Energy Storage Materials: Mitigating the Degradation of Alloy-based Anodes for Lithium and Sodium Ion Batteries

by

Jasper Craig Woodard

A thesis submitted in partial fulfillment of the requirements for the degree of

Doctor of Philosophy

Department of Chemistry
University of Alberta

Abstract

Lithium ion batteries have become a ubiquitous technology for consumer electronics and electric vehicles. Alloying anodes, such as silicon and tin, offer large increases in volumetric energy density compared to conventional graphite anodes. However, the alloying mechanism is accompanied by an expansion of almost 300 %, and repeated expansion and contraction over many cycles leads to particle fracture and pulverization, electrical isolation, and build up of the solid electrolyte interphase (SEI). Electrical isolation of anode material leads to catastrophic capacity loss, while continuous SEI build up causes low Coulombic efficiency during cycling and reduced capacity retention in full cells.

Many strategies have been employed to mitigate the deleterious effects of silicon and tin expansion. Nano-sized silicon structures may reduce the degree of fracturing upon expansion, and mixing of nanoscale silicon with polymer binders and conductive additive can prevent electrical isolation after pulverization. Silicon particle pulverization may also be affected by the formation of the terminal lithium-silicide phase at room temperature, *c*-$Li_{15}Si_4$. The reaction of electrolyte to form SEI can be pre-empted by adding sacrificial additives, such as fluoroethylene carbonate (FEC), which form a stable and passivating SEI on the anode surface. An artificial SEI (a-SEI) might also be employed on silicon anodes prior to cell assembly, with the same goal of passivating the surface and preventing further electrolyte decomposition and SEI build up. Another approach is the use of mixed anodes, which combine graphite with either silicon or tin for lithium ion batteries. Incorporating graphite dilutes the impacts of cell fracturing and of SEI

accumulation, while graphite also prevents the alloying active material from becoming electrically isolated.

This thesis describes four approaches to better understand and mitigate material fracture and continuous SEI build-up. Three of the strategies are performed on silicon anodes in lithium ion batteries, while the final project focuses on porous tin anodes for lithium and sodium ion batteries. In Chapter 2, we examine the effects of forming the *c*-$Li_{15}Si_4$ phase in nano-sized silicon. Contrary to planar thin films of silicon, the *c*-$Li_{15}Si_4$ phase is not associated with greater capacity loss, but it does seem to promote more SEI build-up and reduced Coulombic efficiency, which is especially detrimental to lithium ion full cells. Chapter 3 and Chapter 4 focus on efforts to improve the SEI layer on silicon nanoparticles through the use of a covalently bound a-SEI and electrolyte additives, respectively. We successfully form a-SEI on the surface of silicon anodes. Perfluorinated a-SEI passivates the silicon surface, and improves the Coulombic efficiency over 100 cycles, but still leads to lower overall capacity retention due to poor adhesion with the more flexible polar polymer binders. The relative electrochemical performances of other a-SEI functionalities, such as polyethylene oxides and vinyl ethylene carbonate, depend heavily on the size of silicon and the thickness of the oxide layer to which they are being compared. The SEI can also be manipulated using sacrificial electrolyte additives. We demonstrate that additives containing an alkyne or alkene may plausibly form covalent bonds with the surface of exposed silicon through in-situ electrografting. However, an SEI formed through in-situ electrografting leads to much worse capacity retention than an SEI formed using FEC, potentially due to the self-healing properties of intermolecular

interactions between the SEI and silicon surface in accommodating the colossal expansion of the silicon anode.

Chapter 5 focuses on the use of porous tin anode material for lithium ion (LIB) and sodium ion batteries (NIB). Mixed electrodes of porous tin with graphite and porous tin with hard carbon were used for LIBs and NIBs, respectively, and compared to commercial micron sized tin powder. Pores within tin provide space to accommodate expansion during lithiation or sodiation, while active carbon material dilutes the impacts of tin expansion and fracturing. The addition of up to 10 % p-Sn is associated with larger specific capacity, while still maintaining > 80 % capacity retention over 100 cycles. However, each marginal increase in p-Sn content is associated with lower Coulombic efficiency over all 100 cycles. Porous tin had improved rate capabilities compared to micron sized commercial tin during early cycles, but this distinction dissipated over the course of 100 cycles as micron sized tin fractures and is reduced in size.

Preface

The research described in this thesis was conducted in collaboration with Professor Jillian Buriak. Cell assembly and testing was conducted at NRC-Nano Edmonton. Material characterization was conducted at the University of Alberta NanoFAB. The results are organized into 6 chapters.

Chapter 1 is an introductory chapter which gives a background for alloying anodes in lithium and sodium ion batteries. This is accompanied by a description of the scope of the thesis.

The research in Chapter 2 has been published as: Jasper C. Woodard, W. Peter Kalisvaart, Sayed Youssef Sayed, Brian C. Olsen, Jillian M. Buriak. Beyond Thin Films: Clarifying the Impact of *c*-$Li_{15}Si_4$ Formation in Thin Film, Nanoparticle, and Porous Si Electrodes. *ACS Appl. Mater. Interfaces* **2021**, 13, 32, 38147–38160. Jasper Woodard prepared all samples with silicon nanoparticles and carried out most of the electrochemical testing and characterization with guidance from Dr. Sayed Youssef Sayed. Dr. Peter Kalisvaart prepared the planar and porous films, and performed most electrochemical testing on these materials. Brian Olsen assisted with data processing and prepared the TOC figure for publication. Prof. Jillian Buriak was the supervisor for the project and assisted in preparing the manuscript.

Chapter 3 is being restructured as a manuscript that will be co-authored with Peter Kalisvaart, Sayed Youssef Sayed, and Jillian Buriak. Jasper Woodard performed most synthesis, assembly, testing and characterization. Thin film sputtering and electrochemistry was performed in consultation with Dr. Peter Kalisvaart and Dr. Sayed

Youssef Sayed. X-ray photoelectron spectroscopy was performed by Dr. Shihong Xu at the University of Alberta NanoFAB.

Chapter 4 is unpublished work performed by Jasper Woodard. Dr. Sayed Youssef Sayed assisted directly with electrochemistry on in-situ electrografting.

Chapter 5 is unpublished work conducted in collaboration with the start-up Nanode. Dr. Peter Kalisvaart synthesized the porous tin powder, and both Peter Kalisvaart and Chan Kheong Wong helped with characterization of the porous tin powder. Jasper Woodard performed all slurry and sample preparation, along with all electrochemical tests. The project was supervised by Dr. Bing Cao and Prof. Jillian Buriak.

Acknowledgements

This thesis is the product of tremendous support from a multitude of characters. Above all, I would like to thank Dr. Jillian Buriak for her support and guidance throughout my program. Her experience, expertise, passion, and compassion have made me a better presenter and more rigorous scientist. She has greatly augmented my graduate experience and has my profound appreciation.

I would like to thank my committee members, Prof. Steven Bergens and Prof. Eric Rivard, for their valued direction throughout my program. A special thanks goes to Dr. Lingzi Sang, who agreed to step in as a replacement committee member for my defense, and was also present for my candidacy. Dr. Jonathan Veinot has my similar appreciation for serving as an examiner on both occasions. I would like to thank Dr. Christian Kuss from the University of Manitoba for being my external examiner. I have nothing but gratitude for the time committed for my defense and in reviewing this thesis.

My sincerest gratitude goes out to both past and current members of the Buriak group. First, to Dr. Peter Kalisvaart and Dr. Sayed Youssef Sayed, for invaluable advice and guidance in electrochemistry. Dr. Erik Luber and Brian Olsen, and Tate Hauger deserve particular thanks for lending their considerable scientific knowledge and engineering experience to my every question or problem with instrumentation. A special thanks goes to members of Nanode who supported me during my collaboration, including Dr. Bing Cao, Dr. Jiankuan Li, Chan Kheong “CK” Wong, Josh Douglas, and Yue Wu. Last but not least, all members of the Buriak group, who made my time at the University of Alberta a wonderful experience with their support and inspiration, with specific praise for Dr. Gayashani Ginige, Aaron Kirkey, Dr. Minjia Hu, Dr. Chengcheng Rao, Dr. Mahmoud

Almadhoun, Dr. Hezhen Xie, Dr. Hao Wang, Adrian Velazquez Osorio, Xiang You, and Dr. Youngdong Song.

Many staff members have supported me in tangible and intangible ways, and deserve my explicit gratitude. Special thanks to NRC-Nano members Dr. Michael Fleischauer, Steve Launspach, Dr. Mike Xia, and Paul Conception. I have benefited immensely from the expertise of those within the University of Alberta Analytical Laboratory, NMR services, and NanoFAB: Wayne Moffat, Mark Miskolzie, and Dr. Shihong Xu, to name a few. Special thanks to Dr. Yoram Apelblat, Ryan Lewis, Michael Barteski, Matthew Kingston, and Anita Weiler for tremendous support in a variety of capacities.

Finally, to my friends and family who have enriched my graduate experience and supported me through life, thank you. Of friends, there are too many to name, and I will not insult them in the attempt, but a special note for members of the Chemistry Graduate Students' Society and the memories they hold. Ellen Buckie, my partner in life, has been beside me at every step with love and support. Finally, all my gratitude pours out to my family, parents Brent and Sally, and sister Amelia. You have all brought me here, and it means the world.

Table of Contents

Abstract ..... **ii**

Preface ..... **v**

Acknowledgements ..... **vii**

Table of Contents ..... **ix**

List of Figures ..... **xiv**

List of Tables ..... **xxxvi**

List of Abbreviations ..... **xxxvii**

Chapter 1 Introduction **1**

1.1 Alkali Ion Batteries 1

1.2 Silicon and tin anodes for lithium ion batteries 5

1.2.1 Overview of silicon and tin anodes 5

1.2.2 The solid electrolyte interphase (SEI) 7

1.2.3 Impacts of electrolyte on the SEI 10

1.2.4 Crystalline and amorphous phases of silicon-lithium alloys 13

1.3 Artificial solid electrolyte interphase (a-SEI) 14

1.3.1 Overview of a-SEI 14

1.3.2 Synthesis of an a-SEI 16

1.4 Tin anodes for lithium and sodium ion batteries 17

1.4.1 Lithium-tin alloys 17

1.4.2 Porous tin preparation 20

1.4.3 Tin-graphite and tin-hard carbon electrodes 21

1.5 Thesis overview 25

Chapter 2 Effects of the *c*-$Li_{15}Si_4$ phase on nanoparticle cycling* 27

2.1 Introduction 27

2.2 Results and Discussion 38

2.2.1 Planar and porous Si films 38

2.2.2 Silicon nanoparticles 55

2.3 Conclusions 75

2.4 Experimental section 76

2.4.1 Materials and reagents 76

2.4.2 Preparation of planar and porous Si films 77

2.4.3 Preparation of nanoparticle slurries 79

2.4.4 Electrochemical measurements 80

2.4.5 Characterization 81

Chapter 3 Silicon surface functionalization for artificial solid electrolyte interphase (a-SEI) 82

3.1 Introduction 82

3.2 Thin films, native oxides, and HF vapour etching 91

3.3 Batch variability of commercial, plasma-synthesized silicon nanoparticles 110

3.4 Hydrosilylation of silicon nanoparticles 127

3.5 Surface and binder interaction in a SiNP slurry 146

3.5.1 Establishing surface functionalization 148

3.5.2 Cell replications and reproducibility: 152

3.5.3 Effect of Binder: 155

3.5.4 Effect of surface coverage on capacity: 157

3.6 Mechanochemical synthesis on Si-325 particles 167

3.7 Conclusions 180

3.8 Experimental section 182

3.8.1 Materials and reagents 182

3.8.2 Preparation of silicon thin films 183

3.8.3 Synthesis of 2,5,8,11-tetraoxatetradec-13-ene 183

3.8.4 Hydrogen termination on silicon surfaces 184

3.8.5 Hydrosilylation of silicon surfaces 185

3.8.6 Mechanochemical synthesis 186

3.8.7 Preparation of nanoparticle slurries 187

3.8.8 Electrochemical measurements 187

3.8.9 Characterization 188

Chapter 4 Electrolyte optimization and in-situ functionalization of silicon surfaces 189

4.1 Introduction 189

4.2 Ex-situ electrografting of alkyne additives 194

4.3 Additives for silicon electrodes 205

4.3.1 Silicon thin films 205

4.3.2 Silicon nanoparticles 214

4.4 Additives with Si-325 based electrodes 222

4.5 Conclusions 226
4.6 Experimental section 227
4.6.1 Materials and reagents 227
4.6.2 Ex-situ electrografting 228
4.6.3 Preparation of nanoparticle slurries 229
4.6.4 Electrochemical measurements 229
4.6.5 Characterization 230
Chapter 5 - Porous tin anodes for LIBs and NIBs 231
5.1 Introduction 231
5.2 Porous tin with graphite 237
5.3 Porous tin with hard carbon 251
5.4 Cumulative Coulombic inefficiency 257
5.5 Rate analysis 261
5.6 Resilience to exposures to low temperatures 266
5.7 Conclusions 270
5.8 Experimental section 271
5.8.1 Materials and reagents 271
5.8.2 Synthesis of p-Sn powder 272
5.8.3 Preparation of nanoparticle slurries 272
5.8.4 Electrochemical measurements 273
5.8.5 Characterization 274
Chapter 6 - Thesis summary and outlook 275

6.1 Thesis summary 275

6.2 Future directions 279

6.2.1 High energy ball milling of silicon microparticles 279

6.2.2 Si-graphite anodes with a-SEI 280

6.2.3 a-SEI optimization with design of experiments (DOE) 282

References 285

List of Figures

Figure 1-1. Model of the reliability of the electricity supply in the United States of America using only solar and wind power. The distribution of renewable generation is modelled over different land areas, considering production of 1 x and 1.5 x energy demand. Adding 12 hours of energy storage allows for wind and solar to meet much more of the electricity supply and supports solar heavy mixes of solar/wind generation. Reprinted with permission from reference 6. © 2018 Royal Society of Chemistry. 2

Figure 1-2. Theoretical gravimetric energy and volumetric energy performance for full cells. Lithium, carbon, and silicon anodes are shown in black; nickel manganese cobalt (NMC), nickel cobalt aluminum oxide (NCA), and Li-rich layered oxide cathodes are shown in red. Electrode performance is represented by the centre of each circle, and is displayed alongside the goals set out by US Advanced Battery Consortium (USABC) and European Council for R&D (EUCAR). Reproduced from reference 11. Used under a Creative Commons CC-BY-NC-ND license. 3

Figure 1-3. Lithiation of alloying anode materials, leading to expansion and particle fracture. Reprinted with permission from reference 17. © 2014 American Chemical Society 7

Figure 1-4. *Mosaic model of inorganic and organic microphases on the anode surface. Reproduced from reference 51 under a Creative Commons CC-BY license.* 10

Figure 1-5. Atomic percentage of SEI components in battery electrolyte with and without FEC additive. Reprinted with permission from reference 70. © 2015 American Chemical Society. 12

Figure 1-6. Lithium-silicon phase diagram generated by heat treatment (a) and calculated formation energies (b) for amorphous (green) and crystalline (red) lithium silicide phases.

(Left) adapted with permission from reference 74. © 1990. (Right) reprinted with permission from reference 73. © 2013 American Chemical Society. 13
Figure 1-7. Silicon nanoparticles with an a-SEI of polydopamine (PDA) in a binder of polyacrylic acid (PAA). Hydrogen bonding between Si@PDA and PAA prevents electrical isolation during cycling. Reprinted with permission from reference 87. © 2021 American Chemical Society. 15
Figure 1-8. Covalent bonds formed catalytically at 180 °C between silanol groups on the surface of silicon and carboxymethyl cellulose (CMC) binder Reprinted with permission from reference 97. © 2019 American Chemical Society. 16
Figure 1-9. Hydrocarbon and polyethylene oxide (PEO) a-SEI functionalized on the surface of silicon. Reprinted with permission from reference 90. © 2021 American Chemical Society. 18
Figure 1-10. SnO_2 as an anode material also cannot prevent fracturing or irreversible capacity loss due to SEI buildup. Reprinted with permission from reference 111. © 2015 Institute of Materials, Minerals and Mining and ASM International. 19
Figure 1-11. Li-Sn phase diagram. Reprinted with permission from reference 116. © 1998 Springer Nature. 20
Figure 1-12. Methods of the preparation of Si-graphite or Sn-graphite anodes for lithium ion batteries. Adapted with permission from reference 121. © 2020 John Wiley and Sons. ... 24
Figure 2-1. Voltage curve of the lithiation and delithiation in bulk silicon (top), along with the corresponding phase transitions (bottom). The bottom diagram first outlines phase transitions during the lithiation of crystalline silicon (blue), followed by delithiation from the c-$Li_{15}Si_4$ phase (green) and the subsequent lithiation of amorphous silicon. Phase transitions

in each figure are indicated by Roman numerals. Adapted with permission from references 132 (top), 133 (bottom), and 17 (bottom adaptation). © 2006 Electrochemical Society, © 2007 Electrochemical Society, and © 2014 American Chemical Society, respectively. 28

Figure 2-2. Crystal structure of c-$Li_{15}Si_4$. Reprinted with permission from reference 137. © 2007 American Institute of Physics. 29

Figure 2-3. A representation of the interplay between silicon thin film delamination from Cu foil (orange) and concurrent increase in c-$Li_{15}Si_4$ formation. In thin films, the c-$Li_{15}Si_4$ phase and capacity loss may both be caused by delamination, but positive feedback from c-$Li_{15}Si_4$ formation may also increase the rate of delamination. Adapted from reference 77 under a Creative Commons CC BY-NC-ND license. 31

Figure 2-4. Two-phase lithiation of amorphous silicon nanoparticles attached to a c-Si nanowire during the first lithiation and delithiation cycle. Single phase delithiation was observed because the lithiation was mostly arrested at the highly lithiated amorphous Li_xSi phase. Scale bar 200 nm. Reprinted with permission from reference 142. © 2013 American Chemical Society..... 32

Figure 2-5. Suppression of the c-$Li_{15}Si_4$ phase leading to improved cycling of co-sputtered Si-C films. Reprinted with permission from reference 149. © 2019 American Chemical Society. 35

Figure 2-6. a) Voltage vs capacity plots for planar cells using CC or CCCV protocol after 1 or 50 cycles, as indicated. All cells were lithiated to 5 mV and delithiated to 2V using ~200 mA/g during cycle 1 and ~500 mA/g for subsequent cycles. b) dQ/dV graphs of the same cells, obtained by taking the inverse derivative of a). Peaks in dQ/dV correspond to plateaus

in voltage vs capacity plots. Reprinted with permission from reference 163. © 2021 American Chemical Society. 40

Figure 2-7. *XRD of fully lithiated silicon nanoparticle powder electrodes, identifying the* c-$Li_{15}Si_4$ *phase. Electrodes were lithiated to 5 mV and held at a constant voltage until ~20 mA/g. A polypropylene cover is present to prevent exposing* c-$Li_{15}Si_4$ *to air. Reprinted with permission from reference* 163. *© 2021 American Chemical Society.* 41

Figure 2-8. *a): Comparison of the delithiation capacity retention between CC and CCCV protocols for the planar Si film, b) and c): dQ/dV curves for selected cycles using the CCCV protocol at 5 mV lithiation cut-off voltage and a 10 h CV step. Cells were delithiated to 2 V vs Li using CC cycling only. Cycle 1 was performed at ~200 mA/g, and all subsequent cycles at ~500 mA/g. d): delithiation capacity below 0.35 V vs Li as a fraction of total delithiation capacity vs cycle number for cells with no CV step, and a voltage hold of 2 and 10 hours, as indicated. Reprinted with permission from reference* 163. *© 2021 American Chemical Society.* 42

Figure 2-9. dQ/dV curves for selected cycles of the planar Si film using CC protocol with 5 mV lower lithiation cut-off voltage. Reprinted with permission from reference 163. © 2021 American Chemical Society. 45

Figure 2-10. SEM micrographs of annealed $Si_{0.75}Al_{0.25}$ (x = 0.75), and $Si_{0.30}Al_{0.70}$ (x = 0.30) films after dealloying in 1 M (aq) KOH. Scale bars are 200 nm. Reprinted with permission from reference 163. © 2021 American Chemical Society. 46

Figure 2-11. SEM micrographs of the porous thin Si film morphologies as the percentage of Si is decreased from 75 to 20 at.%. Scale bars are 200 nm. All films were annealed prior to

dealloying. Reprinted with permission from reference 163. © 2021 American Chemical Society. 46

Figure 2-12. SEM micrograph of an as-deposited $Si_{0.30}Al_{0.70}$ film after dealloying in 1 M (aq) KOH. Scale bar is 200 nm. Reprinted with permission from reference 163. © 2021 American Chemical Society..... 48

Figure 2-13. Voltage profiles for the first (CC) and second (CCCV) cycle for the planar Si film, a), and the porous x = 0.30 film, b). The plateau at ~0.15 V characteristic of c-Si is only observed for the porous film in the first cycle as an effect of the annealing step. Reprinted with permission from reference 163. © 2021 American Chemical Society. 48

Figure 2-14. a): Relative delithiation capacity retention of x = 0.75 and x = 0.30 porous films comparing the CC and CCCV protocols at 5 mV lithiation cut-off voltage. Cycle 1 was performed at ~200 mA/g, and all subsequent cycles at ~500 mA/g. b): dQ/dV curves for selected cycles for the x = 0.75 porous film. c): dQ/dV curves for selected cycles for the x = 0.30 porous film. d): relative delithiation capacity below 0.35 V vs Li for x = 0.75 and x = 0.30 for CC and CCCV protocol. Reprinted with permission from reference 163. © 2021 American Chemical Society. 50

Figure 2-15. Relative delithiation capacity vs cycle number for planar and porous Si films in CC mode. Capacity retention in CC as well as CCCV mode is shown in Figure 2-8a for the planar film and Figure 2-14a for the x = 0.30 and x = 0.75 porous films. Reprinted with permission from reference 163. © 2021 American Chemical Society. 51

Figure 2-16. dQ/dV curves of dealloyed $Si_{0.75}Al_{0.25}$ and $Si_{0.30}Al_{0.70}$ films for selected cycles in CC mode. The corresponding dQ/dV curves for CCCV mode for the same films are shown

in Figure 2-14. Reprinted with permission from reference 163. © 2021 American Chemical Society. 52
Figure 2-17. Capacity retention and Coulombic efficiency vs cycle number for porous x = 0.30 films in CC and CCCV mode in carbonate-based electrolyte (a) and CCCV mode in DME-based electrolyte (b). dQ/dV curves in carbonate-based electrolyte (c) and 1 M LiOTf in DME (d). Note that the lithiation dQ/dV peaks shift to lower voltages only in the DME-based electrolyte. Reprinted with permission from reference 163. © 2021 American Chemical Society..... 54
Figure 2-18. SEM micrographs after 6 cycles of porous x = 0.30 films in CCCV mode in carbonate-based electrolyte (left) and DME-based electrolyte (right). Reprinted with permission from reference 163. © 2021 American Chemical Society. 55
Figure 2-19. Delithiation dQ/dV curves (a,b), and charge/discharge curves (c,d) of silicon nanoparticle electrodes lithiated to a cut-off of 5 mV using CCCV (a,c) or CC (b,d) protocol. Plateaus in the delithiation curves correspond to peaks in the dQ/dV curves. All cells were delithiated to 1.5 V vs Li using CC cycling only. Cycles 1-3 were performed at 200 mA/g, and all subsequent cycles at 600 mA/g. Cycle number is indicated in the accompanying legends. Relative (e) and absolute (f) delithiation capacity of the same two cells, with CC or CCCV cycling indicated in the legend. Reprinted with permission from reference 163. © 2021 American Chemical Society..... 57
Figure 2-20. Delithiation dQ/dV curves (a,b), and charge/discharge curves (c,d) of silicon nanoparticle electrodes lithiated to a cut-off of 50 mV using CCCV (a,c) or CC (b,d) protocol. Plateaus in the delithiation curves correspond to peaks in the dQ/dV curves. All cells were delithiated to 1.5 V vs Li using CC cycling only. Cycles 1-3 were performed at 200 mA/g,

and all subsequent cycles at 600 mA/g. Cycle number is indicated in the accompanying legends. Relative (e) and absolute (f) delithiation capacity of the same two cells, with CC or CCCV cycling indicated in the legend. Reprinted with permission from reference 163. © 2021 American Chemical Society..... 59

Figure 2-21. Percentage of delithiation capacity occurring below 0.35 V for silicon nanoparticle electrodes cycled to a lower cut-off of (a) 5 mV and (b) 50 mV vs Li for lithiation. CC and CCCV cycling are indicated in the accompanying legends. Cycles 1--3 were performed at 200 mA/g, and all subsequent cycles at 600 mA/g. All cells were delithiated to 1.5 V using CC protocol. Reprinted with permission from reference 163. © 2021 American Chemical Society..... 60

Figure 2-22. Close up of delithiation dQ/dV for silicon nanoparticle electrodes lithiated to 5 mV (a,b) and 50 mV (c,d) vs Li using CCCV (a,c) and CC (b,d) protocol. Cycle number is indicated in the accompanying legends. Cycles 1--3 were performed at 200 mA/g, and all subsequent cycles at 600 mA/g. All cells were delithiated to 1.5 V using CC protocol. Reprinted with permission from reference 163. © 2021 American Chemical Society..... 62

Figure 2-23. Coulombic efficiency of silicon nanoparticle electrodes cycled with a cut-off of (a) 5 mV and (b) 50 mV vs Li. CC or CCCV lithiation protocol is indicated in the legends. Cycles 1--3 were performed at 200 mA/g, and all subsequent cycles at 600 mA/g. All cells were delithiated to 1.5 V using CC protocol. Reprinted with permission from reference 163. © 2021 American Chemical Society..... 63

Figure 2-24. *Overpotential (ΔV) of (a,b) silicon nanoparticle electrodes and (c,d)* x = *0.30 porous films vs delithiation voltage using GITT at cycle 2 and 12, as indicated. Cells were lithiated to 5 mV using CCCV (a,c) and CC (b,d). All cells used ~200 mA/g for cycle 1. Silicon*

nanoparticle powder electrodes used 600 mA/g for cycles 2-12 and delithiated to 1.5 V. x = *0.30 electrodes used 500 mA/g for cycles 2-12 and delithiated to 2 V. All GITT tests were performed using the higher current, with a 30 minute applied current and 2 hour rest period. Reprinted with permission from reference* 163*. © 2021 American Chemical Society.*..... 64
Figure 2-25. SEM micrographs of silicon nanoparticle electrodes a) prior to cycling and after 10 cycles using b) 5 mV CCCV, c) 5 mV CC, d) 50 mV CCCV, and e) 50 mV CC lithiation protocols. Scale bars are 400 nm. Larger particles are silicon, while smaller particles are Super-P carbon black. Cycles 1-3 used 200 mA/g, while cycles 4-10 used 600 mA/g. All cells were delithiated to 1.5 mV vs Li. Reprinted with permission from reference 163. © 2021 American Chemical Society. 67
Figure 2-26. X-ray photoelectron spectroscopy (XPS) spectra of silicon nanoparticle powder electrodes cycled 10 times using 5 mV or 50 mV cutoffs and CCCV or CC charging protocol, as indicated. The cutoff of 5 mV changes relative peak heights most notably in the F 1s and P 2p spectra, indicating different ratios of SEI products from $LiPF_6$ decomposition. Reprinted with permission from reference 163. © 2021 American Chemical Society. 68
Figure 2-27. dQ/dV curves for selected cycles of x = 0.30 film using CCCV protocol with 50 mV lower lithiation cut-off voltage. Contrary to the 5 mV cut-off shown in Figure 2-14, there is no evidence for c-$Li_{15}Si_4$ in this case. Reprinted with permission from reference 163. © 2021 American Chemical Society..... 69
Figure 2-28. Delithiation dQ/dV for silicon nanoparticle electrodes cycled with a voltage cutoff of 60 mV (a), 70 mV (b), 80 mV (c), and 90 mV (d). Cycle number is indicated in the accompanying legends. All cycles used CCCV cycling, with a charging rate of 200 mA/g for cycles 1--3 and 600 mA/g for all subsequent cycles. All cells were delithiated to 1.5 V using

CC protocol. Reprinted with permission from reference 163. © 2021 American Chemical Society. 71

Figure 2-29. Percentage of delithiation capacity occurring below 0.35V for silicon nanoparticle electrodes cycled under CCCV conditions to varying lithiation cutoffs: 60 mV (green), 70 mV (yellow), 80 mV (blue), 90 mV (red). Cycles 1-3 were performed at 200 mA/g, and all subsequent cycles at 600 mA/g. All cells were delithiated to 1.5 V using CC protocol. Reprinted with permission from reference 163. © 2021 American Chemical Society..... 72

Figure 2-30. *Absolute (a) and relative (b) delithiation capacity of silicon nanoparticle electrodes cycled to cut-off voltages from 5--90 mV, as indicated in the accompanying legends. All cycles used CCCV cycling during lithiation, with a charging rate of 200 mA/g for cycles 1--3 and 600 mA/g for all subsequent cycles. All cells were delithiated to 1.5 V using CC protocol. Reprinted with permission from reference* 163*. © 2021 American Chemical Society.* 72

Figure 2-31. Cumulative irreversibilities due to electrolyte decomposition for silicon nanoparticle electrodes cycled with a lithiation voltage cutoff of 50--80 mV using CCCV protocol, as indicated in the legend. Cycles 1--3 were performed at a charging rate of 200 mA/g with subsequent cycles at 600 mA/g. All cells were delithiated to 1.5 V using CC protocol. Reprinted with permission from reference 163. © 2021 American Chemical Society. 74

Figure 2-32. Coulombic efficiency of silicon nanoparticle electrodes cycled with a constant voltage step and a lithiation cut-off of 5--90 mV vs Li, as indicated in the legend. Cycles 1--3 were performed at 200 mA/g, and all subsequent cycles at 600 mA/g. All cells were

delithiated to 1.5 V using CC protocol. *Reprinted with permission from reference* 163. © *2021 American Chemical Society.*.....75

Figure 2-33. XRD patterns of an $Si_{0.55}Al_{0.45}$ film in the as-deposited state, and after annealing, for 2 hours at 300 deg °C under Ar. The total thickness is 168 nm according to the formula above. Si was chosen as the substrate because of the strong X-ray fluorescence background generated by a stainless steel substrate. Reprinted with permission from reference 163. © 2021 American Chemical Society. 78

Figure 3-1. *Lithium diffusion through a silicon oxide layer of various thicknesses. Reprinted with permission from reference* 94*. © 2021 American Chemical Society.* 83

Figure 3-2. *Bond energies of common carbon and silicon bonds. Reprinted with permission from reference* 101*. © 2002 American Chemical Society.*.....84

Figure 3-3. Stylized mechanism of the formation of $Si\text{-}H_x$ surfaces by HF etching on Si-OH (a, c, d ,and e) and SiO_2 (b) surfaces. Full atomic valencies are omitted for clarity. Reprinted with permission from reference 185. © 2018 Elsevier. Panel B adapted with permission from reference 179. © 2000 American Chemical Society. 86

Figure 3-4. Porous silicon etching in a two-electrode electrochemical cell using a silicon wafer anode and platinum wire cathode. Reprinted with permission from reference 187. © 2012 John Wiley and Sons.....87

Figure 3-5. a-SEI functionalized through click chemistry reactions. Reprinted with permission from reference 91. © 2017 American Chemical Society. 89

Figure 3-6. *Radical hydrosilylation mechanism on the surface of hydrogen terminated silicon. Radical initiation can occur above ~150 °C* via a thermally-mediated reaction

pathway, which can also be initiated using UV light and peroxide initiators. *Adapted with permission from reference* 88*. © 2014 American Chemical Society.* 90
Figure 3-7. XRD of co-sputtered silicon carbon films on copper foil, as reported previously by our group. The 100 nm Si spectrum (black) is identical to the thin films reported here, and shows no signs of crystalline Si peaks. Reprinted with permission from reference 149. © 2019 American Chemical Society. 92
Figure 3-8. 100 nm sputtered silicon on stainless steel before (a, b) and after (c, d) immersion in HF (aq) for 30 seconds, and (e) after an HF Vapour etch with 12 Torr of HF vapour for 5 minutes 94
Figure 3-9. Survey scans (a, c, e) and Si 2p high resolution (b, d, f) XPS of Si sputtered onto stainless steel (a,b), Silicon etched by immersion in 1 % HF (aq) for 30 seconds (c,d), and HF vapour etched (e,f). 95
Figure 3-10. First cycle voltage curves (a,c,e) and dQ/dV (b,d,f) for thin films of silicon with a native oxide oxide (a,b), after HF (aq) immersion (c,d), and after HF vapour etching (e,f). 98
Figure 3-11. Capacity retention over 200 cycles of thin film silicon etched subjected to an HF vapour etch. Cells were cycled in 1 M $LiPF_6$ in 1:1 EC:DEC between 2 – 0.05 mV at a rate of 400 mA/g for cycles 1-3 and 1200 mA/g for subsequent cycles. 99
Figure 3-12. Optical image showing discolouration of silicon films after an HF vapour etch, circled in red for visibility. 100
Figure 3-13. SEM of as-sputtered silicon (top) and after HF vapour etch (bottom). Scale bar 1 μm. 101

Figure 3-14. Increasing the thickness of the SiO_2 layer up to 3 nm, done here by treatment at 400 °C, might further increase capacity retention in some silicon particles. Adapted with permission from reference 194. © 2017 American Chemical Society. 102
Figure 3-15. Transmission FTIR of freshly etched p-Si (blue), and after thermal hydrosilylation with 1-hexadecene (orange). 105
Figure 3-16. *Surface coatings on silicon thin films. Artificial SEI are shown after functionalization with 1-dodecyne (green) and vinyl ethylene carbonate (dark red). For comparison, polyvinylene carbonate (blue) forms in-situ from the decomposition of FEC additive.* 106
Figure 3-17. Specific capacity (a) and Coulombic efficiency (b) over 200 cycles for 100 nm thin films of silicon with a variety of surface functionalities. All cells were cycled in 1 M $LiPF_6$ in 1:1 EC:DEC between 2 – 0.01 mV at a rate of 400 mA/g for cycles 1-3 and 1200 mA/g for subsequent cycles..... 109
Figure 3-18. A schematic representation of the plasma-based process for the synthesis of silicon nanoparticles. Reprinted with permission from reference 202. © 2021 American Chemical Society..... 112
Figure 3-19. **Si-SA1**, **Si-SA2**, and **Si-SA3** silicon particles from Sigma-Aldrich showing different colours and tap densities. 113
Figure 3-20. Silicon nanoparticles **Si-SA1** (left) and **Si-AA1** (right), with both samples in powder form (top) and dispersed in pentane (bottom). 115
Figure 3-21. Specific capacities of **Si-SA1**, **Si-SA2**, and **Si-SA3** over 50 cycles. All cells were cycled with FEC between 1.5 – 0.005 mV at a rate of 200 mA/g for cycles 1-3 and 600 mA/g for subsequent cycles. 116

Figure 3-22. Specific capacities of **Si-SA3**, **Si-AA1**, and **Si-325** over 50 cycles. All cells were cycled with FEC between 1.5 – 0.005 mV at a rate of 200 mA/g for cycles 1-3 and 600 mA/g for subsequent cycles. 116

Figure 3-23. SEM micrograph of a sample of **Si-SA1**, and size analysis represented with an average shifted histogram. 118

Figure 3-24. SEM micrograph of a sample of **Si-SA2**, and size analysis represented with an average shifted histogram. 119

Figure 3-25. SEM micrograph of a sample of **Si-SA3**, and size analysis represented with an average shifted histogram. 120

Figure 3-26. DRIFTS spectra of **Si-SA1**, **Si-SA2**, and **Si-SA3**. 122

Figure 3-27. *XPS of the Si 2p region for **Si-SA1**, **Si-SA2**, and **Si-SA3**.* 124

Figure 3-28. *Powder XRD of **Si-SA1** and **Si-SA3**.* 125

Figure 3-29. **Si-AA1** SEM image showing micron sized particles. Sold as having an average particle size of 100 nm. 126

Figure 3-30. DRIFTS spectrum of **Si-AA1** 126

Figure 3-31. *DRIFTS of as-received **Si-SA2** (blue) and HF (aq) etched SiNPs (orange).* 129

Figure 3-32. Molecules considered for hydrosilylation with hydrogen-terminated silicon. 131

Figure 3-33. DRIFTS of Si-TEG and Si-Dode on **Si-SA2.** 131

Figure 3-34. **Si-SA2** particles after hydrosilylation with VEC (blue), 1:1 - VEC:TEG (grey), and 1:1 - VEC:Dode (orange). 133

Figure 3-35. *Transmission FTIR of neat VEC liquid (blue) and neat TEG liquid (red).* 133

Figure 3-36. *VEC solution sliding down the walls of a polypropylene centrifuge tube. The liquid will not form individual droplets when mixed in polypropylene or glass surfaces, indicative of high surface tension. The VEC is coloured with a suspension of silicon particles, which allows for the observation of strong intermolecular interactions within the neat VEC. The specific experiment pictured is not germane to Section 3.4.* 136

Figure 3-37. Diffuse reflectance infrared Fourier transform spectroscopy (DRIFTS) of various hydrosilylated surfaces of **Si-SA2**. 137

Figure 3-38. FTIR of neat DMAA on a KBr plate. 137

Figure 3-39. XPS spectrum of Si-DMAA. 138

Figure 3-40. Specific capacity and Coulombic efficiency of **Si-SA2** particles over 50 cycles. A native oxide surface (Si-O_x) is compared to HF etched particles (Si-H_x) and functionalized Si-TEG particles. All cells were cycled between 1.5 – 0.005 mV at a rate of 200 mA/g for cycles 1-3 and 600 mA/g for subsequent cycles. 140

Figure 3-41. Specific capacity over 50 cycles of various functionalized **Si-SA2** nanoparticles. All cells were cycled with FEC between 1.5 – 0.005 mV at a rate of 200 mA/g for cycles 1-3 and 600 mA/g for subsequent cycles. 141

Figure 3-42. A slurry of Si-dodecyl functionalized nanoparticles in water. Light brown particles can be seen suspended above the darker brown slurry underneath. 142

Figure 3-43. Cumulative Coulombic inefficiency of as received and functionalized **Si-SA2** nanoparticles. All cells were cycled with FEC between 1.5 – 0.005 mV at a rate of 200 mA/g for cycles 1-3 and 600 mA/g for subsequent cycles. 144

Figure 3-44. *Functional groups prepared through thermal hydrosilylation. Bolded titles are used throughout the text.* 148

Figure 3-45. Diffuse reflectance infrared Fourier transform spectroscopy (DRIFTS) of Si-O_x (black) and Si-H_x (red) terminated silicon nanoparticles. 149
Figure 3-46. DRIFTS of silicon nanoparticles functionalized with TEG (black), 1-dodecene (red), 1:1 TEG:dodecene (blue), and 1H,1H,2H-perfluoro-1-decene (PD, green). 151
Figure 3-47. XPS F 1s spectrum of Si-O_x (blue), and Si-PD (green) particles dispersed on a carbon sticky.. 152
Figure 3-48. Specific capacities of **Si-SA3** slurries prepared in various combinations of binder and solvent. Cells were cycled from 1.5 – 0.005 V, and Cycles 1-3 were performed at 200 mA/g, while the remaining cycles were performed at 600 mA/g. 154
Figure 3-49. *Specific capacities (top) and Coulombic efficiencies (bottom)over 100 cycles for the as received Si-O_x silicon with PVDF in NMP (black), PAA in NMP (red) and PAA in H_2O (blue). All cells were cycled with FEC between 1.5 – 0.005 mV at a rate of 200 mA/g for cycles 1-3 and 600 mA/g for subsequent cycles.* 156
Figure 3-50. *Relative capacity retention of **Si-SA3** particles with various surface functionalities in PVDF/NMP (a), PAA/NMP (b), and PAA/H_2O (c). All cells were cycled with FEC between 1.5 – 0.005 mV at a rate of 200 mA/g for cycles 1-3 and 600 mA/g for subsequent cycles.* 158
Figure 3-51. *Coulombic efficiencies of silicon nanoparticle slurries with various coatings in PVDF/NMP (a), PAA/NMP (b), and PAA/H_2O (c). All cells were cycled with FEC between 1.5 – 0.005 mV at a rate of 200 mA/g for cycles 1-3 and 600 mA/g for subsequent cycles.* 160

Figure 3-52. *Absolute capacity of silicon nanoparticle slurries with various coatings in PVDF (a), PAA/NMP (b), and PAA/H_2O (c). All cells were cycled with FEC between 1.5 – 0.005 mV at a rate of 200 mA/g for cycles 1-3 and 600 mA/g for subsequent cycles.* 162

Figure 3-53. *Electrochemical impedance spectroscopy (EIS) after 3 formation cycles of **Si-SA3** slurry electrodes with different surface functionalizations in PAA/NMP.* 164

Figure 3-54. *Scanning electron microscopy (SEM) micrographs of **Si-SA3** particles in PAA/NMP slurries prior to cycling. Si-O_x (a),* Si-H_x *(b), Si-TEG (c), Si-Dode (d), Si-1:1 (e), Si-PD (f).* 165

Figure 3-55. Scanning electron microscopy (SEM) micrographs of **Si-SA3** particles in PAA/NMP slurries after 10 cycles. Si-O_x (a), Si-H_x (b), Si-TEG (c), Si-Dode (d), Si-1:1 (e), Si-PD (f). 166

Figure 3-56. Schematic of the role and function of alkenes added to the mix of high energy ball milling of silicon wafers. Reprinted with permission from reference 225. © 2015 Springer Nature. 169

Figure 3-57. Poly(vinyl alcohol) coated silicon nanoparticles after high energy ball milling. Reprinted with permission from reference 226. © 2020 American Chemical Society..... 170

Figure 3-58. XRD of as received **Si-325** particles (blue), particles ball milled with octane (red) and particles ball milled with 1-octyne (green). 173

Figure 3-59. *SEM images of as-received **Si-325** (a), **Si-325** ball milled in VEC (b), and **Si-325** ball milled in 1-octyne, prepared in a slurry with carbon Super P and LiPAA (c).* 175

Figure 3-60. Transmission FTIR of **Si-325** particles as received (blue), after milling with octane (orange), 1-octyne (grey) and VEC (green). 176

Figure 3-61. Specific capacity of **Si-325** silicon microparticles as received (Si-O_x) and ball milled in different solvents. Cells were cycled between 1.5 – 0.005 V at 200 mA/g for cycles 1-3, and at 600 mA/g afterwards. 178
Figure 3-62. Cumulative Coulombic inefficiency of **Si-325** silicon microparticles as received (Si-O_x) and ball milled in different solvents. Cells were cycled between 1.5 – 0.005 V at 200 mA/g for cycles 1-3, and at 600 mA/g afterwards. 179
Figure 3-63. ^{1}H-NMR of 2,5,8,11-tetraoxatetradec-13-ene (400 MHz, $CDCl_3$, 25 °C). 184
Figure 4-1. Cross-linked polyethylene oxide polymers in the SEI form in the presence of FEC. Reprinted with permission from reference 69. © 2018 American Chemical Society. 190
Figure 4-2. *Additives considered for study with silicon anodes. Novel additives were considered if there was potential for in-situ electrografting while also either mimicking stable SEI surfaces from the literature or with functional groups that could lead to known polymerization pathways for SEI formation. Blue additives are established in the literature for their high capacity retention and were used for comparison.*[69,240] 191
Figure 4-3. SEI formation by trifluoropropylene carbonate on silicon nanoparticles. Adapted with permission from reference 235. © 2019 John Wiley and Sons. 194
Figure 4-4. a) Electrografting of alkynes on the surface of porous silicon under cathodic (CEG) or anodic (AEG) conditions. b) Cathodic electrografting of various alkynes. Adapted with permission from reference 239. © 1998 Royal Society of Chemistry. 196
Figure 4-5. Open cell set up for electrografting of olefins onto porous silicon. The copper working electrode is shown on the bottom, while the platinum wire counter electrode is

passed through the top and subsequently wrapped in parafilm to prevent electrolyte evaporation. 198
Figure 4-6. Transmission FTIR of p-Si prior to electrografting (a) and after being subjected to a cathodic current (b) and an anodic current (c). 199
Figure 4-7. *EIS of an open cell with a p-Si working electrode and a Pt wire counter electrode using 0.1 - 1 M TBAHP in DCM and 0.1 -0.25 M TBAHP in ACN.* 201
Figure 4-8. *FTIR of CEG with 0.25 M TBAHP in acetonitrile.* 202
Figure 4-9. *FTIR of p-Si subjected to -9 mA/cm^2 current for 120 s in the presence of 3.5 % v/v 1-dodecyne in 1 M $LiPF_6$ in 1:1 EC:DEC standard battery electrolyte. Pt wire was used as the counter electrode.* 203
Figure 4-10. FTIR of p-Si subjected to -9 mA/cm^2 and -900 µA/cm^2 current for a total of 120 s in the presence of 3.5 % v/v 1-dodecyne in 1 M $LiPF_6$ in DCM. Lithium foil was used as the counter electrode. WARNING - lithium metal can react vigorously with dichloromethane and thus these experiments should not be replicated. 204
Figure 4-11. Specific capacities and Coulombic efficiencies of silicon thin film anodes cycled for 200 cycles with 10 wt% of various alkene-containing additives. 207
Figure 4-12. Relative and specific capacities over 200 cycles for silicon thin film anodes sputtered on stainless steel spacer with an HF (aq) etching step and 10 wt% additive or with a-SEI functionalization of the same additive on the surface. 210
Figure 4-13. Relative capacities for silicon thin film anodes sputtered on stainless steel spacer with an HF vapour etching step. Cycled for 200 cycles with a hydrophobic or hydrophilic additive. 212

Figure 4-14. Decomposition of FEC to form PEO and poly(VC) in the silicon SEI. Adapted with permission from reference 57. © 2017 American Chemical Society. 213
Figure 4-15. Relative capacities over 50 cycles of **Si-AA1** particles etched in 5 % HF (aq) with and without the presence of 10 wt% various additives. 216
Figure 4-16. Specific capacities of silicon nanoparticles **Si-SA1** vs **Si-AA1** 217
Figure 4-17. Novel alkene/alkyne additives for carbonate lithium ion battery electrolyte: allyloxytrimethyl silane (ATMS) and 3-dimethylaminopropyne (DMAP) 218
Figure 4-18. Specific capacities of **Si-SA1** particles over 50 cycles with 10 wt% novel alkene or alkyne containing additives. 219
Figure 4-19. Specific capacity of **Si-SA2** nanoparticles with an a-SEI of Pr-TEG-OMe. Cycles 1-3 were carried out a 200 mA/g, and subsequent cycles at 600 mA/g. 221
Figure 4-20. Specific capacity of **Si-325** particles with various additives over 50 cycles. 223
Figure 4-21. ***Si-325*** *particles in mix-THF (purple) and in EC:DEC (red) with* $LiPF_6$. 224
Figure 5-1. Gravimetric and volumetric capacities of common lithium ion battery anodes. Reprinted with permission from reference.17 © 2014 American Chemical Society. 232
Figure 5-2. Full cell and full stack energy density of common lithium ion battery anodes assuming a $LiCoO_2$ cathode. Reprinted with permission from reference 17. © 2014 American Chemical Society. 233
Figure 5-3. Gravimetric capacity of lithium stannide phases relative to carbon. Reprinted with permission from reference 271. © 2021 American Chemical Society. 234
Figure 5-4. Voltage curve of tin lithiation. Plateaus represent transitions to new lithium stannide phases. Reprinted with permission from reference 115. © 1998 The American Physical Society. 235

Figure 5-5. Schematic representation of the melt spinning method for metal and alloy ribbon production. Reproduced from reference 276 under a Creative Commons CC-BY license. 236

Figure 5-6. Photo of commercial < 150 μm Sn powder (left) and synthesized p-Sn powder (right). 238

Figure 5-7. SEM of synthesized p-Sn from meltspun SnAl ribbons (left) and commercial <150 μm tin powder (right). 238

Figure 5-8. *Relative delithiation capacity (top) and specific delithiation capacity (bottom) of graphite and tin at ratios of 100:0, 95:5, 90:10, 80:20, and 70:30. All cells were cycled 100 times at a rate of C/2 based on the combined theoretical capacity of graphite and tin present.* 242

Figure 5-9. Specific delithiation capacity of graphite and tin at ratios of 100:0, 95:5, 90:10, 80:20, and 70:30. All cells were cycled 100 times at a rate of C/2 based on the combined theoretical capacity of graphite and tin present. 243

Figure 5-10. Specific capacity (top) and Coulombic efficiency (bottom) for porous tin and commercial (<150 um) tin, both in graphite:tin ratios of 90:10. Commercial tin cycles are included with (C-90:10 FC) and without (C-90:10) formation cycles. 245

Figure 5-11. *Electrochemical impedance spectroscopy (EIS) of graphite:tin anode mixtures from 100:0, 95:5, 90:10, 80:20, and 70:30 in a lithium ion battery half cell. Commercial < 150 μm Sn particles are shown as C-90:10. Cells underwent two formation cycles before EIS was conducted in a fully lithiated state.* 247

Figure 5-12. X-ray microscopy (XRM) of unlithiated 80:20 graphite:tin (top) and fully lithiated 80:20 graphite:tin (bottom). 250

Figure 5-13. Forms of expansion in mixed graphite:tin electrodes. Reproduced from reference 119 under a Creative Commons CC-BY license. 251
Figure 5-14. *Relative delithiation capacity (top) and specific delithiation capacity (bottom) of hard carbon and tin at ratios of 100:0, 95:5, 90:10, 80:20, and 70:30 in sodium ion batteries. All cells were cycled 100 times at a rate of C/2 based on the combined theoretical capacity of graphite and tin present.* 253
Figure 5-15. Coulombic efficiency in hard carbon:tin mixed electrodes for NIBs at various ratios of active material. 254
Figure 5-16. Specific capacity (top) and Coulombic efficiency (bottom) for NIB with porous tin and commercial (<150 um) tin, both in a ratio of 10:90 with hard carbon. 256
Figure 5-17. Cumulative Coulombic inefficiencies over 100 cycles for tin:graphite anodes in lithium ion batteries. 258
Figure 5-18. A comparison of Cumulative Coulombic inefficiencies in commercial < 150 μm tin for lithium ion batteries. C – 90:10 FC cells describe commercial tin powder cycled with three formation cycles, at 1 x C/20 and 2 x C/10. 259
Figure 5-19. *Cumulative Coulombic inefficiencies of all hard-carbon:Sn anodes in sodium ion batteries.* 260
Figure 5-20. Cumulative Coulombic inefficiencies in NIBs. A comparison of porous tin to commercial tin < 150 μm particles. 261
Figure 5-21. Rate test of LIBs (top) and NIBs (bottom) with carbon:tin ratios of 100:0, 95:5, 90:10, and 80:20. Graphite is used for LIBs and hard carbon is used for NIBs. Rate tests were cycled at C/20 (cycle 1), C/10 (cycles 2-3), C/2 (cycles 4-10), 1C (cycles 11-20), 2C (cycles 21-30), and C/2 (cycles 31-40). 263

Figure 5-22. Rate test of LIB (top) and NIB (bottom) with porous tin and commercial <150 μm tin. Graphite is used for LIBs and hard carbon is used for NIBs. Rate tests were cycled at C/20 (cycle 1), C/10 (cycles 2-3), C/2 (cycles 4-10), 1C (cycles 11-20), 2C (cycles 21-30), and C/2 (cycles 31-40). 264

Figure 5-23. *Specific capacities (top) and Coulombic efficiencies (bottom) over 100 cycles in room temperature and cooled graphite:tin cells with a 90:10 ratio. Cooled cells were placed at – 15 °C for one week and then warmed back to room temperature prior to cycling.* 267

Figure 5-24. *Specific capacities (top) and Coulombic efficiencies (bottom) over 100 cycles in room temperature and cooled hard carbon:tin cells with a 90:10 ratio. Cooled cells were placed at – 15 °C for one week and then warmed back to room temperature prior to cycling.* 269

Figure 6-1. Vibratory and planetary methods of high energy ball milling. Reprinted with permission from reference 298. © 2010 Woodhead Publishing Limited and CRC Press LLC. 280

Figure 6-2. Synthesis of silicon/graphite mixed electrodes using high energy ball milling. Reprinted with permission from reference 300. © 2021 American Chemical Society..... 282

Figure 6-3. Variable choice guided by the principles of design of experiments (DoE). Using such principles is an efficient way to sample a large proportion of parameter space, particularly when variables are correlated and interdependent. Reprinted with permission from reference 310. © 2018 American Chemical Society..... 284

List of Tables

Table 3-1. Static water contact angle measurements on sputtered silicon thin films. 96

Table 3-2. Static water contact angle measurements of silicon surfaces on Si(100) wafers. 103

Table 3-3. Common FTIR frequencies on porous silicon surfaces and selected functional groups of alkynes/alkenes for hydrosilylation. [x]Select peak assignments of common organic compounds as per reference [211]. [y]Silicon surface assignments as per Reference [212]. 128

Table 5-1 R_S, R_{SEI}, and R_{CT} for LIB cells with graphite and tin in ratios varying from 100:0 to 70:30. The data for commercial < 150 μm tin, C-90:10 is also included. 248

List of Abbreviations

Abbreviation	Definition
°	degree
A	amp
AA	acrylamide
ACN	acetonitrile
AEG	anodic electrografting
AFM	atomic force microscopy
aq	aqueous
a-SEI	artificial solid electrolyte interphase
ASH	average shifted histogram
ATMS	allyloytrimethyl silane
b.p.	boiling point
BET	Brunauer-Emmett-Teller
CC	constant current
CCCV	constant-current-constant-voltage
CCI	cumulative Coulombic inefficiency
CE	Coulombic efficiency
CEG	cathodic electrografting
CMC	carboxymethyl cellulose
CV	constant voltage
d	doublet

DCM	dichloromethane
DEC	diethyl carbonate
DMAA	N,N-dimethyl acrylamide
DMAP	3-dimethylamino-1-propyne
DMC	dimethyl carbonate
DME	diethylene glycol dimethyl ether
DME	dimethoxyethane
dode	dodecene
DoE	design of experiments
dq	double of quadruplets
DRIFTS	diffuse reflectance infrared Fourier transform spectroscopy
dt	doublet of triplets
EC	ethylene carbonate
EIS	electrical impedance spectroscopy
EtOAc	ethyl acetate
EUCAR	European council for automotive R&D
EV	electric vehicle
FEC	fluoroethylene carbonate
FTIR	Fourier transform infrared radiation
G	g force or relative centrifugal force
g	gram
GITT	galvanostatic intermittent titration technique
GPa	gigapascal

Gr	graphite
h	hours
HC	hard carbon
HEBM	high energy ball mill
HF (aq)	hydrofluoric acid
ICE	initial Coulombic efficiency
L	litre
LIB	lithium ion batteries
LiOTf	lithium triflate
LiPAA	lithium polyacrylic acid
LLO	Li-rich layered oxide
m	meter; multiplet
m-THF	2-methyl tetrahydrofuran
Na-Alg	sodium alginate
NCA	nickel cobalt aluminum oxide
NIB	sodium ion batteries
NMC	nickel manganese cobalt
PAA	polyacrylic acid
PD	1H,1H,2H-perfluoro-1-decene
PDA	polydopamine
PEO	polyethylene oxide
Pr-TEG	2,5,8,11-tetraoxatetradec-13-ene
p-Si	porous silicon

PVA	poly(vinyl alcohol)
PVDF	polyvinylidene fluoride
rcm	relative centrifugal force
R_{CT}	charge transfer resistance
RIC	relative irreversible capacity
rpm	revolutions per minute
R_S	solution resistance
R_{SEI}	SEI resistance
s	singlet
SEI	solid electrolyte interphase
SEM	scanning electron microscopy
SiMP	silicon microparticle
SiNP	sillicon nanoparticle
SiNW	silicon nanowire
SSRM	scanning-spreading resistance microscopy
TBAHP	tetrabutyl ammonium hexafluorophosphate
THF	tetrahydrofuran
USABC	United States advanced battery consortium
VC	vinylene carbonate
VEC	vinyl ethylene carbonate
W	watt
XPS	X-ray photoelectron spectroscopy
XRD	X-ray diffraction

XRM	X-ray microscopy
Z_w	Warburg element
δ	chemical shift
Ω	ohm

Chapter 1 Introduction

1.1 Alkali Ion Batteries

Countries around the world are pursuing a transition away from legacy fossil fuels towards low carbon energy sources. Canada and the United States have both pledged to reach net-zero carbon emissions in their electricity grids by 2035, including large investments in renewable electricity generation.[1,2] Renewable sources, especially solar and wind, suffer from diurnal production cycles that do not always align with peak energy demand.[3] Periods of high demand and low renewable generation must either be supplemented with fixed energy generation from non-emitting sources, or accommodated through energy storage.[4,5] Modelling by Caldeira et al. shows that 12 hours of energy storage dramatically increases the reliability of solar and wind generation to meet electricity demand in the continental US (Figure 1-1).[6] Chemical energy storage, primarily rechargeable batteries, has gained attention and market share due to their applications in renewable electronics, electric vehicles, and grid energy storage.[7]

Lithium ion batteries (LIBs) have become dominant in the world of rechargeable batteries, with ubiquitous applications as the world transitions from fossil fuel energy to the “electrification of everything”.[7,8] Compared to past battery alternatives, lithium ion batteries have no memory effect, are more energy dense, and can retain capacity for up to 4000 cycles with 4 % loss in capacity.[9,10] Nonetheless, improvements are still being hotly pursued to increase the performance of standard lithium-ion batteries, for example with their use in electric vehicles (EVs). The United States Advanced Battery

Consortium (USABC) and the European Council for Automotive Research (EUCAR) have set goals for EV battery performance, as shown in Figure 1-2 alongside commonly used anode and cathode technologies.[11] While each LIB application may place different weight on various performance metrics, the case of EVs emphasizes the need to increase the gravimetric energy (energy per unit mass) and volumetric energy of lithium ion batteries without compromising performance in terms of cost, calendar life, or cycle life, among other considerations.[12]

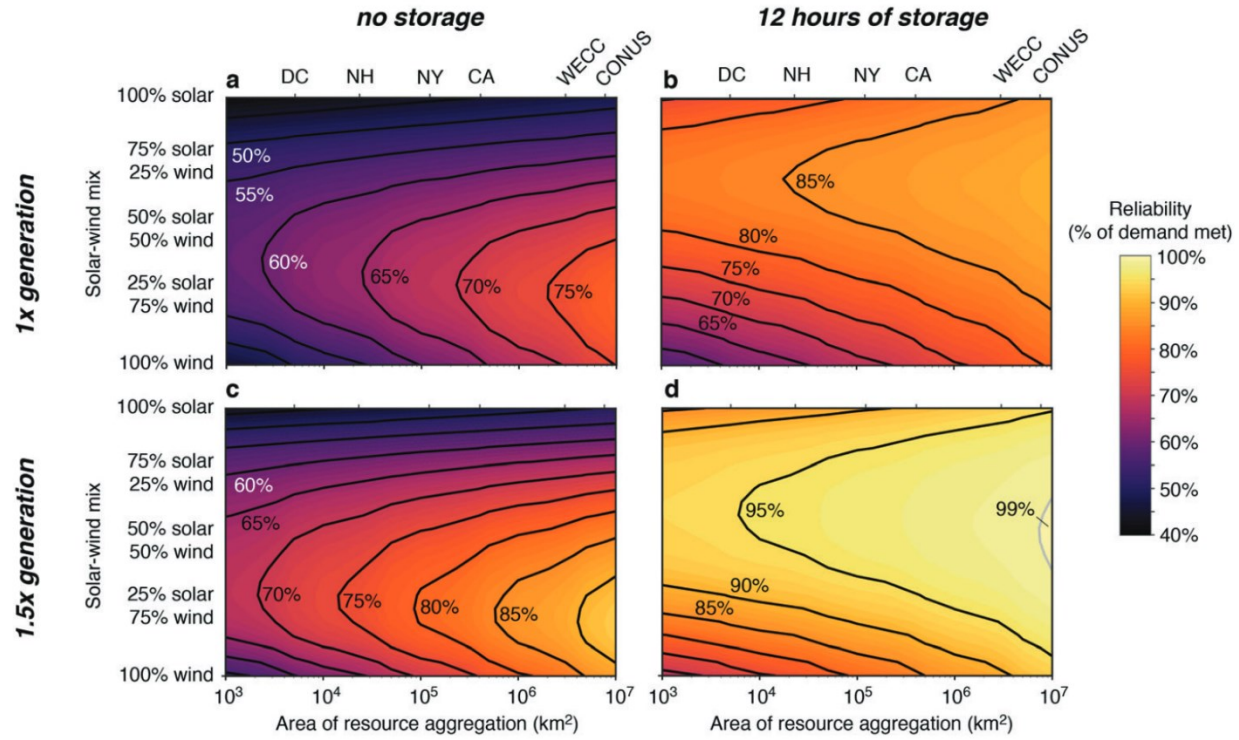

Figure 1-1. Model of the reliability of the electricity supply in the United States of America using only solar and wind power. The distribution of renewable generation is modelled over different land areas, considering production of 1 x and 1.5 x energy demand. Adding 12 hours of energy storage allows for wind and solar to meet much more of the electricity supply and supports solar heavy mixes of solar/wind generation. Reprinted with permission from reference 6. © 2018 Royal Society of Chemistry.

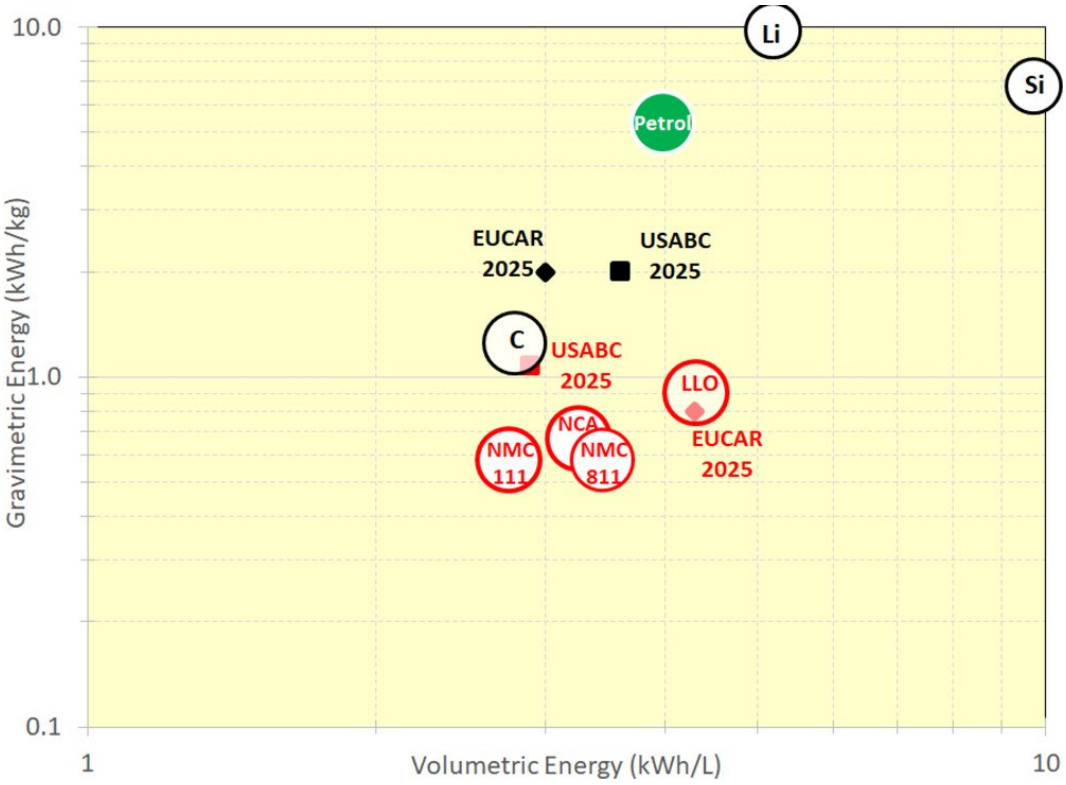

Figure 1-2. Theoretical gravimetric energy and volumetric energy performance for full cells. Lithium, carbon, and silicon anodes are shown in black; nickel manganese cobalt (NMC), nickel cobalt aluminum oxide (NCA), and Li-rich layered oxide cathodes are shown in red. Electrode performance is represented by the centre of each circle, and is displayed alongside the goals set out by US Advanced Battery Consortium (USABC) and European Council for R&D (EUCAR). Reproduced from reference 11. Used under a Creative Commons CC-BY-NC-ND license.

Current battery technology relies overwhelmingly on lithium metal oxides or lithium iron phosphate for the cathode, and graphite for the anode.[13] Graphite anodes react with lithium through an intercalation mechanism, by which lithium intercalates between sheets of graphene, arriving at a fully lithiated state of LiC_6. Graphite anodes have found commercial success due to the confluence of reasonably high specific and

volumetric capacity (c.f. lithium titanate oxide anodes[14]), high Coulombic efficiency (c.f. silicon[15]), and safety to thermal runaway (c.f. lithium[16]). Nevertheless, the promise of silicon anodes is clear from Figure 1-2, and would represent nearly a ten-fold increase in theoretical specific capacity from 372 mAh/g for graphite to 3579 mAh/g for silicon.[17] Silicon, along with other metals like tin, reacts with lithium through an alloying mechanism and reaches a fully lithiated state of $Li_{3.75}Si$. The relationship between specific capacity for the cell and for the anode depends also on the following equation:[18]

$$C_{Cell} = \frac{1}{\left(1/C_A\right) + \left(1/C_C\right) + \left(1/Q_M\right)}$$

where C_{Cell} is the specific capacity of the cell (mAh/g), C_A is the specific capacity of the anode, C_C is the specific capacity of the cathode, and $1/Q_M$ is the specific mass of other cell components. According to this formula, the effect of increasing C_A by transitioning from graphite to silicon is reduced without next generation cathode materials, since the C_C of cathodes such as lithium cobalt oxide is only ~160 mAh/g.[19] A real world comparison between silicon and graphite should focus on a full cell set-up,[20] and highlight volumetric capacity, which is typically more important in most cell applications;[21] however, even with modern day commercial cathodes, silicon represents a 34 % increase in volumetric energy density over graphite. A further consideration in the application of silicon derives from the manufacturing process. Commercial-scale production of silicon metal typically relies on carbothermal reduction of silicon, producing carbon monoxide as a direct by-product, which further reacts in the presence of oxygen to produce carbon dioxide.[22] The energy requirements for reduction are also a drawback for using silicon in low-emissions energy infrastructure, at least using current reduction techniques.[22,23]

Lithium ion batteries have attracted the most attention due to the inherently high specific and volumetric capacity that accompanies lithium as a light element at the top of the periodic table. However, lithium mining faces material constraints as battery production is scaled up, and lithium deposits are highly concentrated in only a few countries in the world.[24] Sodium is a ubiquitous and inexpensive element found all over the world, and sodium ion batteries (NIBs) offer many of the same advantages as lithium ion batteries.[25] Sodium is larger than lithium and has a higher standard electrode potential (-2.71 V vs SHE for Na and -3.02 V vs SHE for Li),[26] so NIBs cannot rival the theoretical energy density of LIBs. Nevertheless, new electrode technologies for NIBs are routinely reaching energy densities above 200 Wh/kg,[27,28] which is competitive with the commercial LIBs, but not yet offering the same cycling stability.[10] Given the aforementioned tradeoffs, LIBs and NIBs are likely to co-exist according to economic and political conditions.[29] This introduction focuses on the chemistry of LIBs, but many of the same principles apply to NIB technologies.

1.2 Silicon and tin anodes for lithium ion batteries

1.2.1 Overview of silicon and tin anodes

Silicon and tin, two elements in the same group of the periodic table with carbon (graphite), have attracted by far the most attention as alloying materials for lithium ion batteries due to many shared advantages over other lithium metal alloys. Both elements are relatively earth abundant and inexpensive, unlike germanium,[30] and non-toxic, unlike lead.[31] They become fully lithiated at low average voltages, 0.400 V vs Li for Si and 0.380 V for Sn, but not too low so as to incur lithium plating, as occurs with

magnesium.[32] The full stack energy densities of silicon and tin are estimated at 976 Wh/L and 941 Wh/L when calculated at their full state of lithiation, which correspond to an improvement over the energy density of graphite of 34 % and 30 %, respectively.[17]

Despite the advantages offered by silicon and tin, both elements also share common weaknesses. The improved specific capacity of these alloying elements is counterbalanced by the colossal expansion of silicon and tin upon alloying with lithium, around 300% in both cases,[33,34] which leads to material fracture and eventual pulverization of the anode material (Figure 1-3). When active material becomes electrically isolated from the rest of the cell, the disconnection is observed as a permanent capacity loss for the lithium ion cell. Furthermore, particle fracture leads to new electrode surfaces exposed during cycling and subsequent consumption of the electrolyte solution to form a solid electrolyte interphase (SEI).[35] The rate capabilities of silicon and tin, which are crucial for fast charging applications, may also be impaired by the increased resistance brought about by SEI build up.[36] Previous attempts to mitigate the deleterious effects of silicon/tin expansion have explored nanoscale morphologies, such as nanoparticles,[37–39] nanowires,[40,41] and nanoporous structures.[42,43] Higher porosity and nanosized structures can also facilitate improved rate capability for silicon anodes, enabling fast charging rates competitive with graphite.[44,45] Other work has explored improving the SEI through thin conformal coatings[46–48] or electrolyte additives.[49–51] What follows is further discussion of the SEI on silicon, although similar principles generally apply to tin anodes as well.

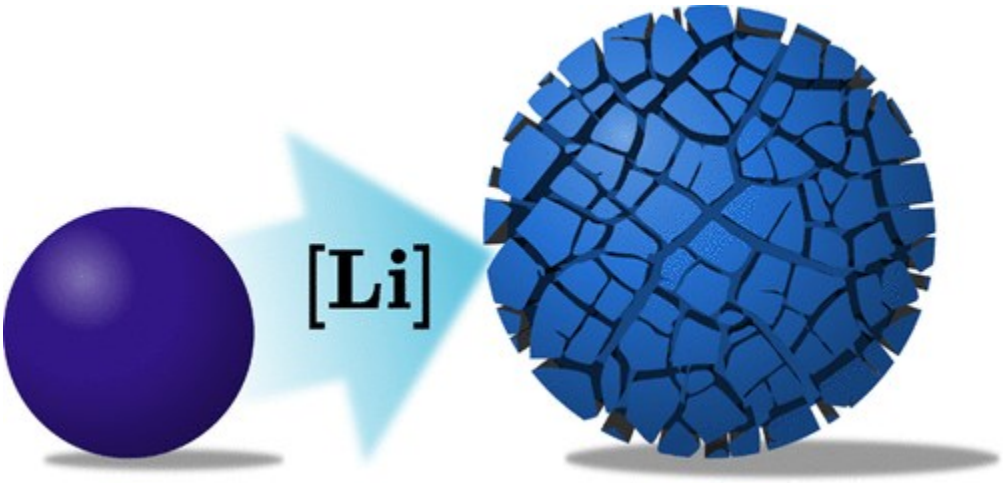

Figure 1-3. Lithiation of alloying anode materials, leading to expansion and particle fracture. Reprinted with permission from reference 17*. © 2014 American Chemical Society.*

1.2.2 The solid electrolyte interphase (SEI)

The solid electrolyte interphase is a layer formed by insoluble degradation products of the solvent and electrolyte on the surface of the anode. SEI can play an important role in battery function, and a thin, robust SEI layer on a silicon surface can prevent further electrolyte degradation and mitigate the effects of expansion upon lithiation.[52] Ideally, the SEI should be highly permeable to lithium ions to allow fast charging.[36,53] It should be electrically insulating between silicon and the electrolyte to passivate the surface and prevent further electrolyte reduction, although silicon not exposed to electrolyte must still have high electric conductivity to the current collector.[54] Furthermore, it must tolerate the stresses of repeated expansion and contraction, while remaining stable and insoluble over a wide range of temperatures and potentials.[55] Multiple strategies have been pursued with the goal of tailoring these SEI properties;

however, maintaining the desired properties is often frustrated by continued SEI growth upon cycling.[56] As silicon expands, new surface area is exposed that can react with and reduce both lithium salts and solvents, irreversibly consuming lithium and further building up the SEI.[57]

The exact nature of the SEI is still a matter of much study, and it depends on the nature of the anode, the potential range of the experiment, the electrolyte, and any electrolyte additives in the cell. Peled et al. developed a well known mosaic model of the SEI on lithium and carbon anodes (Figure 1-4), in which both organic and inorganic microphases are present.[55] Traditionally, an inorganic SEI forms closer to the anode surface, which is produced from decomposition of the $LiPF_6$ electrolyte salt or from reduction of surface oxides.[58] Organic SEI components are then thought to accumulate closer to the soluton, being the products of decomposition from carbonate solvents. Lithium diffusion occurs more quickly through the grain boundaries of these phases.[55] The properties of each phase are complex and depend on the active material being used and the other SEI phases present, which in turn are impacted most strongly by which electrolyte solutions are present.

Research into SEI formation has focused on each aspect of the many factors affecting SEI formation, which extend far beyond electrolyte composition. For example, the current density during the formation steps in lithium ion batteries (typically the first 1-5 cycles) affect the formation of a stable SEI structure, and studies show that lower current densities during the formation steps are preferred for passivating the anode surface.[59,60] Meanwhile, Toney et al. have describe the dependence of SEI growth on the potential during lithiation, and note in particular the role of the native oxide.[61]

According to this model, a high electrical resistivity at the surface of silicon offers a trade-off, leading to a thinner and more homogeneous SEI, but encouraging the growth of inorganic groups with low ionic conductivity, which lowers the rate capability of the cell.[61]

Numerous techniques have been used in analyzing the chemical composition and structure of the SEI on silicon; notably, XPS[62,63] and solid-state NMR[57] have been critical for estimating the exact composition and distribution of functional groups within the SEI. Recently, Han et al. also prepared films of common inorganic SEI components to directly study the properties of the individual components using techniques such as atomic force microscopy (AFM) and scanning-spreading resistance microscopy (SSRM), finding that LiF has a lower ionic conductivity and malleability than other components.[52] However, the performance of individual SEI components is not always an indication of their role in conjunction with other SEI microphases.[36]

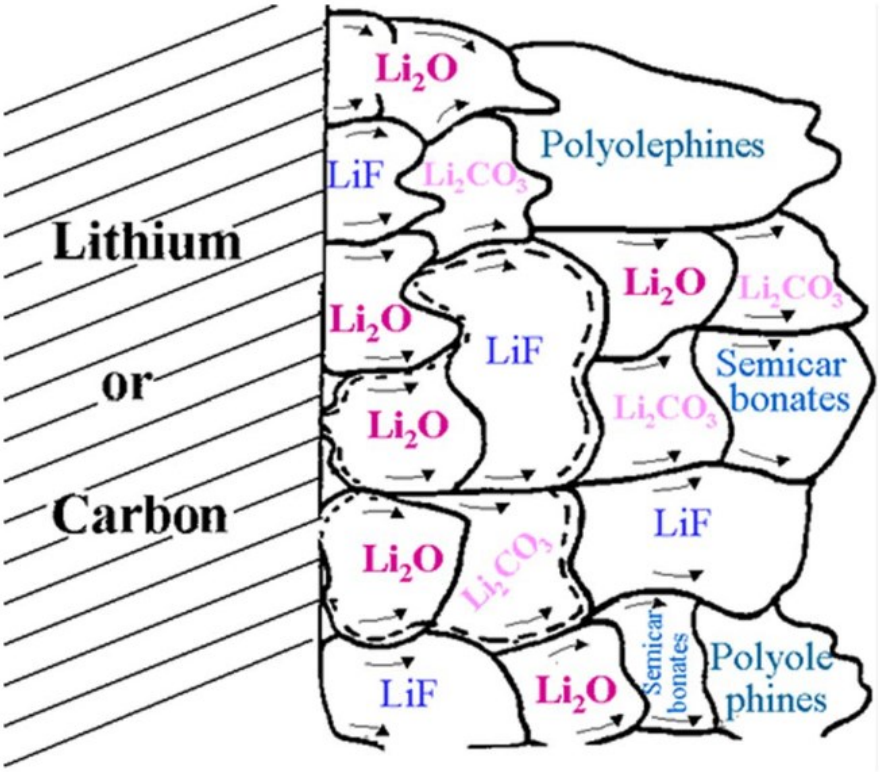

Figure 1-4. *Mosaic model of inorganic and organic microphases on the anode surface. Reproduced from reference 51 under a Creative Commons CC-BY license.*

1.2.3 Impacts of electrolyte on the SEI

Lithium ion battery electrolytes require a polar, aprotic solvent and electrically stable lithium salt to shuttle lithium between the anode and the cathode. $LiPF_6$ has become the lithium salt of choice for most applications due to its balanced properties with regards to the many demands of lithium ion batteries, including ionic mobility and electrochemical stability.[64] Carbonates have long been favoured as the solvent of choice, typically including ethylene carbonate (EC), which is a solid at room temperature, and one or more linear carbonates, such as diethyl carbonate (DEC), which decreases viscosity and lowers the melting point. The contribution of the

carbonates to the SEI has been noted earlier, with $LiPF_6$ decomposing to form LiF especially at high temperatures.[65] Meanwhile, EC and DEC decompose under reductive conditions to contribute to the formation of Li_2CO_3, alongside a myriad of polymerizing SEI components, including polyethylene oxide and polyalkyl chains.[66]

Many additives have been used to improve cycling in lithium ion batteries by improving the quality of the SEI.[51,67,68] Among these, vinylene carbonate (VC) and fluoroethylene carbonate (FEC) are among the most widely used. VC leads to creation of a thin and homogenous coating of organic SEI around silicon particles, mostly consisting of poly(VC) and polyethylene oxide (PEO) fragments.[69] FEC leads to a similar organic SEI, but interspersed with inorganic LiF regions that keep the SEI more permeable to lithium diffusion (Figure 1-5).[36,70] The benefits of the FEC additive seem to correlate with its absolute concentration in the electrolyte, suggesting that its role in stabilizing the SEI stops when the additive is consumed.[71] Other molecules, such as silanes and borate salts, may work as sacrificial additives along the same principle.[72] Sacrificial additives are reduced at a higher voltage than the solvent or electrolyte, and decompose to form a stable, electrically insulating SEI, which prevents reduction of the electrolyte in the future.

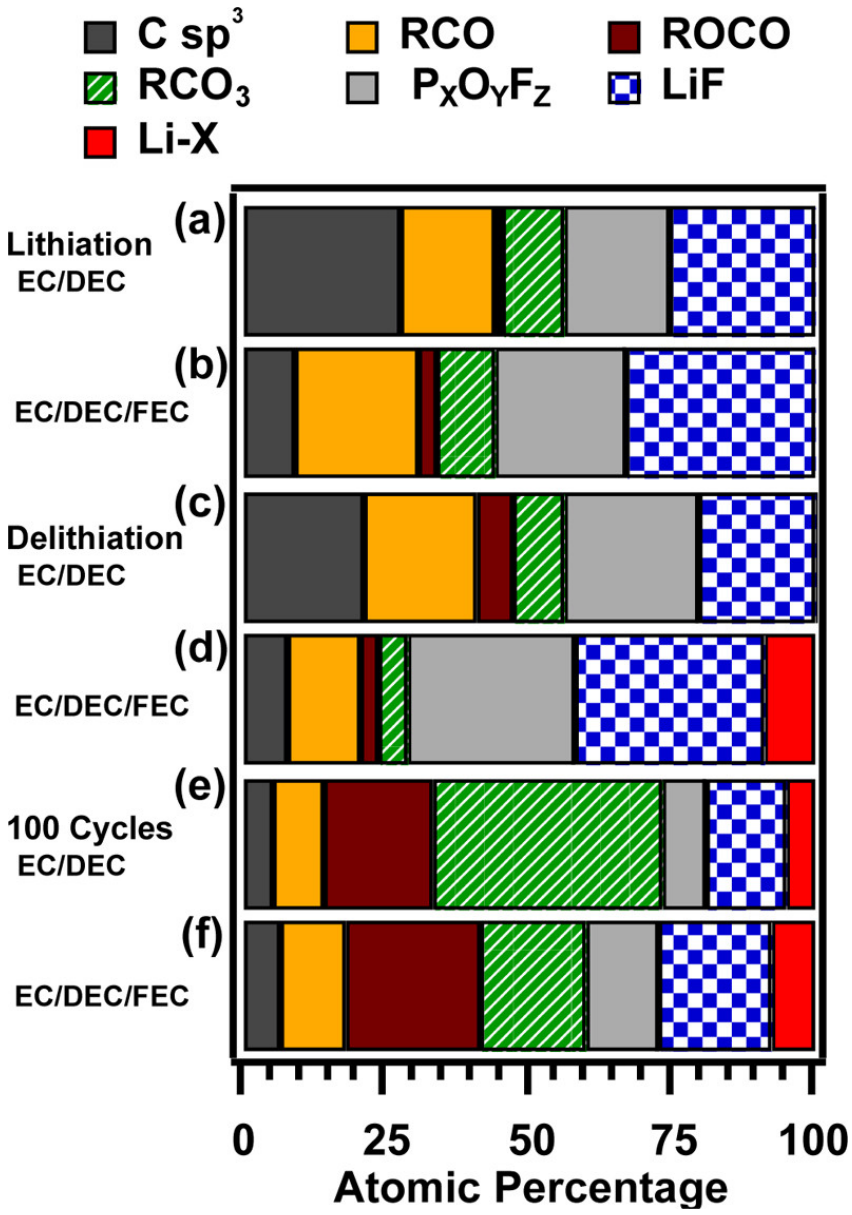

Figure 1-5. Atomic percentage of SEI components in battery electrolyte with and without FEC additive. Reprinted with permission from reference 70. © 2015 American Chemical Society.

1.2.4 Crystalline and amorphous phases of silicon-lithium alloys

The phase diagram of lithium-silicon alloys is associated with different phase transitions, depending on the conditions being used, and the presence of discrete phase transitions may have a further impact on the fracturing and cycle life of silicon anodes. Crystalline lithium silicide phases are thermodynamically favoured during lithiation, as shown in Figure 1-6; however, in practical LIB applications, the lithiation of silicon anodes proceeds rather through the amorphous Li_xSi phase due to kinetic barriers to rearrangement.[73]

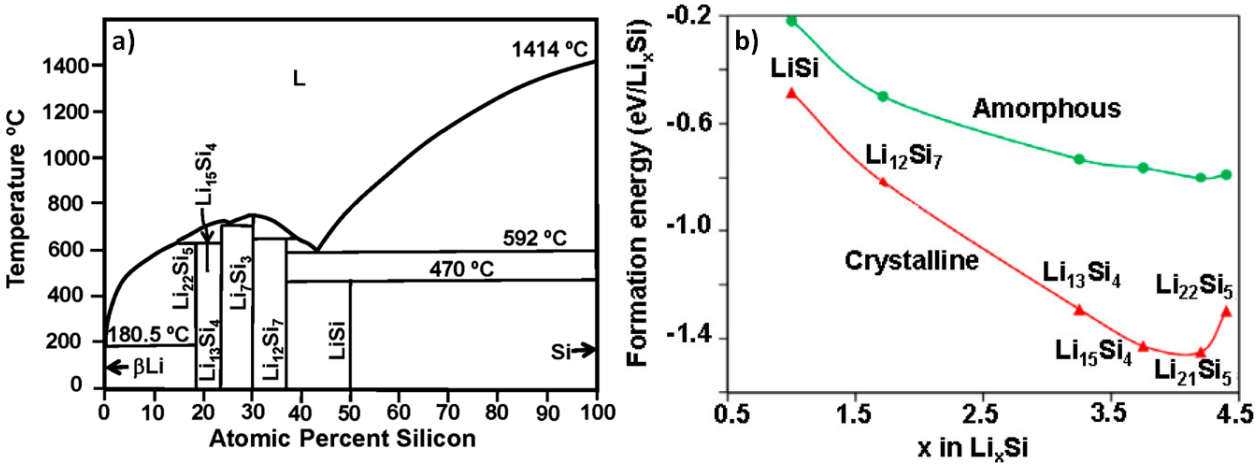

Figure 1-6. Lithium-silicon phase diagram generated by heat treatment (a) and calculated formation energies (b) for amorphous (green) and crystalline (red) lithium silicide phases. (Left) adapted with permission from reference 74. © 1990. (Right) reprinted with permission from reference 73. © 2013 American Chemical Society.

Although the crystalline phase of $Li_{22}Si_5$ is technically the most highly lithiated phase available to a lithium silicon alloy, this phase isn't reached at ambient temperature and pressure;[75] instead, the alloy reaches a metastable *c*-$Li_{15}Si_4$ phase, typically below 50 mV.[33] Similarly to $Li_{22}Si_5$, the $Li_{21}Si_5$ phase has been sought after in

lithium ion batteries due to its high capacity and thermodynamic stability (Figure 1-6b), but is widely accepted to only form above 100 °C due to the high kinetic barrier for rearrangement.[17,76] Previous work has clearly demonstrated that formation of the *c*-$Li_{15}Si_4$ phase is correlated with capacity degradation in thin films, with some evidence that there is a causal relationship between *c*-$Li_{15}Si_4$ phase formation and a loss of capacity.[77] Evidence for this degradation in silicon nanoparticle electrodes is much weaker, and control for *c*-$Li_{15}Si_4$ phase formation using variables such as size or FEC additive,[78,79] which are known to have large impacts on capacity retention regardless of the *c*-$Li_{15}Si_4$ phase.

1.3 Artificial solid electrolyte interphase (a-SEI)

1.3.1 Overview of a-SEI

A common strategy to improve the quality of SEI in silicon involves the conformal coating of silicon with a protective layer, commonly referred to as an artificial solid electrolyte interphase (a-SEI).[80,81] There is no universal definition of an a-SEI, and the term is often used to refer to both homogeneous films deposited on the surface of silicon, as well as molecules covalently bound to the anode. Thin film deposition may occur without covalent bonding to silicon, and has typically used single-component inorganic oxides such as Mn_3O_4,[82] $LiAlO_2$,[83], or Al_2O_3.[84] In a similar fashion, polymer layers are often employed to passivate the silicon surface,[85,86] while in nanoparticle slurry electrodes, they also function to bind the active material to the slurry binder, as shown in Figure 1-7.[87] Due to the large expansion of silicon upon lithiation, it is very beneficial to have strong intermolecular forces such as hydrogen bonding or dipole-

dipole interactions to maintain contact between the active material and the slurry binder.

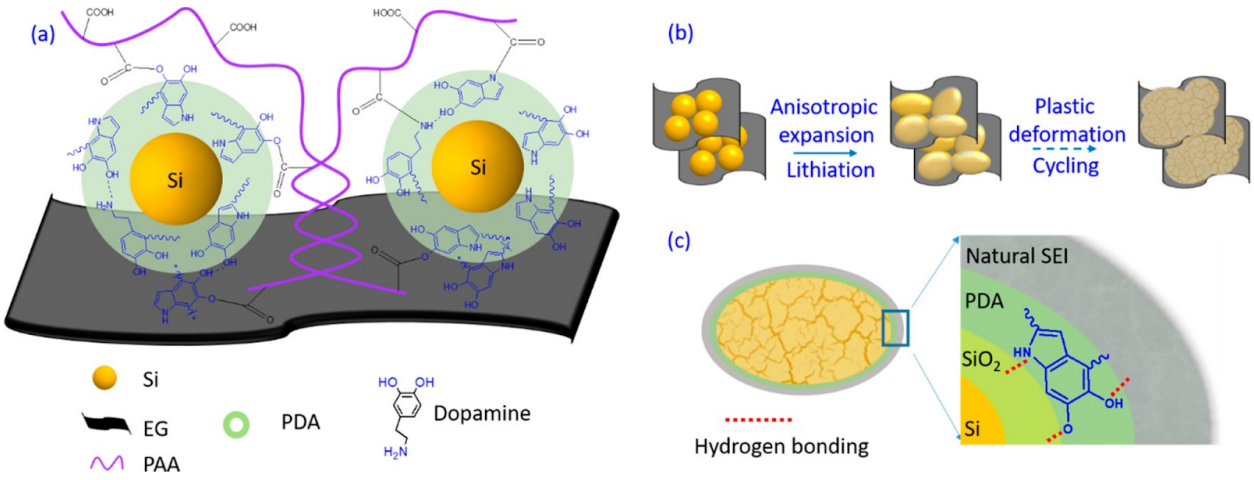

Figure 1-7. Silicon nanoparticles with an a-SEI of polydopamine (PDA) in a binder of polyacrylic acid (PAA). Hydrogen bonding between Si@PDA and PAA prevents electrical isolation during cycling. Reprinted with permission from reference 87. © 2021 American Chemical Society.

Another form of a-SEI builds upon covalent bonds between the silicon surface and the functionalized a-SEI molecules. Taking advantage of the vast history of silicon surface modification,[88,89] thin, conformal layers can be produced on the silicon surface using a vast array of functional groups. A covalently bound a-SEI may be tailored more precisely than a polymer coating, and careful choice of functionality may result in an a-SEI of the desired length and thickness,[90] packing density,[91] and ion permeability.[92] Covalent bonds provide a stronger tether to silicon compared to hydrogen bonding, although hydrogen bonds can provide advantageous self-healing properties to withstand the large expansion and contraction of silicon.[93]

1.3.2 Synthesis of an a-SEI

The chemistry of a-SEI synthesis depends on the nature of the silicon surface. Silicon naturally forms a native oxide layer when exposed to air, typically around 1-3 nm thick.[94] It is possible to coat the oxide layer directly using the chemistry of self-assembled monolayers, however, such surfaces are not stable under alkaline conditions.[95] Covalent bonds to silicon oxides have been employed successfully to tether large polymer a-SEI,[96] and to strengthen the interaction between silicon and polymer binders, as shown in Figure 1-8.[97] When functionalizing the native oxide, the a-SEI is attached via silyl ether or silicon-carbon bonds.

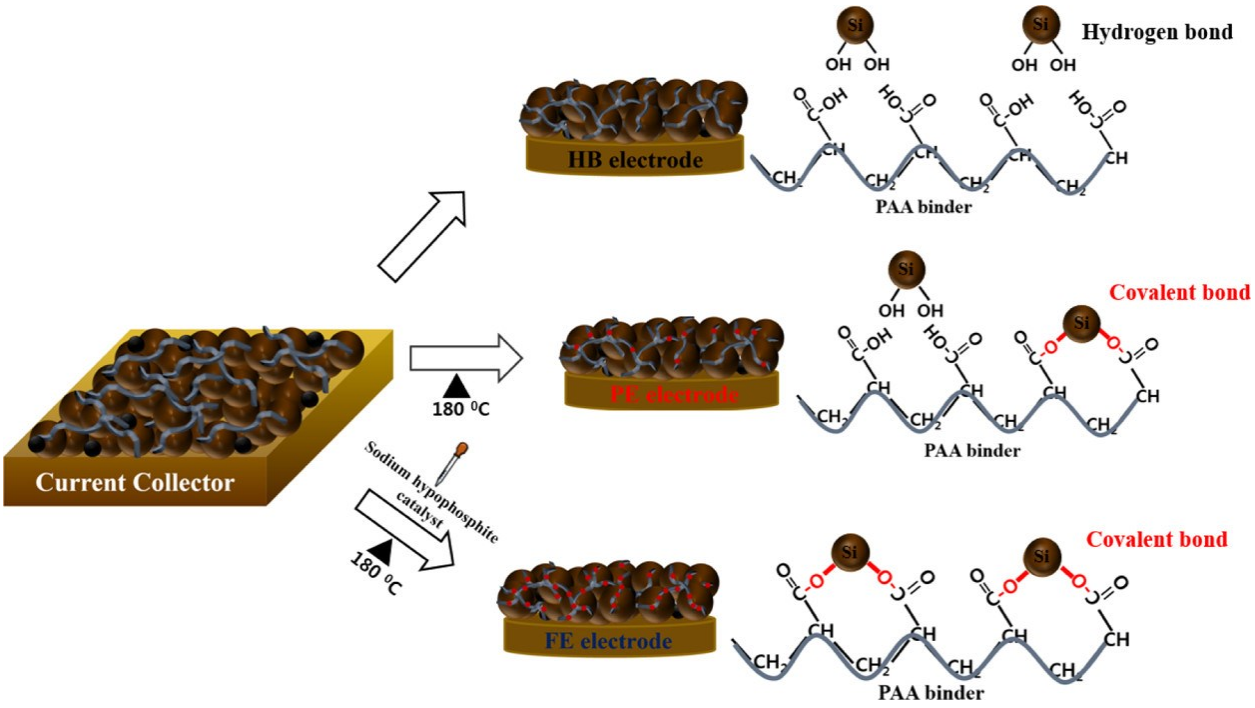

Figure 1-8. Covalent bonds formed catalytically at 180 °C between silanol groups on the surface of silicon and carboxymethyl cellulose (CMC) binder Reprinted with permission from reference 97. © 2019 American Chemical Society.

Covalently bound molecular a-SEI are usually attached through a Si-C bond, formed on the surface of hydrogen terminated silicon.[86,90,91,98,99] Hydrogen-terminated silicon is formed after removal of the silicon oxide using aqueous hydrofluoric acid,[100] which will be explored further in Chapter 3. The chemistry of hydrogen-terminated silicon has been well established, and can be pursued using many different synthesis techniques with a surprisingly large number of mechanisms.[88,101] The work in this thesis will focus on the hydrosilylation of alkenes and alkynes with Si-H_x bonds on the silicon anode, as described in Chapter 3. Using hydrosilylation, one can access wide range of functionalized surfaces of silicon nanoparticles that are stable to harsh chemical conditions due to the covalent Si-C bonding motif. One example is provided in Figure 1-9.[90] The a-SEIs that can be obtained from this chemistry are thus highly tailorable, allowing one to select for the optimal properties with regard to electrical conductivity, ion selectivity and permeability, and silicon-binder cohesion.

1.4 Tin anodes for lithium and sodium ion batteries

1.4.1 Lithium-tin alloys

We have highlighted many of the similarities between silicon and tin anodes; however, the two materials also share notable differences. Tin is inherently more electrically conductive than the semiconductor silicon, with a resistivity of 10^{-7} Ω•m for Sn and $2x10^{3}$ Ω•m for Si, which improves the rate capability of tin anodes.[102] On the other hand, tin is a much heavier element than silicon, and therefore offers poorer specific capacity as a lithium ion battery anode (993 mAh/g for Sn vs 3579 mAh/g for Si),[103] although the volumetric capacity is similar. Perhaps most crucially, while both

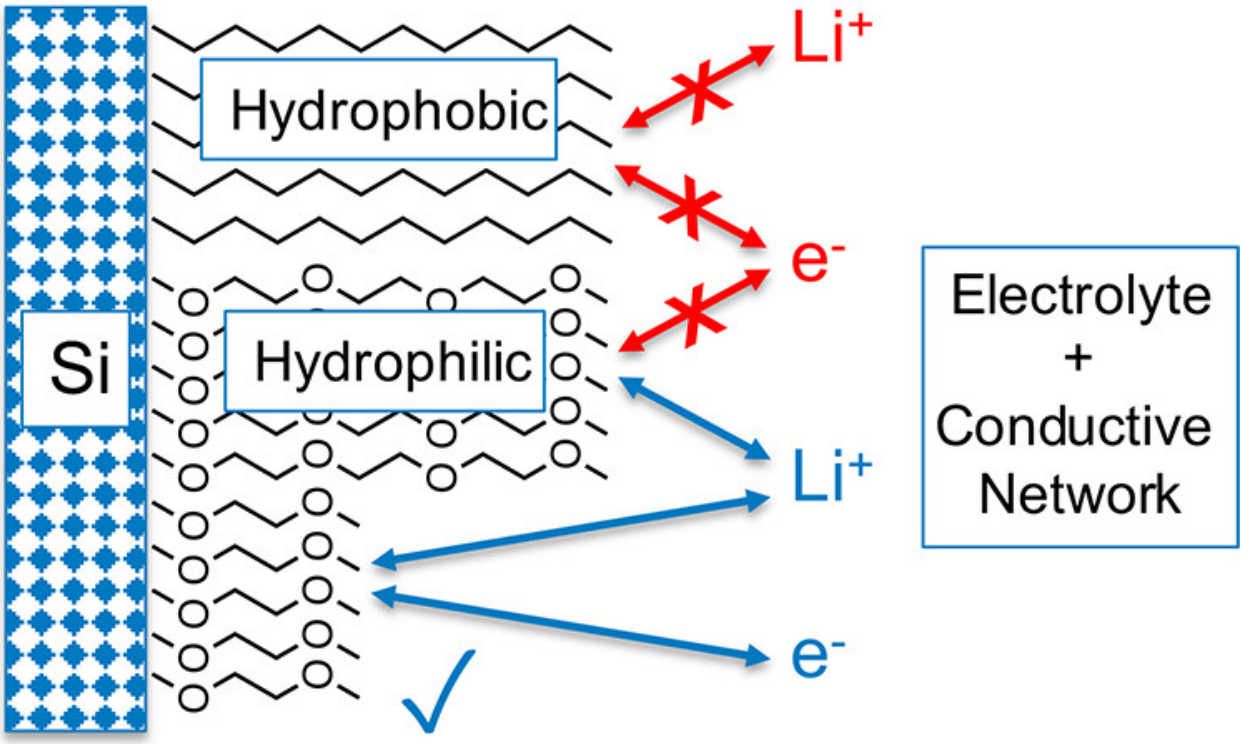

Figure 1-9. Hydrocarbon and polyethylene oxide (PEO) a-SEI functionalized on the surface of silicon. Reprinted with permission from reference 90. © 2021 American Chemical Society.

anodes expand ~300 % during lithiation, tin fractures more easily that silicon.[104] Nanosized tin has arisen as an optimal morphology to mitigate the damage caused by expansion, although the tin remains brittle and subject to fracture and pulverization, even at sizes < 150 nm,[105]. Silicon with sizes < 150 nm is known, however, to be more robust to cycling without fracture, at least during initial cycles.[106–108] Instead, most work looking to harness tin has focused on tin metal alloys,[109,110] tin oxides (Figure 1-10),[111,112] and other tin-main group materials,[113,114] which represents a compromise of lower specific capacity and longer cycle life and higher Coulombic efficiency.

Unlike silicon, tin is lithiated through a series of phase transitions, shown in Figure 1-11.[17] While the theoretical fully lithiated phase is $Li_{22}Sn_5$, this phase is not observed in the bulk of tin during electrochemical testing.[115] Due to the high potential for particle fracture in pure Sn anodes, additional mitigating measures are necessary, such as introducing high porosity and using tin-graphite mixed electrodes.

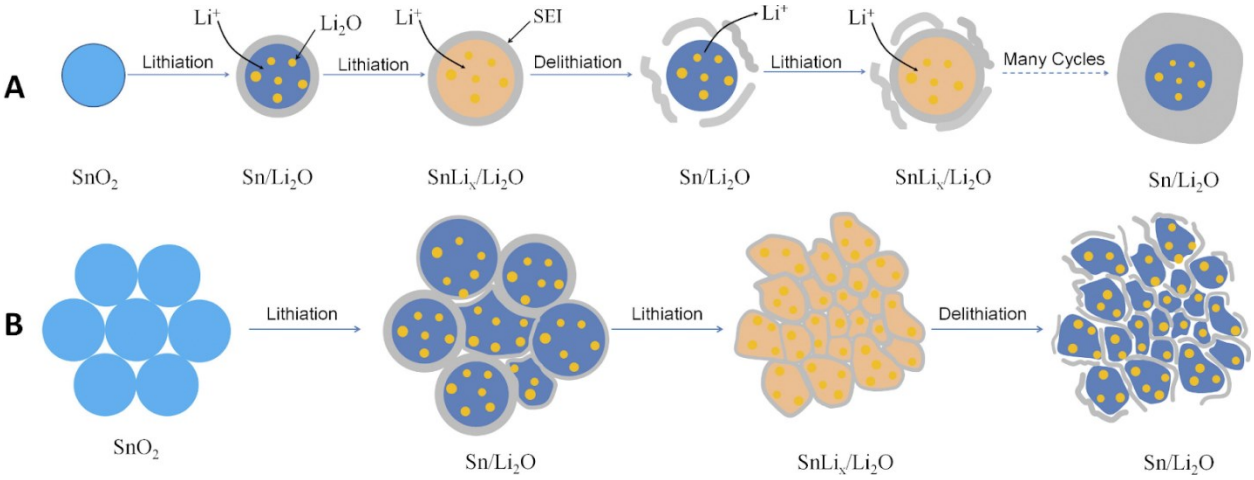

Figure 1-10. SnO_2 as an anode material also cannot prevent fracturing or irreversible capacity loss due to SEI buildup. Reprinted with permission from reference 111. © 2015 Institute of Materials, Minerals and Mining and ASM International.

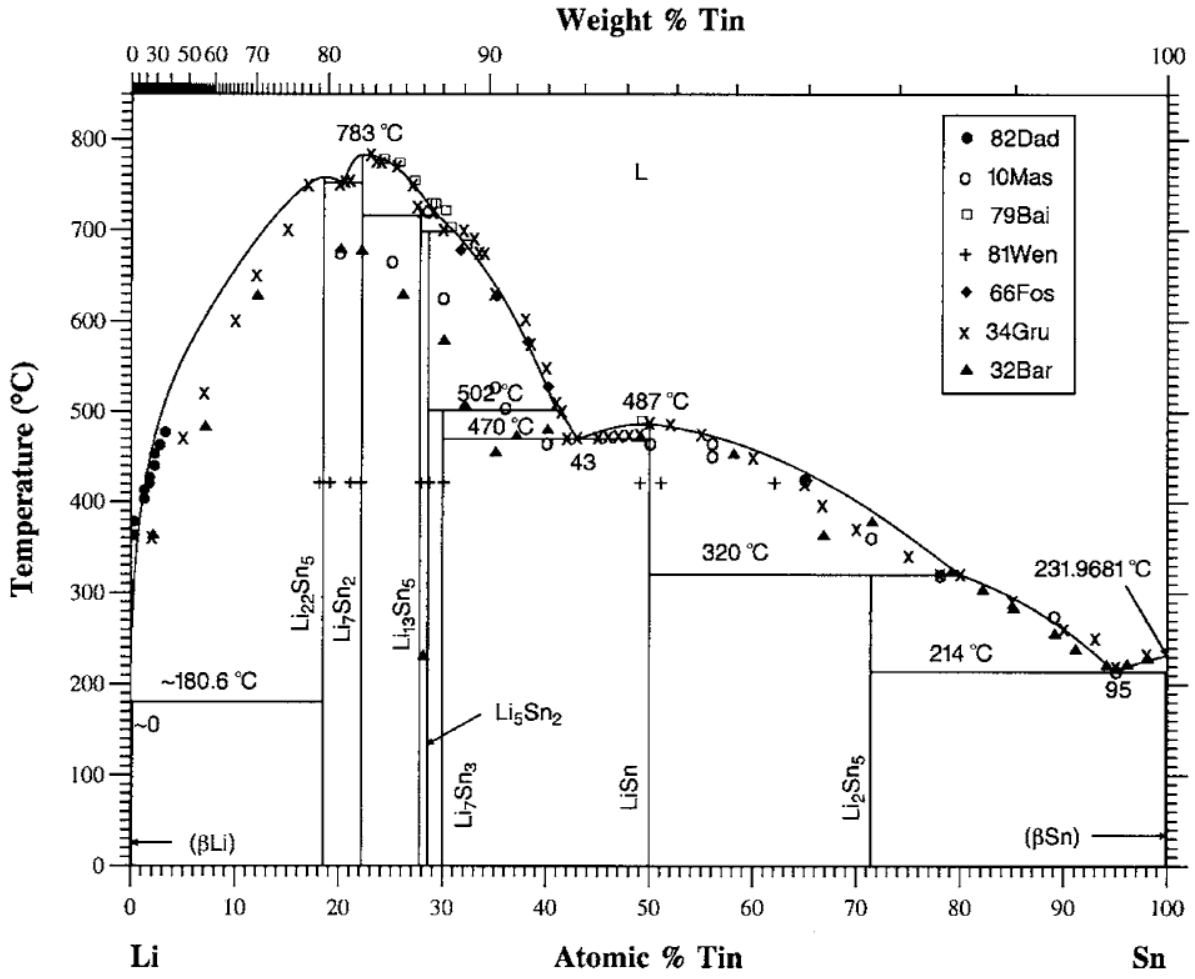

Figure 1-11. Li-Sn phase diagram. Reprinted with permission from reference 116. © 1998 Springer Nature.

1.4.2 Porous tin preparation

Porous tin anodes allow for the expansion of tin to be accommodated by void space in the anode, mitigating the deleterious impacts of expansion.[117] The work on tin anodes described here uses a process for porous tin synthesis developed by Dr. Peter Kalisvaart, and developed within the Buriak group thanks to support from Western

Economic Diversification of the Government of Canada from 2017 to 2022. The work described here to optimize this porous tin powder for use in lithium ion and sodium ion batteries is an industry project carried out with Nanode, a spinoff company from the Buriak group. The porous tin synthesis is based upon a melt-spinning process that produces ribbons of tin and aluminum, followed by an etching step. For porous tin, the goal is to find a material which is highly porous, and with a large surface area to volume ratio, but not so porous as to greatly lower the volumetric capacity of a fully lithiated tin anode.

1.4.3 Tin-graphite and tin-hard carbon electrodes

Another method to mitigate the impacts of tin (or silicon) expansion is the inclusion of graphite in the slurry materials. While tin expansion during lithium alloying reaches ~300 %, graphite intercalation with lithium involves much less expansion, around 13 %.[118] The combination, therefore, of tin and graphite in an anode leads to a reduced overall cell expansion,[119] and graphite acts as a buffer to dilute the effects of particle fracture and pulverization.[120] Graphite is also highly conductive, which is less important for intrinsically conductive tin than for silicon, although due to the lower conductivity of SnO_2, oxide interfaces that form in-situ could reduce electrical contact with the graphite.[9] Graphite can either be blended with tin in a gentle slurry process, or combined into a direct graphite-Sn composite (Figure 1-12), and both approaches have their own advantages.[121] Blended electrodes require a facile stirring process, and don't change the properties of either tin or graphite significantly during anode preparation.[121,122] Composite graphite-Sn electrodes can rely on many fabrication processes. High-energy ball milling has the advantages of simplicity and the potential

for large scale commercial applications; however, care must be taken to avoid degradation of the graphite crystal structure during ball milling.[123,124] Si-graphite and Sn-graphite composite anodes have gained increased attention for their potential to improve specific capacity slightly over all-graphite anodes with minimal loss in Coulombic efficiency or capacity retention.[119,121] The importance of marginal capacity gains is highlighted by the equation for full cell specific capacity outlined in Section 1.1, which leads to much larger gains in full cell capacity for a transition from 350 mAh/g to 450 mAh/g of anode capacity, than for a transition of 3350 mAh/g to 3450 mAh/g.[18]

While graphite works well for both lithium ion batteries and potassium batteries, sodium does not intercalate into the crystalline graphite lattice.[125] The incompatibility of sodium with hard carbon is multifaceted, and must be considered in light of graphite intercalation by both lithium and potassium. LiC_6 compounds allow for a close bond length between lithium and carbon, and modelling indicates non-neglible electron sharing, indicative of a covalent interaction that aids in intercalation.[125] In contrast, sodium and potassium are two large to participate in covalent bonding with graphite, and an ionic bonding interaction can be modelled instead. Due to the decrease in electronegativity down period 1, the formation energy becomes progressively more negative as we examine the larger alkali metals.[125] Sodium exists in a middle ground in which neither ionic bonding nor covalent bonding is strong enough to allow for intercalation with graphite.

Nevertheless, sodium-tin alloys are a promising anode for sodium ion battery technology following the same chemical principles that apply to lithium ion batteries,[17] namely an alloying reaction and high volumetric energy density.[126] A different carbon

material is sought to dilute the effects of tin expansion and improve the capacity retention and Coulombic efficiency of the cell. Hard carbon is the common name for non-graphitizable carbon, or carbonaceous materials which do not form graphite even above 3000 °C.[127] Hard carbon has a capacity of ~ 350 mAh/g in sodium ion batteries depending on the source.[127] The mechanism for sodiation of hard carbon is complicated and was originally hypothesized using a “house of cards” model to involve intercalation between graphene sheets followed by filling of pores within hard carbon.[128,129] Updated models include adsorption at defects in graphene sheets along with intercalation between disordered graphene sheets and pseudo-adsorption in pores, which occur to different degrees depending on the source and nature of the hard carbon.[127,130] We hypothesize that hard carbon and tin mixtures will lead to the same advantages found in silicon graphite anodes, leading to improved capacity at minimal expense of irreversible capacity loss and material fracturing.

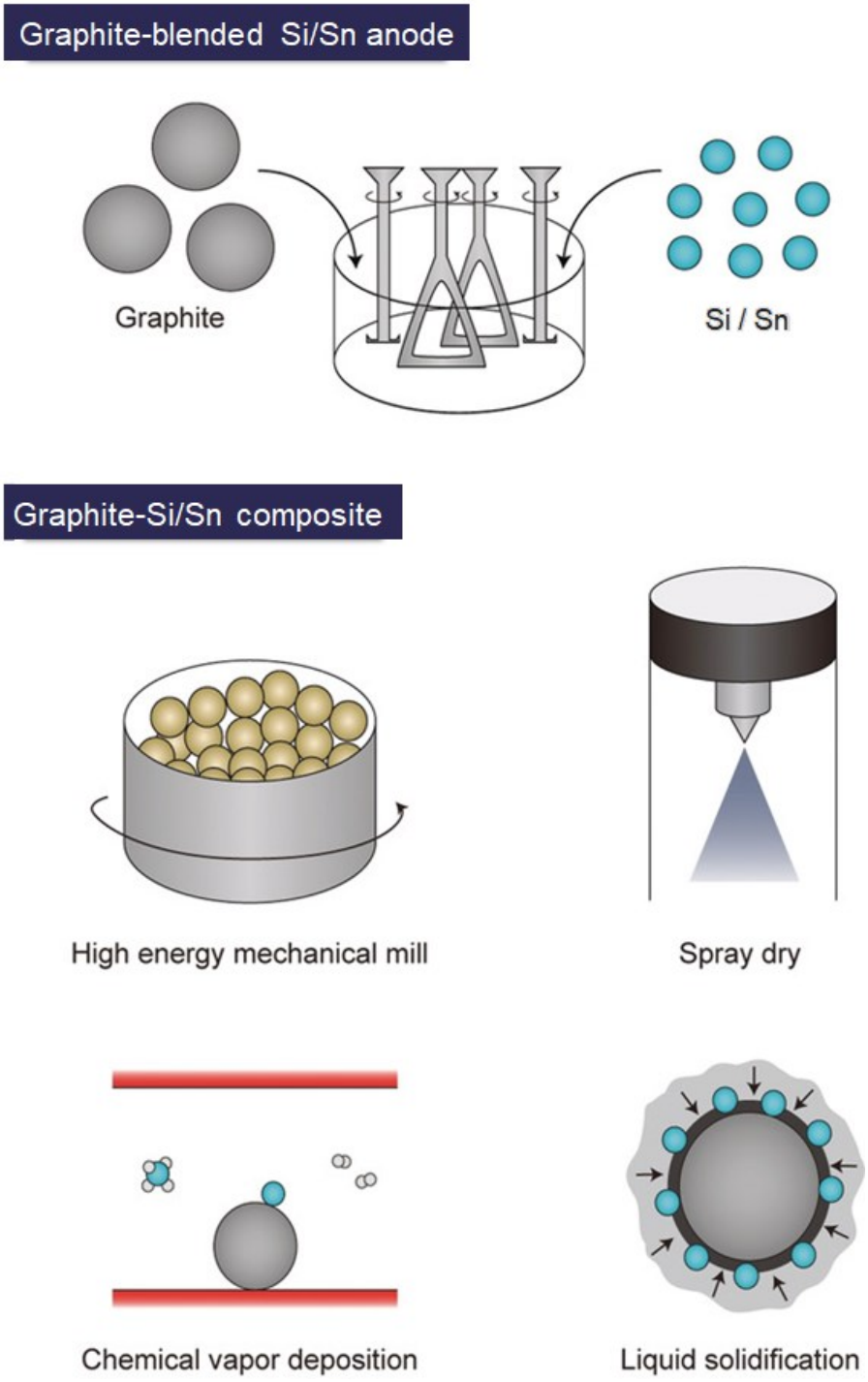

Figure 1-12. Methods of the preparation of Si-graphite or Sn-graphite anodes for lithium ion batteries. Adapted with permission from reference 121. © 2020 John Wiley and Sons.

1.5 Thesis overview

This thesis focuses on alloyed anode materials for alkali-ion batteries, namely, silicon anodes for lithium ion batteries, tin-graphite anodes for lithium ion batteries, and tin-hard carbon anodes for sodium ion batteries. The chemistry of alloying materials is explored, and the electrochemical performance of each material in lithium ion coin cells is demonstrated.

Chapter 2 describes the effect on cycling of the crystallization of amorphous lithium silicide to form the *c*-$Li_{15}Si_4$ phase. We detail the consequences of phase transition in thin films, porous silicon, and silicon nanoparticles. Different cycling protocols were used to control for the presence or absence of the *c*-$Li_{15}Si_4$ phase. We discuss the consequence of *c*-$Li_{15}Si_4$ phase formation on cycling stability and Coulombic efficiency.

Chapter 3 describes the hydrosilylation of silicon nanoparticles to create an artificial solid electrolyte interphase (a-SEI). The benefits of an a-SEI are described in the context of silicon oxide performance, and explored with reference to the chemistry of the a-SEI groups and the interactions between a-SEI and various silicon nanoparticle slurry binders. We also look at the optimization of silicon functionalization and size distribution through a related, radical-based mechanochemical synthesis.

Chapter 4 describes the effect of electrolyte additives on the solid electrolyte interphase on silicon thin films and silicon nanoparticles of varying diameters. Additives include alkenes and alkynes that could react with freshly exposed silicon surfaces via in-situ reactivity, akin to electrografting.

Chapter 5 describes the electrochemical cycling of tin graphite and tin-hard carbon anodes for use in lithium ion batteries and sodium ion batteries. The synthesis and slurry preparation of porous tin is described, and the trade-offs with increased tin content is discussed. A comparison is performed between tin-graphite anodes with porous tin from the melt-spinning process and commercially available micron sized tin particles.

Chapter 2 Effects of the *c*-$Li_{15}Si_4$ phase on nanoparticle cycling*

*The contents of this chapter have been reproduced and/or adapted from the following publication: Woodard, J. C.; Kalisvaart, P.W.; Sayed, S.Y.; Buriak, J. M. Beyond Thin Films: Clarifying the Impact of *c*-$Li_{15}Si_4$ Formation in Thin Film, Nanoparticle, and Porous Si Electrodes, ACS Appl. Mater. Interfaces, 2021, 13, 32, 38160.

2.1 Introduction

Targeted efforts to reduce fracture and improve capacity retention in silicon anodes for lithium ion batteries require an understanding of the alloying processes that occur as the voltage is lowered towards 0 V vs Li during lithiation, and as the voltage is raised again during delithiation. To help visualize the processes that take place during electrochemical cycling, a voltage curve of silicon cycling is shown in Figure 2-1, along with an accompanying diagram of the various phase transitions shown. In the first stages of electrochemical lithiation of crystalline Si, it is directly transformed into highly lithiated amorphous silicon, *a*-Li_xSi, typically at around 0.1 V vs Li.[33,131] The transition is clearly visible in Figure 2-1,[17,132,133] and appears as a plateau labelled I, which only occurs during initial lithiation when the silicon is crystalline.

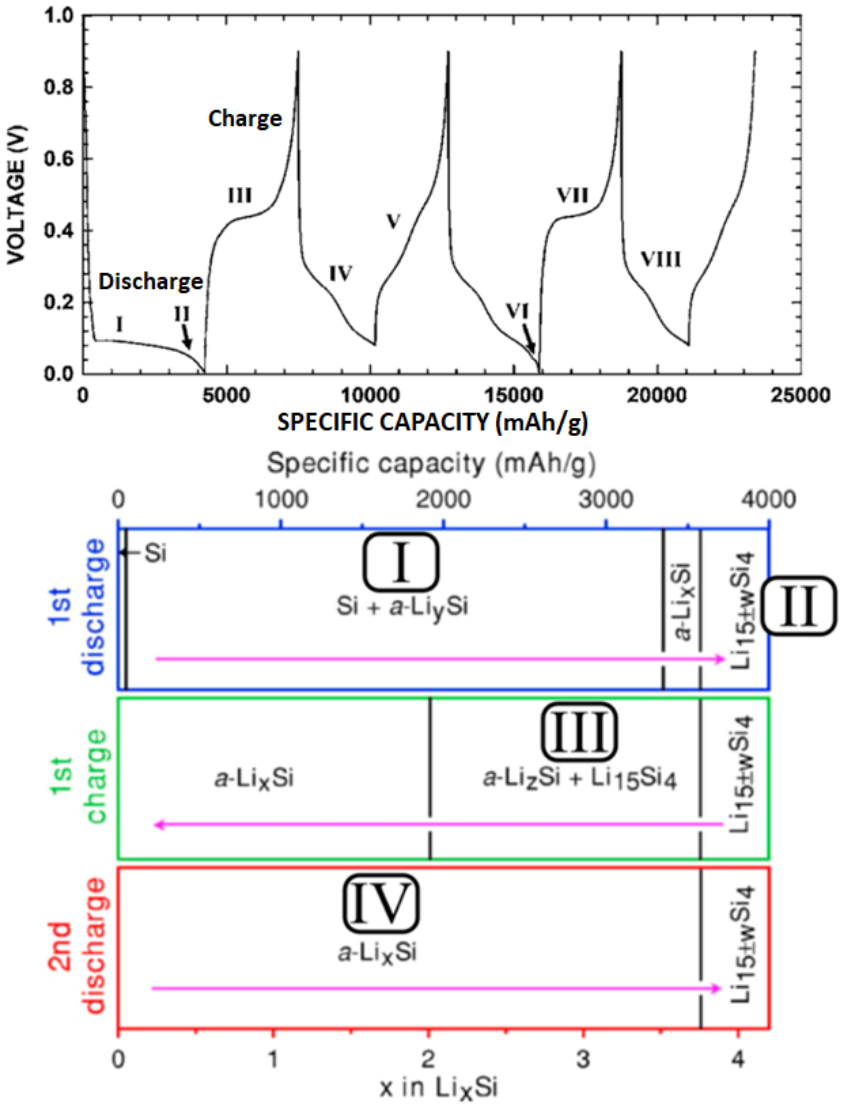

Figure 2-1. Voltage curve of the lithiation and delithiation in bulk silicon (top), along with the corresponding phase transitions (bottom). The bottom diagram first outlines phase transitions during the lithiation of crystalline silicon (blue), followed by delithiation from the c-$Li_{15}Si_4$ phase (green) and the subsequent lithiation of amorphous silicon. Phase transitions in each figure are indicated by Roman numerals. Adapted with permission from references 132 (top), 133 (bottom), and 17 (bottom adaptation). © 2006 Electrochemical Society, © 2007 Electrochemical Society, and © 2014 American Chemical Society, respectively.

The exact value of *x* in *a*-Li_xSi is difficult to determine due to electrolyte decomposition taking place in conjunction with Li insertion into the Si – which correspond to reversible and irreversible lithiaton capacity, respectively. But.the reversible capacity (i.e. the capacity observed during delithiation) associated with this transformation is >3000 mAh/g,[133] and the value of *x* has been reported as 3.4--3.5.[131,134] The terminal stage of lithiation that can be attained at room temperature is a metastable crystalline phase, where *x* = 3.75 (*c*-$Li_{15}Si_4$, Figure 2-2), typically at voltages below 50 mV vs Li.[75,135] The change in *x* specifically associated with this transition is around 0.2 as derived from galvanostatic intermittent titration technique (GITT),[136] and the final transition accounts for approximately 200 mAh/g of specific capacity.

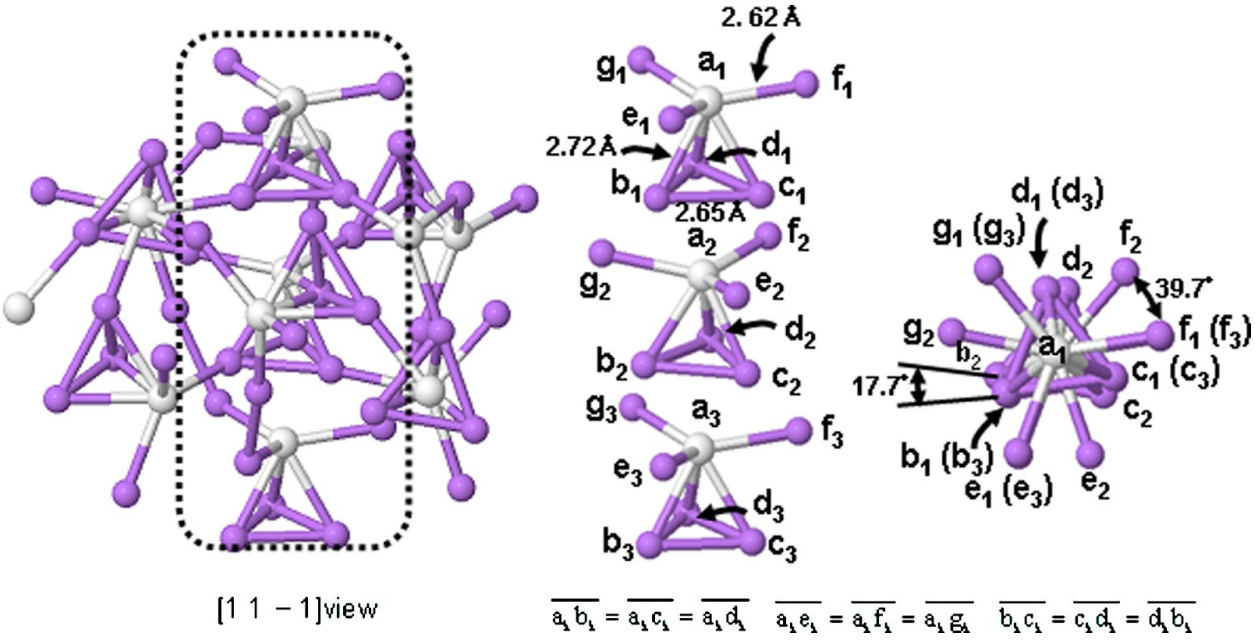

Figure 2-2. Crystal structure of c-$Li_{15}Si_4$. Reprinted with permission from reference 137. © 2007 American Institute of Physics.

Despite the relatively small additional capacity and expansion associated with its formation, *c*-$Li_{15}Si_4$ has been linked to an increased loss of capacity in both silicon thin films,[77,138] and nanoparticles.[78,139] The observed links between delamination, capacity loss, and the *c*-$Li_{15}Si_4$ phase are convoluted in thin films, as demonstrated by the diagram in Figure 2-3.[137] The presence of *c*-$Li_{15}Si_4$ is near-ubiquitous when delamination is observed in thin films, but this crystalline phase is also generally accepted to play an intrinsic role in capacity degradation beyond catastrophic delamination.[140] For instance, lithiation of amorphous lithium silicide, *a*-Li_xSi, to the *c*-$Li_{15}Si_4$ phase may lead to greater fracturing than lithiation ending in the amorphous phase.

The behaviour of *c*-$Li_{15}Si_4$ has been well studied in lithium ion batteries. The $Li_{15}Si_4$ phase is metastable due to the low barriers to rearrangement which present a kinetic barrier to the formation of more heavily lithiated phases such as *c*-$Li_{21}Si_5$ and *c*-$Li_{22}Si_5$.[17,76] *c*-$Li_{15}Si_4$ forms during electrochemical lithiation while lower lithium silicide phases do not form because *c*-$Li_{15}Si_4$ is the lowest lithiated phase in which every silicon atom is fully isolated, again presenting a low kinetic barrier to rearrangement relative to highly lithiated amorphous lithium silicide.[73] Each silicon atom is bonded to six lithium atoms in *c*-$Li_{15}Si_4$ (Figure 2-2), but with two different Si-Li bond lengths.[137] The stability of the *c*-$Li_{15}Si_4$ phase is also of relevance. Under highly reductive conditions, the *c*-$Li_{15}Si_4$ phase could be said to be electron deficient due to the existence of more thermodynamically stable Li-Si phases,[141] and therefore susceptible to reaction with carbonate electrolytes. Indeed, Gao et al. hypothesized that *c*-$Li_{15}Si_4$ phase formation was reversible even at low voltages due to parasitic reactions with the electrolyte.[78]

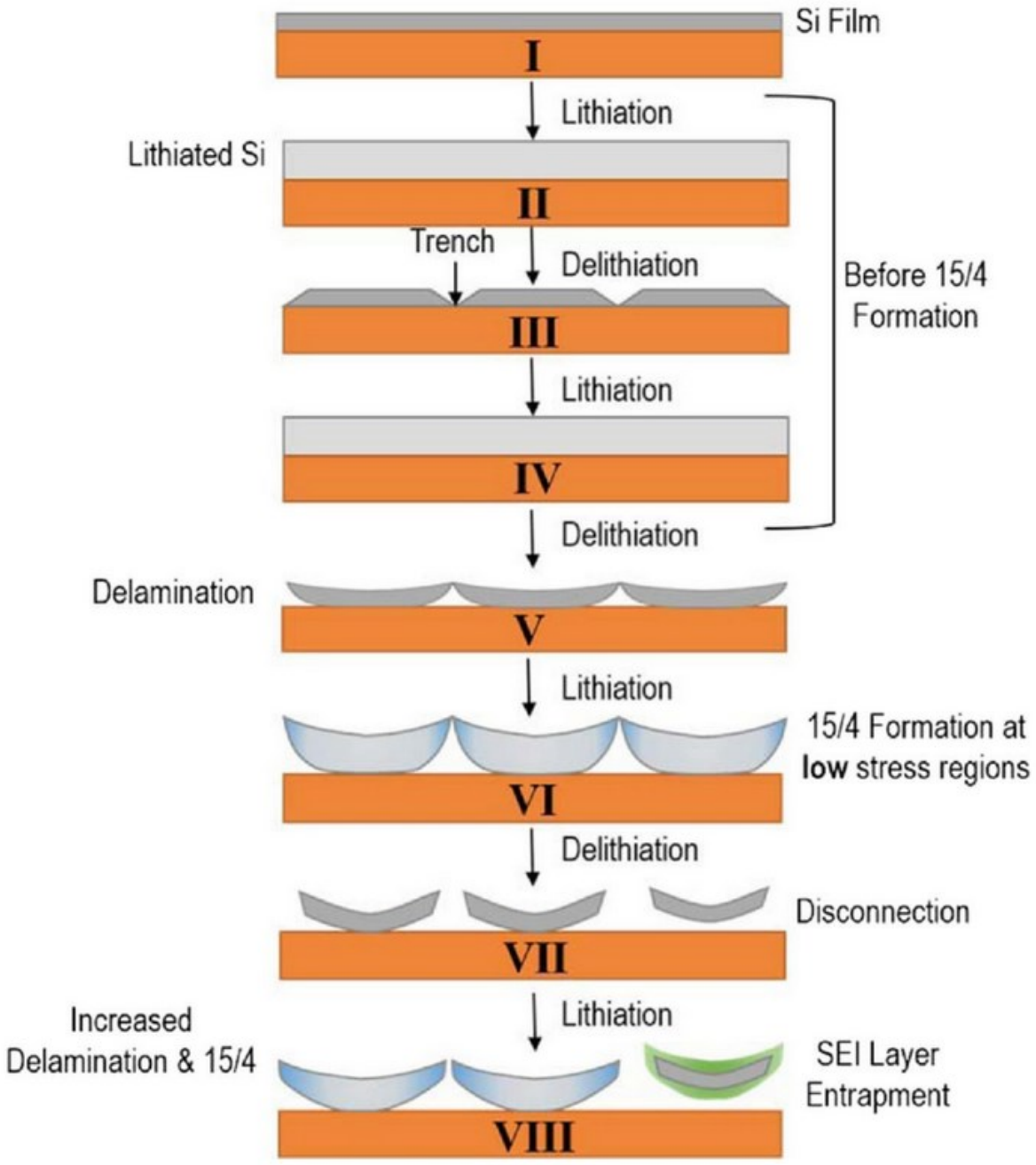

Figure 2-3. A representation of the interplay between silicon thin film delamination from Cu foil (orange) and concurrent increase in c-$Li_{15}Si_4$ formation. In thin films, the c-$Li_{15}Si_4$ phase and capacity loss may both be caused by delamination, but positive feedback from c-$Li_{15}Si_4$ formation may also increase the rate of delamination. Adapted from reference 77 under a Creative Commons CC BY-NC-ND license.

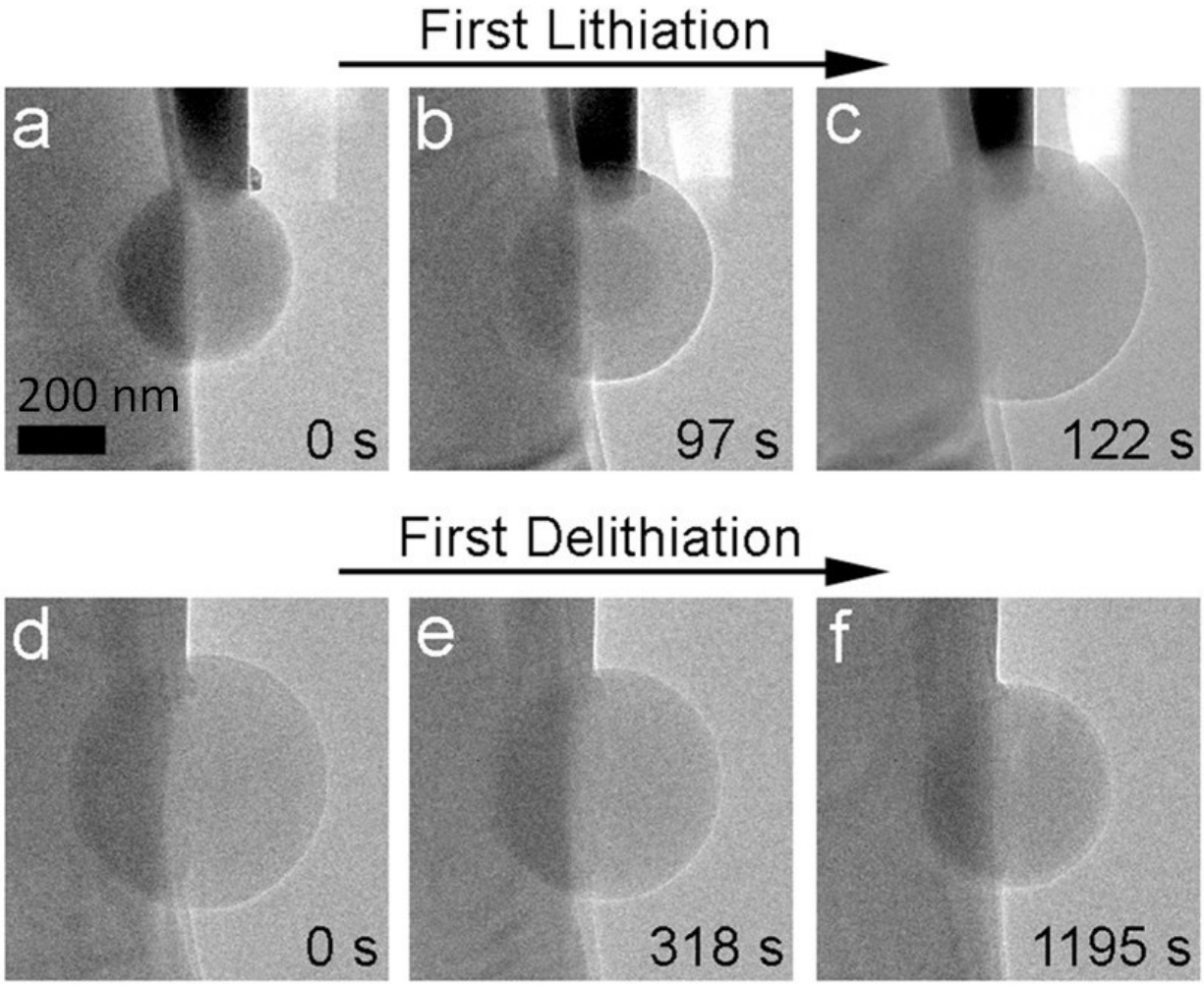

Figure 2-4. Two-phase lithiation of amorphous silicon nanoparticles attached to a c-Si nanowire during the first lithiation and delithiation cycle. Single phase delithiation was observed because the lithiation was mostly arrested at the highly lithiated amorphous Li_xSi phase. Scale bar 200 nm. Reprinted with permission from reference 142. © 2013 American Chemical Society.

With regards to the effect of the *c*-$Li_{15}Si_4$ phase on anode stability, we cannot neglect that the transition from *a*-Li_xSi to *c*-$Li_{3.75}Si$ increases the theoretical capacity by ~ 200 mAh/g, to 3579 mAh/g, and we would expect additional silicon expansion due to this increased capacity regardless of whether the final state is crystalline or not. But

furthermore, formation of *c*-$Li_{15}Si_4$ creates a two-phase boundary between *a*-Li_xSi and *c*-$Li_{15}Si_4$ during lithiation, and between *c*-$Li_{15}Si_4$ and Li_ySi, where y is ~2, during delithiation.[136] Volume changes across a two-phase boundary are associated with increased stress, possibly leading to fracture and capacity loss in alloyed anodes generally,[17] and in silicon specifically (Figure 2-4).[33,106,143] Attempts to directly observe fracture in Si by in-situ TEM have instead overwhelmingly focused on the initial transformation of *c*-Si to Li_xSi,[142] and approaches to mitigate fracturing during this particular transformation by reducing the particle size or using amorphous rather than crystalline Si powder.[106,142,144,145]

The phase transformations associated with formation of *c*-$Li_{15}Si_4$ involve a smaller change in the Li/Si ratio and hence a smaller volume change than the abrupt transformation from pristine silicon to Li-rich *a*-Li_xSi. However, the transition from *c*-Si to *a*-Li_xSi only takes place in the first cycle and only for crystalline Si. There is a strong correlation between formation of the *c*-$Li_{15}Si_4$ phase and capacity loss during long-term cycling. For instance, Xie et al. showed that the onset or acceleration of capacity degradation in 100-nm thick Si films on Cu coincides with the onset of *c*-$Li_{15}Si_4$ formation.[138] Suppression of *c*-$Li_{15}Si_4$ to improve capacity retention can be achieved by keeping the lithiation voltage above the onset of the *c*-$Li_{15}Si_4$ transition, typically above 50 mV.[79,132,135] Higher charging rates will also prevent crystallization to *c*-$Li_{15}Si_4$, and at sufficiently high rates, *c*-$Li_{15}Si_4$ will not form even if the cell is discharged to 0 V vs Li.[78,146,147] Higher charging rates are linked to larger overpotentials due to the IR drop caused by the cell's solution resistance. The use of a constant voltage (CV) step during lithiation, which is standard in commercial cells, also plays a large role in *c*-$Li_{15}Si_4$

formation by increasing the time the electrode is exposed to low voltages.[148] However, there is a potential limit above which *c*-$Li_{15}Si_4$ no longer forms using CV during lithiation as well, as has been demonstrated by Sayed et al.[149]

Recent work has taken advantage of stress-voltage because coupling to suppress the *c*-$Li_{15}Si_4$ phase, a process by which external stress lowers the lithiation voltage of the crystalline transition to *c*-$Li_{15}Si_4$, on the order of ~100-120 mV/GPa as measured in-situ in thin silicon films.[150] Suppressing the transition voltage by 100 mV/GPa can be sufficient to lower the transition below 0 V vs Li and avoid the appearance of the *c*-$Li_{15}Si_4$ phase entirely. The stress-voltage coupling effect has been effectively harnessed to suppress the *c*-$Li_{15}Si_4$ phase through the application of adhesive layers on thin films and capping layers on a variety of silicon morphologies.[77,78,138,149,151,152] One example of reducing *c*-$Li_{15}Si_4$ formation is demonstrate by Sayed et al. in Figure 2-5, in which a combination of tensile stress from adhesive layers and carbon capping layers, with the greatest suppression of the *c*-$Li_{15}Si_4$ phase found for alternating layers of 16 nm of Si and C sputtered onto a copper substrate.[149] Similarly, alloying silicon with inactive transition metals, can also create stress with the same effect of impeding *c*-$Li_{15}Si_4$ formation.[138,139,153–156] The hypothesis that alloying induces stress, thereby improving capacity retention by suppressing *c*-$Li_{15}Si_4$, has been applied to nano- and micron-sized silicon particle electrodes as well as thin films.[153,157,158] However, most, if not all previous studies that find a correlation between the suppression of *c*-$Li_{15}Si_4$ formation and capacity retention achieve this suppression through material changes that are convoluted with other beneficial effects. For instance, a capping layer on top of a Si film can induce clamping, thereby

preventing *c*-$Li_{15}Si_4$ by aforementioned stress-voltage coupling, while also minimizing reactivity with the electrolyte.[152,159–161] Prolonged ball-milling of Si with Mo and W, for instance, increases the proportion of silicide intermetallic and allegedly induces stress, but this processing also reduces the grain size of Si,[157,158] rendering its distribution more homogeneous. Rather than suppressing *c*-$Li_{15}Si_4$ formation by changing the electrode material, a test of the intrinsic effects of *c*-$Li_{15}Si_4$ on capacity retention would, ideally, involve inducing or preventing its formation by adjusting only the experimental conditions while keeping the electrode material constant.

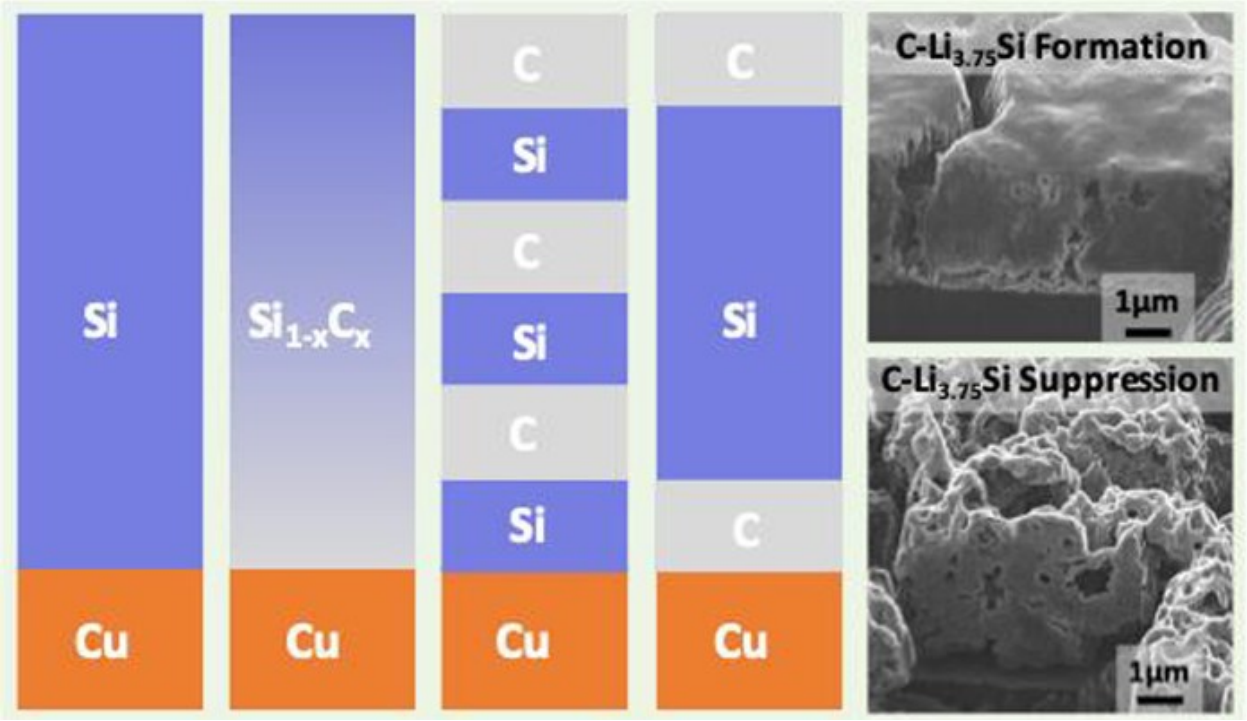

Figure 2-5. Suppression of the c-$Li_{15}Si_4$ phase leading to improved cycling of co-sputtered Si-C films. Reprinted with permission from reference 149. © 2019 American Chemical Society.

In the case of silicon nanoparticles, the role of particle size with regards to suppression of the *c*-$Li_{15}Si_4$ phase and improving capacity retention has been more contentious. It is now well established that nanoparticles below 60 nm form the *c*-$Li_{15}Si_4$ phase less readily than larger particles.[78,79,162] It is easy to confuse the fracture effects of the initial *c*-Si → *a*-Li_xSi transition, which also diminish with decreasing size, and those associated with formation of *c*-$Li_{15}Si_4$. The *c*-$Li_{15}Si_4$ phase is still, however, formed when fracture during the first lithiation is eliminated by using material below a critical size (~150 nm for *c*-Si nanoparticles and ~300 nm for *c*-Si nanowires).[106,145] The multiple impacts of particle size complicate experiments to determine the intrinsic effects of the *c*-$Li_{15}Si_4$ phase in silicon nanoparticles. For example, Gao et al. demonstrated that capacity loss with 120 nm Si nanoparticles was associated with formation of the *c*-$Li_{15}Si_4$ phase at 0 mV vs Li.[78] However, the difference in the quantity of *c*-$Li_{15}Si_4$ formed was correlated with the use of fluoroethylene carbonate as an electrolyte additive, which is known to be beneficial in and of itself.[36,49,70] Smaller 60 nm silicon nanoparticles did not show any formation of the *c*-$Li_{15}Si_4$ phase, even at 0 mV in ex-situ diffraction measurements on fully lithiated material.[78] It was assumed that the increased surface area compared to larger particles prevented the detection of the *c*-$Li_{15}Si_4$ phase because of the enhanced reactivity of *c*-$Li_{15}Si_4$ compared to *a*-Li_xSi as derived from static leakage current measurements.[78] Obrovac et al. also pointed out "polarization induced *c*-$Li_{15}Si_4$ suppression" in the case of nanosized electrodes, which showed no formation of the *c*-$Li_{15}Si_4$ phase near 0 V.[140] Schott et al. observed minimal loss of capacity retention associated with the appearance of *c*-$Li_{15}Si_4$ in silicon/graphite electrodes, when using 5-10 wt% silicon relative to graphite in a blended electrode.[79]

For the smallest nanoparticles, 30-50 nm, the influence of the *c*-$Li_{15}Si_4$ phase on capacity retention, tested by comparing the inclusion or exclusion of a CV step, was minimal. CC cycling consistently showed worse capacity retention, irrespective of cut-off voltage and particle size, which means the CV step likely helps to reduce the effects of increasing polarization.[79]

In the present work, we attempt to establish a generalization of the role of the formation of the *c*-$Li_{15}Si_4$ phase on capacity retention for three different Si morphologies: planar films, porous films, and commercially available Si nanoparticles. From the literature, the detrimental effect of *c*-$Li_{15}Si_4$ is well-established for thin films, but its effect is less clear for nanoparticles of silicon and porous films. We confirm that the *c*-$Li_{15}Si_4$ phase has a significant negative impact on capacity retention of planar films, but has only a small impact on capacity retention in silicon nanoparticles. The upper voltage limit for *c*-$Li_{15}Si_4$ formation is ~80 mV in Si nanoparticles and is dependent on size. We find evidence for higher reactivity of *c*-$Li_{15}Si_4$ with the electrolyte compared to *a*-Li_xSi by comparing cumulative irreversibilities associated with SEI build-up in silicon nanoparticle electrodes with different lithiation cut-off voltages.

2.2 Results and Discussion

2.2.1 Planar and porous Si films

Formation of *c*-$Li_{15}Si_4$ is believed to have an intrinsically detrimental effect on capacity retention in planar Si thin films, and possibly other Si morphologies.[77,78,138,149] As a starting point to test this hypothesis, two cycle life testing protocols are needed in which, using otherwise identical electrodes, *c*-$Li_{15}Si_4$ forms under one set of conditions but not the other. For clarity, we will differentiate between two cycling protocols, one in which lithiation is performed entirely at a constant current (CC), and one protocol in which a constant-current is used until a given voltage cutoff followed by a constant voltage step (CCCV). In a typical experiment with planar and porous films, lithiation was performed from 2 V – 5 mV, using a constant current of ~ 200 mA/g. Under CCCV protocol, the constant current step was followed by a voltage hold at 5 mV, which was held for 10 hours in planar and porous films unless otherwise noted.

Even when using CCCV, *c*-$Li_{15}Si_4$ does not form in the first 18 cycles in Si films on Cu.[138] Therefore, we hypothesized that for the planar 100 nm Si film on stainless steel, *c*-$Li_{15}Si_4$ would not form during CC lithiation, and a comparison between CC and CCCV lithiation would enable us to test the intrinsic detrimental effect of *c*-$Li_{15}Si_4$, or lack thereof. *c*-$Li_{15}Si_4$ is formed at a low lithiation potential of 5 mV,[77,149] but not at 25 mV,[77] or 50 mV vs Li,[149] and therefore, a lithiation potential of 5 mV was chosen for the CV step. The CV step was held for a fixed time of 2-10 hours rather than until a minimum current is reached,[77,138,149] to enable comparisons with porous Si films (*vide*

infra) that have higher surface area and, as a result, a higher rate of Li consumption by electrolyte decomposition.

Figure 2-6 shows voltage profiles and dQ/dV curves for a planar 100 nm Si thin film for the 1st and 50th cycles using CC, and the 50th cycle using CCCV protocol. Using only CC, the voltage profiles show a number of sloping regions during both lithiation and delithiation in both the 1st and 50th cycles. After 50 CCCV cycles, the lithiation profile looks very similar to the 50th CC cycle. However, the 10 hour potential hold at 5 mV causes a dramatic change in the delithiation voltage profile, and a wide plateau at ~0.4 V vs Li is now observed. The dQ/dV curves in Figure 2-6b are obtained by taking the reciprocal of the derivative of the voltage profile. Consequently, a plateau in a voltage profile (small dV) turns into a peak in the dQ/dV curve. The sloping voltage plateaus for all lithiation voltage profiles in Figure 2-6 as well as the delithiation profiles for the CC protocol are transformed into broad peaks in the dQ/dV plot. The flat delithiation profile for the 50th CCCV cycle on the other hand, is visible as a very high, sharp peak centered around 0.42 V which is characteristic of the *c*-$Li_{15}Si_4$ phase. The correlation between this peak in the dQ/dV plot and the *c*-$Li_{15}Si_4$ phase is well established using various techniques,[75,134] and confirmed again here through XRD as shown in the Supplementary Information (Figure 2-7). Small and emerging features are accentuated in a dQ/dV plot compared to a voltage profile. Therefore, observations about whether the *c*-$Li_{15}Si_4$ phase is formed and its onset of appearance will be made by referring to dQ/dV curves rather than voltage profiles.

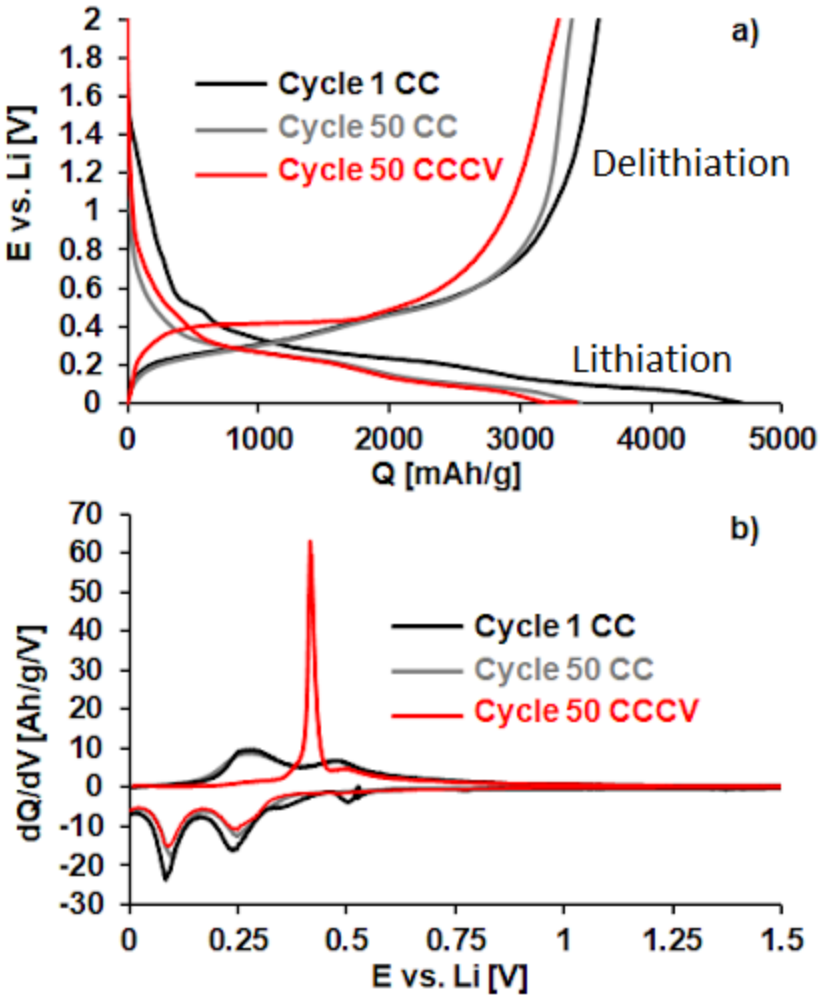

Figure 2-6. a) Voltage vs capacity plots for planar cells using CC or CCCV protocol after 1 or 50 cycles, as indicated. All cells were lithiated to 5 mV and delithiated to 2V using ~200 mA/g during cycle 1 and ~500 mA/g for subsequent cycles. b) dQ/dV graphs of the same cells, obtained by taking the inverse derivative of a). Peaks in dQ/dV correspond to plateaus in voltage vs capacity plots. Reprinted with permission from reference 163. © 2021 American Chemical Society.

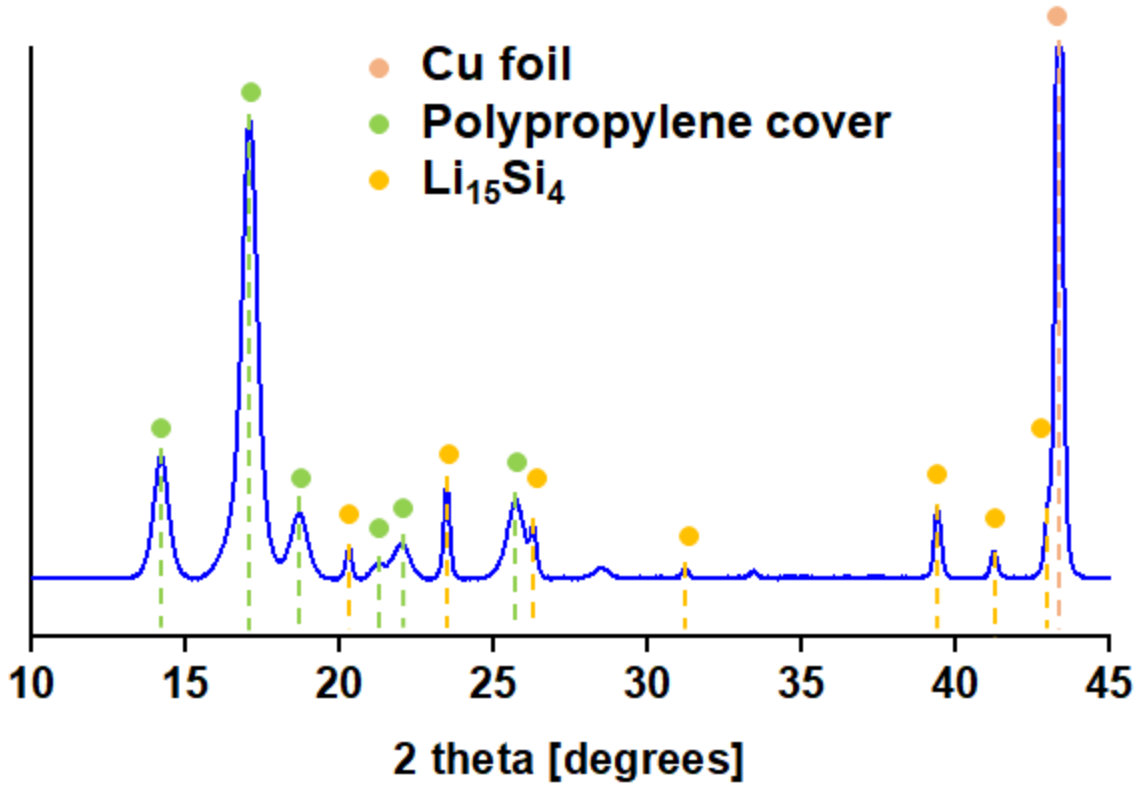

Figure 2-7. *XRD of fully lithiated silicon nanoparticle powder electrodes, identifying the* c-$Li_{15}Si_4$ *phase. Electrodes were lithiated to 5 mV and held at a constant voltage until ~20 mA/g. A polypropylene cover is present to prevent exposing* c-$Li_{15}Si_4$ *to air. Reprinted with permission from reference* 163. *© 2021 American Chemical Society.*

A comparison of the capacity retention with and without a CV step at 5 mV during lithiation and selected dQ/dV curves of the planar Si film is shown in Figure 2-8.

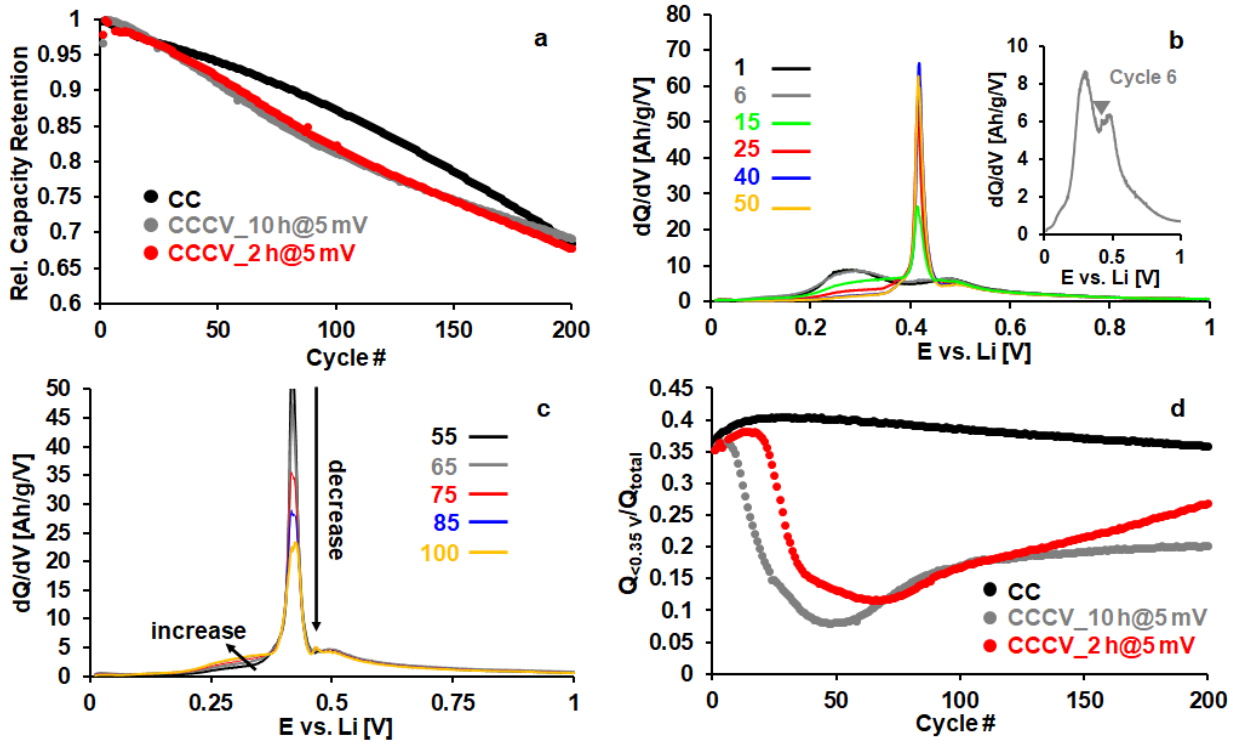

Figure 2-8. *a): Comparison of the delithiation capacity retention between CC and CCCV protocols for the planar Si film, b) and c): dQ/dV curves for selected cycles using the CCCV protocol at 5 mV lithiation cut-off voltage and a 10 h CV step. Cells were delithiated to 2 V vs Li using CC cycling only. Cycle 1 was performed at ~200 mA/g, and all subsequent cycles at ~500 mA/g. d): delithiation capacity below 0.35 V vs Li as a fraction of total delithiation capacity vs cycle number for cells with no CV step, and a voltage hold of 2 and 10 hours, as indicated. Reprinted with permission from reference* 163. *© 2021 American Chemical Society.*

When plotting the capacity retention, the maximum capacity for each film is set to 1. The planar silicon film retains 69 % of its maximum capacity after 200 CC cycles. Capacity degradation is clearly faster for the planar Si film when a CV step is applied compared to CC only, as can be seen in Figure 2-8a, but only between cycle 25 and 125. After this point, the rate of degradation slows and the relative capacity retention after 200 cycles is almost equal for the CC and CCCV protocols. Despite the long potential hold at 5 mV, no trace of *c*-$Li_{15}Si_4$ was observed until the 6th cycle when the CCCV protocol was used. The characteristic peak of *c*-$Li_{15}Si_4$ at ~0.42 V then grows with each cycle and reaches a maximum around cycle 40. The height of the first broad peak at ~0.30 V decreases in the same order, indicating an ever-larger fraction of *c*-$Li_{15}Si_4$, Figure 2-8b. Up to cycle 45, the peak height at 0.42 V is more or less constant and starts to decrease after that point. A closer look at the dQ/dV curves beyond cycle 50 in Figure 2-8c reveals a clear inverse correlation between the height of the *c*-$Li_{15}Si_4$ peak and that of the first amorphous peak centered at ~0.3 V. Figure 2-8d is a plot of the delithiation capacity below 0.35 V, a potential between the peaks of the amorphous and crystalline phase, as a fraction of the total delithiation capacity as a function of cycle number. There is a minimum around cycle 50, where only ~8 % of the total capacity is extracted below 0.35 V, indicating that the fraction of the active material that forms *c*-$Li_{15}Si_4$ is at its maximum there and declines afterwards. Around cycle 100, the amount of *c*-$Li_{15}Si_4$ becomes approximately constant. For planar Si films on Cu, the ratio between *c*-$Li_{15}Si_4$ peak area and the total delithiation capacity has been found to keep increasing, even as the total capacity rapidly declined.[77,138] The observed increase in peak area occurs despite the fact that lower capacities lead to a higher effective cycling

rate, which is known to suppress the formation of *c*-$Li_{15}Si_4$ through increased polarization. The difference in the onset of the increase and decay of the *c*-$Li_{15}Si_4$ peak area in different research works may be due to the choice of substrate, electrode design with and without adhesion, and protective layers or length of the CV step, which was fixed at 10 hours here rather than using a lower current cut-off of 20 mA/g.[138,149] For a shorter CV step of 2 hours instead of 10, the onset of the decline in the capacity below 0.35 V as well as its minimum are shifted by approximately 20 cycles, as per Figure 2-8d. The delithiation capacity below 0.35 V does not reach a plateau, as it does for a 10 h CV step, but instead keeps increasing, indicating an ever declining relative amount of *c*-$Li_{15}Si_4$. This result is likely caused by increasing overpotentials over the course of cycling due to SEI build-up, as well as a higher effective current density during the CC step as the total capacity declines, meaning that a longer CV step favors *c*-$Li_{15}Si_4$ formation. When we exclude the CV step during CC cycling, as shown in Figure 2-9, no trace of *c*-$Li_{15}Si_4$ was noted in the delithiation dQ/dV curves for any cycle. The relative delithiation capacity below 0.35 V is approximately 35-40 % when there is no formation of *c*-$Li_{15}Si_4$. Lower lithiation rates, such as those achieved during a constant voltage hold, are correlated with formation of the *c*-$Li_{15}Si_4$ phase as they increase the quantity of Li inserted within a given voltage window.

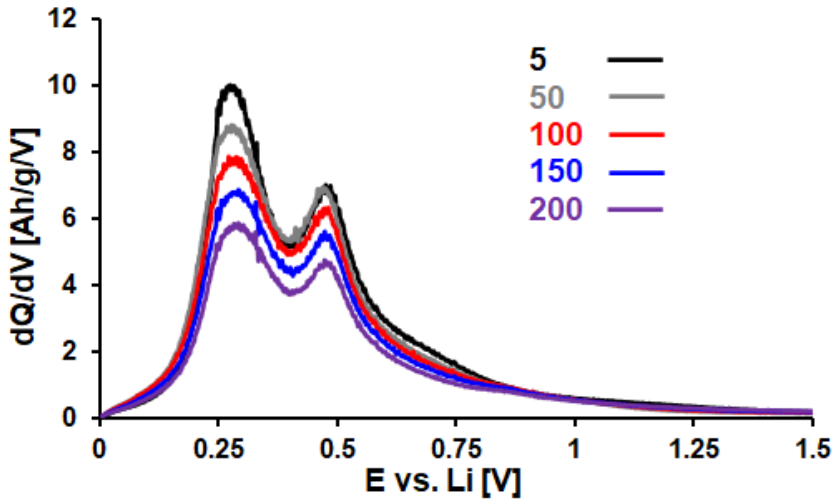

Figure 2-9. dQ/dV curves for selected cycles of the planar Si film using CC protocol with 5 mV lower lithiation cut-off voltage. Reprinted with permission from reference 163. © 2021 American Chemical Society.

Porous Si films can be viewed as intermediate between thin planar films and nanoparticle-based slurry electrodes. All of the active material is interconnected, as in any thin film, but the contact area with the rigid substrate is smaller compared to solid planar films. Due to their porosity, they share similarities with silicon nanoparticle electrodes, although they lack the supportive network of conductive carbon additive particles and binder that comprise such powder electrodes. SEM micrographs of porous silicon films are shown in Figure 2-10 for $Si_{0.75}Al_{0.25}$ (x = 0.75), and $Si_{0.30}Al_{0.70}$ (x = 0.30). Aluminum-silicon films were annealed for 3 hours at 200 – 300 °C under argon, followed by dealloying of aluminum using 1 M $KOH_{(aq)}$. The dealloying step was performed until production of $H_{2(g)}$ ceased, typically 1-2 minutes. At high Si content, the material appears as a planar film with pores up to 40 nm in diameter after dealloying. To contrast, the film with 70 at.% Al, $Si_{0.30}Al_{0.70}$, is more of a porous aggregate of Si nanoparticles with a primary particle size of less than 50 nm. Intermediate compositions

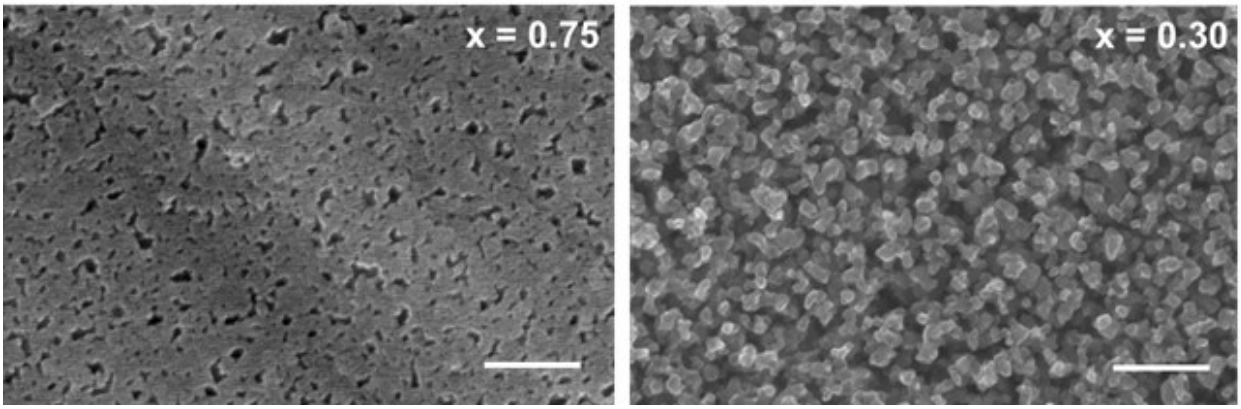

Figure 2-10. SEM micrographs of annealed $Si_{0.75}Al_{0.25}$ (x = 0.75), and $Si_{0.30}Al_{0.70}$ (x = 0.30) films after dealloying in 1 M (aq) KOH. Scale bars are 200 nm. Reprinted with permission from reference 163. © 2021 American Chemical Society.

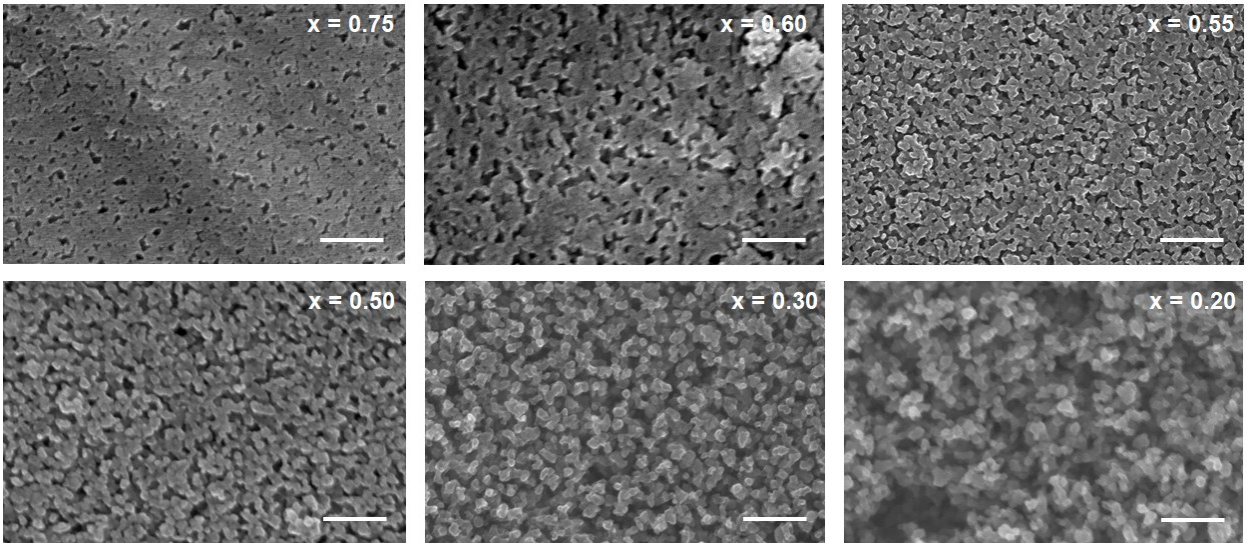

Figure 2-11. SEM micrographs of the porous thin Si film morphologies as the percentage of Si is decreased from 75 to 20 at.%. Scale bars are 200 nm. All films were annealed prior to dealloying. Reprinted with permission from reference 163. © 2021 American Chemical Society.

show a gradual progression between these two morphologies, as shown in Figure 2-11. For $Si_{0.20}Al_{0.80}$, the morphology is virtually identical to $Si_{0.30}Al_{0.70}$ with some deep cavities. Elemental Si films deposited at room-temperature are usually amorphous[138] and the same is true for co-deposited films as shown in the experimental secton. Subsequent annealing induces crystallization of the film and segregation of the Si and Al, resulting in the porous-slab and interconnected-particle morphologies shown in Figure 2-10 and Figure 2-11.

Without the annealing step, films with more than 50% Si cannot be dealloyed in 1 M (aq) KOH. Instead, the films slowly delaminate without any visible bubbling to indicate dissolution of Al. Dealloying the as-deposited $x = 0.30$ film results in a very different morphology as shown in Figure 2-12. Figure 2-13 shows that aside from XRD, crystallinity of Si is also easily deduced from the lithiation voltage profile. The first cycle was carried out in CC mode for all electrodes, to ensure all films had the same starting point when the CV step was initiated. Crystalline Si shows a long flat lithiation plateau at ~0.15 V vs Li, which is observed in the first cycle for the de-alloyed films, as per Figure 2-13b. Amorphous Si, on the other hand, shows a series of sloping plateaus, as observed for the planar Si film (Figure 2-13a) and for the de-alloyed films in the second cycle (Figure 2-13b).

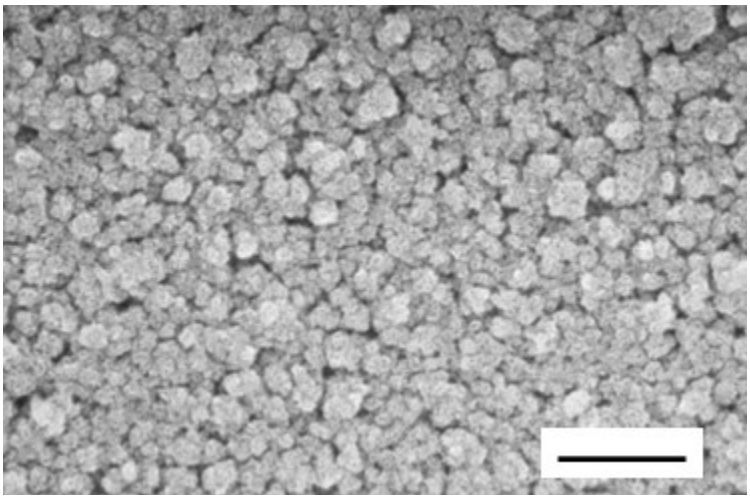

Figure 2-12. SEM micrograph of an as-deposited $Si_{0.30}Al_{0.70}$ film after dealloying in 1 M (aq) KOH. Scale bar is 200 nm. Reprinted with permission from reference 163. © 2021 American Chemical Society.

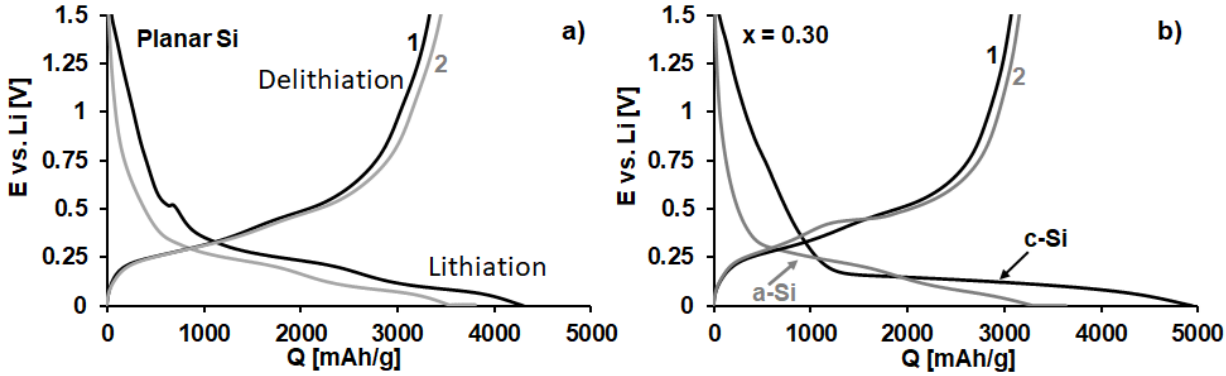

Figure 2-13. Voltage profiles for the first (CC) and second (CCCV) cycle for the planar Si film, a), and the porous x = 0.30 film, b). The plateau at ~0.15 V characteristic of c-Si is only observed for the porous film in the first cycle as an effect of the annealing step. Reprinted with permission from reference 163. © 2021 American Chemical Society.

Figure 2-14 depicts the relative capacity retention of the porous Si films with x = 0.75 and x = 0.30 with and without a CV step at 5 mV. Capacity retention in CC mode for all the porous Si films is shown in Figure 2-15. As can be seen, the capacity retention in CC mode is worse for all the porous films as compared to planar, possibly related to the much higher thickness of the porous films. The thickness of x = 0.30 is 293 nm, while x = 0.75 is 128 nm, as calculated in the experimental section. However, the goal here is not the optimization of the capacity retention of Si films by altering the morphology, but rather the investigation of the relationship of *c*-$Li_{15}Si_4$ and capacity retention for different Si morphologies (planar films, porous films and nanoparticles). For x = 0.75, the capacity is slightly higher after 200 cycles using the CV step, but the electrode cycled in CC mode only degrades faster in the beginning, whereas the CV step causes a relatively faster degradation beyond cycle 50. For x = 0.30 on the other hand, capacity retention is consistently *better* for CV as compared to CC and the difference in relative capacity retention becomes ever larger as cycling progresses. When the porous films are cycled using only constant current (Figure 2-16), no sign of the *c*-$Li_{15}Si_4$ phase is found for x = 0.30, as evidenced by the lack of a peak at 0.42 V. A small peak at ~0.42 V is visible in the first cycle for x = 0.75, and never from the second cycle onwards. The different behavior observed in the first cycle dQ/dV for the two porous films is an early indication that the Si morphology can have an impact on the formation of *c*-$Li_{15}Si_4$, but an additional influence of the different annealing temperature between the x = 0.30 and x = 0.75 films cannot be discounted.

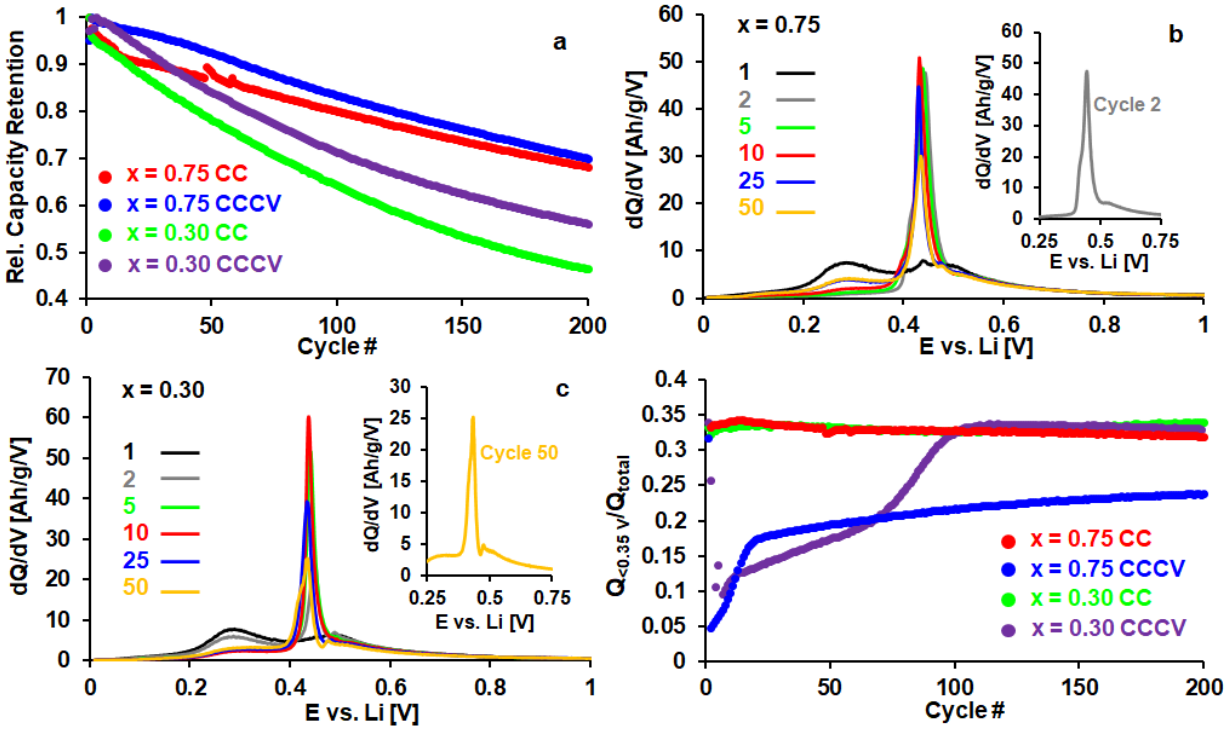

Figure 2-14. a): Relative delithiation capacity retention of x = 0.75 and x = 0.30 porous films comparing the CC and CCCV protocols at 5 mV lithiation cut-off voltage. Cycle 1 was performed at ~200 mA/g, and all subsequent cycles at ~500 mA/g. b): dQ/dV curves for selected cycles for the x = 0.75 porous film. c): dQ/dV curves for selected cycles for the x = 0.30 porous film. d): relative delithiation capacity below 0.35 V vs Li for x = 0.75 and x = 0.30 for CC and CCCV protocol. Reprinted with permission from reference 163. © 2021 American Chemical Society.

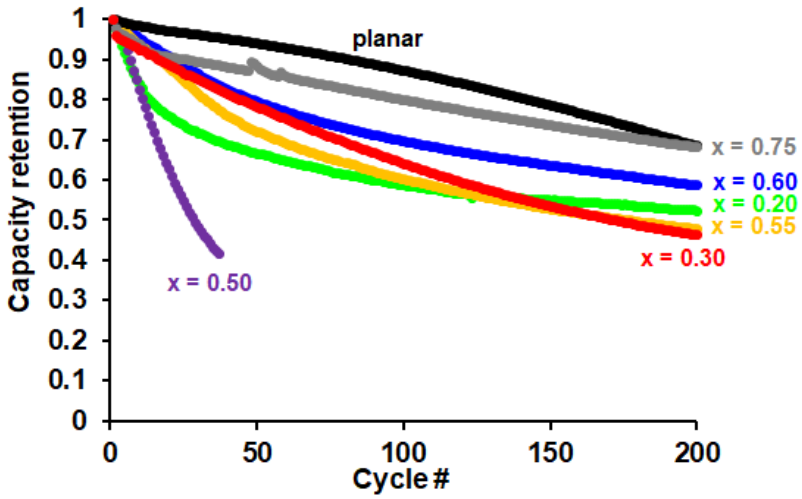

Figure 2-15. Relative delithiation capacity vs cycle number for planar and porous Si films in CC mode. Capacity retention in CC as well as CCCV mode is shown in Figure 2-8a for the planar film and Figure 2-14a for the x = 0.30 and x = 0.75 porous films. Reprinted with permission from reference 163. © 2021 American Chemical Society.

The dQ/dV curves for selected cycles of the x = 0.75 and x = 0.30 porous films using CCCV protocol are also shown in Figure 2-14. For x = 0.75, the amorphous peak around 0.30 V is lowest in the second cycle and therefore, the amount of *c*-$Li_{15}Si_4$ is the highest. The doublet structure of the *c*-$Li_{15}Si_4$ peak has also been observed for C/Si multilayers and Si-Ti alloy films,[138,149] although the spacing between the peaks is much less than the 40 mV separation we observed in Si/C multilayer structures.[149] Although the *c*-$Li_{15}Si_4$ peak *height* increases up to cycle 10, it also narrows and a broad peak around 0.30 V, characteristic of delithiation of amorphous Li_xSi, appears immediately after cycle 2 and starts to increase in height as well. The total capacity has in fact slightly degraded by cycle 10 (2%), so it appears that the tendency of the material to form *c*-$Li_{15}Si_4$ diminishes with cycling. A similar picture emerges for x = 0.30, where the peak at 0.42 V reaches a maximum height around the 8th cycle and where the peak at

0.30 V increases in height between cycle 10 and cycle 50, despite severe degradation of the total capacity, indicating a diminished tendency towards formation of *c*-$Li_{15}Si_4$ as well.

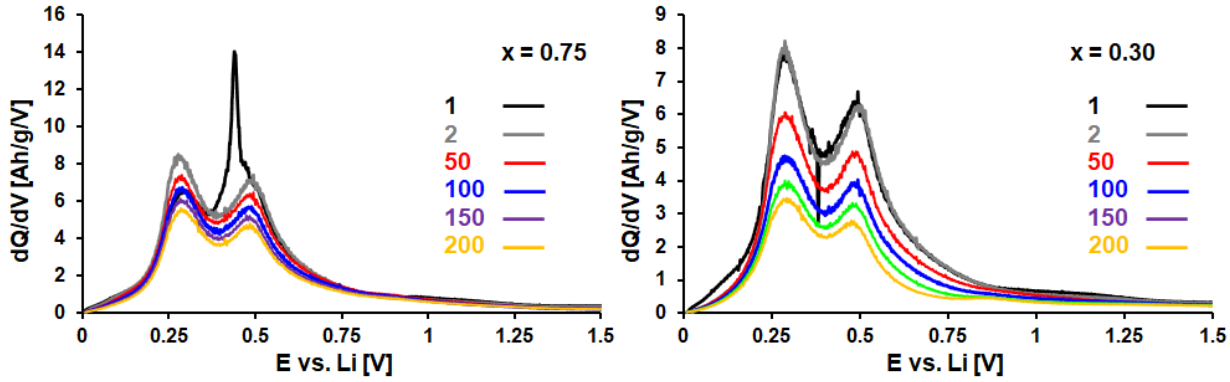

Figure 2-16. dQ/dV curves of dealloyed $Si_{0.75}Al_{0.25}$ and $Si_{0.30}Al_{0.70}$ films for selected cycles in CC mode. The corresponding dQ/dV curves for CCCV mode for the same films are shown in Figure 2-14. Reprinted with permission from reference 163. © 2021 American Chemical Society.

As with planar films, we plot the delithiation capacity below 0.35 V, as a percentage of the total delithiation capacity (Figure 2-14d). This representation helps to visualize that the *c*-$Li_{15}Si_4$ phase only appears in porous films when a CV step is included. When the fully lithiated material remains amorphous, the fraction of the total capacity prior to 0.35 V approaches 35%, as can be seen from Figure 2-14d. The minimal value for $Q_{<0.35}/Q_{total}$ is 0.05 in cycle 2 for x = 0.75 and 0.09 in cycle 7 for x = 0.30 and then slowly decreases with cycling. For x = 0.75, some amount of *c*-$Li_{15}Si_4$ phase is formed in all 200 cycles, whereas for x = 0.30 this contribution ends entirely around cycle 100.

Formation of *c*-$Li_{15}Si_4$ is strongly dependent on stress exerted by a rigid substrate or inert interlayers present in the film.[77,149] Here too, we demonstrated that in a planar Si film, the quantity of *c*-$Li_{15}Si_4$ reaches its maximum around cycle 40, which is believed to be correlated in large part with delamination.[77,138] The porous films are much less constrained by the substrate, resulting in a reversal of the trend, with both the absolute and relative amount of *c*-$Li_{15}Si_4$ diminishing with continued cycling. The decrease is partly due to degradation of the total capacity and partly due to greater overpotentials caused by a higher effective current density, as the capacity declines and SEI builds up. It is worth noting here that for $x = 0.30$ cycled in carbonate-based electrolyte, the peak potentials in the dQ/dV plot do not noticeably shift during cycling (Figure 2-17c), even though their height diminishes. That the amount of *c*-$Li_{15}Si_4$ is strongly correlated with the overpotential during lithiation is illustrated in Figure 2-17d. When 1 M LiOTf in DME is used as the electrolyte, the lithiation dQ/dV peaks are observed to shift to lower voltages and the *c*-$Li_{15}Si_4$ peak around 0.42 V diminishes very rapidly for the $x = 0.30$ porous film.

There are two other possible contributing factors to a decrease in *c*-$Li_{15}Si_4$ formation for the porous silicon films: 1) fracture of the Si particle network, as there are several studies showing an influence of particle size on the tendency to form *c*-$Li_{15}Si_4$ [78,79] and 2): mechanical stress, which might arise as void space is filled by SEI build up that constrains silicon upon expansion. Although thin capping layers have been shown to provide enough stress to suppress *c*-$Li_{15}Si_4$ formation,[138] the SEI is unlikely to be sufficiently mechanically robust to play this role on its own.

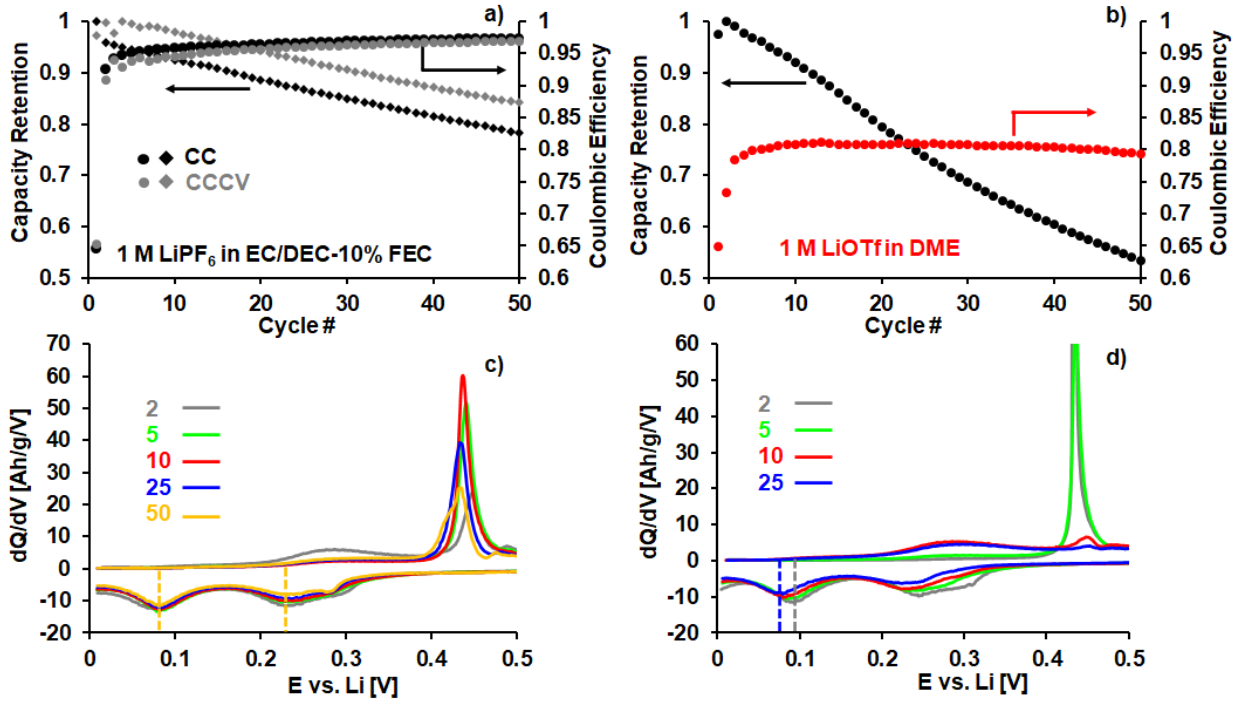

Figure 2-17. Capacity retention and Coulombic efficiency vs cycle number for porous x = 0.30 films in CC and CCCV mode in carbonate-based electrolyte (a) and CCCV mode in DME-based electrolyte (b). dQ/dV curves in carbonate-based electrolyte (c) and 1 M LiOTf in DME (d). Note that the lithiation dQ/dV peaks shift to lower voltages only in the DME-based electrolyte. Reprinted with permission from reference 163. © 2021 American Chemical Society.

The CE of the *x* = 0.30 porous film is typically only around 95% in the early cycles and is lower for the CCCV protocol compared to CC as shown in Figure 2-17a. A thick SEI layer makes material fracture hard to quantify, as seen in Figure 2-18. The influence of particle size on *c*-$Li_{15}Si_4$ formation will be discussed, vide infra, by comparing with commercial Si nanoparticles.

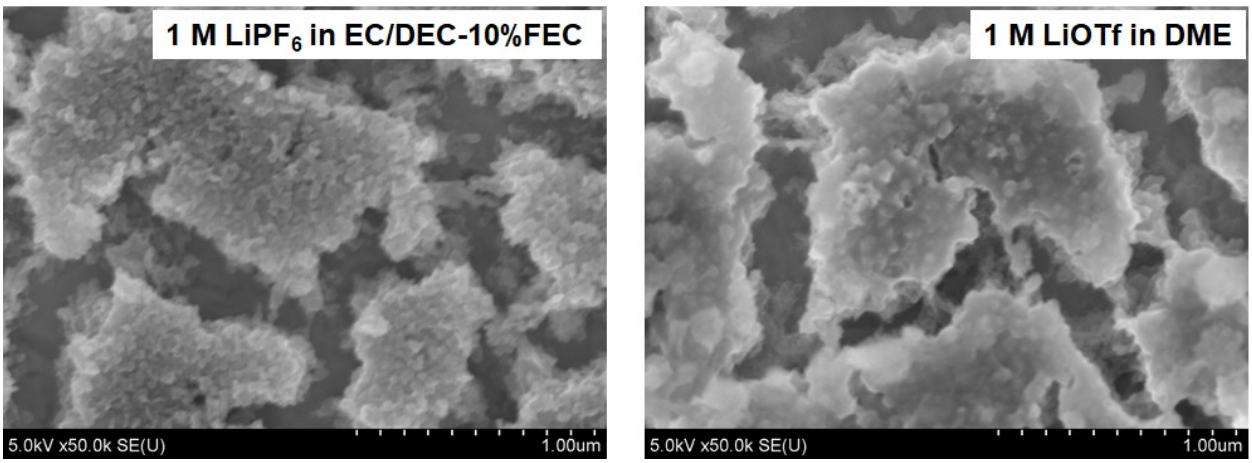

Figure 2-18. SEM micrographs after 6 cycles of porous x = 0.30 films in CCCV mode in carbonate-based electrolyte (left) and DME-based electrolyte (right). Reprinted with permission from reference 163. © 2021 American Chemical Society.

2.2.2 Silicon nanoparticles

~140 nm-diameter commercially available silicon nanoparticles with a 60 wt% loading in a slurry with carbon black (Super P) and lithium polyacrylic acid (LiPAA) as conductive additive and binder, respectively, were used to prepare composite silicon nanoparticle electrodes with an average mass loading of 0.5-0.6 mg/cm^2. An in depth discussion of commercial silicon nanoparticles is discussed in Section 3.3, but all particles used here are **Si-SA3**. We first examine cycling using a deep lithiation cut-off of 5 mV, terminating when the specific current reaches 20 mA/g. The CCCV protocol, terminating when a certain minimum specific current is reached, is usually implemented for safe practical charging of Li-ion batteries, and corresponds to lithiation of the anode active material.[149,164] Therefore, any (detrimental) effects of the CV step on the capacity retention of silicon nanoparticle electrodes are highly technologically relevant. We observe a sharp peak at 0.42 V vs Li in the dQ/dV plot for delithiation (Figure 2-19(a, b)), again, characteristic of the *c*-$Li_{15}Si_4$ phase, and corresponding to the plateau at the

same voltage in Figure 2-19(c, d). When the cell is held at the constant voltage of 5 mV, formation of *c*-$Li_{15}Si_4$ persists until the 50th cycle (Figure 2-19a). However, without a CV step, the dQ/dV indicates delithiation from *c*-$Li_{15}Si_4$ during the initial three cycles at 200 mA/g, but delithiation from amorphous lithium silicide as soon as the current is increased to 600 mA/g (Figure 2-19b). Despite the difference with respect to *c*-$Li_{15}Si_4$ formation, the effect on absolute capacity and capacity retention is comparatively minor. The silicon anodes suffer capacity loss at roughly the same rates whether a CV step is included or not (Figure 2-19e). The maximum capacity is higher when a constant voltage step is used for silicon nanoparticles, reaching 3474 mAh/g and 3354 mAh/g for the CCCV and CC cells, respectively (Figure 2-19f). However, after more than ~20 cycles, both cells approach the same capacity and continue to decay at the same rates.

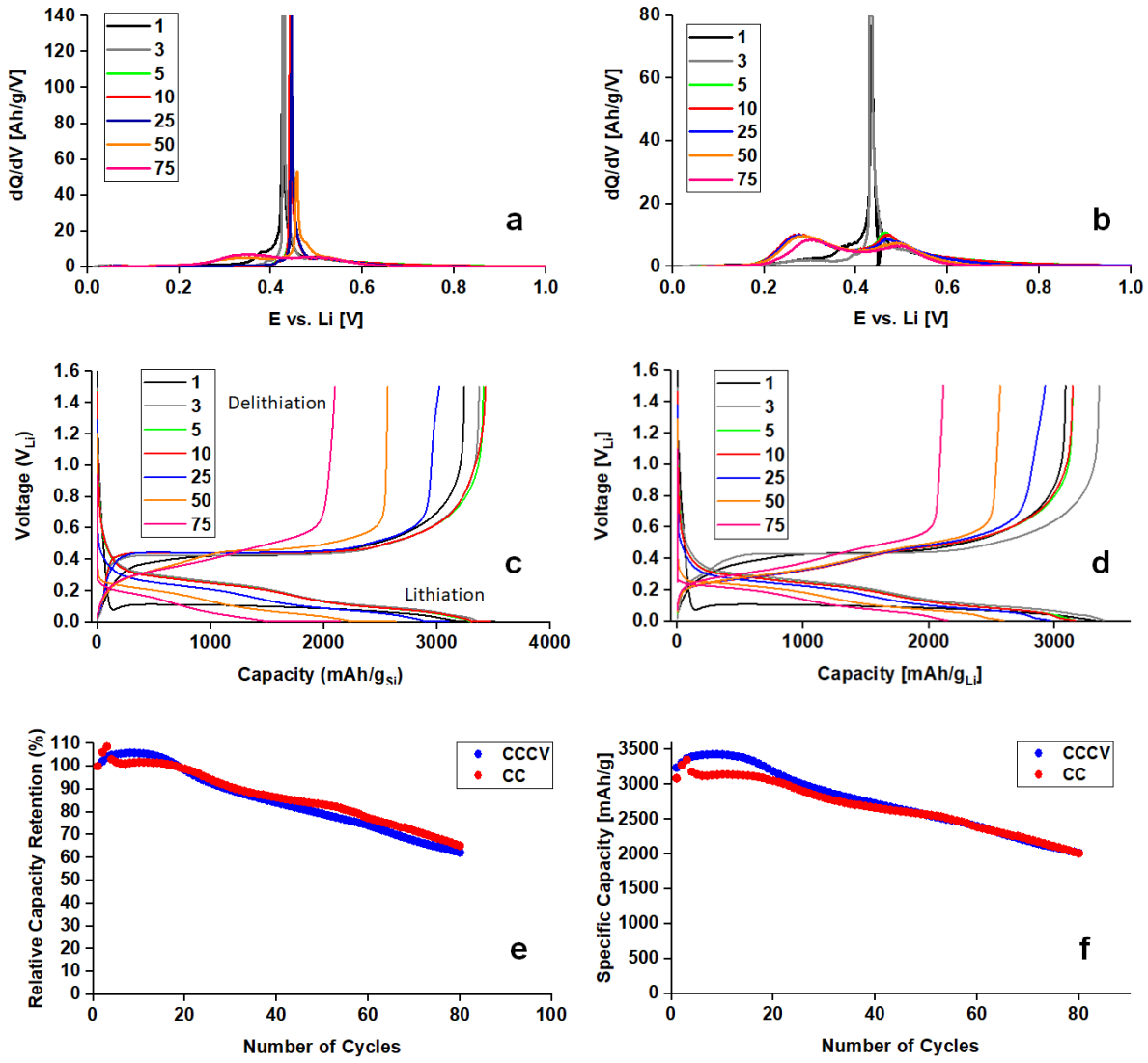

Figure 2-19. Delithiation dQ/dV curves (a,b), and charge/discharge curves (c,d) of silicon nanoparticle electrodes lithiated to a cut-off of 5 mV using CCCV (a,c) or CC (b,d) protocol. Plateaus in the delithiation curves correspond to peaks in the dQ/dV curves. All cells were delithiated to 1.5 V vs Li using CC cycling only. Cycles 1-3 were performed at 200 mA/g, and all subsequent cycles at 600 mA/g. Cycle number is indicated in the accompanying legends. Relative (e) and absolute (f) delithiation capacity of the same two cells, with CC or CCCV cycling indicated in the legend. Reprinted with permission from reference 163. © 2021 American Chemical Society.

50 mV is often considered the line above which *c*-$Li_{15}Si_4$ will not be formed in thin films,[141,149] although there are contrary examples with nanoparticles that show a dependence on size and charging rate.[79,135] Specifically, an increase of particle size above ~70 nm and a decrease of charging rates are associated with more formation of the *c*-$Li_{15}Si_4$ phase.[37,78,79] Accordingly, dQ/dV reveals the presence of *c*-$Li_{15}Si_4$ at 50 mV in the silicon nanoparticle electrodes studied here when a constant voltage step is used (Figure 2-20a). Without a constant voltage step, there is a small *c*-$Li_{15}Si_4$ peak at 0.42 V during the first cycle, and none in subsequent cycles. Including a CV step at 50 mV does come with an increase in capacity, especially in early cycles, going from a maximum capacity of 2809 mAh/g for CC to 3322 mAh/g for the CCCV protocol. Comparisons of capacity retention with and without a constant voltage step are complicated by a fairly large gain in capacity during the first ten cycles (Figure 2-20e). Such a rise indicates incomplete lithiation in the early steps, the cause of which is not clear, but may be related to an improvement of electrolyte access resulting from the expansion and contraction of the Si. Nonetheless, after ~25 cycles, both cells converge towards the same absolute capacity, and relative capacity loss is similar for both. The *c*-$Li_{15}Si_4$ phase still continues to form in the CCCV cell after 25 cycles, but does disappear more quickly with a 50 mV cut-off than with a 5 mV cut-off.

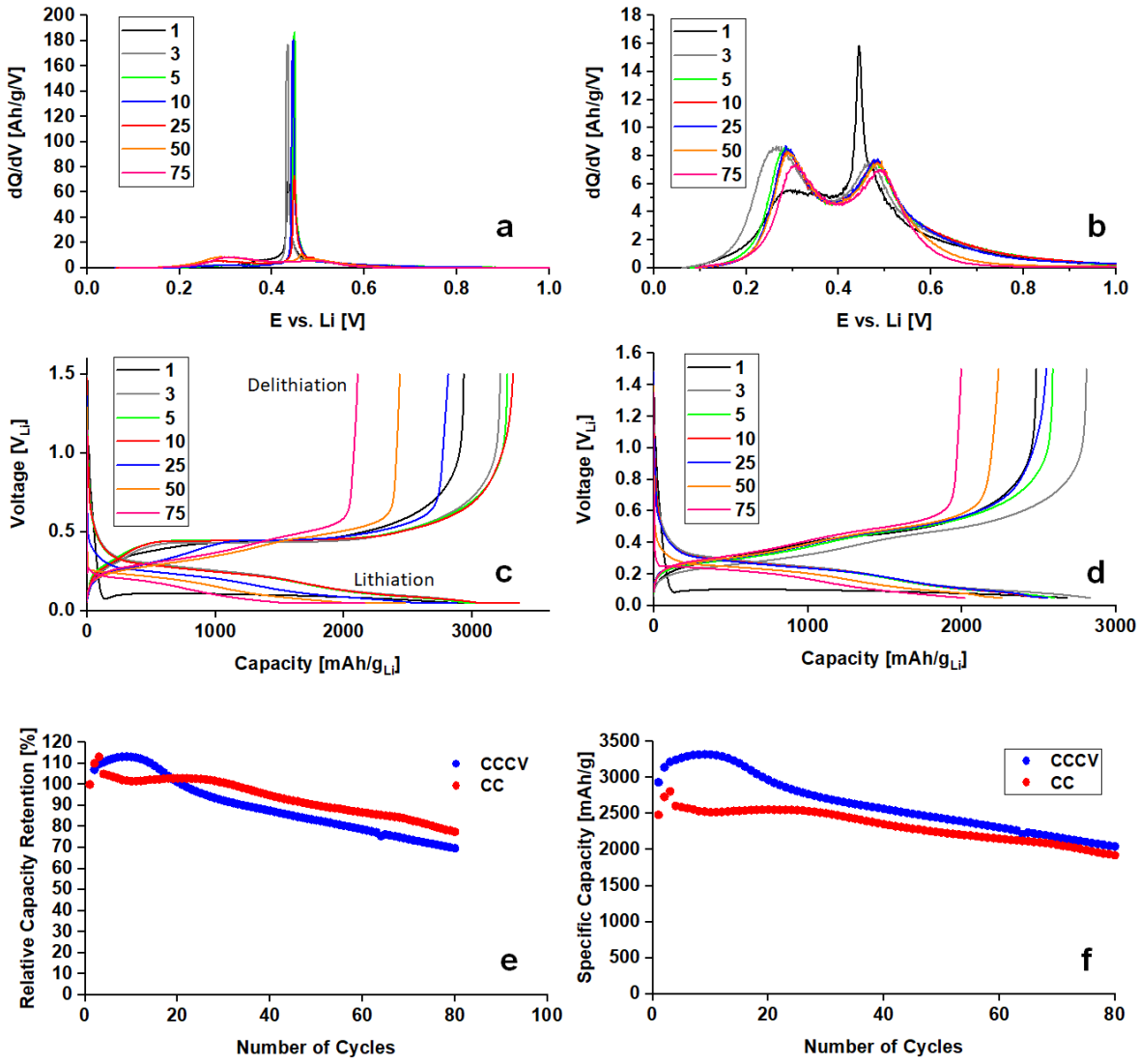

Figure 2-20. Delithiation dQ/dV curves (a,b), and charge/discharge curves (c,d) of silicon nanoparticle electrodes lithiated to a cut-off of 50 mV using CCCV (a,c) or CC (b,d) protocol. Plateaus in the delithiation curves correspond to peaks in the dQ/dV curves. All cells were delithiated to 1.5 V vs Li using CC cycling only. Cycles 1-3 were performed at 200 mA/g, and all subsequent cycles at 600 mA/g. Cycle number is indicated in the accompanying legends. Relative (e) and absolute (f) delithiation capacity of the same two cells, with CC or CCCV cycling indicated in the legend. Reprinted with permission from reference 163. © 2021 American Chemical Society.

As with porous films, we plot the delithiation capacity before 0.35 V as a percentage of the total delithiation capacity (Figure 2-21). Plotting delithiation in this manner helps to clarify the following results. First, we can observe the sharp contrast between cycling the 5 mV CC cells at 200 mA/g (cycles 1--3) and at 600 mA/g (cycles 4--80) (Figure 2-21a), in which *c*-$Li_{15}Si_4$ is present and stable at the lower current, but disappears immediately when higher currents are applied. Using relative delithiation capacity <0.35 V, we can also clearly see that *c*-$Li_{15}Si_4$ stops forming much earlier. With a cut-off of 5 mV and a CV step, the electrodes begin to derive more capacity from *a*-Li_xSi after ~40 cycles, with *c*-$Li_{15}Si_4$ playing a minimal role after ~60 cycles, see Figure 2-21a. However, when the cut-off voltage is increased to 50 mV, the transition away from the *c*-$Li_{15}Si_4$ phase starts and ends at ~20 and ~40 cycles, respectively (Figure 2-21b).

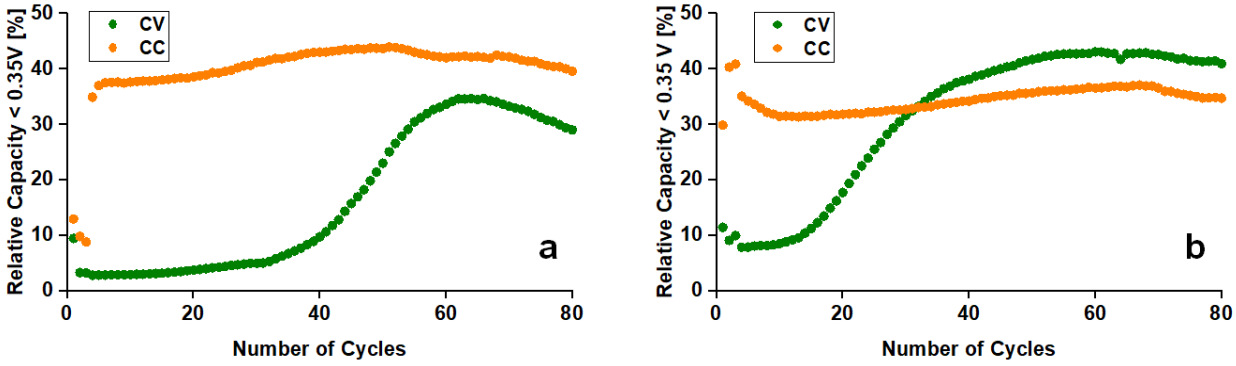

Figure 2-21. Percentage of delithiation capacity occurring below 0.35 V for silicon nanoparticle electrodes cycled to a lower cut-off of (a) 5 mV and (b) 50 mV vs Li for lithiation. CC and CCCV cycling are indicated in the accompanying legends. Cycles 1--3 were performed at 200 mA/g, and all subsequent cycles at 600 mA/g. All cells were delithiated to 1.5 V using CC protocol. Reprinted with permission from reference 163. © 2021 American Chemical Society.

For silicon nanoparticle slurry electrodes, we see evidence of increased polarization in the rightward shift in the delithiation dQ/dVs with increasing cycles, most easily seen in Figure 2-22. Increased polarization is observed using both CC and CCCV cycling, but is more pronounced with the CCCV step. Cycle 75 in the 5 mV CCCV cell, Figure 2-22a, has a peak at ~0.34 V characteristic of delithiation from *a*-Li_xSi, while the corresponding peak in 5 mV CC cells has a maximum at ~0.3 V (Figure 2-22b). This increase in polarization also has a visible effect using a cut-off voltage of 50 mV (Figure 2-22c, d). Both crystalline and amorphous delithiation peaks shift towards higher voltages, and by cycle 75 the peak maxima of *a*-Li_xSi are at 0.33 V and 0.31 V for CCCV and CC cycling respectively. Increased polarization also explains the gradual decline of the relative capacity below 0.35 V that is observed past cycle 65 in Figure 2-21a for CCCV cycling. The larger SEI build-up can also be observed by comparing Coulombic efficiency with and without the constant voltage step (Figure 2-23). Initial Coulombic efficiency is similar with and without a constant voltage step, but after increasing the rate to 600 mA/g, the Coulombic efficiency remains lower with a constant voltage step as more reaction with the electrolyte occurs at low voltages. The lower Coulombic efficiency during CCCV cycling indicates more SEI formation, which impedes full lithium recovery in the delithiation step.[165] More SEI formation is consistent with the larger rightward shifts in the dQ/dV plots, which suggest a higher overpotential (Figure 2-22).

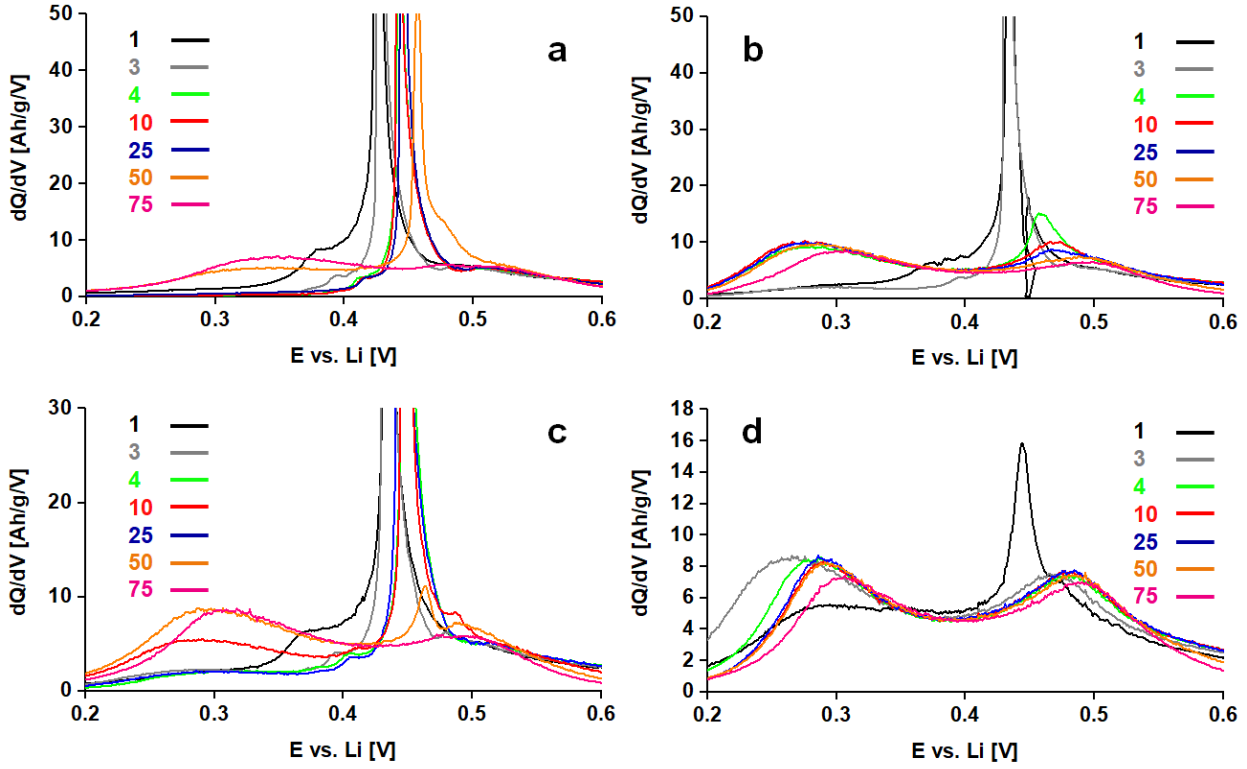

Figure 2-22. Close up of delithiation dQ/dV for silicon nanoparticle electrodes lithiated to 5 mV (a,b) and 50 mV (c,d) vs Li using CCCV (a,c) and CC (b,d) protocol. Cycle number is indicated in the accompanying legends. Cycles 1--3 were performed at 200 mA/g, and all subsequent cycles at 600 mA/g. All cells were delithiated to 1.5 V using CC protocol. Reprinted with permission from reference 163. © 2021 American Chemical Society.

We examine the effect of SEI on overpotential in a more quantitative fashion using the Galvanostatic Intermittent Titration Technique (GITT), in which the applied current is interrupted multiple times during charging and discharging, instead holding the cell at open-circuit voltage. The difference in potential between the applied current step and after the open-circuit voltage step enables the determination of overpotential in the

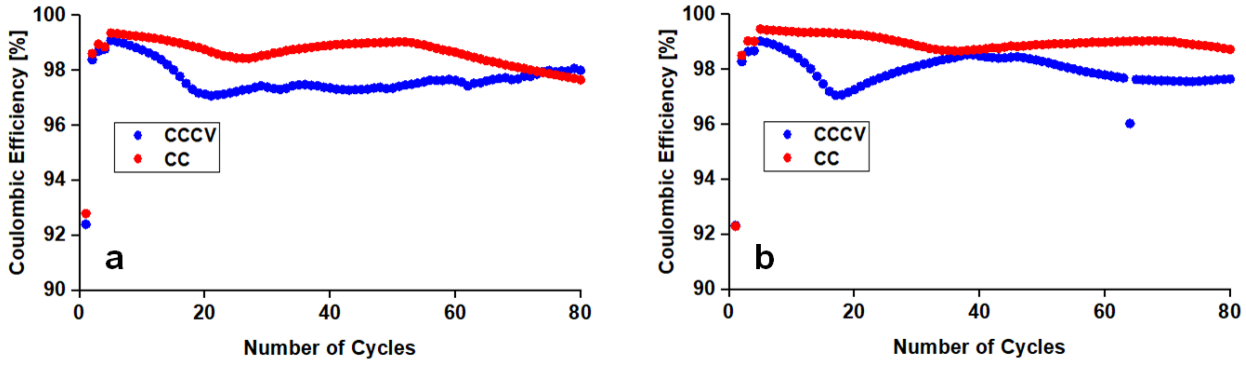

Figure 2-23. Coulombic efficiency of silicon nanoparticle electrodes cycled with a cut-off of (a) 5 mV and (b) 50 mV vs Li. CC or CCCV lithiation protocol is indicated in the legends. Cycles 1--3 were performed at 200 mA/g, and all subsequent cycles at 600 mA/g. All cells were delithiated to 1.5 V using CC protocol. Reprinted with permission from reference 163. © 2021 American Chemical Society.

porous films. Higher overpotentials will lead to less *c*-$Li_{15}Si_4$ formation in all cells. For simplicity, we compare 5 mV CCCV and 5 CC cycles among nanoparticle powder electrodes and porous electrodes with x = 0.30 Figure 2-24 performed using 30 minutes of charging/discharging followed by 2 hours of rest for cycles 2 and 12. The GITT data show a small increase in the overpotential beginning at ~0.45 V after 10 cycles of CCCV. 10 Cycles of CC protocol led to almost no change in overpotential until voltages above 0.7 V. As the cells approach 1.5 V, the cell is already far above the delithiation voltage of *c*-$Li_{15}Si_4$ (~0.42 V vs Li), so we are most concerned by the overpotential between 0.3 and 0.6 V, the range in which we see shifts to higher voltages in the dQ/dV plots (Figure 2-22). We also note that increased cycling does lead to greater overpotentials in x = 0.30 the porous films (Figure 2-24), despite the lack of an observable rightward shift in the dQ/dVs. The increase in overpotential at higher

voltages may be exacerbated by connectivity issues in porous films, which lack binder and conductive additive. No meaningful difference between CCCV and CC cycling is observable in the GITT for *x* = 0.30 porous films.

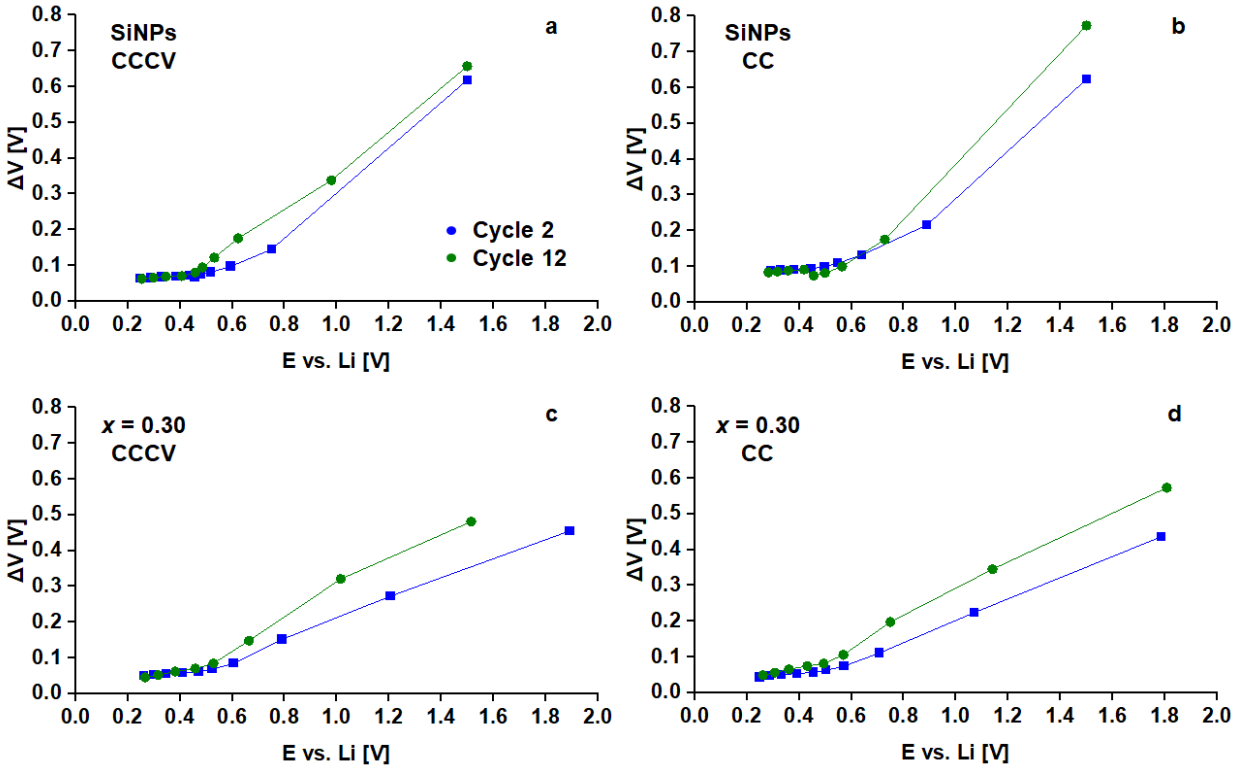

Figure 2-24. *Overpotential (ΔV) of (a,b) silicon nanoparticle electrodes and (c,d)* x = *0.30 porous films vs delithiation voltage using GITT at cycle 2 and 12, as indicated. Cells were lithiated to 5 mV using CCCV (a,c) and CC (b,d). All cells used ~200 mA/g for cycle 1. Silicon nanoparticle powder electrodes used 600 mA/g for cycles 2-12 and delithiated to 1.5 V.* x = *0.30 electrodes used 500 mA/g for cycles 2-12 and delithiated to 2 V. All GITT tests were performed using the higher current, with a 30 minute applied current and 2 hour rest period. Reprinted with permission from reference* 163. *© 2021 American Chemical Society.*

When we re-examine the question of how much impact *c*-$Li_{15}Si_4$ formation has on capacity retention in silicon nanoparticles, the strongest evidence comes from a comparison of the cells cycled with a 5 mV lithiation cut-off in CC and CCCV modes. We find that both absolute capacity and capacity retention are very similar between the two protocols, despite the fact that crystallization stops after the 3rd cycle without a constant voltage step and persists until almost the 60th cycle, with a constant voltage step included. This result shows that formation of the *c*-$Li_{15}Si_4$ phase plays a smaller role in capacity fade for silicon nanoparticle electrodes, as compared to planar films. The x = 0.30 porous film and silicon nanoparticles are very similar in terms of Si morphology as well as capacity retention, despite the porous films not having binder or conductive additive, showing a possible influence of the smaller size of the Si particles in the porous film. To summarize, at 5 mV lithiation cut-off voltage, planar films, porous films and silicon nanoparticle electrodes behave similarly, only showing formation of *c*-$Li_{15}Si_4$ under a CCCV protocol and remaining for the most part amorphous with a CC protocol. However, only the planar film showed a profoundly negative impact on capacity retention, due to formation of the *c*-$Li_{15}Si_4$ phase.

The capacity of the silicon nanoparticle electrodes degrades most rapidly between cycles 15 and 25 (as shown earlier in Figure 2-19e). Approximately half of the capacity degradation between cycles 10 and 60 occurs before the relative delithiation capacity below 0.35 V begins to decrease past cycle 30. From cycle 30 onwards, the degradation rate is more or less constant. Polarization begins to increase around cycle 25 as well, see Figure 2-22a, coinciding with the decline in the amount of *c*-$Li_{15}Si_4$ as evidenced by the decrease in relative delithiation capacity below 0.35 V. Post-mortem

analyses using SEM and X-ray photoelectron spectroscopy (XPS) were carried out on silicon nanoparticle-based electrodes cycled to 5 and 50 mV with and without a CV step. Cells were disassembled using a gas driven decrimper from the MTI corporation under an argon atmosphere. All Si electrodes were manually separated from other cell components and washed with dimethyl carbonate (DMC) before sample preparation. SEM samples were transported under argon and exposed to air for ~30 s prior to data acquisition. The SEM micrographs of the silicon nanoparticle-based electrodes are challenging to interpret as they comprise binder and Super P carbon black, but the initial morphology of the Si particles appears to be better preserved with a CC protocol than using CCCV (Figure 2-25). XPS samples were loaded under argon atmosphere and transported without exposure to air. XPS of cells after 10 cycles shows a relatively similar SEI composition, and no further quantification was pursued (Figure 2-26). 5 mV CCCV cells do stand out for having C-Li bonds present, although this may be a result of small amounts of lithium reacting with carbon black at lower voltages.

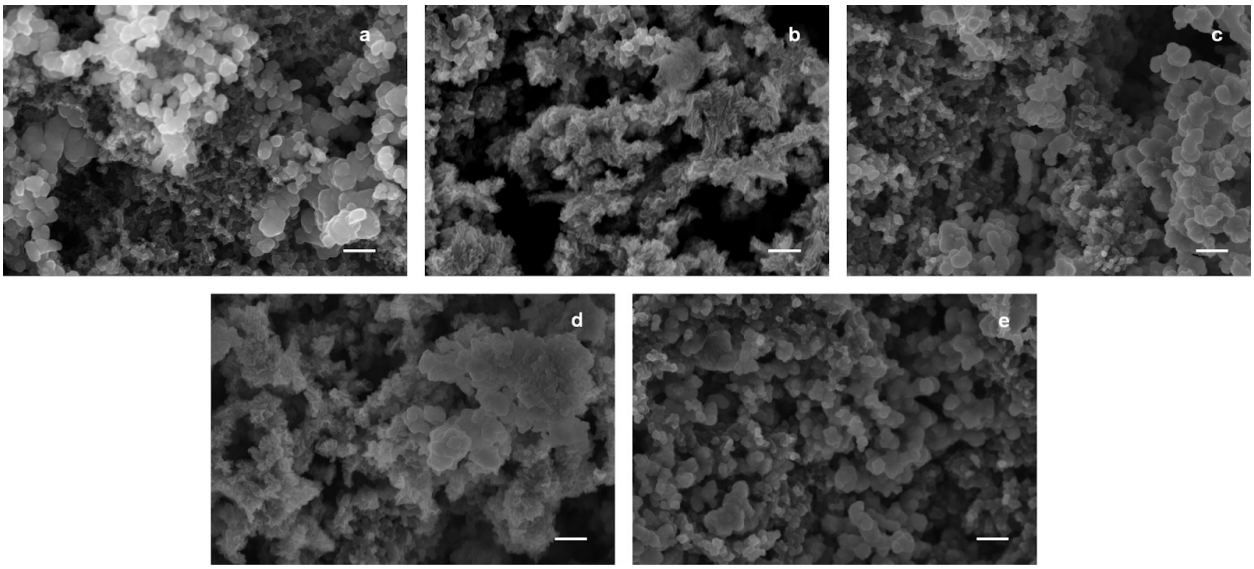

Figure 2-25. SEM micrographs of silicon nanoparticle electrodes a) prior to cycling and after 10 cycles using b) 5 mV CCCV, c) 5 mV CC, d) 50 mV CCCV, and e) 50 mV CC lithiation protocols. Scale bars are 400 nm. Larger particles are silicon, while smaller particles are Super-P carbon black. Cycles 1-3 used 200 mA/g, while cycles 4-10 used 600 mA/g. All cells were delithiated to 1.5 mV vs Li. Reprinted with permission from reference 163. © 2021 American Chemical Society.

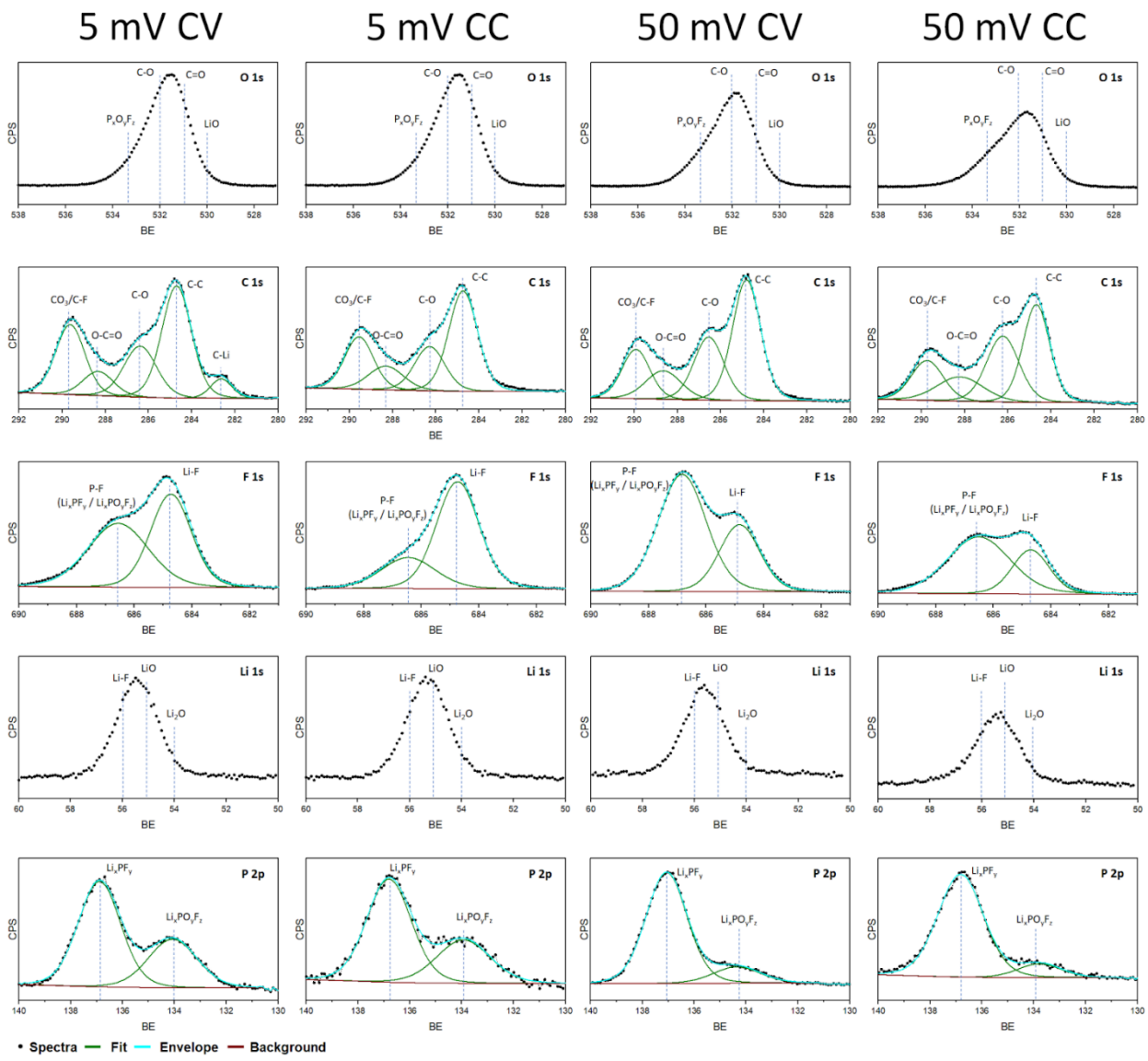

Figure 2-26. X-ray photoelectron spectroscopy (XPS) spectra of silicon nanoparticle powder electrodes cycled 10 times using 5 mV or 50 mV cutoffs and CCCV or CC charging protocol, as indicated. The cutoff of 5 mV changes relative peak heights most notably in the F 1s and P 2p spectra, indicating different ratios of SEI products from $LiPF_6$ decomposition. Reprinted with permission from reference 163. © 2021 American Chemical Society.

At 50 mV, the effects of the constant voltage step on capacity retention are harder to interpret because of a larger change in absolute capacity. However, a similar trend is observed as the rates of capacity decay trend towards the same levels over the long run (Figure 2-20e), even as the amount of *c*-$Li_{15}Si_4$ continues to decline in the CCCV cells. The differences between silicon nanoparticles and porous silicon at 50 mV deserve some note, because while silicon nanoparticles do show formation of *c*-$Li_{15}Si_4$ at 50 mV using a constant voltage step (Figure 2-20a), the *x* = 0.30 porous silicon film remains amorphous (Figure 2-27). Previous studies have typically found that *c*-$Li_{15}Si_4$ does not form50m above 50 mV in thin films[75,149] and nanoparticles smaller than ~70 nm.[78,79] Therefore, our results can be viewed as further confirmation that particle size influences the tendency to form *c*-$Li_{15}Si_4$. The larger commercial silicon nanoparticles (around 140 nm on average, see experimental) still fully crystallize at 50 mV CCCV, while the porous films, in which silicon has a size below ~50 nm (Figure 2-10), do not.

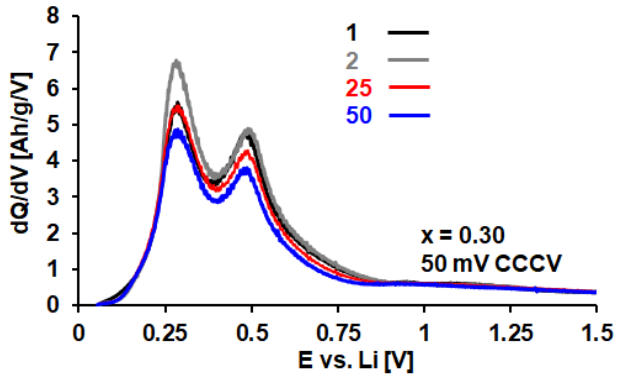

Figure 2-27. dQ/dV curves for selected cycles of x = 0.30 film using CCCV protocol with 50 mV lower lithiation cut-off voltage. Contrary to the 5 mV cut-off shown in Figure 2-14, there is no evidence for c-$Li_{15}Si_4$ in this case. Reprinted with permission from reference 163. © 2021 American Chemical Society.

Previous work has cited a wide range of voltages above which the *c*-$Li_{15}Si_4$ phase does not form in silicon, including 50 mV,[140,141,166] 60 mV,[78] and 70 mV,[17] for a wide variety of Si morphologies and lithiation rates. More recently, Tornheim et al. showed that formation of the *c*-$Li_{15}Si_4$ phase in silicon nanoparticles can occur with cut-off voltages as high as 90 mV, but they only reported the first cycle.[135] As with Tornheim et al., our work applies to silicon nanoparticles >100 nm in size in which the first cycle is run at ~200 mA/g or lower. As shown in Figure 2-28, we observe *c*-$Li_{15}Si_4$ for >25 cycles at 60 mV, 10 cycles at 70 mV, and only on the first cycle for 80 mV, when a constant voltage step is included. There is no evidence of the *c*-$Li_{15}Si_4$ phase at a lithiation cut-off of 90 mV. The relative delithiation capacity below 0.35 V is shown in Figure 2-29. The comparison of cycling with various cut-off voltages in Figure 2-30a can be used as another control for the effect of crystallization on capacity retention, although the differences in the absolute capacity probably play a role as well. The cells with a 5 mV cut-off do clearly show the most rapid loss of relative capacity, and there is a clear relationship between higher cut-off voltages and larger capacity retention at the end of 80 cycles. The nature of this capacity drop is uneven, however, with only minor differences in the rate of capacity loss after cycle 30. The results for 70, 80 and 90 mV in particular, show a very strong similarity. When we look at the absolute capacity in Figure 2-30b, we see that all cut-off voltages tend to converge at a similar absolute capacity in the long run. These findings are relevant for research into capacity limited anode cycling, which has been proposed as a potential compromise to mitigate capacity loss given the relatively high capacity of anodes compared to transition metal oxide cathodes for lithium-ion batteries.[146,167]

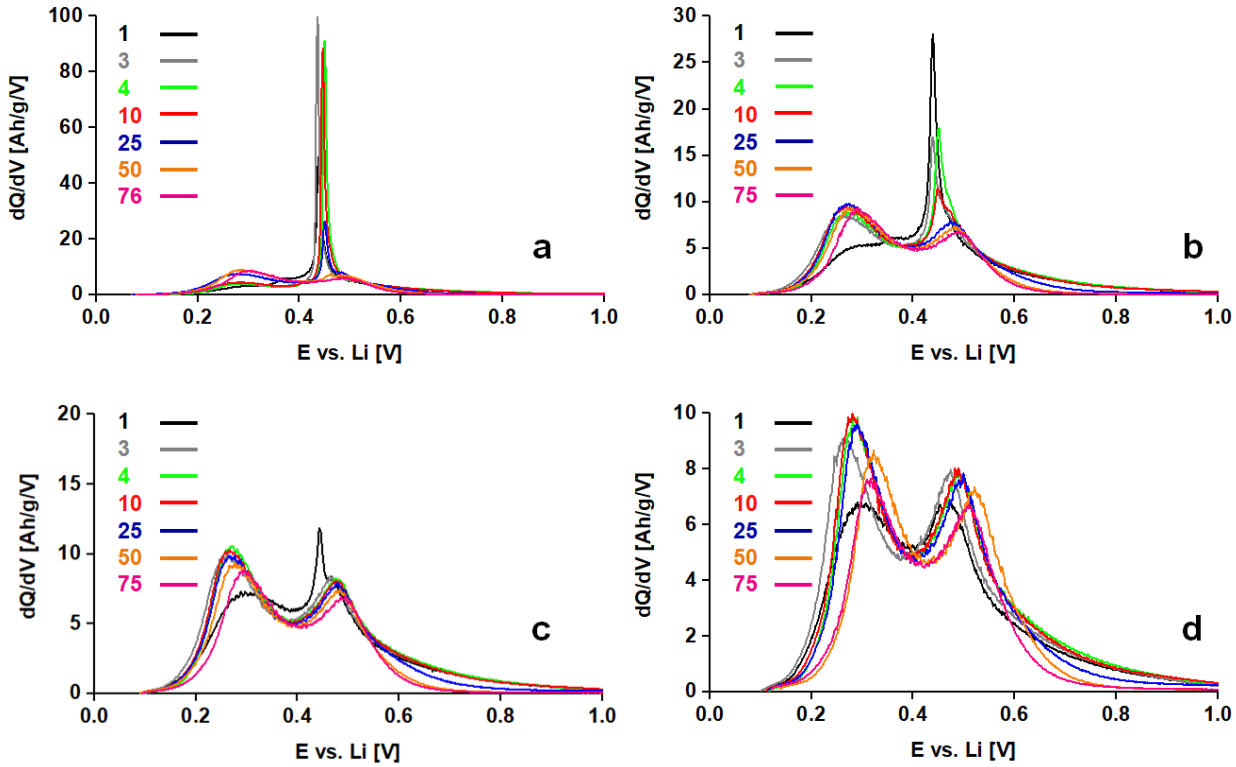

Figure 2-28. Delithiation dQ/dV for silicon nanoparticle electrodes cycled with a voltage cutoff of 60 mV (a), 70 mV (b), 80 mV (c), and 90 mV (d). Cycle number is indicated in the accompanying legends. All cycles used CCCV cycling, with a charging rate of 200 mA/g for cycles 1--3 and 600 mA/g for all subsequent cycles. All cells were delithiated to 1.5 V using CC protocol. Reprinted with permission from reference 163. © 2021 American Chemical Society.

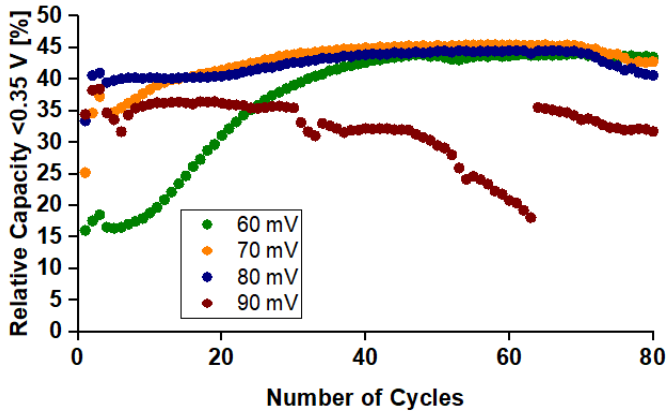

Figure 2-29. Percentage of delithiation capacity occurring below 0.35V for silicon nanoparticle electrodes cycled under CCCV conditions to varying lithiation cutoffs: 60 mV (green), 70 mV (yellow), 80 mV (blue), 90 mV (red). Cycles 1-3 were performed at 200 mA/g, and all subsequent cycles at 600 mA/g. All cells were delithiated to 1.5 V using CC protocol. Reprinted with permission from reference 163. © 2021 American Chemical Society.

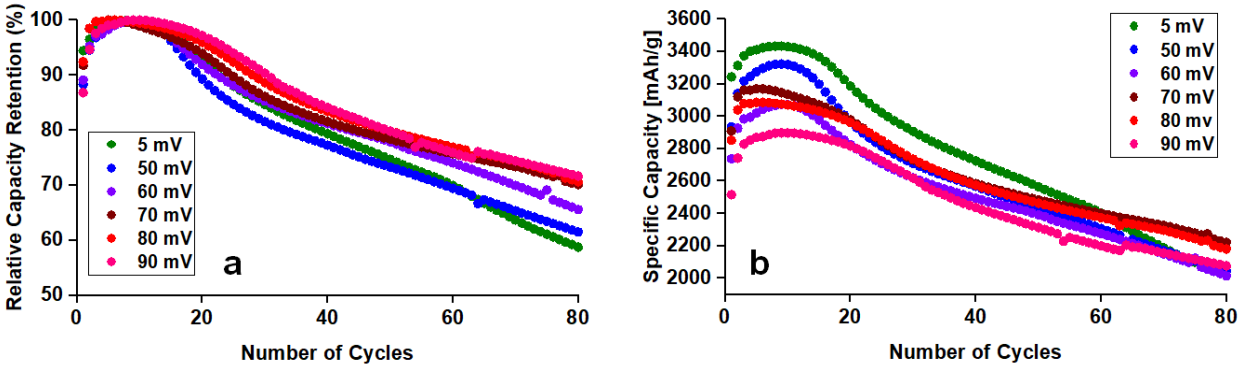

Figure 2-30. *Absolute (a) and relative (b) delithiation capacity of silicon nanoparticle electrodes cycled to cut-off voltages from 5--90 mV, as indicated in the accompanying legends. All cycles used CCCV cycling during lithiation, with a charging rate of 200 mA/g for cycles 1--3 and 600 mA/g for all subsequent cycles. All cells were delithiated to 1.5 V using CC protocol. Reprinted with permission from reference* 163. *© 2021 American Chemical Society.*

The biggest change in the amount of *c*-$Li_{15}Si_4$ and how long *c*-$Li_{15}Si_4$ formation persists, occurs between a 60 and 80 mV lithiation cut-off voltage (Figure 2-28a,c). The lower lithiation plateau of graphite is within the 60--80 mV vs Li voltage interval,[168,169] meaning that in graphite/Si blended electrodes,[170] Si will be exposed to potentials that are right on the cusp of inducing formation of *c*-$Li_{15}Si_4$, depending on size. As suggested by Gao et al., *c*-$Li_{15}Si_4$ may be particularly reactive with the electrolyte,[78] which should result in lower Coulombic efficiency when larger amounts of *c*-$Li_{15}Si_4$ are formed. Figure 2-31 shows a comparison of the cumulative losses due to SEI formation/electrolyte decomposition up to cycle 50, after which little to no *c*-$Li_{15}Si_4$ was observed for 50 mV cut-off. Similar to our previous work,[149] a comparison of irreversible capacities resulting from SEI formation (RIC_{SEI}) can be made by calculating the difference between lithiation capacity at cycle $n + 1$, ${Q_{n+1}}^{Delith}$ and delivered delithiation capacity of the previous cycle, ${Q_n}^{Delith}$, relative to the delithiation capacity at the nth cycle according to the following equation.[37]

$$\sum \mathrm{RIC_{SEI}} = \sum_{n=1}^{N} \frac{Q_{n+1}^{\mathrm{Lith}} - Q_n^{\mathrm{Delith}}}{Q_n^{\mathrm{Delith}}}$$

The advantage of using the equation for RIC_{SEI} rather than the Coulombic efficiency shown in Figure 32 is that it compares the lithiation capacity to the delitiation capacity in the previous cycle. Any lithiation in excess of the previous delithiation capacity can only be ascribed to electrolyte decomposition, especially when the delithiation capacity is itself degrading. There is a consistent downward trend in RIC_{SEI} with increasing cut-off voltage, coinciding with a downward trend in the amount and

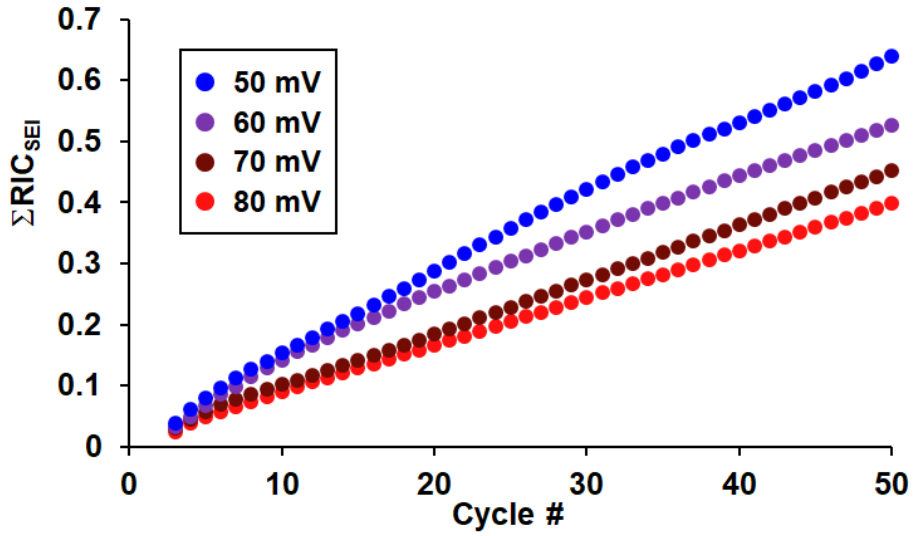

Figure 2-31. Cumulative irreversibilities due to electrolyte decomposition for silicon nanoparticle electrodes cycled with a lithiation voltage cutoff of 50--80 mV using CCCV protocol, as indicated in the legend. Cycles 1--3 were performed at a charging rate of 200 mA/g with subsequent cycles at 600 mA/g. All cells were delithiated to 1.5 V using CC protocol. Reprinted with permission from reference 163. © 2021 American Chemical Society.

persistence of the *c*-$Li_{15}Si_4$ phase. This comparison strongly suggests that *c*-$Li_{15}Si_4$ indeed has higher reactivity towards electrolyte decomposition compared to *a*-Li_xSi. The reactivity of the *c*-$Li_{15}Si_4$ phase with carbonate-based electrolytes is understood to be initiated by removal of Li+ from the lattice via a self-discharge process,[134,141] after which reactions between the electrolyte and charge-imbalanced phase proceed through ring-opening mechanisms to form carbonates, for example.[49] Small differences in the average Coulombic efficiency can have a profound influence on the cycle life of balanced Li-ion full cells.[17]

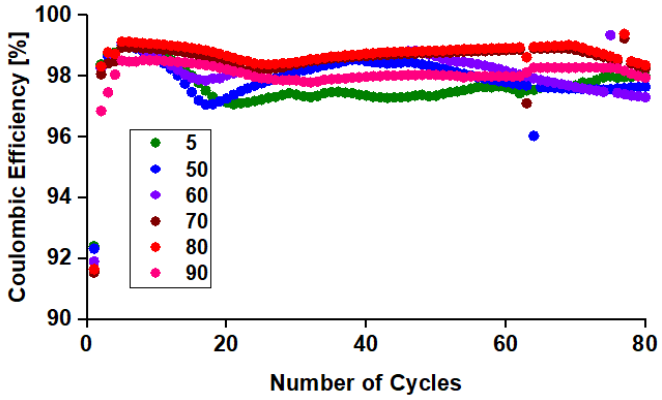

Figure 2-32. Coulombic efficiency of silicon nanoparticle electrodes cycled with a constant voltage step and a lithiation cut-off of 5--90 mV vs Li, as indicated in the legend. Cycles 1--3 were performed at 200 mA/g, and all subsequent cycles at 600 mA/g. All cells were delithiated to 1.5 V using CC protocol. *Reprinted with permission from reference* 163*. © 2021 American Chemical Society.*

2.3 Conclusions

The intrinsic role of *c*-$Li_{15}Si_4$ on capacity retention was examined by modulating the cycling conditions to either maximize or minimize its formation for three distinct Si morphologies: planar films, porous films and silicon nanoparticle electrodes. For all three morphologies, CC cycling minimized the quantity of *c*-$Li_{15}Si_4$ formed, and was only observed for Si nanoparticles at a 5 mV lithiation cut-off and in the first cycle for the porous film with $x = 0.75$. Inclusion of a CV step at 5 mV vs Li eventually induced the formation of *c*-$Li_{15}Si_4$ in every case. For planar films, the quantity of *c*-$Li_{15}Si_4$ first increases up to ~40 cycles, likely related to release of stress by partial delamination, and then decreases until ~80 cycles and remains constant thereafter. In porous Si films as well as Si nanoparticle electrodes, the amount of *c*-$Li_{15}Si_4$ continuously decreases

both absolutely and relatively with respect to the total delithiation capacity as cycling progresses. A causal and general link between the formation of the *c*-$Li_{15}Si_4$ phase and capacity decay was not obvious, as capacity decayed at a similar rate for the CC and CCCV protocols in silicon nanoparticle electrodes and porous Si films. This observation is in contrast to the planar thin films, where it was found that *c*-$Li_{15}Si_4$ is linked to an increased rate of capacity decay between cycle 25 and 125, most likely due to delamination. While the *c*-$Li_{15}Si_4$ phase is not associated with greater capacity loss in porous films and silicon nanoparticles, it does seem to be more reactive with the electrolyte. The larger buildup of SEI is observable both through larger polarization of the electrode and lower Coulombic efficiencies using the CCCV protocol as compared to CC. Increasing the cut-off voltage in CCCV cycling resulted in both lower amounts of *c*-$Li_{15}Si_4$ and lower cumulative irreversibilities due to electrolyte decomposition, confirming the increased reactivity of *c*-$Li_{15}Si_4$ compared to an amorphous phase. Since there is no conclusive evidence for enhanced capacity degradation, the higher reactivity with the electrolyte should be regarded as the main reason for avoiding formation of the *c*-$Li_{15}Si_4$ phase.

2.4 Experimental section

2.4.1 Materials and reagents

Silicon nanoparticles (140 nm, SEM), polyacrylic acid (PAA, Mv = 450,000), lithium hydroxide (LiOH, reagent grade, >98%), 1 M $LiPF_6$ in 1:1 ethylene carbonate:diethyl carbonate (EC/DEC, 1/1 v/v%, battery grade), fluoroethylene carbonate (FEC, >99%, anhydrous), and lithium triflate (LiOTf, 99.995% trace metals

basis) were purchased from Sigma-Aldrich. Potassium hydroxide (KOH, certified ACS), dimethoxyethane (DME, Acros Organics, 99.5%, Max. 0.005% H_2O, grade: extra dry over molecular sieves) was purchased from Fisher. DME was extracted from the stock bottle with a needle and syringe inside an Ar-filled glovebox and passed through a 0.2 um syringe filter prior to use. Carbon black (Super-P) was purchased from Timcal. The silicon nanoparticles were purchased as <100 nm from the manufacturer, but analysis with SEM imaging reveals that most particles are larger than 100 nm, with an average size on the order of ~140 nm, as shown in Figure 3.25. For more discussion of silicon nanoparticles (**Si-SA3)**, see Section 3.3.

2.4.2 Preparation of planar and porous Si films

Stainless steel discs (MTI) of 0.5 mm thickness and 15.5 mm diameter were ultrasonically cleaned with dichloromethane, MilliQ water and isopropanol, and used as substrates. Elemental Si and co-deposited Si-Al films were prepared using an Orion 8 confocal sputtering system (AJA International) in sputter-up configuration. The deposition rate for Si was 0.22 – 0.28 A/s, at 75 – 100 W DC power with an Ar pressure of 4 mTorr. For the co-deposited films, the Al deposition rate was adjusted to yield compositions from 25 to 80 at.% Al.

To obtain a porous Si film, the co-deposited films were annealed on a hotplate under Ar for 3 hours at 200 – 300 °C: For films with ≤ 60 at.% Si, 200 °C was enough to induce crystallization of the Si and phase separation between the Si and Al as determined by XRD, Figure 2-33. For higher Si content, 300 °C was used. To dissolve the Al and obtain a porous Si film, the steel disks were immersed in 1 M (aq) KOH

solution at room temperature for 1--2 min until hydrogen bubbling stopped. After dealloying, to remove residual KOH and water, the films were immersed in MilliQ water (twice) and isopropanol for 5 min each, dried in a vacuum oven at 60 °C for 1 hour and cooled to room temperature while under vacuum. Stainless steel substrates were chosen instead of Cu foil,[138,149] because extensive delamination was observed during KOH immersion in the case of the Cu foil.

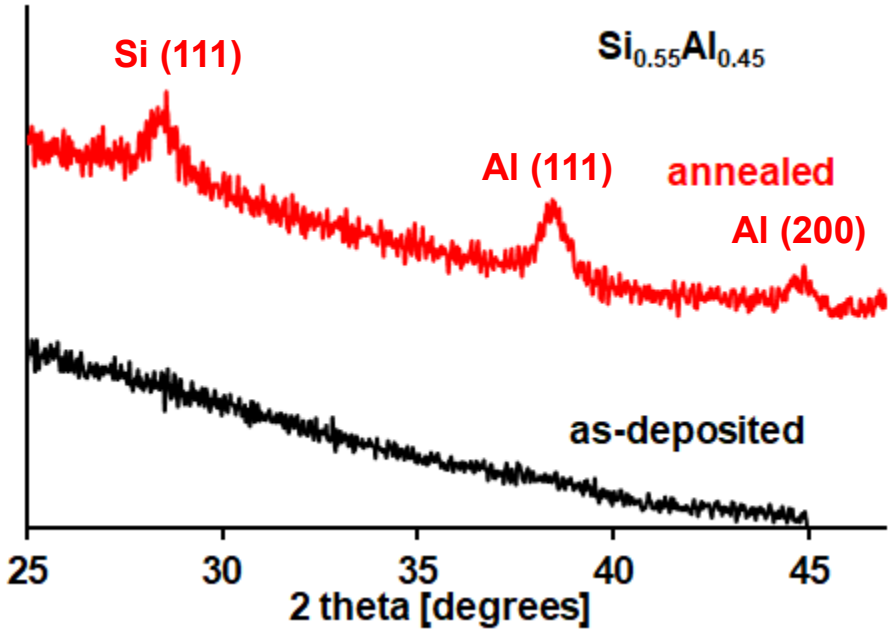

Figure 2-33. XRD patterns of an $Si_{0.55}Al_{0.45}$ film in the as-deposited state, and after annealing, for 2 hours at 300 deg °C under Ar. The total thickness is 168 nm according to the formula above. Si was chosen as the substrate because of the strong X-ray fluorescence background generated by a stainless steel substrate. Reprinted with permission from reference 163. © 2021 American Chemical Society.

Using this method, we were able to produce porous silicon films between 20 and 75 at.% Si. Constant-current cycling data will be presented for all compositions. The influence of a constant-voltage step is tested for 30 and 75 at.% Si only.

The nominal thickness of planar elemental Si films was 100 nm. The co-deposited films had identical areal Si as compared to the loading of the planar films, resulting in an as-deposited thickness greater than 100 nm, as calculated as follows:

$$t(\mathrm{nm}) = 100\left(1 + \frac{1-x}{x} \times \frac{V_{m,Al}}{V_{m,Si}}\right)$$

with *x* as the atomic fraction of Si in the film, and $V_{m,Al}$ and $V_{m,Si}$ as the molar volumes of Al and Si, which are 10.00 and 12.06 cm^3/mol, respectively. A film with 30 at.% Si has an estimated as-deposited thickness of 293 nm according to the above formula.

Samples were weighed using a Mettler Toledo XP6U balance with a readability of 0.1 µg and a repeatability of 0.4 µg. The weight of a 100 nm planar Si film was typically around 40 µg. For the co-deposited films, the weight of Si was calculated assuming the composition of the as-deposited film was nominal. Using these weights and assuming complete removal of the Al during immersion in the aqueous KOH, the specific delithiation capacity in the first cycle was typically 3000--3200 mAh/g_{Si} for the porous films.

2.4.3 Preparation of nanoparticle slurries

LiPAA binder was prepared by titrating PAA in water with saturated LiOH (aq), creating an 8.5% LiPAA solution at pH ≈ 7.2. Slurries were prepared in an ambient atmosphere by combining as-purchased Si nanoparticles, Super-P and LiPAA in a 60:20:20 ratio and diluting with water (~160% mass of slurry). The solution was mixed in

a planetary ball mill (Changsha Tianchuang Powder Technology Co.) at 500 rpm for 60 min total in a polyurethane vial using zirconia balls (~500% mass of slurry). The slurry was cast onto copper foil (battery grade, 10 μm) at a cast height of 100 μm and dried overnight at 120 °C under vacuum. Discs were punched with a diameter of 15 mm, then dried again at 120 °C under vacuum for 16 hours and brought directly under inert atmosphere. The average mass loading was 0.5-0.6 mg/cm^2.

2.4.4 Electrochemical measurements

1 M $LiPF_6$ in EC/DEC (1/1 v/v%) with 10 wt% FEC additive and 1 M LiOTf in DME were used as electrolytes, with 45 μL total used per cell. All cells were assembled under an argon atmosphere using 2032 coin cells with Li metal foil (MTI) counter electrodes and single layer polypropylene--polyethylene--polypropylene separators with a porosity of 39% (Celgard™ 2325). Cycle life testing was performed on an Arbin BT2000 battery testing system at 25 °C using two different lithiation protocols; constant-current (CC) and constant-current-constant-voltage (CCCV). In CC measurements, electrodes were lithiated to the cut-off voltage using only a constant current. For the CCCV protocol, lithiation was held at the low cut-off voltage until a prescribed end-point. Delithiation was performed only using constant-current using the same specific current as for lithiation. Planar and porous films were cycled between 0.005 and 2 V vs Li at a current density of 4 μA/cm^2 for the first cycle and 10 μA/cm^2 for subsequent cycles, corresponding to ~200 and 500 mA/g, respectively. Constant voltage steps were held for 10 hours in porous and planar films. For nanoparticle-based electrodes, cells were cycled between 1.5 V and various low cut-offs using 200 mA/g for the initial 3 cycles with 600 mA/g for all subsequent cycles. Constant voltage steps were held until

reaching a current of 20 mA/g. Galvanostatic Intermittent Titration Technique (GITT) was performed using a Biologic BCS-805 battery testing system, with an applied current for 30 min followed by a 2 h relaxation step. Applied currents were ~500 mA/g for porous films and 600 mA/g for nanoparticle electrodes. Cycling for GITT involved 1 cycle at 200 mA/g for either porous films or nanoparticle electrodes, with all following cycles at 500 mA/g or 600 mA/g, respectively.

2.4.5 Characterization

Scanning electron microscopy (SEM) was carried out using a Zeiss Sigma Field Emission SEM at accelerating voltages of 5-10 kV. X-ray photoelectron spectroscopy (XPS) was performed using a Kratos AXIS ultra spectrometer with monochromatic Al Kα radiation (hv = 1486.6 eV, spot size ~100 μm) and under ultrahigh vacuum (10^{-9} Torr). X-ray diffraction (XRD) analysis was performed with an AXS diffractometer (Bruker, d8 Discover, Madison, WI) using Cu Kα radiation (1.5406 Å). The *c*-$Li_{15}Si_4$ phase was induced by lithiating a cell to 5 mV with a CV hold until the current reached 20 mA/g. *c*-$Li_{15}Si_4$ was protected from air by using a sealed polypropylene cover. All post-mortem anodes were washed three times with dimethyl carbonate (DMC) in an inert atmosphere prior to analysis.

Chapter 3 Silicon surface functionalization for artificial solid electrolyte interphase (a-SEI)

3.1 Introduction

The surface of the silicon itself has a large impact on the cycling of silicon anodes in lithium ion batteries. First, upon cycling and lithium insertion and deinsertion, silicon reacts with electrolyte and solvent to form SEI, and the nature of the silicon surface impacts the products of those reactions.[94] Second, any oxides of silicon at these interfaces will be reduced by lithium during the first lithiation cycle to irreversibly form inorganic products, leading to irreversible capacity loss as the lithium is consumed.[171] Third, in silicon nanoparticle (SiNP) electrodes, the silicon surface interacts with binder material and conductive carbon additive(s), maintaining electrical contact with the cell throughout expansion and contraction in the anode.[172] A change of functional groups on the surface of silicon will play a critical role with respect to continuity of electrical connections and hence conductivity between the silicon and other slurry components.

Commercial silicon nanoparticles produced via plasma synthesis contain a substantial amount of native oxide, typically a layer around 1-3 nm thick.[94] The oxide layer may interact with the binder to maintain electrode cohesion,[97] but reduces theoretical specific capacity because it is not electrochemically active.[173,174] The silicon oxide layer reacts with lithium in the first cycle and is reduced to Si(0), leading to the production of Li_2O or lithium silicates in the SEI.[175] In addition, the SiO_x layer diminishes electron transport rates[176] and suppresses silicon expansion in small (<50 nm) nanowires,[177] especially with thicker layers of SiO_x. Above a thickness of 3 nm, lithium

diffusion is inhibited and SiO_x can cause non-uniform lithium deposition through pinholes (Figure 3-1).[94]

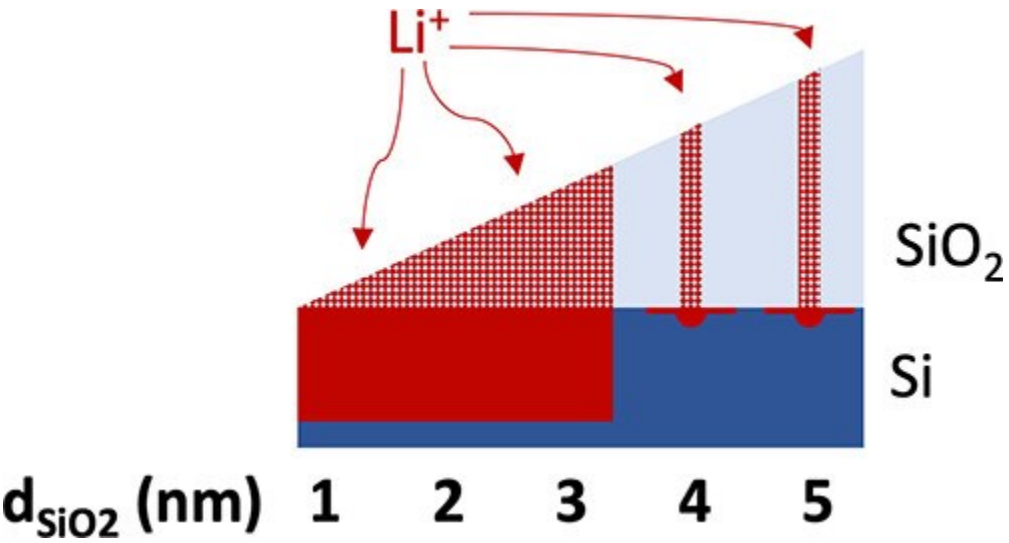

Figure 3-1. *Lithium diffusion through a silicon oxide layer of various thicknesses. Reprinted with permission from reference* 94. *© 2021 American Chemical Society.*

Early work suggested that removing the SiO_x layer on silicon could increase the specific capacity of silicon particles and lead to improved Coulombic efficiency (CE) during the first cycles.[174,178] The native oxide is easily removed with an aqueous HF etch to arrive at a hydride-terminated surface, which could then react with lithium without the irreversible capacity loss associated with reduction of the oxide by lithium. HF (aq) etching is a mainstay of the semiconductor industry, to etch both elemental silicon and silicon oxide to produce a hydride- terminated surface.[100,179,180]

The chemistries of HF etching of SiO_2 and of elemental silicon are related, but follow different mechanisms.[181] We will consider only the chemistry of aqueous HF (aq) since these are the conditions most widely used, and applied in this work. In the case of

SiO_2, the reaction proceeds by nucleophilic attack of the highly electropositive silicon centre by a fluoride-based species such as the highly polarized HF molecule, its dimer $(HF)_2$, or one of the anions F^- or HF_2^-, depending upon the pH.[182,183] While the Si-O bond is extremely strong (368 kJ/mol), the silicon-fluorine bond is stronger (582 kJ/mol), and thus the thermodynamically driven reaction is one that leads to the maximum number of Si-F bonds in the product (Figure 3-2).[101] The silicon atoms from SiO_2 are converted into fluosilicic acid, H_2SiF_6, with 6 fluorine atoms per silicon atom (SiF_6^{2-}), accompanied by the production of water.[100]

$SiO_2 + HF\ (aq) \rightarrow 2\ H^+ + SiF_6^{2-} + 2\ H_2O$

element	self	H	C	O	F	Cl	Br	I
C	292−360	416		336	485	327	285	213
Si	210−250 (bulk) 310−340 (disilane) 105−126 (disilene)	323	369	368	582	391	310	234

Figure 3-2. *Bond energies (in kJ/mol) of common carbon and silicon bonds. Reprinted with permission from reference* 101*. © 2002 American Chemical Society.*

For bulk silicon, on the other hand, (Figure 3-3, A), the chemistry is driven by nucleophilic attack on the silicon-silicon bonds in the crystalline lattice by fluoride. Silicon-silicon bonds in an isolated disilane are relatively strong (310-340 kJ/mol), but in a crystalline lattice of diamondoid silicon, the Si-Si bonds are considerably weaker (210 - 250 kJ/mol.[101,181,184] Starting with a thin native oxide, after removal of the surface SiO_x, HF (aq) the silicon centers of the remaining Si-OH groups are attacked

preferentially by fluoride species as they are highly polarized, leading to Si-Si bond cleavage. The resulting anionic silicon centre in the lattice is be rapidly protonated, resulting in Si-H bond formation (note that this reaction is almost certainly concerted, as shown by Chabal and co-workers in Figure 3).[185] Due to the low polarizability of the Si-H groups, they persist and are thus metastable - although they are less favoured thermodynamically compared to Si-F bonds (323 kJ/mol versus 582 kJ/mol), they are not reactive under these conditions and thus represent a kinetic product.[100,186] The bulk silicon product is Si-H_x-terminated as a result.

Porous silicon is a high surface area version of hydrogen terminated silicon, produced through a modification of the HF etch described above. The most common etching condition is electrochemically driven, and is typically carried out in galvanostatic mode with or without illumination depending upon the doping (n- or p-type) to generate holes at the surface that rapidly increase the rate of etching (Figure 3-4).[187]

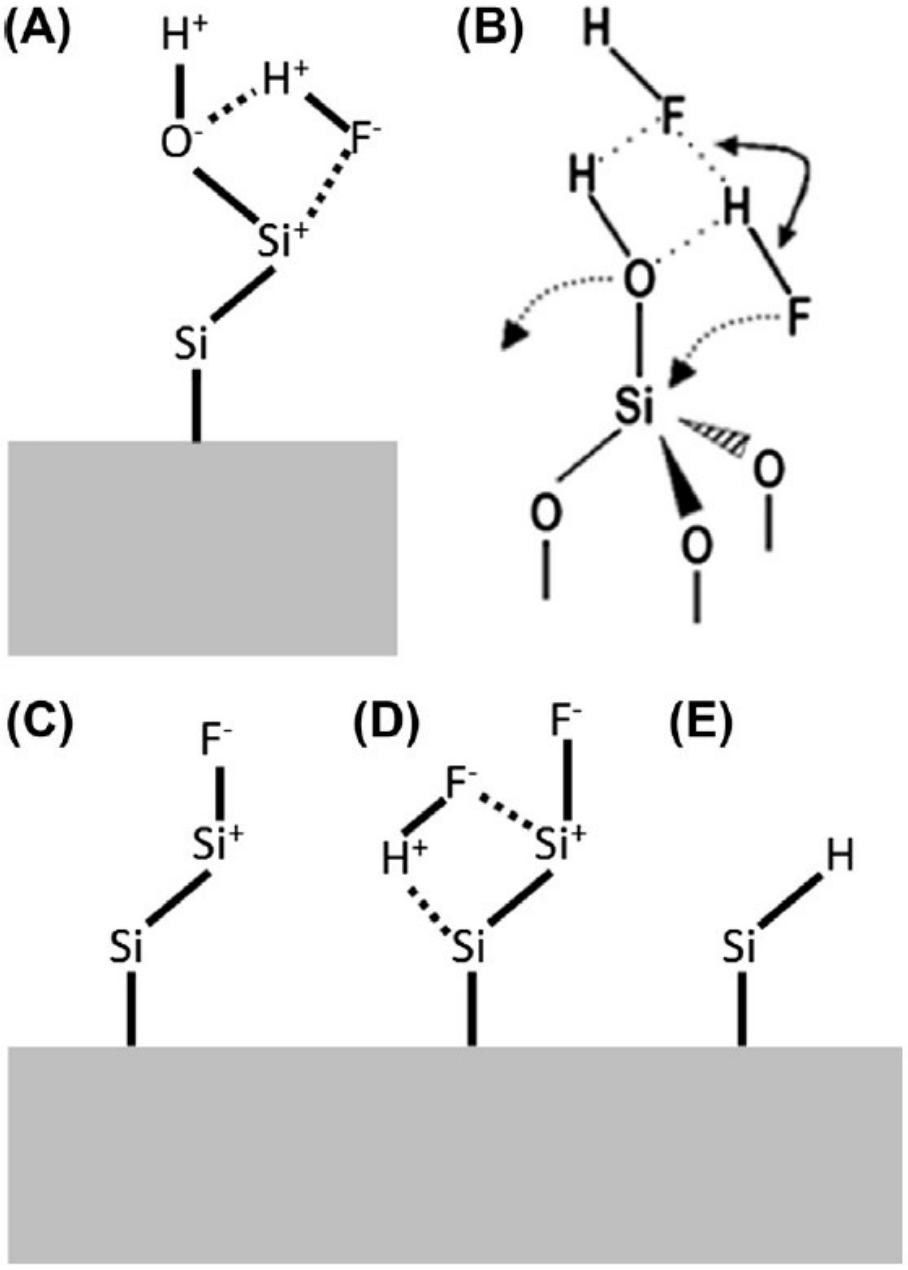

Figure 3-3. Stylized mechanism of the formation of Si-H_x surfaces by HF etching on Si-OH (a, c, d ,and e) and SiO_2 (b) surfaces. Full atomic valencies are omitted for clarity. Reprinted with permission from reference 185. © 2018 Elsevier. Panel B adapted with permission from reference 179. © 2000 American Chemical Society.

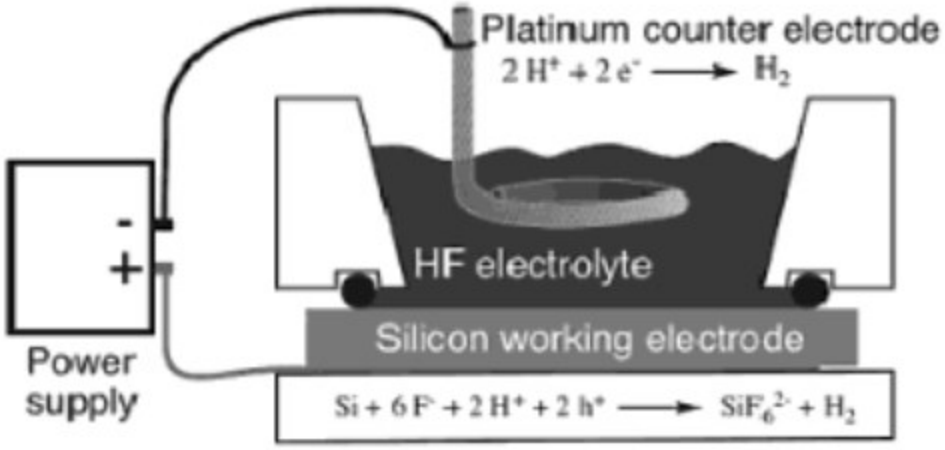

Figure 3-4. Porous silicon etching in a two-electrode electrochemical cell using a silicon wafer anode and platinum wire cathode. Reprinted with permission from reference 187. © 2012 John Wiley and Sons.

HF (aq) etching procedures can be applied to silicon anode materials to change the properties for lithium ion batteries. Xun et al. found that removal of the oxide with HF (aq) increases the total capacity of silicon nanoparticle-based electrodes for lithium ion cells from ~1320 mAh/g to ~3600 mAh/g.[174,178] These cells comprised 50 nm hydride-terminated silicon nanoparticles, synthesized through chemical vapour deposition and etched in aqueous HF, and used a PVDF binder, which is the typical binder used with graphite electrodes. PVDF binder is less commonly used with silicon electrodes because the nature of the intermolecular interactions with hydrophilic SiO_x surfaces are based upon weak van der Waals forces.[87] In earlier work, however, Magasinski et al. showed that hydrophilic binders such as polyacrylic acid (PAA) and carboxymethyl cellulose (CMC) were superior for silicon nanoparticle electrode performance even

when using hydrophobic Si-H_x-terminated silicon nanoparticles.[188] Since then, many others have demonstrated that hydrophilic binders such as PAA, LiPAA, CMC, and sodium alginate (Na-Alg) with silicon lead to better cycling performance, in part due to the high elasticity of these polymeric compounds that can accommodate the large silicon expansion and contraction during each cycle.[189–191]

Using hydrophilic binders, the presence of a silica layer is reliably beneficial for capacity retention, with some dispute over the ideal thickness.[172,192,193] The effect of an oxide layer on the initial capacity is often minimal,[94,194] with the exception of small particles <10 nm in size, in which SiO_x cannot be reduced to Si(0) due to competing reactions with the electrolyte on the large surface area.[173] Assuming thin SiO_x layers and a particle size of at least 50 nm, the effect of a native oxide on the initial Coulombic efficiency is also minimal.[94,195]

Moving beyond the effects of a surface oxide of silicon, it is also possible to integrate other functional groups on the silicon surfaces, forming what is termed an artificial solid electrolyte interphase (a-SEI). One of the earliest examples of this work was performed by Gao et al. using click chemistry to attach various derivatives of ethylene carbonate and polyethylene oxide to the surface of oxide-coated silicon nanoparticles (Figure 3-5).[91] The a-SEI formed via this method enabled much longer capacity retention in their 50 nm silicon particles, and remained above 80% of initial capacity for 100 cycles with their most highly optimized a-SEI, compared to only 4 cycles for the as-received silicon particles. The theoretical benefits of an a-SEI touch on every aspect of silicon surfaces addressed at the beginning of this chapter. a-SEI can passivate the surface of silicon and prevent electrochemical reactions with the solvent

and electrolyte. The a-SEI replaces or encapsulates the native oxide, and minimizes or prevents the characteristic first cycle irreversible capacity loss that accompanies the reduction of the SiO_x by lithium. Finally, the a-SEI can be tuned to have strong intermolecular forces with the carbon additive and binder in a nanoparticle slurry electrode to ensure cohesion and electrochemical contact. This final point will be explored more fully in Section 3.5.

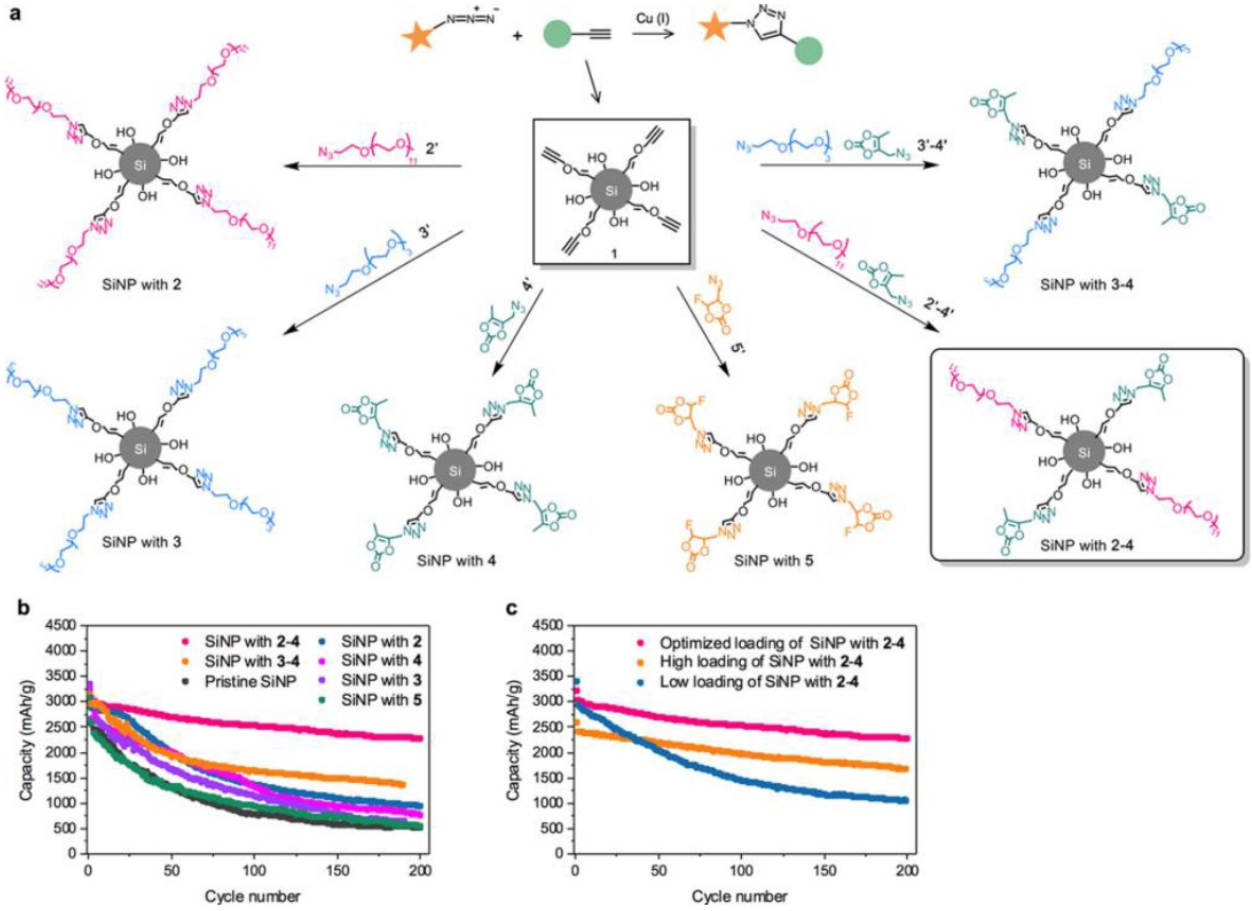

Figure 3-5. a-SEI functionalized through click chemistry reactions. Reprinted with permission from reference 91. © 2017 American Chemical Society.

In this work, we decided to apply the vast repertoire of surface chemistries on silicon that produce a hydrolytically stable and unpolarized silicon-carbon bond (362 kJ/mol). Hydrosilylation is a class of reactions that is well-established on silicon surfaces, going back to the seminal papers of Linford and Chidsey in 1993 and 1995.[88,196,197] As they described, thermal hydrosilylation is a clean and efficient approach to forming silicon-carbon bonds on hydride-terminated silicon via what is an insertion reaction of an unsaturated alkene or alkyne into a surface-bound Si-H group. We chose to use thermal hydrosilylation as a means of covalently attaching various molecules to the surface of silicon to form a hydrolytically stable a-SEI to passivate the silicon surface. Thermal hydrosilylation proceeds via radical chemistry, involving homolytic cleavage of a Si-H group above 150 °C to form a silicon-based radical that then reacts with unsaturated hydrocarbons with no apparent energy barrier, as shown in Figure 3-6.[101,197] In this way, a variety of a-SEI's can be accessed using hydrogen-terminated silicon as the basis, and choosing either neat or mixed alkynes/alkenes to form monolayers on the surface.

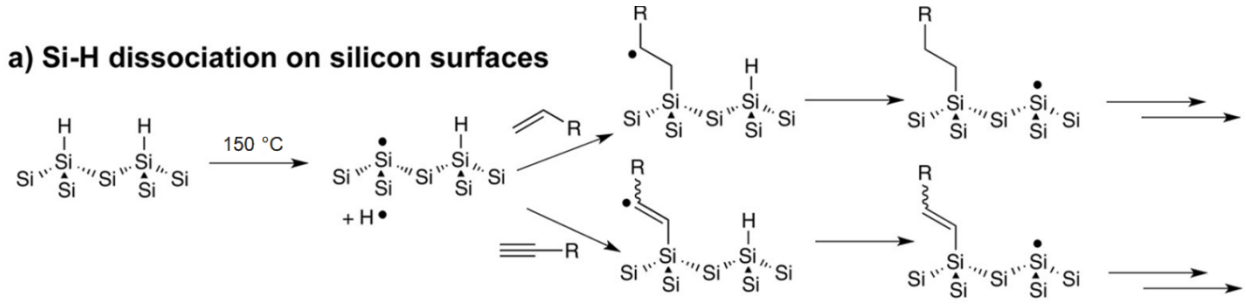

Figure 3-6. *Radical hydrosilylation mechanism on the surface of hydrogen terminated silicon. Radical initiation can occur above ~150 °C* via a thermally-mediated reaction pathway, which can also be initiated using UV light and peroxide initiators. *Adapted with permission from reference* 88*. © 2014 American Chemical Society.*

In this chapter, we detail the synthesis and performance of a-SEI produced via hydrosilylation on silicon surfaces for use in lithium ion battery anodes. We begin by characterizing a-SEI on porous silicon and silicon thin films in Section 3.2. We move on to explore a-SEI on silicon nanoparticles, detailing the differences in nanoparticle capacity in Section 3.3, then observing a-SEI on lower capacity particles in Section 3.4. We perform a systematic analysis of a-SEI on high capacity silicon nanoparticles in Section 3.5 and outline the effects of slurry binder on silicon performance. Finally, in Section 3.6, we explore high energy ball milling as a radical initiator to enable a related mechanochemical synthesis of silicon nanoparticles with an a-SEI.

3.2 Thin films, native oxides, and HF vapour etching

Initially, we studied the effect of modulating the composition of silicon surfaces using the simplest platform that does not require binder or conductive carbon additives to avoid compounded and convoluting effects. To start, we used 100 nm-thin films of amorphous silicon that were prepared by sputter deposition using a planar magnetron process on stainless steel. Thin films reduce the system complexity to enable focus on the interaction between the silicon surface and the electrolyte. The amorphous nature of these films was determined through XRD (Figure 3-7), and was validated in the first cycle dQ/dV plots vide infra (Figure 3-10). Cycling was carried out using 1 M $LiPF_6$ in 1:1 ethylene carbonate:diethyl carbonate (EC:DEC).

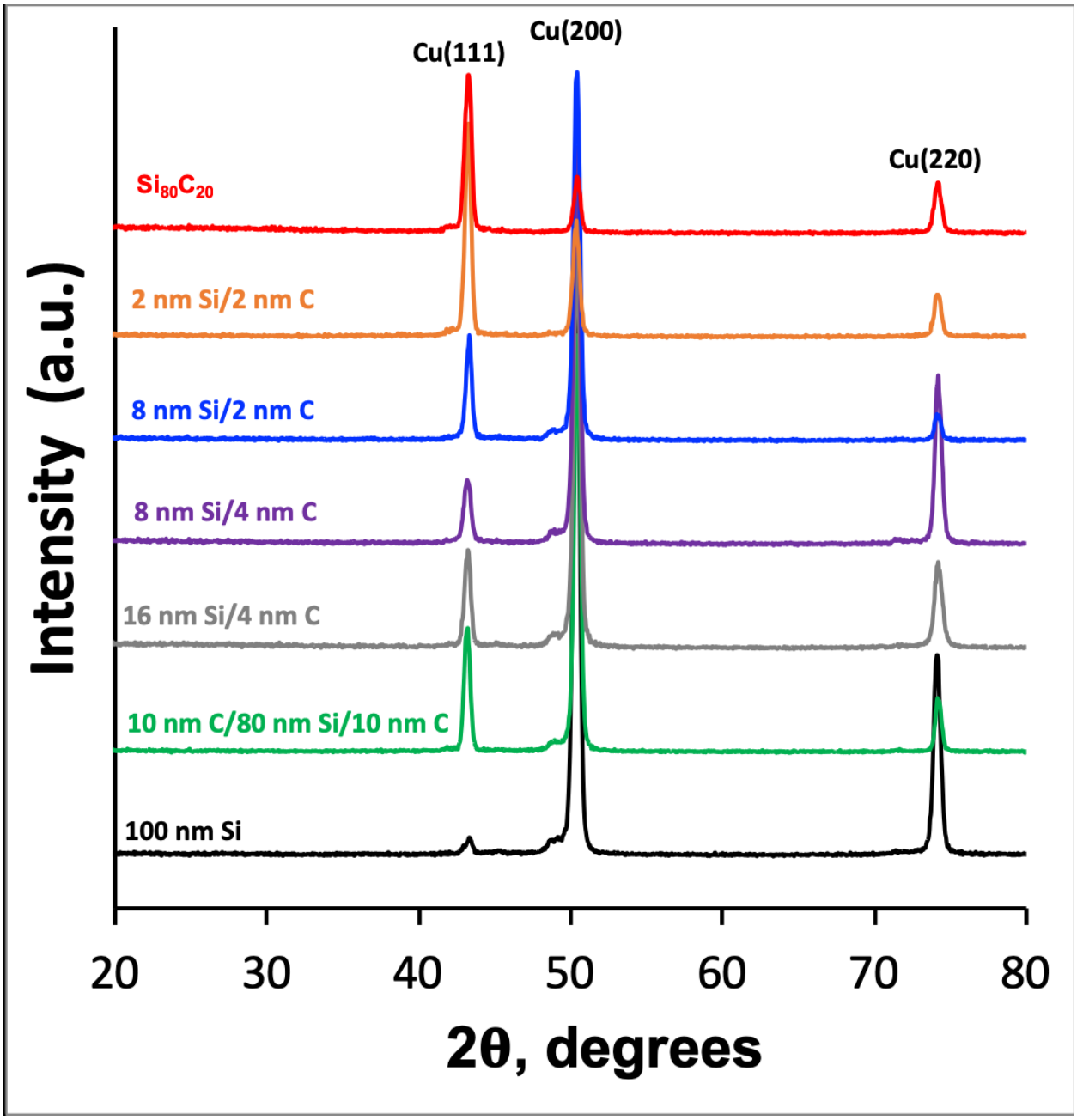

Figure 3-7. XRD of co-sputtered silicon carbon films on copper foil, as reported previously by our group. The 100 nm Si spectrum (black) is identical to the thin films reported here, and shows no signs of crystalline Si peaks. Reprinted with permission from reference 149. © 2019 American Chemical Society.

As stated in the introduction, general acknowledgement has emerged that removal of the native oxide is detrimental to silicon cycling above a size of ~10 nm.[173,193,194] With thin films, we explored cells with a native oxide, and cells whose oxide had been removed by immersing in HF (aq) or with an HF vapour etch. For immersion, we placed these 100 nm-thin films of silicon on stainless steel discs into 1 mL of 1 % HF (aq), and left the disc without stirring for 30 seconds. To compensate for stainless steel corrosion by the HF (aq), we also etched an unmodified stainless steel disc and measured weight loss, using the assumption that mass loss for thin film samples would be half as large with one side of the stainless steel exposed to the HF (aq). A typical HF vapour etch involved placing 100 nm thin film silicon face up in a memsstar Orbis Alpha HF vapour etching instrument. The system was evacuated, and then the silicon surface was exposed to 12 Torr of HF vapour for 5 minutes.

Samples with a native oxide and hydrogen termination prepared by an immersion etch and an HF vapour etch were characterized via XPS and water contact angle measurments. The variation of the appearance of the surface can be monitored with the naken eye, as shown in Figure 3-8. As-sputtered films were violet in colour, and quickly changed to turquoise during immersion in HF (aq), while the thin films became orange after exposure to HF vapour. As per XPS (Figure 3-9), the survey scan of silicon immersed in 1 % HF (aq) reveals iron and chromium 2p on the surface , which suggests contamination from the stainless steel. XPS of the thin film of silicon after the HF vapour etch shows no iron or chromium on the surface during a survey scan, and shows a sharp decrease in the degree of Si(2+) in scans of the Si 2p peak (Figure 3-9f). Silicon thin films immersed in HF (aq) show little reduction in the oxide peak, which is

predominantly due to the acquisition protocol. The XPS analyses of samples etched via HF (aq) immersion were conducted two days after the sample was submitted, which could have resulted in further oxidation.[198] However, upon realization of the issue of contamination by metals from the stainless steel, we did not pursue additional XPS analyses with less air exposure of these samples. The sample with the least amount of oxidation in the XPS spectrum as per the Si 2p region was the one etched with HF vapour and exposed to air for less than 20 minutes (Figure 3-9).

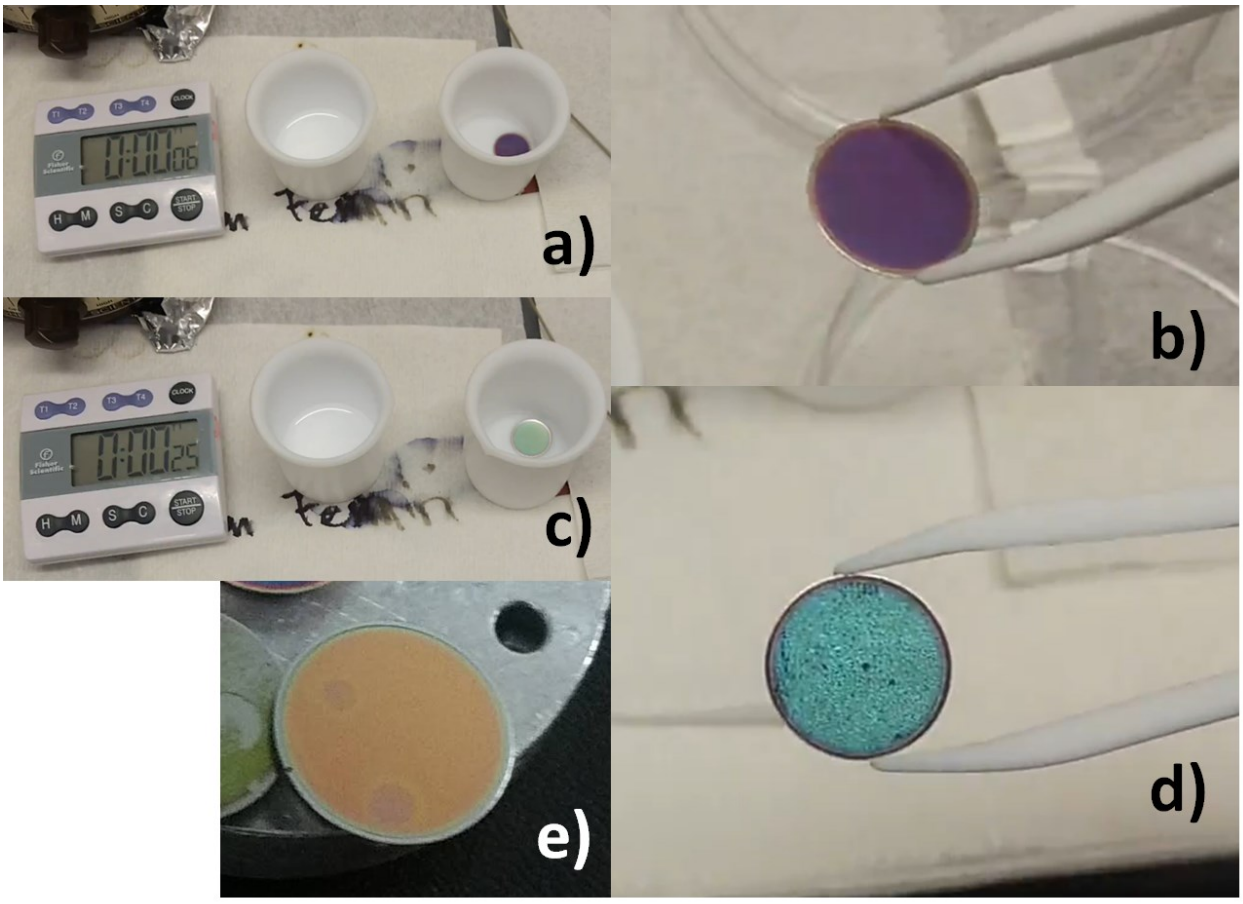

Figure 3-8. 100 nm sputtered silicon on stainless steel before (a, b) and after (c, d) immersion in HF (aq) for 30 seconds, and (e) after an HF Vapour etch with 12 Torr of HF vapour for 5 minutes.

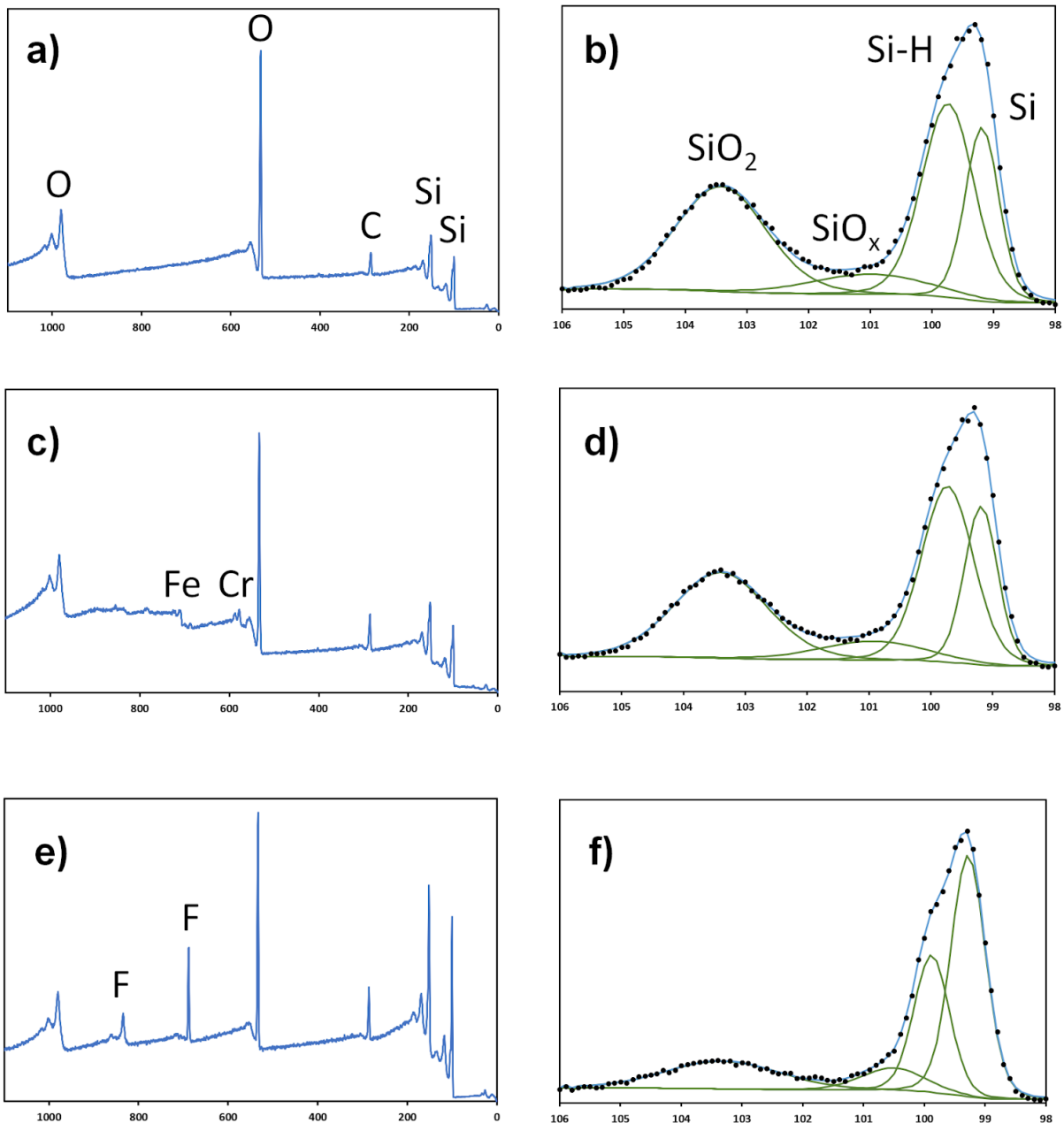

Figure 3-9. Survey scans (a, c, e) and Si 2p high resolution (b, d, f) XPS of Si sputtered onto stainless steel (a,b), Silicon etched by immersion in 1 % HF (aq) for 30 seconds (c,d), and HF vapour etched (e,f).

The contact angle measurements were carried out with water on the silicon thin films to determine hydrophilicity as a proxy for quantifying the level of oxidation. Measurements were carried out within 30 s following immersion in HF (aq) to minimize time exposed to air, while samples treated with HF vapour were transported under vacuum and analyzed within 1 hour. Immersion in HF (aq) resulted in the highest contact angle (= most hydrophobic surface), with a static water contact angle of 70 °, which is typical of a Si-H_x-terminated silicon surface. This result suggests that the oxide content of the HF (aq) etched silicon thin films is low, but increases with exposure to air after etching since the XPS measurements had shown a high degree of oxidation after storage for two days in air. HF vapour etching also resulted in an increase of the contact angle of silicon to 41 °, which is less than the samples prepared by immersion in HF (aq). HF (aq) immersion clearly resulted in the highest water contact angle, but oxidizes rapidly due to cross-contamination from transition metals. HF vapour etching also has a hydrophobic surface from hydrogen termination. Both methods of removing the oxide will be explored for further applications below.

Surface	**100 nm Si (as-is)**	**Treated with HF (aq), 30 s**	**Treated with $HF_{(g)}$, 12 Torr, 5 min**
Contact angle (°)	23.2	70.1	40.8

Table 3-1. *Static water contact angle measurements on sputtered silicon thin films.*

We perform electrochemical cycling in lithium ion half cells for silicon thin films with a native oxide and after both HF (aq) and HF vapour etching. The first cycle voltage curve for each of the silicon surfaces, along with the dQ/dV, which represents the inverse derivative of a voltage plot with respect to capacity, is shown in Figure 3-10. The first cycle dQ/dV reveals that all thin films remain amorphous, as noted by the lack of a sharp peak at 150 mV during the initial lithiation, which is characteristic of the transition from crystalline silicon to an amorphous lithium silicide. The first cycle voltage curve also demonstrates that an HF vapour etch leads to larger initial capacities during the first lithiation and delithiation, as well as a higher initial Coulombic efficiency, as represented by the ratio in capacity between the lithiation step and the delithiation step. The lower capacity and initial Coulombic efficiency observed with the native oxide is presumably due to irreversible reactions between lithium and the oxide, which represent both efficiency losses and the lower per weight capacity of silicon oxide compared to silicon. Silicon thin films immersed in 1 % HF (aq) show slightly lower capacity than films with the native oxide, suggesting that the oxide layer was not cleanly removed during the immersion step, or re-oxidized during cell preparation.

The specific capacity over 200 cycles is shown in Figure 3-11. Here we see clear evidence that removal of the silicon oxide entails a trade-off between initial capacity and capacity retention. Films exposed to an HF vapour etch show much higher capacities, beginning at 3878 mAh/g compared to 3257 mAh/g for as-sputtered silicon with the native oxide. All cells begin with three cycles at lower current, 400 mA/g, followed by subsequent cycling at 1200 mA/g. HF vapour etched cells deteriorate rapidly at the 1200 mA/g rate relative to as-sputtered samples, and by cycle 50 the capacity retention

reached 34 % and 62 %, respectively. It may be that an SEI formed by a combination of lithium reacting with the oxide surface and the decomposition of the electrolyte and solvent stabilize the thin films as they cycle.

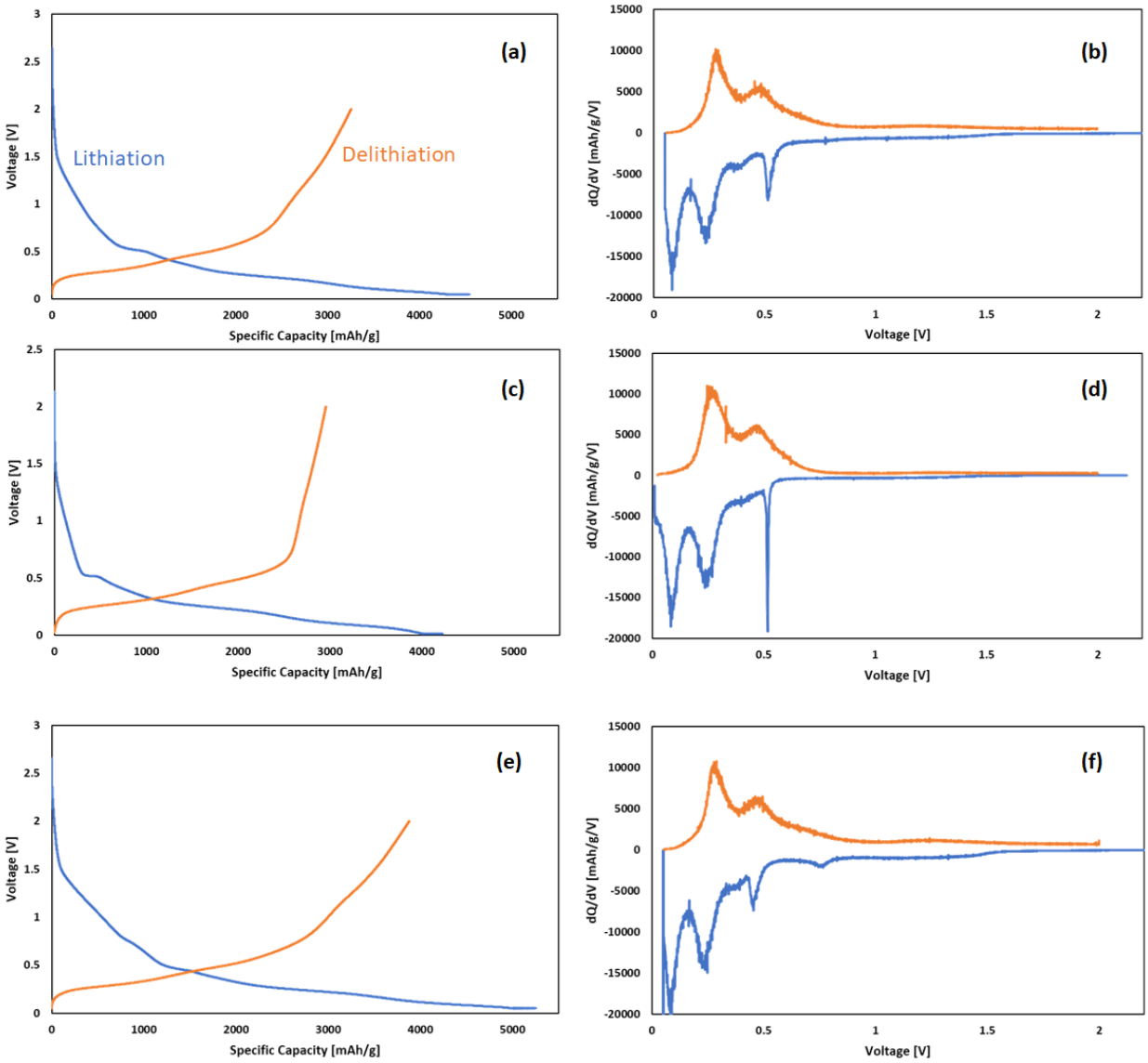

Figure 3-10. First cycle voltage curves (a,c,e) and dQ/dV (b,d,f) for thin films of silicon with a native oxide oxide (a,b), after HF (aq) immersion (c,d), and after HF vapour etching (e,f).

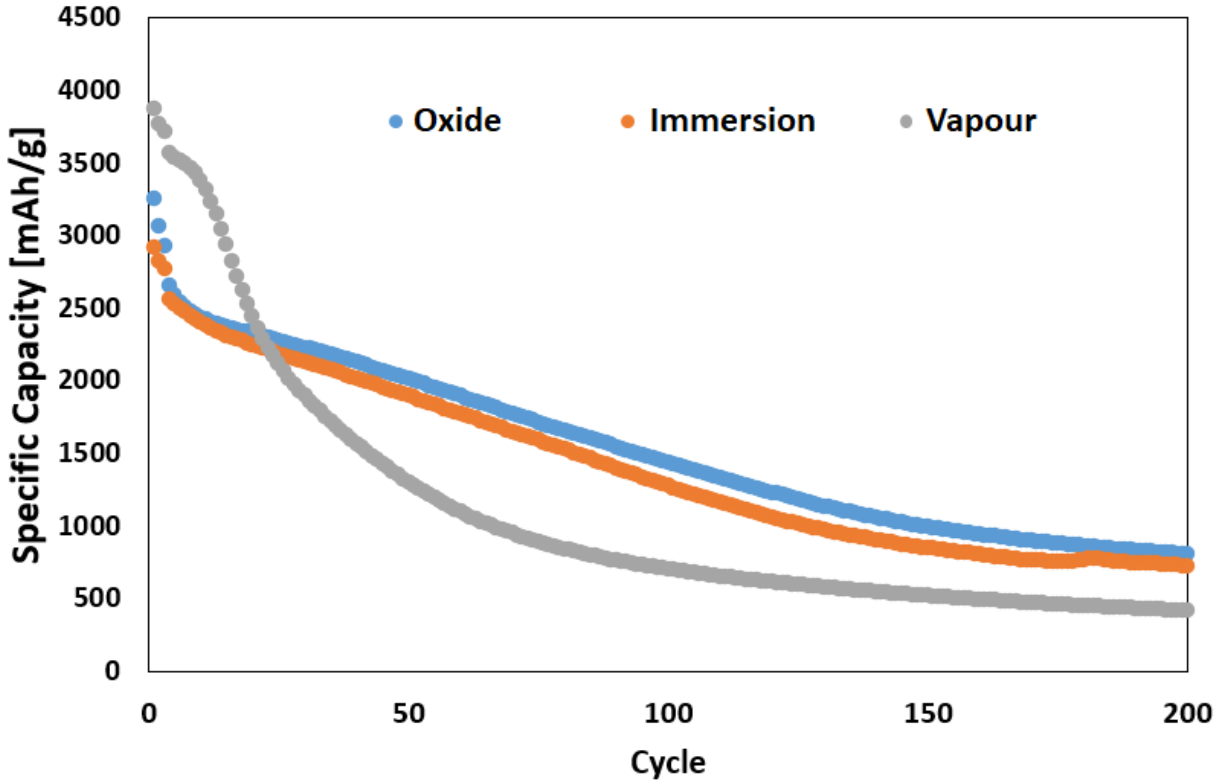

Figure 3-11. Capacity retention over 200 cycles of thin film silicon etched subjected to an HF vapour etch. Cells were cycled in 1 M $LiPF_6$ in 1:1 EC:DEC between 2 – 0.05 mV at a rate of 400 mA/g for cycles 1-3 and 1200 mA/g for subsequent cycles.

We should not rule out that the vapour etching step itself produced a large change in the morphology or the structural integrity of the silicon thin films, perhaps making it easier for them to delaminate. Visually, the HF vapour etching process reveals possible nonuniformity of the HF vapour step. Silicon surfaces transition from violet to orange during the vapour etching step, but often the discs will contain patches of discolouration visible as light violet circles, as outlined in Figure 3-12. However, discs for cell cycling were chosen from among samples with no visible signs of inhomogeneity. A top down SEM image of Si thin films before and after HF vapour

etching is shown in Figure 3-13. The surface remains generally smooth after the HF vapour etch, but further conclusions are difficult due to the selective nature of SEM.

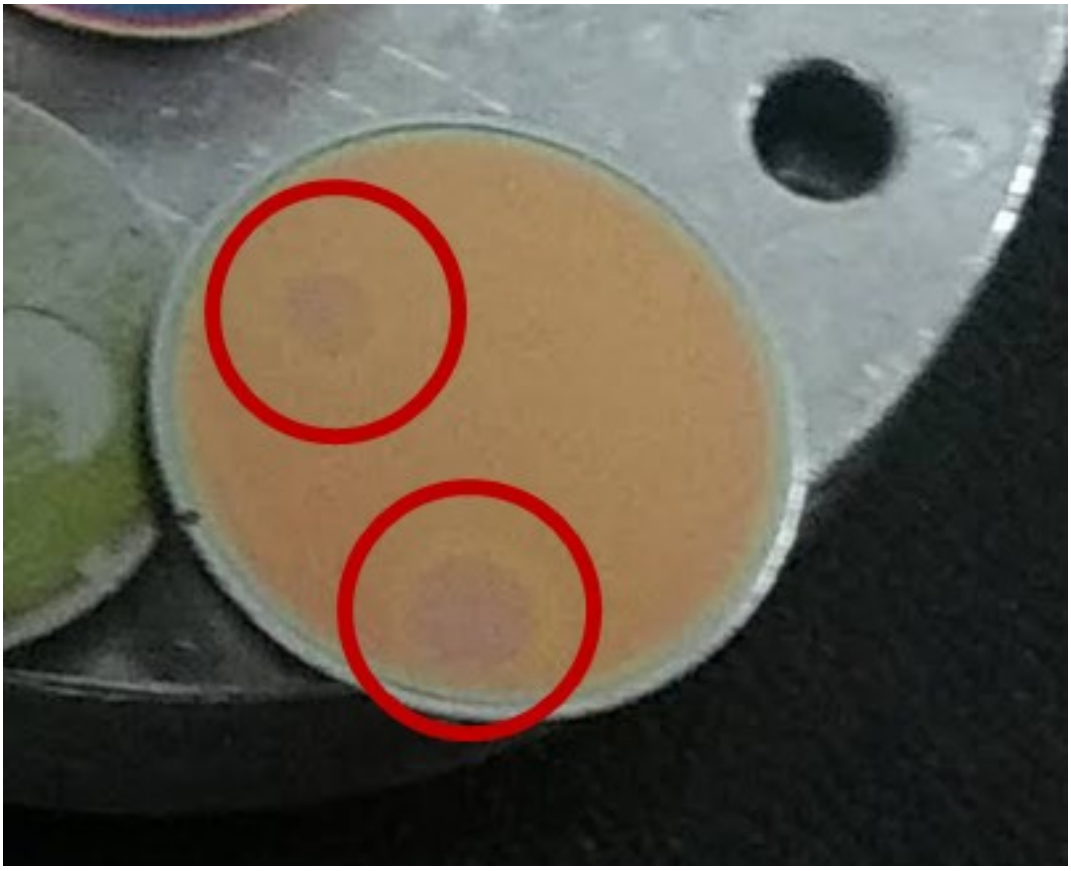

Figure 3-12. Optical image showing discolouration of silicon films after an HF vapour etch, circled in red for visibility.

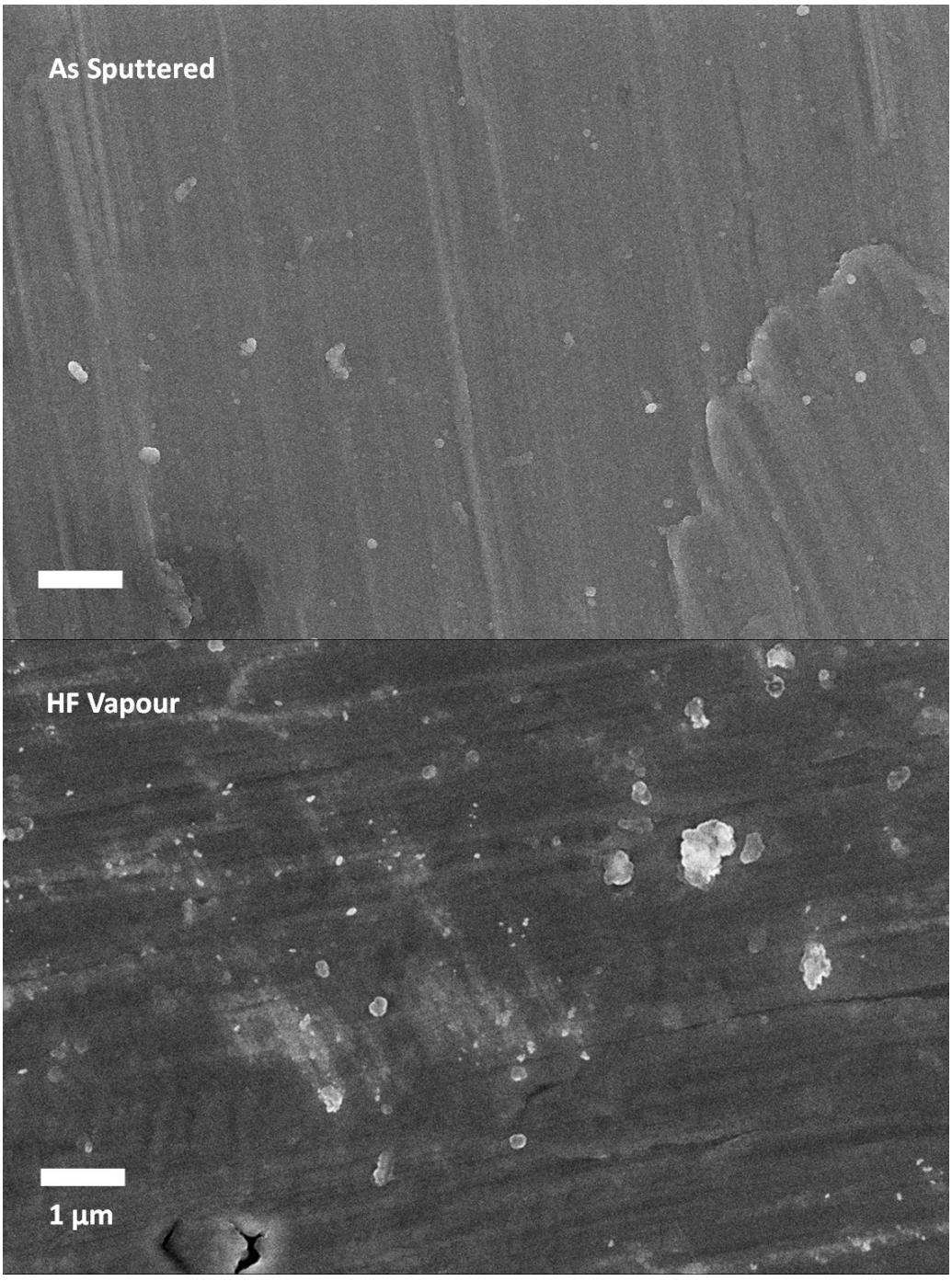

Figure 3-13. SEM of as-sputtered silicon (top) and after HF vapour etch (bottom). Scale bar 1 µm.

We have only observed the effect of a native oxide vs hydrogen termination on thin films, which matches with more recent observations for hydrogen termination seen in the literature for silicon nanoparticles.[194] We find that removing the native oxide increases the initial capacity, just as early studies using PVDF binder or studies on small (< 10 nm) nanoparticles.[178] Early research with silicon nanoparticles in polar binders like PAA and CMC also removed the oxide layer to increase capacity,[188] but the higher capacity retention observed with a native oxide is now accepted as outweighing costs to capacity for larger nanoparticles.[193] It has even been shown that artificially thicker SiO_2 layers could further increase capacity retention up to ~3 nm (Figure 3-14),[194] although we do not explore thicker SiO_2 layers in this work.

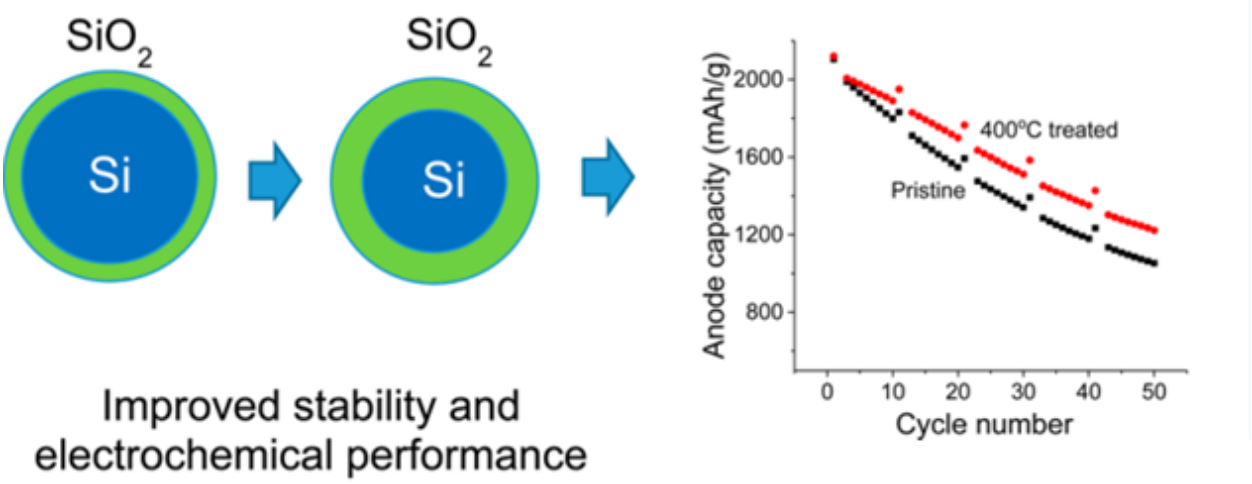

Figure 3-14. Increasing the thickness of the SiO_2 layer up to 3 nm, done here by treatment at 400 °C, might further increase capacity retention in some silicon particles. Adapted with permission from reference 194. © 2017 American Chemical Society.

Hydrosilylation is a reaction between Si-H groups and an unsaturated carbon-carbon bond such as an alkene or alkyne to create a covalent Si-C bond linkage, described in Section 3.1. Having established the baseline for native oxide-capped and HF-treated silicon thin films, we investigated different surface coatings prepared via hydrosilylation. The simplest hydrosilylation chemistry is thermal hydrosilylation with an alkene or alkyne, as demonstrated first by Chidsey and co-workers in 1995, as it requires no additional additives or complex apparatus.[197] Using the conditions of Sieval et al (1998), P-doped, n-type <100> Si wafers (1-5 Ω) were first etched with a 2 % HF (aq) solution for 2 minutes, producing a hydrogen terminated silicon surface.[199] After etching, the silicon wafer was immersed in 2 mL of neat distilled 1-dodecyne and heated at 170 °C for 2 hours while argon was bubbled in gently on the surface of the 1-dodecyne. The alkene or alkyne can also be diluted in mesitylene (1:10 v:v) and refluxed at 165 °C.[200] The modification of the surface properties can be easily seen in the changing water contact angle (Table 3-2), which becomes increasingly hydrophobic as the surface changes from Si-O_x, to Si-H_x, to Si-dodecyne. These contact angle values are similar to those found in the original work by Sieval et al.[200]

Surface	**Si(100) Wafer (native oxide)**	**H_x-Si-terminated Si(100)**	**Dodecenyl-terminated Si(100)**
Contact Angle (°)	48.3	75.0	101.0

Table 3-2. Static water contact angle measurements of silicon surfaces on Si(100) wafers.

Porous silicon (p-Si) is an excellent platform for investigating the surface chemistry of silicon by Fourier transform infrared radiation (FTIR) spectroscopy because of the high surface area of the material coupled with the IR transmissivity of lightly doped silicon. A small number of scans in transmission mode leads to high signal-to-noise ratios, as shown in Figure 3-15. In the preliminary studies, the alkene/alkyne was varied, and included 1-dodecyne, 1-hexadecene, and 1-dodecene, and not surprisingly, all behaved similarly as is established in the literature. The FTIR spectrum of freshly etched silicon is shown in Figure 3-15 in blue. The feature at 2100 cm^{-1} is visible in both functionalized and unfunctionalized silicon and corresponds to Si-H_x stretching modes that are not adjacent to oxidized silicon. These features are well defined and resolve into separate SiH, SiH_2, and SiH_3 maxima. Upon reaction with 1-hexadecene, the orange plot in Figure 3-15, the FTIR spectrum of porous silicon shows strong sp^3 hybridized ν(C-H_x) stretching in the region of 2800 - 3000 cm^{-1}, and no features corresponding to the alkene group at 1640 cm^{-1}, thus indicating covalent bonding with the silicon surface. Upon hydrosilylation, the ν(Si-H_x) feature broadens and appears smoother, as is established in the literature, due to the increased number of distinct Si-H_x binding environments that merge into one large feature centered around 2100 cm^{-1}. Figure 3-15 (orange) also reveals signs of oxidation, including a small feature at 2250 cm^{-1} that corresponds to the oxygen backbonded ν(Si-H_x) stretch, and a larger feature at 1050 cm^{-1}, corresponding to ν(Si-O) stretching. Oxidation is due to trace water and/or oxygen present at levels that enable oxidation to compete with the hydrosilylation reaction.[200,201] The mesitylene solvent and the olefin were distilled and passed through activated alumina under inert atmosphere, accompanied by drying steps to reduce

exposure to water and air prior to and during the reaction. To reduce the level of oxidation, higher concentrations of alkene would prevent competitive oxidation with respect to hydrosilylation.

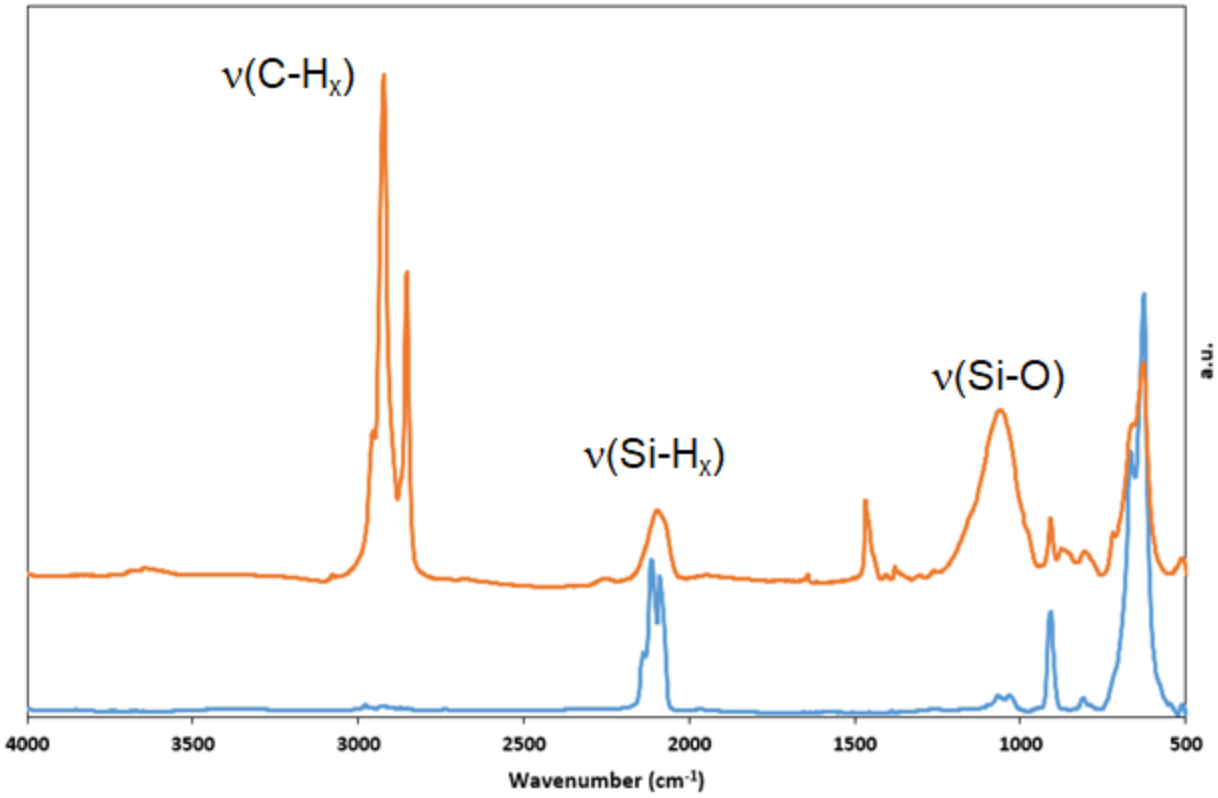

Figure 3-15. Transmission FTIR of freshly etched p-Si (blue), and after thermal hydrosilylation with 1-hexadecene (orange).

Having successfully hydrosilylated porous silicon, we then aimed to test a major hypothesis for our a-SEI research in lithium ion battery coin cells. We hypothesized that functional groups similar to those found in a naturally forming silicon SEI would increase first cycle Coulombic efficiency and the capacity retention. We further hypothesized that non-polar a-SEI would have different properties from polar a-SEI, both in terms of lithium diffusivity and chemical interactions with other cell components. Intermolecular

forces between the polar carbonate groups of VEC and components of the SEI during cycling may engender a thinner, more robust SEI, while 1-dodecyne may prove more electrochemically inert and should avoid reduction with lithium. Based on the results, polar and non-polar components could be mixed to tailor the a-SEI with synergistic effects from both functional groups.

We performed hydrosilylation with a non-polar hydrocarbon, in this case 1-dodecyne in lieu of 1-hexadecene, and with vinyl ethylene carbonate (VEC) as a polar surface that mimics the nature of a stable SEI.[57] The Grey group has used solid state NMR to characterize the insoluble products of fluoroethylene carbonate decomposition in a lithium ion cell, which is known to form a stable SEI with high capacity retention. Among the products are poly-vinylene carbonate, shown in Figure 3-16 in blue, which we mimic with a monolayer comprising the hydrosilylated product of VEC, shown in dark red.

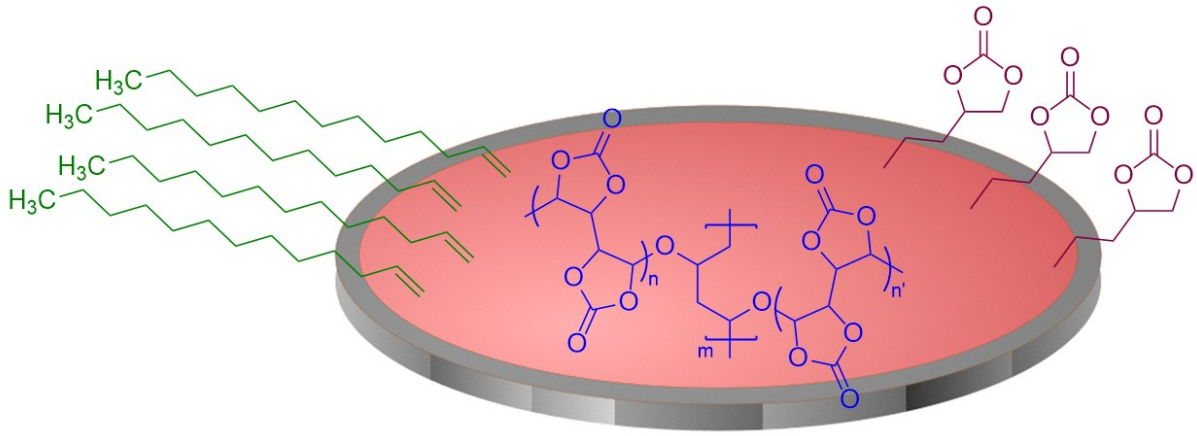

Figure 3-16. *Surface coatings on silicon thin films. Artificial SEI are shown after functionalization with 1-dodecyne (green) and vinyl ethylene carbonate (dark red). For comparison, polyvinylene carbonate (blue) forms in-situ from the decomposition of FEC additive.*

The porous silicon samples could not be adapted for use in a lithium ion battery coin cell, and we therefore moved on to hydrosilylation of silicon thin films. The process for sputtering and etching silicon has been described earlier in this chapter, and these thin film experiments were hydrogen-terminated using immersion in aqueous HF. The experiments were performed before XPS measurements showed contamination with iron (vide supra); however, the silicon surface was transferred directly from the HF (aq) immersion to a round bottom flask under inert atmosphere, so significant oxidation is unlikely. Hydrosilylation was very similar to that performed on porous silicon, and so to conserve expensive reagents such as VEC, the reactions were carried out with the alkyne/alkene in mesitylene in a 1:10 v/v ratio, as described earlier.[200]

Here, we focus on the effects of a pre-hydrosilylation step on the initial Coulombic efficiency (ICE) and the specific capacity retention of these cells based upon thin films of silicon. Figure 3-17 shows over 200 cycles of Si-O_x, Si-H_x, Si-Dodecene, and Si-VEC samples of silicon that represent the native oxide- and Si-H_x-capped surfaces as the controls, with 1-dodecyne and VEC hydrosilylated as above. As can be seen, the cells comprising the silicon with native oxide surfaces show the highest capacity and cycling stability, while the silicon with Si-H_x- and 1-dodecenyl-termination have the lowest. The silicon hydrosilylated with VEC shows similar performance to the silicon terminated with native Si-O_x, having a slightly reduced initial capacity but almost superimposable profile over 200 cycles. One of the primary hypotheses for use of an a-SEI was improved Coulombic efficiency that results from protecting the silicon surfaces, thus reducing the quantity of in-situ SEI formation from electrolyte decomposition. Figure 3-17b shows the plots of Coulombic efficiency of the same samples, and as can

be seen, samples functionalized with an a-SEI do not have a higher ICE relative to the native oxide.

Although studies on silicon thin films help to simplify the lithium ion cell by removing slurry components such as conductive additives and binders, it has major drawbacks for this type of study. Characterization of the surface is more difficult because FTIR analysis of these silicon thin films is not feasible. The absolute specific capacity of each cell is uncertain due to mass lost during the HF etching step, which may be due to both the loss of silicon and the etching of other elements in the stainless steel. In one experiment, it was found that 6.8 μg were lost during a 30 second immersion in 1 % HF (aq), which corresponded to 18% of the initial mass of silicon. There is also a trade-off between the need to quickly process the freshly prepared hydride-terminated-Si samples and to weigh them on a balance capable of 1 μg precision, which is not located in the same building as other processing steps. In consideration of these limitations, we moved on from hydrosilylation on thin film silicon samples to silicon nanoparticles (SiNPs), which are prepared in much larger quantities and can be characterized by IR spectroscopy after producing pellets for transmission FTIR or through diffuse reflectance infrared Fourier transform spectroscopy (DRIFTS).

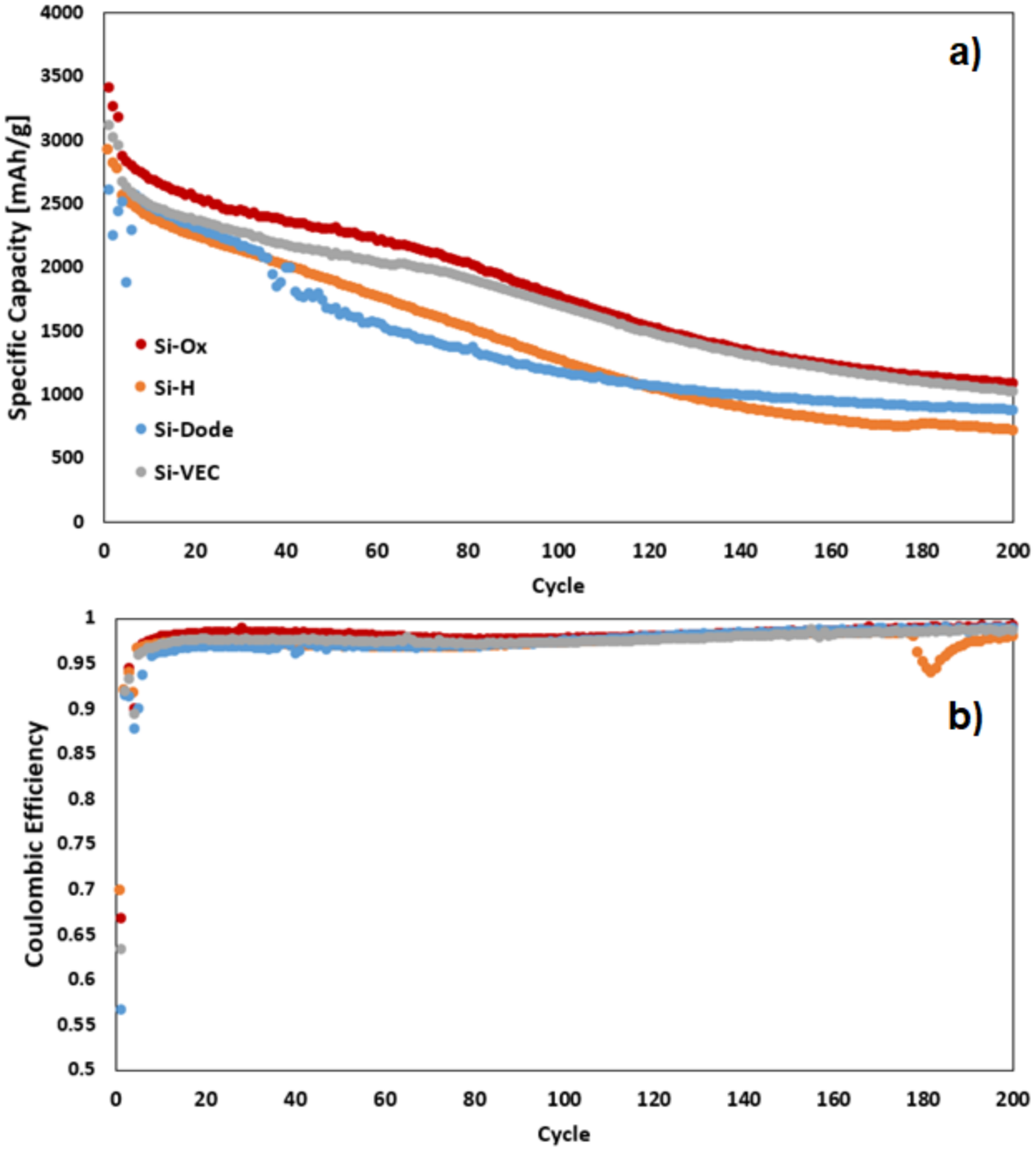

Figure 3-17. Specific capacity (a) and Coulombic efficiency (b) over 200 cycles for 100 nm thin films of silicon with a variety of surface functionalities. All cells were cycled in 1 M $LiPF_6$ in 1:1 EC:DEC between 2 – 0.01 mV at a rate of 400 mA/g for cycles 1-3 and 1200 mA/g for subsequent cycles.

3.3 Batch variability of commercial, plasma-synthesized silicon nanoparticles

Despite the advantages of studying SiNPs, the source of these particles could be a confounding variable. SiNPs must be processed as electrode slurries to be integrated with the coin cell architecture and to ensure stable conductive contact between silicon and the cell. The use of slurry electrodes requires a conductive carbon additive and a polymer binder, both of which increase the level of complexity of the system with respect to analyzing the effects of an a-SEI. While thin films of silicon were made in-house in the University of Alberta's Centre for Nanofabrication by sputtering, and can be tailored, silicon nanoparticles need to be purchased from commercial sources. These silicon particles are synthesized by a plasma-based process, and we observed significant batch-to-batch variability, a critical aspect that will be explored in detail, vide supra. We therefore had to remove this variability by purchasing a large quantity from one batch from a supplier to ensure consistency across the prepared cells, although earlier experiments will be reported from different silicon sources.

Plasma synthesis is considered as a high throughput method for producing silicon nanoparticles via thermal or nonthermal conversion of a silane source into Si(0) nanoparticles. Developing and popularizing this method of silicon nanoparticle synthesis is largely attributed to the Kortshagen group,[202] while more recently, the Neale group has explored plasma synthesis and its tunable properties for lithium ion battery applications.[98,203] A schematic of the thermal method as per Kortshagen and co-workers is shown in Figure 3-18.[202] A mixture of an inert gas and a silicon precursor, SiH_4, is admitted to the quartz chamber, and decomposition of the silane takes place in

the small volume surrounded by copper rings to which a radiofrequency power (200 W, 27 MHz in this case) is applied to generate a plasma. The formed silicon particles are then collected in a filter or solvent. Since this apparatus is highly specialized, we needed to source our silicon nanoparticles from commercial distributors, who for this work were Sigma-Aldrich and Alfa Aesar.

We ordered three containers from Sigma-Aldrich, and two from Alfa Aesar, all five of which were advertised as < 100 nm in size as determined by TEM. We also ordered a sixth sample, 325 mesh silicon supplied from Sigma-Aldrich, which corresponds to silicon < 44 μm in size that has been passed through a 325 mesh sieve; size was confirmed by SEM (Figure 3-59). For simplicity, the samples are labeled chronologically by the time of ordering: **Si-SA1**, **Si-SA2**, and **Si-SA3** are the nanoparticle batches supplied by Sigma-Aldrich under the same catalogue number, **Si-AA1** and **Si-AA2** are from Alfa Aesar, and **Si-325** refers to a 325 mesh silicon from Sigma-Aldrich. Both **Si-AA1** and **Si-AA2** are likely derived from the same batch as they appear very similar, and so only **Si-AA1** will be discussed hereafter. The 4 batches appear obviously different to the naked eye and showed very significant differences in electrochemical cycling. Figure 3-19 shows that the three **Si-SA1**, **Si-SA2**, and **Si-SA3** samples purchased from Sigma-Aldrich have distinctly different colours and behaviour towards static; meanwhile, Figure 3-20 shows the difference between **Si-SA1** and **Si-AA1** both as received and dispersed in pentane. We first discuss differences in **Si-SA** samples, before returning to the samples from Alfa Aesar and **Si-325**.

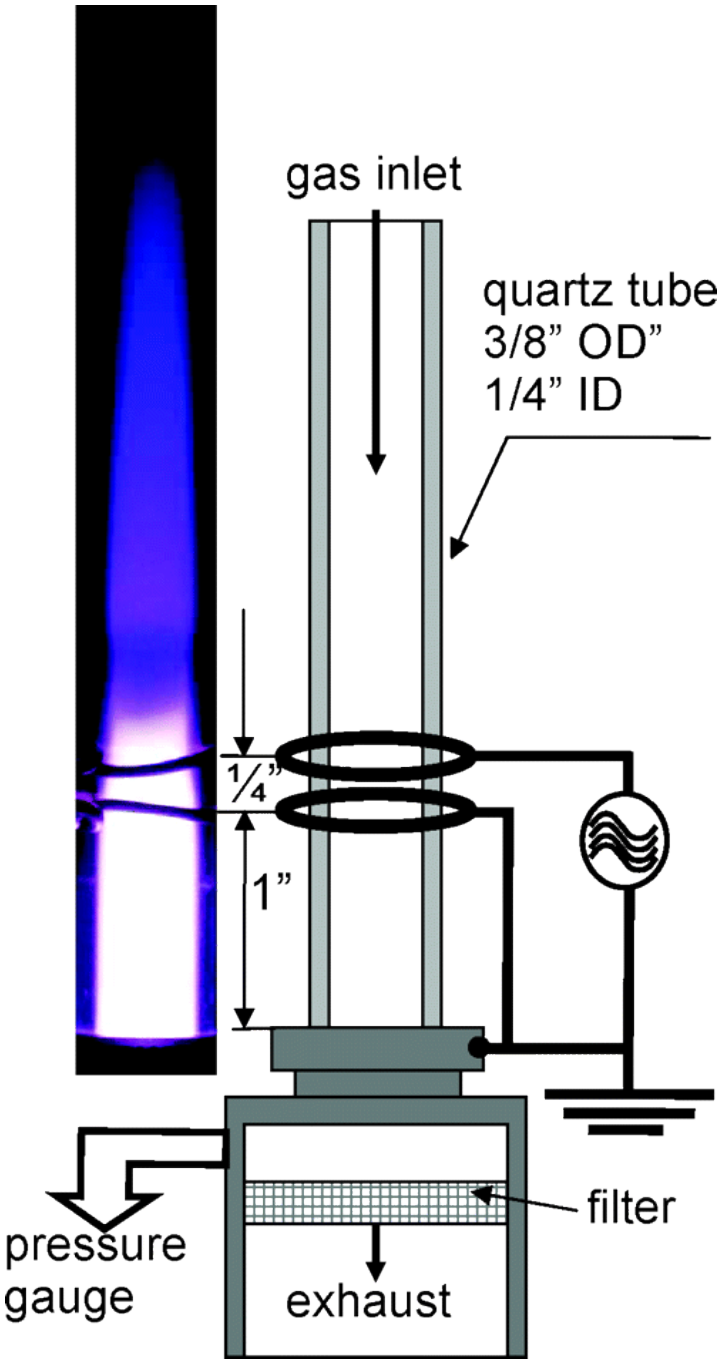

Figure 3-18. A schematic representation of the plasma-based process for the synthesis of silicon nanoparticles. Reprinted with permission from reference 202. © 2021 American Chemical Society.

All three Sigma-Aldrich samples, **Si-SA1**, **Si-SA2**, and **Si-SA3**, were used in a 60:20:20 ratio with Super P Carbon black and LiPAA in water to make silicon electrode slurries, and cycling in lithium ion battery cells is shown in Figure 3-21. **Si-SA1** and **Si-SA2** have much lower initial capacities, of 2153 mAh/g and 1733 mAh/g, or 60 % and 48 % of theoretical capacity, respectively. **Si-SA3** attains 3520 mAh/g on the first cycle, corresponding to 98 % of theoretical capacity, but has slightly lower capacity retention over 50 cycles. **Si-SA3** matches the theoretical properties of silicon anodes

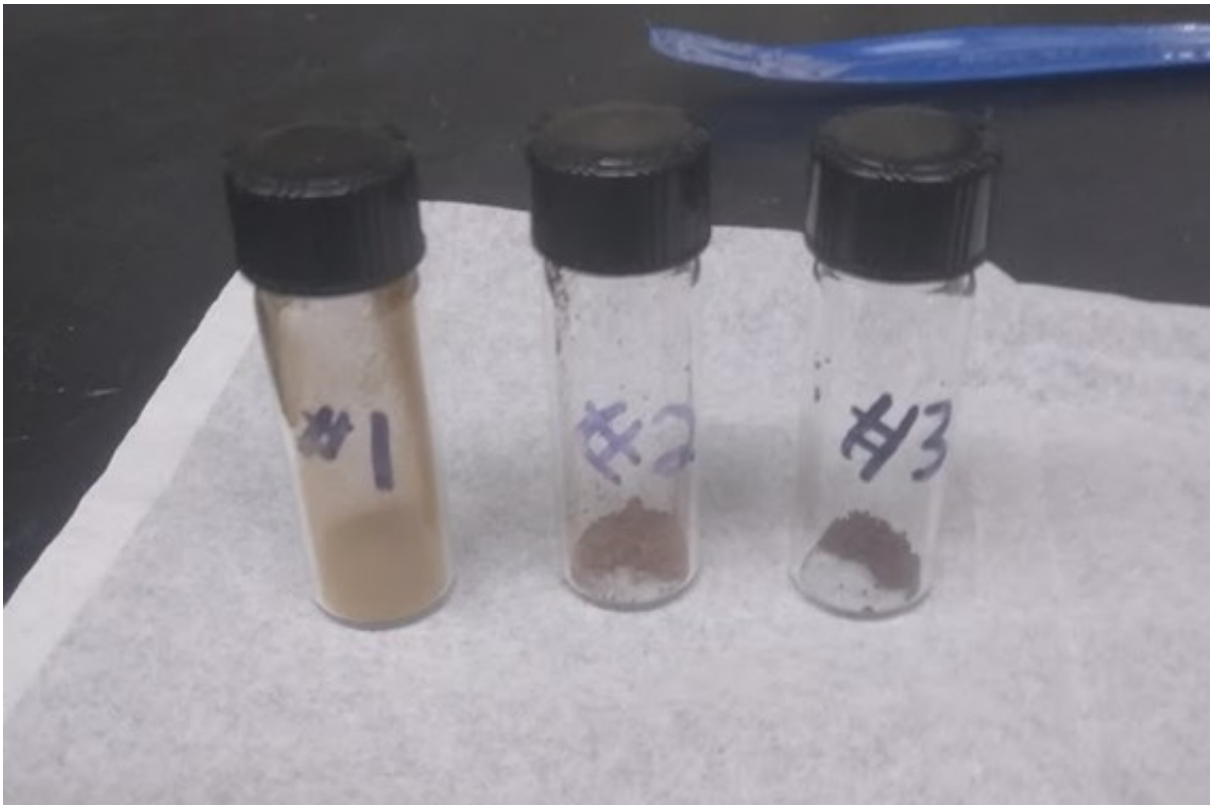

*Figure 3-19. **Si-SA1**, **Si-SA2**, and **Si-SA3** silicon particles from Sigma-Aldrich showing different colours and tap densities.*

much more closely, along with the known poor cycling efficiency due to the problematic pulverization of silicon upon electrochemical cycling with lithium. Clearly, these three samples from Sigma-Aldrich differ in appearance and performance, and so we then carried out a more thorough characterization to try to better understand the morphology and chemistry of these materials. In practical applications, **Si-SA2** was used for preliminary synthesis and electrochemical tests of an a-SEI, outlined in Section 3.4, while **Si-SA3** was used for a systematic study of a-SEI and binder interactions in Section 3.5. The large **Si-325** and **Si-AA1** particles, Figure 3-22, show the most rapid decrease of capacity retention, most likely due to fragmentation during cycling. Large silicon particles have long been associated with increased pulverization during the expansion and contraction of silicon during lithiation.[204]

*Figure 3-20. Silicon nanoparticles **Si-SA1** (left) and **Si-AA1** (right), with both samples in powder form (top) and dispersed in pentane (bottom).*

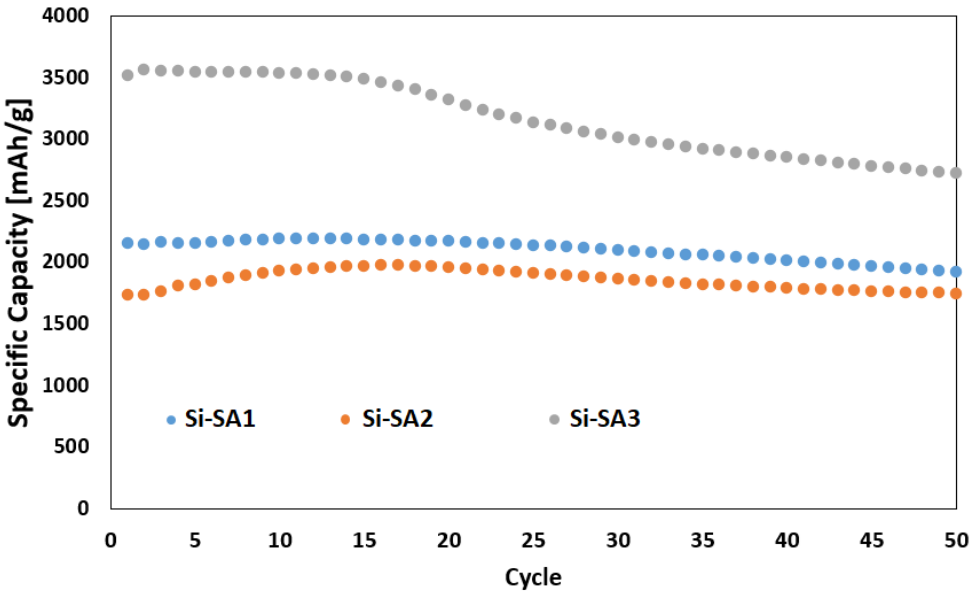

*Figure 3-21. Specific capacities of **Si-SA1**, **Si-SA2**, and **Si-SA3** over 50 cycles. All cells were cycled with FEC between 1.5 – 0.005 mV at a rate of 200 mA/g for cycles 1-3 and 600 mA/g for subsequent cycles.*

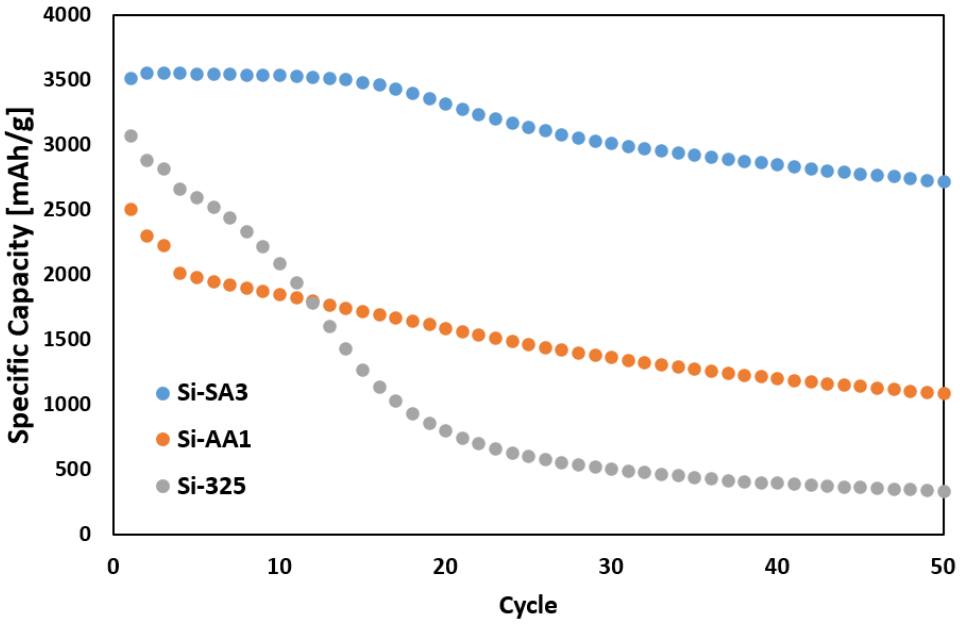

*Figure 3-22. Specific capacities of **Si-SA3**, **Si-AA1**, and **Si-325** over 50 cycles. All cells were cycled with FEC between 1.5 – 0.005 mV at a rate of 200 mA/g for cycles 1-3 and 600 mA/g for subsequent cycles.*

The most obvious starting place would be an analysis of particle size. Using SEM, the 3 samples from Sigma-Aldrich were sized manually using at least 200 measurements (Figure 3-23, Figure 3-24, and Figure 3-25), which yields a statistically significant size difference between **Si-SA3** particles and both **Si-SA1** and **Si-SA2**. **Si-SA3** particles have an average diameter of ~140 nm, larger than both ~ 60 nm for **Si-SA1** particles and ~80 nm for **Si-SA2**. The size distribution is represented by an average shifted histogram (ASH), which reduces the bias of traditional histograms that occurs when choosing bin size and location.[205] The distribution shows a narrow peak near to the average diameter with a long tail of larger sized particles. 150 nm has traditionally been considered the critical size below which particle fracture no longer occurs when lithiating crystalline silicon nanoparticles,[106] although some particle fracture is likely to occur eventually, even with smaller sizes.[206] Nevertheless, 140 nm average diameter **Si-SA3** particles may exist in an ideal size range to provide high specific capacity due to low oxide content, with higher capacity retention compared to larger, micron sized particles, as will be discussed vide infra.

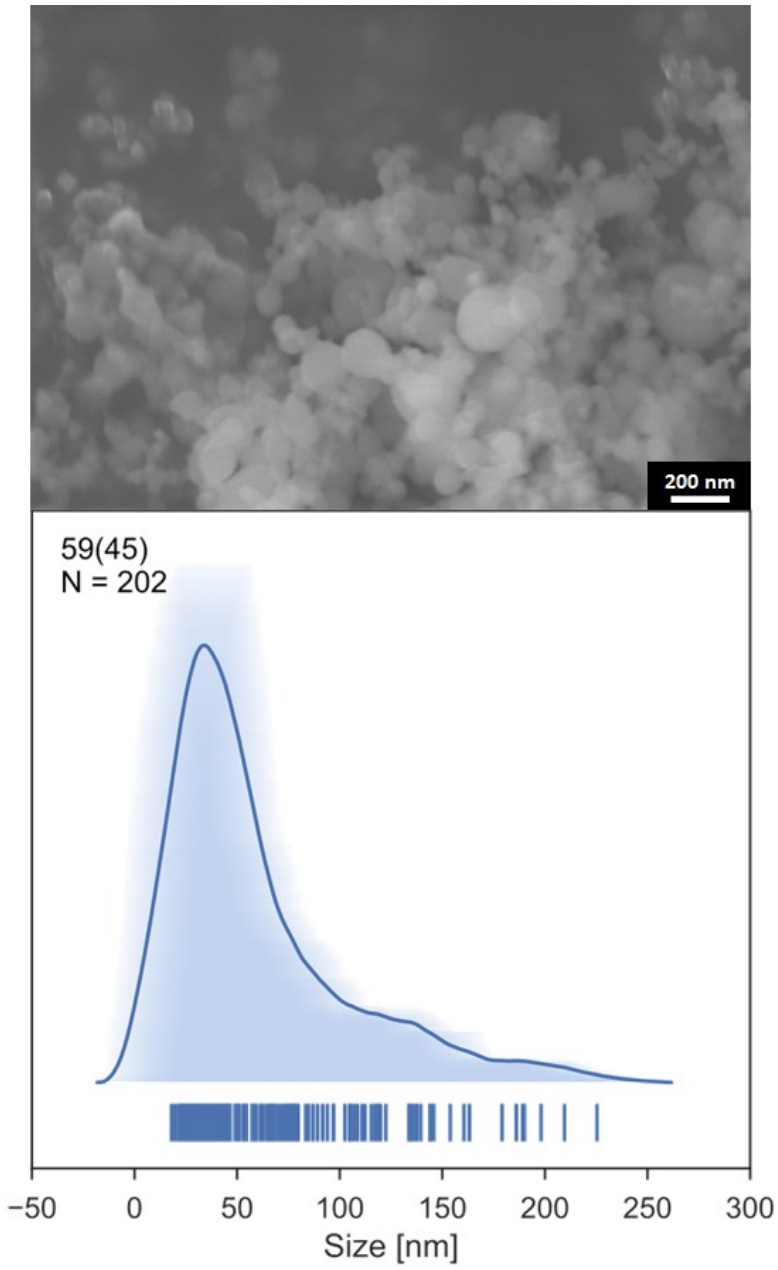

*Figure 3-23. SEM micrograph of a sample of **Si-SA1**, and size analysis represented with an average shifted histogram.*

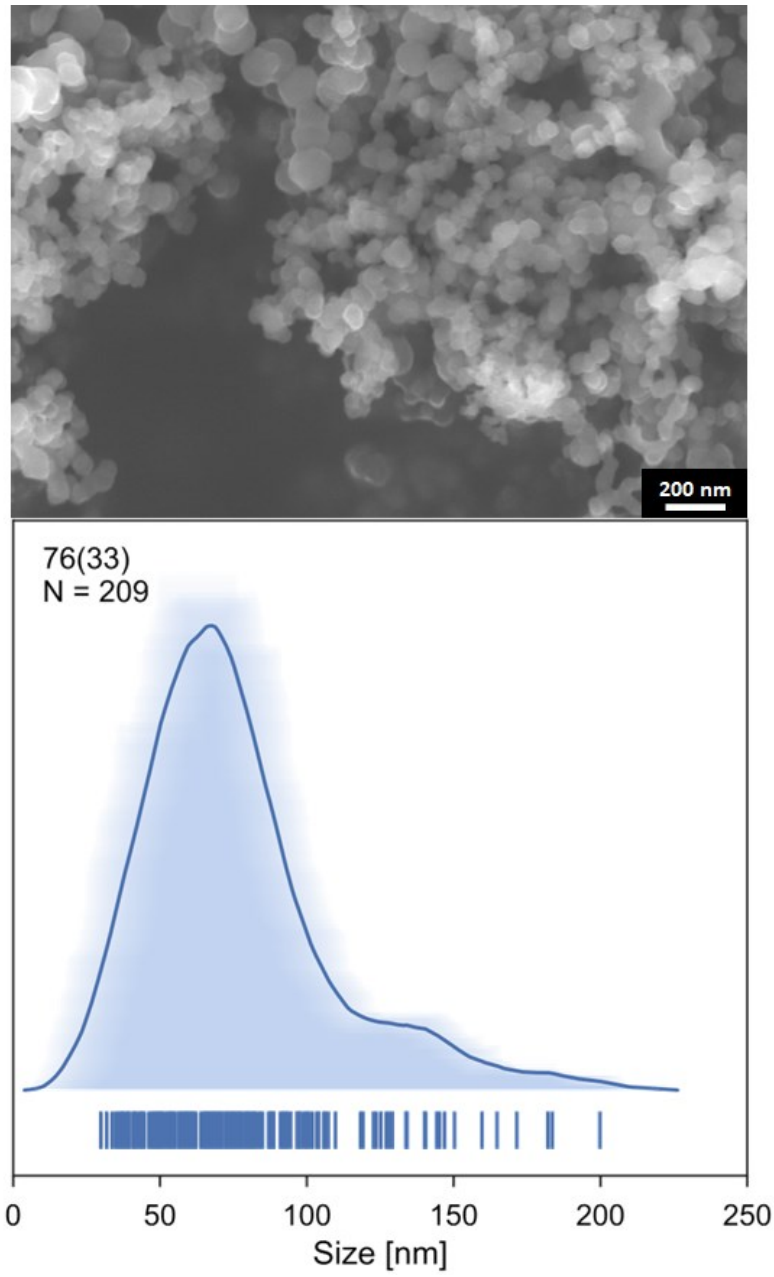

*Figure 3-24. SEM micrograph of a sample of **Si-SA2**, and size analysis represented with an average shifted histogram.*

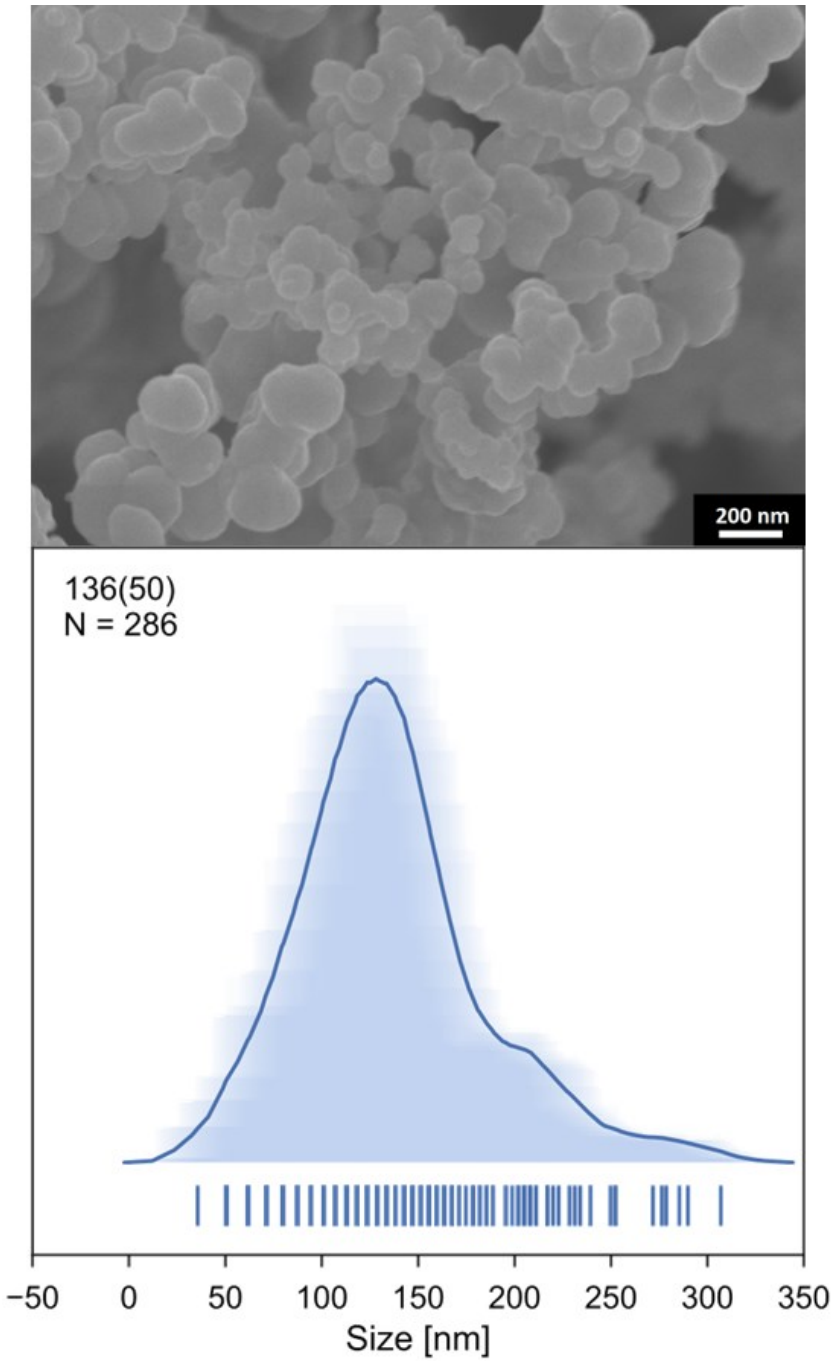

*Figure 3-25. SEM micrograph of a sample of **Si-SA3**, and size analysis represented with an average shifted histogram.*

Moving on to chemical analysis, the DRIFTS/FTIR spectra of the three samples from Sigma-Aldrich, **Si-SA1**, **Si-SA2**, and **Si-SA3** in KBr, are shown in Figure 3-26. The only features visible in these spectra correspond to ν(Si-H_x) in the region of 2100 - 2250 cm^{-1}, the broad ν(Si-O) mode centered around 1100 cm^{-1}, a non-hydrogen bonded ν(OH) stretch at 3740 cm^{-1}, and a feature around 900 cm^{-1}. Looking more closely at **Si-SA1**, the ν(Si-H_x) is predominantly oxygen backbonded as the feature is centered around 2250 cm^{-1}. In **Si-SA2**, however, the small feature at 2100 cm^{-1} corresponds to the ν(Si-H_x) that is not oxygen backbonded, pointing to decreased levels of oxidation proximal to the Si-H_x groups in this sample. In **Si-SA3**, the Si-H_x mode is insignificant, most likely due to the larger particle sizes and smaller surface area to bulk ratio. Meanwhile, the sharp feature at 3740 cm^{-1}, the ν(OH), identifies the presence of non-hydrogen bonded Si-OH groups. The ν(Si-O) stretch in **Si-SA3** is much narrower and shifted to higher energies than that in the **Si-SA1** and **Si-SA2** samples, suggesting that the **Si-SA3** sample comprises little bulk Si-O-Si, and predominantly Si-OH. These differences are subtle, and due to the transparency of the silicon to IR, it is unclear whether these differences are manifested on the surface and/or in the bulk of the nanoparticles (the core).

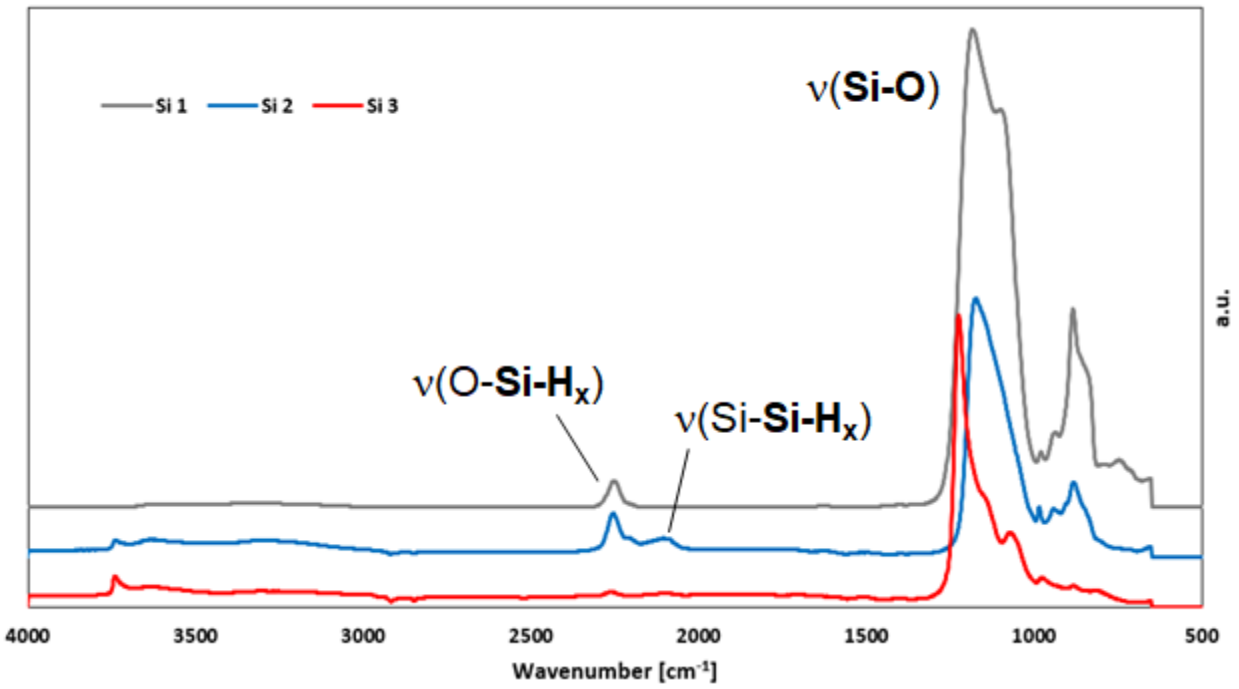

*Figure 3-26. DRIFTS spectra of **Si-SA1**, **Si-SA2**, and **Si-SA3**.*

Following the IR spectroscopy results, X-ray photoelectron spectroscopy (XPS) was carried out to provide insights into the quantity of oxidation in each of the three samples. A survey scan of each of **Si-SA1**, **Si-SA2**, and **Si-SA3** was carried out to determine the relative elemental composition on the surface of each particle, and we highlight the Si 2p peak to determine the oxidation state of silicon on the surface (Figure 3-27). Outside of more adventitious carbon in the scan of **Si-SA1**, the spectra of **Si-SA2** and **Si-SA3** look very similar at low resolution. At high resolution, however, the samples appear very different with respect to the oxidation state of the silicon, as can be determined by analysis of the Si 2p binding energy region. **Si-SA1** is dominated by the high binding energy feature at 102 eV that corresponds to Si(IV)/silica - although the **Si-SA1** spectrum is broadened slightly due to surface charging and the Si(IV) peak arises closer to 104 eV.[207] The **Si-SA2**, on the other hand, has two features, the larger higher

binding energy mode at 102 eV, and a smaller lower energy feature at 99 eV corresponding to Si(0). **Si-SA3** also comprises these two features corresponding to Si(IV) and Si(0) in an approximately 50:50 ratio. Since XPS is a surface-centric analytical technique with a penetration depth of ~10 nm, the high surface area nature of these silicon nanoparticles will have some component of the bulk. We can, however, conclude that **Si-SA3** has the most elemental Si(0), and that **Si-SA1** and **Si-SA2** are relatively more oxidized. These XPS results align with the results of the FTIR spectroscopy, as the spectrum of **Si-SA3** points to less Si-O-Si (silica), as well as the expectations from particle size in SEM.

Finally, we present differences in the crystallite size between **Si-SA1** and **Si-SA3** (Figure 3-28). Crystallite size can be determined through X-ray Diffraction (XRD) using the modified Scherrer equation:[208]

$$L=K\lambda/\beta\cos\theta$$

where L is the nanocrystallite size, K is a shape factor set to 0.9, β is the full width at half max of each peak at a given diffraction angle, θ. The **Si-SA3** particles have an average crystallite size of 11 nm, and 22 nm for **Si-SA1**. These results indicate that the as-received commercial particles comprise small nanocrystallites with an unknown fraction of amorphous silicon. Particle stress is known to be greater in crystalline silicon particles compared to amorphous particles,[106,142] and smaller crystallite sizes are associated with less fracturing and increased capacity retention.[209,210] Our results suggest that **Si-SA3** particles have a larger particle size and low surface area to volume ratio, while also having smaller crystalline domains that could minimize stress during expansion.

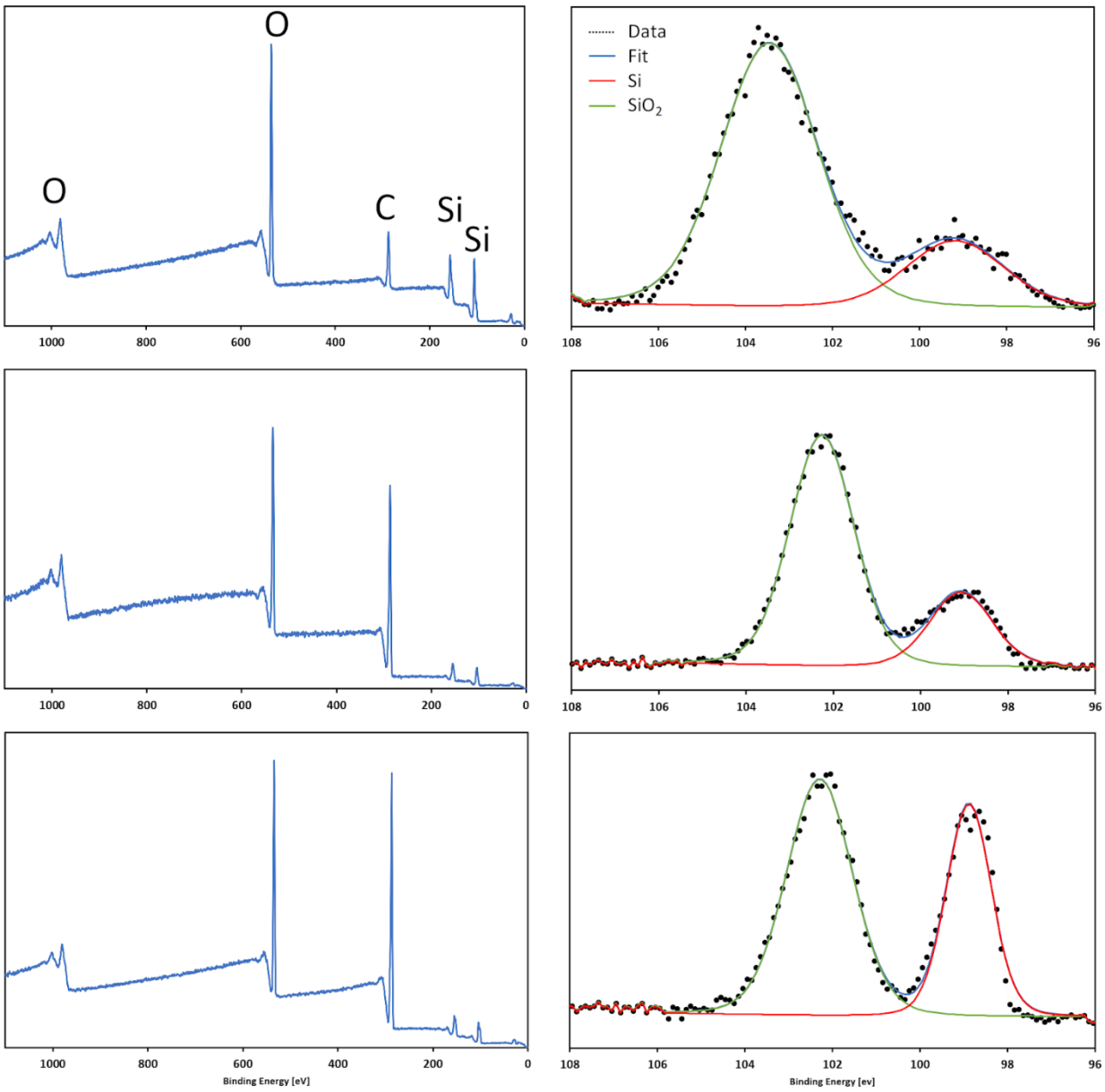

Figure 3-27. *XPS of the Si 2p region for* ***Si-SA1****,* ***Si-SA2****, and* ***Si-SA3****.*

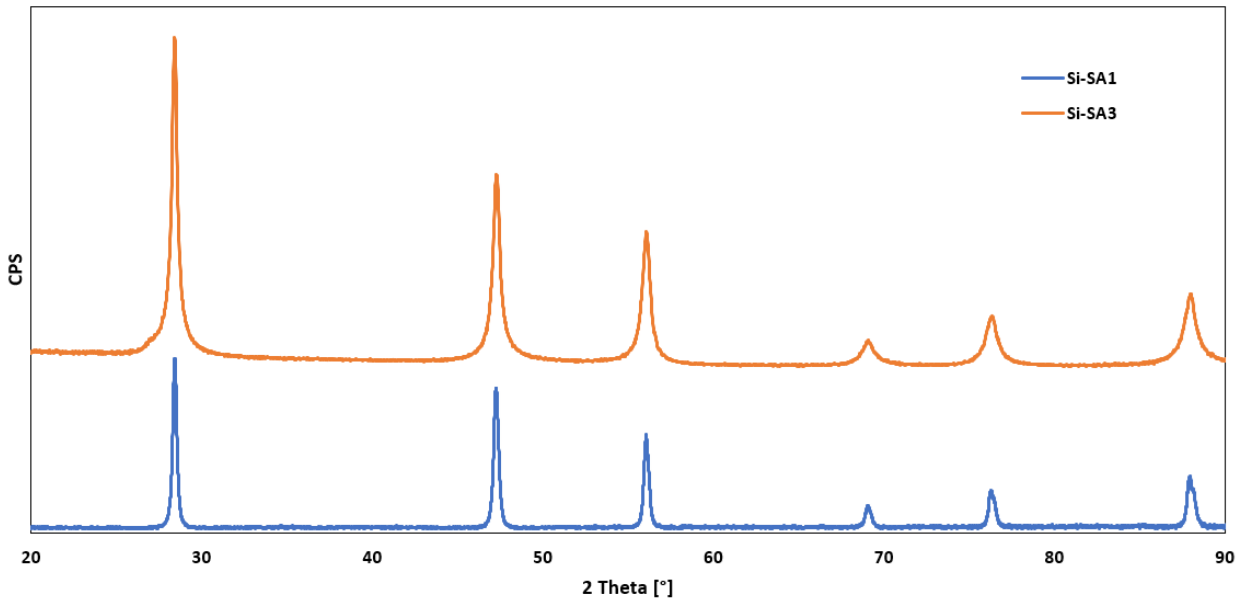

Figure 3-28. *Powder XRD of **Si-SA1** and **Si-SA3**.*

Silicon from Alfa Aesar was also purchased for use as nanoparticles with an average particle size of 100 nm. However, in contrast to silicon samples from Sigma-Aldrich, **Si-AA1** particles comprise micron-sized particles as shown in Figure 3-29. Conducting a representative count of the particles was deemed unrealistic due to the large distribution and, but many particles < 100 nm are present alongside particles > 5 µm. DRIFTS was performed for **Si-AA1** particles (Figure 3-30), however, very little could be observed other than ν(Si-O) stretching due to the very low surface to area ratio for particles this large. **Si-AA** particles will be referenced briefly in Chapter 4, but were generally disregarded for experimentation due to the large sizes of particles present.

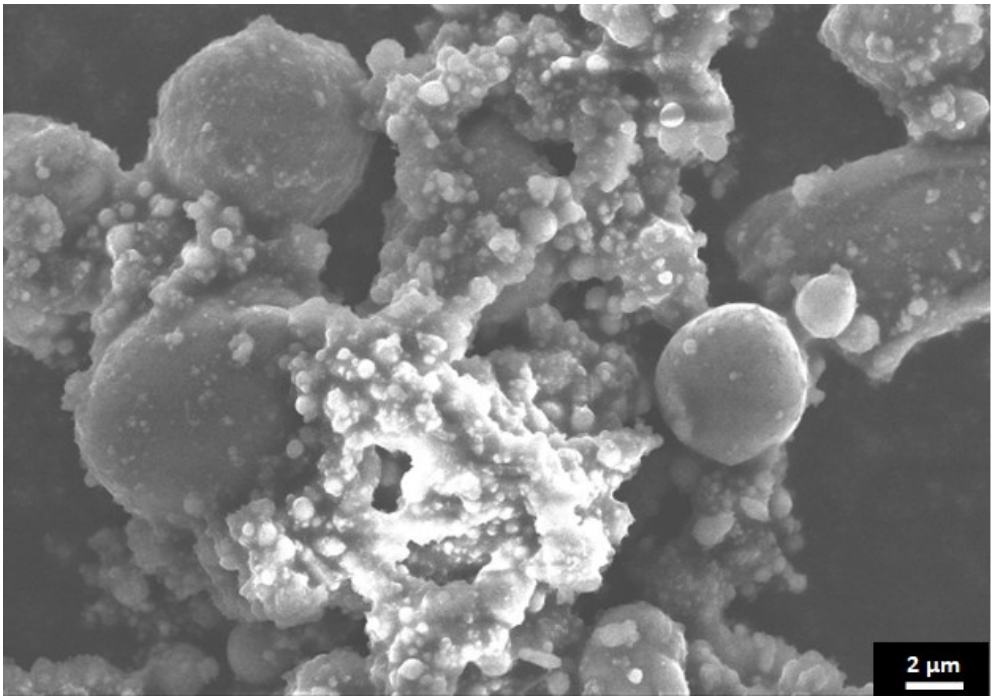

*Figure 3-29. **Si-AA1** SEM image showing micron sized particles. Sold as having an average particle size of 100 nm.*

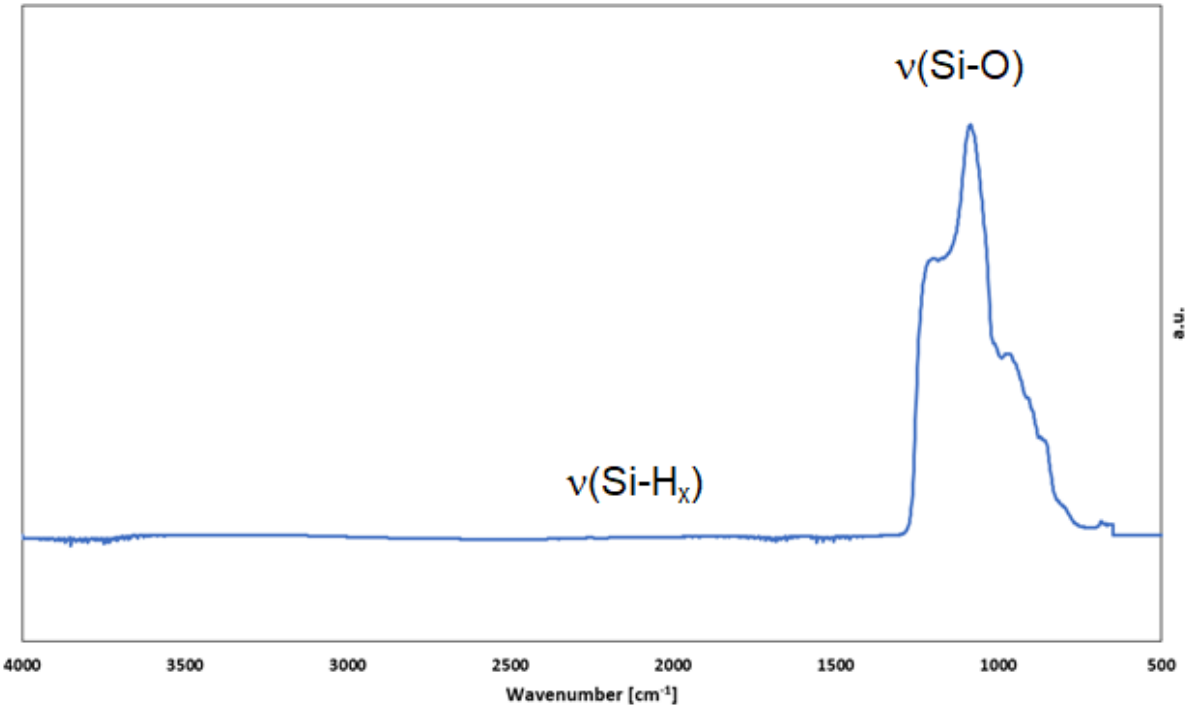

*Figure 3-30. DRIFTS spectrum of **Si-AA1**.*

3.4 Hydrosilylation of silicon nanoparticles

In this section, we focus on hydrosilylation for silicon nanoparticles to determine the effect of artificial surface coverages as part of a slurry electrode. This work focuses on expanding the list of functional groups that could be used as an a-SEI, and is performed on **Si-SA2**, which was commercially available at the time, while a more systematic analysis of a-SEI in lithium ion half-cells with different binders is performed with **Si-SA3** and described in Section 3.5. Silicon nanoparticles have a higher surface area than the thin films described in Section 3.2, and thus the influence of the surface is expected to be more apparent. Silicon nanoparticles are also able to scale more easily for commercial purposes than thin films, as well as integrating into existing cell infrastructure, using many of the slurry mixing methods currently used for graphite anodes. We examine silicon with a native oxide (Si-O_x), hydrogen-terminated silicon (Si-H_x) and a variety of a-SEI using both polar aprotic and nonpolar functionalities. The HF etching step was performed by immersing SiNPs in a solution of 5 % HF, 10 % ethanol, and 85 % water (solution A) for 10 minutes, then isolating the particles through vacuum filtration, and washing with a 4:1 water:ethanol solution followed by pentane.

Assignment	Frequency (cm^{-1})[y]	**Assignment**	Frequency (cm^{-1})
ν(Si-**O-H**)	3,660 (sharp)	ν(Si-**Si-H$_3$**)	2,142
ν(**H-O-H**) (ads.)	3,600 (broad)	ν(Si-**Si-H$_2$**)	2,108
ν(**C-H**) (sp^2)	3100 - 3000[x]	ν(Si-**Si-H**)	2,087
ν(**C-H**) (sp^3)	3000 - 2850[x]	ν(**C=O**) (carbonate)	1,760 - 1660[x]
ν(O$_3$-**Si-H**)	2,256	ν(**C-O**)	1,260 - 1,050[x]
ν(O$_2$-**Si-H$_2$**)	2,200	ν(**Si-O-Si**)	1,050
ν(O$_1$-**Si-H$_3$**)	2,160	δ(**Si-H$_2$**)	916

Table 3-3. Common FTIR frequencies on porous silicon surfaces and selected functional groups of alkynes/alkenes for hydrosilylation. [x]Select peak assignments of common organic compounds as per reference [211]. [y]Silicon surface assignments as per Reference [212].

The particles were dried using vacuum filtration and further washed with pentane. The particles were then characterized via diffuse reflectance FTIR (DRIFTS), and notable peak shifts for the hydrosilylation of silicon nanoparticles are shown in Table 3-3. As described earlier, for as-received **Si-SA2** nanopowder, Figure 3-31 (blue), three main features are noted, in particular the features at 2230 cm^{-1} and 2100 cm^{-1} corresponding to oxygen backbonded Si-H_x groups, $\nu(O_xSiH_{4-x})$, and the smaller feature at 2100 cm^{-1}, which corresponds to the group of ν(Si-H_x) stretches not proximal to Si-O

groups. There is also a broad and intense mode at 1100 cm^{-1} which corresponds to the Si-O stretching mode. Upon treatment with 5 % HF (aq), Figure 3-31 (orange), the DRIFTS spectrum shows that the primary feature is the ν(Si-H_x) stretch with no oxygen backbonding, pointing to a surface dominated by Si-H_x groups and little oxidation. The δ_s(Si-H2) scissor mode can be clearly seen at ~850 cm^{-1}, and is only apparent in p-Si samples with little or no surface oxidation.

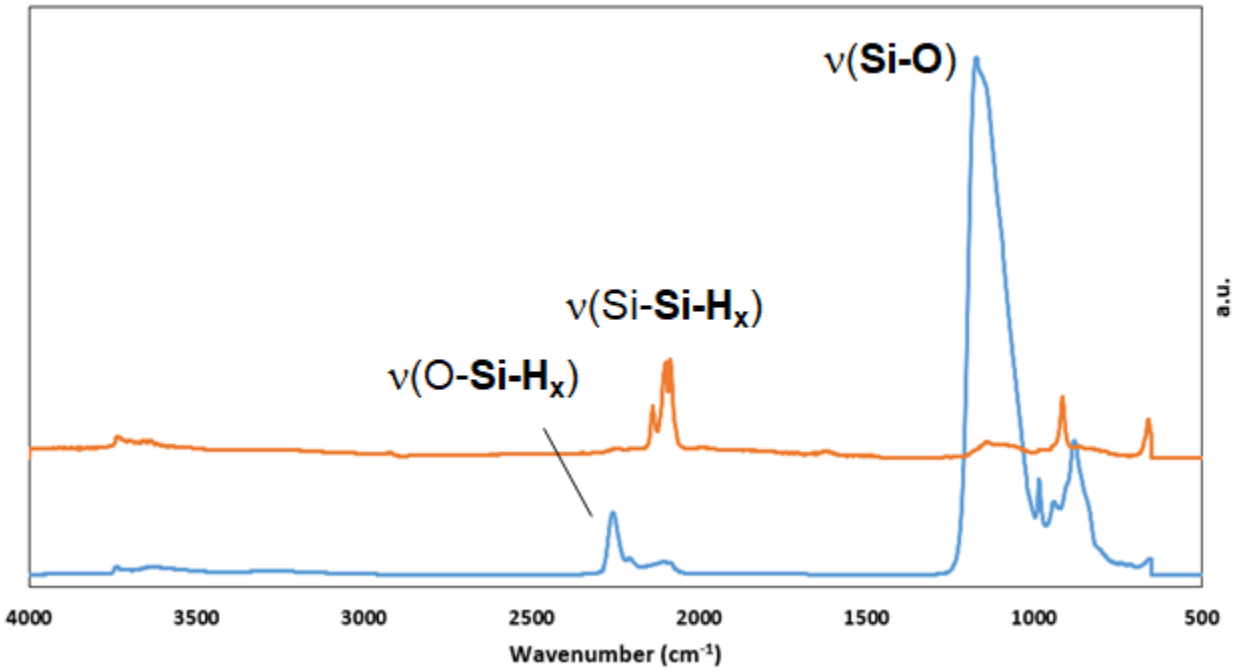

Figure 3-31. *DRIFTS of as-received **Si-SA2** (blue) and HF (aq) etched SiNPs (orange).*

Hydrosilylation was carried out on the Si-H_x-terminated silicon nanopowders with six unsaturated molecules, and two binary combinations of molecules (Figure 3-32). Hx-Si-terminated nanoparticles were stirred in a 10 % v/v solution of alkyne/alkene in mesitylene under refluxing conditions (165 °C) for 2 hours. The nanoparticle product was centrifuged and decanted three times and washed with pentane between each

centrifuge step to remove mesitylene and alkyne/alkene, followed by drying under vacuum for 16 hours. The results with TEG and 1-dodecene were characterized using DRIFTS and confirm straightforward hydrosilylation (Figure 3-33). Hydrosilylation with 1-dodecene (Si-Dode) proceeded smoothly with little oxidation as demonstrated by the absence of the features at ~1100 cm^{-1} and 2250 cm^{-1} that correspond to the ν(Si-O) and oxygen backbonded $\nu(Si-H_x)$ stretching modes, respectively. A small feature corresponding to ν(Si-O) is typically observed even in $Si-H_x$ samples. The strong sp^3 hybridized ν(C-H)features centered around 2900 cm^{-1} - 3000 cm^{-1} are characteristic of the dodecyl functionality. In the case of the oligoethylene-terminated olefin, TEG, hydrosilylation is also evidenced by $\nu(C-H_x)$ stretching in the 2900 cm^{-1} - 3000 cm^{-1} region, as well as ν(C-O) stretching at 1100 cm^{-1}. The characteristic ν(C-O) stretching modes overlap with the ν(Si-O)-Si stretches. A low broad feature in the region of 3300 cm^{-1} to 3500 cm^{-1} can be seen, which corresponds to hydrogen bonded OH groups. Considering the hygroscopic nature of oligoethylene, absorbed water likely contributes to this feature, in addition to any oxidation of the silicon surface itself (Si-OH groups). The diagnostic feature for oxidation of the silicon surface is the oxygen backbonded $\nu(Si-H_x)$ stretch at 2250 cm^{-1}, which is not visible in Figure 33.

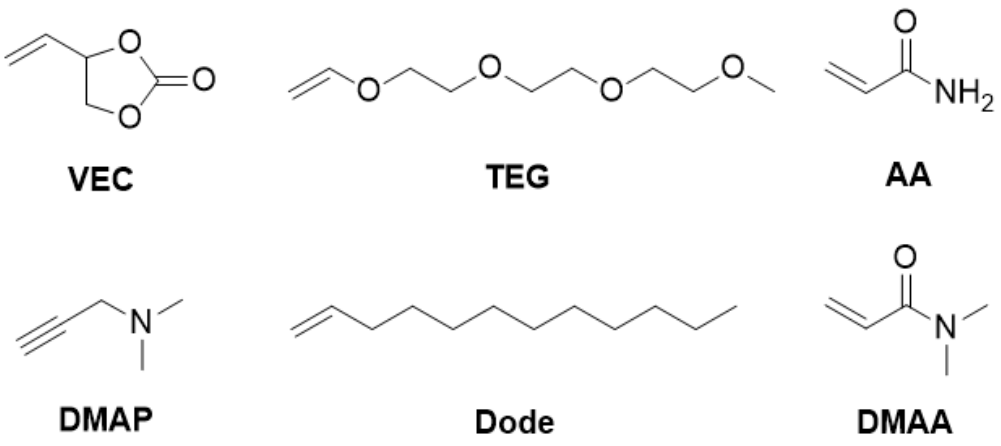

Figure 3-32. Molecules considered for hydrosilylation with hydrogen-terminated silicon.

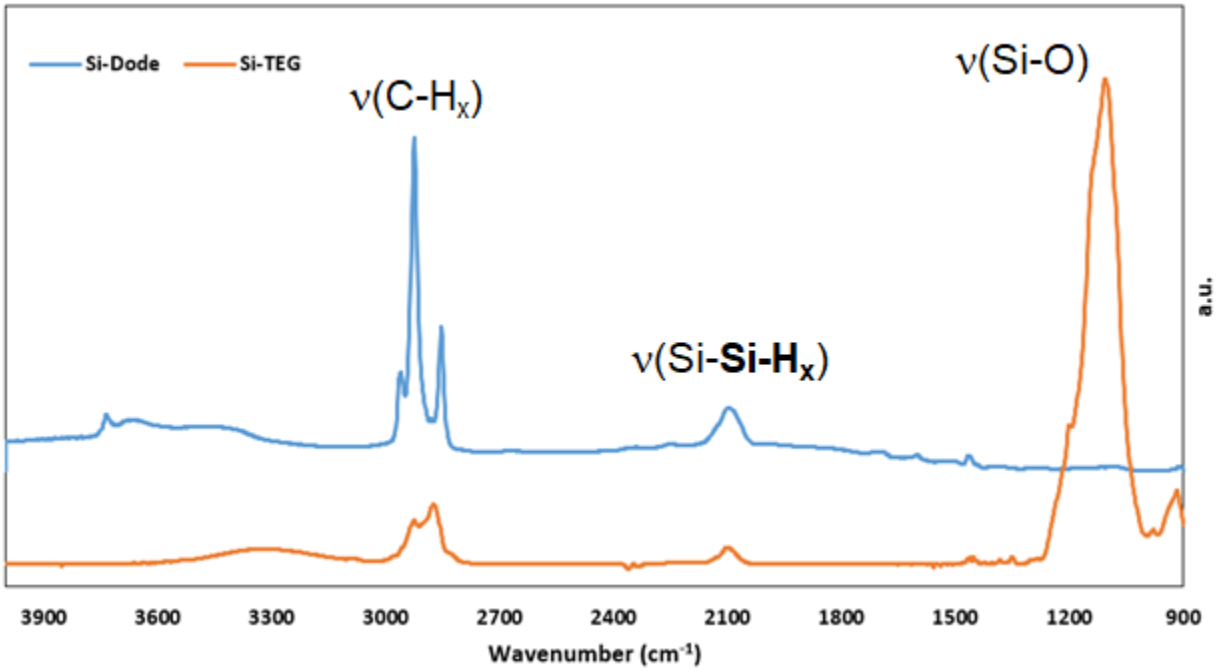

*Figure 3-33. DRIFTS of Si-TEG and Si-Dode on **Si-SA2.***

VEC was hypothesized to be a candidate for stable a-SEI since the molecule is closely related to the carbonate electrolytes that decompose and form an SEI in-situ, for example sharing the five-centred ring found in ethylene carbonate. Hydrosilylation with the VEC molecule, as well as 1:1 v/v hydrosilylation with VEC and either 1-dodecene or TEG (Figure 3-34) resulted in interfaces with substantial oxidation, as determined by FTIR. To prevent oxidation during each hydrosilylation reaction, argon was bubbled through the system, and one end was capped with a condenser filled with $CaCl_2$. The degree of oxidation observed in the DRIFTS spectra suggests that there was insufficient positive pressure preventing oxygen from entering the system, and an oil bubbler should be used in future experiments. The oxygen backbonded $\nu(Si\text{-}H_x)$ stretch at ~2250 cm^{-1} along with $\nu(sp^3\ C\text{-}H_x)$ and $\nu(C\text{-}O)$ stretches are observed in each spectrum as above, as well as a complex group of features near 1100 cm^{-1}. A $\nu(C{=}O)$ stretch that corresponds to the carbonate group is expected to appear close to 1700 cm^{-1} - 1800 cm^{-1}, and is observed at 1818 cm^{-1} in neat VEC (Figure 3-35). Si-VEC has an intense peak at 1788 cm^{-1}, while spectra of Si-VEC:Dode and Si-VEC:TEG have $\nu(C{=}O)$ peaks of weaker, though varying intensities at 1710 cm^{-1} and 1788 cm^{-1}. For Si-VEC:TEG, the $\nu(C{=}O)$ stretching peaks are weaker, and the chemistry seems to be dominated by oxidation possibly from residual water in TEG.

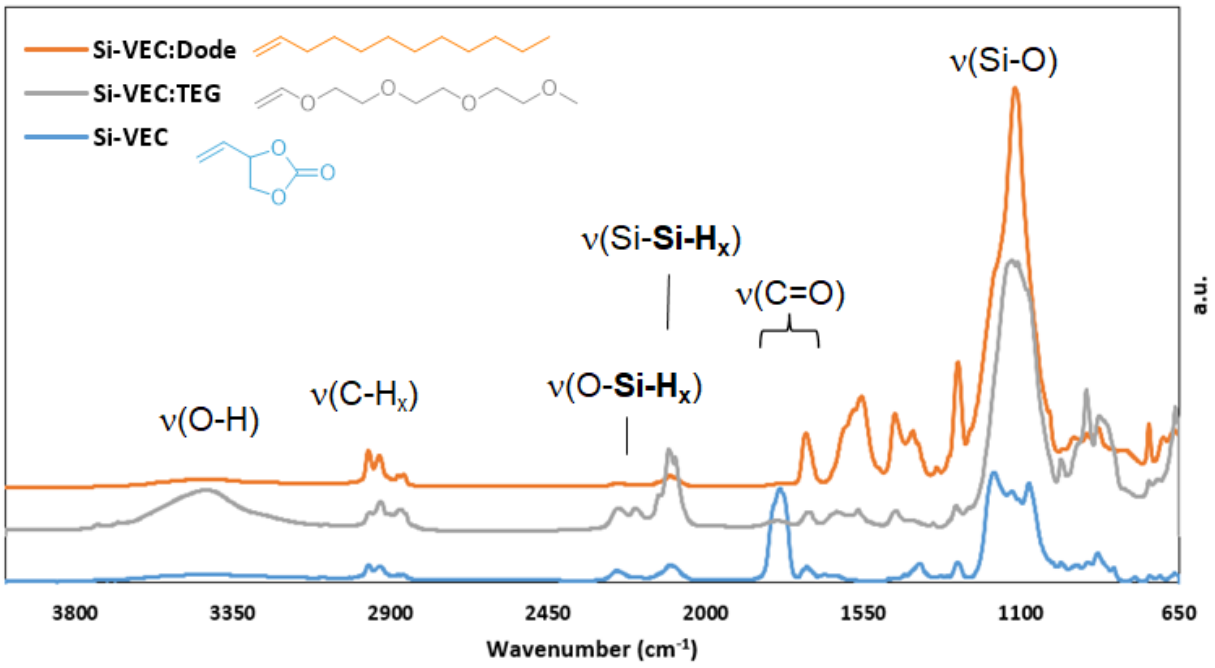

*Figure 3-34. **Si-SA2** particles after hydrosilylation with VEC (blue), 1:1 - VEC:TEG (grey), and 1:1 - VEC:Dode (orange).*

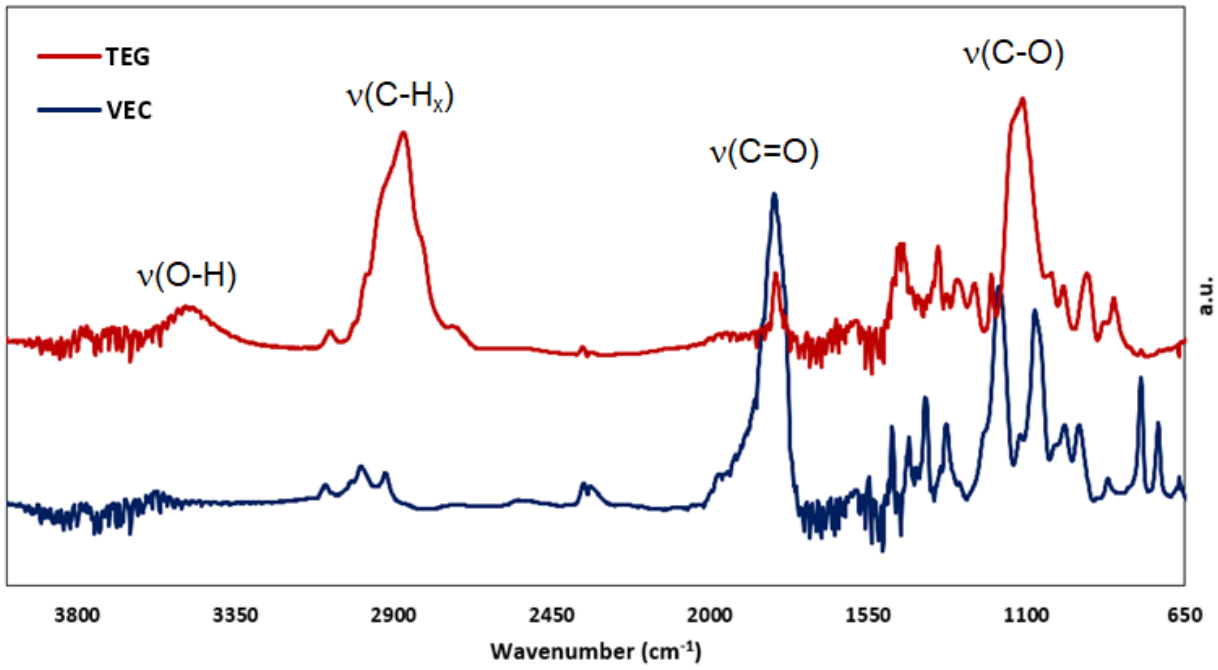

Figure 3-35. *Transmission FTIR of neat VEC liquid (blue) and neat TEG liquid (red).*

Two interactions of note could occur prior to cell assembly: oxidation by residual water or oxygen to form surface silanol groups, and physisorption of the alkenes/alkynes on the surface of silicon, particularly VEC. Oxidation is clearly seen in the DRIFTS spectra of some hydrosilylated silicon particles, such as Si-VEC:TEG in Figure 3-34. However, many silicon slurry recipes are mixed in water, which reduces the requirement for a low level of spurious oxidation occurring alongside the hydrosilylation chemistry (since some degree of reaction with residual water is therefore inevitable). Furthermore, as discussed in Section 3.2, the presence of a native oxide and surface silanol groups is not necessarily deleterious to silicon cycling. It is unclear whether physisorption of VEC is occurring during any of the hydrosilylation reactions described here; however, VEC has a very high surface tension (visible to the naked eye with colouring, Figure 3-36), and a high boiling point (237 °C). The standard procedure for cleaning hydrosilylated particles involved centrifuge washes with pentane, which would be less effective due to minimal solubility of VEC in pentane and the strong intermolecular forces between VEC molecules, and evacuation of the particles overnight at room temperature, which would be hampered by the high boiling point. The presence of VEC during slurry mixing - although it would be much diluted in water - could affect the mixing of silicon nanoparticles with other components, and would at least lower the mass of silicon added when weighing ingredients. If true, the lower mass would, in turn, actualize as a lower apparent specific capacity for Si-VEC. After the slurry is prepared, however, cells are exposed to < 20 Torr at 120 °C, which - for a boiling point of 237 °C, should result in the removal of most residual VEC prior to cell assembly, if indeed VEC is adsorbed in our sample.

Finally, hydrosilylation was carried out with three other molecules from Figure 3-37, acrylamide (AA), N,N-dimethyl acrylamide (DMAA), and 3-dimethylamino-1-propyne (DMAP); the DRIFTS results are shown in Figure 3-38. Results with acrylamide appear successful, with minimal oxidation seen at 2250 cm^{-1}, ν(C=O) at 1710 cm^{-1} and expected features corresponding to $\nu(C\text{-}H_x)$ and ν(C-N) (~ 2900 cm^{-1} and 1150 cm^{-1}, respectively). The spectrum resulting from the hydrosilylation of DMAP is hard to interpret due to a very intense broad peak at 1228 cm^{-1}. This peak may conceivably be due to C-N stretching from the covalently bound amine, but obscures other expected features, such as those in the $\nu(C\text{-}H_x)$ region. For Si-DMAA, we compare the broad peak at 3000 cm^{-1} and the many carbonyl peaks at 1650 cm^{-1} to a spectrum of neat DMAA liquid on a KBr plate, and observe very similar vibrations at these wavelengths for the hydrosilylated sample. We can also identify the attachment of DMAA using XPS, because it can detect the nitrogen in DMAA due to the high surface sensitivity of XPS. A low resolution XPS spectrum of Si-DMAA in Figure 3-39 shows a signal from the N 1s peak at 400 eV, the expected binding energy for an amine, which serves as further evidence for the presence of DMAA on the silicon surface.

Figure 3-36. *VEC solution sliding down the walls of a polypropylene centrifuge tube. The liquid will not form individual droplets when mixed in polypropylene or glass surfaces, indicative of high surface tension. The VEC is coloured with a suspension of silicon particles, which allows for the observation of strong intermolecular interactions within the neat VEC. The specific experiment pictured is not germane to Section 3.4.*

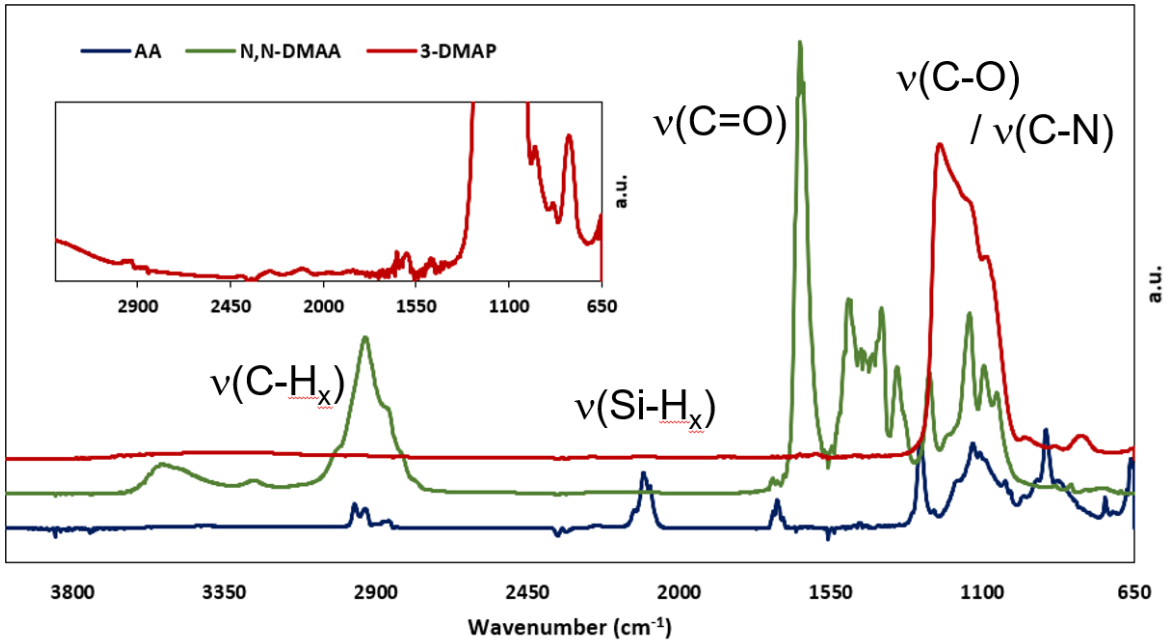

Figure 3-37. Diffuse reflectance infrared Fourier transform spectroscopy (DRIFTS) of various hydrosilylated surfaces of **Si-SA2**.

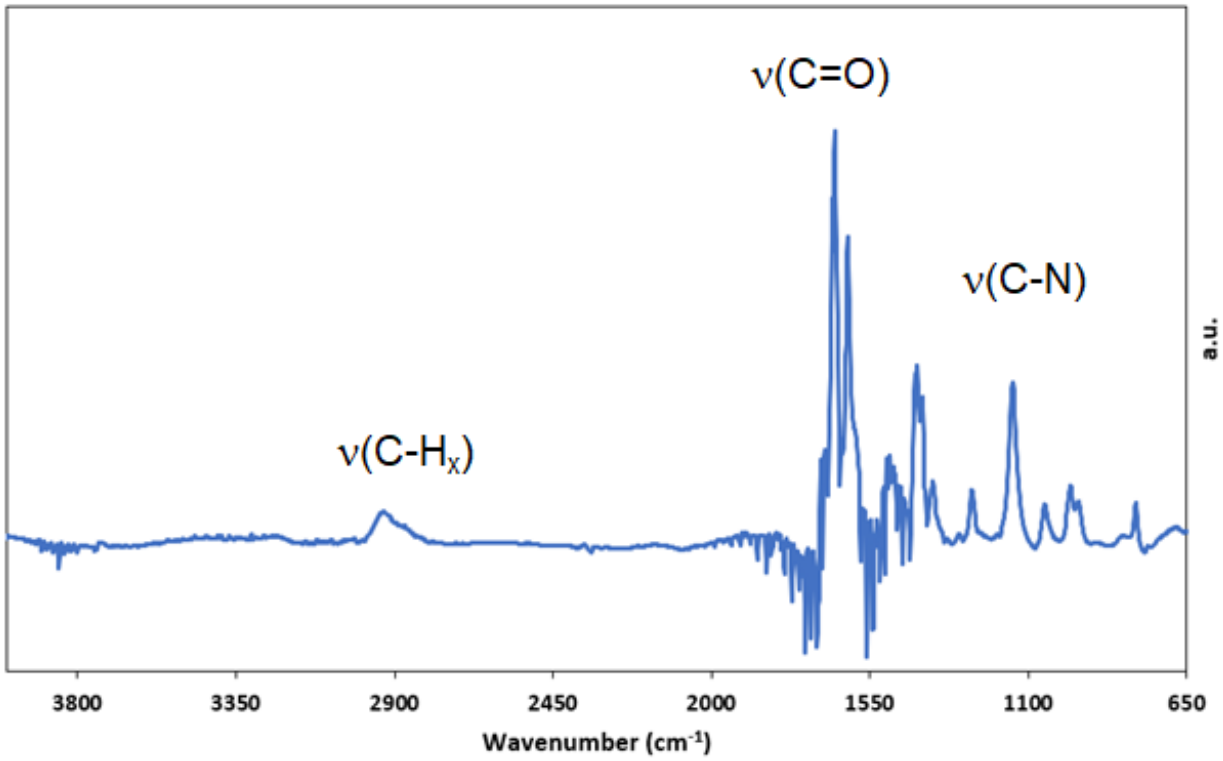

Figure 3-38. FTIR of neat DMAA on a KBr plate.

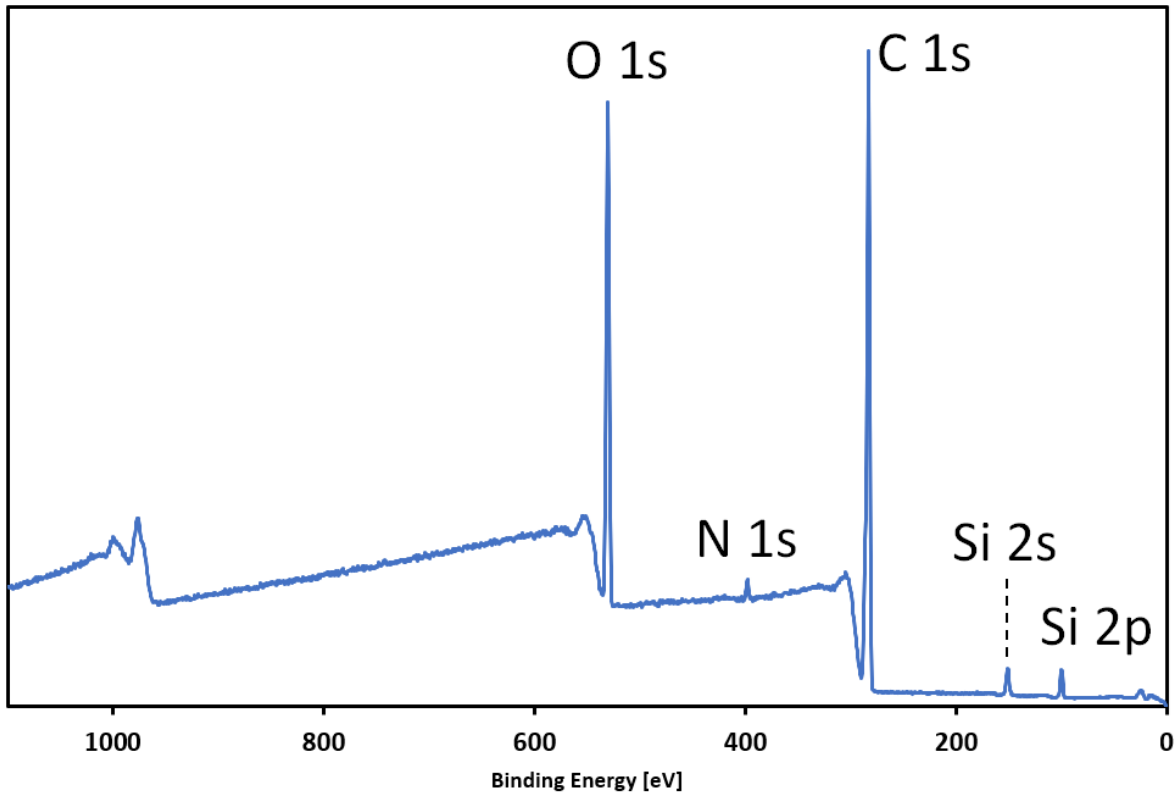

Figure 3-39. XPS spectrum of Si-DMAA.

We did not proceed to cell assembly with the silicon functionalized by amine or amide functional groups - AA, DMAA, and DMAP. The yields required for cell assembly were high, and further work was transitioned to **Si-SA3** particles, as outlined in Section 3.3 and further explored in Section 3.5. Unlike an N,N-dimethyl acrylamide coating, acrylamide could lead to high levels of irreversible capacity in early cycles due to being protic. Protic surfaces and electrolyte also pose a safety risk due to the release of hydrogen gas upon reduction in the cell. Amides and amines also have fewer analogues in the literature, both as a-SEI and as naturally occurring SEI components, although N,N-dimethylacrylamide has been used as an electrolyte additive.[213] Future work could focus on similar functional groups, even including protic a-SEI for silicon nanoparticles,

given that silicon with a native oxide and protic silanol groups is now accepted to perform well under many circumstances.

Of the selected silicon a-SEIs, we proceeded to produce slurries for electrochemical testing in coin cells. Slurries were produced using a 60:20:20 ratio of **Si-SA2** SiNPs, Timcal Super P conductive carbon additive, and lithium polyacrylic acid (LiPAA) used as a 6-10 % solution in water. The mixture was then ball milled in a teflon vial with zirconia balls, milling for one hour at 500 rpm. Slurries were cast onto copper at a height of 100 μm using a doctor blade. We minimize the impact of residual water as strictly as possible by drying under vacuum at 120 °C, both before punching and weighing our disks and before bringing the discs into the glove box. The copper discs were assembled into coin cells using 1 M $LiPF_6$ in 1:1 EC:DEC as the electrolyte, with 10 wt% FEC as electrolyte additive. All cells were cycled between 2 V and 5 mV, using 3 formation cycles at 200 mA/g followed by subsequent cycling at 600 mA/g.

As discussed in Section 3.3, initial capacity was low for **Si-SA2** nanoparticles, beginning at 1730 mAh/g, or 48 % of theoretical capacity (Figure 3-40). Specific capacity was very similar for particles etched with hydrofluoric acid, although we expect the hydrogen termination to be partially removed during slurry preparation in water, but the Coulombic efficiency of as-received **Si-SA2** nanoparticles is much lower without an HF etch to remove the native oxide, with an initial Coulombic efficiency (ICE) of 60.2 % for Si-O_x compared to 80.7 % for Si-H_x terminated particles. Functionalization with an olefin group – which also entailed an HF (aq) etch prior to hydrosilylation – was able to dramatically improve initial capacity, for example to 2749 mAh/g for Si-TEG, or 77 % of theoretical capacity.

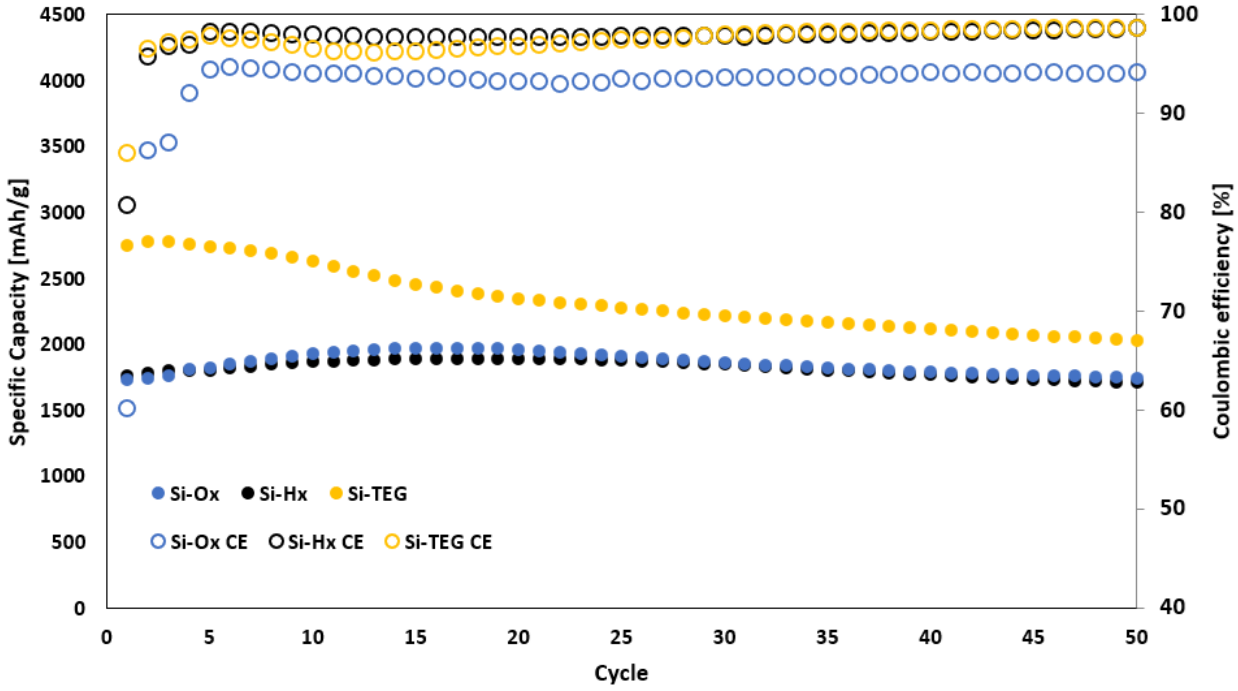

*Figure 3-40. Specific capacity and Coulombic efficiency of **Si-SA2** particles over 50 cycles. A native oxide surface (Si-O_x) is compared to HF etched particles (Si-H_x) and functionalized Si-TEG particles. All cells were cycled between 1.5 – 0.005 mV at a rate of 200 mA/g for cycles 1-3 and 600 mA/g for subsequent cycles.*

When we compare the different functionalizations (Figure 3-41), two main findings present themselves. First, Si-Dode particles perform the worst. The initial capacity begins at 868 mAh/g, while the lowest capacity with any other functionalized silicon nanoparticle sample is 2605 mAh/g. We hypothesize that dodecyl functionalities on **Si-SA2** degrades silicon cycling for two main reasons. 1) The hydrophobic monolayer of dodecyl groups may impede lithium diffusivity through the a-SEI more than other surface coatings. Lithium ions will have a greater activation barrier to diffusion through a non-polar coating, and the unbranched aliphatic structure of the dodecyl group should allow for more efficient packing and higher density of substitutions

on the surface. 2) Non-polar coatings on the surface of silicon will interact less favourably with the polar functionalities on LiPAA binder, with the hydroxide and carboxylic acid groups known to be on the surface of conductive carbon additive,[214] and with the water used as a solvent during ball milling. The chemical incompatibility of the dodecyl-terminated surfaces with the other slurry components is visible in Figure 3-42, which shows a mixed slurry of Si-Dode in which a dark brown liquid is stirred to reveal the contrast with a light brown film on top. Some Si-Dode particles float on top of the water solution, preventing homogeneous mixing under the conditions used for other particles, and not ameliorating upon 30 additional minutes of ball milling. We explore the differences with samples hydrosilylated with 1-dodecene, vide infra.

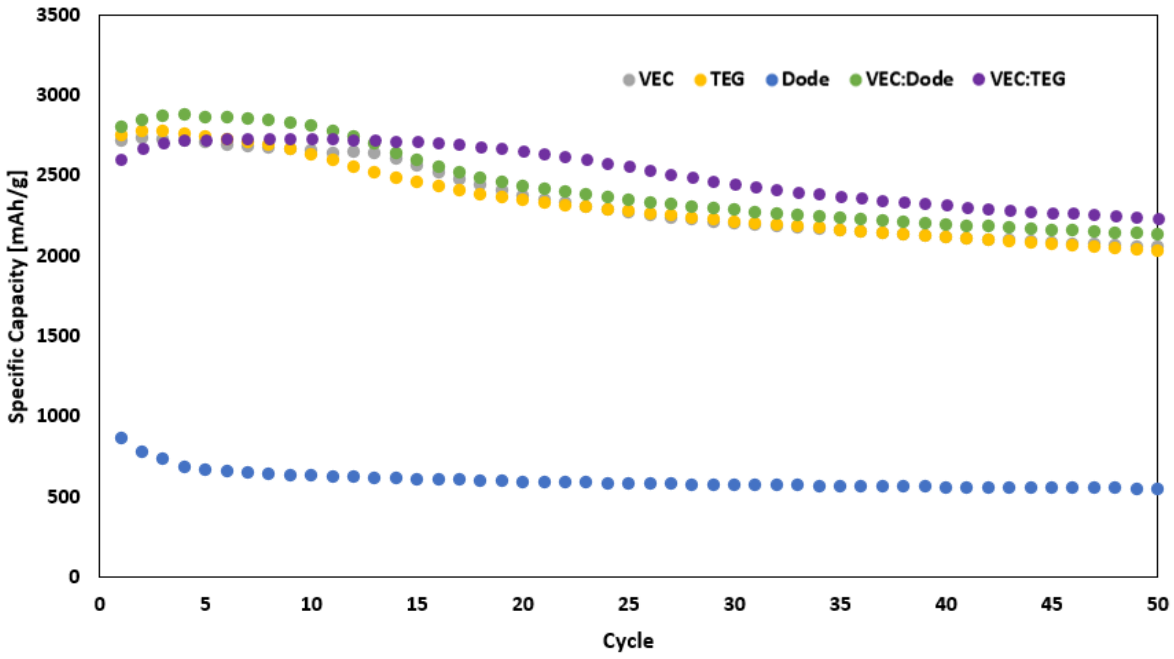

*Figure 3-41. Specific capacity over 50 cycles of various functionalized **Si-SA2** nanoparticles. All cells were cycled with FEC between 1.5 – 0.005 mV at a rate of 200 mA/g for cycles 1-3 and 600 mA/g for subsequent cycles.*

Figure 3-42. A slurry of Si-dodecyl functionalized nanoparticles in water. Light brown particles can be seen suspended above the darker brown slurry underneath.

Si-VEC:TEG particles offered the highest capacity retention, as well as the highest absolute capacity after 50 cycles (purple data, Figure 3-41). Si-VEC:TEG is a strong candidate for providing the strongest protection to silicon and the highest capacity retention. VEC and TEG mimic the organic components of a stable SEI formed from the decomposition of FEC. Solid state NMR studies performed by the Grey group have found that FEC naturally forms poly-VC[57] and polyethylene oxide[69] chains in the SEI of silicon nanowires (SiNWs), associated with high capacity retention and Coulombic efficiency. Furthermore, the Si-VEC:TEG particles mirror the work of Gao et al using click chemistry to form a-SEI on the surface of silicon. Gao and coworkers also mixed a polyethylene oxide derivative and an alkylene carbonate derivative to co-functionalize silicon and achieve their highest capacity retention. Our results on **Si-SA2**

also suggest that this may be a promising strategy to improve cycling of silicon anodes in lithium ion batteries.

The cumulative Coulombic inefficiency (CCI) of each cell is displayed in Figure 3-43. CCI is the sum of all Coulombic efficiency losses, equal to the area above the curve in a tradition Coulombic efficiency graph, and calculated according to the equation,

$$CCI = \left(1 - \frac{Q_{Delithiation}}{Q_{Lithiation}}\right) x\ 100\ \%$$

We include silicon nanoparticles capped with Si-O_x and Si-H_x along with all of the functionalized SiNPs, leading to many overlapping data points. There are two main takeaways. First, the CCI for as received particles with a native oxide is more than twice as high after 50 cycles compared to all other surface coatings. The high CCI of Si-O_x is in direct contradiction to the studies on silicon thin films, in which the native oxide had the lowest CCI, and occurs despite the fact that the silicon particles capped with Si-O_x and Si-H_x had similar initial capacities and capacity retentions. Secondly, Si-VEC:TEG has the lowest CCI after 50 cycles, again suggesting that synergistic effects between particles with similar functional groups may be the best method of improving capacity retention. However, even for Si-VEC:TEG, the CCI exceeds 1 after 40 cycles, indicating total cell death if tested on a full cell, all else being equal. It is clear that the conditions used here are still not close to improving silicon for commercial applications.

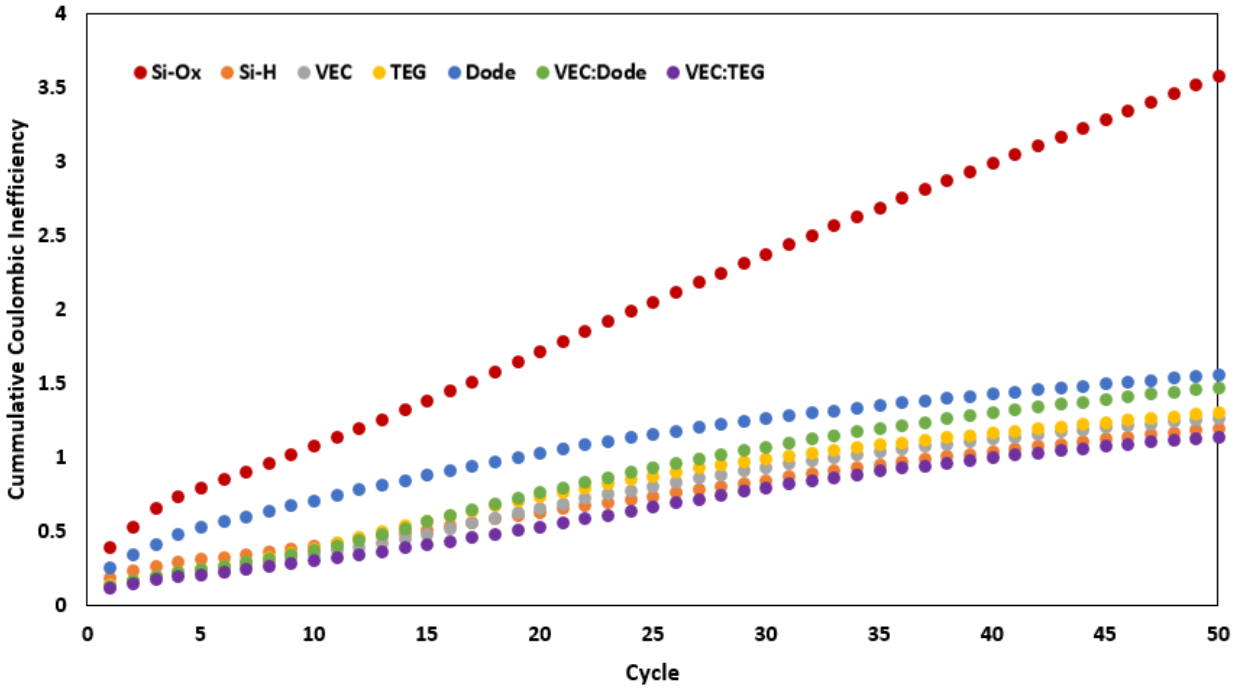

*Figure 3-43. Cumulative Coulombic inefficiency of as received and functionalized **Si-SA2** nanoparticles. All cells were cycled with FEC between 1.5 – 0.005 mV at a rate of 200 mA/g for cycles 1-3 and 600 mA/g for subsequent cycles.*

Ultimately, the results from **Si-SA2** particles still have many drawbacks that we want to build upon. First, the as-received silicon particles have very low capacity and low Coulombic efficiency, calling into question the validity of further comparisons with functionalized nanoparticles against this baseline. Hydrosilylation of Si-VEC may have failed to remove VEC liquid from the surface of silicon prior to slurry preparation, and oxidation was not constant between samples. We also fail to distinguish between the effects of a-SEI on lithium diffusivity and surface stability vs the effects on mixing between the a-SEI and a polar binder in water.

The replicability of each experiment leaves much to be desired. Most silicon samples were tested using both 5 and 50 mV cut-offs and while including or excluding a

constant voltage step during lithiation, the results of which follow the general pattern expected from the chemistry outlined in Chapter 2. Having the 4 cell results for each slurry gives qualitative reassurance that our results at 5 mV using CCCV protocol are within the right absolute capacity range, however, the majority of tests were carried out without replications, and all the data presented are the result of a single test. At the time that these tests were performed, it was common for literature studies to use silicon nanoparticles with low initial capacity and/or low capacity retention,[86,87,90,92,98,99,215] and it was common for studies to present data without replication;[44,151,216–218] however, these practices leave the results open to error from a variety of sources, and some journals have started to require replications if the battery performance is a key part of the results.[219] Very poor performance could result from a single catastrophic mistake during slurry preparation or similar error. Furthermore, slurry making and cell preparation both contain a number of “artisanal” steps that may improve in quality over time. The first slurries mixed using hydrosilylated nanoparticles may perform slightly less well due to slower and less practiced assembly, without ever suffering from a “mistake” during assembly. By employing a more systematic study of hydrosilylation on new silicon nanoparticles, we hope to improve on some aspects of Section 3.4 with **Si-SA3** particles.

3.5 Surface and binder interaction in a SiNP slurry

Despite the failings of PVDF as a binder for hydrogen terminated silicon nanoparticles, recent work has returned to this polymer for use with silicon electrodes functionalized with hydrophobic interfaces to form an artificial SEI (a-SEI).[99] Qian and coworkers showed that the attachment of perfluorinated dodecyl groups to the surface of porous silicon nanoparticles repelled electrolyte and increased van der Waals interactions with the PVDF binder.[99] The Coulombic efficiency of the first cycle increased from 60% to 88%, which was accompanied by reduction of the quantity of electrolyte breakdown into SEI, which is especially beneficial to capacity retention in a full cell.[99] However, the comparison of hydrophobic particles in PVDF to hydrophilic particles in PVDF may be inappropriate given that hydrophilic particles have stronger intermolecular forces with hydrophilic binders.[220]

More recently, Schulze et al. have compared hydrophobic and hydrophilic surface of silicon using PAA,[90] which is generally considered a more elastic binder associated with longer cycling in silicon nanoparticles.[188,221] Their control silicon consisted of silicon functionalized with the same molecule as their solvent, NMP, by reacting silicon with the carbonyl group of NMP to produce a silyl ether linkage. Due to using PAA binder rather than PVDF, they find that hydrophobic surfaces are associated with very poor capacity retention and coulombic efficiency. Hydrophilic PEO surfaces, on the other hand, have higher initial capacities, capacity retentions, and coulombic efficiencies than their control silicon. Interestingly, longer lengths of PEO were found to reduce capacity retention, likely due to electronic insulation from the conductive additive; however, this contrasts with the work of Gao et al. who found that silicon

functionalized with longer PEO chains had higher capacity retention.[91] This work by Schulze et al. does not provide any comparison to silicon with a native oxide, which is already known to interact well with commonly used hydrophilic binders, and the native oxide has minimal impact on first cycle Coulombic efficiency for sufficiently small particles.[94]

Without a control slurry, it is difficult to compare the effects of different silicon nanoparticle surfaces between research groups, as there are significant differences in average particle size, the source of particles that can affect the surface coverage, and the binder chosen. To the best of our knowledge, nothing has been published on a covalently bound a-SEI that compares the proposed surfaces to both hydrophobic and hydrophilic binders. Hesitancy to research both a-SEI surfaces and binders simultaneously may stem from a traditional belief in many scientists that experiments should proceed “one variable at a time”. However, single variable analysis can be insufficient when the two variables are highly correlated, as is the case with silicon surface functionalizations and the binders used for nanoparticle slurry electrodes. Herein, we compare six surfaces on otherwise identical silicon nanoparticle electrodes (Figure 3-44): Si-O_x, Si-H_x, Si-TEG, Si-Dode, Si-1:1, Si-PD. Each silicon sample is tested with both PVDF and PAA in NMP, as well as PAA in H_2O to determine the effects during mixing. We establish a silicon nanoparticle slurry with a native oxide that has high initial capacity, moderate capacity retention over 100 cycles (67 %), and initial Coulombic efficiency (ICE) above 90% in polar binder. We demonstrate the ability of silicon surface modification to improve the cycling performance of a high performing silicon anode.

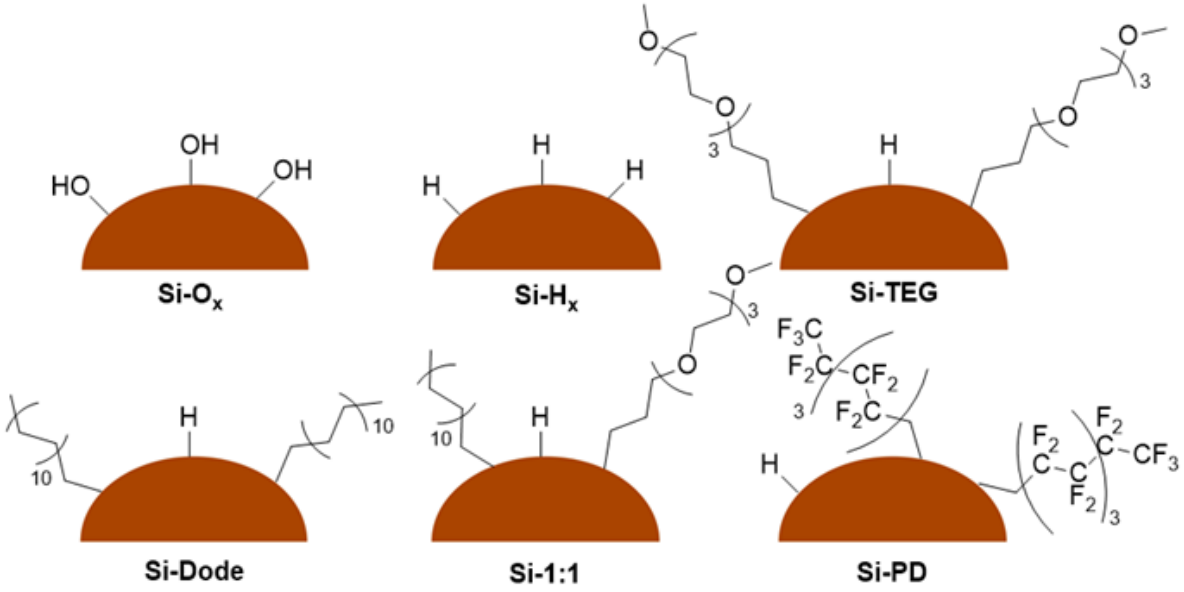

Figure 3-44. *Functional groups prepared through thermal hydrosilylation. Bolded titles are used throughout the text.*

3.5.1 Establishing surface functionalization

Native oxide-terminated **Si-SA3** nanoparticles, ~140 nm in size as determined by SEM (Section 3.3), were used as received when applicable. For hydrogen-terminated silicon, the native oxide was removed by stirring in a solution of 5 % HF, 10 % ethanol, and 85 % water for 5 minutes. The particles were filtered and further immersed in the same HF solution two more times before being rinsed with 4:1 H_2O:EtOH. Particles were subsequently dried under a nitrogen stream overnight to ensure full removal of water before a hydrosilylation step. Removal of the oxide layer was confirmed by Diffuse Reflectance Infrared Fourier Transform Spectroscopy (DRIFTS, Figure 3-45). After reacting with HF (aq), the DRIFTS spectrum indicates removal of the oxygen backbonded H_x-Si-O vibration at ~2200 cm^{-1} and the Si-O-Si stretch at 1200 cm^{-1}.

Meanwhile, the presence of $\nu(Si\text{-}H_x)$ stretching without oxygen backbonding is noted at 2100 cm^{-1}, as well as some adventitious hydrocarbon. H_x-Si-terminated particles were then used directly for slurry preparation, with preparation done under an inert atmosphere in anhydrous NMP to prevent oxidation. H_x-Si slurries were prepared in PAA/H_2O to complete the matrix of surfaces and binders, although it is unlikely that the hydride functionalities would survive ball milling in water without any oxidation.

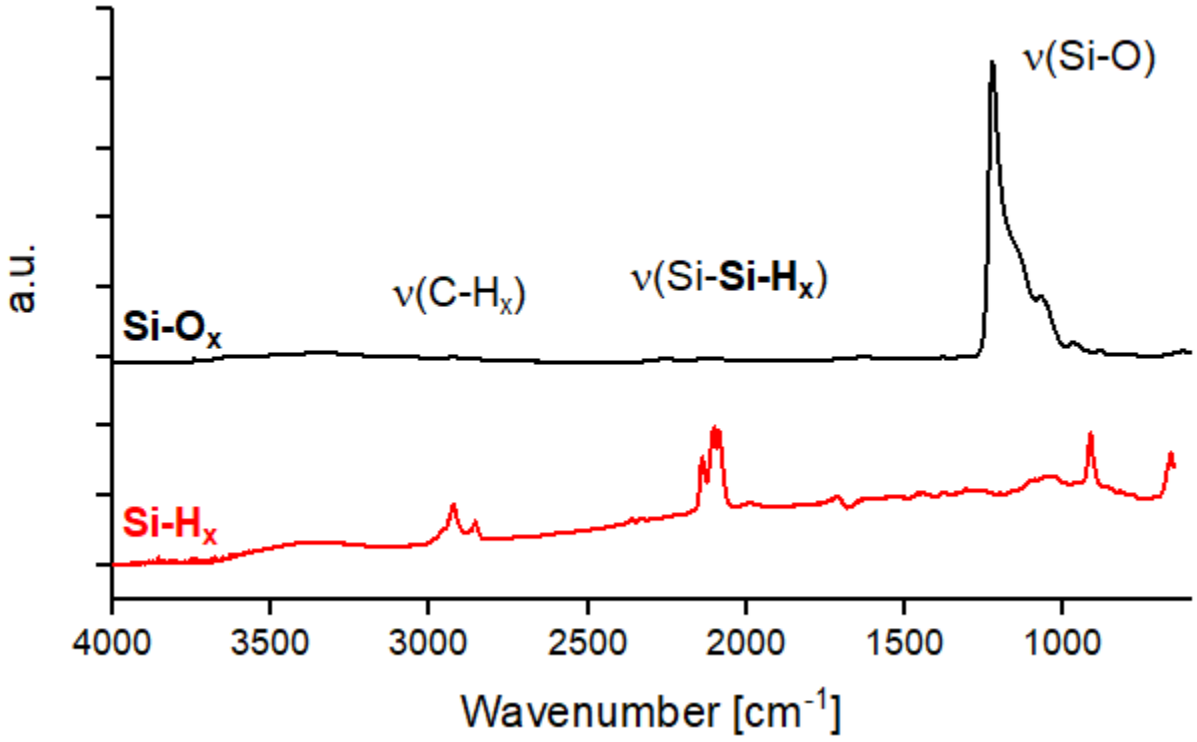

Figure 3-45. Diffuse reflectance infrared Fourier transform spectroscopy (DRIFTS) of Si-O_x (black) and Si-H_x (red) terminated silicon nanoparticles.

Hydrogen-terminated silicon particles were functionalized using thermal hydrosilylation. The molecule of interest was diluted 10:1 in mesitylene, and dry silicon particles were added. The solution was refluxed at 165°C for two hours, and functionalization was confirmed again using DRIFTS (Figure 3-46). The region of interest is between 2800 cm^{-1} and 3000 cm^{-1}, showing C-H stretching frequencies of the covalently bonded dodecyl and TEG moieties (Figure 3-46, black, red). The FTIR for a 1:1 v/v mixture of 1-dodecene and TEG is inconclusive, but is consistent with both molecules bonded to the surface. Oxidation is a possible competing pathway in the presence of water, and is most easily observed at 2200 cm^{-1} as $\nu(Si\text{-}H_x)$ stretching where silicon is bound to oxygen, which is minimal in most samples. O-H stretching observed at 3400 cm^{-1} is at least partially attributed to acquisition conditions (seen in CO_2 and H_20 stretching frequencies) which could not be corrected for.

Most surface functionalizations can be tracked due to characteristic peaks in the $C\text{-}H_x$ stretching region. Perfluorinated 1-decene is harder to recognize, as the $\nu(C\text{-}H_x)$ would be small, and the $\nu(C\text{-}F)$ at ~1100 cm^{-1} would be largely overshadowed by the Si-O-Si stretching peak. To further confirm the correct surface coatings, we performed XPS on slurries prior to cycling to identify the presence of fluorine on the surface of silicon (Figure 3-47).

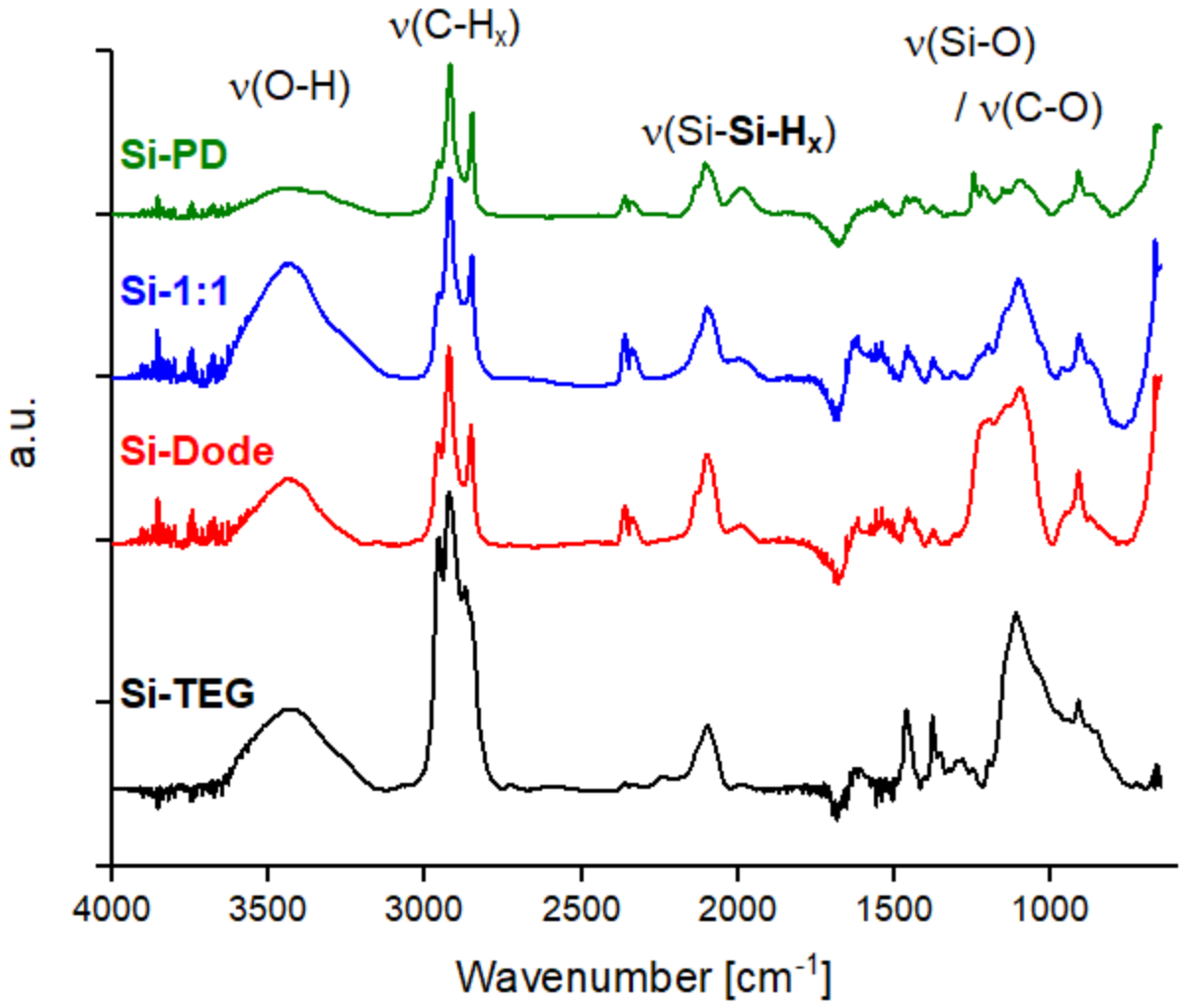

Figure 3-46. DRIFTS of silicon nanoparticles functionalized with TEG (black), 1-dodecene (red), 1:1 TEG:dodecene (blue), and 1H,1H,2H-perfluoro-1-decene (PD, green).

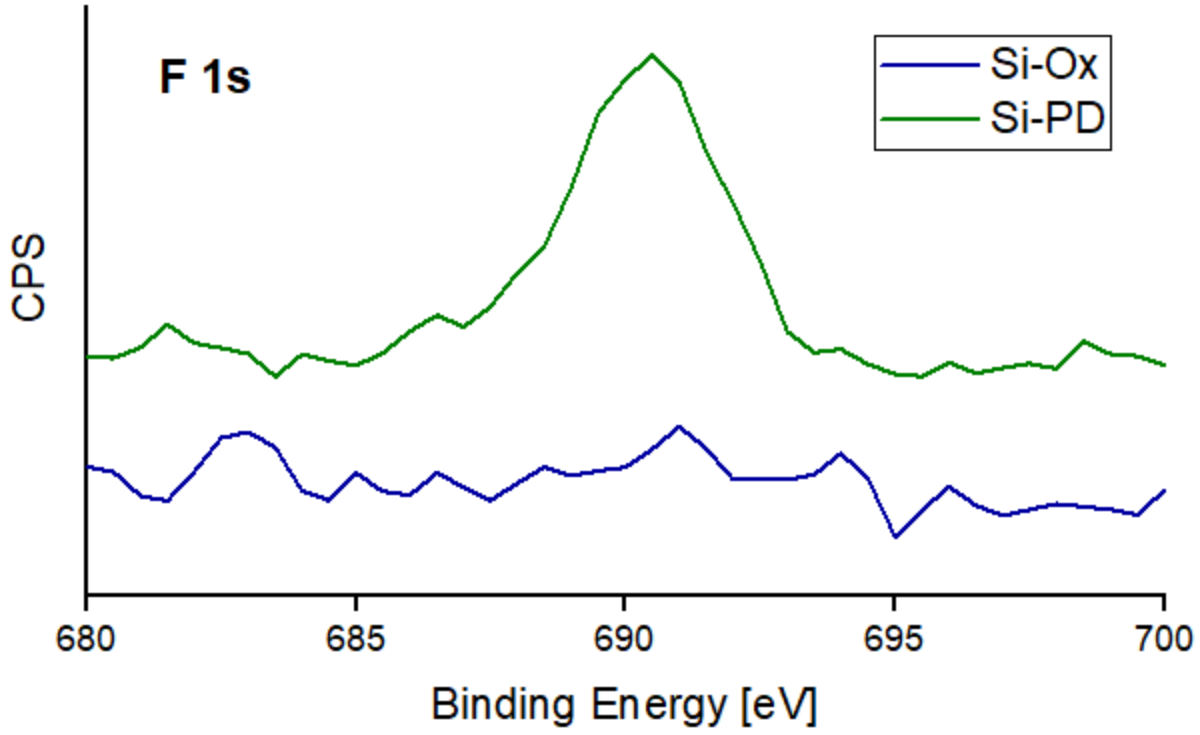

Figure 3-47. XPS F 1s spectrum of Si-O_x (blue), and Si-PD (green) particles dispersed on a carbon sticky..

3.5.2 Cell replications and reproducibility:

The goal of this project was to present all cycling data as the average of three identical replications, to minimize the effect of the environment or of assembly error on the results. In an ideal setting, each replication would have involved a separate hydrosilylation and slurry preparation for each cell test, so as to mitigate variation in those preparation processes as well. Considering reasonable restraints on time and material, however, we choose to perform three replications on each cell cycle using discs punched from the same slurry material. The goal of using three replications has drawbacks, however, as can be discussed with reference to specific capacity data in Figure 3-48. **Si-SA3** particles were cycled three times in each of PVDF/NMP,

PAA/NMP, and PAA/H_2O, and the effect of binder on performance will be discussed further in Section 3.5.2, while here we focus on replicability. For PVDF/NMP slurries (black dots), all three cells fell into a narrow distribution, and the standard deviation of each capacity measurement never exceeded 3 %. The data displayed for PAA/NMP (red dots) is the result of only two experiments, and as such the standard deviation reaches a maximum of 6 % of capacity. The third cell ran for three cycles at a comparable capacity, but failed catastrophically during cycle 4 for unknown reasons. Ideally, experiments would be monitored closely and reproduced immediately in the case of a failed experiment. However, due to the length of time required for each experiment and the inability to catch cycling failure immediately, reproduced experiments often could not be performed until weeks or months after the initial cells had begun cycling. Unfortunately, slurries that were stored for weeks often displayed a drop in capacity of ~ 10 %, which would artificially lower the absolute specific capacity and raise the uncertainty for these experiments relative to cells that were each cycled directly after slurry mixing. slurries were stored under an inert atmosphere in which cell assembly took place, and may have scavenged volatile electrolyte molecules or other contaminants over the course of many weeks. Finally, we turn to the data for PAA/H_2O (blue dots). PAA/H_2O as a binder and solvent combination often led to irregular capacity over 100 cycles, as will be discussed later on, and it specifically led to irregular cycling in one replication of the Si-O_x particles in Figure 3-48, which results in large swings in capacity after cycle 79 and a standard deviation of 12 % relative to capacity. While exceptionally poor performance in a single cell could be discarded and replaced with

another experiment, deciding when to replace a poor experiment would fundamentally be a judgement call.

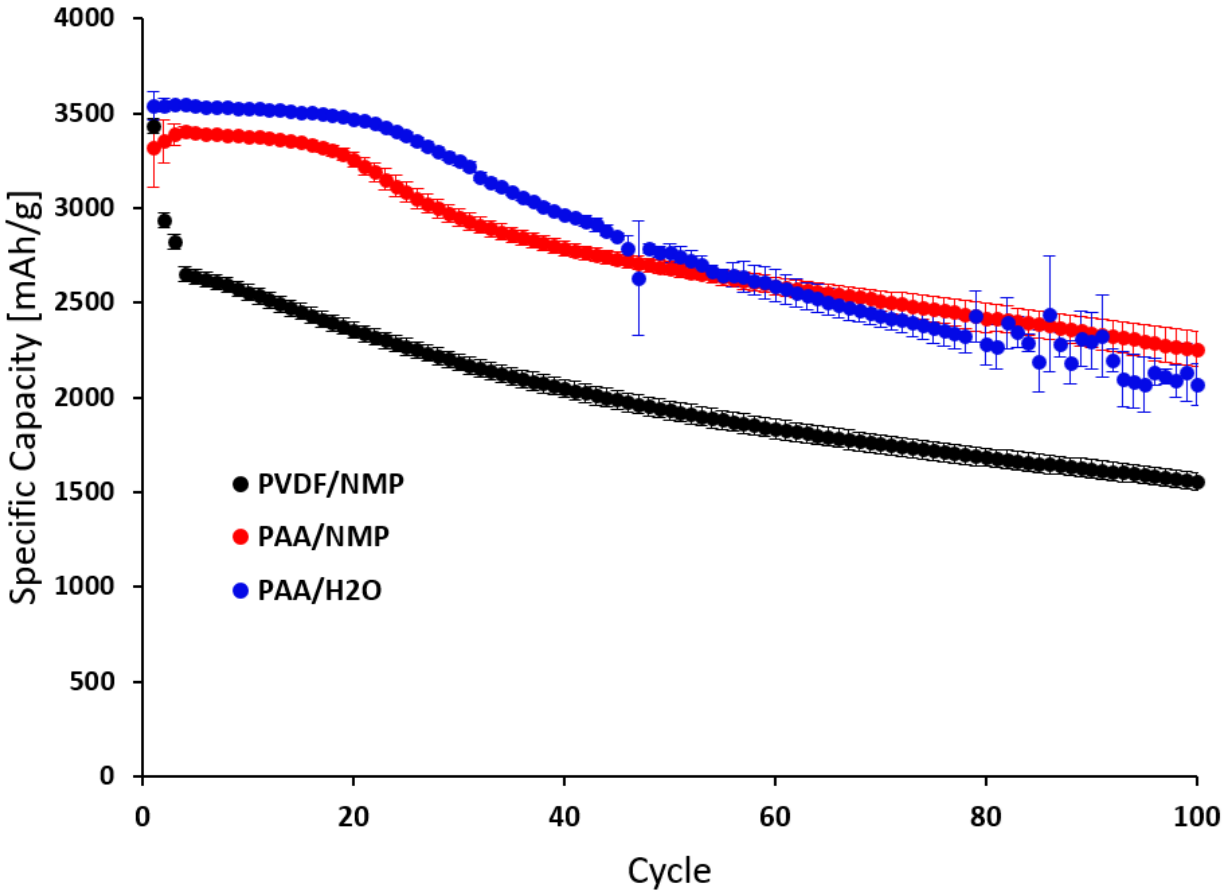

*Figure 3-48. Specific capacities of **Si-SA3** slurries prepared in various combinations of binder and solvent. Cells were cycled from 1.5 – 0.005 V, and Cycles 1-3 were performed at 200 mA/g, while the remaining cycles were performed at 600 mA/g.*

Due to the difficulties of reporting three replications for each cell, we choose instead to report the cycling results of the champion cell for each set of three replications. Choosing the champion cell was done to maximize the capacity retention at cycle 100 relative to the maximum specific capacity, as well as to avoid erratic cycling in

which capacity rose and fell with no distinct pattern due to cell failure, or unnaturally low initial capacity due to a long time in storage. We believe that choosing the best performing cell is the most objective method for comparing cycling data, by removing decisions about which lower performing cells to include in the averages. Choosing the best cell of three replications also improves the replicability of our work as compared to the results detailed in Section 3.4, and is an improvement on the current practices on reporting cell performance,[44,151,216–218] as described earlier.

3.5.3 Effect of Binder:

We first want to confirm the effects of polar and non-polar binders on silicon nanoparticle cycling, and we focus on the capacity retention and Coulombic efficiency in the first 100 cycles for PVDF in NMP, PAA in NMP, and PAA in water (Figure 3-49). All electrodes produce a very similar initial capacity at approximately 3500 mAh/g, but PVDF quickly loses capacity compared to the PAA binder, and remains at a lower capacity for all 100 cycles. Silicon cycled with PVDF binder has noticeably worse Coulombic efficiency over the first 4 cycles.

Our results confirm the lower capacity retention and Coulombic efficiency expected when using PVDF binder, due in part to the low elastic modulus of PVDF compared to PAA[188] as well as the superior interaction between the COOH groups of PAA and the OH groups of silicon.[220] Slurries made with PAA in water behave similarly to PAA in NMP initially, but lose capacity more quickly. Some degree of neutralization to LiPAA is understood to improve ICE and capacity retention in water,[222] but we used PAA in both techniques for consistency.

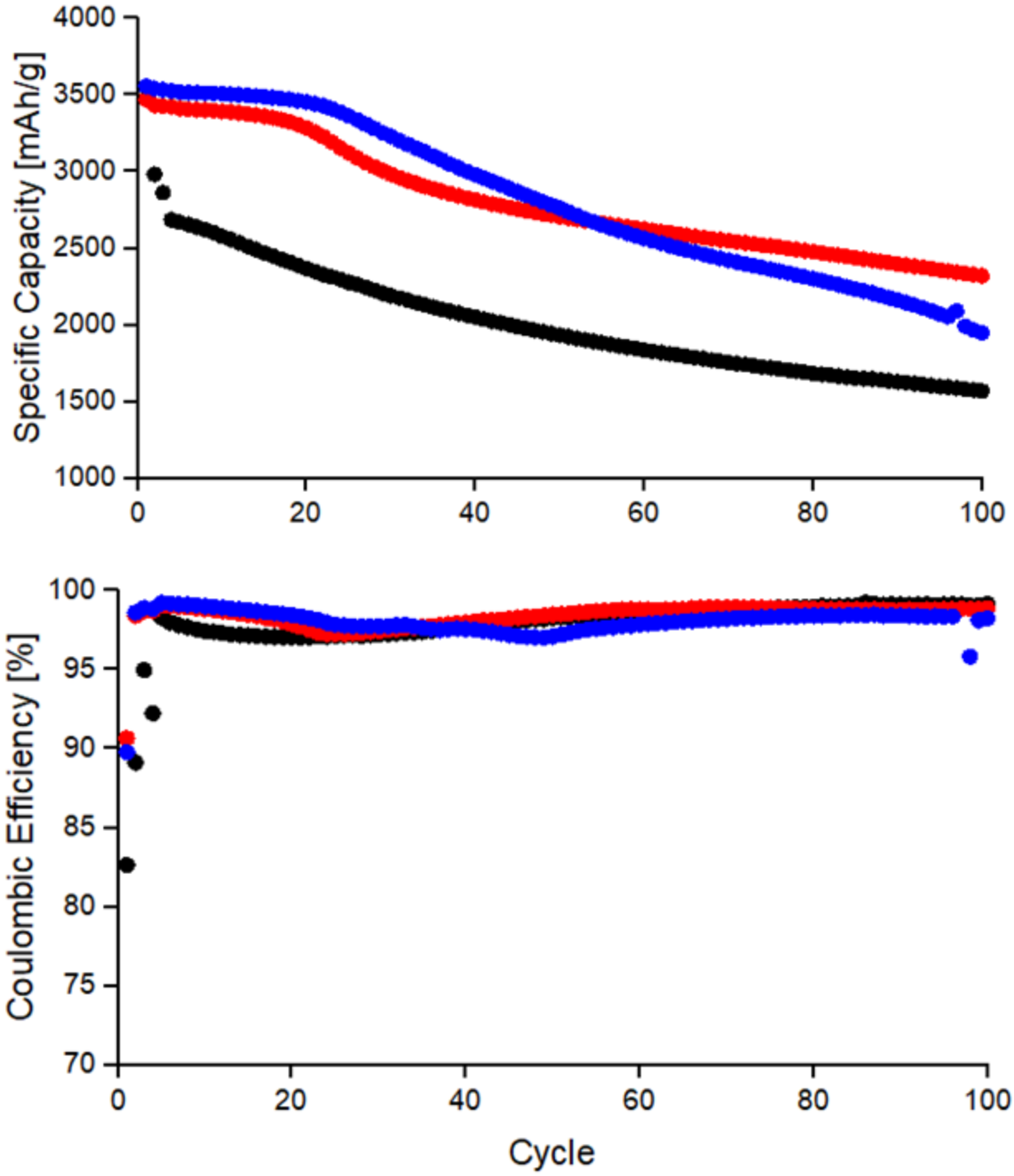

Figure 3-49. *Specific capacities (top) and Coulombic efficiencies (bottom)over 100 cycles for the as received Si-O_x silicon with PVDF in NMP (black), PAA in NMP (red) and PAA in H_2O (blue). All cells were cycled with FEC between 1.5 – 0.005 mV at a rate of 200 mA/g for cycles 1-3 and 600 mA/g for subsequent cycles.*

3.5.4 Effect of surface coverage on capacity:

Cells were tracked over 100 cycles in all solvents, and the best data of three replications (as described in section 3.5.2) are shown in Figure 3-50. Unlike previous research, the as received Si-O_x particles lead to some of the best capacity retention for all binders and solvents. The capacity retention with non-polar surface coatings in PVDF is contradictory. Si-PD had the best capacity retention of all coatings, best seen when standardized vs maximum capacity (Figure 3-50, a). Si-H_x compares favourably to Si-PD until 80 cycles. Meanwhile, Si-Dode had the worst capacity retention of all surface coatings. All non-polar coatings had poor capacity retention over 100 cycles in PAA/NMP, relative to the baseline for as-received particles. Polar surface coatings - notably coatings that included Si-TEG - did worse than Si-O_x in both PVDF and PAA binders. PAA/H_2O cycling (Figure 3-50, c) showed instability after 50 cycles for functionalized particles, suggesting that slurry compositions and distributions were affected by milling in the polar, protic solvent.

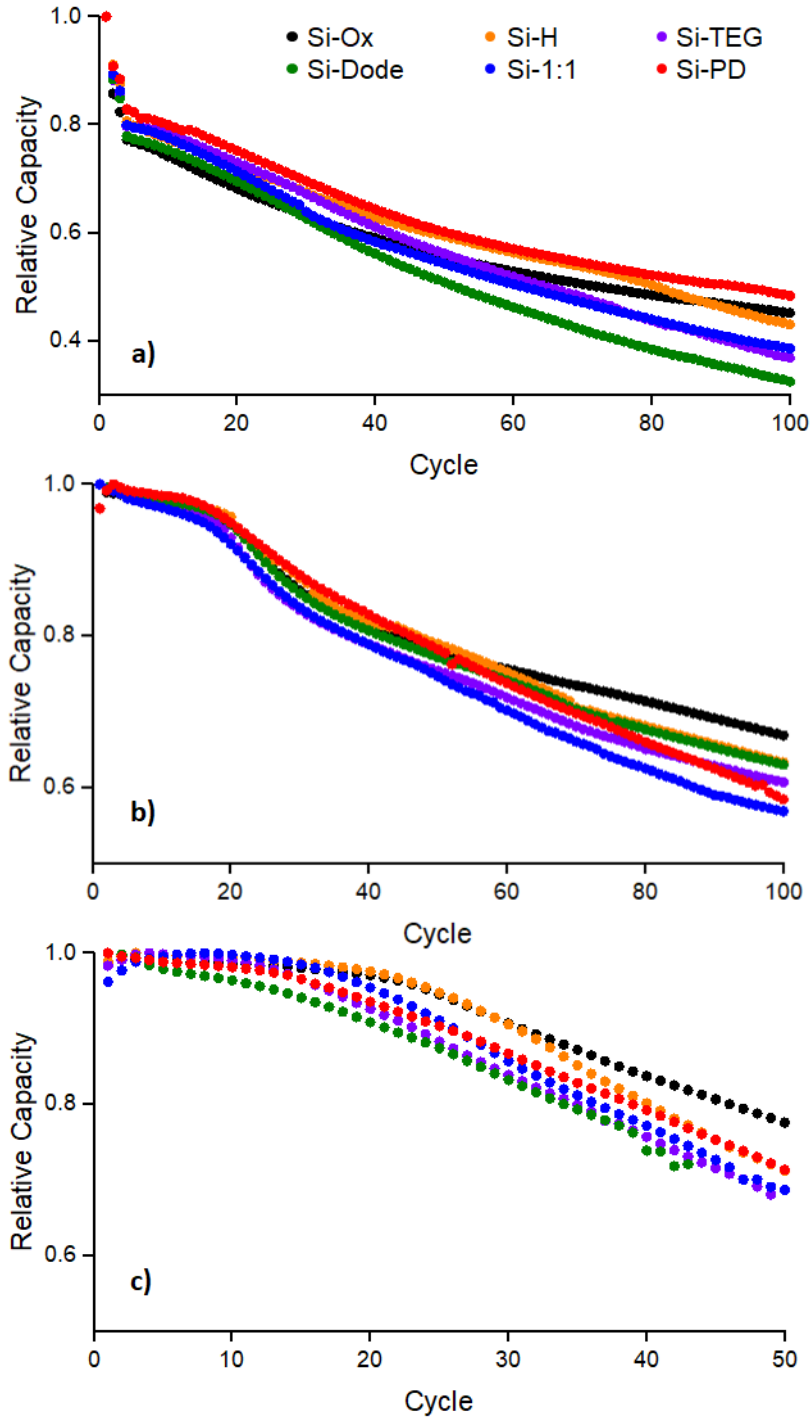

Figure 3-50. *Relative capacity retention of **Si-SA3** particles with various surface functionalities in PVDF/NMP (a), PAA/NMP (b), and PAA/H_2O (c). All cells were cycled with FEC between 1.5 – 0.005 mV at a rate of 200 mA/g for cycles 1-3 and 600 mA/g for subsequent cycles.*

The high performance of PD-Si in PVDF is consistent with previous work,[99] and could stem from stronger interactions between the non-polar fluorinated surface of the silicon nanoparticles and the non-polar silicon surface of PVDF. Despite the improvement in PVDF, all cells in PAA/NMP were able to outperform Si-PD in PVDF after 100 cycles, indicating that the benefits caused by Si-PD to PVDF intermolecular forces are overshadowed by the superior binding properties of PAA. Dode-Si does not perform well in PVDF despite also being a nonpolar functionalization, which may be due to lower lithium diffusivity.

Si-O_x based slurries also demonstrate high ICE in most settings (Figure 3-51). Whenever NMP was used as the solvent, Si-O_x samples demonstrated high ICE's relative to other coatings (83 % for PVDF and 90.6 % for PAA). With PAA/H_2O, the polar surfaces of Si-O_x and Si-TEG show lower ICE's of 89.7 % and 86.8 % respectively. HF treatment to remove the native oxide has previously been proposed as a simple way to improve first cycle Coulombic efficiency, but we only find this to be the case for slurries prepared in water. Polar silicon surfaces may retain trace amounts of adsorbed water that persists through the evacuation processes and react irreversibly during the first lithiation.

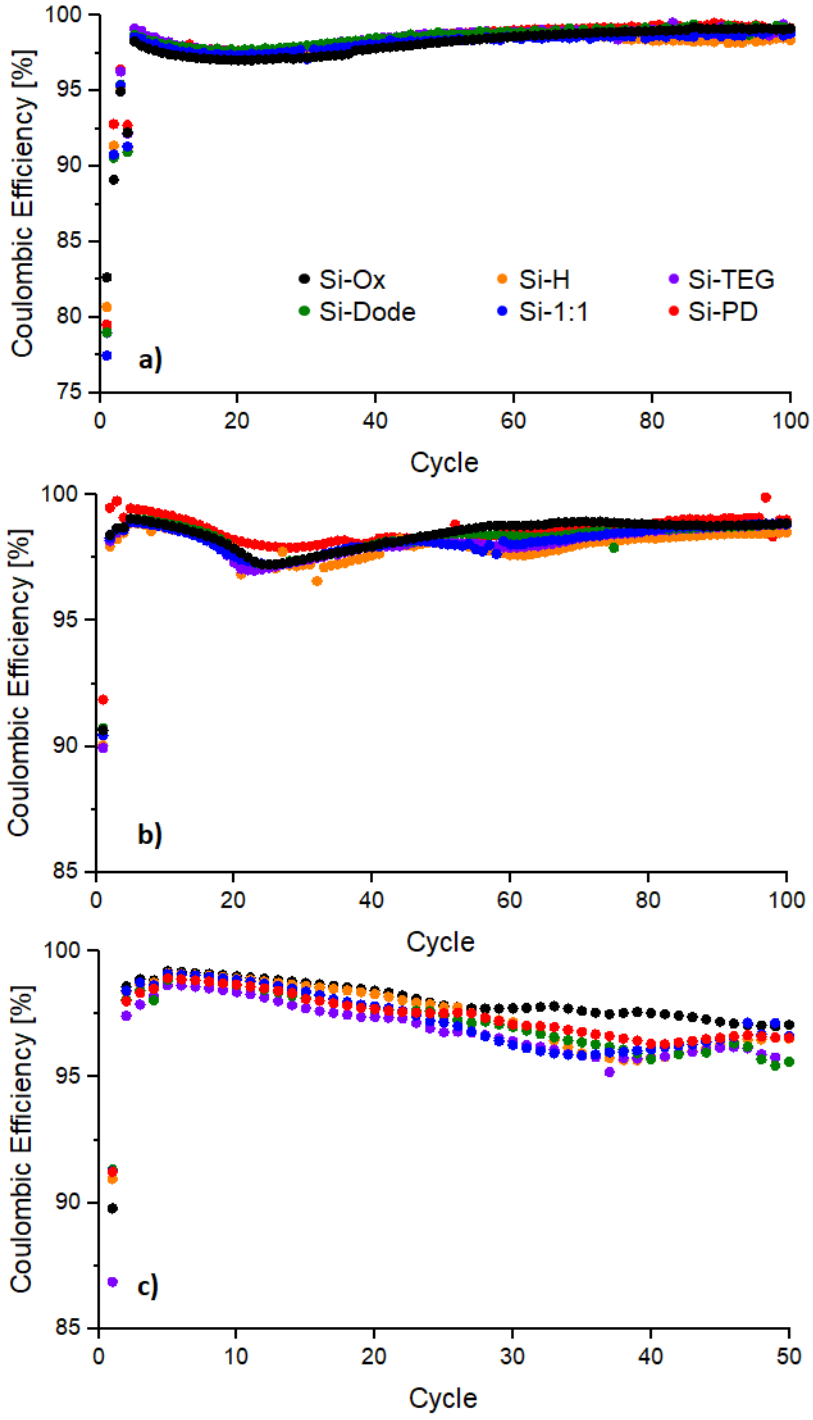

Figure 3-51. *Coulombic efficiencies of silicon nanoparticle slurries with various coatings in PVDF/NMP (a), PAA/NMP (b), and PAA/H_2O (c). All cells were cycled with FEC between 1.5 – 0.005 mV at a rate of 200 mA/g for cycles 1-3 and 600 mA/g for subsequent cycles.*

Absolute initial capacities with **Si-SA3** nanoparticles are close to theoretical for all surface coatings (Figure 3-52), and competitive with results from the literature. Si-O_x in a slurry with PAA/NMP achieved an initial capacity of 3468 mAh/g, 67 % capacity retention after 100 cycles, and an initial Coulombic efficiency of 90.6 %. This is in contrast to the controls used in other studies on artificial-SEI, which typically achieve less that 33 % capacity retention over 100 cycles,[91,99,215,220] have an initial capacity below 2000 mAh/g,[86,98,223] do both,[92] or have no control.[90] Of these nine papers with artificial SEIs, three were able to achieve 100 cycles with greater than 50% capacity retention and above 2000 mAh/g.[86,91] This metric was achieved by every surface coating reported here in PAA/NMP except for Si-PD and Si-1:1 (1960 and 1932 mAh/g, respectively). Gao et al also use a much inferior control of oxide-terminated silicon (<30 % capacity retention after 100 cycles) but achieve exceptional absolute capacity and capacity retention (~2500mAh/g and 72 % after 200 cycles, respectively), and high first cycle Coulombic efficiency (91.3 %) with bifunctionalized silicon that is further optimized for degree of functionalization. The results from Gao et al. suggest that the performance of our functionalized silicon particles should not be viewed as a ceiling for the potential of an artificial SEI to improve silicon cycling. Our research highlights the tradeoffs between a-SEI research and binder choice, as well as the relative importance of surface optimization given high performing silicon slurries. Direct hydrosilylation of olefins on the surface of hydrogen terminated silicon, as performed here, may also provide more options for further a-SEI research.

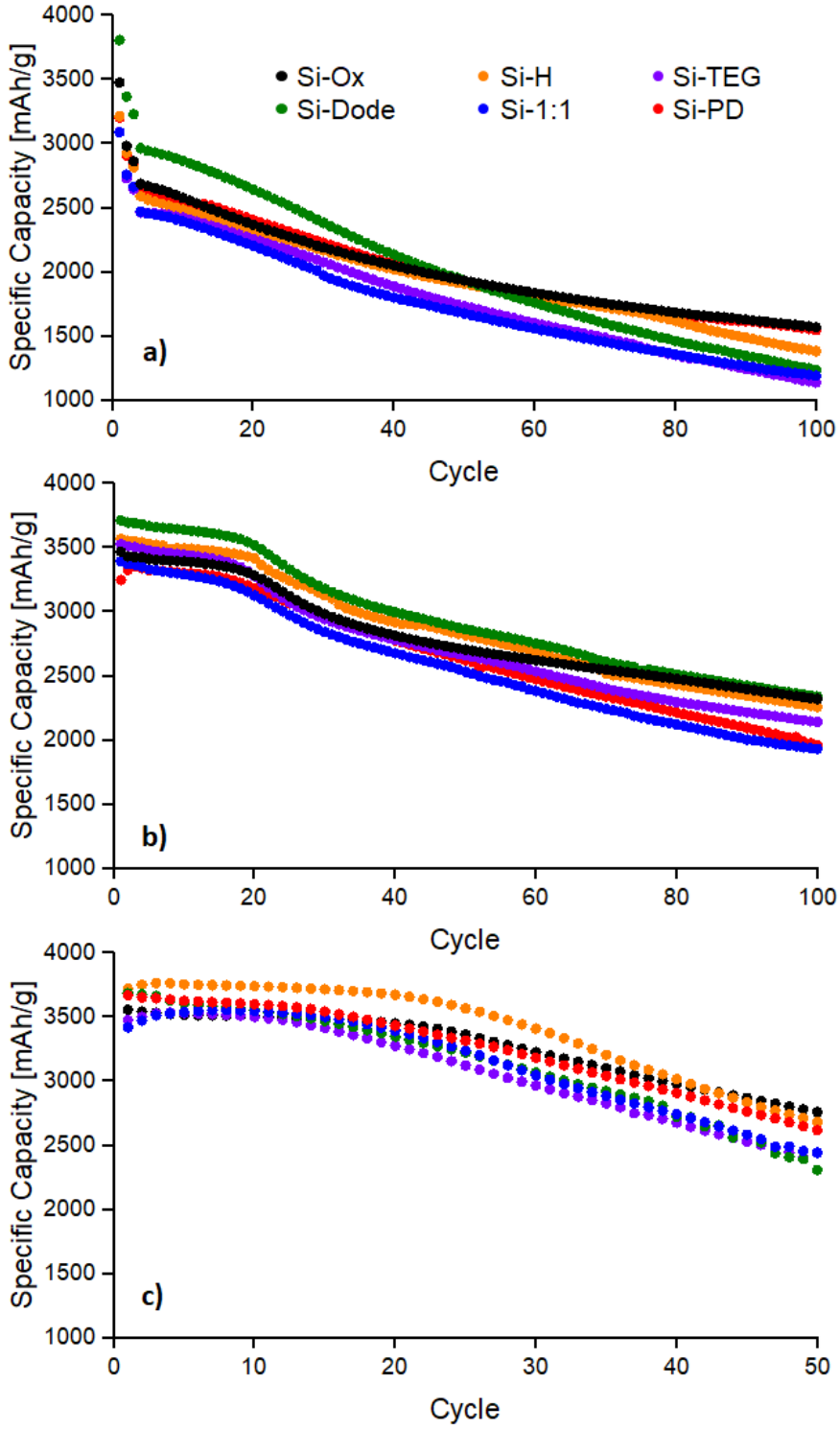

Figure 3-52. *Absolute capacity of silicon nanoparticle slurries with various coatings in PVDF (a), PAA/NMP (b), and PAA/H_2O (c). All cells were cycled with FEC between 1.5 – 0.005 mV at a rate of 200 mA/g for cycles 1-3 and 600 mA/g for subsequent cycles.*

Slurries made with PAA binder lead to the most stable cycling, so now we focus on characterization of these cells to elucidate the effects of surface coverage on cycling. We perform potentiostatic electrical impedance spectroscopy (EIS) on all cells after the three formation cycles at 200 mA/g (Figure 3-53). We find high solution resistance for many of the cells after 3 cycles, reaching 150 Ω for Si-Dode. The resistance at higher frequencies is associated with the SEI, and forms the first small semicircle. We observe that only the Si-PD coating mitigates SEI formation compared to the as received particles, which is consistent with its high initial Coulombic efficiency in Figure 3-51. This is also consistent with a high initial capacity retention for Si-PD samples in PAA/NMP. However, the high hydrophobicity of the fluorinated groups lead to weak interaction with the binder and poor cycling after 100 cycles.

The surface functionalization on silicon would also affect slurry dispersion via the interaction of active material with carbon additive and binder. We seek to analyze the distribution and composition before and after 10 cycles in PAA/NMP. We continue to focus on the cells prepared with PAA/NMP as they have the least capacity decay after 100 cycles. SEM of taken before cycling demonstrate a similar distribution of larger silicon nanoparticles and smaller Super P particles across all surface coatings (Figure 3-54). After 10 cycles we observe greater particle agglomeration, and some amount of silicon pulverization is visible at higher magnification (Figure 3-55). Si-PD appears to mitigate particle pulverization early on, but quantification is difficult.

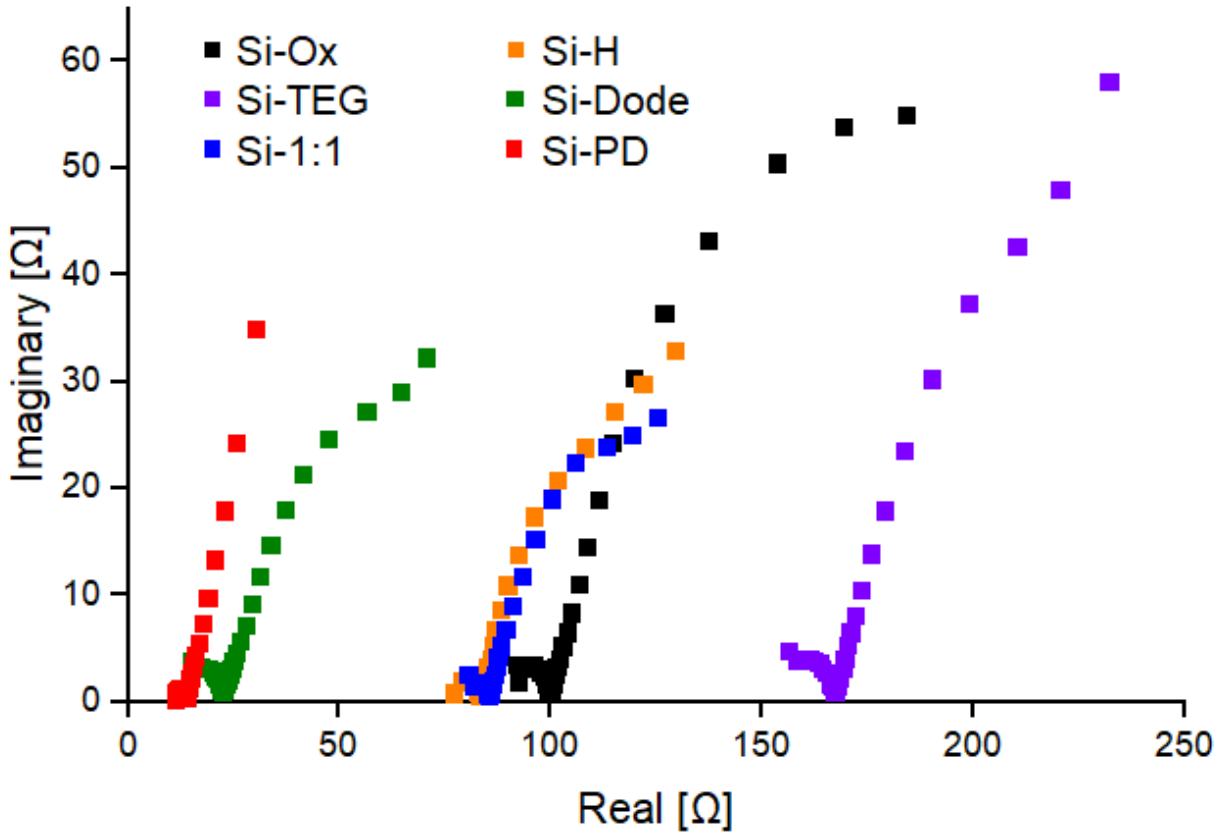

Surface	R_s	R_{SEI}
Si-O_x	88.1	12.8
Si-H_x	76.6	7.60
Si-TEG	150	16.9
Si-Dode	10.0	13.6
Si-1:1	76.1	10.2
Si-PD	11.2	2.90

Figure 3-53. *Electrochemical impedance spectroscopy (EIS) after 3 formation cycles of* ***Si-SA3*** *slurry electrodes with different surface functionalizations in PAA/NMP.*

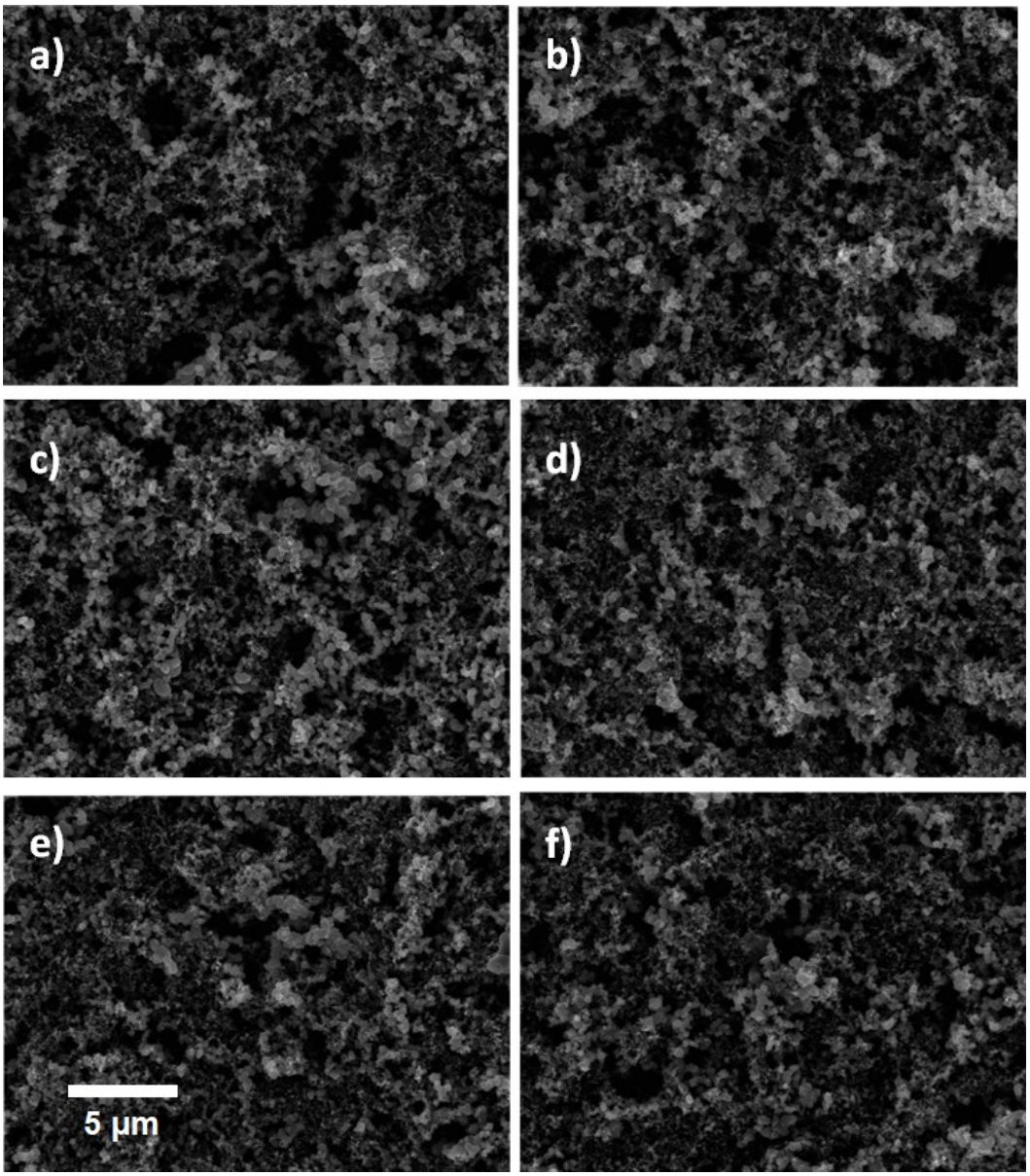

Figure 3-54. *Scanning electron microscopy (SEM) micrographs of* ***Si-SA3*** *particles in PAA/NMP slurries prior to cycling. Si-*O_x *(a),* Si-H_x *(b), Si-TEG (c), Si-Dode (d), Si-1:1 (e), Si-PD (f).*

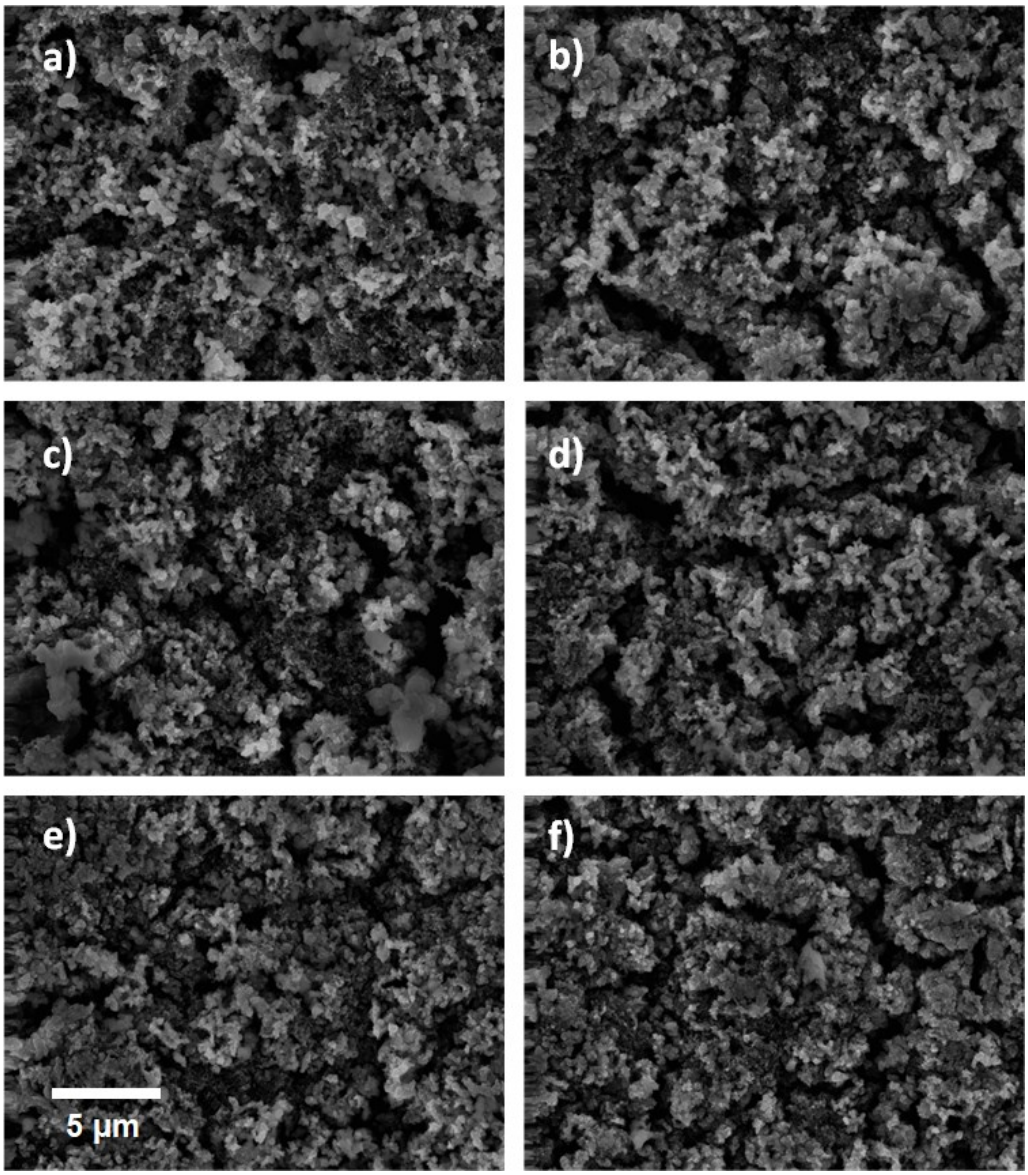

*Figure 3-55. Scanning electron microscopy (SEM) micrographs of **Si-SA3** particles in PAA/NMP slurries after 10 cycles. Si-O_x (a), Si-H_x (b), Si-TEG (c), Si-Dode (d), Si-1:1 (e), Si-PD (f).*

In conclusion, we analyzed silicon nanoparticle slurries with six different surface functionalizations in both polar and nonpolar binder combinations. We find that using nonpolar Si-PD along with nonpolar PVDF binder leads to superior capacity retention over 100 cycles, but that this effect is overshadowed by the inferior performance of PVDF as a binder for lithium ion batteries. Si-PD performs poorly when paired with PAA binder due to the weak interaction between the hydrophobic silicon and hydrophilic binder. We confirm that removing the native oxide on silicon prior to slurry preparation primarily degrades cycling performance, especially in superior polar binders, with dubious benefits to initial capacity for 140 nm particles.

We electrochemical cycling performance that was close to the theoretical maximum from as-received Si-O_x based slurries, including an initial capacity of 3468 mAh/g, 67 % capacity retention after 100 cycles, and an initial Coulombic efficiency of 90.6 %. We were unable to find an artificial SEI that could improve the performance of these Si-O_x slurries in PAA/NMP over 100 cycles. Further research should focus on multifunctional interfaces comprising mixtures of polar functional groups, and greater control of the synthesis conditions. However, our research highlights that cycling improvements from silicon with an a-SEI should be viewed in the context of high-performing silicon anodes, which are better able to underline the benefits provided by the additional synthesis steps.

3.6 Mechanochemical synthesis on Si-325 particles

The focus of the work in this chapter is the reduction in size and surface functionalization of micron sized silicon particles prior to cycling. Hydrosilylation of

commercial silicon nanoparticles (~140 nm in diameter) did not lead to improvements of capacity retention of silicon nanoparticle-based anodes. The critical size of silicon, below which fracturing of the silicon nanomaterial can be avoided, remains controversial,[15] although it is typically cited at 150 nm for crystalline particles.[106] It is possible that **Si-SA3** particles are still comparatively large and fracture during cycling, exposing fresh silicon surfaces that undergo reactions with the electrolyte to form the typical SEI. In addition, even small improvements in cell cycling could have commercial applications if the number of processing processing steps could be reduced, and if the silicon source is less expensive. Following on this idea, multiple groups have shown that micron-sized crystalline silicon, often a waste product of industrial applications, particularly silicon microprocessor fabs - can be reduced to the nanoscale by high energy ball milling. Furthermore, work such as that by Hallman et al. and Xu et al. (Figure 3-56) has shown that introducing alkyne molecules during high energy ball milling can lead to covalent attachment of the alkyne molecule to the silicon surface through mechanochemical synthesis.[224,225] Both authors further claim that silicon wafer feedstock can be reduced to a particle size < 10 nm during the high energy ball milling, which is similar to the particle sizes used by Neale and co-workers at NREL.. Neither of the ball milling groups tested their SiNPs in lithium ion batteries, and thus the combination of a one step process for generation of nanoscale silicon materials and covalent functionalization of the silicon makes this approach interesting. Another advantage of this ball milling approach is that the silicon would not require treatment with HF (aq) to generate hydride termination, avoiding an expensive and dangerous processing step.

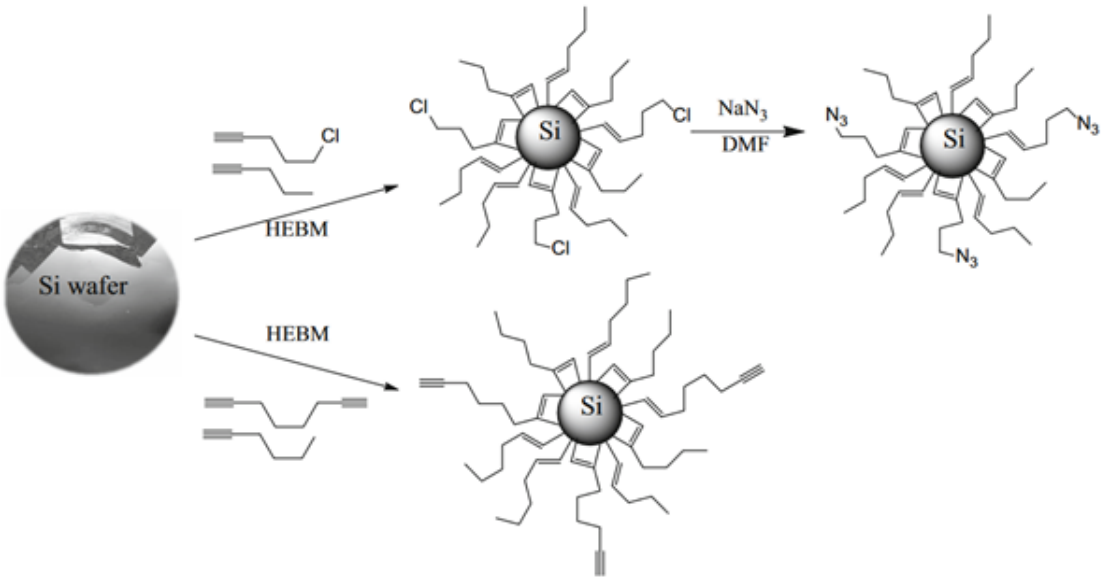

Figure 3-56. Schematic of the role and function of alkenes added to the mix of high energy ball milling of silicon wafers. Reprinted with permission from reference 225. © 2015 Springer Nature.

In recent work, Shi et al. used 325 mesh (<44 μm) crystalline silicon microparticles for high energy ball milling with poly(vinyl alcohol) (PVA), as outlined in Figure 3-57.[226] They covalently attach PVA polymers to the surface of silicon via silyl ether bonds, and through ball milling they are able to reduce the silicon particle size from 44 μm to ~200 nm. Cell cycling does show much higher capacity retention after 100 cycles using 5 % PVA during the high energy ball mill step. However, the group also noted large differences in the size and agglomeration of their particles whether PVA is included, and it is possible that the change to cycling capacity and Coulombic efficiency were due mostly to the decrease in size associated with ball milling in the presence of PVA.

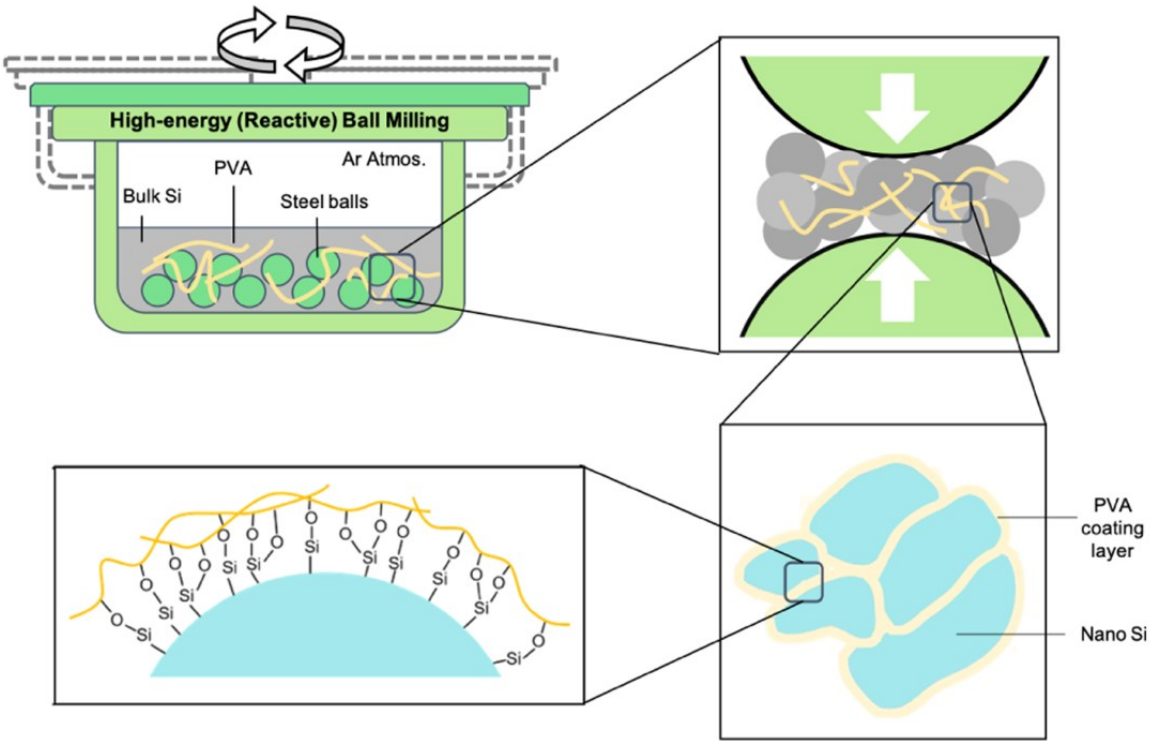

Figure 3-57. Poly(vinyl alcohol) coated silicon nanoparticles after high energy ball milling. Reprinted with permission from reference 226. © 2020 American Chemical Society.

In this work, we aimed to produce silicon nanoparticles by ball milling 33 μm silicon microparticles (termed silicon 325 here). It is our hypothesis based partly on experience outlined in Section 3.3 that 150 nm is an important target for attaining silicon that will not quickly lose capacity due to particle cracking and pulverization upon cycling. While Hallman focused upon alkynes,[224] chemomechanical reactivity on silicon is very versatile and also proceeds with other hydrocarbon-based classes of molecules, including alkenes, epoxides, aldehydes, alcohols, alkyl halides, and acid chlorides, as demonstrated by Linford and co-workers.[227]

Si-325 was milled with three solvents: 1-octane, 1-octyne, and VEC. 1-octane is expected to be non-reactive and is a control solvent. 1-octyne and VEC were chosen as two contrasting reactive molecules, with 1-octyne leading to short aliphatic alkyl group coverage, and VEC presumably resulting in a cyclic carbonate that resembles the electrolytes used in the half cells. The Pr-TEG-OMe molecule described in Sections 3.2 and 3.4 was not initially screened due to the large volume of solution required for ball milling, although dilution with hydrocarbon solvents was considered for future applications. We modelled our mechanochemical synthesis after Hallman et al.,[228] and in a typical experiment, Si 325 mesh (1.786 g) was mixed with 25 mL of neat alkyne/alkene in a teflon ball milling vial, along with zirconia balls ranging from 0.5 cm to 1.2 cm (13.6 g). The mixture was milled at 500 rpm for 12 hours, leaving a brown suspension. The suspension was transferred to a centrifuge tube by pipette, where it was centrifuged at 500 G for 30 minutes. For characterization of particles in octane and 1-octyne, the suspension was concentrated by removing half (~12 mL) of the supernatant, and manually agitating the deposited particles in the remaining liquid. This suspension was pipetted onto the desired substrate for characterization by SEM, FTIR, or XRD. At the higher concentration, the hydrocarbons were removed after 10 minutes in air, which was followed by at least 10 minutes under vacuum for full removal. For slurry mixing, the remaining hydrocarbon solvent was decanted, and the particles were evacuated overnight to remove residual 1-octyne and octane.

Isolating particles after mechanochemical synthesis was more difficult with VEC than with hydrocarbon suspensions. Particles in octane and 1-octyne solutions separated neatly after centrifugation into a colourless supernatant and a brown solid,

which could be isolated to obtain particle yields of 84 % and 69 %, respectively. Using VEC, however, centrifugal separation was incomplete as the supernatant remained light brown. Removal of the supernatant resulted in a yield of only 16% for those particles, indicating a large number of particles that remained suspended in the VEC liquid. Drying particles was also more difficult because VEC has a boiling point of 237 °C compared to 126 °C for octane and 121 °C for 1-octyne. We found that decanting as much liquid as possible, followed by vacuum overnight, was sufficient to produce a dry powder, although we believe that heating up to 120 °C under vacuum would improve the evaporation process with no effect on the particles themselves.

Of primary importance was determining the effect of ball milling on particle size. First, we use particle X-ray diffraction (XRD) to determine the effect of ball milling on the crystallite size. The sizes of the crystallites in the Si 325 mesh microparticles differs from that of the particles themselves, as revealed by the XRD spectra in Figure 3-58. As discussed in Section 3.3, crystallite size was determined using the modified Scherrer equation:[208]

$$L = K\lambda/\beta\cos\theta$$

where L is the nanocrystallite size, K is a shape factor set to 0.9, β is the full width at half max of each peak at a given diffraction angle, θ. Using this equation, we determined that Si 325 comprises crystallites of 56 nm, which decreases to 42 nm and 48 nm for particles milled in octane and 1-octyne, respectively. The fact that the Si 325 comprises particles of 50-60 nm on average reveals that this material is polycrystalline

and represents agglomerations of much smaller crystallites. A particle size in the range of 50 nm may be preferable to prevent particle pulverization during cycling,[106,142] but another method of characterization is needed to determine the sizes of the actual particles themselves.

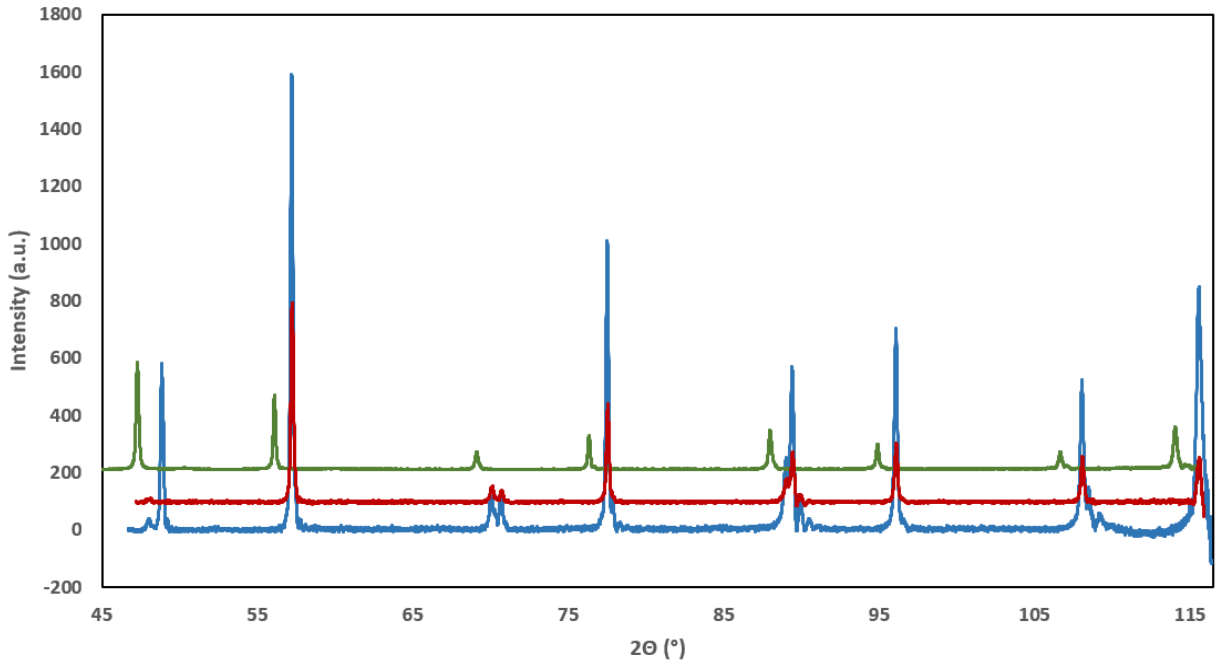

*Figure 3-58. XRD of as received **Si-325** particles (blue), particles ball milled with octane (red) and particles ball milled with 1-octyne (green).*

SEM was then used to image the as-received particles. Beginning with Si 325 mesh particles in Figure 3-59a, the particles are of various shapes with rough edges, and the largest are between 10-20 μm in size. Attempts to size each particle in an image are complicated by the particle shape, but the largest particles reach 3-4 μm at their narrowest point, and 5-10 μm at the widest point. We then examined the particles milled for 12 hours in VEC and trapped in the bottom after centrifuge (Figure 3-59c). The silicon particles have retained their oblong and irregular shape, but have also lost

many of the largest particles, with an approximate average size of 500 nm for Si-VEC, with the largest particles in the range of 1-2 μm. Silicon milled with 1-octyne was observed after mixing with other slurry components for cell testing, and revealed the continued presence of silicon particles between 5-10 μm, which are comparable in size to the starting material, and fail to prevent early pulverization as seen during our tests of Si 325 mesh particles (Figure 3-61, vide infra).

The inability to sufficiently reduce particle size using our ball milling method led to the early abandonment of this project, as it seemed clear that any surface modification would be insufficient for protecting against catastrophic capacity loss over 50 cycles in particles above. Below, we outline further particle characterization and cell tests, but we consider this hypothesis untested due to our inability to reduce or sufficiently filter out micron-sized silicon particles for slurry preparation. We believe that our ball milling instrument may have been incapable of sufficient rotational speed to provide the shearing force required for reducing all silicon particles to sub 150 nm size. We use a Tencan planetary ball mill set to 500 rpm. In contrast, the work of Brian Mitchell uses a SPEX 8000D high energy ball mill (HEBM), capable of both figure-8 rotation laterally along with vertical tilting.[229] Similar experiments from the Yunfeng Lu group use a Retsch Emax HEBM at 1000 rpm, and attain an average particle size of 200 nm.[226]

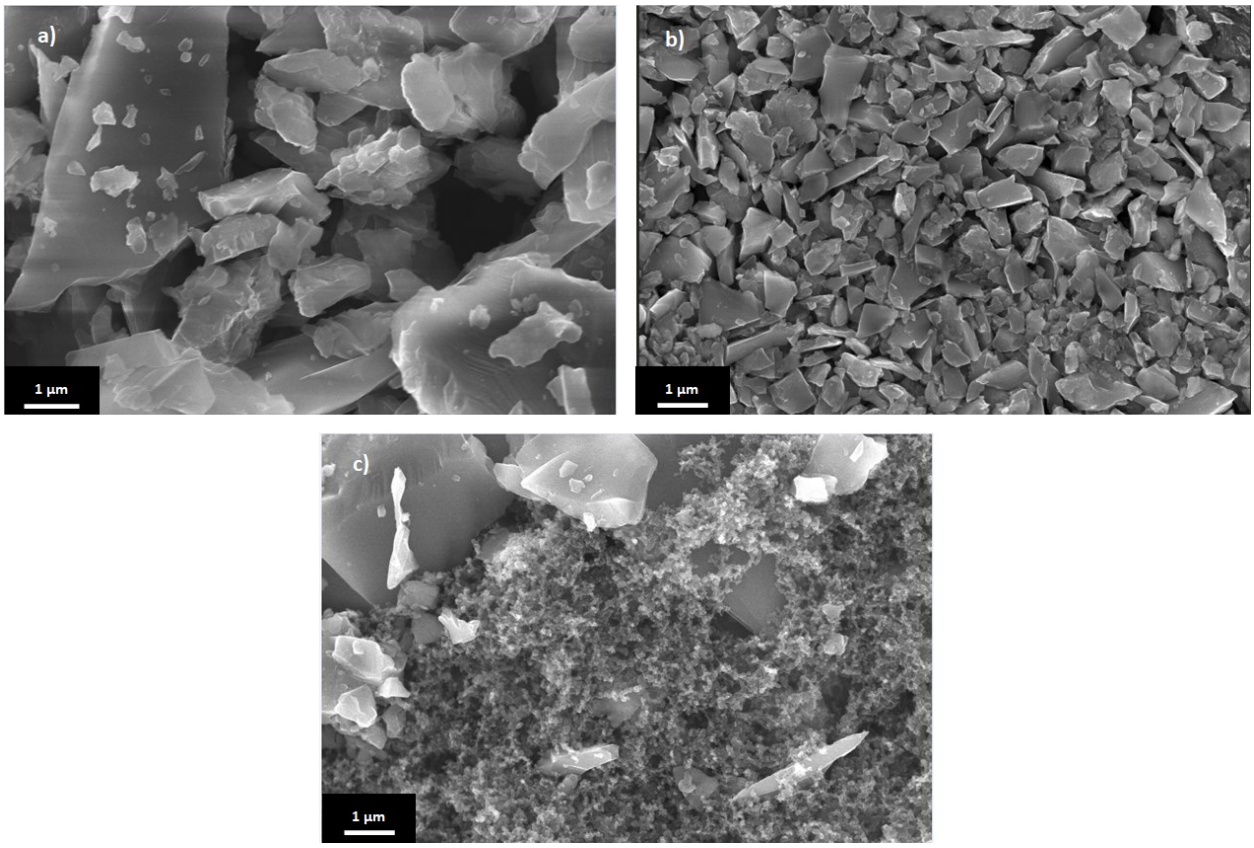

Figure 3-59. *SEM images of as-received **Si-325** (a), **Si-325** ball milled in VEC (b), and **Si-325** ball milled in 1-octyne, prepared in a slurry with carbon Super P and LiPAA (c).*

Of all the samples performed, **Si-325** ball milled with VEC came the closest to reaching the desired size, with an average particle size of ~ 500 nm by SEM. Furthermore, many particles were clearly suspended in the supernatant after centrifugation, and these particles may have been of an even smaller diameter. It was difficult to cleanly remove large volumes of VEC (b.p. 237 °C) to characterize the particles in the supernatant, and we chose not to pursue this project further when we could not reliably replicate mechanochemical synthesis with 1-octyne. However, future research should examine mechanochemical synthesis with VEC as a promising way to produce smaller silicon particles at relatively lower milling rates.

In spite of the particle sizes being larger than we anticipated, FTIR analyses of the ball milled powders were carried out for completeness. Transmission FTIR spectra using KBr plates are shown in Figure 3-60. The Si-octenyl spectrum shows characteristic $\nu(C\text{-}H_x)$ in the region of 3000 cm^{-1} to 2900 cm^{-1}. As stated earlier, the feature at 1100 cm^{-1} results from the $\nu(Si\text{-}O\text{-}Si)$ stretching mode. Finally, the spectrum of Si-VEC indicates $\nu(Si\text{-}H_x)$ at 2100 cm^{-1}, $\nu(C{=}O)$ at 1790 cm^{-1}, and a mixture of $\nu(C\text{-}O)$ and $\nu(Si\text{-}O\text{-}Si)$ between 1100 and 1300 cm^{-1}, which we would expect for silicon with VEC hydrosilylated on the surface. However, stretching above ~2500 cm^{-1} becomes too difficult to distinguish due to noise at the higher frequencies. $\nu(Si\text{-}H_x)$ vibrations are minimal in each spectrum due to the small surface area to volume ratio of the **Si-325** particles.

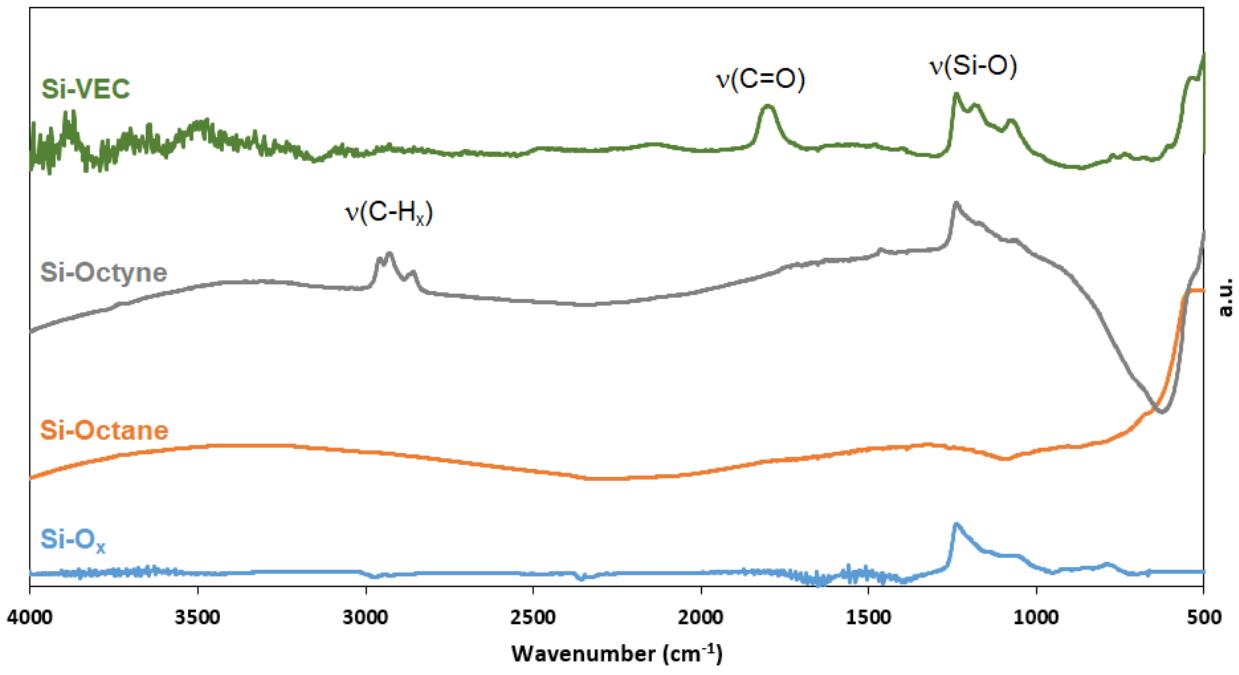

*Figure 3-60. Transmission FTIR of **Si-325** particles as received (blue), after milling with octane (orange), 1-octyne (grey) and VEC (green).*

We take the FTIR results as sufficient evidence that we have at least partially functionalized the silicon surface. We then use these silicon nanoparticles to prepare slurry electrodes along with Super P conductive carbon and LiPAA binder in a water solvent. Results for the first 50 cycles are shown in Figure 3-61. While all cells were tested in 1 M $LiPF_6$ with a variety of additives, only cycles performed with FEC are shown here for having the highest capacity retention. The first and most important conclusion is that all cells lose 75 % of their capacity by cycle 20, typical of the pulverization and capacity loss observed in micron sized particles. Ball milling fails to reduce the size of silicon, as we observed in SEM images, leading to a lack of stability. VEC-Si begins at a surprisingly low initial capacity, only 1158 mAh/g compared to 3073 mAh/g for as-received 325 mesh SiMPs. We hypothesize that this is predominantly due to the low yields during reactive ball milling with VEC, which led to a smaller mass of functionalized particles during slurry preparation and worse mixing with the carbon additive and binder components. It is likely that the initial capacity of Si-VEC could be raised to a similar level to the as received particles if yields were improved, if reactive ball milling were conducted at a much larger scale, or if we mixed the product from more than two experiments. However, our inability to reduce the particle size in 1-octyne milled silicon, and the lower specific capacity Si-VEC particles, dissuaded us from further attempts at mechanochemical synthesis without a high energy ball mill.

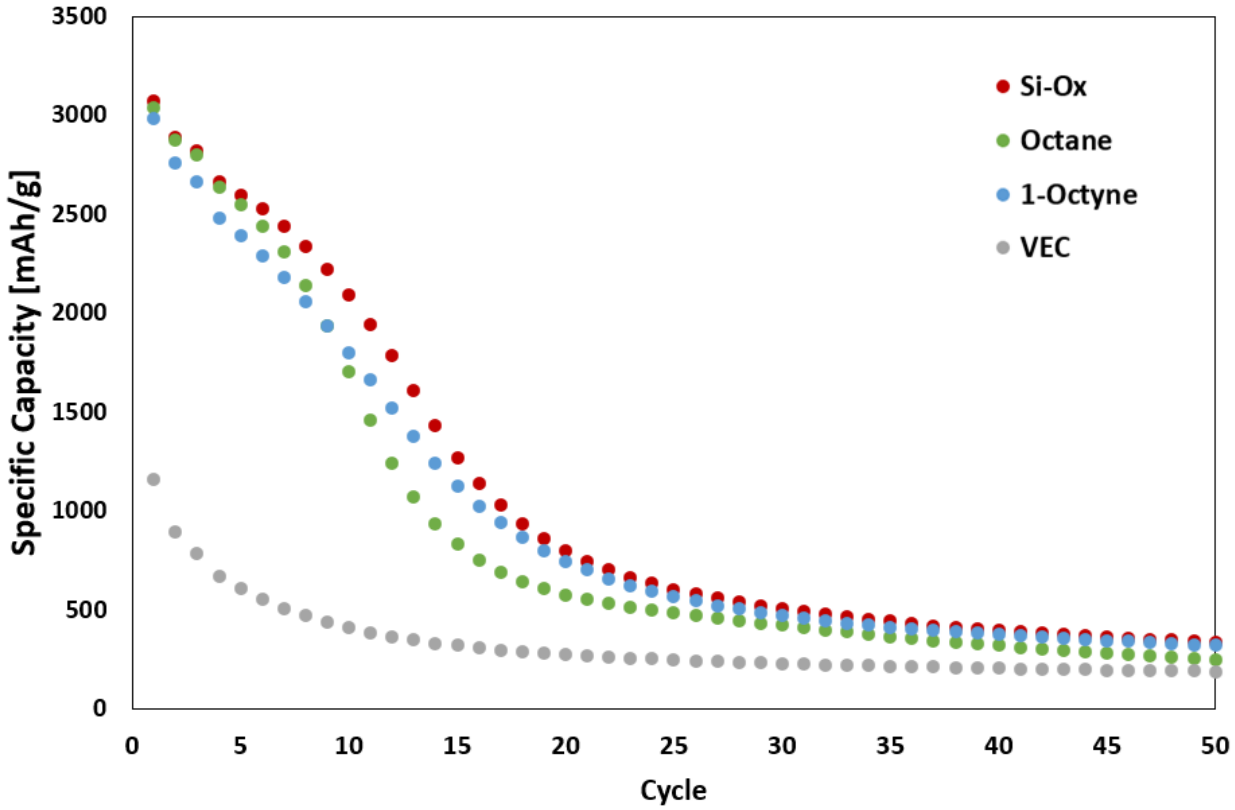

*Figure 3-61. Specific capacity of **Si-325** silicon microparticles as received (Si-O_x) and ball milled in different solvents. Cells were cycled between 1.5 – 0.005 V at 200 mA/g for cycles 1-3, and at 600 mA/g afterwards.*

The cumulative Coulombic inefficiency shown in Figure 3-62 mirrors the results of specific capacity, with as received SiMPs showing the best performance, particularly in cycles 1-20. The Coulombic efficiency of Si-VEC particles is originally low before flattening out early; however, we cannot compare the Coulombic efficiencies of particles with dramatically different specific capacities, as Coulombic efficiency always approaches 100 % as capacity approaches zero.

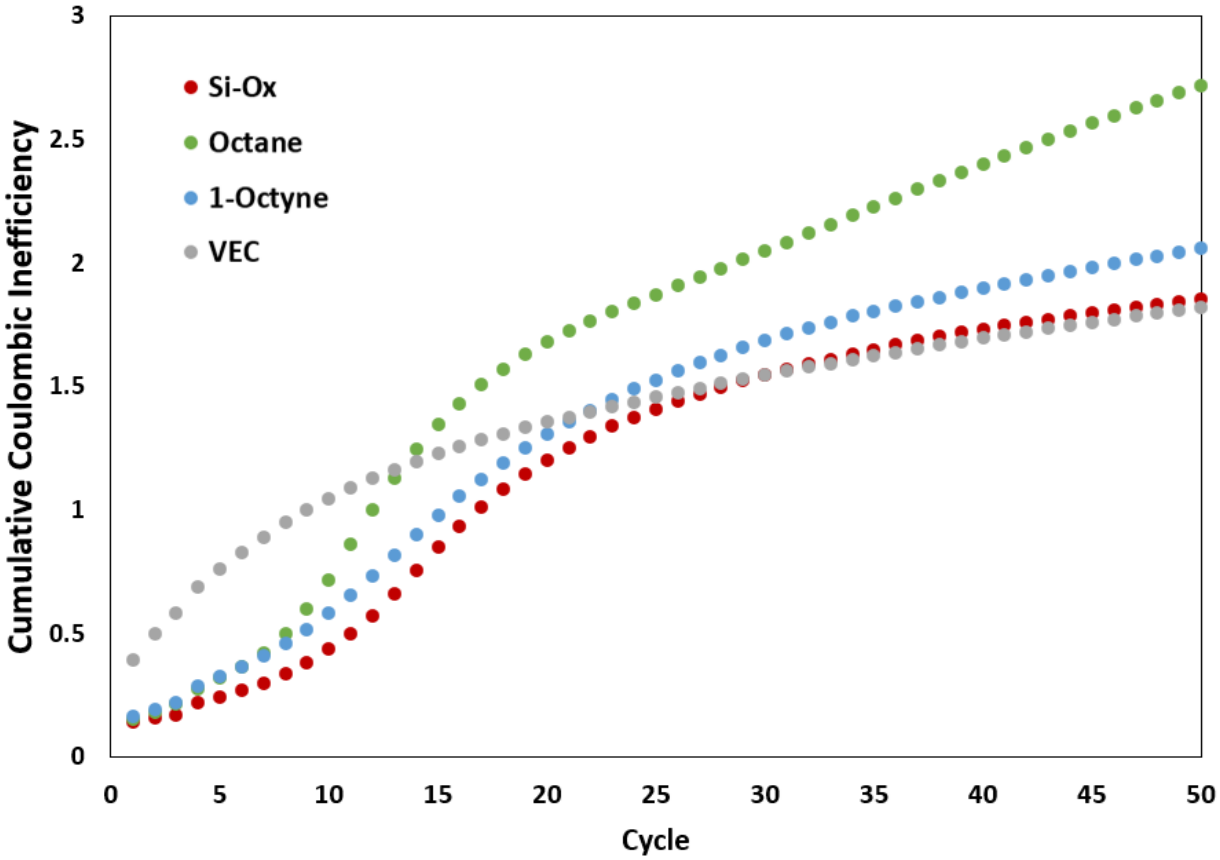

*Figure 3-62. Cumulative Coulombic inefficiency of **Si-325** silicon microparticles as received (Si-O_x) and ball milled in different solvents. Cells were cycled between 1.5 – 0.005 V at 200 mA/g for cycles 1-3, and at 600 mA/g afterwards.*

3.7 Conclusions

We demonstrate that an a-SEI can be achieved by direct thermal hydrosilylation on silicon surfaces under moderate heating conditions (165 °C) and with easily attainable chemical precursors. We demonstrate the basics of thermal hydrosilylation on the surface of porous silicon using FTIR, and export this process to thin films of sputtered silicon; however, we examine only a cursory number of functionalizations on silicon thin films, and the a-SEI do not improve capacity retention compared to a native oxide.

We outline a similar method of thermal hydrosilylation of alkenes onto the surface of silicon nanoparticles to create an a-SEI. We attempt functionalization of two different samples of silicon nanoparticles, **Si-SA2** and **Si-SA3**, which have different sizes and different specific capacities. **Si-SA2** has a low specific capacity, and we find polar a-SEI generally leads to superior capacity retention compared to long alkyl chains, as we believe that long alkyl chains passivate the surface so that they become electrically isolated from the binder and the rest of the cell. When we functionalize **Si-SA2** with both TEG and VEC simultaneously, we attain higher specific capacities and good capacity retention. Mixing components in the a-SEI replicates the naturally formed SEI of high capacity retention cells with FEC additive,[69] and is consistent with the published findings of a-SEI formed with silyl ether bonds and click chemistry.[91]

We also form a-SEI on **Si-SA3** particles, which have a higher specific capacity than **Si-SA2**, and which have a high capacity retention compared to many particles used in the literature.[91,99,215,220] The a-SEI silicon particles are functionalized with a mixture of polar and non-polar surface coatings, are prepared with both non-polar PVDF

binder as well as polar PAA binder. We confirm that Si-PD surfaces lead to superior capacity retention in PVDF binder and improved Coulombic efficiency overall, but we also confirm that PAA binder leads to superior capacity retention for all silicon functionalizations. Polar surfaces did not improve capacity retention or Coulombic efficiency in **Si-SA3** particles. We suggest that this does not represent an upper limit to capacity retention with this method, and future research seeking to improve high performing particles such as **Si-SA3** might require mixed use of polar alkenes in the a-SEI and an optimization of alkene loading volumes. Meanwhile, future work should explore the stabilizing influence of Si-PD particles in silicon-graphite mixed electrodes, for which there is less overall expansion in the electrode and PVDF binder is more frequently used.

Finally, we use mechanochemical synthesis to functionalize the surface of silicon microparticles. This project was abandoned quickly when we were unable to reduce the size of **Si-325** milled in 1-octyne below 150 nm, as we were using a planetary ball mill at 500 rpm, while previous work had used high energy ball milling at 1000 rpm. Nevertheless, we were able to successfully functionalize the surface of silicon with 1-octyne and VEC, and prepared slurries for electrochemical testing. 1-octyne functionalization had little effect on specific capacity or Coulombic efficiency, as predicted by the small surface area to volume ratio for micron sized particles. **Si-325** milled in VEC appeared to be reduced in size to the ~ 500 nm range, but was difficult to isolate and led to very low specific capacity. Future research would include better characterisation of Si-VEC particles that remain suspended in solution, and should focus on high energy ball milling to reduce particle sizes further.

3.8 Experimental section

3.8.1 Materials and reagents

Silicon wafers (100, prime-grade, n-type, P-doped, 1-10 Ω•cm) were purchased from Virginia Semiconductor, Inc. Ethanol (anhydrous), sodium hydride (NaH, dry, 90%), allyl bromide (reagent grade, 97%), mesitylene (98%), tetrahydrofuran (99.9 %), triethylene glycol monomethyl ether (95%), vinyl ethylene carbonate (VEC, 99%), 1-dodecene (95%), 1H,1H,2H-perfluoro-1-decene (PD, 99%), 3-dimethylamino-1-propyne (97%), acrylamide (99 %), N,N-dimethyl acrylamide (99%, contains 500 ppm inhibitor), and fluoroethylene carbonate (FEC, >99 %, anhydrous) were purchased from Sigma-Aldrich. Molecular sieves (type 4Å), and magnesium sulphate ($MgSO_4$, anhydrous) were purchased from Caledon Laboratory Chemicals. Hydrofluoric acid (HF, 49% in water) was purchased from J.T. Baker. Tetrahydrofuran (THF) was purified by a solvent purification system (Innovative Technology, Inc.) and dried over molecular sieves for 24 hours before use. Mesitylene was distilled before use. All other reagents were used as received unless otherwise specified.

Silicon nanoparticles (<100 nm, TEM), silicon powder (325 mesh), polyacrylic acid (PAA, Mv = 450,000), lithium hydroxide (LiOH, reagent grade, 98%), polyvinylidene fluoride (PVDF, average Mw = ~534,000), and 1 M $LiPF_6$ in 1:1 ethylene carbonate:diethyl carbonate (EC/DEC, 1/1 v/v%, battery grade), were purchased from Sigma-Aldrich. Carbon black (Super-P) was purchased from Timcal. More details on the size of silicon nanoparticles is detailed in Section 3.3. Stainless steel discs (304) of 0.5 mm thickness and 15.5 mm diameter were used as spacers. All spacers, springs, and caps for 2032 coin cells were purchased from MTI.

3.8.2 Preparation of silicon thin films

Stainless steel discs (MTI) of 0.5 mm thickness and 15.5 mm diameter were ultrasonically cleaned with dichloromethane, MilliQ water and isopropanol, and used as substrates. Elemental Si films were prepared using an Orion 8 confocal sputtering system (AJA International) in sputter-up configuration. The deposition rate for Si was 0.22--0.28 A/s, at 75 –100 W DC power with an Ar pressure of 4 mTorr.

3.8.3 Synthesis of 2,5,8,11-tetraoxatetradec-13-ene

The synthesis was adapted from previous work Shin and Moon (2018).[230] NaH (0.875 g, 1.2 eq) and dried THF (25 mL) were added to a 100 mL round bottom flask under inert Ar atmosphere. At 0 ºC, triethylene glycol monomethyl ether (4.86 mL) was added dropwise to the solution, turning a dull yellow, and stirred for 30 minutes. The solution was allowed to return to room temperature before we slowly added allyl bromide (3.14 mL, 1.2 eq), turning the solution milk white, and stirring for 2 hours. The solution was quenched with 10 mL water. The organic layer was extracted with a pipette, and the product was further extracted three times with 15 mL CH_2Cl_2. The solution was dried with magnesium sulphate and gravity filtered, before solvent was removed by rotary evaporation (4.72 g crude, 76%). 2.55 g of crude product were purified through a silica column using 1:1 hexanes:ethyl acetate (EtOAc), yielding the product as a colourless oil (1.93 g, 75.7% yield). R_f = 0.21 (TLC, SiO_2, hexanes:EtOAc = 10)

^{1}H-NMR, Figure 3-63 (400 MHz, $CDCl_3$, 25 °C, δ): 5.96 – 5.88 (m, 1H; C<u>H</u>=CH_2), 5.27 (dq, *J* = 1.6 and 17.2 Hz, 1H; CH = C<u>H</u>$_2$), 5.17 (dd, *J* = 1.6 and 10.4 Hz, 1H; CH = C<u>H</u>$_2$), 4.02 (dt, *J* = 1.2 and 5.6 Hz, 2H; OC<u>H</u>$_2$CH = CH_2), 3.67 – 3.64 (m, 8H; OC<u>H</u>$_2$), 3.60 (m, 2H; OC<u>H</u>$_2$), 3.55 (m, 2H; OC<u>H</u>$_2$), 3.38 (s, 3H; OC<u>H</u>$_3$).

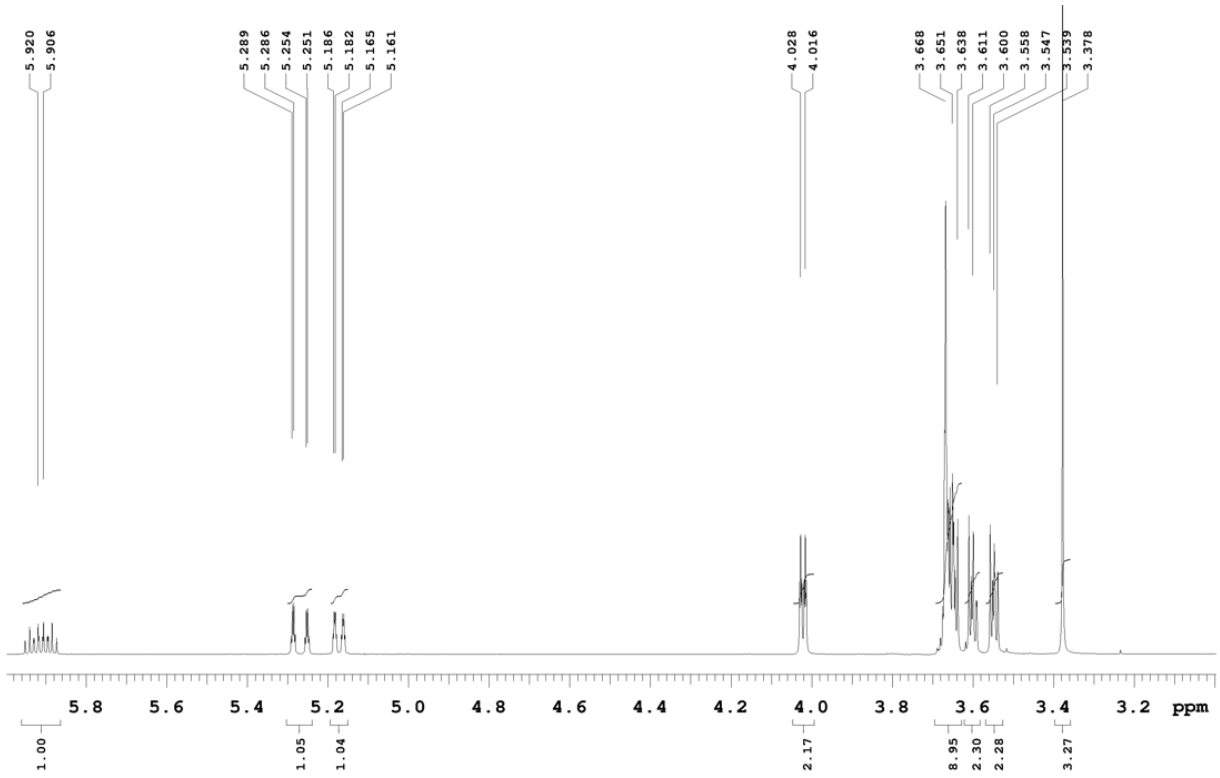

Figure 3-63. ^{1}H-NMR of 2,5,8,11-tetraoxatetradec-13-ene (400 MHz, $CDCl_3$, 25 °C).

3.8.4 Hydrogen termination on silicon surfaces

Warning – hydrofluoric acid (HF) must be handled with extreme caution. Appropriate PPE is required, including a face shield. Silicon thin films were etched by full immersion in 1 % HF (aq) solution for 30 seconds, followed by liberal washing of the surface with ethanol. Samples were dried under argon and left exposed to air for no more than 24 hours unless otherwise specified. No protocols were taken to protect the

backside of the stainless steel. HF vapour etching was conducted using a memsstar Orbis Alpha HF Vapour etching instrument.

Porous silicon was prepared from Si 100 wafers, according to methods previously described in our group.[231] Silicon wafers were sonicated in a bath of 1:1 acetone:ethanol for 10 minutes, then rinsed with ethanol and dried under flowing argon. The polished surface was exposed to a 24.5% HF/25.5% H_2O/50% EtOH solution, and placed in a circuit with an Al foil anode and Pt wire loop as cathode. The silicon was anodized for 90 s at 7.6 mA cm^{-2}, followed by 76 mA cm^{-2} for 120 s under full white-light illumination with an ELH bulb (~40 mW cm^{-2}). The freshly etched porous silicon was rinsed with excess ethanol and excess pentane, and dried under an argon stream. Further functionalization or characterization was pursued as soon as possible, always within 24 hours.

As received silicon nanoparticles (typically ~600 mg) were immersed in a solution of 85:10:5 H_2O:ethanol:HF, at a ratio of ~5 mL solution / 100 g of particles. The mixture was stirred in a teflon beaker for 5 minutes before being filtered using filter paper. Components were exposed twice more to the same HF solution to ensure full removal of the oxide layer. The silicon nanoparticles were then washed three times with ~10 mL of 4:1 H_2O:ethanol to remove HF and placed under a stream of nitrogen until dry. This product was used directly for experiments with hydrogen-terminated silicon (H-Si).

3.8.5 Hydrosilylation of silicon surfaces

In an argon filled glove-box, 1 mL of alkene/alkyne and 10 mL of mesitylene were passed through alumina columns and added to a 3-neck round bottom flask. The

glassware was moved to a Schlenk line and flushed with argon, after which we attached a reflux condenser and a drying tube with calcium chloride.

Dried hydride-terminated silicon was added to the round bottom flask under positive pressure. The solution was allowed to reflux at 165 °C for two hours. We removed the heat, then extracted the solution in a centrifuge tube using hexane as necessary. The solution was centrifuged three times, decanting and rinsing with hexanes in between. The final product was dried under argon and finally placed under vacuum overnight.

3.8.6 Mechanochemical synthesis

In a typical synthesis, silicon powder (325 mesh, 1.7860 g) was mixed with olefin (25 mL) in a teflon milling vial. Zirconia balls (~13.5 g) of were used for milling, with typical diameters of 0.5 cm (x 4), 1.0 cm (x 2) and 1.2 cm (x 1). The material was placed in a planetary ball mill and milled at 500 rpm for 12 hours. The suspension was pipetted semi-quantitatively to a polypropylene centrifuge tube, and centrifuged at 500 rcm for 30 minutes. For characterization of particles in 1-octyne or octane, all but ~7 mL of supernatant was decanted, and the suspension was re-agitated to disperse silicon particles. The suspension was pipetted onto substrates for characterization, and dried for 10 minutes in air and 10 minutes under vacuum. Remaining particles for cell assembly were dried under the same conditions in the centrifuge tube.

3.8.7 Preparation of nanoparticle slurries

Lithium polyacrylic acid was prepared as described in Section 2.4. Slurries were prepared in either water or NMP by combining Si nanoparticles, Super-P and binder in a 60:20:20 mass ratio and diluting with solvent (~160% mass of dry materials). The solution was mixed in a planetary ball mill (Changsha Tianchuang Powder Technology Co.) at 500 rpm for 60 min total in a teflon vial using zirconia balls (4 x 0.5 cm, 2 x 1.0 cm, 2 x 1.2 cm, 1 x 1.5 cm; ~500% mass of slurry). The slurry was cast onto copper foil (battery grade, 10 μm) at a cast height of 100 μm and dried overnight at 120 °C under vacuum. Slurries prepared with NMP were prepared in an Argon glove box whenever possible to prevent oxidation, including during solvent addition and slurry casting. Discs were punched with a diameter of 15 mm, then dried again at 120 °C under vacuum for 16 hours and brought directly under inert atmosphere. The average mass loading was 0.5-0.6 mg/cm^2. Samples were weighed using a Mettler Toledo XP6U balance with a readability of 0.1 μg and a repeatability of 0.4 μg.

3.8.8 Electrochemical measurements

1 M $LiPF_6$ in EC/DEC (1/1 v/v%) with 10 wt% FEC additive was used as electrolytes, with 45 μL total used per cell. All cells were assembled under an argon atmosphere using 2032 coin cells with Li metal foil (MTI) counter electrodes and single layer polypropylene–polyethylene–polypropylene separators with a porosity of 39% (Celgard™ 2325). Cycle life testing was performed on an Arbin BT2000 battery testing system at 25 °C using between the range of 1.5 and 0.005 V. Three formation cycles at 200 mA/g were followed by cycles at 600 mA/g, and all cycles used a constant voltage

step during lithiation of 20 mA/g and 60 mA/g, respectively. Potentiostatic Electrochemical Impedance Spectroscopy (EIS) was performed using a Biologic BCS-805 battery testing system, scanning between 10 kHz and 10 mHz. Cells underwent two full formation cycles as well as lithiation at 200 mA/g, then were left to reach open circuit voltage for three hours prior to EIS. These same cells were left to reach a total of 10 cycles for post-cycling SEM.

3.8.9 Characterization

Scanning Electron Microscopy (SEM) was carried out using a Zeiss Sigma Field Emission SEM at accelerating voltages of 5-10 kV. X-ray photoelectron spectroscopy (XPS) was performed using a Kratos AXIS ultra spectrometer with monochromatic Al Kα radiation (hv = 1486.6 eV, spot size ~100 μm) and under ultrahigh vacuum (10^{-9} Torr). X-Ray diffraction was performed on a Bruker D-8 X-ray diffractometer using Cu Kα radiation (1.5406 Å). Coin cell dissassembly was performed using a gas driven decrimper (MTI corporation), and all post-mortem anodes were washed with dimethyl carbonate (DMC) in an inert atmosphere prior to analysis. Infrared spectroscopy (diffuse reflectance and transmission) was performed using a Nicolet IS50 spectrometer. Contact angle measurements were performed on a Ramé-Hart goniometer (Model 100-00) to obtain a semi-quantitative measurement for the degree of oxidation on the silicon surface.

Chapter 4 Electrolyte optimization and in-situ functionalization of silicon surfaces

4.1 Introduction

The previous chapter discussed optimizing the solid-electrolyte interphase (SEI) prior to cycling through the creation of covalent bonds to silicon. Electrolyte additives have long been examined for their potential to improve the quality of the SEI in lithium ion battery electrodes during cycling.[49,69,71,232–238] Due to the large expansion of silicon upon lithiation, unfunctionalized surfaces are exposed and react with the electrolyte to form fresh SEI, regardless of the initial silicon surface. Many additives function by being less electrochemically stable than the electrolyte and decomposing into SEI components at relatively high voltages, which prevents the electrolyte itself from decomposing. A good electrolyte additive should break down into the components of a stable and high performing SEI, improving such metrics as high lithium diffusivity and high tolerance to electrode expansion. Among the best electrolyte additives that have been identified is fluoroethylene carbonate (FEC), which decomposes at 0.9 volts to form polyethylene oxide (PEO) chains and lithium fluoride (Figure 4-1).[36] The PEO creates flexibility in the SEI, as it is able to maintain contact with the silicon surface through dipole-dipole forces even during large expansion. Meanwhile, nanocrystalline LiF domains become enmeshed in the PEO matrix and causes defects in the otherwise uniform SEI, as determined by XRD.[36] These LiF defects ensure that there are channels of high lithium diffusivity through the SEI.

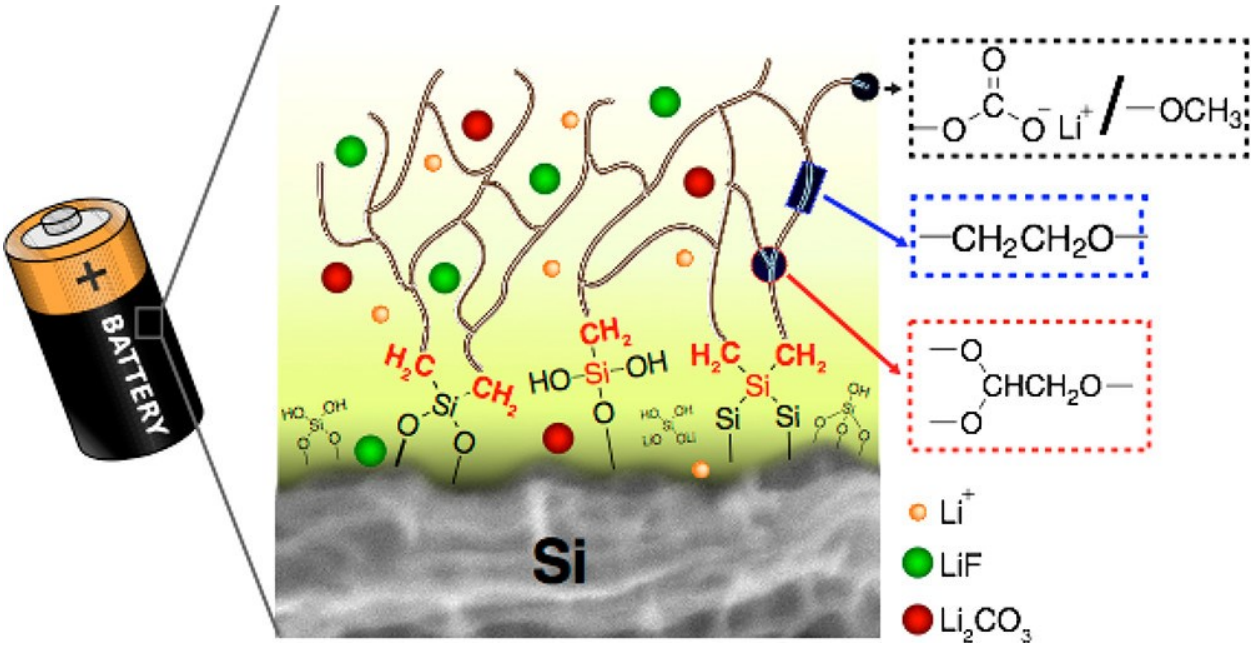

Figure 4-1. Cross-linked polyethylene oxide polymers in the SEI form in the presence of FEC. Reprinted with permission from reference 69. © 2018 American Chemical Society.

In this chapter, we investigate the application of known reactivity of alkenes and alkynes via electrografting to provide a means of controlling the SEI that forms in-situ. It has been previously established that alkynes and alkenes can be covalently bonded to hydride-terminated silicon surfaces under either cathodic (alkynes) and anodic (alkynes and alkenes) galvanostatic conditions.[239] We aimed to replicate this work and then apply the principles of in-situ electrografting to half cells during cycling. Functional groups containing an alkyne or alkene could be used as an additive in the electrolyte to undergo electrografting on newly exposed silicon surfaces. The efforts to carry out ex-situ electrografting on porous silicon are detailed first, with a subsequent discussion of the implications for additives to lithium ion battery electrolyte. A list of additives considered for this work is shown in Figure 4-2.

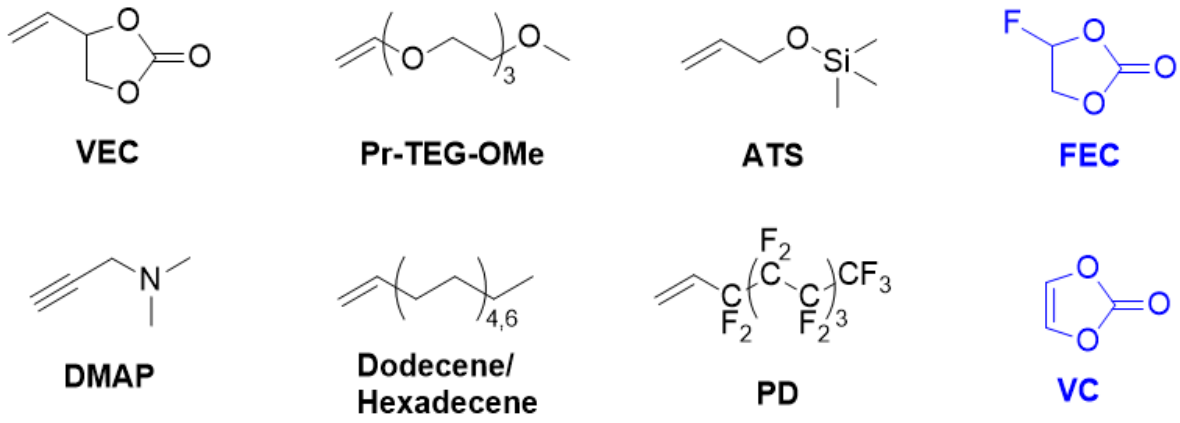

Figure 4-2. *Additives considered for study with silicon anodes. Novel additives were considered if there was potential for in-situ electrografting while also either mimicking stable SEI surfaces from the literature or with functional groups that could lead to known polymerization pathways for SEI formation. Blue additives are established in the literature for their high capacity retention and were used for comparison.*[69,240]

The working hypothesis driving this work is that electrolyte additives with an alkene/alkyne functionality would not only react with freshly exposed silicon surfaces, but could also repair gaps in the SEI caused by silicon fracture during cycling. Electrolyte additives could supplement the SEI formed by solvent decomposition, or could lead to a new a-SEI, that could theoretically graft onto the silicon surface and recreate a thin and uniform layer of organic SEI during cycling. It was important therefore to determine if the reaction of these alkene and alkynes could compete with well known sacrificial electrolyte additives such as FEC and VC during cycling.

The functional groups on the added alkenes and alkynes needed to be considered carefully. Additives were non-protic to avoid reduction by lithium, and

included functional groups homologous to additives in the literature,[57,69] as well as novel functional groups of interest. We generally chose molecules with a terminal alkene or alkyne that would react via radical chemistry and/or electrograting but which also contained functional groups and chemistries similar to additives proposed in the literature. For example, highly fluorinated electrolyte additives have shown success in stabilizing silicon anode cycling in the literature,[235,241,242] typically by decomposing to form a chemically resistant SEI at relatively high voltages (Figure 4-3), and we were curious if highly fluorinated functional groups capable of in-situ reactivity with silicon would provide the same stabilizing effects.

As with other chapters, the research on additives was performed on half cells – sometimes referred to as lithium-metal cells to avoid confusion[20] - in which silicon represents the positive electrode in contrast to a lithium foil negative electrode. The use of lithium foil electrodes leads to certain benefits associated with the functionally unlimited supply of lithium and standardization between different experiments, and lithium-metal cells are common in research on electrolyte additives for lithium ion batteries.[50,71,243] Nevertheless, the use of a half cell setup comes with notable disadvantages. As noted in chapter 3, an unlimited supply of lithium can mask a loss of capacity that arises due to irreversible capacity loss during lithiation; however, such a capacity loss can be approximated through a proper examination of Coulombic efficiency.[244] More important for additives is the interaction of the lithium negative electrode with the electrolyte additives. Electrolyte additives may affect lithium plating, build up an interphase on the lithium surface, and subsequently alter the effective voltage experienced by the silicon electrode.[20,245] For a combination of the above

reasons, full cell setups using cathode materials without a surplus of lithium (e.g. NMC111) have become more popular for studies of lithium ion battery additives.[238,246,247]

The additives of interest were initially screened using thin film silicon electrodes, and then repeated for silicon nanoparticle (SiNP)- and silicon microparticle (SiMP)-based electrodes, the latter being more prone to cracking. The larger microparticles of silicon would be expected to result in formation of more SEI via reactions between electrolyte additives and fresh surface exposed on these cracked microparticles. The role of an additive could be more apparent with these ether-based solvents, and the larger size of the silicon microparticles would show the effect of an additive more readily due to the greater amount of fresh surface area exposed during prolonged cycling. Conversely, silicon microparticle-based electrodes with standard solvents and electrolytes generally lose capacity so quickly that new insights into stabilizing cycling are needed.[93,248] For example, Choi et al. stabilized SiMP cycling by integrating polyrotaxanes into the PAA binder, which held together pulverized silicon material through a ring sliding mechanism.[249] We briefly explore ex-situ electrografting for silicon microparticles, and also consider the potential of olefinated electrolyte additives in a mixed-THF ether based solvent system .[250] The working hypothesis for this project is that larger silicon particles would be expected to involve more reactions with electrolyte additives, accentuating the effect on SEI stability, while mixed-THF solvents might improve the capacity retention sufficiently to allow time for the electrolyte additives to function on SiMP electrode systems.

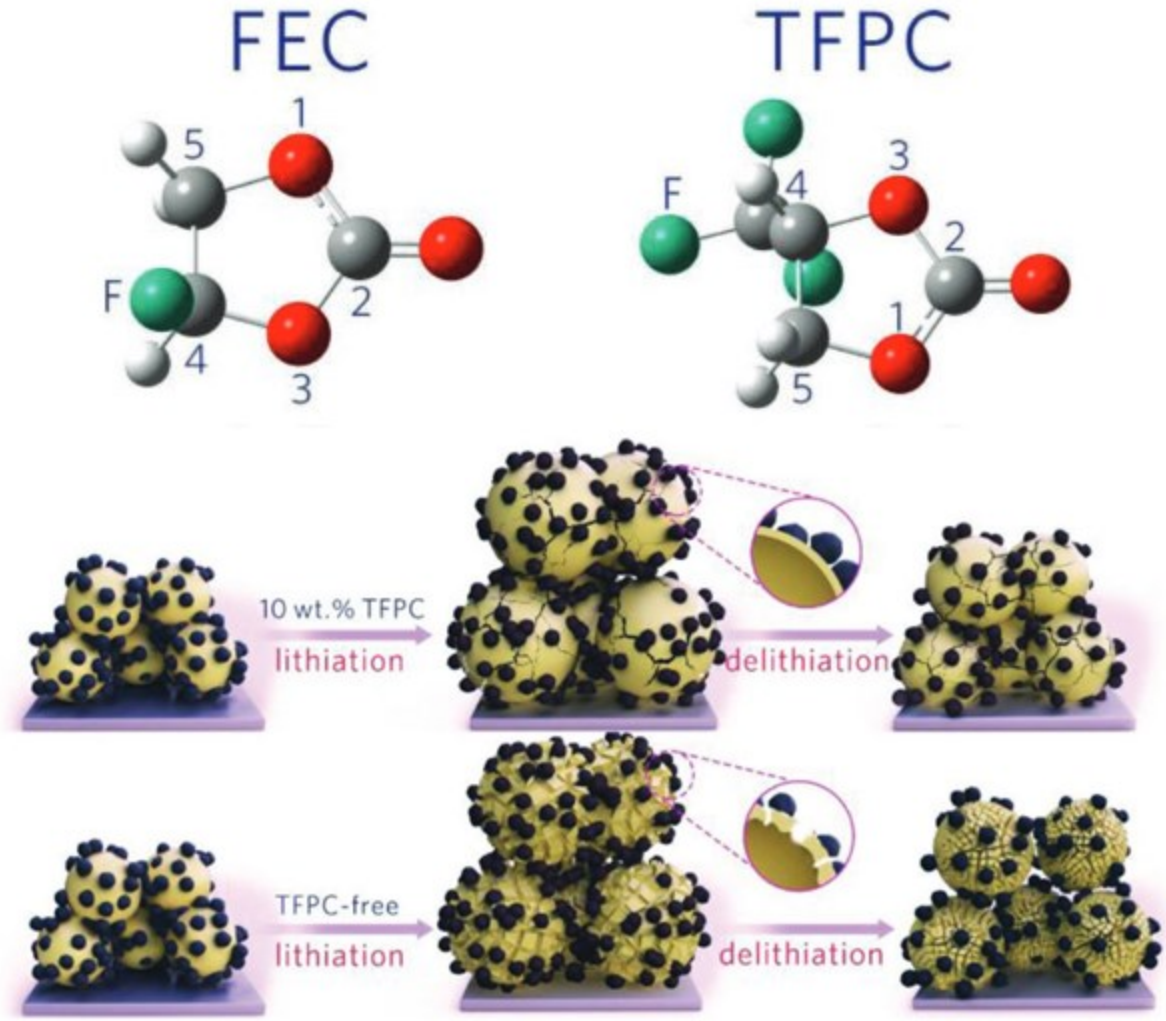

Figure 4-3. SEI formation by trifluoropropylene carbonate on silicon nanoparticles. Adapted with permission from reference 235. © 2019 John Wiley and Sons.

4.2 Ex-situ electrografting of alkyne additives

In Chapter 3, we explored thermally driven hydrosilylation to covalently bond functional groups on the surface of silicon through silicon-carbon bonds. Just as olefins can be hydrosilylated using a thermal driving force, an electrochemical driving force can also be used to initiate carbon-silicon bonding. Early work by Robins et al. established

that anodic and cathodic electrografting can drive covalent chemistry between alkynes (and alkenes) and the surface of hydrogen-terminated silicon. With alkynes, cathodic electrografting (CEG) leads to covalent bonding of an intact alkyne attached through a silicon-carbon bond (Figure 4-4). The presumptive mechanism involves the formation of silyl anion under negative bias. The silyl anion is able to deprotonate a terminal alkyne, leading to a carbanion which reacts with a weak Si-Si bond.[101] Cathodic electrografting does not work for terminal alkenes.

For anodic electrografting (AEG), both alkynes and alkenes undergo covalent bonding to the silicon, as shown in Figure 4-4a.[239] In contrast to CEG, the unsaturated carbons are reduced during AEG, likely proceeding via cationic hydrosilylation when exposed to a positive bias.[101] Since batteries involve the flow of current during cycling, we hypothesized that in-situ electrografting could occur on the surface of silicon, and thus alkynes or alkenes added to the electrolyte could be grafted via similar chemistry. The resulting covalent chemistry could therefore lead to in-situ formation of a stable SEI that would not react further with the electrolyte. First steps of this investigation required reproducing the original conditions of electrografting but using the same electrolyte as that in a lithium ion battery half cell.

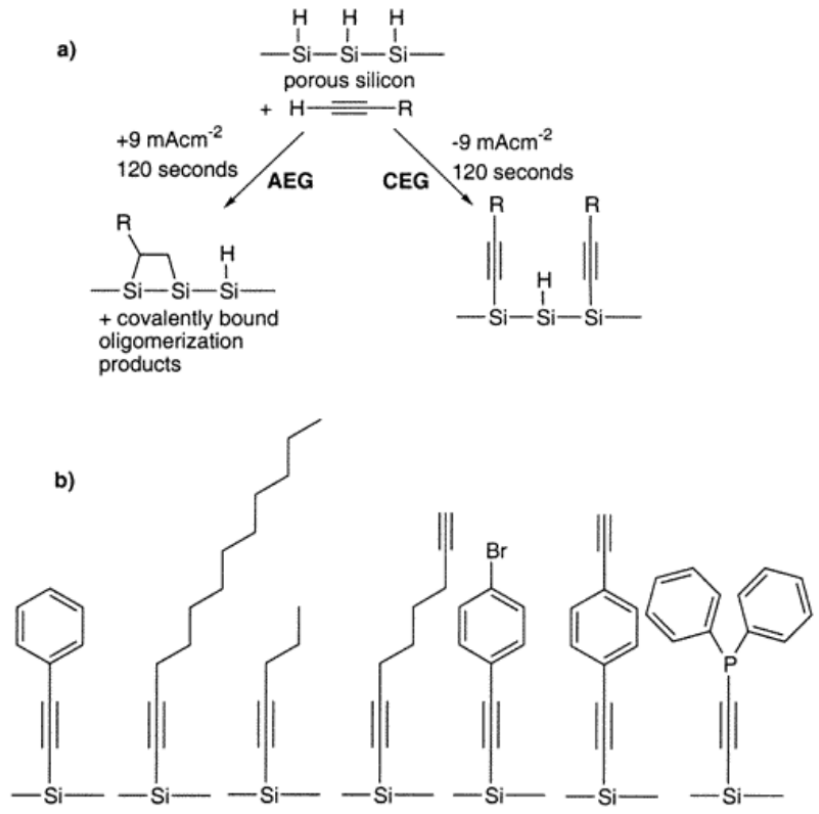

Figure 4-4. a) Electrografting of alkynes on the surface of porous silicon under cathodic (CEG) or anodic (AEG) conditions. b) Cathodic electrografting of various alkynes. Adapted with permission from reference 239. © 1998 Royal Society of Chemistry.

The test bed for this electrografting work was high surface area porous silicon by assembling an open cell in an argon filled glove box (Figure 4-5). 1-Dodecyne (35 µL) was added to a 1 mL solution of 0.1 M tetrabutyl ammonium hexafluorophosphate (TBAHP) in dichloromethane (DCM), as per Robins et al. The open cell allowed us to experiment with hydride-terminated porous silicon made from silicon wafers, which would not otherwise fit into a lithium ion battery coin cell. Porous silicon is a high surface area material ideal for characterization with FTIR,[187] and the cell allowed for easy, modular assembly and disassembly, also ideal for short experiments and efficient post-

mortem characterization. Porous silicon was placed on a copper current collector using a Galinstan eutectic to improve conductivity. The porous silicon was sandwiched between two teflon discs with an O-ring. The upper disc carried battery electrolyte and additives, and funneled to a hole 0.7 cm in diameter. Teflon discs of the same size were used for etching silicon wafers to obtain porous silicon, so all of the porous silicon was exposed to electrolyte. Finally, the cell was clamped shut to prevent evaporation by a glass hose adapter with an O-ring seal. A platinum wire was fitted through the glass hose adapter to act as a counter electrode and adjusted to be within 1 mm of the surface of the porous silicon. The opening containing the platinum electrode was further sealed with parafilm, as shown in Figure 4-5.

Preliminary results for 0.1 M TBAHP with cathodic electrografting (-9 $mAcm^{-2}$ for 120 seconds) were analyzed by transmission mode FTIR. Figure 4-6 demonstrates the differences observed between porous silicon, and silicon subject to cathodic electrografting and anodic electrografting. The 1-dodecyne $\nu(C\text{-}H_x)$ modes at ~2950 cm^{-1} and ~3000 cm^{-1} are consistent with a decyl group, and the shoulder at 2175 cm^{-1}, labeled in Figure 4-6b, is consistent with the ≡Si-**C≡R** group. Broadening of the $Si\text{-}H_x$ feature around 2100 cm^{-1} is also suggestive of functionalization.[251]

Figure 4-5. Open cell set up for electrografting of olefins onto porous silicon. The copper working electrode is shown on the bottom, while the platinum wire counter electrode is passed through the top and subsequently wrapped in parafilm to prevent electrolyte evaporation.

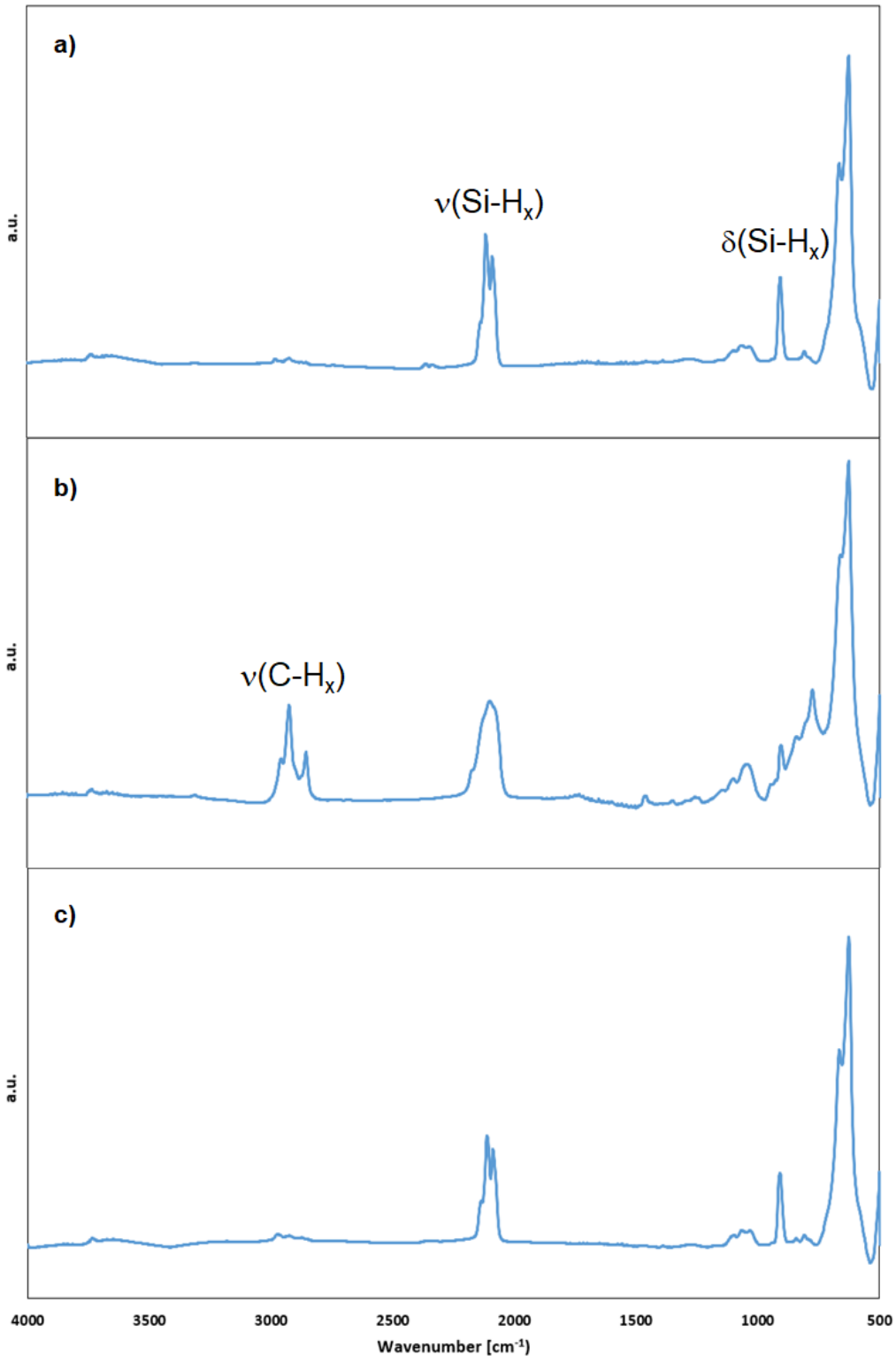

Figure 4-6. Transmission FTIR of p-Si prior to electrografting (a) and after being subjected to a cathodic current (b) and an anodic current (c).

Conversely, when an anodic current was used to induce anodic electrografting, the necessary current needed, 9 mA/cm^2, could not be reached and no change on the surface of the silicon was observed by FTIR (Figure 4-6c). The highest sustainable anodic current was three orders of magnitude less, 9 μA/cm^2. We investigated the cause of this high resistance with electrochemical impedance spectroscopy (EIS). Initially, the solution resistance (R_S) of the system was found to be very high, ~760 Ω. We aimed to improve the R_S via minimizing the distance between the platinum wire and the surface of the porous silicon, as well as applying a GaIn eutectic to improve the conductivity between the silicon 5and the conductive metal contact. The combination of these factors reduced solution resistance to ~300 Ω. A key difference between our first attempts at electrografting and the material we were replicating was the resistivity of the silicon wafer, as we were using 1-10 Ω•cm silicon, while Robins et al. had used 0.65 - 0.95 Ω•cm. Lower resistivity silicon (0.677 Ω•cm) had little effect on solution resistance, and we were still unable to perform anodic electrografting under anodic galvanostatic conditions. More highly doped silicon (0.005 Ω•cm) is unsuitable for research into silicon electrografting because it is opaque to infrared light, which would make characterization much more difficult by FTIR.

In order to reduce the resistance with the open cell and allow for high anodic current over 120 s, we increased the concentration of electrolyte in our solution. The solution resistance was inversely correlated with the concentration of TBAHP, as shown in Figure 4-7, and a further reduction in the solution resistance was enabled by replacing dichloromethane with acetonitrile (ACN). The lowest resistances observed were 163 Ω with 1 M TBAHP in DCM and 64 Ω for 0.25 M TBAHP in ACN, which are

the solubility limits for TBAHP. Even at 64 Ω, we were unable to reach the 9 mA/cm^2 current for 2 minutes, and all attempts to apply lower positive currents for any period of time (such as 90 μA/cm^2 for 20 minutes), failed to lead to any apparent C-H$_x$ stretching modes in FTIR, compared to a control in which no current was applied. In addition, ACN also led primarily to oxidation of the porous silicon, as shown in Figure 4-8, as is expected based on prior observations with water-miscible solvents.[252] Competing reactions with trace water in the solvent result in surface oxidation as exemplified by the observation of oxygen backbonded Si-H$_x$ stretches at 2200 cm^{-1}, and the Si-O-Si stretching mode around 1100 cm^{-1},[253] as well as possible grafting of the butyl groups from the TBAHP cation (which would lead to the ν(C-H$_x$) that correspond with that of a butyl group as per Figure 4-8).[254]

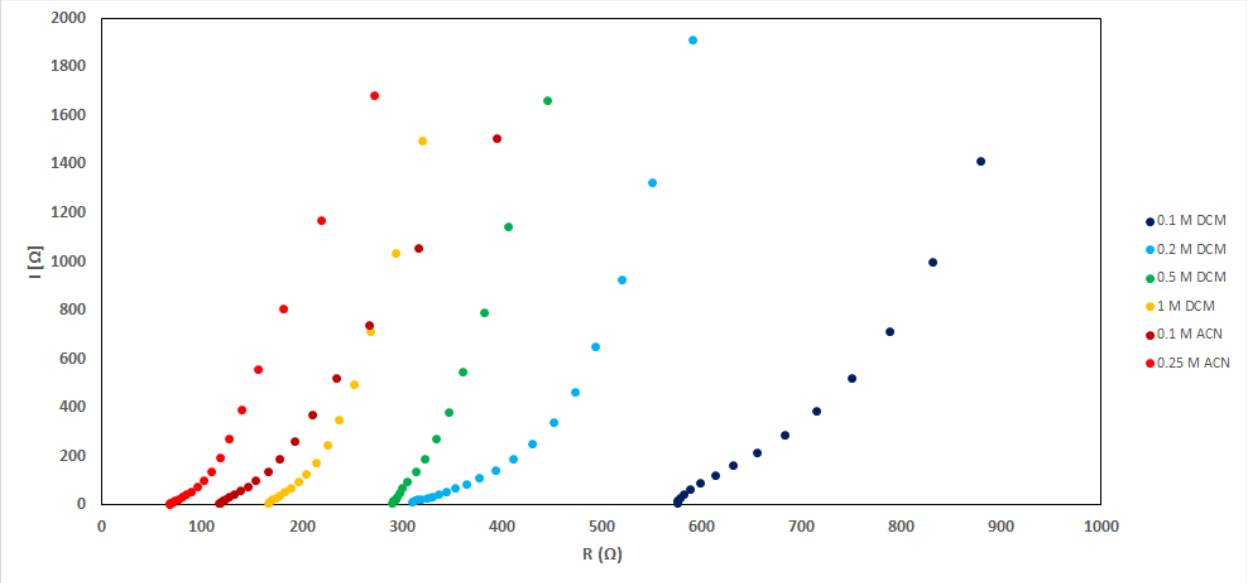

Figure 4-7. *EIS of an open cell with a p-Si working electrode and a Pt wire counter electrode using 0.1 - 1 M TBAHP in DCM and 0.1 -0.25 M TBAHP in ACN.*

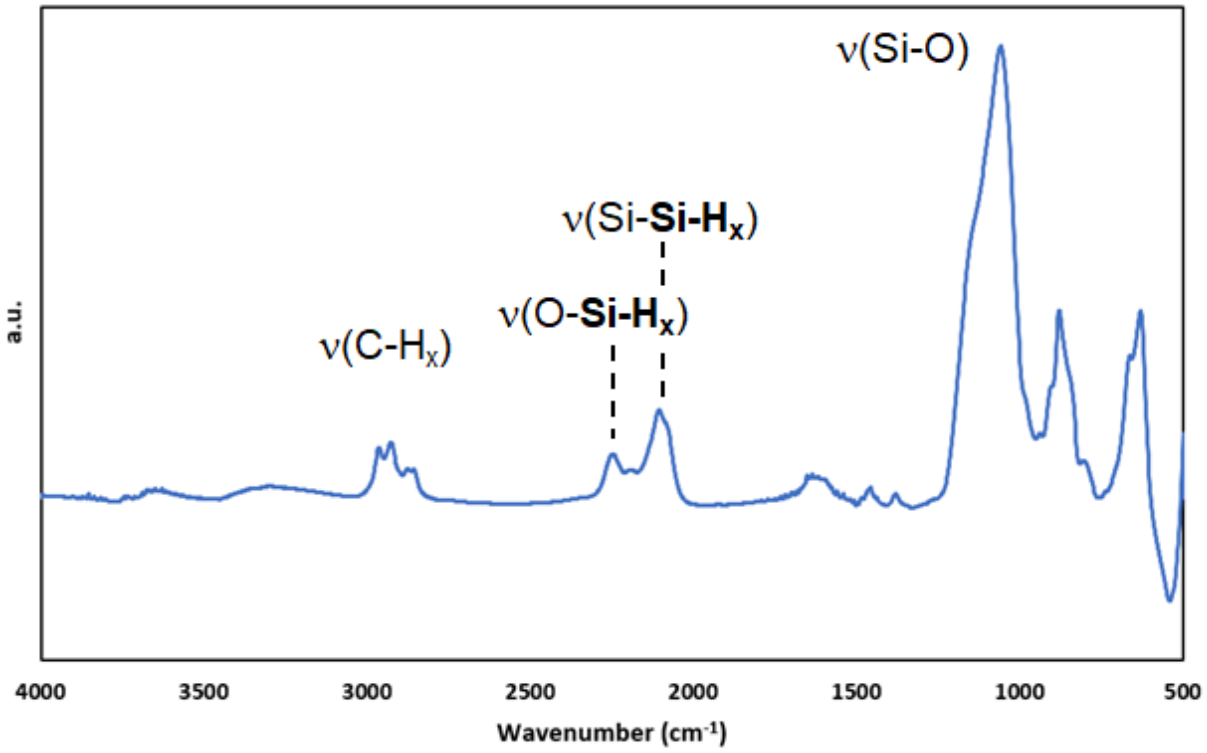

Figure 4-8. *FTIR of CEG with 0.25 M TBAHP in acetonitrile.*

Accepting that anodic electrografting was not working with our apparatus, we aimed to mimic the conditions of a lithium ion battery half cell using an open cell set-up. Initial experiments retained the platinum electrode and substituted 1 M $LiPF_6$ with EC:DEC and 3.5 % v/v 1-dodecyne as the electrolyte. However, the 1-dodecyne was not soluble, and the solubility issues were not detected in early tests. The solution resistance was measured at 120 Ω, and although high anodic currents were still not possible within the voltage window, the FTIR spectrum of the porous silicon sample subjected to cathodic electrografting is shown in Figure 4-9. Significant oxidation is observed, as evidenced by the ν(Si-O-Si) at 1100 cm^{-1}, the broad hydrogen bonded ν(O-H) around 3400 cm^{-1}, and other features likely due to decomposition products from

the battery electrolyte and solvent. In many ways, this process mirrors SEI formation that occurs during battery cycling. It is unclear to what degree 1-dodecyne is incorporated onto the silicon surface, especially given the poor solubility.

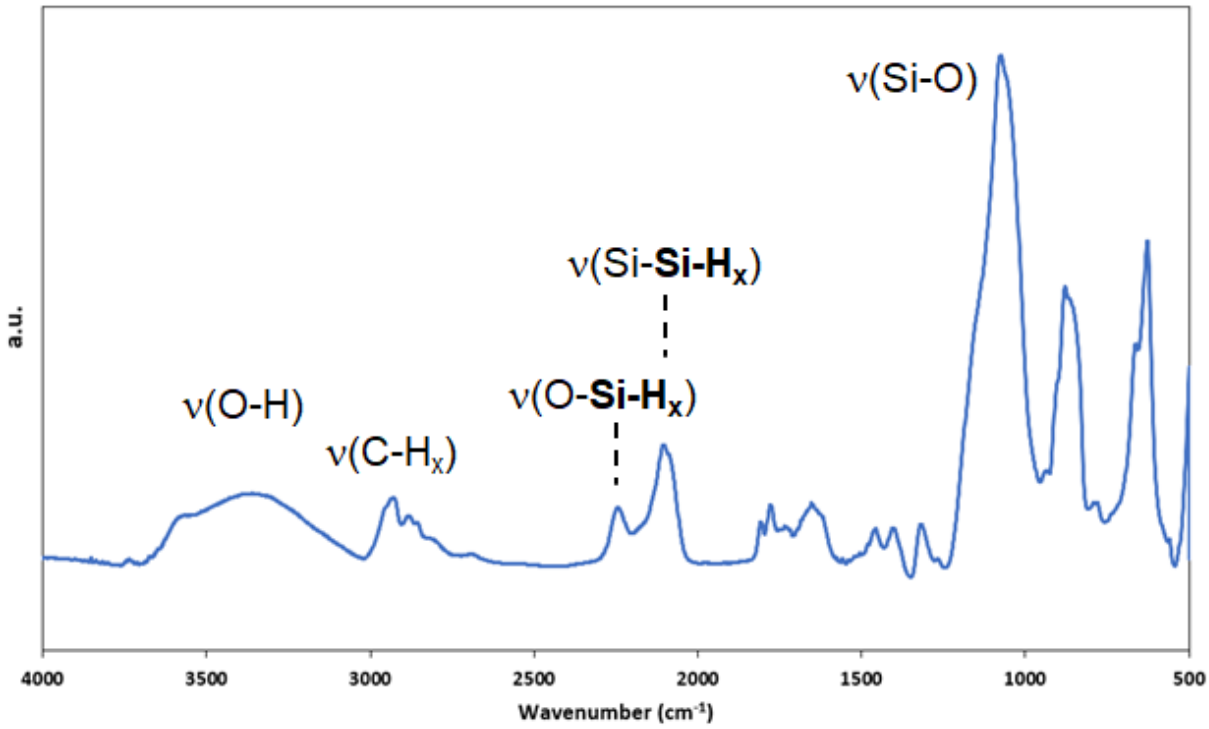

Figure 4-9. *FTIR of p-Si subjected to -9 mA/cm^2 current for 120 s in the presence of 3.5 % v/v 1-dodecyne in 1 M $LiPF_6$ in 1:1 EC:DEC standard battery electrolyte. Pt wire was used as the counter electrode.*

Using a small strip of lithium metal as the counter electrode, 5 mm in width, was placed within 1 mm of the surface of porous silicon. WARNING, the use of lithium with DCM is dangerous, as DCM can and will react vigorously with alkali metals.[255,256] Because lithium is the least reactive of the alkali metals and only 1 mL of solvent was used in the inert atmosphere glovebox, the experiment was completed without incident, but we do not recommend repeating this experiment due to safety considerations. 0.5 M

TBAHP in DCM was the electrolyte, with 35 µL of 1-dodecyne for electrografting. Cell failure was observed after a short time (<20 seconds) and the voltage limits were exceeded. The FTIR spectrum (Figure 4-10) shows C-H_x stretching that does not correspond with a decyl group as evidenced by the high ratio between the heights of the $\nu(CH_3)$ at 2960 cm^{-1} and the $\nu_{as}(C\text{-}H_2)$ at ~2915 cm^{-1}. We propose that this area of the FTIR spectrum suggests possible electrografting of the dichloromethane as per Sailor and co-workers,[257] lithium reduction of DCM that lead to active methyl species (radicals, methyl anions) that can attack the silicon surface,[251] and possible electrografting of the butyl groups of TBAHP.[254]

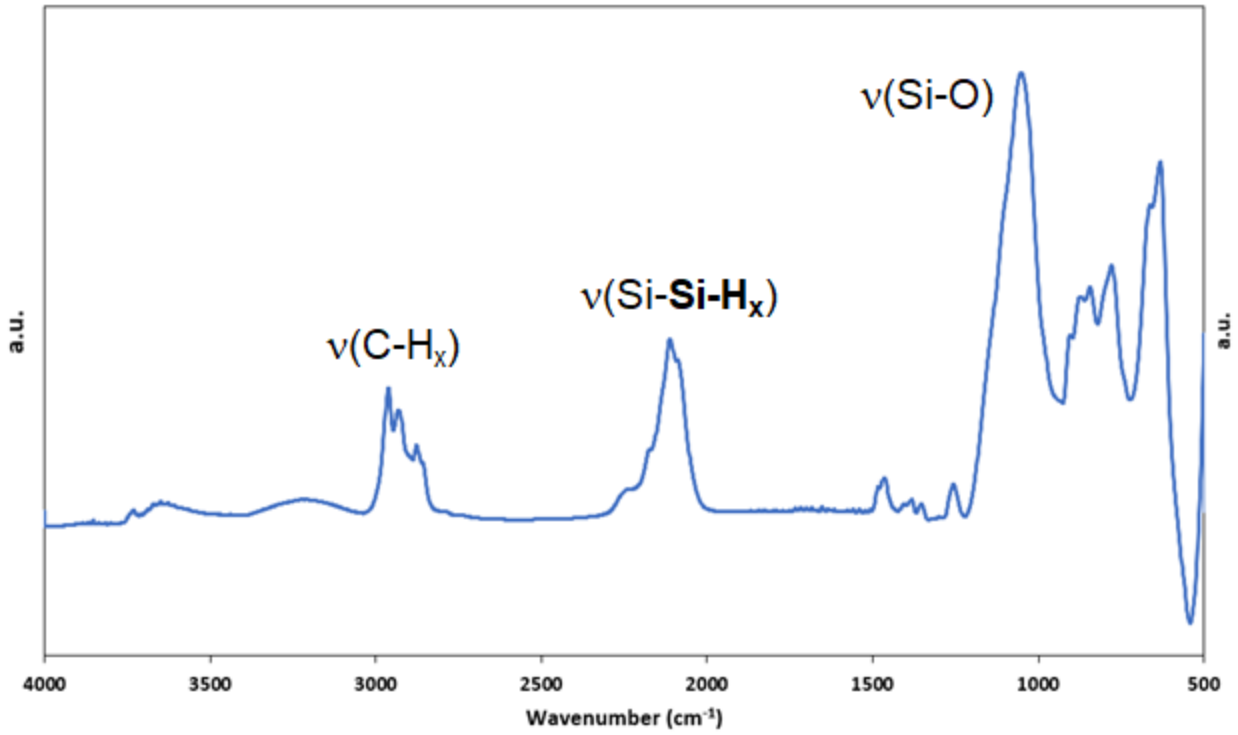

Figure 4-10. FTIR of p-Si subjected to -9 mA/cm² and -900 µA/cm² current for a total of 120 s in the presence of 3.5 % v/v 1-dodecyne in 1 M $LiPF_6$ in DCM. Lithium foil was used as the counter electrode. WARNING - lithium metal can react vigorously with dichloromethane and thus these experiments should not be replicated.

To summarize, replication of cathodic electrografting was successful, but anodic was not. We demonstrated that cathodic electrografting in conditions similar to those encountered in a lithium ion battery cell, although possible, competes with side reactions from the decomposition of solvent components at low voltages, as well as oxidation in the presence of any residual water. Examination of the effect of this process in lithium ion battery half cells, and whether in-situ formation of a covalently bound monolayer on the surface of freshly exposed silicon has any effects during cycling.

4.3 Additives for silicon electrodes

4.3.1 Silicon thin films

Preliminary screening of electrolyte additives was carried out using thin films of silicon sputtered onto stainless steel. Thin films are a useful platform as they simplify the model of lithium ion battery half cells since they do not require the addition of binder and a conductive additive, and the artisanal slurry formation step. The simplicity of these thin film anodes enables a less convoluted observation of the effect of electrolyte additives on the solid-electrolyte interphase. 100 μm of amorphous silicon was sputtered onto either copper or stainless steel spacers, and for the electrolyte, additives were added at 10 wt% to a solution of 1 M $LiPF_6$ in 1:1 EC:DEC.

The first and simplest experiments into the effects of additives involved as-sputtered silicon on copper foils, which would rapidly oxidize in air, yielding a surface coating of silicon oxides. The surface oxide would not react with an alkene via in-situ electrografting; however, fresh silicon surfaces not capped by silicon oxide would be exposed during lithiation as the silicon expands and fractures, and we hypothesize

that olefins present in the electrolyte will react with newly formed, highly reactive silicon radicals to form alkylated species on the surface in what is termed chemomechanical silicon chemistry.[227] These alkyl groups could then form a covalently bound SEI that could passivate the surface of the silicon from further reaction with the electrolyte and - depending on the additive used and other cell components - anchor the silicon together to prevent disconnection. Simple olefins and alkynes were initially explored, including 1-hexadecene, vinyl ethylene carbonate, and propargyl ether. We also compared the cycling results to electrolyte without additive, and electrolyte with 10 wt% fluoroethylene carbonate (FEC), since FEC is a proven, optimized additive for silicon anodes with respect to prolonged LIB cycling.

The additive results are shown in Figure 4-11 for the first 200 cycles. FEC stood out as the electrolyte additive that resulted in the most stable cycling performance for silicon thin films, showing ~56 % capacity retention after 100 cycles, and 36% after 200 cycles. The effect of FEC on thin films is well attested to in the literature,[232,258] although comparisons to reports of capacity retention are complicated by factors such as the substrate on which silicon is sputtered,[77] as described in Section 2.2.1. All cells dropped to less than 20 % of initial capacity by the end of the experiment. Nevertheless, a clear trend is observed whereby all olefin-containing additives were associated with poorer capacity retention in the first 100 cycles. The first cycle Coulombic efficiency is expected to be lower when using additives,[242] because sacrificial electrolyte additives react with lithium under reductive conditions, ideally forming a stable SEI which would minimize further electrolyte degradation. In our case, silicon thin films without an additive had the highest first cycle Coulombic efficiency, at 84 %. While the half cell with the FEC

2additive had a low first cycle Coulombic efficiency, it quickly stabilized and reached 98 % CE by cycle 15. Conversely the olefinic additives had both a low first cycle CE and lower CE throughout compared to the neat electrolyte mixture.

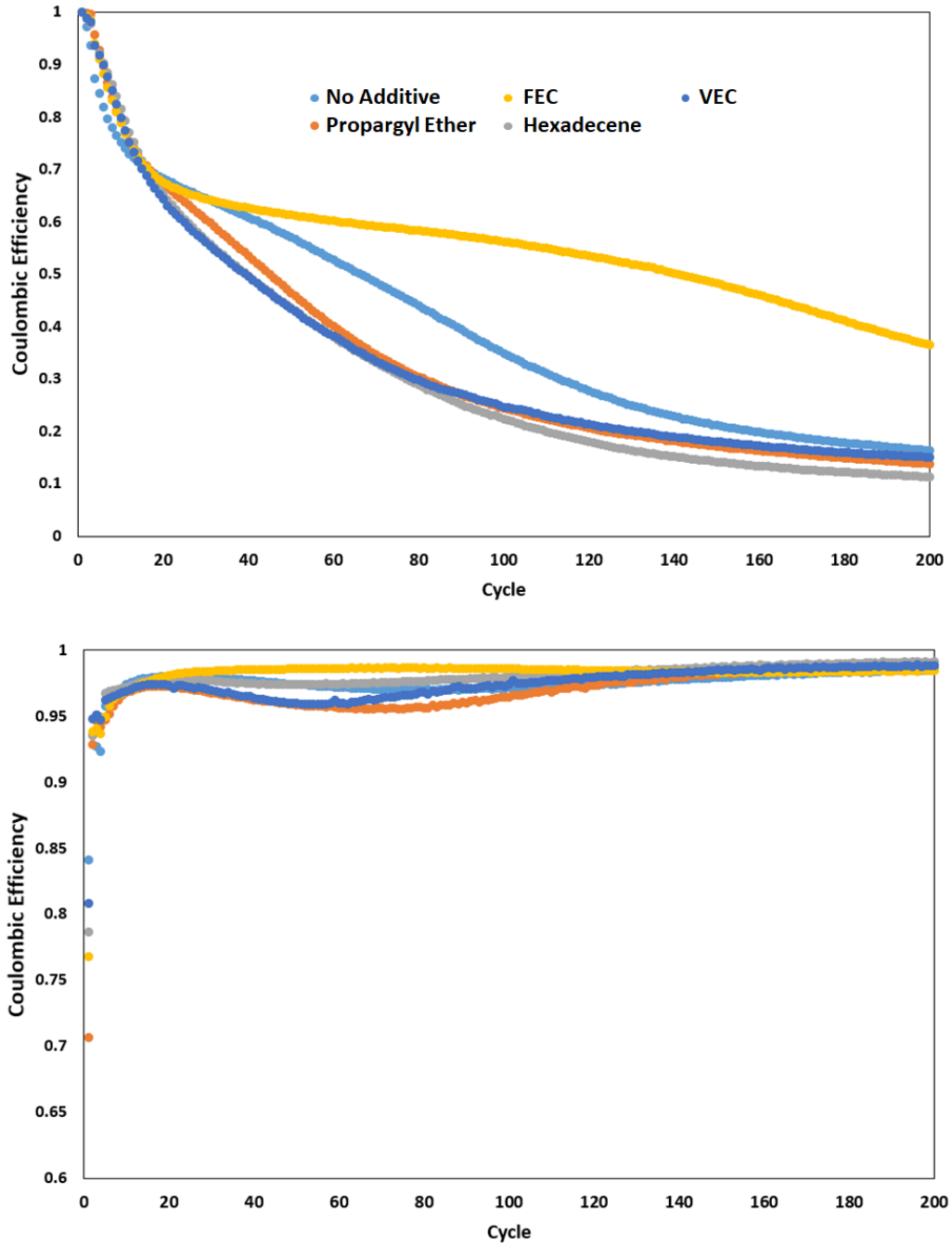

Figure 4-11. Specific capacities and Coulombic efficiencies of silicon thin film anodes cycled for 200 cycles with 10 wt% of various alkene-containing additives.

A next logical step was to test the effect of olefinic additives with silicon thin films treated with HF (aq) to remove the native oxide; much of this research was done concurrently with investigations on the role of surface chemistry of silicon outlined in Chapter 3. As described in Chapter 3, exposure of the silicon surface to HF (aq) produces a silicon hydride-capped surface. We first attempted HF (aq) exposure on thin film samples sputtered on stainless steel discs as we believed that the stainless steel might be more resilient to HF etching. The native oxide was removed by fully immersing the stainless steel discs in a solution of 1 % HF (aq) etch for 1 minute. As in Chapter 3, we were interested in the effects of both hydrophobic and hydrophilic additives on the formation and composition of the SEI. We used 1-dodecyne and vinyl ethylene carbonate (VEC) as the hydrophobic and hydrophilic additives respectively, and compared the effect on sputtered films with a native oxide and with hydrogen terminated silicon. These cells were then compared to silicon pretreated via thermal hydrosilylation (see Section 3.2) with 1-dodecyne and VEC in the presence of the same additive. The hypothesis tested was whether in-situ electrografting would bolster the effect of additives and produce a protective surface coating as new surface area is exposed due to fracturing during cycling.

Relative capacity retention is shown in Figure 4-12. We find that all cells decay to below 60 % capacity retention after 100 cycles. and below 40 % capacity retention after 200 cycles. Si-VEC that was pretreated with a hydrosilylation step generally had better capacity retention than hydrogen terminated silicon with any additives, while the cycling of the Si-Dode hydrosilylated silicon film was unstable. For more discussion on the results observed for hydrosilylation with unsaturated hydrocarbons, see Section 3.2.

With regard to additives, the VEC additive improved capacity retention of hydrogen-terminated silicon relative to solutions with no additive. 1-dodecene has poor solubility in battery electrolyte, and it is difficult to extrapolate from these results because the concentration of additive is in question. Hydrogen-terminated silicon thin films still appear to benefit from the presence of even small amounts of 1-dodecene as an additive. None of the observed capacity retentions rival that of FEC on thin film silicon sputtered on a copper substrate (Figure 4-11).

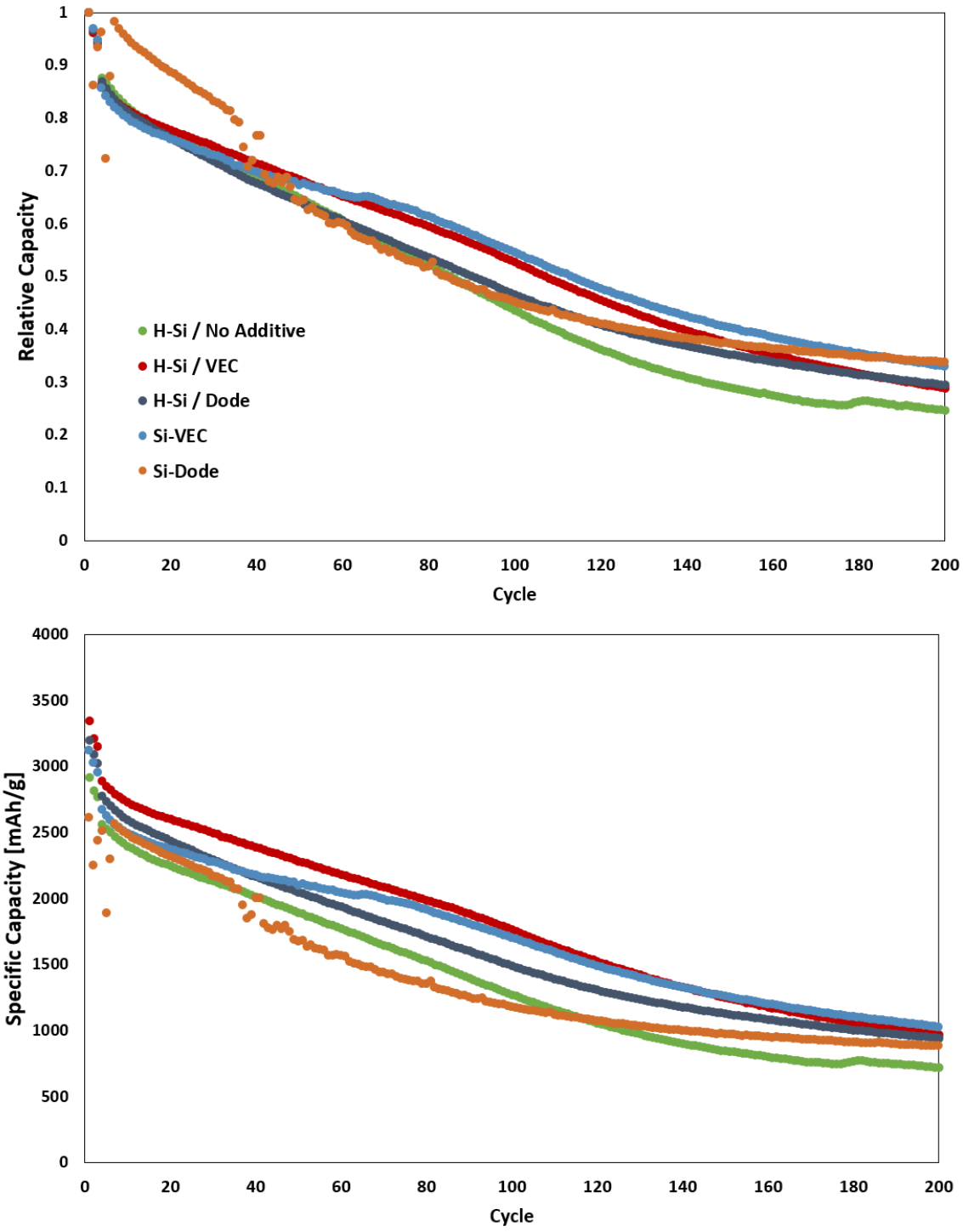

Figure 4-12. Relative and specific capacities over 200 cycles for silicon thin film anodes sputtered on stainless steel spacer with an HF (aq) etching step and 10 wt% additive or with a-SEI functionalization of the same additive on the surface.

Following on the results of the silicon that had been treated with HF (aq), we studied silicon subjected to an HF vapour etch, which was shown in Chapter 3 to remove the native oxide on silicon while avoiding immersion and potential contamination, as had been observed with an HF (aq) solution. Figure 4-13 demonstrates 200 cycles with no electrolyte additive, with 10 wt% VEC, and 10 wt% 1H,1H,2H-perfluoro-1-decene (PD). Perfluorinated decene was chosen in lieu of the 1-hexadecene and 1-dodecene additives explored in earlier experiments. Highly fluorinated compounds have been explored as electrolyte additives in the past with some success,[235,241] and we chose a molecule that also contained a terminal alkene to undergo in-situ electrografting and react with silicon radicals that form upon fracture. The VEC additive appears to stabilize the initially hydrogen-terminated silicon anode slightly after 20 cycles, but the cycling retention of silicon after an HF vapour etch remains very poor (< 20 % after 200 cycles) regardless of the olefinic additives chosen. The addition of 10 wt% perfluorinated decene appears to have no effect on the performance of silicon after an HF vapour etch, with a simple explanation. We subsequently observed that the perfluorinated 1-decene was entirely immiscible with EC:DEC battery solvent - separating immediately after mixing, and that we had been mistaken in thinking that the additive had mixed. The need to find miscible solvents largely limits the range of non-polar additives available to non-perfluorinated molecules.

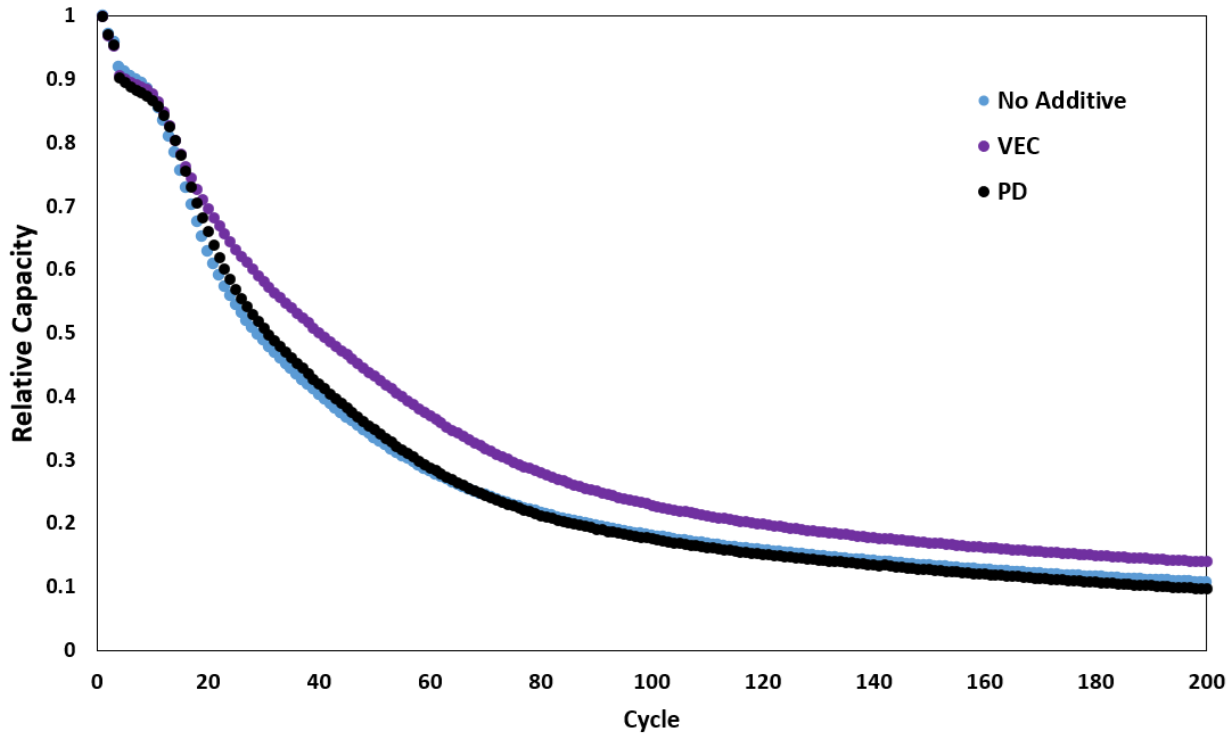

Figure 4-13. Relative capacities for silicon thin film anodes sputtered on stainless steel spacer with an HF vapour etching step. Cycled for 200 cycles with a hydrophobic or hydrophilic additive.

The improvement observed with VEC on hydrogen-terminated silicon is consistent with in-situ electrografting and covalent SEI formation, but is also consistent with other electrochemical reduction products forming non-covalently bound SEI components. Fluoroethylene carbonate and vinylene carbonate, for example, are known to decompose under reductive conditions along a number of well studied pathways to form LiF and polyethylene oxide products (Figure 4-14).[57] However, VEC does not have the same reductive initiation pathways to drive the formation of an EC radical as does FEC.[57] FEC is reduced to form an EC radical with the loss of LiF, while a similar pathway for VEC would involve the formation of pyrophoric vinyllithium. Without the

formation of an EC radical intermediate, VEC would not go through the same reduction mechanisms to form stable, cross-linked polyethylene oxide in the SEI as do both FEC and VC.[69] Nevertheless, VEC still has a lower LUMO than either of the solvent compounds EC or DEC,[259] and would therefore be reduced first during lithiation to form SEI during lithiation. We do not have sufficient results to state the mechanisms for VEC decomposition under reductive conditions, but some degree of branched polymer formation could occur due to the unsaturated carbon bonds.[69] Ideally, our results would have been compared to similar additives without an olefin, such as butylene carbonate. In the following Section, we outline a partial exploration of the impacts of olefinic vs non-olefinic additives on a silicon nanoparticle-based slurry electrode.

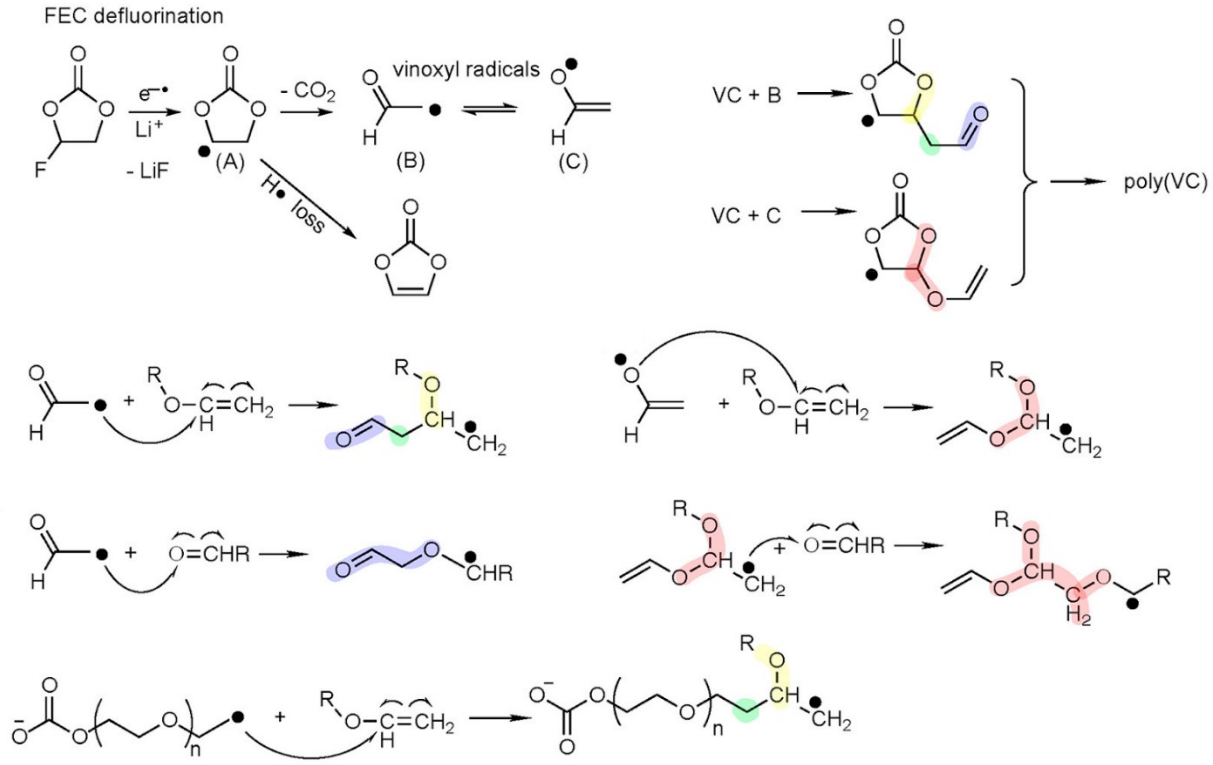

Figure 4-14. Decomposition of FEC to form PEO and poly(VC) in the silicon SEI. Adapted with permission from reference 57. © 2017 American Chemical Society.

4.3.2 Silicon nanoparticles

Since the surface area of nanoparticle-based anodes is much higher than that of sputter deposited thin films, silicon nanoparticle-based slurry electrodes might better uncover the effects of additives and surface pretreatments. Slurry-based electrodes are also similar to what would be used in commercial applications of silicon-based anodes. Silicon nanoparticles were purchased from a commercial source, either Sigma-Aldrich or Alfa Aesar, and were stated to have sizes < 100 nm as determined by TEM. While additive comparisons are valid within a given batch of silicon nanoparticles, we observed sufficient cross-batch variation between silicon nanoparticle batches as supplied from Sigma-Aldrich that comparisons between experiments were not always possible. More details on the silicon nanoparticle samples can be found in Section 3.3. Initial experiments were performed with small scale synthesis methods for preparing slurries, such as mixing with stir bars and drop casting onto stainless steel, but such approaches led to poor homogeneity and reproducibility. Best practices for silicon slurry preparation involves ball milling of slurry components with relatively large volumes of silicon per cast, which resulted in rapid consumption of silicon nanoparticles, thus requiring new and different batches. Briefly, a typical experiment combines SiNPs (867 mg), Timcal conductive carbon (Super P, 290 mg), and a binder solution of PAA (289 mg, 8.48 % in water). The ingredients are mixed in a Teflon ball milling vial with zirconia milling balls and extra water to attain the appropriate viscosity. The resulting slurry is milled and cast on copper film using a doctor blade before being vacuum dried and brought under inert atmosphere for cell assembly.

We used HF (aq)-etched silicon nanoparticles obtained from Alfa Aesar, labeled **Si-AA1** to again compare olefinic additives. Vinyl ethylene carbonate was alongside the high performing additive of fluoroethylene carbonate. 1-dodecene, and perfluorinated 1-decene were again used as non-polar electrolyte additives, but we reiterate their poor solubility in EC:DEC solvent. Once again, FEC led to the highest capacity retention (Figure 4-15), although capacity retention was low with the Alfa Aesar particles. FEC does not have an olefinic group and therefore is not a candidate for in-situ electrografting, instead leading to more stable cycling via decomposition products LiF and polyethylene oxide fragments, which contribute to a stable SEI composition as established in the literature.[36,69] Additive VEC, which is a candidate for in-situ electrografting, underperforms both FEC and as-received 1 M $LiPF_6$ in 1:1 EC:DEC without an additive. The fast capacity fade in the presence of VEC suggests that in-situ electrografting of VEC may a poor method for stabilizing the SEI of silicon nanoparticles prepared via the slurry method. We hypothesize that the poor capacity retention observed with even the FEC additive is a result of the large size of some particles obtained from Alfa Aesar (Figure 3-29). A general trend observed with the commercial particles used here is that a larger particle size often leads to higher initial capacity at the expense of capacity retention, which will be explored further later in this chapter. 1-dodecene is poorly miscible in battery electrolyte and perfluorinated 1-decene is immiscible. The results of 1-dodecene and perfluorinated 1-decene are included here after thorough mixing with the electrolyte to show that the inclusion of an immiscible hydrophobic additive can lead to cell death.

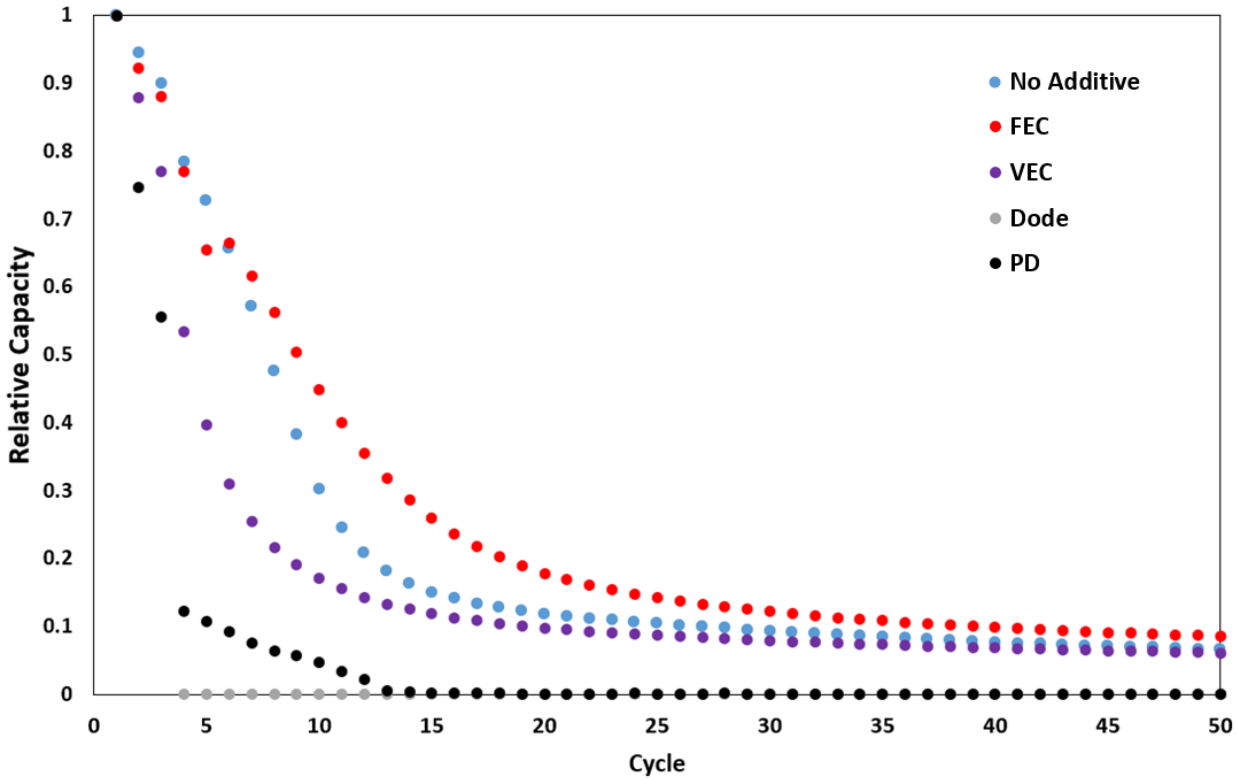

*Figure 4-15. Relative capacities over 50 cycles of **Si-AA1** particles etched in 5 % HF (aq) with and without the presence of 10 wt% various additives.*

Following these tests, we experimented with silicon nanoparticles from Sigma-Aldrich, labeled **Si-SA1**, which have an average size of 60 nm as determined by SEM (Section 3.3). While electrodes comprising these particles generally start at a lower specific capacity than those using particles obtained from Alfa Aesar, their capacity retention was much higher (Figure 4-16), with **Si-SA1** achieving 70 % capacity retention after 50 cycles compared to the 26 % capacity retention of **Si-AA1**. We did not experiment with non-polar additives, as we had realized their incompatibility with carbonate solvents, however we introduced two new olefin containing electrolytes (Figure 4-17). Allyloytrimethyl silane (ATMS) is an olefinic derivative of a family of compounds containing trimethyl silane that were studied by Ryu et al to improve stability

in silicon anodes.[260–262] 3-Dimethylaminopropyne (DMAP) is a commercially available tertiary amine, which combines the necessary components of being a polar aprotic additive - necessary for mixing with carbonate solvents without being reduced by lithium - and also contains an alkyne that renders the molecule susceptible to in-situ electrografting and reactivity with silicon radicals under chemomechanical conditions (following fracture). Amides have been used successfully as electrolyte additives for silicon anodes,[213,263] but the compatibility of nucleophilic amines is unknown.

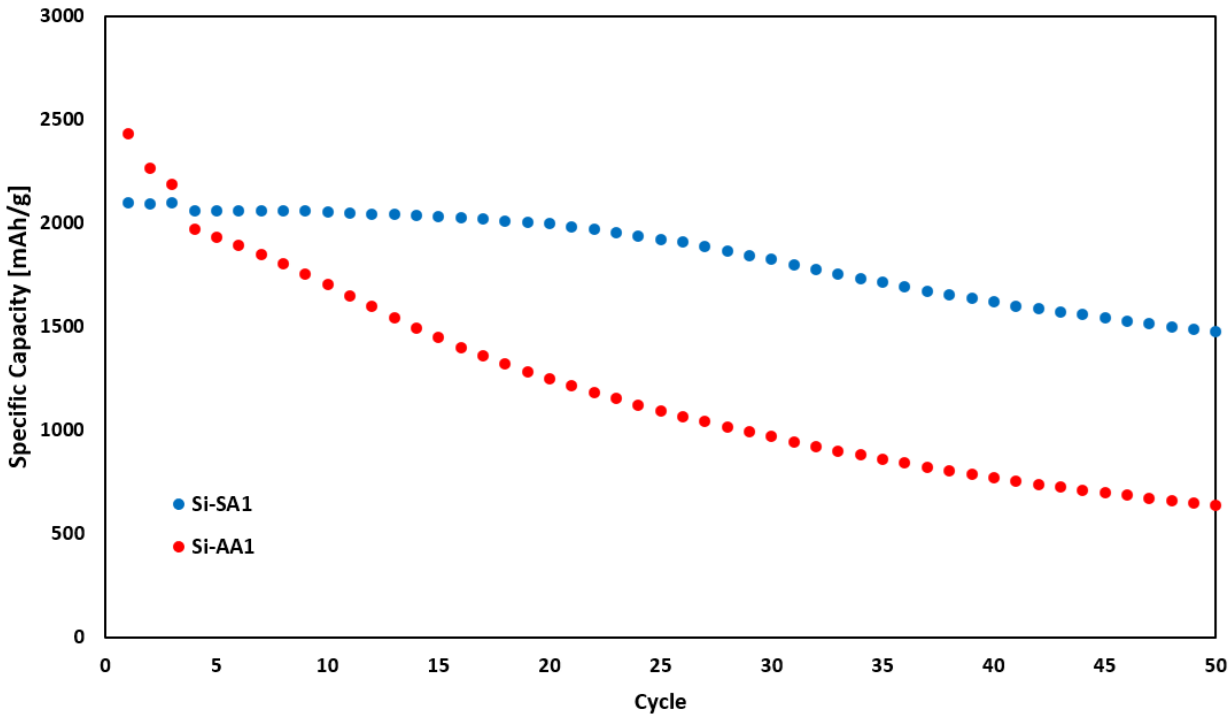

*Figure 4-16. Specific capacities of silicon nanoparticles **Si-SA1** vs **Si-AA1**.*

allyloxytrimethyl silane **3-dimethylaminopropyne**

Figure 4-17. Novel alkene/alkyne additives for carbonate lithium ion battery electrolyte: allyloxytrimethyl silane (ATMS) and 3-dimethylaminopropyne (DMAP).

The specific capacity of **Si-SA1** slurries over 50 cycles are shown in Figure 4-18. All of the cells had an initial capacity of ~2000 mAh/g, but additives VEC and ATMS led to lower cycling capacities of the silicon anode after ~10 cycles compared to as-received $LiPF_6$ electrolyte in carbonate solvent without an additive. DMAP caused instability in cell cycling and catastrophic failure after 40 cycles. We hypothesize that the nucleophilic amine on DMAP attacks the silicon substrate, leading to oxidation and electrical isolation of the silicon, similar to problems with hydrosilylation observed in Chapter 3. From both **Si-AA1** and **Si-SA1**, we find no evidence for the ability of olefinic additives to passivate silicon surfaces through the formation of more stable SEI.

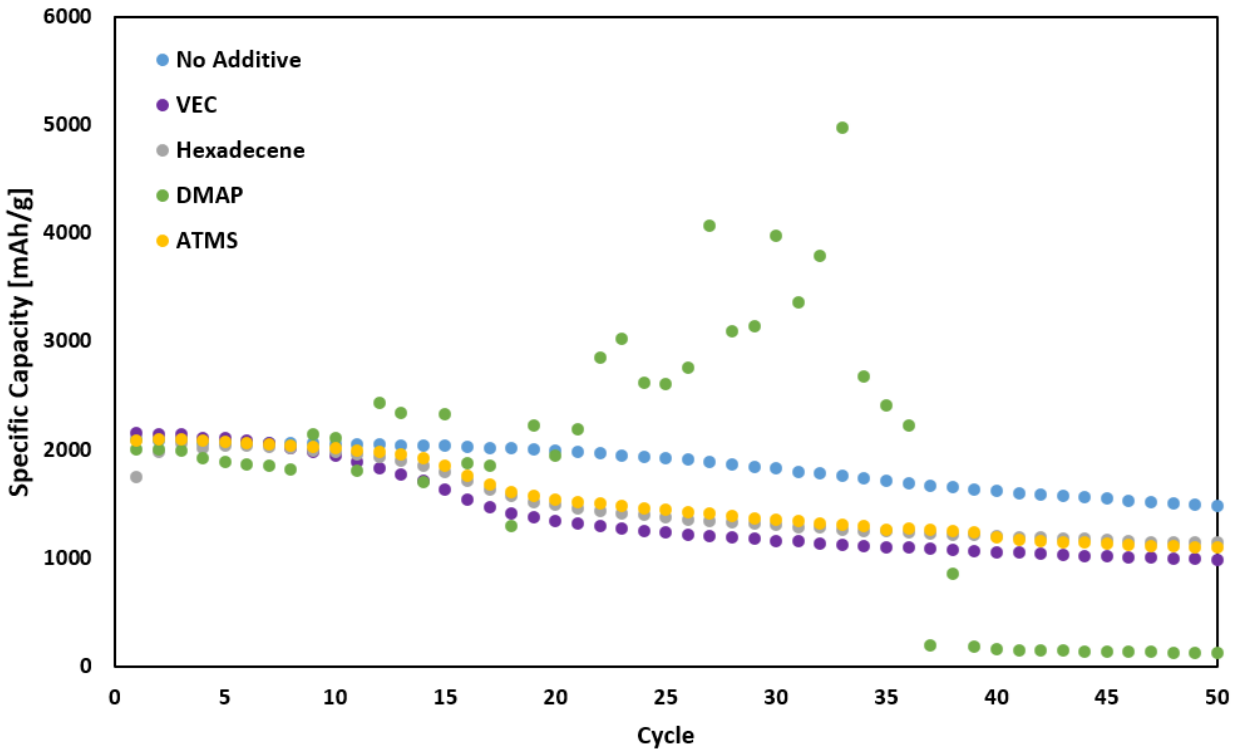

*Figure 4-18. Specific capacities of **Si-SA1** particles over 50 cycles with 10 wt% novel alkene or alkyne containing additives.*

As mentioned previously, the large mass of silicon nanoparticles required for slurry preparation (~800 mg) necessitated new orders of nanoparticles with separate batch numbers and properties. Further experiments were carried out with a new batch of silicon ordered from Sigma-Aldrich **(Si-SA2)**. As shown in Section 3.3, the size distribution of **Si-SA2** was ~80 nm based on SEM.

As discussed in the introduction, a central hypothesis to this chapter builds off the work on a-SEI in Chapter 3 to introduce olefinated additives with functionalized silicon nanoparticles. In-situ electrografting could bolster the effects of a-SEI, and theoretically replace holes in the a-SEI that are made by newly exposed silicon upon fracture during cycling. At a minimum, we wanted to test if the inclusion of a polar

alkene could be used as both the functional group for electrografting and the additive in 1 M $LiPF_6$ in EC:DEC. We are testing the idea that in-situ electrografting could create a self-repairing a-SEI which could provide more uniform protection than the decomposition of either the as-received electrolyte or the literature additives of FEC and vinylene carbonate (VC).

The specific capacities of hydrosilylated silicon samples in various additives is shown in Figure 4-19. We choose to hydrosilylate **Si-SA2** with olefin terminated triethylene oxide monomethyl ether (Pr-TEG), which mimics the polyethylene oxide fragments often found in stable SEIs, and we use the same Pr-TEG as a 10 % v/v additive in the electrolyte. As demonstrated by the capacity retention at cycle 50, our novel olefinated additive once again led to worse capacity retention than electrolyte without additive under these conditions. The inclusion of FEC, with or without the complementary additive VC, led to much improved capacity retention over the 50 cycles studied, although cycling in the presence of FEC is known to deteriorate after the FEC has been consumed.[71]

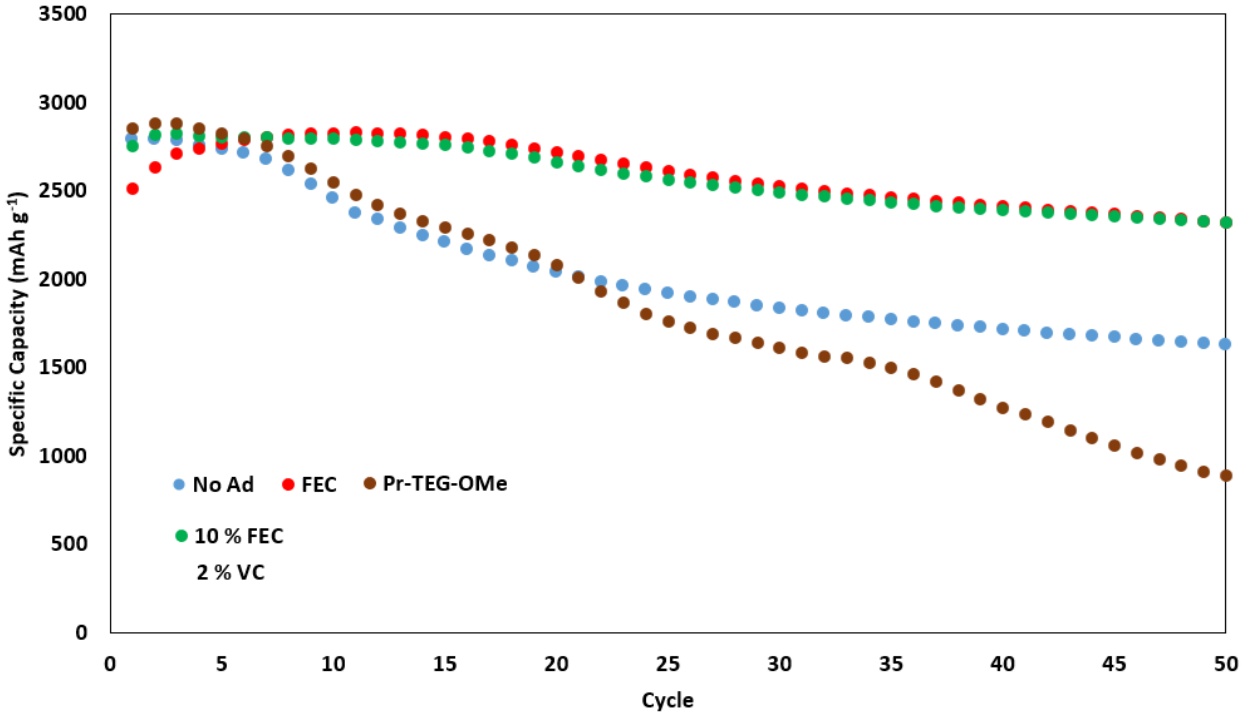

*Figure 4-19. Specific capacity of **Si-SA2** nanoparticles with an a-SEI of Pr-TEG-OMe. Cycles 1-3 were carried out a 200 mA/g, and subsequent cycles at 600 mA/g.*

With these results, we do not feel that we have exhausted all options for olefin terminated additives, nor all combinations of surface and additive mixtures, but we do feel that we have sufficient evidence to suggest that in-situ electrografting is an unlikely target for creating a stable and passivating SEI in silicon nanoparticle anodes. Briefly, we explore the possibility that in-situ electrografting could improve the capacity retention of larger silicon particles on the micro scale, before discussing the possible chemistry behind the poor cycling performance of alkyne/alkene terminated additives.

4.4 Additives with Si-325 based electrodes

Our final attempt to explore additives for in-situ electrografting was using much larger silicon microparticles (SiMPs), which have a size below 44 μm as described in Section). Unlike silicon nanoparticles, larger microparticles typically start very near to the theoretical capacity of 3579 mAh/g, but undergo large drops in relative capacity as expansion and contraction rapidly leads to pulverization in the larger particles. The role of an additive could be more apparent with this electrode system, as the larger size of the silicon microparticles would show the effect of an additive more readily due to the greater amount of fresh surface area exposed during prolonged cycling. Nevertheless, cycling over 50 cycles is shown in the same 1 M $LiPF_6$ in 1:1 EC:DEC is shown in Figure 4-20, with and without olefinated additives. All cycling decays at similar rates, rapidly reaching <15 % capacity retention prior to 20 cycles regardless of which additives were included. FEC is able to improve cycling slightly, but the cells with SiMPs still reach 15 % by cycle 33. The capacity decay in SiMPs is so rapid that the effect of additives may not be apparent.

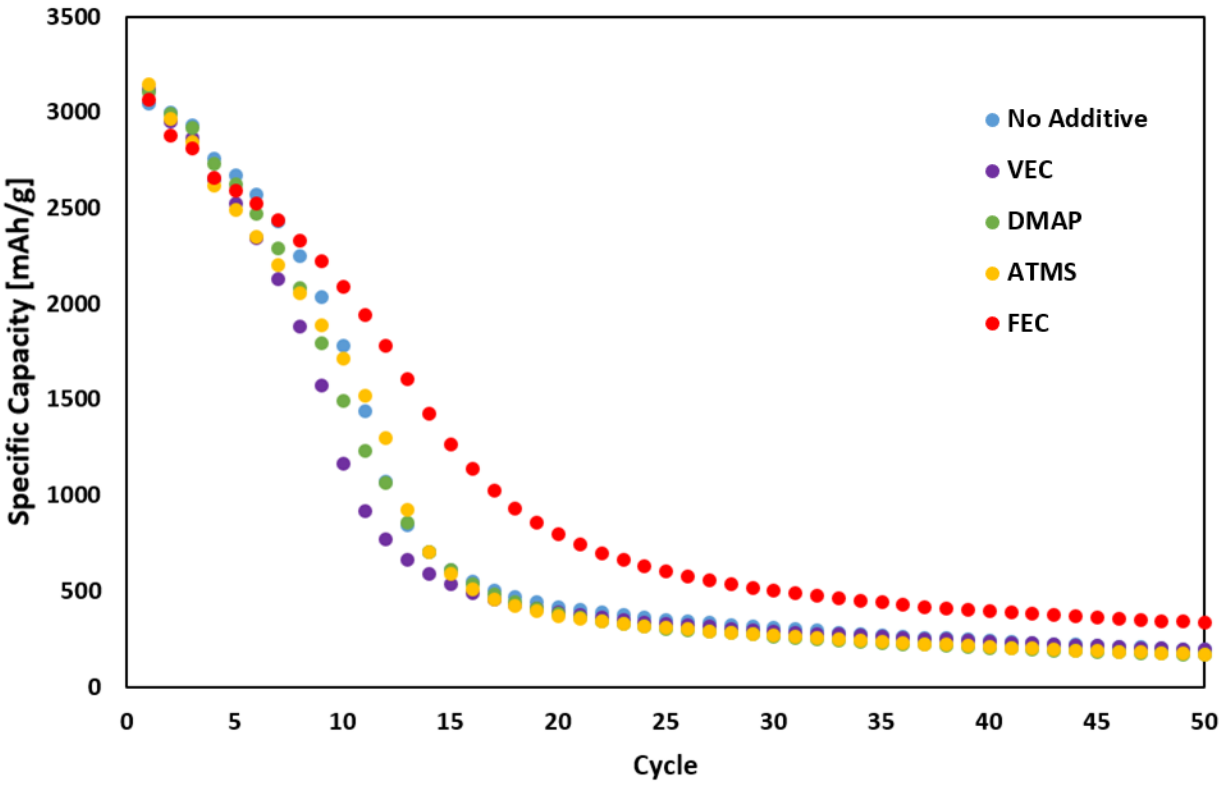

*Figure 4-20. Specific capacity of **Si-325** particles with various additives over 50 cycles.*

In a final effort to find a platform in which in-situ electrografting would lead to a more stable SEI and longer capacity retention, we explore the use of ether solvents to prolong the cycling of SiMPs. Here we aim to build upon an approach initially described by Chen et al. that showed that the use of an ether-based solvent enabled long-lived silicon microparticle electrodes.[250] They find that a solution of 2 M $LiPF_6$ in 1:1 THF:1-methyl THF results in a thin, uniform SEI of inorganic LiF, which allows for high capacity retention (> 80 %) for up to 200 cycles in SiMPs. The working hypothesis for this project is the establishment of a stable solvent/electrolyte system for these larger silicon particles (microparticles), that avoids the use of carbonate electrodes that decompose during cycling. We were able to improve on the cyclability of SiMPs substantially using a mix-THF solvent, as shown in Figure 4-21, but we were unable to reproduce the stability

shown in Chen et al. (2020) and our cells slowly lose capacity over 50 cycles and continue to show catastrophic capacity degradation by cycle 100. Due to our inability to reproduce the effect of a mixed-THF solvent system, further work using electrolyte additives in this ether-based electrolyte was abandoned.

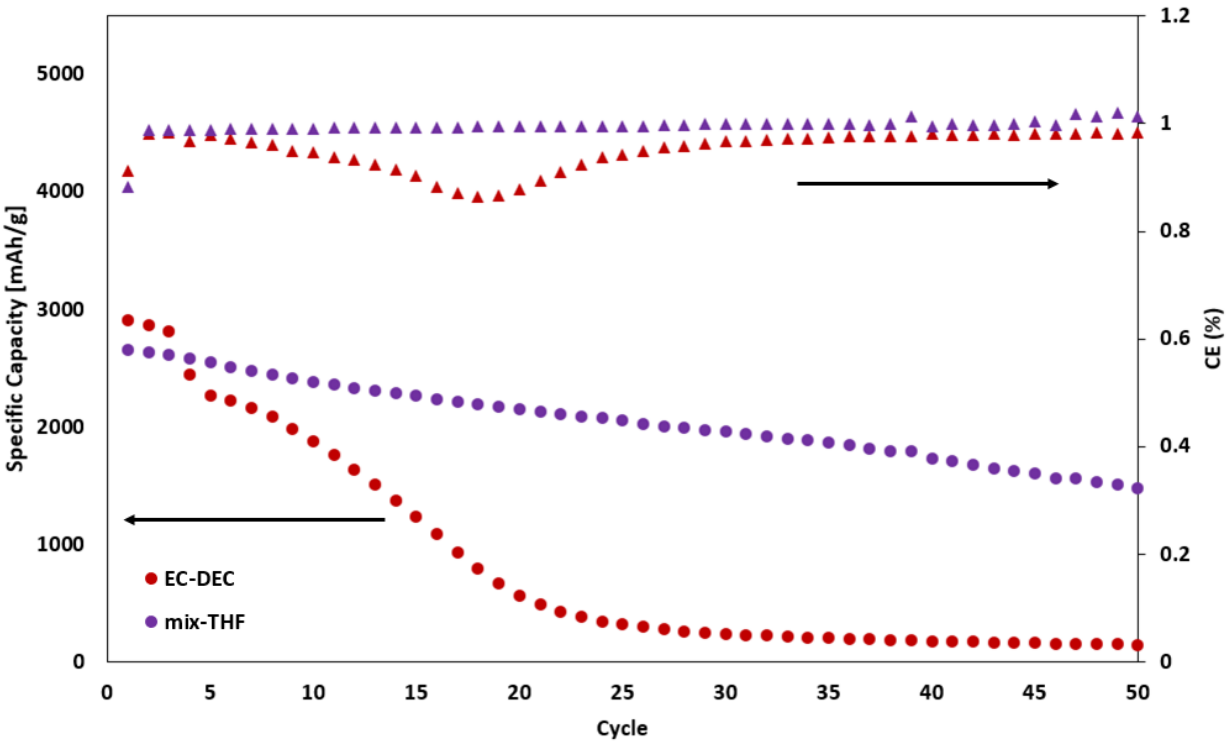

Figure 4-21. ***Si-325*** *particles in mix-THF (purple) and in EC:DEC (red) with* $LiPF_6$.

We believe there is sufficient proof that in-situ electrografting with the molecules we have considered is unlikely to offer improvements on the SEI formed from electrochemical degradation of high performing additives such as FEC. It is possible that covalent bonds are fundamentally less desirable for many aspects of the SEI, because they do not offer the same self-healing properties of a flexible SEI bound through intermolecular forces. Dipole-dipole bonding between a flexible SEI and an expanding and contracting silicon surface may offer stability that our additives were

unable to mimic. In some tests, the addition of alkyne/alkene terminated additives led to worse capacity retention than electrolyte with no additives at all, which we postulate may occur for one of at least two reasons. A minor impact of electrolyte additives is that they dilute the concentration of lithium salt because we did not add more $LiPF_6$ along with the additive. For example, a 10 wt% addition of VEC corresponds to ~0.9 M $LiPF_6$. 1 M $LiPF_6$ is close to ideal for ionic conductivity, and recent studies have pointed towards even higher concentrations of $LiPF_6$ for superior SEI formation,[264,265] therefore a concentration of only 0.9 M is not ideal. Furthermore, lithium diffusion through the SEI typically benefits from an inorganic SEI layer, primarily LiF,[36] which forms close to the silicon surface according to the mosaic model of SEI formation.[55] It is possible that covalent bonding of organic groups to the silicon surface disrupt the natural formation of inorganic SEI microphases. In Chapter 3, we suggest that a covalently bound a-SEI must be optimized for molecular loading so as to achieve the optimal degree of surface coverage with organic molecules. The SEI formed by in-situ electrografting cannot be controlled in this way and leads to inferior capacity retention in many of our silicon nanoparticle cells.

We must also consider the choice of alkenes and alkynes used as additives in this chapter. We were interested in contrasting the effect of polar additives for in-situ electrografting vs non-polar additives but did not find a non-polar additive with suitable solubility in carbonate solvents. Non-polar additives are unlikely to be fruitful for future research, and the study of electrolyte-phobic surfaces require the use of an a-SEI.[99] Future research should focus on novel additives capable of further cross-linking chemistry after being bound to the silicon surface. Using additives capable of in-situ

polymerization could favour mechanical flexibility and ion mobility in the a-SEI. Molecular additives such as dienes and dichalcogenides might also be able to anchor silicon fragments together through in-situ cross linking reactions.

4.5 Conclusions

The incorporation of additives such as FEC into lithium ion battery electrolyte is an established method of improving the stability of silicon anodes through their decomposition products, which form a stable SEI on the silicon surface and protect the surface from further reaction with the solvent and electrolyte. We confirm the beneficial nature of FEC on both silicon thin film and nanoparticle slurry electrodes. We explored olefinic additives based on the SEI components, with the idea that they could protect the surface of silicon through in-situ electrografting to create a robust, covalently bound SEI. We find that covalent bonding between an unsaturated hydrocarbon and hydrogen terminated silicon can occur under reductive conditions by exposing silicon to 1-dodecyne acetonitrile or dichloromethane; however, we do not find a non-polar alkene with suitable solubility in carbonate solvents. When we attempt electrografting of 1-dodecyne in battery solvent of 1 M $LiPF_6$ in 1:1 EC:DEC we mostly observe the reductive decomposition of electrolyte products.

Screening of simple monofunctional olefinic additives did not reveal any improvement of capacity retention for as-sputtered silicon thin films or as-received silicon nanoparticles compared to 1 M $LiPF_6$ electrolyte in 1:1 EC:DEC solvent with no additive. There was some evidence that vinyl ethylene carbonate improved the capacity retention on thin films that were treated with HF to remove the native oxide; however,

the improvement in capacity retention could not be replicated for silicon nanoparticles treated with HF before slurry preparation, and the improvement observed in thin films was still inferior to the protection offered by the established additive FEC. Non-polar additives are entirely unsuitable in carbonate solvents and should have been abandoned earlier, while polar additives may covalently attach to the surface of silicon, but do not provide superior passivation compared to SEI built of insoluble decomposition products. In-situ electrografting does not offer the same control over the degree of surface functionalization as a well optimized a-SEI, while also not offering the same passivating layer as FEC. A thin and robust organic SEI may benefit from flexible intermolecular forces which hold together silicon and slurry binder, and may offer “self-healing” properties which are more advantageous for mitigating the reactivity associated with expanding and contracting silicon.

4.6 Experimental section

4.6.1 Materials and reagents

Ethanol (99 %), 1-dodecyne (98 %), 1-dodecene (95 %), 1H,1H,2H-perfluoro-1-decene (PD, 99 %), 3-diamino-1-propyne (97 %), allyloxytrimethylsilane (reagent), vinyl ethylene carbonate (VEC, 99 %), and fluoroethylene carbonate (FEC, >99 %, anhydrous) were purchased from Sigma-Aldrich. Acetonitrile and dichloromethane were purified by a solvent purification system (Innovative Technology, Inc.) and placed over molecular sieves for 24 hours before use. All other reagents were used as received unless otherwise specified.

Silicon nanoparticles were purchased from Sigma-Aldrich (< 100 nm, TEM) and Alfa Aesar (APS = 100 nm), and silicon powder (325 mesh, < 44 μm) were purchased from Sigma-Aldrich. Polyacrylic acid (PAA, Mv = 450,000), lithium hydroxide (LiOH, reagent grade, 98%), 1 M $LiPF_6$ in 1:1 ethylene carbonate:diethyl carbonate (EC/DEC, 1/1 v/v%, battery grade), tetrahydrofuran (THF, anhydrous, ≥99.9%, inhibitor-free), and 2-methyl tetrahydrofuran (m-THF, anhydrous, ≥99.9%, inhibitor-free), were purchased from Sigma-Aldrich. Lithium hexafluorophosphate salt and vinylene carbonate were purchased from Gotion. Carbon black (Super-P) was purchased from Timcal. Stainless steel discs (MTI) of 0.5 mm thickness and 15.5 mm diameter were used as spacers. Functionalized silicon particles, Lithium polyacrylic acid (LiPAA), and 2,5,8,11-tetraoxatetradec-13-ene (Pr-TEG) were synthesized according to procedures described in Chapter 3.

4.6.2 Ex-situ electrografting

Porous silicon was prepared as described in Section 3.8. Newly etched porous silicon was transported directly to an argon-filled glove box with minimal exposure to air. The porous silicon was placed on a copper current collector with a GaIn eutectic to improve conductivity. The current collector was switched from aluminum initially due to the incompatibility of aluminum with Galinstan. Teflon discs were clamped to either side of the porous silicon with an o-ring to ensure no leakage of solvent during electrografting. PTFE O-rings were sufficient for DCM, but Viton-GFLT O-rings were used for acetonitrile or battery solvents. The upper disc carried battery electrolyte and additives, and funneled to a hole 0.7 cm in diameter. A straight platinum wire was used

as the counter electrode, and adjusted as close as possible to the surface of porous silicon. Parafilm was used to exclude air from the set-up and prevent evaporation. Final experiments were performed on P type, B-doped silicon with a resistivity of 0.677 Ω•cm, as confirmed by a four-point probe. All electrochemistry on this system was performed using a BioLogic SP-200. After electrografting, all wafers were washed with DCM, then pentane, and then dried under an argon stream prior to characterization by FTIR.

4.6.3 Preparation of nanoparticle slurries

Slurries were prepared by combining Si nanoparticles, Super-P and LiPAA in a 60:20:20 ratio and diluting with solvent (~160% mass of dry materials). The solution was mixed in a planetary ball mill (Changsha Tianchuang Powder Technology Co.) at 500 rpm for 60 min total in a teflon vial using zirconia balls (~500% mass of slurry). The slurry was cast onto copper foil (battery grade, 10 μm) at a cast height of 100 μm and dried overnight at 120 °C under vacuum. Discs were punched with a diameter of 15 mm, then dried again at 120 °C under vacuum for 16 hours and brought directly under inert atmosphere. The average mass loading was 0.5-0.6 mg/cm^2.

4.6.4 Electrochemical measurements

1 M $LiPF_6$ in EC/DEC (1/1 v/v%) with 10 wt% additive, when applicable, was used as electrolyte, with 45 μL total used per cell. All cells were assembled under an argon atmosphere using 2032 coin cells with Li metal foil (MTI) counter electrodes and single layer polypropylene-polyethylene-polypropylene separators with a porosity of 39% (Celgard™ 2325). Cycle life testing was performed on an Arbin BT2000 battery

testing system at 25 °C using between the range of 1.5 and 0.005 V. Three formation cycles at 200 mA/g were followed by cycles at 600 mA/g, and all cycles used a constant voltage step during lithiation of 20 mA/g and 60 mA/g, respectively. Potentiostatic Electrochemical Impedance Spectroscopy (EIS) was performed using a Biologic BCS-805 battery testing system, scanning between 10 kHz and 10 mHz. Cells underwent two full formation cycles as well as lithiation at 200 mA/g, then were left to reach open circuit voltage for three hours prior to EIS. These same cells were left to reach a total of 10 cycles for post-cycling SEM.

4.6.5 Characterization

Scanning Electron Microscopy (SEM) was carried out using a Zeiss Sigma Field Emission SEM at accelerating voltages of 5-10 kV. Coin cell dissassembly was performed using a gas driven decrimper (MTI corporation), and all post-mortem anodes were washed with dimethyl carbonate (DMC) in an inert atmosphere prior to analysis. Diffuse Reflectance Infrared Fourier Transform Spectroscopy (DRIFTS) was performed using a Nicolet IS50 spectrometer.

Chapter 5 - Porous tin anodes for LIBs and NIBs

5.1 Introduction

Just as silicon anodes alloy with lithium, other group (IV) elements can accommodate lithium atoms with a specific capacity higher than that of graphite.[266] As can be seen in Figure 5-1, silicon has a far higher specific capacity than other alloying metals, but only a moderately higher volumetric capacity (calculated in the fully lithiated state).[17] The volumetric capacity must also be considered alongside the lithiation voltage for each anode material as it contributes to the overall power that the cell can produce in a full cell configuration. Full stack energy density is the best representation of the performance required for battery commercialization.[267] When full cell voltage and capacity are considered, silicon is one of many elements with a high stack energy density compared to graphite (Figure 5-2). However, due to the confluence of safety, non-toxicity, and elemental abundance, the vast majority of research has until now focused upon silicon and tin.[266,268,269] Silicon is relatively more earth abundant than tin;[270] nevertheless, tin has a similarly high energy density compared to silicon and is more intrinsically conductive.[102] In this chapter, we describe the development of porous tin electrodes for alkali-ion battery anodes, described below, and this chapter aims to explore the use of porous tin as an anode active material. This work was partly funded by the University of Alberta spinoff, Nanode Battery Technologies, and was carried out in collaboration with Drs. Bing Cao, Peter Kalisvaart, and Jiankuan Li. The research described here contributes to their goals of scale-up and commercialization of a ‘drop-in’ tin-based anode for commercial production of full LIB cells.

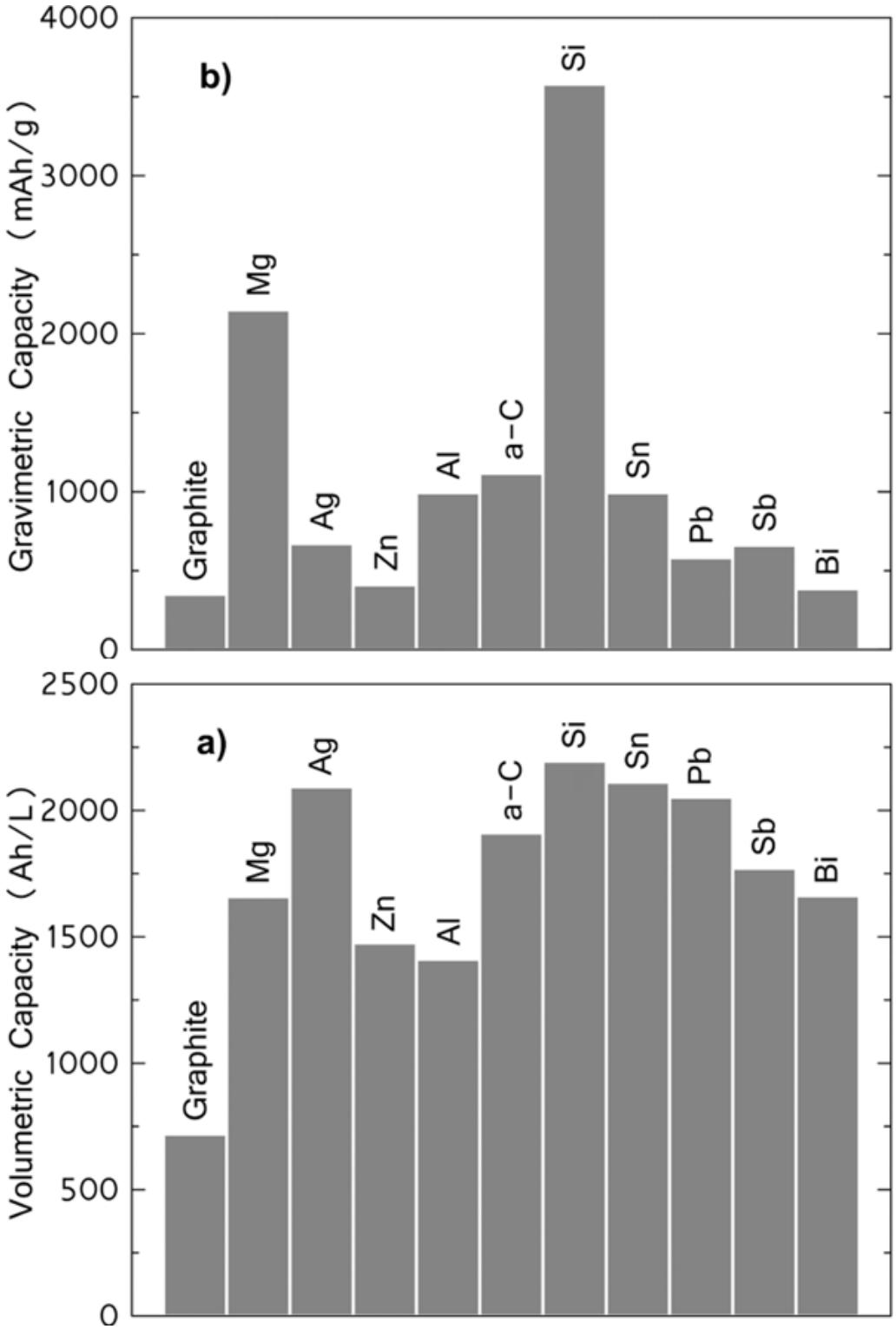

Figure 5-1. Gravimetric and volumetric capacities of common lithium ion battery anodes.

Reprinted with permission from reference 17. © 2014 American Chemical Society.

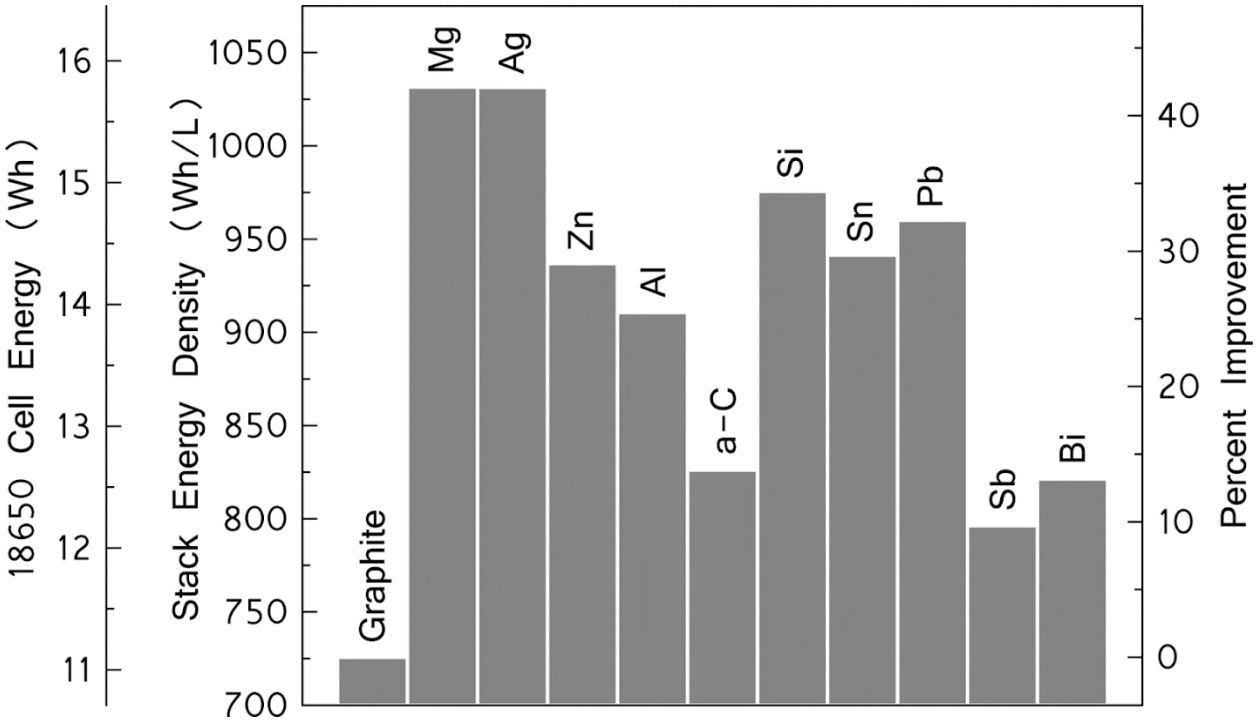

Figure 5-2. Full cell and full stack energy density of common lithium ion battery anodes assuming a $LiCoO_2$ cathode. Reprinted with permission from reference 17*. © 2014 American Chemical Society.*

Like silicon, tin alloys with alkali metals accompanied by a high storage capacity of lithium per unit of mass, but as with silicon, the alloying is accompanied by a large volume expansion (~300 %) during lithiation or sodiation.[103] A crucial metric for commercial applications of lithium ion batteries is a high stack energy density, and the theoretical full cell stack energy density of tin is very competitive with that of silicon (941 Wh/L for tin vs 976 Wh/L for silicon and 726 Wh/L for graphite).[17] An improvement of more than 200 Wh/L would represent a large improvement of anode technology if the challenges associated with the anode expansion can be overcome.

During lithiation, tin progresses through several crystalline phases, and some of the later phases are shown alongside their gravimetric and volumetric capacities relative

to carbon in Figure 5-3.[271] At higher Li:Sn ratios beyond $Li_{2.5}Sn$, the crystalline phases are slow to form, and bulk Li_xSn has only been lithiated to approximately x = 3.4-3.8 (Figure 5-4).[34] Bulk tin fails to reach $Li_{4.4}Sn$ mostly due to low atom mobility;[17] The stress between a fully lithiated outer shell and a less lithiated inner core may contribute to cracking and fracture of tin particles even at sizes as low as 10 nm, although the critical size remains controversial.[105] Many of the approaches hypothesized and tested to relieve this stress have been based upon the use of tin-metal alloys such as Sn-Co, Sn-Cu, and Sn-Ni;[272–274] as well as encapsulation tin within carbon spheres.[104,275] Tin-alloy and tin-carbon anode materials have been reviewed extensively.[9,103,268]

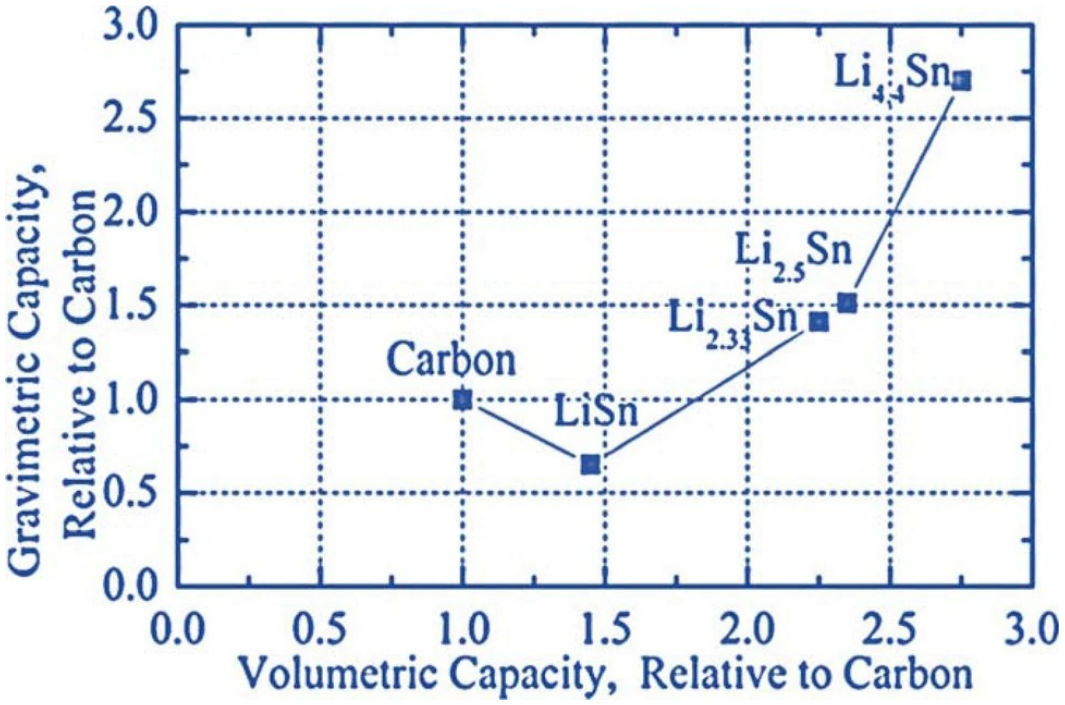

Figure 5-3. Gravimetric capacity of lithium stannide phases relative to carbon. Reprinted with permission from reference 271. © 2021 American Chemical Society.

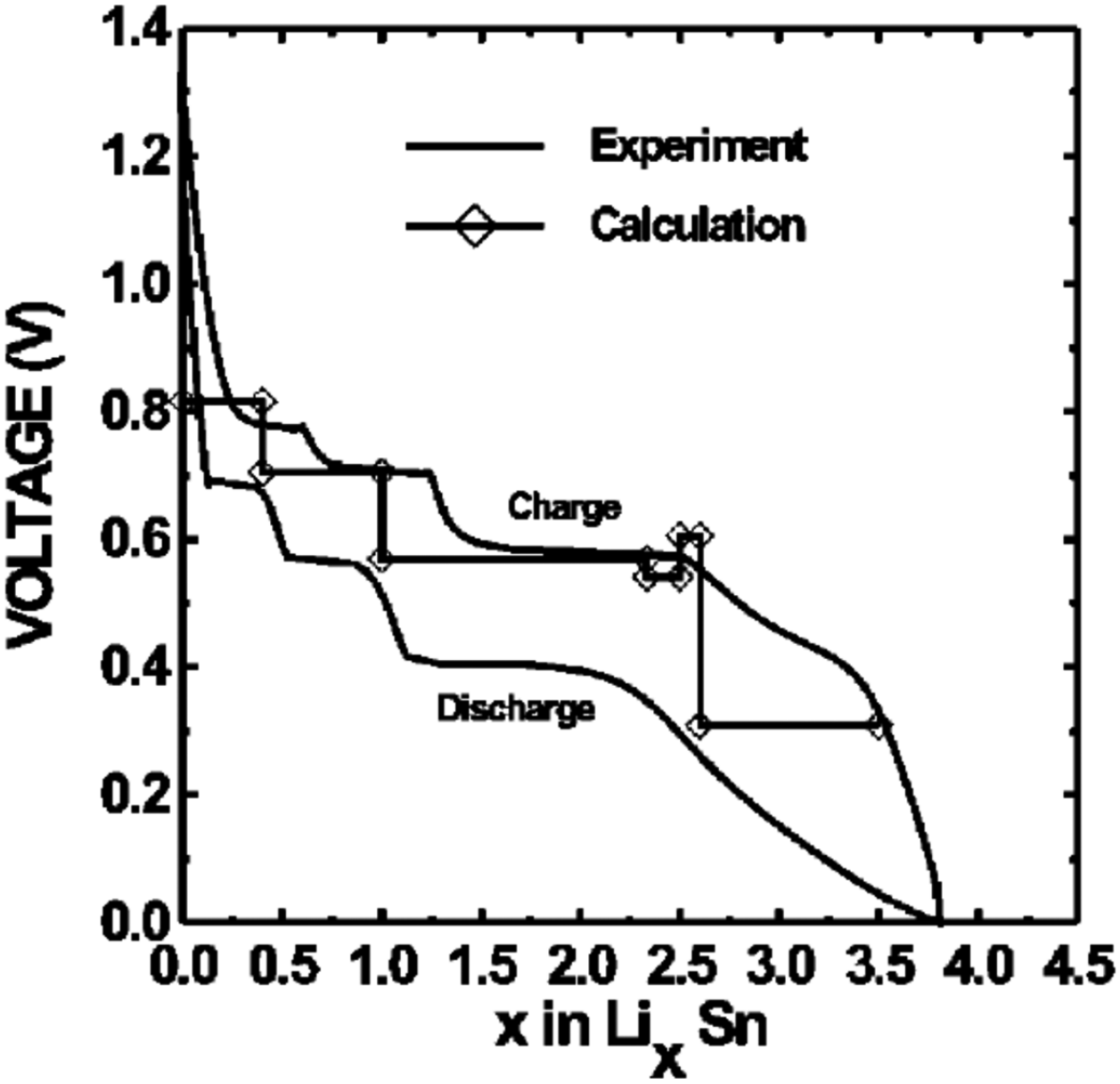

Figure 5-4. Voltage curve of tin lithiation. Plateaus represent transitions to new lithium stannide phases. Reprinted with permission from reference 115. © 1998 The American Physical Society.

Funded by a 5-year Western Economic Diversification grant, our research group developed a new method to produce porous tin, which is now being further studied by Nanode for possible commercialization. The hypothesis tested here is that the porous tin can mitigate capacity loss during cycling due to the large volume expansion of tin upon lithiation and sodiation. The porous tin in question is prepared through the melt spinning of tin ribbons. Melt spinning has already been established as a method of producing tin alloy electrodes for lithium ion and sodium ion batteries, and the process is shown schematically in Figure 5-5.[276] The ribbons of metal used in LIBs and NIBs are formed from molten metal in a crucible that is ejected onto a rotating copper wheel. The melt spinning process is capable of producing alloys which can be used as electrode materials directly[277] or treated to form porous powders of a desired specification.[278–280]

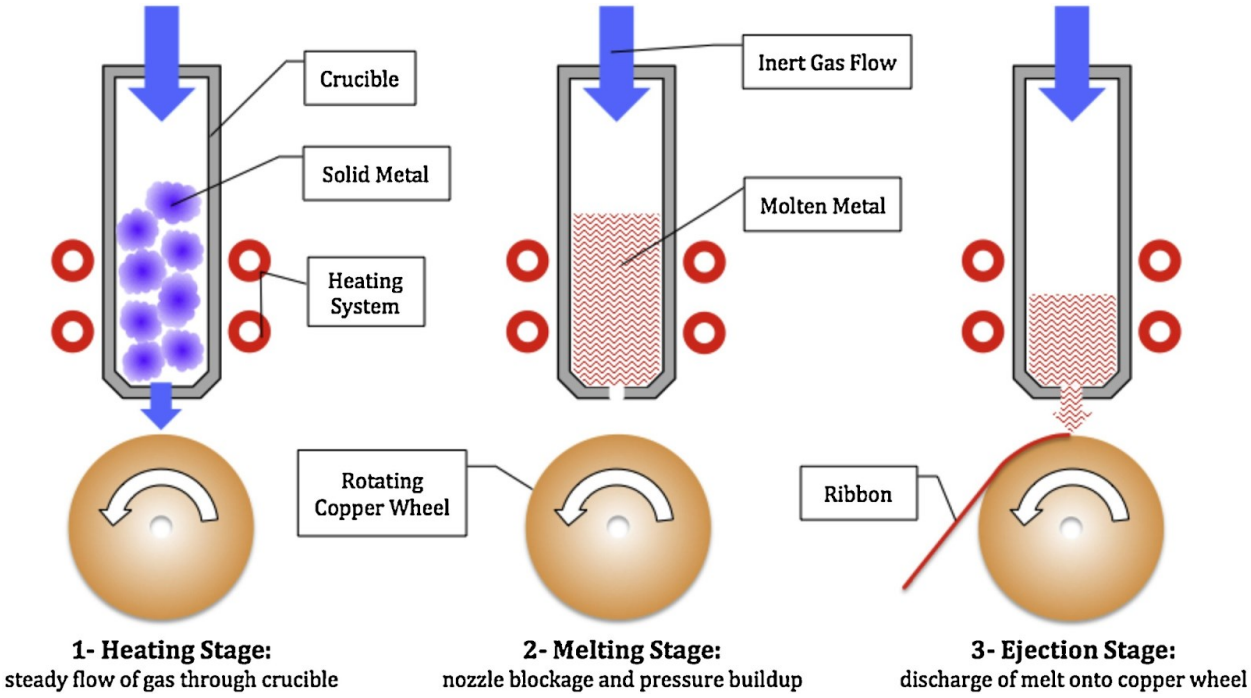

Figure 5-5. Schematic representation of the melt spinning method for metal and alloy ribbon production. Reproduced from reference 276 under a Creative Commons CC-BY license.

Combining small amounts of active material with graphite or hard carbon is viewed as a promising path for the commercialization of silicon.[121] By using a metal-graphite anode, there is far less reliance on non-active material such as binders and conductive additives to maintain the tin (or silicon) within conductive contact of the cell. Graphite is not suitable for NIBs due to poor chemical bonding between the Na and C atoms during intercalation, as described in Chapter 1.[125] Instead, a variety of non-graphitizable carbons, commonly called “hard carbon”, have been successfully applied towards sodium ion batteries. The technical definition of hard carbons encompass carbonaceous materials that do not transition into graphite even above 3000 °C, and instead feature highly disordered graphene sheets.[127,281] Accordingly, we will use tin-graphite mixtures for anodes in lithium ion cells, and tin-hard carbon mixtures for anodes in sodium ion cells.

5.2 Porous tin with graphite

Prior work in our group, now being carried out at Nanode, showed that porous tin can be prepared by melt spinning Sn:Al 1:1 w/w % ribbons, followed by etching in 1 M KOH (aq) at room temperature until no hydrogen bubbles are observed, which removes the aluminum and results in a dark grey powder (Figure 5-6). The resulting material is porous tin with an average pore size below 36 nm and a surface area 2.35 m^2g^{-1} as measured by the Brunauer-Emmett-Teller (BET) method. The morphology of our p-Sn powder can be seen from Scanning electron microscopy (Figure 5-7) and is contrasted to commercial tin powder sold < 150 μm.

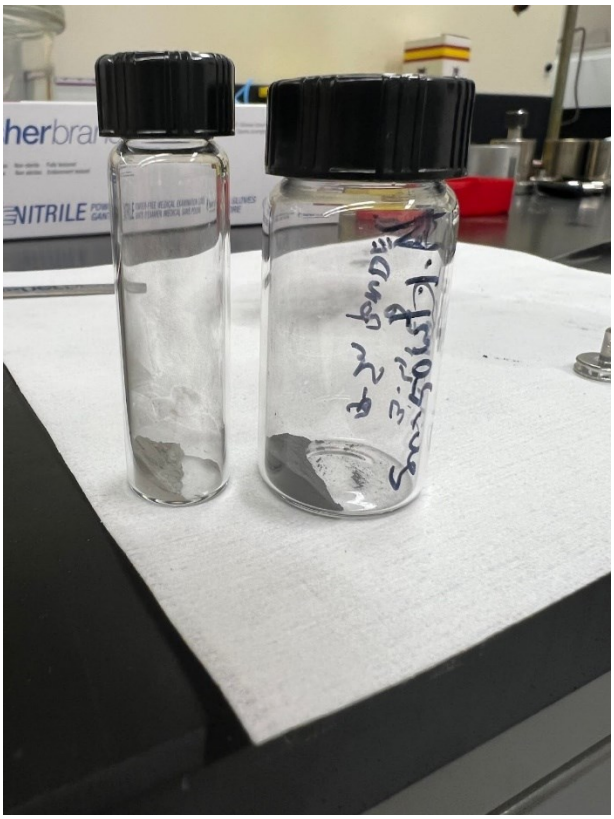

Figure 5-6. Photo of commercial < 150 µm Sn powder (left) and synthesized p-Sn powder (right).

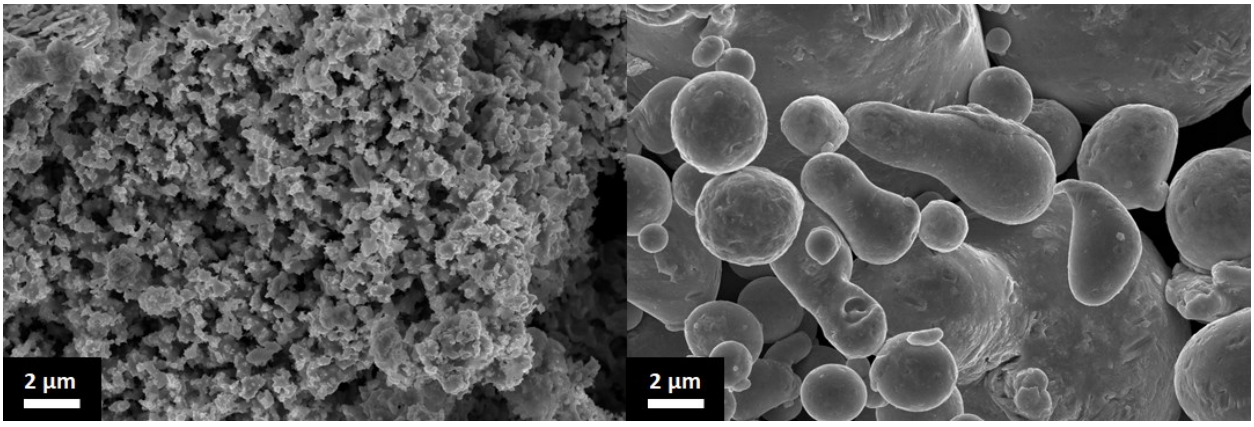

Figure 5-7. SEM of synthesized p-Sn from meltspun SnAl ribbons (left) and commercial <150 µm tin powder (right).

The porous tin materials produced via melt spinning were mixed with graphite in the case of LIBs, and hard carbon for NIBs. Smaller percentages of tin are also expected to lead to less electrode swelling on the macroscale, which is important for maintaining electrode structure and avoiding pressure on the cell casing.[121] Graphite has been explored for use with tin, and early studies with 325 mesh (<44 μm) tin[120,282] confirmed that tin could increase the specific capacity, but never exceeded 20 cycles. Later studies of nanosized tin and tin derivatives with graphite[283–285] enabled stable cycling for up to 40 cycles with pure tin, and 100 cycles with tin alloys. The starting point for the work described here uses small amounts of porous tin with graphite or hard carbon as a means of increasing anode capacity while minimizing the failure mechanisms associated with expansion in pure tin sufficiently to maintain 80 % capacity retention over 100 cycles. A common failure mechanism for tin in lithium ion batteries involves pulverization of the tin particles caused by tensile stress between a fully lithiated tin surface and a partially lithiated tin core.[286] The tensile stress leads to cracks and pores upon delithiation. Graphite will help to maintain conductive contact with the pulverized tin, and also lower the total swelling of the composite electrode.

A secondary goal of this research involves comparing the results obtained using porous tin to those using commercially available tin microparticles. Through this comparison, we explore the potential for porous tin with active carbon material to stabilize the cycle life of tin. Finally, we investigate the cycling chemistry of porous tin using impedance spectroscopy and post-cycling analysis.

As described above, mixing tin with graphite should allow for an increase in the specific capacity of an anode without confronting the issues of expansion that arise with majority tin anodes.[121] The first step is to establish an acceptable baseline for electrodes comprising 100% graphite. Unlike tin anodes, graphite only expands ~10% during lithiation[17] and is intrinsically conductive. Previous work has demonstrated that slurries can be prepared with a high ratio of 95% active material, 4 % binder, and 1% carbon additive,[170] and many similar ratios.[121] The initial results for 100 % graphite anodes were well below the theoretical specific capacity of 357 mAh/g, with an initial value of only 208 mAh/g (Figure 5-8), and attaining an initial capacity at, or in excess of 360 mAh/g is common in the literature.[287] A low initial capacity may be acceptable because the primary goal of this research is to establish the relative benefits of adding porous tin from melt-spun ribbons while achieving stability over 100 cycles, and the absolute capacity of each slurry is of secondary importance.

Cycling rates for tin-carbon mixed electrodes were not described in mA/g, due to the varying theoretical capacities present with varying levels of tin. The C-rate of a battery is a convenient way to describe charging and discharging rates across different cells, whereby 1C is defined as the rate required to fully discharge in one hour. In contrast, 2C is double the current, or a rate required to discharge in 30 minutes, while C/2 is half the current, and would complete a discharge in two hours. The initial tests on tin-graphite cells were optimized for high-throughput to determine what percentage of tin was compatible with cycling stability over 100 cycles. To this end, tin-graphite anodes were run at a rate of C/2 with no CV steps and no formation cycles, despite knowing that cells would obtain a higher initial capacity if lower rates were used for the first

cycles. As will be shown, rate tests confirmed that 100% graphite can reach a high initial capacity of ~340 mAh/g at low currents.

We cycled slurries containing graphite and porous tin (Gr:Sn) in ratios of 100:0, 95:5, 90:10, 80:20, and 70:30 for 100 cycles, and present the delithiation capacities (Figure 5-8) and Coulombic efficiencies (Figure 5-9). Our goal is to determine what percentage of tin is compatible with stable cycling (>80 % capacity retention) over 100 cycles, and to quantify the specific capacity gained with higher amounts of tin. We observe a clear trend when adding larger percentages of porous tin to the slurry mixture. Higher tin content is associated with greater initial capacity, but is inversely correlated to capacity retention over 100 cycles. 95:5 Gr:Sn achieves an initial capacity of only 310 mAh/g, (Figure 5-8) but retains 95% capacity over 100 cycles (Figure 5-8). This capacity retention is slightly below that of 90:10 Gr:Sn anodes, which maintain 98% capacity after 100 cycles. Conversely, 70:30 Gr:Sn anodes achieve a higher initial capacity of 350 mAh/g, but fade to 70% capacity retention after 100 cycles. 90:10 Gr:Sn cells reverse this trend slightly by having a lower initial capacity than 95:5 cells (300 mAh/g vs 310 mAh/g), but we do not have the number of cells required to determine if this is statistically significant.

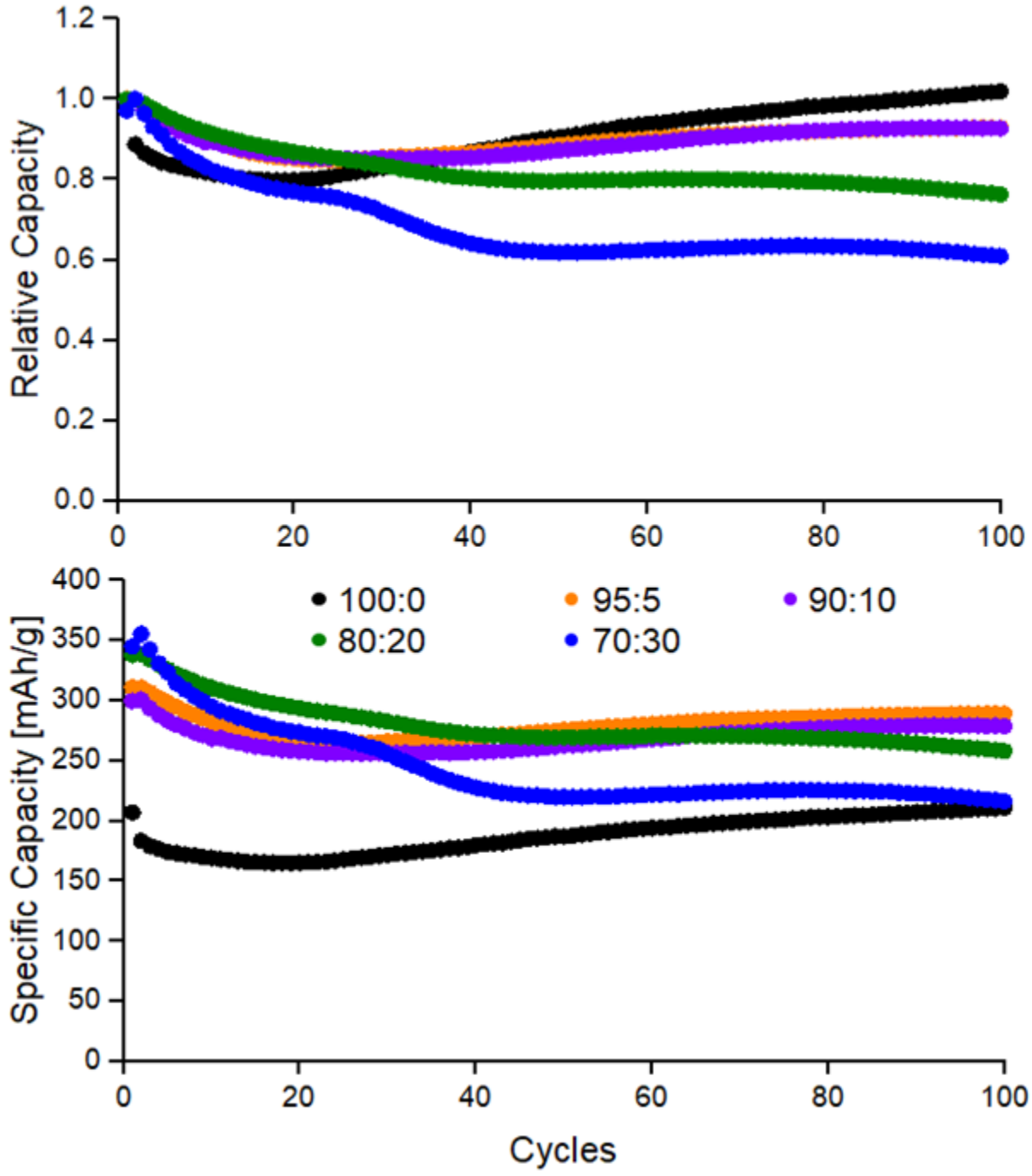

Figure 5-8. *Relative delithiation capacity (top) and specific delithiation capacity (bottom) of graphite and tin at ratios of 100:0, 95:5, 90:10, 80:20, and 70:30. All cells were cycled 100 times at a rate of C/2 based on the combined theoretical capacity of graphite and tin present.*

We see further trends of the effect of varying tin content by examining the early cycles of Coulombic efficiency. Higher tin content leads to lower initial Coulombic efficiency (ICE) and continued lower Coulombic efficiency for all 100 cycles, presumably due to unwanted reactions on the surface of tin during the large expansion. 95:5 Gr:Sn has the highest ICE of all cells, matching its anomalously high initial capacity in Figure 5-8, which was larger than the initial capacity of 90:10 Gr:Sn. These results do suggest, however, that small amounts of tin might be added to graphite to increase the capacity with minimal losses to efficiency in early cycles. Nevertheless, further optimization is required.

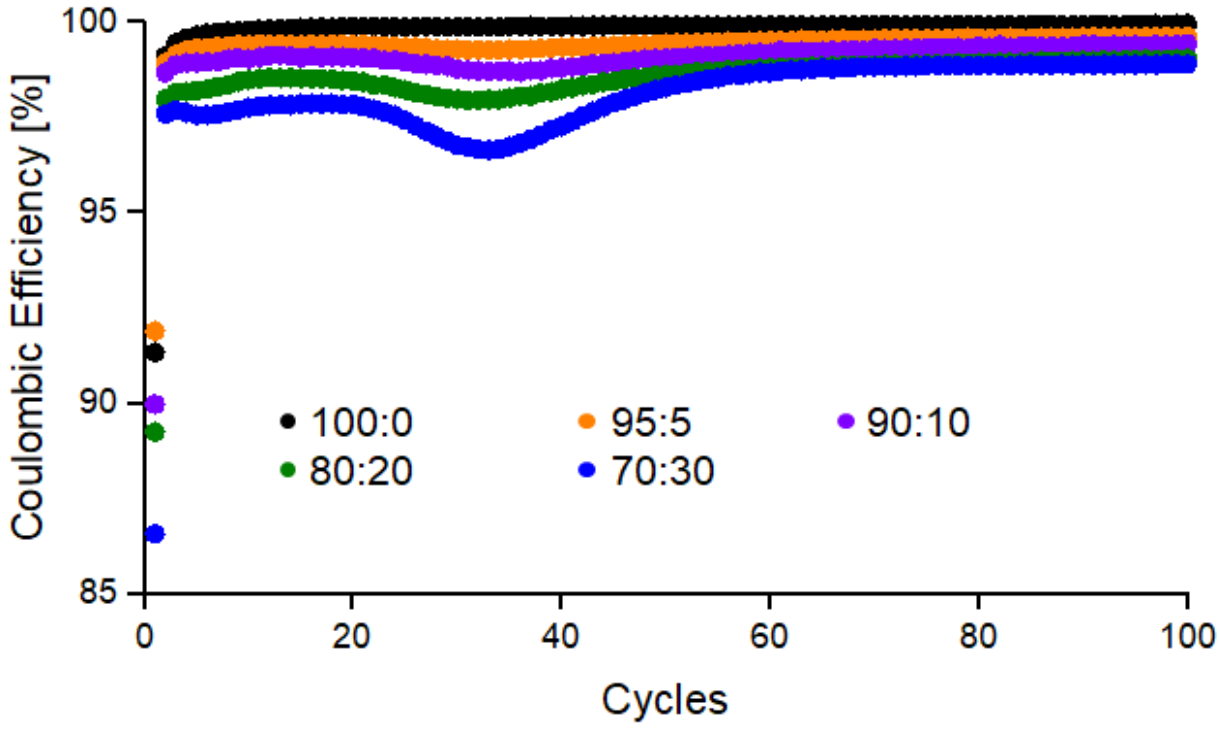

Figure 5-9. Specific delithiation capacity of graphite and tin at ratios of 100:0, 95:5, 90:10, 80:20, and 70:30. All cells were cycled 100 times at a rate of C/2 based on the combined theoretical capacity of graphite and tin present.

We then added 10 % w/w commercial tin powder (<150 um, Sigma-Aldrich) to graphite slurries to compare the effects of commercial tin powder vs the porous tin from melt spinning. As shown in Figure 5-10, absolute capacity begins lower for 10 % commercial tin (C – 90:10) than for 10 % porous tin (90:10) in graphite slurries. The capacity fades before rising again to above its original capacity maximum. Coulombic efficiency is also much lower for commercial tin than for porous tin (81 % vs 90 %). These results are both obtained using cycling without lower rate formation steps, and we hypothesize that larger particle sizes pose a challenge for high capacity at high cycling rates. For commercial tin only, we perform 3 formation cycles before testing the lithium ion battery (C – 90:10 FC) and observe much higher initial capacity at rates of C/10 and C/20, which falls to ~66 % capacity in a single cycle as the current is increased to C/2. Capacity falls to ~50 % in the commercial tin anodes before returning slowly after cycle 30. We hypothesize that this is due to smaller particles being formed by pulverization, which lithium is again able to penetrate at the higher C/2 rate. Nevertheless, the capacity after 100 cycles remains lower using commercial tin particles whether formation steps are included or not. Further experiments on the effects of cycle rate will be described later in this chapter.

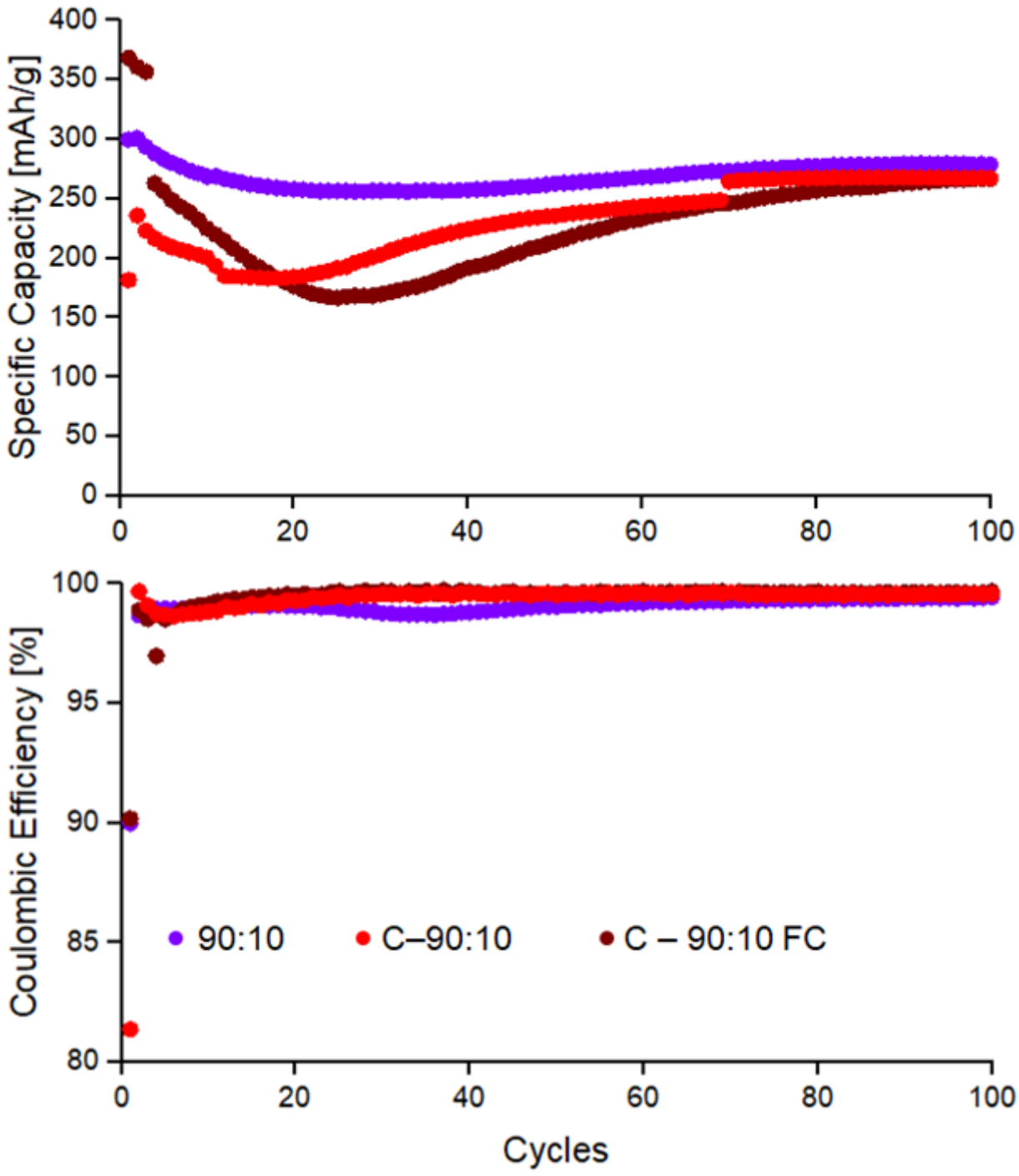

Figure 5-10. Specific capacity (top) and Coulombic efficiency (bottom) for porous tin and commercial (<150 um) tin, both in graphite:tin ratios of 90:10. Commercial tin cycles are included with (C-90:10 FC) and without (C-90:10) formation cycles.

Formation of the SEI on the surface of the porous tin should increase the resistance associated with the solid electrolyte interphase, and therefore should be apparent through electrochemical impedance spectroscopy (EIS). For these tests, cells were first subjected to formation cycles at C/20 and C/10, before testing for impedance of a lithiated cell (Figure 5-11). R_s - which occurs at the highest frequencies given by the x-intercept at the beginning of the Nyquist plot, was high for all cells tested. Nevertheless, significant differences were noted between the various cell recipes. An EIS plot contains three basic elements: (i) the smallest semicircle in each plot occurs at high frequencies, and represents the resistance provided by the SEI (R_{SEI}); (ii) the larger semicircle corresponds to charge transfer resistance (R_{CT}); and (iii) the trailing line represents the Warburg element (Z_w), as outlined in the model circuit of Figure 5-11. The values for R_s, R_{SEI}, and R_{CT} are listed in Table 5-1.

As can be seen from the data in Figure 5-11 and Table 5-1, no obvious linear trends can be observed for R_{SEI} or R_{CT}. As mentioned previously, the R_S is high for all ratios of porous and commercial tin, but is especially high for 100 % graphite anodes, which causes the black plot of 100:0 Gr:Sn to appear distinct from the other results. For 100:0 Gr:Sn only, we performed a replication to achieve some small statistical power and we confirm that the R_S is much higher than for other slurries (Table 5-1). Since there was only one test run on cells containing porous or commercial tin, reproducibility may be an issue. Given that higher percentages of porous tin were associated with lower Coulombic efficiencies, we hypothesized that some of the irreversible capacity

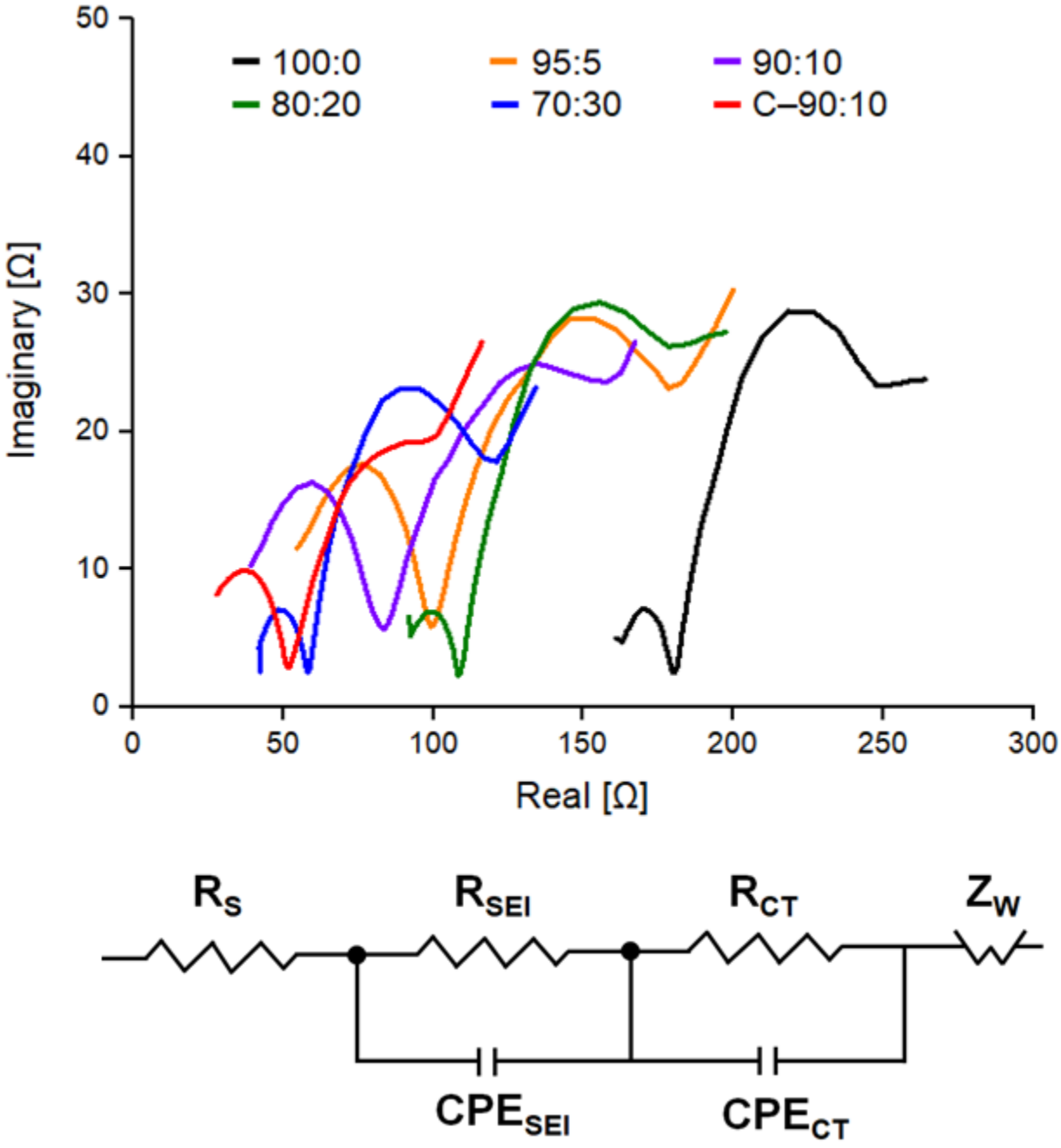

Figure 5-11. *Electrochemical impedance spectroscopy (EIS) of graphite:tin anode mixtures from 100:0, 95:5, 90:10, 80:20, and 70:30 in a lithium ion battery half cell. Commercial < 150 μm Sn particles are shown as C-90:10. Cells underwent two formation cycles before EIS was conducted in a fully lithiated state.*

loss represented by the low Coulombic efficiency would manifest in a thicker SEI and therefore a higher R_{SEI}. 95:5 and 90:10 Gr:Sn cells do show higher R_{SEI} than pure graphite cells, but this observation disappears at higher concentrations of porous tin.

Given the scattered nature of the EIS results on porous tin, and potential problems with reproducibility, it is unwise to search for significant meaning in the comparisons to commercial <150 μm tin electrodes (Figure 5-11, red line). Nevertheless, we note that the C-90:10 anodes not only had a lower R_S and R_{CT} than the 90:10 porous tin homologue, but also a lower R_S and R_{CT} than all of the porous tin and 100 % graphite samples.

Table 5-1 R_S, R_{SEI}, and R_{CT} for LIB cells with graphite and tin in ratios varying from 100:0 to 70:30. The data for commercial < 150 μm tin, C-90:10 is also included.

Cell	**R_S**	**R_{SEI}**	**R_{CT}**
100:0	158 (5)	26 (4)	87 (3)
95:5	44	61	119
90:10	27	61	118
80:20	88	23	100
70:30	39	21	77
C-90:10	19	36	75

The expansion of tin due to lithiation can be observed using cross-sectional X-ray microscopy (XRM), which allows us to examine the thickness of fully lithiated samples without exposure to ambient atmosphere. Figure 5-12 shows an electrode containing 80 % graphite and 20 % tin. In the unlithiated sample, the slurry is composed of distinct particle clusters stacked on top of the copper sheet. The variability of the slurry composition makes it difficult to obtain a single thickness measurement for the sheet, but it appears that the slurry shrinks during drying from a casting height of 100 μm to a thickness on the order of 30 μm. Upon lithiation, the slurry seems to expand slightly, but all regions remain at or below 40 μm thick. Modelling by Otero et al. suggests that expansion in tin-graphite electrodes can be represented with either small volume expansion and a concomitant reduction in porosity, or considered with constant porosity and a large increase in volume (Figure 5-13).[119] Considering a scenario in which porosity and lithiation are both kept constant, we would expect a 60 % growth in active material from tin alloying alone, based on 300 % expansion in the 20 % porous tin material. We suggest that there is both a reduction in pore size, as well as unrelated micron sized void space visible from the XRM image of the unlithiated sample (Figure 5-12) Therefore electrode expansion in 80:20 Gr:Sn slurries results in only ~20 % expansion based on the median measurements.

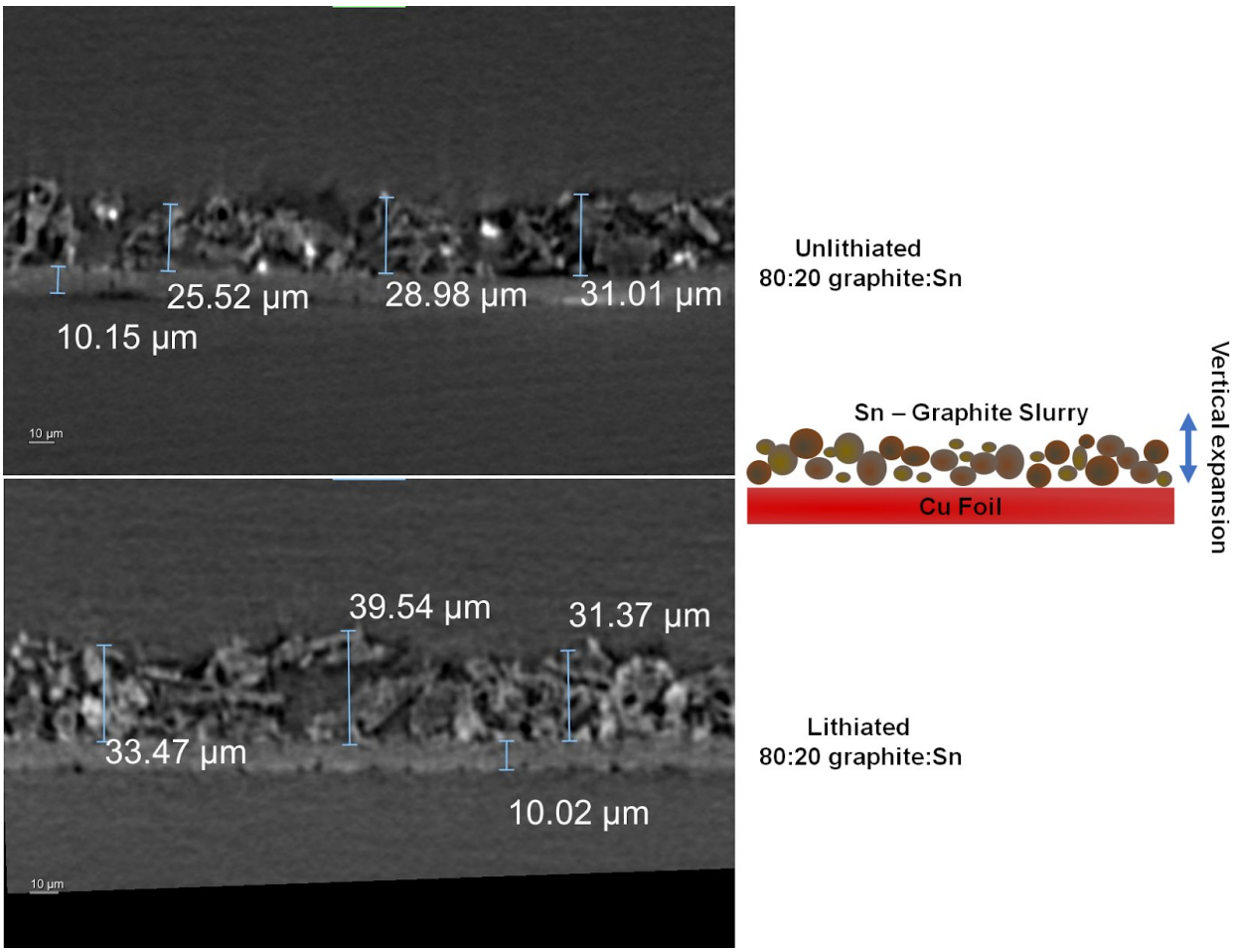

Figure 5-12. X-ray microscopy (XRM) of unlithiated 80:20 graphite:tin (top) and fully lithiated 80:20 graphite:tin (bottom).

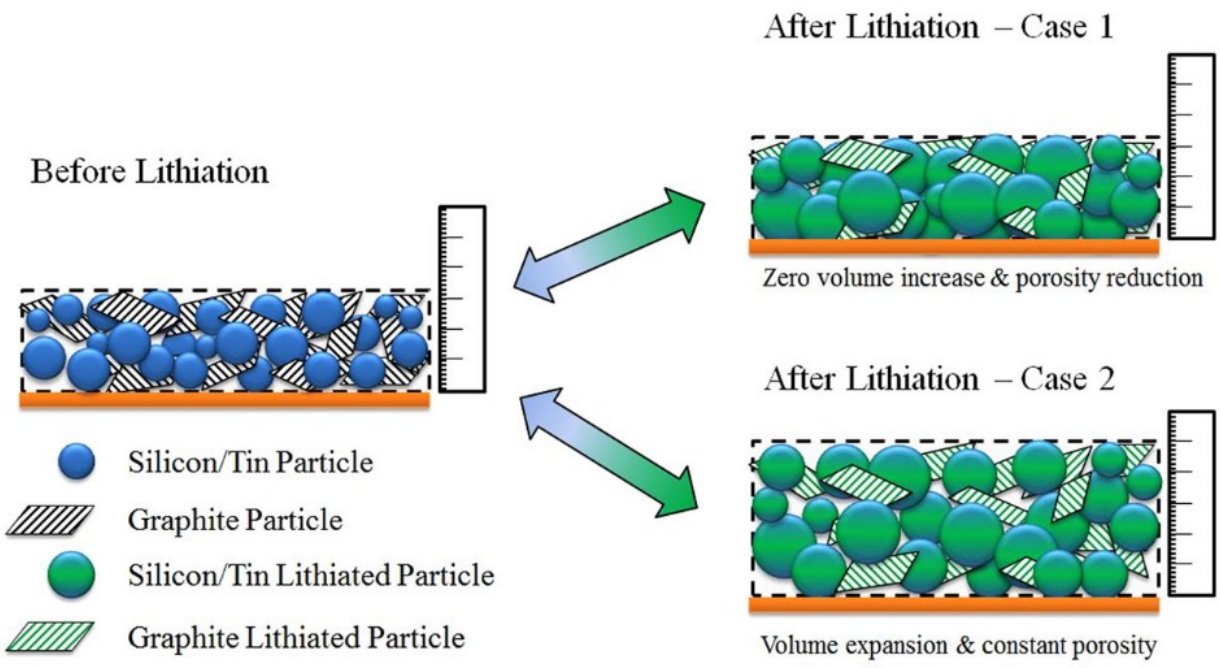

Figure 5-13. Forms of expansion in mixed graphite:tin electrodes. Reproduced from reference 119 under a Creative Commons CC-BY license.

5.3 Porous tin with hard carbon

Graphite does not lead to high capacity in sodium ion batteries as sodium does not intercalate well between the sheets of graphene, despite the fact that both lithium and potassium ion batteries work well. There are many reasons for the low capacity which still represent an active area of research, but in general the problems relate to poor orbital overlap between sodium and tightly packed graphene layers, which lead to a positive enthalpy of formation. Sodium intercalation has both poor covalent interactions (c.f. lithium) and poor ionic interactions (c.f. potassium).[125,288] Hard carbon has been used successfully with sodium instead to some success, with a theoretical capacity ranging between 350 to 400 mAh/g, depending on the source and structure of

the hard carbon.[127] As with graphite, adding small amounts of alloying metals such as tin is viewed as a promising way to increase the capacity of hard carbon for sodium while avoiding the catastrophic capacity loss associated with tin expansion upon sodiation.

With sodium ion batteries, we began with 3 formation cycles at lower rates - C/20 for cycle 1 and C/10 for cycles 2 and 3, which include a constant voltage (CV) step afterwards. Formation cycles are important for establishing a stable SEI on the surface of tin, and by including them in sodium ion battery half cells, an increase in the absolute specific capacity might be observed with longer cycling. The initial capacity of 100% hard carbon was determined to be 295 mAh/g in sodium ion battery half cells. The capacity dropped from 288 mAh/g to 278 mAh/g between cycles 3 and 4, displaying the effect of increasing the rate from C/10 to C/2 and removing the CV step. However, the capacity remained at 270 mAh/g by cycle 100, displaying a 91 % capacity retention at cycle 100.

A recognizable pattern was observed when incorporating 5, 10 and 20 % porous tin into hard carbon (Figure 5-14). Greater proportions of tin were associated with a higher initial capacity, while also being accompanied by lower capacity retention over 100 cycles. 20 % tin was associated with an initial capacity of 351 mAh/g, but a final capacity of 259 mAh/g, representing 74% capacity retention over 100 cycles. Increasing to 30 % tin failed to produce stable cycling over more than 20 cycles, and is not included here.

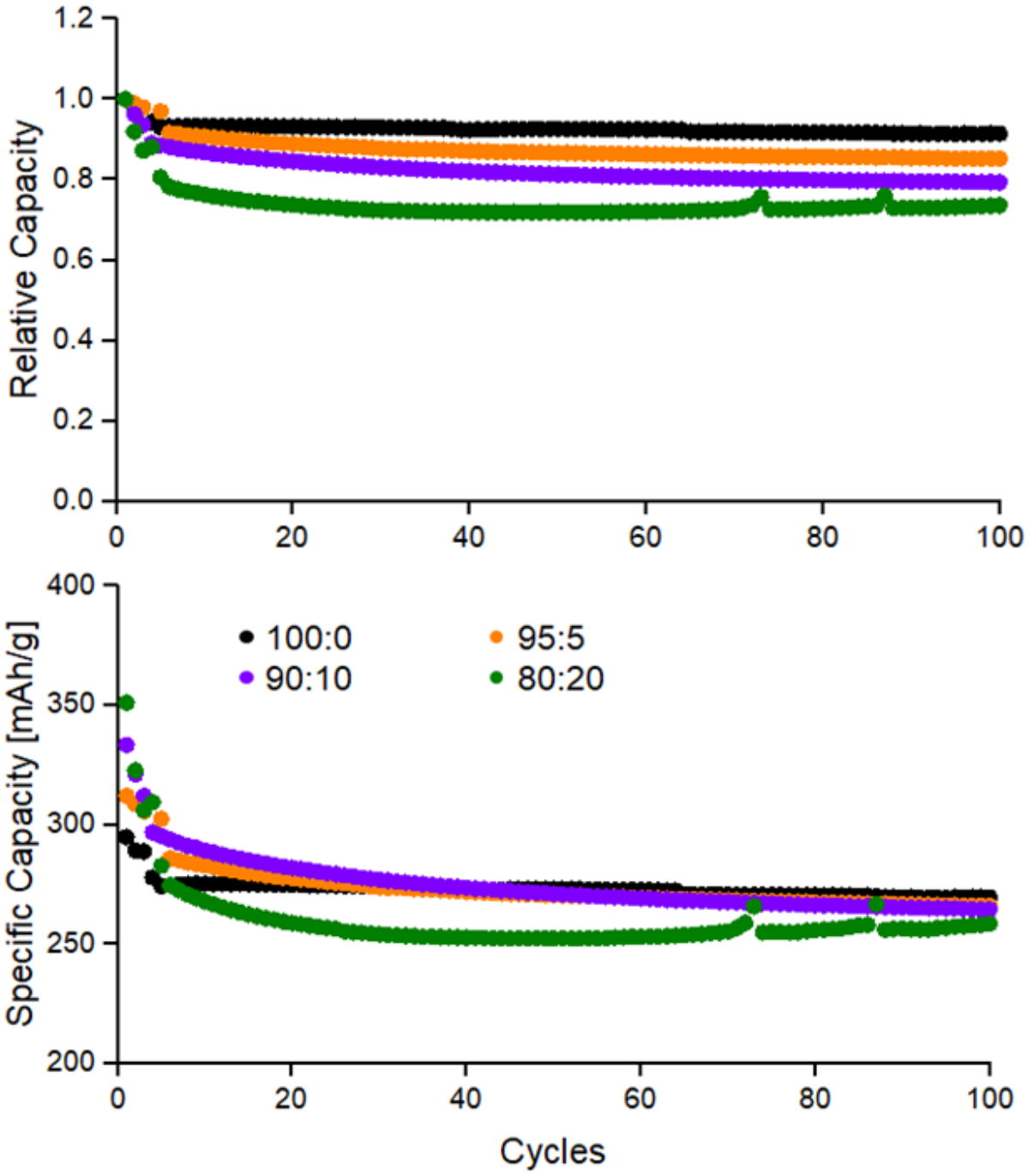

Figure 5-14. *Relative delithiation capacity (top) and specific delithiation capacity (bottom) of hard carbon and tin at ratios of 100:0, 95:5, 90:10, 80:20, and 70:30 in sodium ion batteries. All cells were cycled 100 times at a rate of C/2 based on the combined theoretical capacity of graphite and tin present.*

The ICE of each cell also follows a predictable pattern, as the efficiency of the first cycle becomes lower with an increasing quantity of porous tin (Figure 5-15). We hypothesize that this relationship is due to the irreversible reaction of electrolyte with the exposed surface of tin upon expansion. The Coulombic efficiency does arrive at much higher values for all sodium ion battery half cells investigated here, as compared with their lithium ion battery homologues. This difference may explain part of the high capacity retention that we observed in cells with no more than 10 % tin. Sodium ion batteries used $NaPF_6$ in diethylene glycol dimethyl ether (DME) as the electrolyte, which is known to be more stable under reductive conditions than EC:DEC.[289]

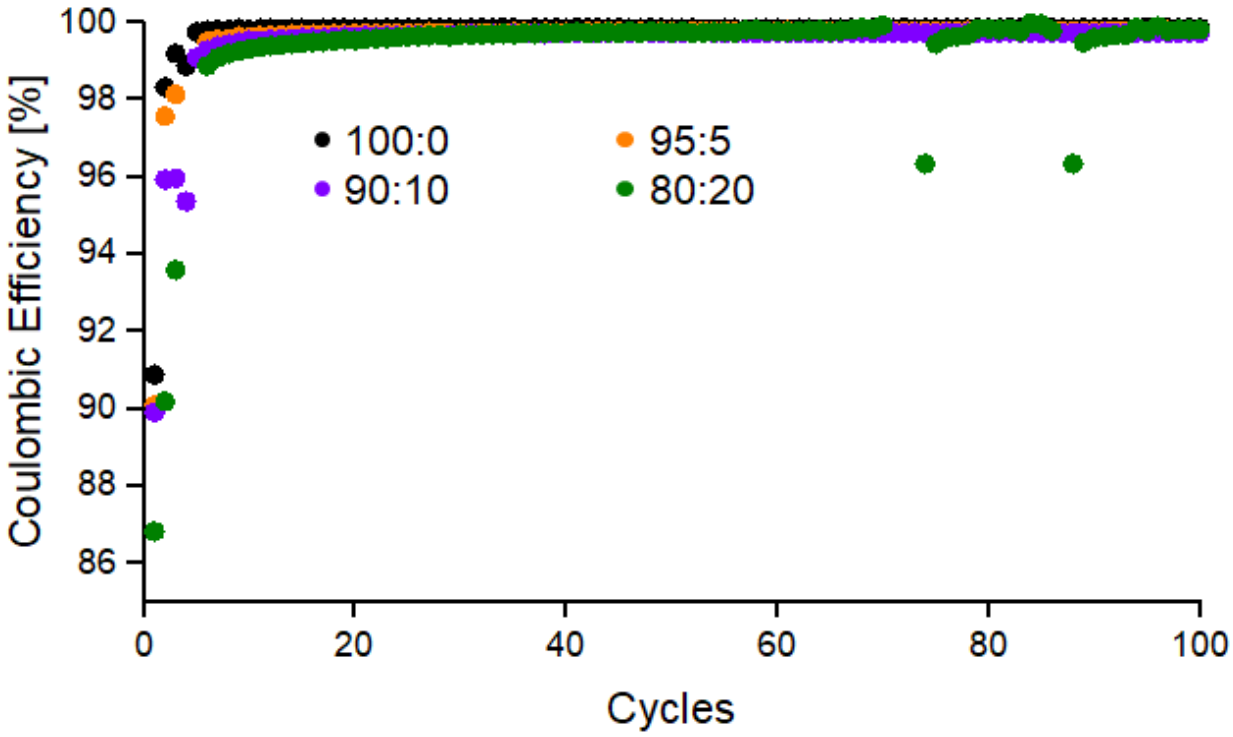

Figure 5-15. Coulombic efficiency in hard carbon:tin mixed electrodes for NIBs at various ratios of active material.

For sodium ion batteries, a similar trend was seen with commercial tin particles, although in this case all cells were cycled with 3 formation cycles at the beginning (Figure 5-16). The inclusion of formation cycles was sufficient to bring commercial tin capacity level with the capacity reached by 10 % porous tin. However, the capacity of electrodes containing 10 % porous tin decreased immediately after the cycling rate was increased to C/2, from 311 mAh/g to only 219 mAh/g. The capacity of commercial tin electrodes eventually mirrored that of 10 % porous tin electrodes, but it involved jumps in capacity, presumably rising as tin became permeable by sodium at high rates due to pulverization, or falling as pulverized tin lost conductive contact with the cell.

We also attempted to analyze NIBs using EIS to determine the contribution of SEI impedance to the cell at each concentration of porous tin. EIS has been used for this purpose before,[290,291] but was unsuccessful in every case, and led to both a nonsensical Nyquist plot during the impedance measurement, as well as the catastrophic capacity loss for multiple cycles after the measurement. The cause of such poor impedance measurements is unknown, and surprising for a non-destructive characterization technique, but it held true for all tin concentrations and often for replicated experiments. Possible contributing factors include unstable conditions in DEC solvent at lower frequencies, or even unwanted reactions of sodium during the three hour low voltage OCV step that proceeds EIS measurements. However, we emphasize that such factors would be unlikely and a more fulsome explanation was not pursued. Ideally, an exploration of the effects of EIS on our NIB cells would have included multiple measurements within different frequency ranges, and at different states of charge.

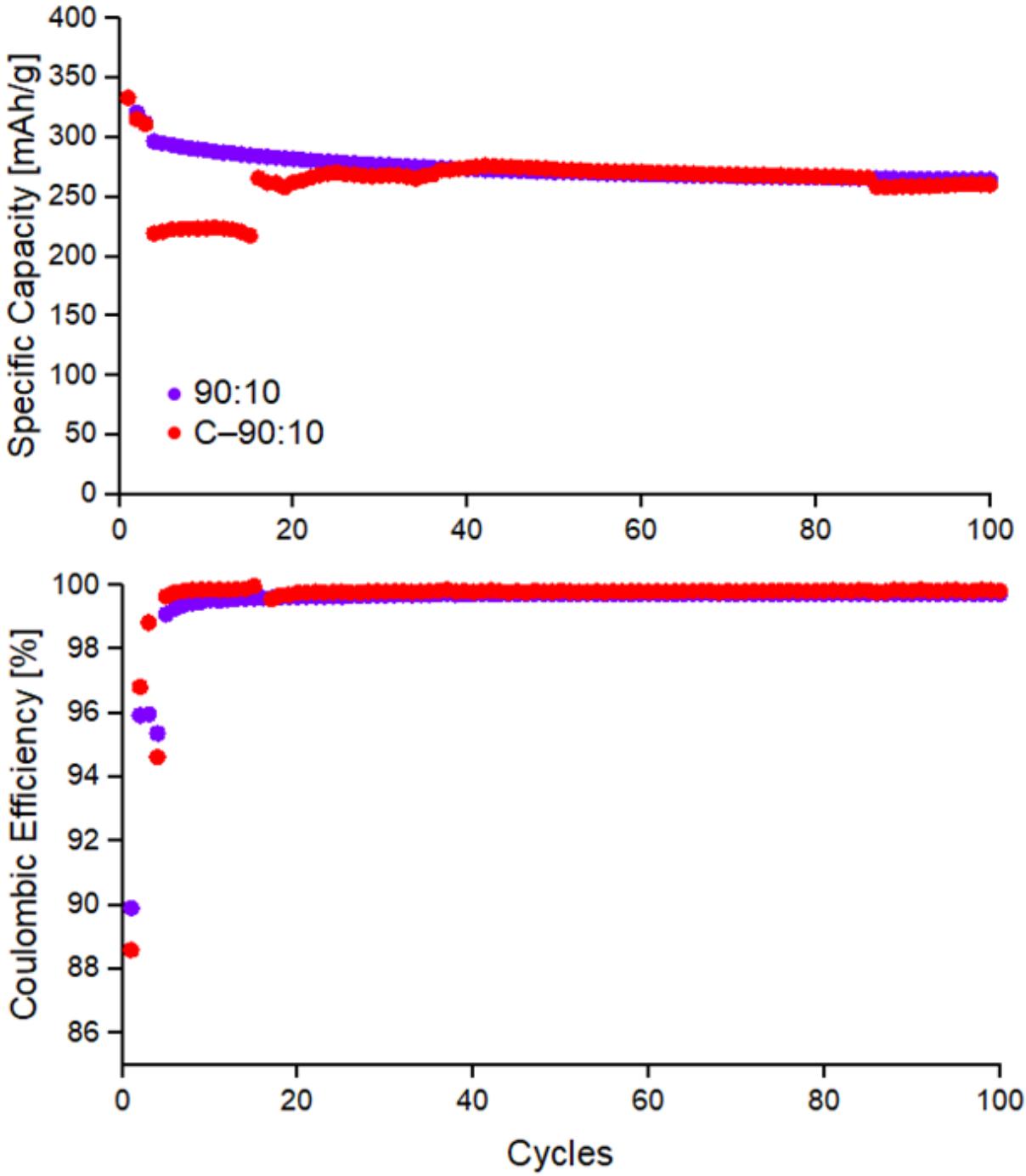

Figure 5-16. Specific capacity (top) and Coulombic efficiency (bottom) for NIB with porous tin and commercial (<150 um) tin, both in a ratio of 10:90 with hard carbon.

5.4 Cumulative Coulombic inefficiency

First cycle initial Coulombic efficiency (ICE) provides useful information on SEI formation with a single number. ICE is especially powerful for indicating the effects of surface coverage on silicon surface reactivity with the electrolyte, such as examined in Chapter 3. However, over many cycles, it can be more useful to look at cumulative Coulombic inefficiency (CCI), which is the sum of all efficiency lost according to the following formula

$$CCI = \left(1 - \frac{Q_{Delithiation}}{Q_{Lithiation}}\right) x\ 100\ \%$$

For tin-graphite anodes in lithium ion batteries, the CCI follows a predictable trend with increasing percentages of porous tin (Figure 5-17). 100 % graphite anodes have 20 % irreversible capacity after 100 cycles, while with 70 % graphite and 30 % tin, the electrodes lose 196 % irreversible capacity, which is only possible due to the functionally limitless amount of lithium available in a half cell. The cells diverge immediately, with higher Coulombic inefficiency associated with larger amounts of tin from the first 10 cycles. However, tin-graphite cells undergo a noticeable rise in CCI from cycles 30-40, indicating side reactions between tin and the electrolyte increase at this period during cycling.

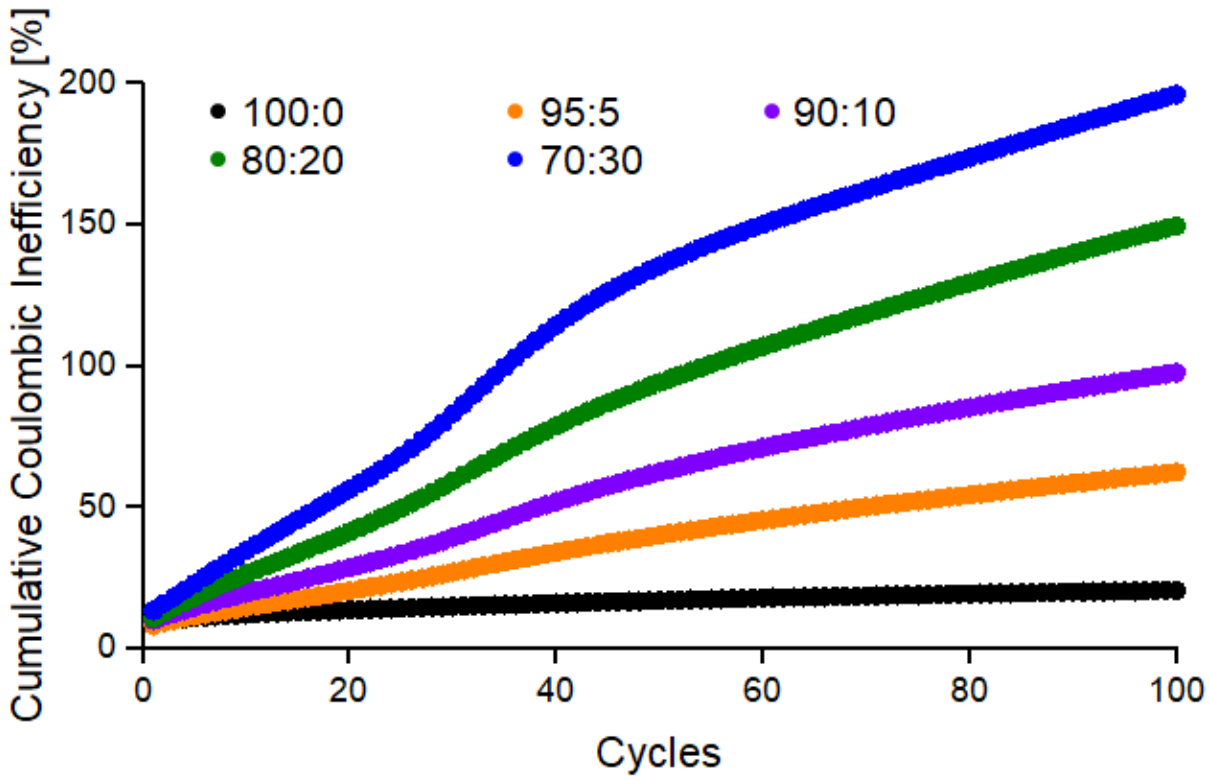

Figure 5-17. Cumulative Coulombic inefficiencies over 100 cycles for tin:graphite anodes in lithium ion batteries.

Examining the CCI data for < 150 um tin electrodes, we find that the commercial tin electrodes have higher Coulombic efficiencies after cycle 20. This corresponds to cycles in which C-90:10 slurries are regaining absolute capacity, as shown in Figure 5-18. While the effect of high irreversible capacity loss on absolute capacity can be masked in half cells, it leads to catastrophic capacity loss in full cells when lithium availability is limited. These results suggest that our porous tin samples are poorly suited for incorporation in commercial graphite anodes under the conditions studied.

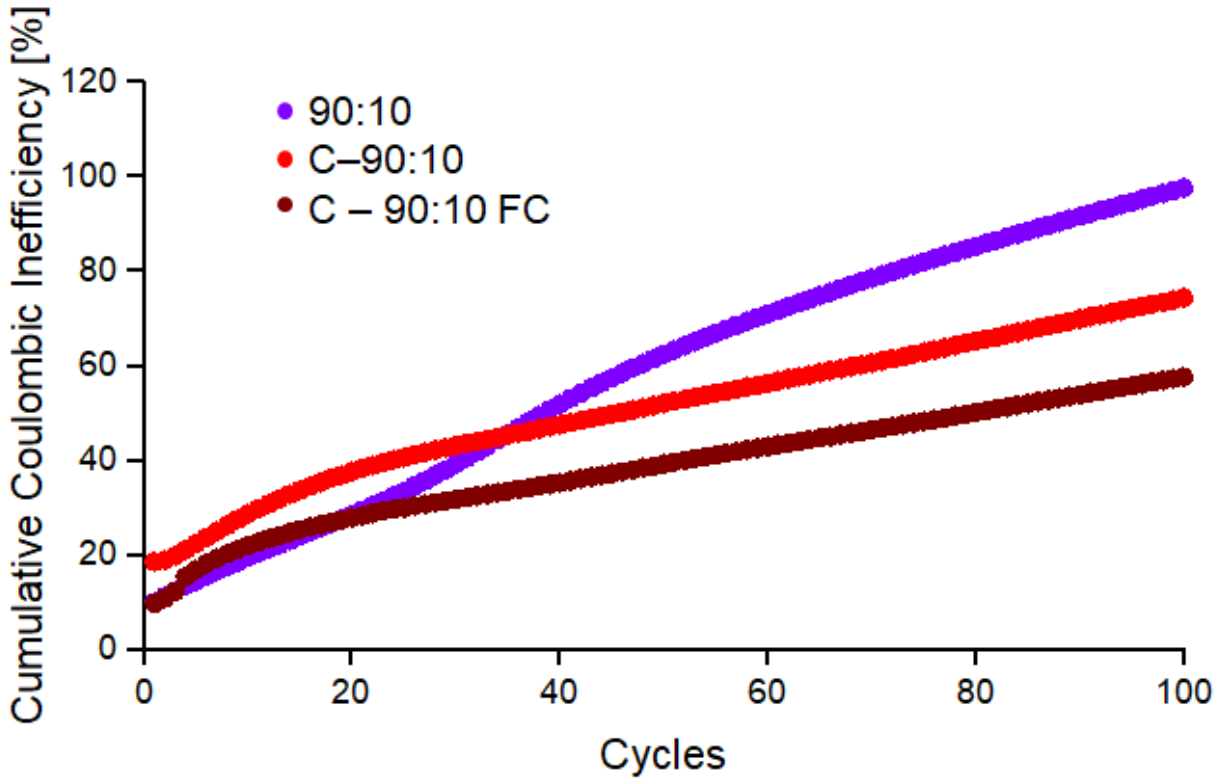

Figure 5-18. A comparison of Cumulative Coulombic inefficiencies in commercial < 150 μm tin for lithium ion batteries. C – 90:10 FC cells describe commercial tin powder cycled with three formation cycles, at 1 x C/20 and 2 x C/10.

When mixed with hard carbon, porous tin also leads to larger cumulative Coulombic inefficiency in sodium ion batteries (Figure 5-19). While 100 % hard carbon has a higher CCI after 100 cycles than 100 % graphite (27 % vs 20 %), the CCI after 100 cycles for tin - hard carbon electrodes was noticeably lower than with their lithium ion battery analogues (56 % vs 150 % for an 80:20 carbon:tin ratio). Furthermore, most of the divergence in CCI is observed within the first 3 formation cycles, and further cycling occurs with similar irreversible capacity loss for each cell recipe. The exception remains the 100 % hard carbon electrode, which has a noticeably smaller slope in

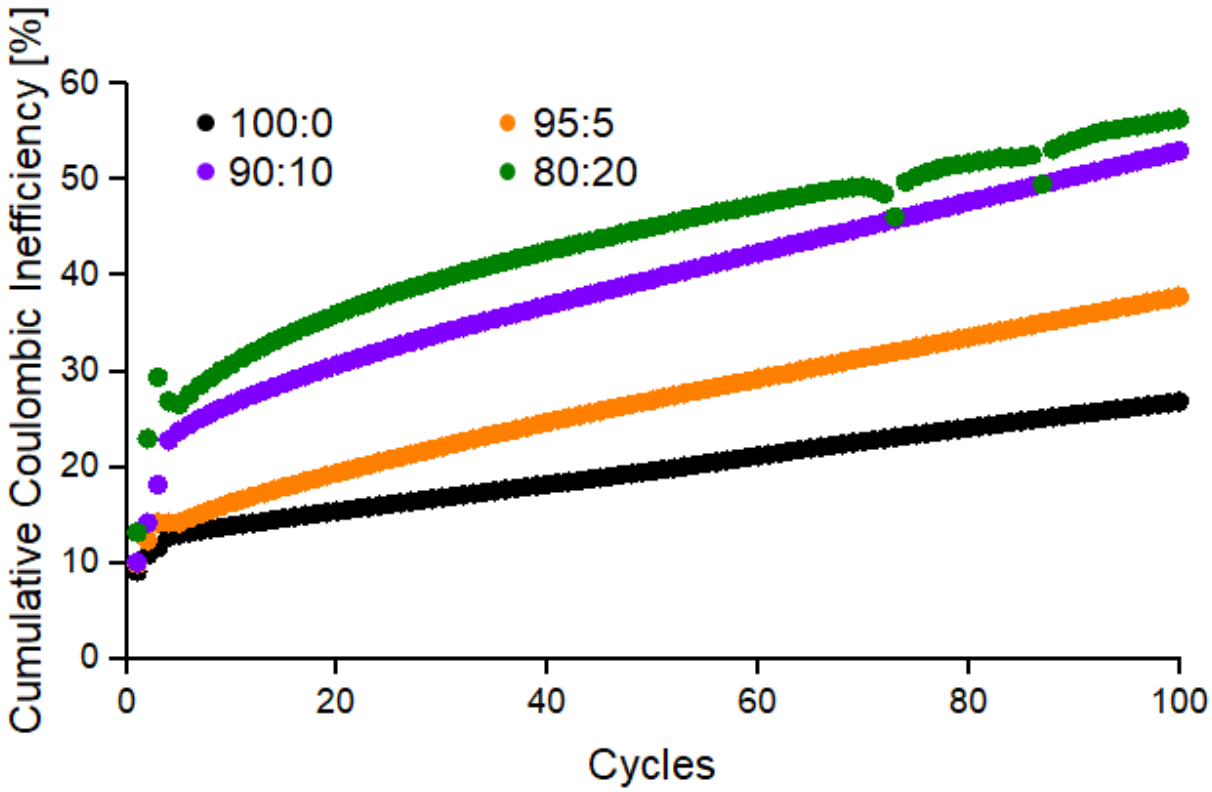

Figure 5-19. *Cumulative Coulombic inefficiencies of all hard-carbon:Sn anodes in sodium ion batteries.*

When commercial < 150 um tin is examined for CCI, we observe similar Coulombic efficiencies for the first three formation cycles (Figure 5-20). Less than 150 um tin electrodes settle into a lower slope caused by higher Coulombic efficiencies after cycle 4. The lower Coulombic efficiency at a rate of C/2 is observed in porous tin samples despite initially lower specific capacities (Figure 5-16).

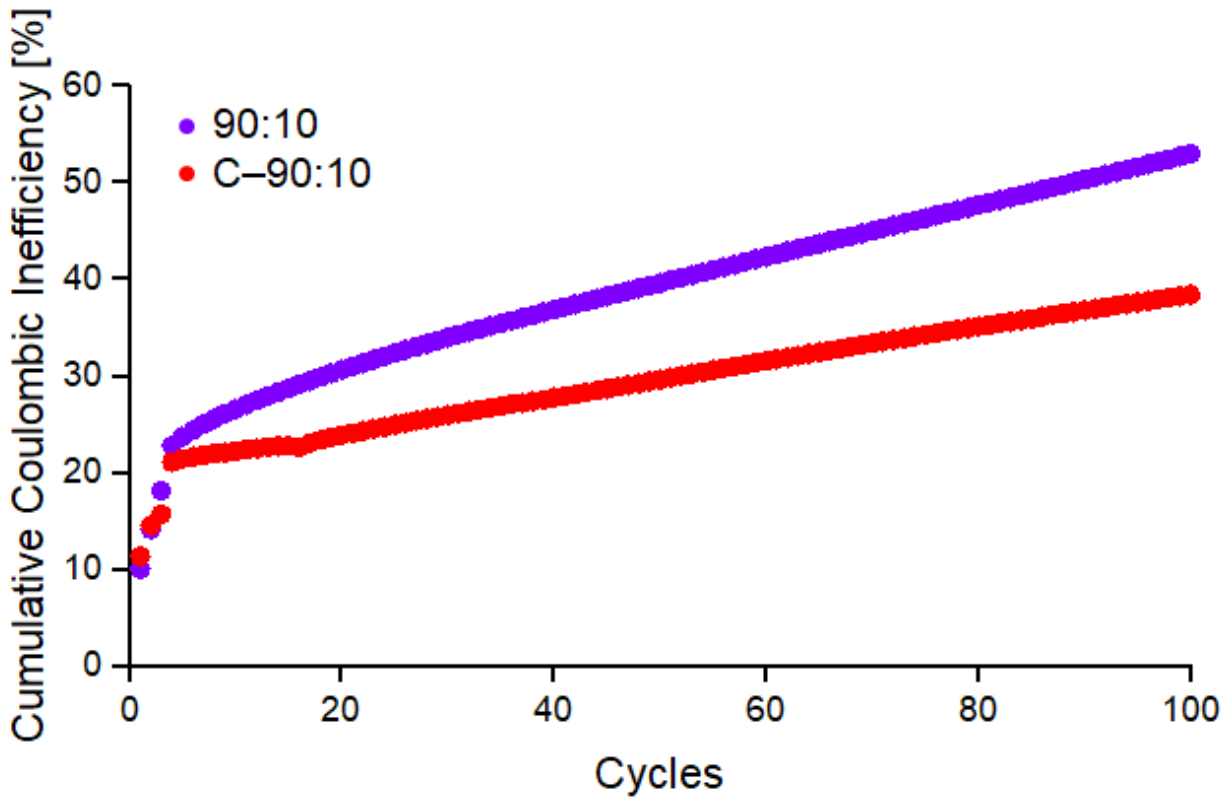

Figure 5-20. Cumulative Coulombic inefficiencies in NIBs. A comparison of porous tin to commercial tin < 150 μm particles.

5.5 Rate analysis

We performed a rate analysis on each of the highest performing cells for both lithium and sodium ion batteries. We considered it important to begin with 3 formation cycles, one at C/20 and two at C/10, each including a CV step. Afterwards, the rate was varied between C/2 and 2C, as shown in Figure 5-21. The general trend was clear, however: the results are complicated by anomalies that we did not have the statistical power to resolve. For lithium ion batteries, we again found that initial capacity was generally increased as the percentage of tin was increased, however 5 % tin was an outlier with capacities below that of 100% graphite anodes at all rates. All cells were

only performed once, so the replicability is in question, particularly the absolute value of the specific capacity. It also appears that higher percentages of tin lead to poorer performance at rates of C and 2C, by comparing 80:20 and 90:10 cells, although this finding cannot be untangled from the general tendency of higher tin loadings to decay more quickly with added cycles.

Sodium ion batteries were also tested at rates between C/2 and 2C, with formation steps at C/20 and C/10. Once again, we observed the general trend that higher porous tin content increases the first cycle specific capacity, while decreasing the capacity at cycle 40, which is conducted at C/2. Results at higher rates were mixed, and the 80:20 cells saw catastrophic capacity loss when rates of C/2 were initially conducted before recovering between cycles 30-40. Meanwhile, 95:5 and 90:10 cells remained above 200 mAh/g even at rates of 2C. 90:10 HC:p-Sn cells were able to maintain a capacity above 250 mAh/g even at a rate of 2C, which corresponds to 75 % of its initial capacity.

We also cycled commercial tin at different rates in Figure 5-22, confirming many observations of the cells that were run over 100 cycles. 10 % commercial tin begins at or near the same capacity as 10 % porous tin for the formation cycles at C/20 and C/10, but commercial <150 um tin has a lower capacity at higher rates. Commercial tin appears much worse in sodium ion batteries due to the aforementioned excellent performance of 90:10 porous tin cells at 1C and 2C rates.

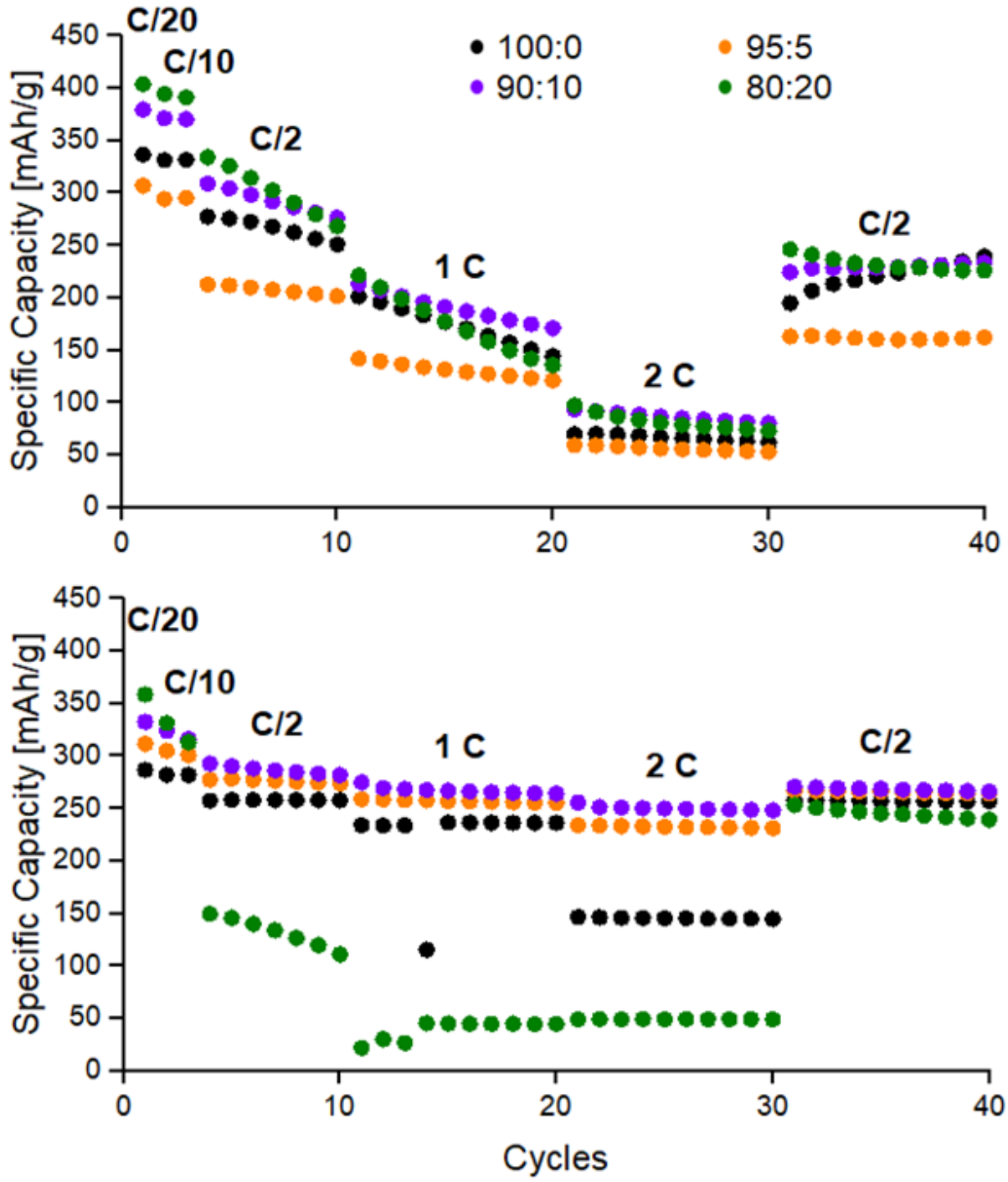

Figure 5-21. Rate test of LIBs (top) and NIBs (bottom) with carbon:tin ratios of 100:0, 95:5, 90:10, and 80:20. Graphite is used for LIBs and hard carbon is used for NIBs. Rate tests were cycled at C/20 (cycle 1), C/10 (cycles 2-3), C/2 (cycles 4-10), 1C (cycles 11-20), 2C (cycles 21-30), and C/2 (cycles 31-40).

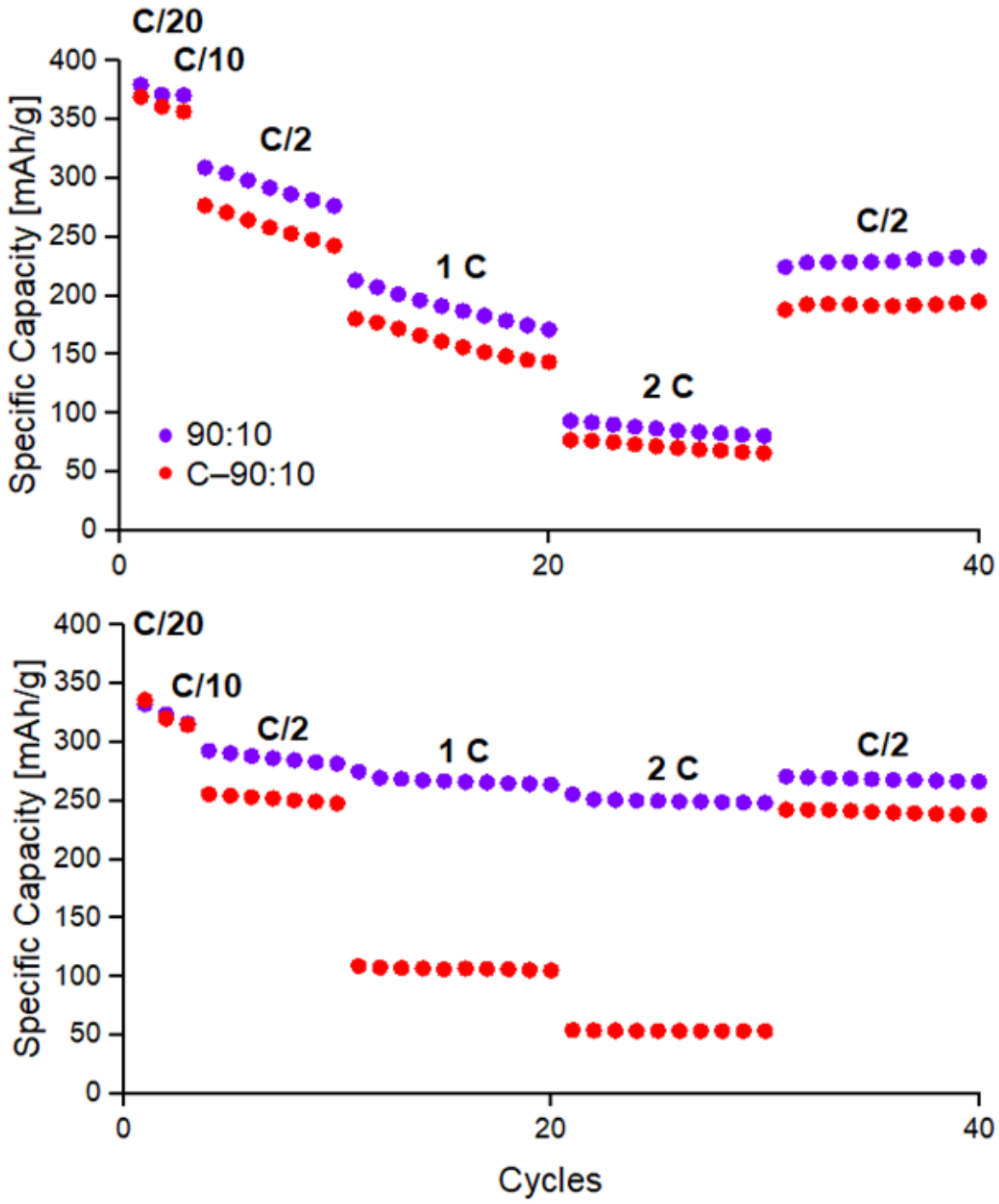

Figure 5-22. Rate test of LIB (top) and NIB (bottom) with porous tin and commercial <150 μm tin. Graphite is used for LIBs and hard carbon is used for NIBs. Rate tests were cycled at C/20 (cycle 1), C/10 (cycles 2-3), C/2 (cycles 4-10), 1C (cycles 11-20), 2C (cycles 21-30), and C/2 (cycles 31-40).

The results above suggest a model in which porous tin is always able to increase the initial specific capacity of active carbon materials, whether for lithium ion batteries or sodium ion batteries. The gain in specific capacity is expected,[292] and represents, in LIBs, the simultaneous intercalation of lithium in graphite and alloying of lithium with tin. The rise in specific capacity with addition of tin is relatively modest compared to the specific capacity of silicon observed in earlier chapters, mostly due to the high atomic mass of tin. The rise in the initial volumetric capacity when incorporating tin with graphite would be larger if we could reliably calculate volume for all the electrodes studied. The primary drawback of tin is the capacity loss associated with particle fracture and electrical isolation, even at small particle sizes.[105] Our results indicate that graphite or hard carbon is capable of diluting the effects of overall cell expansion up until a maximum of 10 % tin content. Above 10 %, we hypothesize that the overall cell expansion may increase significantly.[293] Capacity loss may follow because there is no longer enough graphite to maintain contact with all of the fractured tin, some of which becomes electrically isolated and is lost as capacity. While graphite is able to maintain contact with fractured tin within the 10 % threshold, graphite does not mitigate the effects of tin fracture on Coulombic efficiency. When tin expands and fractures, new surface is exposed and reacts with the electrolyte, leading to irreversible capacity loss and SEI accumulation.[294] The small size of our porous tin is not sufficient to prevent particle fracture and increase Coulombic efficiency.

Porous tin had superior rate capability to <150 μm tin, but with no improvement in capacity retention. The rationale once again comes back to the very small size at which tin is found to fracture.[105] Both micron sized tin particles and p-Sn powder fracture

during lithiation, but with a 90:10 Gr:Sn or HC:Sn ratio, the active carbon material is sufficient to mitigate the effects of fracture and maintain all active material within conductive contact. Also, after many cycles, < 150 μm tin is reduced to a similar size as our p-Sn material, and the rate capabilities of both materials become similar.

5.6 Resilience to exposures to low temperatures

It is important for commercial applications of lithium ion batteries to understand the effect on performance when exposed to low temperatures. α-Sn is a more brittle phase of tin which is capable of forming below 13 °C, and may affect battery cycling under some conditions.[295] On the other hand, previous research has indicated that both tin-coated graphite as well as tin particles may actually improve intercalation kinetics below -20 °C.[296] To test the effect of low temperatures on our cell robustness, we manufactured cells and stored them in a freezer at -15 °C for 7 days. The cells were then removed from the freezer and allowed to return to room temperature before cycling began.

For lithium ion batteries, the results were made difficult to compare because of the desire to include formation cycles for all later cells. While formation cycles were deemed unnecessary for the initial LIB tests to obtain a quick comparison, best practice should include formation cycles at low currents, and we wanted to include these for the cells stored at low temperature. In Figure 5-23, we find that the low temperature cell has higher absolute capacity, while having much lower initial Coulombic efficiency. This is not necessarily an expected result of storing at low temperatures, and results may be confounded by the addition of formation cycles early on.

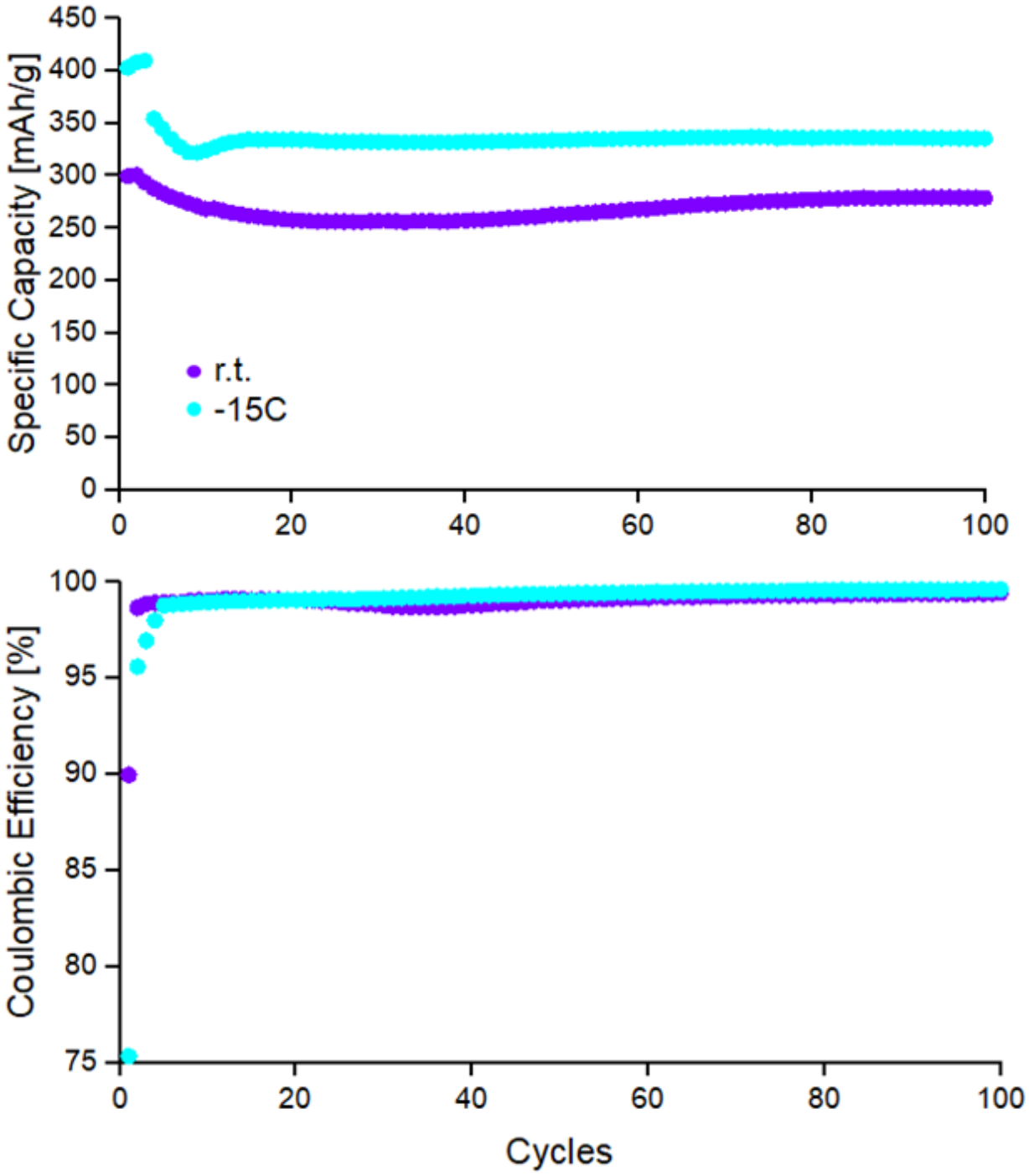

Figure 5-23. *Specific capacities (top) and Coulombic efficiencies (bottom) over 100 cycles in room temperature and cooled graphite:tin cells with a 90:10 ratio. Cooled cells were placed at – 15 °C for one week and then warmed back to room temperature prior to cycling.*

With sodium ion batteries, when cycling parameters were kept constant between the two conditions, little change was observed for the cell stored at -15 °C for one week (Figure 5-24). The specific capacity at cycle 1 was 335 mAh/g for the cooled cell vs 333 mAh/g for the baseline. After 100 cycles, this decays to 257 mAh/g vs 264 mAh/g for cooled vs baseline. All electrochemistry was performed at room temperature. The difference in specific capacity is not considered to be significant, and suggests that the tin based cell for sodium ion batteries is resilient to storage at -15 °C (and certainly below 13 °C) for one week without significant deterioration. Unlike the chilled cell for LIBs, the first cycle Coulombic efficiency was high and in line with its room temperature equivalent, reaching 90.3 % for the cell cooled to -15 °C and 89.9 % for the control.

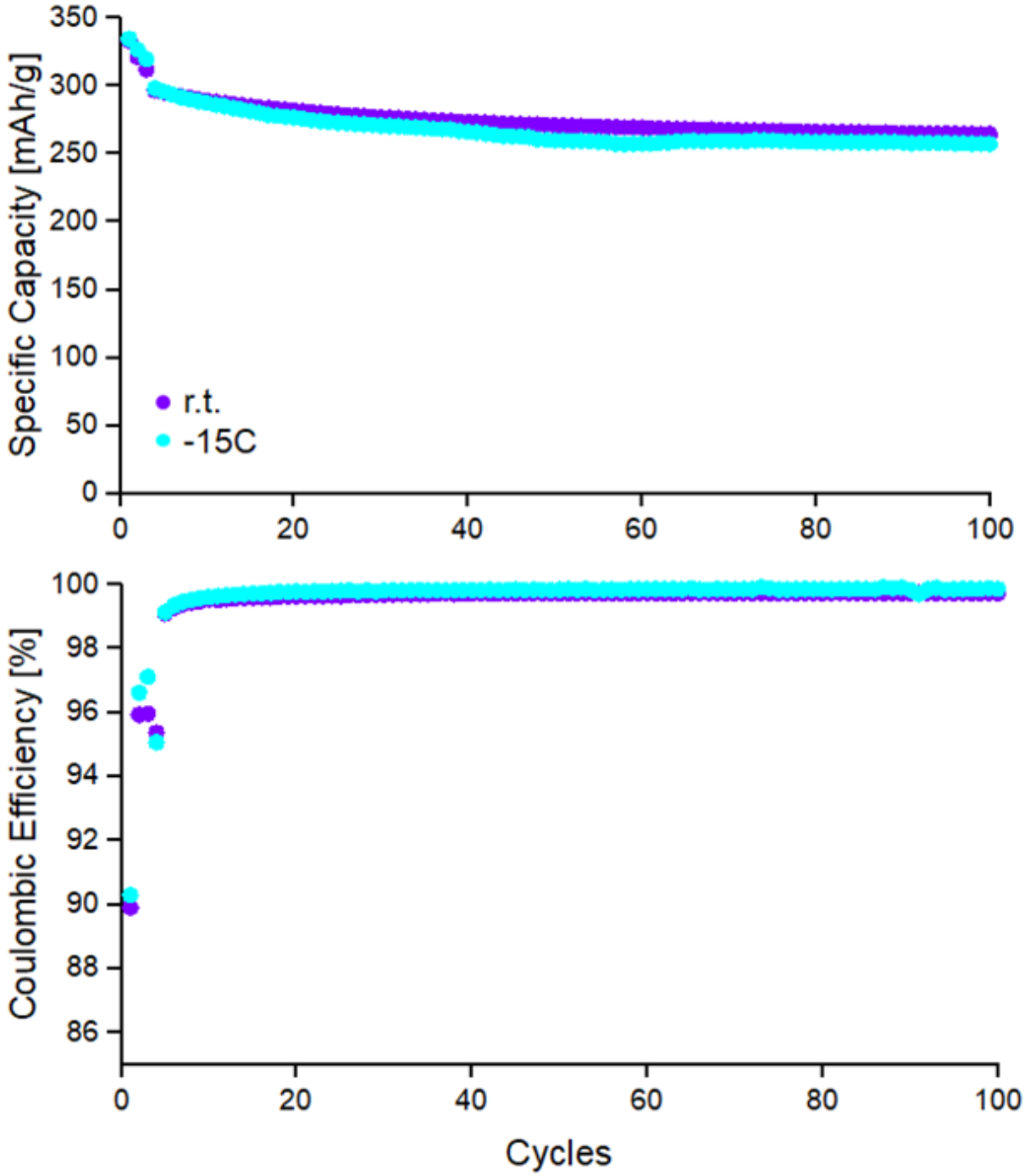

Figure 5-24. *Specific capacities (top) and Coulombic efficiencies (bottom) over 100 cycles in room temperature and cooled hard carbon:tin cells with a 90:10 ratio. Cooled cells were placed at – 15 °C for one week and then warmed back to room temperature prior to cycling.*

5.7 Conclusions

Porous tin was successfully prepared and characterized from a ribbon of 50/50 w/w % silicon and aluminum, which was made using a melt spinning process. We mixed electrode slurries using up to 30 % porous tin with graphite for use in lithium ion batteries, as well as up to 20 % porous tin with hard carbon for use in sodium ion batteries. Using a LIB half-cell, we achieve > 80 % capacity retention after 100 cycles with 95:5 and 90:10 Gr:Sn cells. For NIB half cells, we achieve > 80 % capacity retention with only 95:5 HC:Sn cells, although 90:10 HC:Sn cells remain at 79 % by cycle 100. The porous tin anodes seemed largely resilient to storage at cold temperatures, and cycling was largely unaffected by one week at -15 °C, especially in NIBs. We compared 10 % porous tin cells with cells containing 10% of a commercial <150 μm tin powder, and found that the porous tin had superior performance initially at rates equal to or exceeding C/2. The poorer rate performance of commercial tin particles under these conditions is likely due to limited lithium diffusion through the large particles, resulting in lower specific capacities at earlier cycles; however, commercial tin recovers to the levels seen with porous tin after 100 cycles, presumably because it fractures into smaller particles. The similar capacity retention after 100 cycles can be ascribed to the very small size at which tin particles fracture,[105] occurring even with our porous tin samples, and leading to electrically isolated anode material. Commercial tin also has superior Coulombic efficiency to the porous tin samples analyzed.

Despite achieving the goal of cycle life over 100 cycles, all additions of tin were reliably associated with lower relative capacity after 100 cycles compared to pure carbon anodes. More importantly, 80 % capacity retention was only possible in LIB and

NIB half cells, in which an alkali foil counter electrode provides a functionally unlimited source of lithium. By plotting cumulative Coulombic inefficiency, we demonstrate that even 5 % porous tin contributes to the irreversible loss of lithium, including a 62.4 % irreversible capacity loss with 95:5 Gr:Sn after 100 cycles, and 37.8 % irreversible capacity loss after 100 cycles with 95:5 HC:Sn. While graphite and hard carbon are able to dilute the overall anode expansion, the active carbon materials do not prevent electrolyte decomposition on the newly exposed surfaces of fracture tin particles. For future research, the Coulombic inefficiencies may be partly avoidable by using slow formation cycles and prelithiation of the anode. An important direction for future exploration of tin-graphite and tin-hard carbon technology is to include tests of LIB and NIB full cells using high quality commercial cathodes.

5.8 Experimental section

5.8.1 Materials and reagents

Aluminum (7-8 μm max) and tin (100 mesh) metal powders were purchased from Sigma-Aldrich. Polyacrylic acid (PAA, Mv = 450,000), lithium hydroxide (LiOH, reagent grade, 98 %), 1 M $LiPF_6$ in 1:1 ethylene carbonate:diethyl carbonate (EC/DEC, 1/1 v/v%, battery grade), sodium hexafluorophosphate (99.99 %), metallic sodium (99.9 %), diethylene glycol dimethyl ether (anhydrous, 99.5 %), and fluoroethylene carbonate (FEC, >99 %, anhydrous) were purchased from Sigma-Aldrich. Sodium hydroxide (pellets, certified ACS) was purchased from Fisher Scientific. Graphite (MCMB) and hard carbon (D50) was purchased from MSE supplies. Carbon black (Super-P) was

purchased from Timcal. Stainless steel discs (MTI) of 0.5 mm thickness and 15.5 mm diameter were used as spacers.

5.8.2 Synthesis of p-Sn powder

Tin and aluminum were mixed in a 1:1 wt % ratio and processed through a single-roller melt spinner with a surface velocity of 28 m/s. The material became brittle after aging the ribbons in air for a sufficient length of time, and it was subsequently ball milled with a tungsten carbide milling vessel and tungsten carbide balls at 500 rpm for 5 hours. The ratio between milling balls and SnAl material was 20:1 wt %. Aluminum was removed by immersing the powder in 1 M KOH (aq) until hydrogen bubbling ceased, which was an indicator that dissolution of Al was complete. The powder was washed with MilliQ water and dried under vacuum at room temperature. The resulting powder was characterized using SEM and BET. The specific surface area of the powder was 2.35 m^2/g. The pore volume as determined by BET was 0.013 cc/g of pores below 36 nm diameter. The volume fraction of Al based on the nominal composition is 73 %, which is equivalent to 0.1 cc/g. BET used nitrogen as an adsorbate,

5.8.3 Preparation of nanoparticle slurries

Slurries were prepared by combining active material (carbon and porous tin), conductive carbon Super P, and LiPAA or NaPAA binder in a 95:1:4 ratio and diluting in water (~120 % mass of dry materials). Less water was used with higher tin proportions to maintain the same viscosity due to the greater density of tin. The solution was mixed in a planetary ball mill (Changsha Tianchuang Powder Technology Co.) at 500 rpm for

60 min total in a teflon vial using zirconia balls (typically 4 x 0.7 cm, 2 x 1.0 cm, 2 x 1.2 cm, 2 x 1.5 cm; ~500% mass of slurry). The slurry was cast onto copper foil (battery grade, 10 μm) at a cast height of 100 μm and dried overnight at 120 °C under vacuum. Discs were punched with a diameter of 15 mm, then dried again at 120 °C under vacuum for 16 hours and brought directly under inert atmosphere. The average mass loading was 1.8 - 2.8 mg/cm^2, depending on the ratio of carbon to tin. Samples were weighed using a Mettler Toledo XP6U balance with a readability of 0.1 μg and a repeatability of 0.4 μg.

5.8.4 Electrochemical measurements

1 M $LiPF_6$ in EC/DEC (1/1 v/v%) with 10 wt% FEC additive was used as electrolyte for lithium ion batteries, and 1M $NaPF_6$ in diethylene glycol dimethyl ether was used as the electrolyte for sodium ion batteries. 100 μL of electrolyte was used for porous tin cells. All cells were assembled under an argon atmosphere using 2032 coin cells with Li metal foil (MTI) counter electrodes and single layer polypropylene-polyethylene-polypropylene separators with a porosity of 39 % (Celgard™ 2325). Cycle life testing was performed on an Arbin BT2000 battery testing system at 25 °C using between the range of 1.5 and 0.001 V. Preliminary tests on lithium ion batteries were performed at a rate of C/2 for all cycles, using only constant current protocol. All future tests were performed with three formation cycles, cycle 1 a C/20, and cycles 2-3 at C/10, with a constant voltage hold at C/50 and at C/20 for the respective formation cycles. Further cycling was performed at a rate of C/2 without a constant voltage hold. All C rates were calculated depending on the ratio of carbon to tin, using a theoretical

specific capacity of 372 mAh/g for graphite and 993 mAh/g for Sn in LIBs, and 350 mAh/g for hard carbon and 847 mAh/g for Sn with NIBs. Potentiostatic Electrochemical Impedance Spectroscopy (EIS) was performed using a Biologic BCS-805 battery testing system, scanning between 10 kHz and 10 mHz. Cells underwent two full formation cycles as well as lithiation at C/10, then were left to reach open circuit voltage for three hours prior to EIS. These same cells were left to reach a total of 10 cycles for post-cycling SEM.

5.8.5 Characterization

Scanning Electron Microscopy (SEM) was carried out using a Zeiss Sigma Field Emission SEM at accelerating voltages of 5-10 kV. Coin cell dissassembly was performed using a gas driven decrimper (MTI corporation), and all post-mortem anodes were washed with dimethyl carbonate (DMC) in an inert atmosphere prior to analysis. Diffuse Reflectance Infrared Fourier Transform Spectroscopy (DRIFTS) was performed using a Nicolet IS50 spectrometer. Surface area measurements using Brunauer Emmett Teller (BET) theory were conducted using an Autosorb Quantochrome 1MP. X-ray Microscopy (XRM) was performed on a ZEISS Xradia Versa 620 X-Ray Microscope. For XRM, 1 mm strips of sample were wrapped in parafilm to protect lithiated samples from air.

Chapter 6 - Thesis summary and outlook

6.1 Thesis summary

Alloying anode materials have been studied for use in lithium and sodium ion batteries. The primary goal of this thesis was to improve capacity retention and Coulombic efficiency in silicon and tin anodes by mitigating the impacts of anode fracture during lithiation - electrical isolation from material fracture, and irreversible capacity loss from reactions with the electrolyte. We examine the effects of nano-size morphologies, electrolyte additives, and formation of the *c*-$Li_{15}Si_4$ phase in silicon. We also present an approach toward the preparation of a-SEI on the surface of silicon and examine the effect on capacity retention and Coulombic efficiency. Tin anodes are examined with regard to nano scale morphologies and mixed graphite or hard carbon anodes. Highlights of each project and summarized in the following sections.

Chapter 1 introduces LIBs along with the use of silicon and tin anodes to improve the specific and volumetric capacities of LIBs. We discuss the fundamentals of lithium-silicon and lithium-tin alloys, along with the colossal expansion of silicon and tin and the formation of solid electrolyte interphase (SEI). Silicon is further described in terms of its interaction with the electrolyte for SEI formation, as well as the lithiation phases observed in a silicon anode, particularly the terminal *c*-$Li_{15}Si_4$ phase. Furthermore, we introduce the concept of the artificial SEI (a-SEI) and its preparation. Finally, tin anodes are described to introduce our work on porous tin powders on mixed carbon-tin anodes for lithium and sodium ion batteries.

In Chapter 2, we contrast the effects of forming the *c*-$Li_{15}Si_4$ phase in silicon thin films and porous films versus forming the same phase in silicon nanoparticle electrodes.

We focus on the effects of a constant voltage hold step, which increases the amount of *c*-$Li_{15}Si_4$ phase built up by exposing the electrodes to a lower current during the voltage hold, but we also analyze SiNPs at different cut-off voltages, which changes the degree of *c*-$Li_{15}Si_4$ phase formation. Understanding the effect of the *c*-$Li_{15}Si_4$ phase is important to inform future research on its suppression, and gives researchers more information when choosing the optimal cycling profile for testing silicon anode materials. Previous work has suggested that the *c*-$Li_{15}Si_4$ phase is intrinsically detrimental to silicon nanoparticle electrodes, even in the half-cell set up.[78] We find that the *c*-$Li_{15}Si_4$ phase is associated with capacity loss in planar Si films, likely due to delamination, but is not associated with capacity loss in porous films or SiNPs. Nevertheless, Coulombic efficiency is lower with the formation of the *c*-$Li_{15}Si_4$ phase, which would lead to poorer capacity retention in a full cell set up. This work contributes to the literature on *c*-$Li_{15}Si_4$ formation by suggesting that the negative effects of the *c*-$Li_{15}Si_4$ phase in <150 nm sized silicon electrodes is limited to greater reactivity with the electrolyte and larger SEI buildup, which mostly affects capacity in full cells without a lithium metal counter electrode.

Chapter 3 describes the functionalization of silicon anodes to create an a-SEI. The use of an a-SEI follows up on the work of Chapter 2 by aiming to improve Coulombic efficiency in silicon electrodes and limit SEI build up during cycling, regardless of *c*-$Li_{15}Si_4$ phase formation. Functionalization of the surfaces of silicon thin films and silicon nanoparticles was carried out using thermal hydrosilylation. We also functionalized silicon microparticles using ball milling to reduce the sizes of the microparticles, but we were unsuccessful in achieving sufficient size reduction of the

micron sized particles. Functionalized thin films and nanoparticles were assembled into lithium ion coin cells. We showed that the relative performance of SiNP functionalization depends overwhelmingly on the performance of SiNPs used as a control. SiNPs below 80 nm had a larger fraction of silicon oxide on the surface and a comparatively lower initial capacity, so that functionalized silicon could improve on the initial capacity while maintaining high capacity retention. However, larger 140 nm SiNPs with a native oxide had a relatively high initial capacity along with high capacity retention, and unfunctionalized silicon achieved better capacity retention, so long as we used the most effective binder, polyacrylic acid (PAA). The thickness of native oxide on 140 nm particles compromises well in the trade-off between (i) high initial capacity and (ii) strong intermolecular bonds with both the binder and the SEI formed by decomposition of FEC. Previous work in the literature has already established covalently bound a-SEI with organic functional groups through a variety of methods.[90–92,99] Our main contribution was to study the tradeoff between silicon surface passivation and surface-binder interactions, while we also highlight the importance of a high-quality control anode for silicon nanoparticle studies, which hampers comparisons between many literature examples. Improving on the properties of high capacity silicon with a native oxide requires the added variable of molecular loading to optimize the degree of functionalization on our particles.

Chapter 4 describes the role of electrolyte additives in the formation of SEI on silicon anodes. Electrolyte additives work complementarily with Chapter 3, by contributing the SEI on the surface of the silicon anode, and by repairing gaps in SEI coverage that inevitably form during silicon expansion. Electrolyte additives have

received considerable attention in the literature, and a wide variety of sacrificial additives – which are reduced at relatively high voltages to produce stable SEI products – have achieved widespread adoption.[36,69,297] We explored a subset of electrolyte additives that contained an alkene or alkyne functionality, based the hypothesis that they could covalently bond via electrografting to the surface of newly exposed hydrogen-terminated silicon during cycling. First, we demonstrated cathodic electrografting (CEG) of an alkyne on the surface of porous silicon and found that CEG occurs in competition with solvent decomposition in the presence of carbonate-based solvents or in the presence of a lithium counter electrode. Long term cycling results with alkyne/alkene electrolytes were in some cases consistent with in-situ electrografting to form SEI, but the molecules chosen here did not result in improved capacity retention when compared to non-alkene/alkyne electrolyte additives such as FEC.

Chapter 5 addresses the use of porous tin in conjunction with graphite or hard carbon anodes for lithium ion batteries and sodium ion batteries. Silicon graphite mixtures are common in the literature, but tin-graphite and tin-hard carbon mixtures are less commonly studied.[120,282,283,296] We report a novel synthesis of porous tin produced from a melt-spun ribbon of 1:1 wt% Sn:Al, as described in Chapter 5. Porous tin mixed with graphite or hard carbon led to increased specific capacity compared to pure carbon-based anodes, but at the cost of capacity retention. We show that porous tin improves on the rate capability of commercial tin microparticles, but does not improve on the capacity retention over 100 cycles. Importantly, anodes containing porous tin had much lower Coulombic efficiency over the course of 100 cycles, and the cumulative

effect would pose a large detriment to porous tin powder incorporated into an alkali ion full cell set up.

6.2 Future directions

6.2.1 High energy ball milling of silicon microparticles

As described in Section 3.6, ball milling of silicon 325 mesh microparticles with VEC showed promise for reducing the size of silicon microparticles and to functionalize silicon particles with VEC. However, 15 hours of milling did not reduce the particle size below 150 nm, and separating Si-VEC particles from the VEC solution proved difficult. Future work should try to reproduce this process using a high energy ball mill (HEBM) - either a vibratory mill, or a planetary ball mill capable of > 1000 rpm (Figure 6-1) to further reduce the size of silicon microparticles.[298] With the ability to achieve sub-150 nm Si-VEC particles, milling time could be adjusted to achieve the optimal size dispersion and surface area to volume ratio, as judged by the specific capacity and Coulombic efficiency of the resulting electrode slurries. The process of Si-VEC separation could be improved significantly by increasing the rate of centrifugation using an ultracentrifuge. Si-octenyl particles could be separated from the supernatant using a centrifugal force of 500 G, however, this clearly wasn't enough to separate Si-VEC particles for the size distribution that we observed.

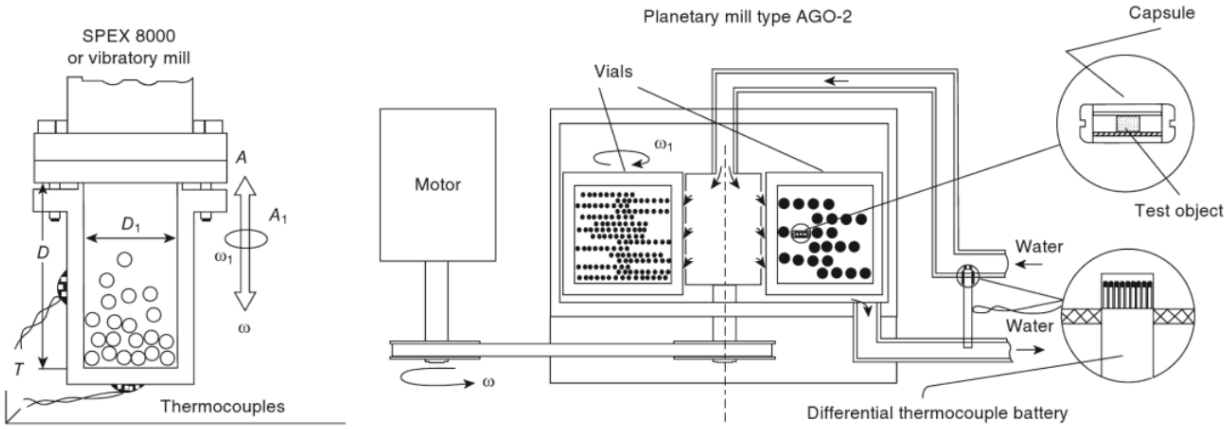

Figure 6-1. Vibratory and planetary methods of high energy ball milling. Reprinted with permission from reference 298. © 2010 Woodhead Publishing Limited and CRC Press LLC.

Lithium ion batteries have been made with polymer coatings or carbon coatings synthesized through high energy ball milling.[226,299] Si-VEC particles could be obtained using adequate instrumentation, including a high energy ball mill and ultracentrifuge, and other thin, robust a-SEI silicon surfaces should be explored, such as polyethylene oxide chains of varying lengths or N,N-dimethylacrylamide. Future research should explore silicon microparticles milled in a HEBM with two or three solvents to further tune the SEI prior to cell assembly.

6.2.2 Si-graphite anodes with a-SEI

In Section 3.5, we noted difficulties improving capacity retention with an a-SEI in high performing silicon nanoparticle anodes with a native oxide. However, the one silicon functionalization that resulted in improved capacity retention compared to the native oxide was 1H,1H,2H-perfluoro-1-decene, using a PVDF binder. Our Si-PD

nanoparticles also had a higher Coulombic efficiency than silicon with a native oxide, even in the presence of a PAA binder. Future research could overcome the limitation of the poor compatibility between Si-PD and non-polar binders such as PVDF by incorporating functionalized SiNPs into silicon graphite slurry mixtures, analogous to the work done with tin in Chapter 6. Common methods of preparing silicon graphite slurries, such as those shown in figure 6-2,[300] could be easily adapted to incorporate functionalized SiNPs, including SiNPs functionalized by mechanochemical synthesis using a HEBM. All graphite anodes still typically use PVDF binders, and while many silicon graphite mixtures use polar binders such as PAA or CMC instead, PVDF remains a good option for silicon-graphite mixed electrodes due to the much lower levels of overall volume expansion. This approach would have environmental drawbacks. Lithium ion batteries have been trying to pivot away from PVDF and NMP as binder and solvent, respectively, in favour of more environmentally responsible aqueous slurry preparation.[301] Meanwhile, perfluorinated molecules such as 1H,1H,2H-perfluoro-1-decene are potent greenhouse gases.[302] Alternative hydrophobic a-SEIs would be preferable for large scale anode synthesis.

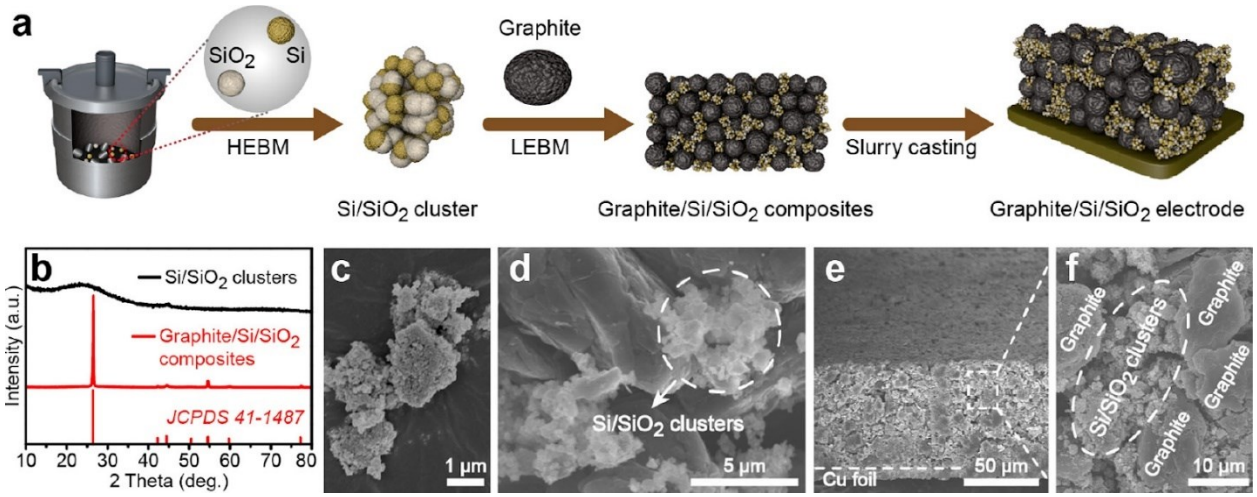

Figure 6-2. Synthesis of silicon/graphite mixed electrodes using high energy ball milling. Reprinted with permission from reference 300. © 2021 American Chemical Society.

6.2.3 a-SEI optimization with design of experiments (DOE)

Lithium ion battery testing involves dozens of variables that interact in dependent ways. For example, we demonstrated in Chapter 2 that a variable such as particle size can have different effects on capacity retention depending on the cut-off voltage or the inclusion of a constant voltage step during lithiation. While engineering and related industries, and life and medical sciences are well-accustomed to interrogating multiple variables simultaneously via design of experiments and ANOVA analyses, academic research in the physical sciences tends to prefer one-variable-at-a-time experimentation.[303–308] We varied silicon surface structure and slurry binder concurrently within Section 3.5, but the cut-off voltage and use of CCCV mode during lithiation were left unchanged. However, it became clear that improvements with a-SEI would require optimizing the loading of alkenes/alkynes for hydrosilylation, as had been seen in previous research.[91] Multiple variables would need to be modified simultaneously in order to tease out these convoluted factors. Future research should

also consider molecules that we did not use for coin cell assembly, such as N,N-dimethyl acrylamide and 3-amino-1-propyne as outline in Section 3.4, as well as novel additives such as dienes, chalcogenides, and dichalcogenides, each of which has well established mechanisms of silicon surface functionalization.[231,309] Ideally research would also consider hydrosilylation with two or more molecules. Finally, the matrix of binders should be expanded to include more polar, flexible binders known for high capacity retention with silicon anodes - such as carboxymethyl cellulose (CMC) - as well as alkali salts in water, such as LiPAA and NaCMC. The variables of a-SEI molecules, molecular loading, and binder choice are all intimately linked, and deserve to be compared across the same batch of silicon nanoparticles. A conservative experimental design with 6 a-SEI (3 molecules and 3 binary combinations), 3 levels of molecular loading,[91] and 3 binders would involve 54 unique silicon slurries and leave out many possible a-SEI molecules and binders. Situations with large numbers of experiments and a need for replications can benefit from design of experiments (DoE) with machine learning-based analyses.[310–313]

Machine learning describes techniques for data processing that allow for rapid interpretation of results across multiple variables and many experiments, and have become much more user friendly in the materials community in recent years.[314,315] In the aforementioned example, the data processing would still require 54 experiments, which is where principles from the field of DoE arrive to conserve time and expand the number of variables that are open for exploration. At its most fundamental, the principles of DoE guide the choice of variables in a round of experiments so that specific variable combinations can be ignored while still representing a large portion of the

parameter space being investigated (Figure 6-3). Recent tutorials outline its benefits to analytical or material chemistry.[310,316] Future research should focus first on the use of DoE for optimization of an a-SEI on SiNPs obtained from hydrosilylation or from mechanochemical reactivity, while further research should also use DoE to elucidate the role of related variables, such as silicon size, the choice of carbon additive, and the ratio of silicon to carbon additive to binder in the slurry.

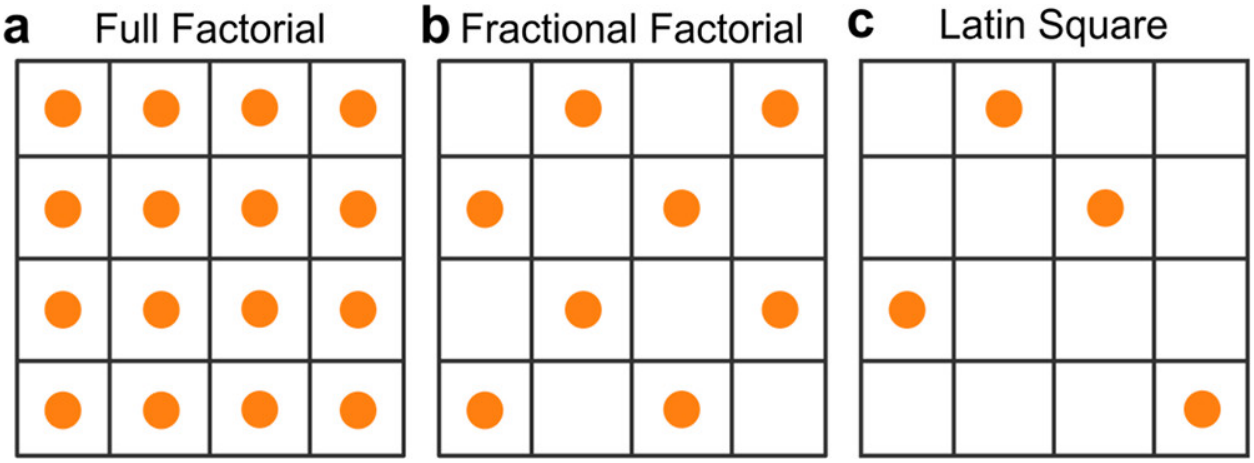

Figure 6-3. Variable choice guided by the principles of design of experiments (DoE). Using such principles is an efficient way to sample a large proportion of parameter space, particularly when variables are correlated and interdependent. Reprinted with permission from reference 310. © 2018 American Chemical Society.

References

(1) Environment and Climate Change Canada. *A clean electricity standard in support of a net-zero electricity sector: discussion paper*. https://www.canada.ca/en/environment-climate-change/services/canadian-environmental-protection-act-registry/achieving-net-zero-emissions-electricity-generation-discussion-paper.html (accessed 2022-08-31).

(2) Department of Energy. *2021: DOE Moves At Lightning Speed Toward Clean Energy Goals*. Energy.gov. https://www.energy.gov/articles/2021-doe-moves-lightning-speed-toward-clean-energy-goals (accessed 2022-08-31).

(3) Lewis, N. S.; Nocera, D. G. Powering the Planet: Chemical Challenges in Solar Energy Utilization. *Proc. Natl. Acad. Sci.* **2006**, *103* (43), 15729–15735. https://doi.org/10.1073/pnas.0603395103.

(4) Alberizzi, J. C.; Frigola, J. M.; Rossi, M.; Renzi, M. Optimal Sizing of a Hybrid Renewable Energy System: Importance of Data Selection with Highly Variable Renewable Energy Sources. *Energy Convers. Manag.* **2020**, *223*, 113303. https://doi.org/10.1016/j.enconman.2020.113303.

(5) Li, Y.; Wang, C.; Li, G.; Chen, C. Optimal Scheduling of Integrated Demand Response-Enabled Integrated Energy Systems with Uncertain Renewable Generations: A Stackelberg Game Approach. *Energy Convers. Manag.* **2021**, *235*, 113996. https://doi.org/10.1016/j.enconman.2021.113996.

(6) Shaner, M. R.; Davis, S. J.; Lewis, N. S.; Caldeira, K. Geophysical Constraints on the Reliability of Solar and Wind Power in the United States. *Energy Environ. Sci.* **2018**, *11* (4), 914–925. https://doi.org/10.1039/C7EE03029K.

(7) Tarascon, J.-M.; Armand, M. Issues and Challenges Facing Rechargeable Lithium Batteries. *Nature* **2001**, *414* (6861), 359–367. https://doi.org/10.1038/35104644.

(8) Luntz, A. C.; Voss, J.; Reuter, K. Interfacial Challenges in Solid-State Li Ion Batteries. *J. Phys. Chem. Lett.* **2015**, *6* (22), 4599–4604. https://doi.org/10.1021/acs.jpclett.5b02352.

(9) Mou, H.; Xiao, W.; Miao, C.; Li, R.; Yu, L. Tin and Tin Compound Materials as Anodes in Lithium-Ion and Sodium-Ion Batteries: A Review. *Front. Chem.* **2020**, *8*.

(10) Harlow, J. E.; Ma, X.; Li, J.; Logan, E.; Liu, Y.; Zhang, N.; Ma, L.; Glazier, S. L.; Cormier, M. M. E.; Genovese, M.; Buteau, S.; Cameron, A.; Stark, J. E.; Dahn, J. R. A Wide Range of Testing Results on an Excellent Lithium-Ion Cell Chemistry to Be Used as Benchmarks for New Battery Technologies. *J. Electrochem. Soc.* **2019**, *166* (13), A3031. https://doi.org/10.1149/2.0981913jes.

(11) Masias, A.; Marcicki, J.; Paxton, W. A. Opportunities and Challenges of Lithium Ion Batteries in Automotive Applications. *ACS Energy Lett.* **2021**, *6* (2), 621–630. https://doi.org/10.1021/acsenergylett.0c02584.

(12) Schmuch, R.; Wagner, R.; Hörpel, G.; Placke, T.; Winter, M. Performance and Cost of Materials for Lithium-Based Rechargeable Automotive Batteries. *Nat. Energy* **2018**, *3* (4), 267–278. https://doi.org/10.1038/s41560-018-0107-2.

(13) Li, M.; Lu, J.; Chen, Z.; Amine, K. 30 Years of Lithium-Ion Batteries. *Adv. Mater.* **2018**, *30* (33), 1800561. https://doi.org/10.1002/adma.201800561.

(14) Sandhya, C. P.; John, B.; Gouri, C. Lithium Titanate as Anode Material for Lithium-Ion Cells: A Review. *Ionics* **2014**, *20* (5), 601–620. https://doi.org/10.1007/s11581-014-1113-4.

(15) Zhao, X.; Lehto, V.-P. Challenges and Prospects of Nanosized Silicon Anodes in Lithium-Ion Batteries. *Nanotechnology* **2020**, *32* (4), 042002. https://doi.org/10.1088/1361-6528/abb850.

(16) Cheng, X.-B.; Zhang, R.; Zhao, C.-Z.; Zhang, Q. Toward Safe Lithium Metal Anode in Rechargeable Batteries: A Review. *Chem. Rev.* **2017**, *117* (15), 10403–10473. https://doi.org/10.1021/acs.chemrev.7b00115.

(17) Obrovac, M. N.; Chevrier, V. L. Alloy Negative Electrodes for Li-Ion Batteries. *Chem. Rev.* **2014**, *114* (23), 11444–11502. https://doi.org/10.1021/cr500207g.

(18) Kasavajjula, U.; Wang, C.; Appleby, A. J. Nano- and Bulk-Silicon-Based Insertion Anodes for Lithium-Ion Secondary Cells. *J. Power Sources* **2007**, *163* (2), 1003–1039. https://doi.org/10.1016/j.jpowsour.2006.09.084.

(19) Chen, Z.; Zhang, W.; Yang, Z. A Review on Cathode Materials for Advanced Lithium Ion Batteries: Microstructure Designs and Performance Regulations. *Nanotechnology* **2019**, *31* (1), 012001. https://doi.org/10.1088/1361-6528/ab4447.

(20) Nölle, R.; Beltrop, K.; Holtstiege, F.; Kasnatscheew, J.; Placke, T.; Winter, M. A Reality Check and Tutorial on Electrochemical Characterization of Battery Cell Materials: How to Choose the Appropriate Cell Setup. *Mater. Today* **2020**, *32*, 131–146. https://doi.org/10.1016/j.mattod.2019.07.002.

(21) Gogotsi, Y.; Simon, P. True Performance Metrics in Electrochemical Energy Storage. *Science* **2011**, *334* (6058), 917–918. https://doi.org/10.1126/science.1213003.

(22) Sævarsdottir, G.; Kvande, H.; Magnusson, T. Greenhouse Gas Emissions from Silicon Production -Development of Carbon Footprint with Changing Energy

Systems. Rochester, NY September 12, 2021. https://doi.org/10.2139/ssrn.3926088.

(23) Zhu, G.; Luo, W.; Wang, L.; Jiang, W.; Yang, J. Silicon: Toward Eco-Friendly Reduction Techniques for Lithium-Ion Battery Applications. *J. Mater. Chem. A* **2019**, *7* (43), 24715–24737. https://doi.org/10.1039/C9TA08554H.

(24) Meng, F.; McNeice, J.; Zadeh, S. S.; Ghahreman, A. Review of Lithium Production and Recovery from Minerals, Brines, and Lithium-Ion Batteries. *Miner. Process. Extr. Metall. Rev.* **2021**, *42* (2), 123–141. https://doi.org/10.1080/08827508.2019.1668387.

(25) Vaalma, C.; Buchholz, D.; Weil, M.; Passerini, S. A Cost and Resource Analysis of Sodium-Ion Batteries. *Nat. Rev. Mater.* **2018**, *3* (4), 18013. https://doi.org/10.1038/natrevmats.2018.13.

(26) Hwang, J.-Y.; Myung, S.-T.; Sun, Y.-K. Sodium-Ion Batteries: Present and Future. *Chem. Soc. Rev.* **2017**, *46* (12), 3529–3614. https://doi.org/10.1039/C6CS00776G.

(27) Chayambuka, K.; Mulder, G.; Danilov, D. L.; Notten, P. H. L. Sodium-Ion Battery Materials and Electrochemical Properties Reviewed. *Adv. Energy Mater.* **2018**, *8* (16), 1800079. https://doi.org/10.1002/aenm.201800079.

(28) Yabuuchi, N.; Kubota, K.; Dahbi, M.; Komaba, S. Research Development on Sodium-Ion Batteries. *Chem. Rev.* **2014**, *114* (23), 11636–11682. https://doi.org/10.1021/cr500192f.

(29) Deng, J.; Luo, W.-B.; Chou, S.-L.; Liu, H.-K.; Dou, S.-X. Sodium-Ion Batteries: From Academic Research to Practical Commercialization. *Adv. Energy Mater.* **2018**, *8* (4), 1701428. https://doi.org/10.1002/aenm.201701428.

(30) Liu, Y.; Zhang, S.; Zhu, T. Germanium-Based Electrode Materials for Lithium-Ion Batteries. *ChemElectroChem* **2014**, *1* (4), 706–713. https://doi.org/10.1002/celc.201300195.

(31) Guo, A.; Chen, E.; Wygant, B. R.; Heller, A.; Mullins, C. B. Lead Oxide Microparticles Coated by Ethylenediamine-Cross-Linked Graphene Oxide for Lithium Ion Battery Anodes. *ACS Appl. Energy Mater.* **2019**, *2* (5), 3017–3020. https://doi.org/10.1021/acsaem.9b00401.

(32) Zhang, Z.; Zhao, M.; Xia, M.; Qi, R.; Liu, M.; Nie, J.; Wang, Z. L.; Lu, X. Magnesium Anodes with Extended Cycling Stability for Lithium-Ion Batteries. *Adv. Funct. Mater.* **2019**, *29* (41), 1806400. https://doi.org/10.1002/adfm.201806400.

(33) McDowell, M. T.; Lee, S. W.; Nix, W. D.; Cui, Y. 25th Anniversary Article: Understanding the Lithiation of Silicon and Other Alloying Anodes for Lithium-Ion Batteries. *Adv. Mater.* **2013**, *25* (36), 4966–4985. https://doi.org/10.1002/adma.201301795.

(34) Zhang, F.; Wang, J.; Liu, S.; Du, Y. Effects of the Volume Changes and Elastic-Strain Energies on the Phase Transition in the Li-Sn Battery. *J. Power Sources* **2016**, *330*, 111–119. https://doi.org/10.1016/j.jpowsour.2016.08.136.

(35) Stetson, C.; Yin, Y.; Norman, A.; Harvey, S. P.; Schnabel, M.; Ban, C.; Jiang, C.-S.; DeCaluwe, S. C.; Al-Jassim, M. Evolution of Solid Electrolyte Interphase and

Active Material in the Silicon Wafer Model System. *J. Power Sources* **2021**, *482*, 228946. https://doi.org/10.1016/j.jpowsour.2020.228946.

(36) Jaumann, T.; Balach, J.; Langklotz, U.; Sauchuk, V.; Fritsch, M.; Michaelis, A.; Teltevskij, V.; Mikhailova, D.; Oswald, S.; Klose, M.; Stephani, G.; Hauser, R.; Eckert, J.; Giebeler, L. Lifetime vs. Rate Capability: Understanding the Role of FEC and VC in High-Energy Li-Ion Batteries with Nano-Silicon Anodes. *Energy Storage Mater.* **2017**, *6*, 26–35. https://doi.org/10.1016/j.ensm.2016.08.002.

(37) Gauthier, M.; Mazouzi, D.; Reyter, D.; Lestriez, B.; Moreau, P.; Guyomard, D.; Roue, L. A Low-Cost and High Performance Ball-Milled Si-Based Negative Electrode for High-Energy Li-Ion Batteries. *Energy Env. Sci* **2013**, *6* (7), 2145–2155. https://doi.org/10.1039/C3EE41318G.

(38) Beattie, S. D.; Larcher, D.; Morcrette, M.; Simon, B.; Tarascon, J.-M. Si Electrodes for Li-Ion Batteries—A New Way to Look at an Old Problem. *J. Electrochem. Soc.* **2008**, *155* (2), A158–A163. https://doi.org/10.1149/1.2817828.

(39) Lindgren, F.; Rehnlund, D.; Pan, R.; Pettersson, J.; Younesi, R.; Xu, C.; Gustafsson, T.; Edström, K.; Nyholm, L. On the Capacity Losses Seen for Optimized Nano-Si Composite Electrodes in Li-Metal Half-Cells. *Adv. Energy Mater.* **2019**, *9* (33), 1901608. https://doi.org/10.1002/aenm.201901608.

(40) Jeong, Y. K.; Huang, W.; Vilá, R. A.; Huang, W.; Wang, J.; Kim, S. C.; Kim, Y. S.; Zhao, J.; Cui, Y. Microclusters of Kinked Silicon Nanowires Synthesized by a Recyclable Iodide Process for High-Performance Lithium-Ion Battery Anodes. *Adv. Energy Mater.* **2020**, *10* (41), 2002108. https://doi.org/10.1002/aenm.202002108.

(41) Chan, C. K.; Peng, H.; Liu, G.; McIlwrath, K.; Zhang, X. F.; Huggins, R. A.; Cui, Y. High-Performance Lithium Battery Anodes Using Silicon Nanowires. *Nat. Nanotechnol.* **2008**, *3* (1), 31–35. https://doi.org/10.1038/nnano.2007.411.

(42) Li, X.; Gu, M.; Hu, S.; Kennard, R.; Yan, P.; Chen, X.; Wang, C.; Sailor, M. J.; Zhang, J.-G.; Liu, J. Mesoporous Silicon Sponge as an Anti-Pulverization Structure for High-Performance Lithium-Ion Battery Anodes. *Nat. Commun.* **2014**, *5* (1), 1–7. https://doi.org/10.1038/ncomms5105.

(43) Jia, H.; Zheng, J.; Song, J.; Luo, L.; Yi, R.; Estevez, L.; Zhao, W.; Patel, R.; Li, X.; Zhang, J.-G. A Novel Approach to Synthesize Micrometer-Sized Porous Silicon as a High Performance Anode for Lithium-Ion Batteries. *Nano Energy* **2018**, *50*, 589–597. https://doi.org/10.1016/j.nanoen.2018.05.048.

(44) Wang, B.; Ryu, J.; Choi, S.; Zhang, X.; Pribat, D.; Li, X.; Zhi, L.; Park, S.; Ruoff, R. S. Ultrafast-Charging Silicon-Based Coral-Like Network Anodes for Lithium-Ion Batteries with High Energy and Power Densities. *ACS Nano* **2019**, *13* (2), 2307–2315. https://doi.org/10.1021/acsnano.8b09034.

(45) Weiss, M.; Ruess, R.; Kasnatscheew, J.; Levartovsky, Y.; Levy, N. R.; Minnmann, P.; Stolz, L.; Waldmann, T.; Wohlfahrt-Mehrens, M.; Aurbach, D.; Winter, M.; Ein-Eli, Y.; Janek, J. Fast Charging of Lithium-Ion Batteries: A Review of Materials Aspects. *Adv. Energy Mater.* **2021**, *11* (33), 2101126. https://doi.org/10.1002/aenm.202101126.

(46) Lin, J.; Peng, H.; Kim, J.-H.; Wygant, B. R.; Meyerson, M. L.; Rodriguez, R.; Liu, Y.; Kawashima, K.; Gu, D.; Peng, D.-L.; Guo, H.; Heller, A.; Mullins, C. B. Lithium

Fluoride Coated Silicon Nanocolumns as Anodes for Lithium Ion Batteries. *ACS Appl. Mater. Interfaces* **2020**. https://doi.org/10.1021/acsami.9b23106.

(47) Patnaik, S. G.; Jayakumar, T. P.; Sawamura, Y.; Matsumi, N. Defined Poly(Borosiloxane) as an Artificial Solid Electrolyte Interphase Layer for Thin-Film Silicon Anodes. *ACS Appl. Energy Mater.* **2021**, *4* (3), 2241–2247. https://doi.org/10.1021/acsaem.0c02749.

(48) Yan, Y.; He, Y.-S.; Zhao, X.; Zhao, W.; Ma, Z.-F.; Yang, X. Regulating Adhesion of Solid-Electrolyte Interphase to Silicon via Covalent Bonding Strategy towards High Coulombic-Efficiency Anodes. *Nano Energy* **2021**, *84*, 105935. https://doi.org/10.1016/j.nanoen.2021.105935.

(49) Etacheri, V.; Haik, O.; Goffer, Y.; Roberts, G. A.; Stefan, I. C.; Fasching, R.; Aurbach, D. Effect of Fluoroethylene Carbonate (FEC) on the Performance and Surface Chemistry of Si-Nanowire Li-Ion Battery Anodes. *Langmuir* **2012**, *28* (1), 965–976. https://doi.org/10.1021/la203712s.

(50) Markevich, E.; Salitra, G.; Aurbach, D. Fluoroethylene Carbonate as an Important Component for the Formation of an Effective Solid Electrolyte Interphase on Anodes and Cathodes for Advanced Li-Ion Batteries. *ACS Energy Lett.* **2017**, *2* (6), 1337–1345. https://doi.org/10.1021/acsenergylett.7b00163.

(51) Kim, K.; Ma, H.; Park, S.; Choi, N.-S. Electrolyte-Additive-Driven Interfacial Engineering for High-Capacity Electrodes in Lithium-Ion Batteries: Promise and Challenges. *ACS Energy Lett.* **2020**, *5* (5), 1537–1553. https://doi.org/10.1021/acsenergylett.0c00468.

(52) Han, S.-D.; Wood, K. N.; Stetson, C.; Norman, A. G.; Brumbach, M. T.; Coyle, J.; Xu, Y.; Harvey, S. P.; Teeter, G.; Zakutayev, A.; Burrell, A. K. Intrinsic Properties of Individual Inorganic Silicon–Electrolyte Interphase Constituents. *ACS Appl. Mater. Interfaces* **2019**, *11* (50), 46993–47002. https://doi.org/10.1021/acsami.9b18252.

(53) Gargh, P.; Sarkar, A.; Lui, Y. H.; Shen, S.; Hu, C.; Hu, S.; Nlebedim, I. C.; Shrotriya, P. Correlating Capacity Fade with Film Resistance Loss in Fast Charging of Lithium-Ion Battery. *J. Power Sources* **2021**, *485*, 229360. https://doi.org/10.1016/j.jpowsour.2020.229360.

(54) Stetson, C.; Yoon, T.; Coyle, J.; Nemeth, W.; Young, M.; Norman, A.; Pylypenko, S.; Ban, C.; Jiang, C.-S.; Al-Jassim, M.; Burrell, A. Three-Dimensional Electronic Resistivity Mapping of Solid Electrolyte Interphase on Si Anode Materials. *Nano Energy* **2018**, *55* (C). https://doi.org/10.1016/j.nanoen.2018.11.007.

(55) Peled, E.; Menkin, S. Review—SEI: Past, Present and Future. *J. Electrochem. Soc.* **2017**, *164* (7), A1703–A1719. https://doi.org/10.1149/2.1441707jes.

(56) Yin, Y.; Arca, E.; Wang, L.; Yang, G.; Schnabel, M.; Cao, L.; Xiao, C.; Zhou, H.; Liu, P.; Nanda, J.; Teeter, G.; Eichhorn, B.; Xu, K.; Burrell, A.; Ban, C. Nonpassivated Silicon Anode Surface. *ACS Appl. Mater. Interfaces* **2020**, *12* (23), 26593–26600. https://doi.org/10.1021/acsami.0c03799.

(57) Jin, Y.; Kneusels, N.-J. H.; Magusin, P. C. M. M.; Kim, G.; Castillo-Martínez, E.; Marbella, L. E.; Kerber, R. N.; Howe, D. J.; Paul, S.; Liu, T.; Grey, C. P. Identifying the Structural Basis for the Increased Stability of the Solid Electrolyte Interphase

Formed on Silicon with the Additive Fluoroethylene Carbonate. *J. Am. Chem. Soc.* **2017**, *139* (42), 14992–15004. https://doi.org/10.1021/jacs.7b06834.

(58) Peled, E.; Golodnitsky, D.; Ardel, G. Advanced Model for Solid Electrolyte Interphase Electrodes in Liquid and Polymer Electrolytes. *J. Electrochem. Soc.* **1997**, *144* (8), L208. https://doi.org/10.1149/1.1837858.

(59) Zhu, T.; Hu, Q.; Yan, G.; Wang, J.; Wang, Z.; Guo, H.; Li, X.; Peng, W. Manipulating the Composition and Structure of Solid Electrolyte Interphase at Graphite Anode by Adjusting the Formation Condition. *Energy Technol.* **2019**, *7* (9), 1900273. https://doi.org/10.1002/ente.201900273.

(60) Zhang, W.; Cai, T. H.; Sheldon, B. W. The Impact of Initial SEI Formation Conditions on Strain-Induced Capacity Losses in Silicon Electrodes. *Adv. Energy Mater.* **2019**, *9* (5), 1803066. https://doi.org/10.1002/aenm.201803066.

(61) Cao, C.; Abate, I. I.; Sivonxay, E.; Shyam, B.; Jia, C.; Moritz, B.; Devereaux, T. P.; Persson, K. A.; Steinrück, H.-G.; Toney, M. F. Solid Electrolyte Interphase on Native Oxide-Terminated Silicon Anodes for Li-Ion Batteries. *Joule* **2019**, *3* (3), 762–781. https://doi.org/10.1016/j.joule.2018.12.013.

(62) Schroder, K. W.; Celio, H.; Webb, L. J.; Stevenson, K. J. Examining Solid Electrolyte Interphase Formation on Crystalline Silicon Electrodes: Influence of Electrochemical Preparation and Ambient Exposure Conditions. *J. Phys. Chem. C* **2012**, *116* (37), 19737–19747. https://doi.org/10.1021/jp307372m.

(63) Philippe, B.; Dedryvère, R.; Allouche, J.; Lindgren, F.; Gorgoi, M.; Rensmo, H.; Gonbeau, D.; Edström, K. Nanosilicon Electrodes for Lithium-Ion Batteries: Interfacial Mechanisms Studied by Hard and Soft X-Ray Photoelectron

Spectroscopy. *Chem. Mater.* **2012**, *24* (6), 1107–1115. https://doi.org/10.1021/cm2034195.

(64) Xu, K. Nonaqueous Liquid Electrolytes for Lithium-Based Rechargeable Batteries. *Chem. Rev.* **2004**, *104* (10), 4303–4418. https://doi.org/10.1021/cr030203g.

(65) Campion, C. L.; Li, W.; Lucht, B. L. Thermal Decomposition of LiPF6-Based Electrolytes for Lithium-Ion Batteries. *J. Electrochem. Soc.* **2005**, *152* (12), A2327–A2334. https://doi.org/10.1149/1.2083267.

(66) Michan, A. L.; Divitini, G.; Pell, A. J.; Leskes, M.; Ducati, C.; Grey, C. P. Solid Electrolyte Interphase Growth and Capacity Loss in Silicon Electrodes. *J. Am. Chem. Soc.* **2016**, *138* (25), 7918–7931. https://doi.org/10.1021/jacs.6b02882.

(67) Li, F.; Xu, J.; Hou, Z.; Li, M.; Yang, R. Silicon Anodes for High-Performance Storage Devices: Structural Design, Material Compounding, Advances in Electrolytes and Binders. *ChemNanoMat* **2020**, *6* (6), 720–738. https://doi.org/10.1002/cnma.201900708.

(68) Xu, Z.; Yang, J.; Li, H.; Nuli, Y.; Wang, J. Electrolytes for Advanced Lithium Ion Batteries Using Silicon-Based Anodes. *J. Mater. Chem. A* **2019**, *7* (16), 9432–9446. https://doi.org/10.1039/C9TA01876J.

(69) Jin, Y.; Kneusels, N.-J. H.; Marbella, L. E.; Castillo-Martínez, E.; Magusin, P. C. M. M.; Weatherup, R. S.; Jónsson, E.; Liu, T.; Paul, S.; Grey, C. P. Understanding Fluoroethylene Carbonate and Vinylene Carbonate Based Electrolytes for Si Anodes in Lithium Ion Batteries with NMR Spectroscopy. *J. Am. Chem. Soc.* **2018**, *140* (31), 9854–9867. https://doi.org/10.1021/jacs.8b03408.

(70) Schroder, K.; Alvarado, J.; Yersak, T. A.; Li, J.; Dudney, N.; Webb, L. J.; Meng, Y. S.; Stevenson, K. J. The Effect of Fluoroethylene Carbonate as an Additive on the Solid Electrolyte Interphase on Silicon Lithium-Ion Electrodes. *Chem. Mater.* **2015**, *27* (16), 5531–5542. https://doi.org/10.1021/acs.chemmater.5b01627.

(71) Jung, R.; Metzger, M.; Haering, D.; Solchenbach, S.; Marino, C.; Tsiouvaras, N.; Stinner, C.; Gasteiger, H. A. Consumption of Fluoroethylene Carbonate (FEC) on Si-C Composite Electrodes for Li-Ion Batteries. *J. Electrochem. Soc.* **2016**, *163* (8), A1705–A1716. https://doi.org/10.1149/2.0951608jes.

(72) Eshetu, G. G.; Figgemeier, E. Confronting the Challenges of Next-Generation Silicon Anode-Based Lithium-Ion Batteries: Role of Designer Electrolyte Additives and Polymeric Binders. *ChemSusChem* **2019**, *12* (12), 2515–2539. https://doi.org/10.1002/cssc.201900209.

(73) Gu, M.; Wang, Z.; Connell, J. G.; Perea, D. E.; Lauhon, L. J.; Gao, F.; Wang, C. Electronic Origin for the Phase Transition from Amorphous LixSi to Crystalline Li15Si4. *ACS Nano* **2013**, *7* (7), 6303–6309. https://doi.org/10.1021/nn402349j.

(74) Okamoto, H. The Li-Si (Lithium-Silicon) System. *Bull. Alloy Phase Diagr.* **1990**, *11* (3), 306–312. https://doi.org/10.1007/BF03029305.

(75) Obrovac, M. N.; Christensen, L. Structural Changes in Silicon Anodes during Lithium Insertion/Extraction. *Electrochem. Solid-State Lett.* **2004**, *7* (5), A93–A96. https://doi.org/10.1149/1.1652421.

(76) Kwon, J. Y.; Ryu, J. H.; Oh, S. M. Performance of Electrochemically Generated Li21Si5 Phase for Lithium-Ion Batteries. *Electrochimica Acta* **2010**, *55* (27), 8051–8055. https://doi.org/10.1016/j.electacta.2010.01.054.

(77) Iaboni, D. S. M.; Obrovac, M. N. Li15Si4 Formation in Silicon Thin Film Negative Electrodes. *J. Electrochem. Soc.* **2016**, *163* (2), A255–A261. https://doi.org/10.1149/2.0551602jes.

(78) Gao, H.; Xiao, L.; Plümel, I.; Xu, G.-L.; Ren, Y.; Zuo, X.; Liu, Y.; Schulz, C.; Wiggers, H.; Amine, K.; Chen, Z. Parasitic Reactions in Nanosized Silicon Anodes for Lithium-Ion Batteries. *Nano Lett.* **2017**, *17* (3), 1512–1519. https://doi.org/10.1021/acs.nanolett.6b04551.

(79) Schott, T.; Robert, R.; Ulmann, P. A.; Lanz, P.; Zürcher, S.; Spahr, M. E.; Novák, P.; Trabesinger, S. Cycling Behavior of Silicon-Containing Graphite Electrodes, Part A: Effect of the Lithiation Protocol. *J. Phys. Chem. C* **2017**, *121* (34), 18423–18429. https://doi.org/10.1021/acs.jpcc.7b05919.

(80) Zhang, Y.; Du, N.; Yang, D. Designing Superior Solid Electrolyte Interfaces on Silicon Anodes for High-Performance Lithium-Ion Batteries. *Nanoscale* **2019**, *11* (41), 19086–19104. https://doi.org/10.1039/C9NR05748J.

(81) Ge, M.; Cao, C.; Biesold, G. M.; Sewell, C. D.; Hao, S.-M.; Huang, J.; Zhang, W.; Lai, Y.; Lin, Z. Recent Advances in Silicon-Based Electrodes: From Fundamental Research toward Practical Applications. *Adv. Mater.* **2021**, *33* (16), 2004577. https://doi.org/10.1002/adma.202004577.

(82) Stram, L.; Miroshnikov, Y.; Zitoun, D. Lithiation Kinetics in Silicon/Mn3O4 Core–Shell Nanoparticles Anodes for Li-Ion Battery. *Chem. Mater.* **2019**, *31* (20), 8320–8327. https://doi.org/10.1021/acs.chemmater.9b01470.

(83) Ai, Q.; Li, D.; Guo, J.; Hou, G.; Sun, Q.; Sun, Q.; Xu, X.; Zhai, W.; Zhang, L.; Feng, J.; Si, P.; Lou, J.; Ci, L. Artificial Solid Electrolyte Interphase Coating to

Reduce Lithium Trapping in Silicon Anode for High Performance Lithium-Ion Batteries. *Adv. Mater. Interfaces* **2019**, *6* (21), 1901187. https://doi.org/10.1002/admi.201901187.

(84) Ronneburg, A.; Silvi, L.; Cooper, J.; Harbauer, K.; Ballauff, M.; Risse, S. Solid Electrolyte Interphase Layer Formation during Lithiation of Single-Crystal Silicon Electrodes with a Protective Aluminum Oxide Coating. *ACS Appl. Mater. Interfaces* **2021**, *13* (18), 21241–21249. https://doi.org/10.1021/acsami.1c01725.

(85) Li, J.; Dudney, N. J.; Nanda, J.; Liang, C. Artificial Solid Electrolyte Interphase To Address the Electrochemical Degradation of Silicon Electrodes. *ACS Appl. Mater. Interfaces* **2014**, *6* (13), 10083–10088. https://doi.org/10.1021/am5009419.

(86) Jiang, S.; Hu, B.; Sahore, R.; Zhang, L.; Liu, H.; Zhang, L.; Lu, W.; Zhao, B.; Zhang, Z. Surface-Functionalized Silicon Nanoparticles as Anode Material for Lithium-Ion Battery. *ACS Appl. Mater. Interfaces* **2018**, *10* (51), 44924–44931. https://doi.org/10.1021/acsami.8b17729.

(87) Li, Y.; Lu, J.; Wang, Z.; Wang, X.; Yuan, H.; Qin, N.; Yi, Z.; Chen, Z.; Gu, S.; Lu, Z. Suppressing Continuous Volume Expansion of Si Nanoparticles by an Artificial Solid Electrolyte Interphase for High-Performance Lithium-Ion Batteries. *ACS Sustain. Chem. Eng.* **2021**, *9* (24), 8059–8068. https://doi.org/10.1021/acssuschemeng.0c08964.

(88) Buriak, J. M. Illuminating Silicon Surface Hydrosilylation: An Unexpected Plurality of Mechanisms. *Chem. Mater.* **2014**, *26* (1), 763–772. https://doi.org/10.1021/cm402120f.

(89) van Druenen, M.; Collins, G.; Glynn, C.; O'Dwyer, C.; Holmes, J. D. Functionalization of SiO2 Surfaces for Si Monolayer Doping with Minimal Carbon Contamination. *ACS Appl. Mater. Interfaces* **2018**, *10* (2), 2191–2201. https://doi.org/10.1021/acsami.7b16950.

(90) Schulze, M. C.; Carroll, G. M.; Martin, T. R.; Sanchez-Rivera, K.; Urias, F.; Neale, N. R. Hydrophobic versus Hydrophilic Interfacial Coatings on Silicon Nanoparticles Teach Us How to Design the Solid Electrolyte Interphase in Silicon-Based Li-Ion Battery Anodes. *ACS Appl. Energy Mater.* **2021**. https://doi.org/10.1021/acsaem.0c02817.

(91) Gao, Y.; Yi, R.; Li, Y. C.; Song, J.; Chen, S.; Huang, Q.; Mallouk, T. E.; Wang, D. General Method of Manipulating Formation, Composition, and Morphology of Solid-Electrolyte Interphases for Stable Li-Alloy Anodes. *J. Am. Chem. Soc.* **2017**, *139* (48), 17359–17367. https://doi.org/10.1021/jacs.7b07584.

(92) Hailu, A. G.; Wang, F.-M.; Ramar, A.; Tiong, P.-W. L.; Yeh, N.-H.; Hsu, C.-C.; Chang, Y.-J.; Chen, M.-M.; Chen, T.-W.; Huang, C.-W.; Yu, P.-X.; Chang, C.-K.; Hsing, C.-D. R.; Merinda, L.; Wang, C.-C.; Kahsay, B. A. Tailoring of a Reinforcing and Artificial Self-Assembled Alkyl Sulfonic Acid Layer Electrolyte Interphase on Silicon as an Anode for High-Energy-Density Lithium-Ion Batteries. *Electrochimica Acta* **2022**, *421*, 140489. https://doi.org/10.1016/j.electacta.2022.140489.

(93) Xu, Z.; Yang, J.; Zhang, T.; Nuli, Y.; Wang, J.; Hirano, S. Silicon Microparticle Anodes with Self-Healing Multiple Network Binder. *Joule* **2018**, *2* (5), 950–961. https://doi.org/10.1016/j.joule.2018.02.012.

(94) Schnabel, M.; Harvey, S. P.; Arca, E.; Stetson, C.; Teeter, G.; Ban, C.; Stradins, P. Surface SiO2 Thickness Controls Uniform-to-Localized Transition in Lithiation of Silicon Anodes for Lithium-Ion Batteries. *ACS Appl. Mater. Interfaces* **2020**, *12* (24), 27017–27028. https://doi.org/10.1021/acsami.0c03158.

(95) Onclin, S.; Ravoo, B. J.; Reinhoudt, D. N. Engineering Silicon Oxide Surfaces Using Self-Assembled Monolayers. *Angew. Chem. Int. Ed.* **2005**, *44* (39), 6282–6304. https://doi.org/10.1002/anie.200500633.

(96) Shen, B. H.; Veith, G. M.; Tenhaeff, W. E. Silicon Surface Tethered Polymer as Artificial Solid Electrolyte Interface. *Sci. Rep.* **2018**, *8* (1), 11549. https://doi.org/10.1038/s41598-018-30000-z.

(97) Jung, C.-H.; Kim, K.-H.; Hong, S.-H. Stable Silicon Anode for Lithium-Ion Batteries through Covalent Bond Formation with a Binder via Esterification. *ACS Appl. Mater. Interfaces* **2019**, *11* (30), 26753–26763. https://doi.org/10.1021/acsami.9b03866.

(98) Jiang, S.; Hu, B.; Sahore, R.; Liu, H.; Pach, G. F.; Carroll, G. M.; Zhang, L.; Zhao, B.; Neale, N. R.; Zhang, Z. Tailoring the Surface of Silicon Nanoparticles for Enhanced Chemical and Electrochemical Stability for Li-Ion Batteries. *ACS Appl. Energy Mater.* **2019**, *2* (9), 6176–6183. https://doi.org/10.1021/acsaem.9b01601.

(99) Qian, C.; Zhao, J.; Sun, Y.; Lee, H. R.; Luo, L.; Makaremi, M.; Mukherjee, S.; Wang, J.; Zu, C.; Xia, M.; Wang, C.; Singh, C. V.; Cui, Y.; Ozin, G. A. Electrolyte-Phobic Surface for the Next-Generation Nanostructured Battery Electrodes. *Nano Lett.* **2020**, *20* (10), 7455–7462. https://doi.org/10.1021/acs.nanolett.0c02880.

(100) Trucks, G. W.; Raghavachari, K.; Higashi, G. S.; Chabal, Y. J. Mechanism of HF Etching of Silicon Surfaces: A Theoretical Understanding of Hydrogen Passivation. *Phys. Rev. Lett.* **1990**, *65* (4), 504–507. https://doi.org/10.1103/PhysRevLett.65.504.

(101) Buriak, J. M. Organometallic Chemistry on Silicon and Germanium Surfaces. *Chem. Rev.* **2002**, *102* (5), 1271–1308. https://doi.org/10.1021/cr000064s.

(102) Zhong, L.; Beaudette, C.; Guo, J.; Bozhilov, K.; Mangolini, L. Tin Nanoparticles as an Effective Conductive Additive in Silicon Anodes. *Sci. Rep.* **2016**, *6* (1), 30952. https://doi.org/10.1038/srep30952.

(103) Xin, F.; Whittingham, M. S. Challenges and Development of Tin-Based Anode with High Volumetric Capacity for Li-Ion Batteries. *Electrochem. Energy Rev.* **2020**, *3* (4), 643–655. https://doi.org/10.1007/s41918-020-00082-3.

(104) Xu, Y.; Liu, Q.; Zhu, Y.; Liu, Y.; Langrock, A.; Zachariah, M. R.; Wang, C. Uniform Nano-Sn/C Composite Anodes for Lithium Ion Batteries. *Nano Lett.* **2013**, *13* (2), 470–474. https://doi.org/10.1021/nl303823k.

(105) Pender, J. P.; Jha, G.; Youn, D. H.; Ziegler, J. M.; Andoni, I.; Choi, E. J.; Heller, A.; Dunn, B. S.; Weiss, P. S.; Penner, R. M.; Mullins, C. B. Electrode Degradation in Lithium-Ion Batteries. *ACS Nano* **2020**, *14* (2), 1243–1295. https://doi.org/10.1021/acsnano.9b04365.

(106) Liu, X. H.; Zhong, L.; Huang, S.; Mao, S. X.; Zhu, T.; Huang, J. Y. Size-Dependent Fracture of Silicon Nanoparticles During Lithiation. *ACS Nano* **2012**, *6* (2), 1522–1531. https://doi.org/10.1021/nn204476h.

(107) Leblanc, D.; Wang, C.; He, Y.; Bélanger, D.; Zaghib, K. In Situ Transmission Electron Microscopy Observations of Lithiation of Spherical Silicon Nanopowder Produced by Induced Plasma Atomization. *J. Power Sources* **2015**, *279*, 522–527. https://doi.org/10.1016/j.jpowsour.2014.12.060.

(108) Chen, C.-Y.; Sano, T.; Tsuda, T.; Ui, K.; Oshima, Y.; Yamagata, M.; Ishikawa, M.; Haruta, M.; Doi, T.; Inaba, M.; Kuwabata, S. In Situ Scanning Electron Microscopy of Silicon Anode Reactions in Lithium-Ion Batteries during Charge/Discharge Processes. *Sci. Rep.* **2016**, *6* (1), 36153. https://doi.org/10.1038/srep36153.

(109) Li, J.; Xu, X.; Luo, Z.; Zhang, C.; Yu, X.; Zuo, Y.; Zhang, T.; Tang, P.; Arbiol, J.; Llorca, J.; Liu, J.; Cabot, A. Compositionally Tuned NixSn Alloys as Anode Materials for Lithium-Ion and Sodium-Ion Batteries with a High Pseudocapacitive Contribution. *Electrochimica Acta* **2019**, *304*, 246–254. https://doi.org/10.1016/j.electacta.2019.02.098.

(110) Park, M.-G.; Lee, D.-H.; Jung, H.; Choi, J.-H.; Park, C.-M. Sn-Based Nanocomposite for Li-Ion Battery Anode with High Energy Density, Rate Capability, and Reversibility. *ACS Nano* **2018**, *12* (3), 2955–2967. https://doi.org/10.1021/acsnano.8b00586.

(111) Zhang, M.; Wang, T.; Cao, G. Promises and Challenges of Tin-Based Compounds as Anode Materials for Lithium-Ion Batteries. *Int. Mater. Rev.* **2015**, *60* (6), 330–352. https://doi.org/10.1179/1743280415Y.0000000004.

(112) Jiang, B.; He, Y.; Li, B.; Zhao, S.; Wang, S.; He, Y.-B.; Lin, Z. Polymer-Templated Formation of Polydopamine-Coated SnO2 Nanocrystals: Anodes for Cyclable

Lithium-Ion Batteries. *Angew. Chem. Int. Ed.* **2017**, *56* (7), 1869–1872. https://doi.org/10.1002/anie.201611160.

(113) Jiang, Y.; Song, D.; Wu, J.; Wang, Z.; Huang, S.; Xu, Y.; Chen, Z.; Zhao, B.; Zhang, J. Sandwich-like SnS2/Graphene/SnS2 with Expanded Interlayer Distance as High-Rate Lithium/Sodium-Ion Battery Anode Materials. *ACS Nano* **2019**, *13* (8), 9100–9111. https://doi.org/10.1021/acsnano.9b03330.

(114) Wang, J.; Luo, C.; Mao, J.; Zhu, Y.; Fan, X.; Gao, T.; Mignerey, A. C.; Wang, C. Solid-State Fabrication of SnS2/C Nanospheres for High-Performance Sodium Ion Battery Anode. *ACS Appl. Mater. Interfaces* **2015**, *7* (21), 11476–11481. https://doi.org/10.1021/acsami.5b02413.

(115) Courtney, I. A.; Tse, J. S.; Mao, O.; Hafner, J.; Dahn, J. R. Ab Initio Calculation of the Lithium-Tin Voltage Profile. *Phys. Rev. B* **1998**, *58* (23), 15583–15588. https://doi.org/10.1103/PhysRevB.58.15583.

(116) Sangster, J.; Bale, C. W. The Li-Sn (Lithium-Tin) System. *J. Phase Equilibria* **1998**, *19* (1), 70–75. https://doi.org/10.1007/s12385-006-5008-6.

(117) Wang, L.; Ni, Y.; Lei, K.; Dong, H.; Tian, S.; Li, F. 3D Porous Tin Created by Tuning the Redox Potential Acts as an Advanced Electrode for Sodium-Ion Batteries. *ChemSusChem* **2018**, *11* (19), 3376–3381. https://doi.org/10.1002/cssc.201801662.

(118) Schweidler, S.; de Biasi, L.; Schiele, A.; Hartmann, P.; Brezesinski, T.; Janek, J. Volume Changes of Graphite Anodes Revisited: A Combined Operando X-Ray Diffraction and In Situ Pressure Analysis Study. *J. Phys. Chem. C* **2018**, *122* (16), 8829–8835. https://doi.org/10.1021/acs.jpcc.8b01873.

(119) Otero, M.; Heim, C.; Leiva, E. P. M.; Wagner, N.; Friedrich, A. Design-Considerations Regarding Silicon/Graphite and Tin/Graphite Composite Electrodes for Lithium-Ion Batteries. *Sci. Rep.* **2018**, *8* (1), 15851. https://doi.org/10.1038/s41598-018-33405-y.

(120) Datta, M. K.; Epur, R.; Saha, P.; Kadakia, K.; Park, S. K.; Kumta, P. N. Tin and Graphite Based Nanocomposites: Potential Anode for Sodium Ion Batteries. *J. Power Sources* **2013**, *225*, 316–322. https://doi.org/10.1016/j.jpowsour.2012.10.014.

(121) Chae, S.; Choi, S.-H.; Kim, N.; Sung, J.; Cho, J. Integration of Graphite and Silicon Anodes for the Commercialization of High-Energy Lithium-Ion Batteries. *Angew. Chem. Int. Ed.* **2020**, *59* (1), 110–135. https://doi.org/10.1002/anie.201902085.

(122) Sohn, M.; Lee, D. G.; Park, H.-I.; Park, C.; Choi, J.-H.; Kim, H. Microstructure Controlled Porous Silicon Particles as a High Capacity Lithium Storage Material via Dual Step Pore Engineering. *Adv. Funct. Mater.* **2018**, *28* (23), 1800855. https://doi.org/10.1002/adfm.201800855.

(123) Yoon, Y. S.; Jee, S. H.; Lee, S. H.; Nam, S. C. Nano Si-Coated Graphite Composite Anode Synthesized by Semi-Mass Production Ball Milling for Lithium Secondary Batteries. *Surf. Coat. Technol.* **2011**, *206* (2), 553–558. https://doi.org/10.1016/j.surfcoat.2011.07.076.

(124) Wang, C. S.; Wu, G. T.; Zhang, X. B.; Qi, Z. F.; Li, W. Z. Lithium Insertion in Carbon-Silicon Composite Materials Produced by Mechanical Milling. *J. Electrochem. Soc.* **1998**, *145* (8), 2751. https://doi.org/10.1149/1.1838709.

(125) Moriwake, H.; Kuwabara, A.; Fisher, C. A. J.; Ikuhara, Y. Why Is Sodium-Intercalated Graphite Unstable? *RSC Adv.* **2017**, *7* (58), 36550–36554. https://doi.org/10.1039/C7RA06777A.

(126) Palaniselvam, T.; Babu, B.; Moon, H.; Hasa, I.; Santhosha, A. L.; Goktas, M.; Sun, Y.-N.; Zhao, L.; Han, B.-H.; Passerini, S.; Balducci, A.; Adelhelm, P. Tin-Containing Graphite for Sodium-Ion Batteries and Hybrid Capacitors. *Batter. Supercaps* **2021**, *4* (1), 173–182. https://doi.org/10.1002/batt.202000196.

(127) Dou, X.; Hasa, I.; Saurel, D.; Vaalma, C.; Wu, L.; Buchholz, D.; Bresser, D.; Komaba, S.; Passerini, S. Hard Carbons for Sodium-Ion Batteries: Structure, Analysis, Sustainability, and Electrochemistry. *Mater. Today* **2019**, *23*, 87–104. https://doi.org/10.1016/j.mattod.2018.12.040.

(128) Bommier, C.; Surta, T. W.; Dolgos, M.; Ji, X. New Mechanistic Insights on Na-Ion Storage in Nongraphitizable Carbon. *Nano Lett.* **2015**, *15* (9), 5888–5892. https://doi.org/10.1021/acs.nanolett.5b01969.

(129) Stevens, D. A.; Dahn, J. R. The Mechanisms of Lithium and Sodium Insertion in Carbon Materials. *J. Electrochem. Soc.* **2001**, *148* (8), A803–A811. https://doi.org/10.1149/1.1379565.

(130) Zhang, B.; Ghimbeu, C. M.; Laberty, C.; Vix-Guterl, C.; Tarascon, J.-M. Correlation Between Microstructure and Na Storage Behavior in Hard Carbon. *Adv. Energy Mater.* **2016**, *6* (1), 1501588. https://doi.org/10.1002/aenm.201501588.

(131) Ogata, K.; Salager, E.; Kerr, C. J.; Fraser, A. E.; Ducati, C.; Morris, A. J.; Hofmann, S.; Grey, C. P. Revealing Lithium–Silicide Phase Transformations in

Nano-Structured Silicon-Based Lithium Ion Batteries via in Situ NMR Spectroscopy. *Nat. Commun.* **2014**, *5*, 3217.

(132) Obrovac, M. N.; Krause, L. J. Reversible Cycling of Crystalline Silicon Powder. *J. Electrochem. Soc.* **2006**, *154* (2), A103. https://doi.org/10.1149/1.2402112.

(133) Li, J.; Dahn, J. R. An In Situ X-Ray Diffraction Study of the Reaction of Li with Crystalline Si. *J. Electrochem. Soc.* **2007**, *154* (3), A156–A161. https://doi.org/10.1149/1.2409862.

(134) Key, B.; Bhattacharyya, R.; Morcrette, M.; Seznéc, V.; Tarascon, J.-M.; Grey, C. P. Real-Time NMR Investigations of Structural Changes in Silicon Electrodes for Lithium-Ion Batteries. *J. Am. Chem. Soc.* **2009**, *131* (26), 9239–9249. https://doi.org/10.1021/ja8086278.

(135) Tornheim, A.; Trask, S. E.; Zhang, Z. Communication—Effect of Lower Cutoff Voltage on the 1st Cycle Performance of Silicon Electrodes. *J. Electrochem. Soc.* **2019**, *166* (2), A132. https://doi.org/10.1149/2.0111902jes.

(136) Baggetto, L.; Oudenhoven, J. F. M.; van Dongen, T.; Klootwijk, J. H.; Mulder, M.; Niessen, R. A. H.; de Croon, M. H. J. M.; Notten, P. H. L. On the Electrochemistry of an Anode Stack for All-Solid-State 3D-Integrated Batteries. *J. Power Sources* **2009**, *189* (1), 402–410. https://doi.org/10.1016/j.jpowsour.2008.07.076.

(137) Kubota, Y.; Escaño, M. C. S.; Nakanishi, H.; Kasai, H. Crystal and Electronic Structure of Li15Si4. *J. Appl. Phys.* **2007**, *102* (5), 053704. https://doi.org/10.1063/1.2775999.

(138) Xie, H.; Sayed, S. Y.; Kalisvaart, W. P.; Schaper, S. J.; Müller-Buschbaum, P.; Luber, E. J.; Olsen, B. C.; Haese, M.; Buriak, J. M. Adhesion and Surface Layers

on Silicon Anodes Suppress Formation of C-$Li_{3.75}Si$ and Solid-Electrolyte Interphase. *ACS Appl. Energy Mater.* **2020**, *3* (2), 1609–1616. https://doi.org/10.1021/acsaem.9b02090.

(139) Wang, Y.; Cao, S.; Kalinina, M.; Zheng, L.; Li, L.; Zhu, M.; Obrovac, M. N. Lithium Insertion in Nanostructured Si1-XTix Alloys. *J. Electrochem. Soc.* **2017**, *164* (13), A3006–A3010. https://doi.org/10.1149/2.0491713jes.

(140) Obrovac, M. N. Si-Alloy Negative Electrodes for Li-Ion Batteries. *Curr. Opin. Electrochem.* **2018**, *9*, 8–17. https://doi.org/10.1016/j.coelec.2018.02.002.

(141) Bärmann, P.; Krueger, B.; Casino, S.; Winter, M.; Placke, T.; Wittstock, G. Impact of the Crystalline $Li_{15}Si_4$ Phase on the Self-Discharge Mechanism of Silicon Negative Electrodes in Organic Electrolytes. *ACS Appl. Mater. Interfaces* **2020**. https://doi.org/10.1021/acsami.0c16742.

(142) McDowell, M. T.; Lee, S. W.; Harris, J. T.; Korgel, B. A.; Wang, C.; Nix, W. D.; Cui, Y. In Situ TEM of Two-Phase Lithiation of Amorphous Silicon Nanospheres. *Nano Lett.* **2013**, *13* (2), 758–764. https://doi.org/10.1021/nl3044508.

(143) Zhao, K.; Pharr, M.; Wan, Q.; Wang, W. L.; Kaxiras, E.; Vlassak, J. J.; Suo, Z. Concurrent Reaction and Plasticity during Initial Lithiation of Crystalline Silicon in Lithium-Ion Batteries. *J. Electrochem. Soc.* **2011**, *159* (3), A238. https://doi.org/10.1149/2.020203jes.

(144) Lee, S. W.; McDowell, M. T.; Berla, L. A.; Nix, W. D.; Cui, Y. Fracture of Crystalline Silicon Nanopillars during Electrochemical Lithium Insertion. *Proc. Natl. Acad. Sci.* **2012**, *109* (11), 4080–4085. https://doi.org/10.1073/pnas.1201088109.

(145) Ryu, I.; Choi, J. W.; Cui, Y.; Nix, W. D. Size-Dependent Fracture of Si Nanowire Battery Anodes. *J. Mech. Phys. Solids* **2011**, *59* (9), 1717–1730. https://doi.org/10.1016/j.jmps.2011.06.003.

(146) Erk, C.; Brezesinski, T.; Sommer, H.; Schneider, R.; Janek, J. Toward Silicon Anodes for Next-Generation Lithium Ion Batteries: A Comparative Performance Study of Various Polymer Binders and Silicon Nanopowders. *ACS Appl. Mater. Interfaces* **2013**, *5* (15), 7299–7307. https://doi.org/10.1021/am401642c.

(147) Misra, S.; Liu, N.; Nelson, J.; Hong, S. S.; Cui, Y.; Toney, M. F. In Situ X-Ray Diffraction Studies of (De)Lithiation Mechanism in Silicon Nanowire Anodes. *ACS Nano* **2012**, *6* (6), 5465–5473. https://doi.org/10.1021/nn301339g.

(148) Chevrier, V. L.; Liu, L.; Le, D. B.; Lund, J.; Molla, B.; Reimer, K.; Krause, L. J.; Jensen, L. D.; Figgemeier, E.; Eberman, K. W. Evaluating Si-Based Materials for Li-Ion Batteries in Commercially Relevant Negative Electrodes. *J. Electrochem. Soc.* **2014**, *161* (5), A783–A791. https://doi.org/10.1149/2.066405jes.

(149) Sayed, S. Y.; Kalisvaart, W. P.; Olsen, B. C.; Luber, E. J.; Xie, H.; Buriak, J. M. Alternating Silicon and Carbon Multilayer-Structured Anodes Suppress Formation of the c-Li3.75Si Phase. *Chem. Mater.* **2019**, *31* (17), 6578–6589. https://doi.org/10.1021/acs.chemmater.9b00389.

(150) Sethuraman, V. A.; Srinivasan, V.; Bower, A. F.; Guduru, P. R. In Situ Measurements of Stress-Potential Coupling in Lithiated Silicon. *J. Electrochem. Soc.* **2010**, *157* (11), A1253–A1261. https://doi.org/10.1149/1.3489378.

(151) Bernard, P.; Alper, J. P.; Haon, C.; Herlin-Boime, N.; Chandesris, M. Electrochemical Analysis of Silicon Nanoparticle Lithiation – Effect of Crystallinity

and Carbon Coating Quantity. *J. Power Sources* **2019**, *435*, 226769. https://doi.org/10.1016/j.jpowsour.2019.226769.

(152) Memarzadeh Lotfabad, E.; Kalisvaart, P.; Kohandehghan, A.; Cui, K.; Kupsta, M.; Farbod, B.; Mitlin, D. Si Nanotubes ALD Coated with TiO 2 , TiN or Al 2 O 3 as High Performance Lithium Ion Battery Anodes. *J. Mater. Chem. A* **2014**, *2* (8), 2504–2516. https://doi.org/10.1039/C3TA14302C.

(153) Du, Z.; Hatchard, T. D.; Dunlap, R. A.; Obrovac, M. N. Combinatorial Investigations of Ni-Si Negative Electrode Materials for Li-Ion Batteries. *J. Electrochem. Soc.* **2015**, *162* (9), A1858–A1863. https://doi.org/10.1149/2.0731509jes.

(154) Du, Z.; Ellis, S. N.; Dunlap, R. A.; Obrovac, M. N. NixSi1-x Alloys Prepared by Mechanical Milling as Negative Electrode Materials for Lithium Ion Batteries. *J. Electrochem. Soc.* **2016**, *163* (2), A13–A18. https://doi.org/10.1149/2.0011602jes.

(155) Du, Z.; Liu, H.; Ellis, S. N.; Dunlap, R. A.; Zhu, M.; Obrovac, M. N. Electrochemistry of CuxSi1−x Alloys in Li Cells. *J. Electrochem. Soc.* **2016**, *163* (7), A1275–A1279. https://doi.org/10.1149/2.0811607jes.

(156) Liu, Y.; Sun, W.; Lan, X.; Hu, R.; Cui, J.; Liu, J.; Liu, J.; Zhang, Y.; Zhu, M. Adding Metal Carbides to Suppress the Crystalline $Li_{15}Si_4$ Formation: A Route toward Cycling Durable Si-Based Anodes for Lithium-Ion Batteries. *ACS Appl. Mater. Interfaces* **2019**, *11* (42), 38727–38736. https://doi.org/10.1021/acsami.9b13024.

(157) Liu, Y.; Bennett, J. C.; Obrovac, M. N. Ball Milled Si-W Alloys: Part II. Thermal Behavior and Performance in Li Cells. *J. Electrochem. Soc.* **2019**, *166* (13), A2791. https://doi.org/10.1149/2.1571912jes.

(158) Cao, S.; Gracious, S.; Bennett, J. C.; Obrovac, M. N. Synthesis, Lithium Insertion and Thermal Stability of Si–Mo Alloys. *J. Electrochem. Soc.* **2020**, *167* (13), 130531. https://doi.org/10.1149/1945-7111/abba91.

(159) Halim, M.; Kim, J. S.; Choi, J.-G.; Lee, J. K. Electrochemical Characterization of Carbon Coated Bundle-Type Silicon Nanorod for Anode Material in Lithium Ion Secondary Batteries. *Appl. Surf. Sci.* **2015**, *334*, 115–122. https://doi.org/10.1016/j.apsusc.2014.08.085.

(160) Kim, S. J.; Kargar, A.; Wang, D.; Graham, G. W.; Pan, X. Lithiation of Rutile TiO2-Coated Si NWs Observed by in Situ TEM. *Chem. Mater.* **2015**, *27* (20), 6929–6933. https://doi.org/10.1021/acs.chemmater.5b02565.

(161) Shin, J.; Cho, E. Agglomeration Mechanism and a Protective Role of Al2O3 for Prolonged Cycle Life of Si Anode in Lithium-Ion Batteries. *Chem. Mater.* **2018**, *30* (10), 3233–3243. https://doi.org/10.1021/acs.chemmater.8b00145.

(162) Gan, C.; Zhang, C.; Wen, W.; Liu, Y.; Chen, J.; Xie, Q.; Luo, X. Enhancing Delithiation Reversibility of $Li_{15}Si_4$ Alloy of Silicon Nanoparticles-Carbon/Graphite Anode Materials for Stable-Cycling Lithium Ion Batteries by Restricting the Silicon Particle Size. *ACS Appl. Mater. Interfaces* **2019**, *11* (39), 35809–35819. https://doi.org/10.1021/acsami.9b13750.

(163) Woodard, J. C.; Kalisvaart, W. P.; Sayed, S. Y.; Olsen, B. C.; Buriak, J. M. Beyond Thin Films: Clarifying the Impact of c-Li15Si4 Formation in Thin Film, Nanoparticle, and Porous Si Electrodes. *ACS Appl. Mater. Interfaces* **2021**. https://doi.org/10.1021/acsami.1c04293.

(164) Keil, P.; Jossen, A. Charging Protocols for Lithium-Ion Batteries and Their Impact on Cycle Life—An Experimental Study with Different 18650 High-Power Cells. *J. Energy Storage* **2016**, *6*, 125–141. https://doi.org/10.1016/j.est.2016.02.005.

(165) Wetjen, M.; Pritzl, D.; Jung, R.; Solchenbach, S.; Ghadimi, R.; Gasteiger, H. A. Differentiating the Degradation Phenomena in Silicon-Graphite Electrodes for Lithium-Ion Batteries. *J. Electrochem. Soc.* **2017**, *164* (12), A2840–A2852. https://doi.org/10.1149/2.1921712jes.

(166) Jiang, Y.; Offer, G.; Jiang, J.; Marinescu, M.; Wang, H. Voltage Hysteresis Model for Silicon Electrodes for Lithium Ion Batteries, Including Multi-Step Phase Transformations, Crystallization and Amorphization. *J. Electrochem. Soc.* **2020**, *167* (13), 130533. https://doi.org/10.1149/1945-7111/abbbba.

(167) Marinaro, M.; Weinberger, M.; Wohlfahrt-Mehrens, M. Toward Pre-Lithiatied High Areal Capacity Silicon Anodes for Lithium-Ion Batteries. *Electrochimica Acta* **2016**, *206*, 99–107. https://doi.org/10.1016/j.electacta.2016.03.139.

(168) Zheng, T.; Dahn, J. R. The Effect of Turbostratic Disorder on the Staging Transitions in Lithium Intercalated Graphite. *Synth. Met.* **1995**, *73* (1), 1–7. https://doi.org/10.1016/0379-6779(95)03289-4.

(169) Zheng, T.; Reimers, J. N.; Dahn, J. R. Effect of Turbostratic Disorder in Graphitic Carbon Hosts on the Intercalation of Lithium. *Phys. Rev. B* **1995**, *51* (2), 734–741. https://doi.org/10.1103/PhysRevB.51.734.

(170) Jeschull, F.; Surace, Y.; Zürcher, S.; Lari, G.; Spahr, M. E.; Novák, P.; Trabesinger, S. Graphite Particle-Size Induced Morphological and Performance

Changes of Graphite–Silicon Electrodes. *J. Electrochem. Soc.* **2020**, *167* (10), 100535. https://doi.org/10.1149/1945-7111/ab9b9a.

(171) Sun, L.; Liu, Y.; Wu, J.; Shao, R.; Jiang, R.; Tie, Z.; Jin, Z. A Review on Recent Advances for Boosting Initial Coulombic Efficiency of Silicon Anodic Lithium Ion Batteries. *Small* **2022**, *18* (5), 2102894. https://doi.org/10.1002/smll.202102894.

(172) Sun, S.; He, D.; Li, P.; Liu, Y.; Wan, Q.; Tan, Q.; Liu, Z.; An, F.; Gong, G.; Qu, X. Improved Adhesion of Cross-Linked Binder and SiO2-Coating Enhances Structural and Cyclic Stability of Silicon Electrodes for Lithium-Ion Batteries. *J. Power Sources* **2020**, *454*, 227907. https://doi.org/10.1016/j.jpowsour.2020.227907.

(173) Carroll, G. M.; Schulze, M. C.; Martin, T. R.; Pach, G. F.; Coyle, J. E.; Teeter, G.; Neale, N. R. SiO2 Is Wasted Space in Single-Nanometer-Scale Silicon Nanoparticle-Based Composite Anodes for Li-Ion Electrochemical Energy Storage. *ACS Appl. Energy Mater.* **2020**. https://doi.org/10.1021/acsaem.0c01934.

(174) Xun, S.; Song, X.; Wang, L.; Grass, M. E.; Liu, Z.; Battaglia, V. S.; Liu, G. The Effects of Native Oxide Surface Layer on the Electrochemical Performance of Si Nanoparticle-Based Electrodes. *J. Electrochem. Soc.* **2011**, *158* (12), A1260–A1266. https://doi.org/10.1149/2.007112jes.

(175) Liang, C.; Zhou, L.; Zhou, C.; Huang, H.; Liang, S.; Xia, Y.; Gan, Y.; Tao, X.; Zhang, J.; Zhang, W. Submicron Silica as High−capacity Lithium Storage Material with Superior Cycling Performance. *Mater. Res. Bull.* **2017**, *96*, 347–353. https://doi.org/10.1016/j.materresbull.2017.03.072.

(176) Bülter, H.; Sternad, M.; Wilkening, M.; Wittstock, G. Impact of the Native SiO2 Surface Layer on the Electron Transfer at Amorphous Si Electrodes. *ECS Trans.* **2015**, *68* (2), 1. https://doi.org/10.1149/06802.0001ecst.

(177) McDowell, M. T.; Lee, S. W.; Ryu, I.; Wu, H.; Nix, W. D.; Choi, J. W.; Cui, Y. Novel Size and Surface Oxide Effects in Silicon Nanowires as Lithium Battery Anodes. *Nano Lett.* **2011**, *11* (9), 4018–4025. https://doi.org/10.1021/nl202630n.

(178) Xun, S.; Song, X.; Grass, M. E.; Roseguo, D. K.; Liu, Z.; Battaglia, V. S.; Liu, G. Improved Initial Performance of Si Nanoparticles by Surface Oxide Reduction for Lithium-Ion Battery Application. *Electrochem. Solid State Lett.* **2011**, *14* (5), A61. https://doi.org/10.1149/1.3559765.

(179) Knotter, D. M. Etching Mechanism of Vitreous Silicon Dioxide in HF-Based Solutions. *J. Am. Chem. Soc.* **2000**, *122* (18), 4345–4351. https://doi.org/10.1021/ja993803z.

(180) Kang, J. K.; Musgrave, C. B. The Mechanism of HF/H2O Chemical Etching of SiO2. *J. Chem. Phys.* **2002**, *116* (1), 275–280. https://doi.org/10.1063/1.1420729.

(181) Ubara, H.; Imura, T.; Hiraki, A. Formation of Si□H Bonds on the Surface of Microcrystalline Silicon Covered with SiOx by HF Treatment. *Solid State Commun.* **1984**, *50* (7), 673–675. https://doi.org/10.1016/0038-1098(84)90156-X.

(182) Judge, J. S. A Study of the Dissolution of SiO2 in Acidic Fluoride Solutions. *J. Electrochem. Soc.* **1971**, *118* (11), 1772. https://doi.org/10.1149/1.2407835.

(183) Verhaverbeke, S.; Teerlinck, I.; Vinckier, C.; Stevens, G.; Cartuyvels, R.; Heyns, M. M. The Etching Mechanisms of SiO2 in Hydrofluoric Acid. *J. Electrochem. Soc.* **1994**, *141* (10), 2852. https://doi.org/10.1149/1.2059243.

(184) Walsh, R. Bond Dissociation Energy Values in Silicon-Containing Compounds and Some of Their Implications. *Acc. Chem. Res.* **1981**, *14* (8), 246–252. https://doi.org/10.1021/ar00068a004.

(185) Rupich, S. M.; Chabal, Y. J. Chapter 9 - Surface Chemical Composition and Morphology. In *Handbook of Silicon Wafer Cleaning Technology (Third Edition)*; Reinhardt, K. A., Kern, W., Eds.; William Andrew Publishing, 2018; pp 505–577. https://doi.org/10.1016/B978-0-323-51084-4.00009-5.

(186) Dhar, S.; Seitz, O.; Halls, M. D.; Choi, S.; Chabal, Y. J.; Feldman, L. C. Chemical Properties of Oxidized Silicon Carbide Surfaces upon Etching in Hydrofluoric Acid. *J. Am. Chem. Soc.* **2009**, *131* (46), 16808–16813. https://doi.org/10.1021/ja9053465.

(187) Sailor, M. J. *Porous Silicon in Practice: Preparation, Characterization and Applications*; John Wiley & Sons, 2012, pp 176-179

(188) Magasinski, A.; Zdyrko, B.; Kovalenko, I.; Hertzberg, B.; Burtovyy, R.; Huebner, C. F.; Fuller, T. F.; Luzinov, I.; Yushin, G. Toward Efficient Binders for Li-Ion Battery Si-Based Anodes: Polyacrylic Acid. *ACS Appl. Mater. Interfaces* **2010**, *2* (11), 3004–3010. https://doi.org/10.1021/am100871y.

(189) Jeschull, F.; Scott, F.; Trabesinger, S. Interactions of Silicon Nanoparticles with Carboxymethyl Cellulose and Carboxylic Acids in Negative Electrodes of Lithium-Ion Batteries. *J. Power Sources* **2019**, *431*, 63–74. https://doi.org/10.1016/j.jpowsour.2019.05.036.

(190) Lee, M.; Reddi, R. K. R.; Choi, J.; Liu, J.; Huang, X.; Cho, H.; Kim, J.-H. In-Operando AFM Characterization of Mechanical Property Evolution of Si Anode

Binders in Liquid Electrolyte. *ACS Appl. Energy Mater.* **2020**, *3* (2), 1899–1907. https://doi.org/10.1021/acsaem.9b02332.

(191) Chen, Z.; Zhang, H.; Dong, T.; Mu, P.; Rong, X.; Li, Z. Uncovering the Chemistry of Cross-Linked Polymer Binders via Chemical Bonds for Silicon-Based Electrodes. *ACS Appl. Mater. Interfaces* **2020**, *12* (42), 47164–47180. https://doi.org/10.1021/acsami.0c12519.

(192) Yu, B.-C.; Hwa, Y.; Park, C.-M.; Kim, J.-H.; Sohn, H.-J. Effect of Oxide Layer Thickness to Nano–Si Anode for Li-Ion Batteries. *RSC Adv.* **2013**, *3* (24), 9408–9413. https://doi.org/10.1039/C3RA41006D.

(193) Schnabel, M.; Arca, E.; Ha, Y.; Stetson, C.; Teeter, G.; Han, S.-D.; Stradins, P. Enhanced Interfacial Stability of Si Anodes for Li-Ion Batteries via Surface SiO2 Coating. *ACS Appl. Energy Mater.* **2020**, *3* (9), 8842–8849. https://doi.org/10.1021/acsaem.0c01337.

(194) Zhang, L.; Liu, Y.; Key, B.; Trask, S. E.; Yang, Z.; Lu, W. Silicon Nanoparticles: Stability in Aqueous Slurries and the Optimization of the Oxide Layer Thickness for Optimal Electrochemical Performance. *ACS Appl. Mater. Interfaces* **2017**, *9* (38), 32727–32736. https://doi.org/10.1021/acsami.7b09149.

(195) Maddipatla, R.; Loka, C.; Lee, K.-S. Electrochemical Performance of an Ultrathin Surface Oxide-Modulated Nano-Si Anode Confined in a Graphite Matrix for Highly Reversible Lithium-Ion Batteries. *ACS Appl. Mater. Interfaces* **2020**, *12* (49), 54608–54618. https://doi.org/10.1021/acsami.0c14978.

(196) Linford, M. R.; Chidsey, C. E. D. Alkyl Monolayers Covalently Bonded to Silicon Surfaces. *J. Am. Chem. Soc.* **1993**, *115* (26), 12631–12632. https://doi.org/10.1021/ja00079a071.

(197) Linford, M. R.; Fenter, P.; Eisenberger, P. M.; Chidsey, C. E. D. Alkyl Monolayers on Silicon Prepared from 1-Alkenes and Hydrogen-Terminated Silicon. *J. Am. Chem. Soc.* **1995**, *117* (11), 3145–3155. https://doi.org/10.1021/ja00116a019.

(198) Trushin, M.; Vyvenko, O.; Seifert, W.; Jia, G.; Kittler, M. Iron–Oxygen Interaction in Silicon: A Combined XBIC/XRF-EBIC-DLTS Study of Precipitation and Complex Building. *Phys. B Condens. Matter* **2009**, *404* (23), 4645–4648. https://doi.org/10.1016/j.physb.2009.08.132.

(199) Sieval, A. B.; Demirel, A. L.; Nissink, J. W. M.; Linford, M. R.; van der Maas, J. H.; de Jeu, W. H.; Zuilhof, H.; Sudhölter, E. J. R. Highly Stable Si−C Linked Functionalized Monolayers on the Silicon (100) Surface. *Langmuir* **1998**, *14* (7), 1759–1768. https://doi.org/10.1021/la971139z.

(200) Sieval, A. B.; Vleeming, V.; Zuilhof, H.; Sudhölter, E. J. R. An Improved Method for the Preparation of Organic Monolayers of 1-Alkenes on Hydrogen-Terminated Silicon Surfaces. *Langmuir* **1999**, *15* (23), 8288–8291. https://doi.org/10.1021/la9904962.

(201) Ogata, Y.; Niki, H.; Sakka, T.; Iwasaki, M. Oxidation of Porous Silicon under Water Vapor Environment. *J. Electrochem. Soc.* **1995**, *142* (5), 1595–1601. https://doi.org/10.1149/1.2048619.

(202) Mangolini, L.; Thimsen, E.; Kortshagen, U. High-Yield Plasma Synthesis of Luminescent Silicon Nanocrystals. *Nano Lett.* **2005**, *5* (4), 655–659. https://doi.org/10.1021/nl050066y.

(203) Seitzinger, C. L.; Sacci, R. L.; Coyle, J. E.; Apblett, C. A.; Hays, K. A.; Armstrong, R. R.; Rogers, A. M.; Armstrong, B. L.; Bennet, T. H.; Neale, N. R.; Veith, G. M. Intrinsic Chemical Reactivity of Silicon Electrode Materials: Gas Evolution. *Chem. Mater.* **2020**, *32* (7), 3199–3210. https://doi.org/10.1021/acs.chemmater.0c00308.

(204) Wu, S.; Yu, B.; Wu, Z.; Fang, S.; Shi, B.; Yang, J. Effect of Particle Size Distribution on the Electrochemical Performance of Micro-Sized Silicon-Based Negative Materials. *RSC Adv.* **2018**, *8* (16), 8544–8551. https://doi.org/10.1039/C8RA00539G.

(205) Anderson, S. L.; Luber, E. J.; Olsen, B. C.; Buriak, J. M. Substance over Subjectivity: Moving beyond the Histogram. *Chem. Mater.* **2016**, *28* (17), 5973–5975. https://doi.org/10.1021/acs.chemmater.6b03430.

(206) Zuo, X.; Zhu, J.; Müller-Buschbaum, P.; Cheng, Y.-J. Silicon Based Lithium-Ion Battery Anodes: A Chronicle Perspective Review. *Nano Energy* **2017**, *31*, 113–143. https://doi.org/10.1016/j.nanoen.2016.11.013.

(207) Baer, D. R.; Artyushkova, K.; Cohen, H.; Easton, C. D.; Engelhard, M.; Gengenbach, T. R.; Greczynski, G.; Mack, P.; Morgan, D. J.; Roberts, A. XPS Guide: Charge Neutralization and Binding Energy Referencing for Insulating Samples. *J. Vac. Sci. Technol. A* **2020**, *38* (3), 031204. https://doi.org/10.1116/6.0000057.

(208) Monshi, A.; Foroughi, M. R.; Monshi, M. R. Modified Scherrer Equation to Estimate More Accurately Nano-Crystallite Size Using XRD. *World J. Nano Sci. Eng.* **2012**, *2* (3), 154–160. https://doi.org/10.4236/wjnse.2012.23020.

(209) Luo, Z.; Fan, D.; Liu, X.; Mao, H.; Yao, C.; Deng, Z. High Performance Silicon Carbon Composite Anode Materials for Lithium Ion Batteries. *J. Power Sources* **2009**, *189* (1), 16–21. https://doi.org/10.1016/j.jpowsour.2008.12.068.

(210) Yim, C.-H.; M. Courtel, F.; Abu-Lebdeh, Y. A High Capacity Silicon–Graphite Composite as Anode for Lithium-Ion Batteries Using Low Content Amorphous Silicon and Compatible Binders. *J. Mater. Chem. A* **2013**, *1* (28), 8234–8243. https://doi.org/10.1039/C3TA10883J.

(211) *12.8: Infrared Spectra of Some Common Functional Groups*. Chemistry LibreTexts. https://chem.libretexts.org/Bookshelves/Organic_Chemistry/Organic_Chemistry_(McMurry)/12%3A_Structure_Determination_-_Mass_Spectrometry_and_Infrared_Spectroscopy/12.08%3A_Infrared_Spectra_of_Some_Common_Functional_Groups (accessed 2022-08-29).

(212) Huck, L. T.; Buriak, J. M. Silicon-Carbon Bond Formation on Porous Silicon. In *Handbook of Porous Silicon*; Canham, L. T., Ed.; Springer, 2014; pp 683–693.

(213) Zhu, G.; Yang, S.; Wang, Y.; Qu, Q.; Zheng, H. Dimethylacrylamide, a Novel Electrolyte Additive, Can Improve the Electrochemical Performances of Silicon Anodes in Lithium-Ion Batteries. *RSC Adv.* **2018**, *9* (1), 435–443. https://doi.org/10.1039/C8RA07988A.

(214) Liu, S.; Zeng, X.; Liu, D.; Wang, S.; Zhang, L.; Zhao, R.; Kang, F.; Li, B. Understanding the Conductive Carbon Additive on Electrode/Electrolyte Interface Formation in Lithium-Ion Batteries via in Situ Scanning Electrochemical Microscopy. *Front. Chem.* **2020**, *8*, 114. https://doi.org/10.3389/fchem.2020.00114.

(215) Fan, S.; Wang, H.; Qian, J.; Cao, Y.; Yang, H.; Ai, X.; Zhong, F. Covalently Bonded Silicon/Carbon Nanocomposites as Cycle-Stable Anodes for Li-Ion Batteries. *ACS Appl. Mater. Interfaces* **2020**, *12* (14), 16411–16416. https://doi.org/10.1021/acsami.0c00676.

(216) Park, J.; Suh, S.; Jeong, S.; Kim, H.-J. New Approach for the High Electrochemical Performance of Silicon Anode in Lithium-Ion Battery: A Rapid and Large Surface Treatment Using a High-Energy Pulsed Laser. *J. Power Sources* **2021**, *491*, 229573. https://doi.org/10.1016/j.jpowsour.2021.229573.

(217) Yao, D.; Feng, J.; Wang, J.; Deng, Y.; Wang, C. Synthesis of Silicon Anode Binders with Ultra-High Content of Catechol Groups and the Effect of Molecular Weight on Battery Performance. *J. Power Sources* **2020**, *463*, 228188. https://doi.org/10.1016/j.jpowsour.2020.228188.

(218) Chuang, Y.-P.; Lin, Y.-L.; Wang, C.-C.; Hong, J.-L. Dual Cross-Linked Polymer Networks Derived from the Hyperbranched Poly(Ethyleneimine) and Poly(Acrylic Acid) as Efficient Binders for Silicon Anodes in Lithium-Ion Batteries. *ACS Appl. Energy Mater.* **2021**, *4* (2), 1583–1592. https://doi.org/10.1021/acsaem.0c02802.

(219) Stephan, A. K. Standardized Battery Reporting Guidelines. *Joule* **2021**, *5* (1), 1–2. https://doi.org/10.1016/j.joule.2020.12.026.

(220) Li, S.; Liu, Y.-M.; Zhang, Y.-C.; Song, Y.; Wang, G.-K.; Liu, Y.-X.; Wu, Z.-G.; Zhong, B.-H.; Zhong, Y.-J.; Guo, X.-D. A Review of Rational Design and Investigation of Binders Applied in Silicon-Based Anodes for Lithium-Ion Batteries. *J. Power Sources* **2021**, *485*, 229331. https://doi.org/10.1016/j.jpowsour.2020.229331.

(221) Browning, K. L.; Sacci, R. L.; Doucet, M.; Browning, J. F.; Kim, J. R.; Veith, G. M. The Study of the Binder Poly(Acrylic Acid) and Its Role in Concomitant Solid–Electrolyte Interphase Formation on Si Anodes. *ACS Appl. Mater. Interfaces* **2020**, *12* (8), 10018–10030. https://doi.org/10.1021/acsami.9b22382.

(222) Xiong, J.; Dupré, N.; Mazouzi, D.; Guyomard, D.; Roué, L.; Lestriez, B. Influence of the Polyacrylic Acid Binder Neutralization Degree on the Initial Electrochemical Behavior of a Silicon/Graphite Electrode. *ACS Appl. Mater. Interfaces* **2021**, *13* (24), 28304–28323. https://doi.org/10.1021/acsami.1c06683.

(223) Li, C.; Shi, T.; Li, D.; Yoshitake, H.; Wang, H. Effect of Surface Modification on Electrochemical Performance of Nano-Sized Si as an Anode Material for Li-Ion Batteries. *RSC Adv.* **2016**, *6* (41), 34715–34723. https://doi.org/10.1039/C5RA28021D.

(224) Hallmann, S.; Fink, M. J.; Mitchell, B. S. Mechanochemical Synthesis of Functionalized Silicon Nanoparticles with Terminal Chlorine Groups. *J. Mater. Res.* **2011**, *26* (8), 1052–1060. https://doi.org/10.1557/jmr.2011.31.

(225) Xu, Z.; Li, Y.; Zhang, B.; Purkait, T.; Alb, A.; Mitchell, B. S.; Grayson, S. M.; Fink, M. J. Water-Soluble PEGylated Silicon Nanoparticles and Their Assembly into

Swellable Nanoparticle Aggregates. *J. Nanoparticle Res.* **2015**, *17* (1), 56. https://doi.org/10.1007/s11051-015-2869-9.

(226) Shi, W.; Wu, H. B.; Baucom, J.; Li, X.; Ma, S.; Chen, G.; Lu, Y. Covalently Bonded Si–Polymer Nanocomposites Enabled by Mechanochemical Synthesis as Durable Anode Materials. *ACS Appl. Mater. Interfaces* **2020**, *12* (35), 39127–39134. https://doi.org/10.1021/acsami.0c09938.

(227) Yang, L.; Lua, Y.-Y.; Lee, M. V.; Linford, M. R. Chemomechanical Functionalization and Patterning of Silicon. *Acc. Chem. Res.* **2005**, *38* (12), 933–942. https://doi.org/10.1021/ar040242u.

(228) Hallmann, S.; Fink, M. J.; Mitchell, B. S. Wetting Properties of Silicon Films from Alkyl-Passivated Particles Produced by Mechanochemical Synthesis. *J. Colloid Interface Sci.* **2010**, *348* (2), 634–641. https://doi.org/10.1016/j.jcis.2010.05.003.

(229) Heintz, A. S.; Fink, M. J.; Mitchell, B. S. Mechanochemical Synthesis of Blue Luminescent Alkyl/Alkenyl-Passivated Silicon Nanoparticles. *Adv. Mater.* **2007**, *19* (22), 3984–3988. https://doi.org/10.1002/adma.200602752.

(230) Shin, H.; Moon, B. Careful Investigation of the Hydrosilylation of Olefins at Poly(Ethylene Glycol) Chain Ends and Development of a New Silyl Hydride to Avoid Side Reactions. *J. Polym. Sci. Part Polym. Chem.* **2018**, *56* (5), 527–536. https://doi.org/10.1002/pola.28924.

(231) Hu, M.; Liu, F.; Buriak, J. M. Expanding the Repertoire of Molecular Linkages to Silicon: Si–S, Si–Se, and Si–Te Bonds. *ACS Appl. Mater. Interfaces* **2016**, *8* (17), 11091–11099. https://doi.org/10.1021/acsami.6b00784.

(232) Choi, N.-S.; Yew, K. H.; Lee, K. Y.; Sung, M.; Kim, H.; Kim, S.-S. Effect of Fluoroethylene Carbonate Additive on Interfacial Properties of Silicon Thin-Film Electrode. *J. Power Sources* **2006**, *161* (2), 1254–1259. https://doi.org/10.1016/j.jpowsour.2006.05.049.

(233) Song, S.-W.; Baek, S.-W. Silane-Derived SEI Stabilization on Thin-Film Electrodes of Nanocrystalline Si for Lithium Batteries. *Electrochem. Solid State Lett.* **2008**, *12* (2), A23. https://doi.org/10.1149/1.3028216.

(234) Nguyen, C. C.; Seo, D. M.; Chandrasiri, K. W. D. K.; Lucht, B. L. Improved Cycling Performance of a Si Nanoparticle Anode Utilizing Citric Acid as a Surface-Modifying Agent. *Langmuir* **2017**, *33* (37), 9254–9261. https://doi.org/10.1021/acs.langmuir.6b04310.

(235) Hu, Z.; Zhao, L.; Jiang, T.; Liu, J.; Rashid, A.; Sun, P.; Wang, G.; Yan, C.; Zhang, L. Trifluoropropylene Carbonate-Driven Interface Regulation Enabling Greatly Enhanced Lithium Storage Durability of Silicon-Based Anodes. *Adv. Funct. Mater.* **2019**, *29* (45), 1906548. https://doi.org/10.1002/adfm.201906548.

(236) Wei, C.; Obrovac, M. N. Small Molecule Slurry Additives for Si Alloy Coatings with CMC/SBR Binder. *J. Electrochem. Soc.* **2019**, *166* (14), A3217. https://doi.org/10.1149/2.0311914jes.

(237) Park, S.; Jeong, S. Y.; Lee, T. K.; Park, M. W.; Lim, H. Y.; Sung, J.; Cho, J.; Kwak, S. K.; Hong, S. Y.; Choi, N.-S. Replacing Conventional Battery Electrolyte Additives with Dioxolone Derivatives for High-Energy-Density Lithium-Ion Batteries. *Nat. Commun.* **2021**, *12* (1), 838. https://doi.org/10.1038/s41467-021-21106-6.

(238) Nölle, R.; Schmiegel, J.-P.; Winter, M.; Placke, T. Tailoring Electrolyte Additives with Synergistic Functional Moieties for Silicon Negative Electrode-Based Lithium Ion Batteries: A Case Study on Lactic Acid O-Carboxyanhydride. *Chem. Mater.* **2020**, *32* (1), 173–185. https://doi.org/10.1021/acs.chemmater.9b03173.

(239) Robins, E. G.; Stewart, M. P.; Buriak, J. M. Anodic and Cathodic Electrografting of Alkynes on Porous Silicon. *Chem. Commun.* **1999**, No. 24, 2479–2480. https://doi.org/10.1039/A906726D.

(240) Nguyen, C. C.; Lucht, B. L. Comparative Study of Fluoroethylene Carbonate and Vinylene Carbonate for Silicon Anodes in Lithium Ion Batteries. *J. Electrochem. Soc.* **2014**, *161* (12), A1933. https://doi.org/10.1149/2.0731412jes.

(241) Zeng, G.; An, Y.; Xiong, S.; Feng, J. Nonflammable Fluorinated Carbonate Electrolyte with High Salt-to-Solvent Ratios Enables Stable Silicon-Based Anode for Next-Generation Lithium-Ion Batteries. *ACS Appl. Mater. Interfaces* **2019**, *11* (26), 23229–23235. https://doi.org/10.1021/acsami.9b05570.

(242) Nölle, R.; Achazi, A. J.; Kaghazchi, P.; Winter, M.; Placke, T. Pentafluorophenyl Isocyanate as an Effective Electrolyte Additive for Improved Performance of Silicon-Based Lithium-Ion Full Cells. *ACS Appl. Mater. Interfaces* **2018**, *10* (33), 28187–28198. https://doi.org/10.1021/acsami.8b07683.

(243) Veith, G. M.; Doucet, M.; Sacci, R. L.; Vacaliuc, B.; Baldwin, J. K.; Browning, J. F. Determination of the Solid Electrolyte Interphase Structure Grown on a Silicon Electrode Using a Fluoroethylene Carbonate Additive. *Sci. Rep.* **2017**, *7* (1), 1–15. https://doi.org/10.1038/s41598-017-06555-8.

(244) Schulze, M. C.; Neale, N. R. Half-Cell Cumulative Efficiency Forecasts Full-Cell Capacity Retention in Lithium-Ion Batteries. *ACS Energy Lett.* **2021**, 1082–1086. https://doi.org/10.1021/acsenergylett.1c00173.

(245) He, X.; Bresser, D.; Passerini, S.; Baakes, F.; Krewer, U.; Lopez, J.; Mallia, C. T.; Shao-Horn, Y.; Cekic-Laskovic, I.; Wiemers-Meyer, S.; Soto, F. A.; Ponce, V.; Seminario, J. M.; Balbuena, P. B.; Jia, H.; Xu, W.; Xu, Y.; Wang, C.; Horstmann, B.; Amine, R.; Su, C.-C.; Shi, J.; Amine, K.; Winter, M.; Latz, A.; Kostecki, R. The Passivity of Lithium Electrodes in Liquid Electrolytes for Secondary Batteries. *Nat. Rev. Mater.* **2021**, *6* (11), 1036–1052. https://doi.org/10.1038/s41578-021-00345-5.

(246) Zhao, R.; Wang, S.; Liu, D.; Liu, Y.; Lv, X.; Zeng, X.; Li, B. Effect of Fluoroethylene Carbonate on Solid Electrolyte Interphase Formation of the SiO/C Anode Observed by In Situ Atomic Force Microscopy. *ACS Appl. Energy Mater.* **2021**, *4* (1), 492–499. https://doi.org/10.1021/acsaem.0c02399.

(247) Haridas, A. K.; Nguyen, Q. A.; Terlier, T.; Blaser, R.; Biswal, S. L. Investigating the Compatibility of TTMSP and FEC Electrolyte Additives for LiNi0.5Mn0.3Co0.2O2 (NMC)–Silicon Lithium-Ion Batteries. *ACS Appl. Mater. Interfaces* **2021**, *13* (2), 2662–2673. https://doi.org/10.1021/acsami.0c19347.

(248) Wang, C.; Wu, H.; Chen, Z.; McDowell, M. T.; Cui, Y.; Bao, Z. Self-Healing Chemistry Enables the Stable Operation of Silicon Microparticle Anodes for High-Energy Lithium-Ion Batteries. *Nat. Chem.* **2013**, *5* (12), 1042–1048. https://doi.org/10.1038/nchem.1802.

(249) Choi, S.; Kwon, T.; Coskun, A.; Choi, J. W. Highly Elastic Binders Integrating Polyrotaxanes for Silicon Microparticle Anodes in Lithium Ion Batteries. *Science* **2017**, *357* (6348), 279–283. https://doi.org/10.1126/science.aal4373.

(250) Chen, J.; Fan, X.; Li, Q.; Yang, H.; Khoshi, M. R.; Xu, Y.; Hwang, S.; Chen, L.; Ji, X.; Yang, C.; He, H.; Wang, C.; Garfunkel, E.; Su, D.; Borodin, O.; Wang, C. Electrolyte Design for LiF-Rich Solid–Electrolyte Interfaces to Enable High-Performance Microsized Alloy Anodes for Batteries. *Nat. Energy* **2020**, 1–12. https://doi.org/10.1038/s41560-020-0601-1.

(251) Song, J. H.; Sailor, M. J. *Reaction of Photoluminescent Porous Silicon Surfaces with Lithium Reagents To Form Silicon−Carbon Bound Surface Species*. ACS Publications. https://doi.org/10.1021/ic980303i.

(252) Bateman, J. E.; Eagling, R. D.; Horrocks, B. R.; Houlton, A.; Worrall, D. R. Rôle for Organic Molecules in the Oxidation of Porous Silicon. *Chem. Commun.* **1997**, No. 23, 2275–2276. https://doi.org/10.1039/A707107H.

(253) Sailor, M. J. Chemical Reactivity and Surface Chemistry of Porous Silicon. In *Handbook of Porous Silicon*; Canham, L., Ed.; Springer International Publishing: Cham, 2017; pp 1–20. https://doi.org/10.1007/978-3-319-04508-5_37-2.

(254) Wang, D.; Buriak, J. M. Electrochemically Driven Organic Monolayer Formation on Silicon Surfaces Using Alkylammonium and Alkylphosphonium Reagents. *Surf. Sci.* **2005**, *590* (2), 154–161. https://doi.org/10.1016/j.susc.2005.06.018.

(255) Saffer, A.; Davis, T. W. Reaction of Methylene Chloride and Other Halide Vapors with Sodium. *J. Am. Chem. Soc.* **1945**, *67* (4), 641–645. https://doi.org/10.1021/ja01220a039.

(256) Sax, N. I.; Sax, N. I.; Feiner, B. *Dangerous Properties of Industrial Materials*, 6th ed.; Van Nostrand Reinhold, 1984.

(257) Gurtner, C.; Wun, A. W.; Sailor, M. J. Surface Modification of Porous Silicon by Electrochemical Reduction of Organo Halides. *Angew. Chem. Int. Ed.* **1999**, *38* (13–14), 1966–1968. https://doi.org/10.1002/(SICI)1521-3773(19990712)38:13/14<1966::AID-ANIE1966>3.0.CO;2-5.

(258) Kim, J. S.; Byun, D.; Lee, J. K. Electrochemical Characteristics of Amorphous Silicon Thin Film Electrode with Fluoroethylene Carbonate Additive. *Curr. Appl. Phys.* **2014**, *14* (4), 596–602. https://doi.org/10.1016/j.cap.2014.02.008.

(259) Zuo, X.; Wu, J.; Zhao, M.; Wang, C.; Liu, J.; Nan, J. Vinyl Ethylene Carbonate as an Electrolyte Additive for High-Voltage LiNi0.4Mn0.4Co0.2O2/Graphite Li-Ion Batteries. *Ionics* **2016**, *22* (2), 201–208. https://doi.org/10.1007/s11581-015-1536-6.

(260) Ryu, Y.-G.; Lee, S.; Mah, S.; Lee, D. J.; Kwon, K.; Hwang, S.; Doo, S. Electrochemical Behaviors of Silicon Electrode in Lithium Salt Solution Containing Alkoxy Silane Additives. *J. Electrochem. Soc.* **2008**, *155* (8), A583. https://doi.org/10.1149/1.2940310.

(261) Choi, H.; Nguyen, C. C.; Song, S.-W. Control of Surface Chemistry and Electrochemical Performance of Carbon-Coated Silicon Anode Using Silane-Based Self-Assembly for Rechargeable Lithium Batteries. *Bull. Korean Chem. Soc.* **2010**, *31* (9), 2519–2526. https://doi.org/10.5012/bkcs.2010.31.9.2519.

(262) Aupperle, F.; von Aspern, N.; Berghus, D.; Weber, F.; Eshetu, G. G.; Winter, M.; Figgemeier, E. The Role of Electrolyte Additives on the Interfacial Chemistry and

Thermal Reactivity of Si-Anode-Based Li-Ion Battery. *ACS Appl. Energy Mater.* **2019**, *2* (9), 6513–6527. https://doi.org/10.1021/acsaem.9b01094.

(263) Xu, Z.; Yang, J.; Qian, J.; Zhang, T.; Nuli, Y.; Chen, R.; Wang, J. Bicomponent Electrolyte Additive Excelling Fluoroethylene Carbonate for High Performance Si-Based Anodes and Lithiated Si-S Batteries. *Energy Storage Mater.* **2019**, *20*, 388–394. https://doi.org/10.1016/j.ensm.2018.11.001.

(264) Borodin, O.; Self, J.; Persson, K. A.; Wang, C.; Xu, K. Uncharted Waters: Super-Concentrated Electrolytes. *Joule* **2020**, *4* (1), 69–100. https://doi.org/10.1016/j.joule.2019.12.007.

(265) Arano, K.; Begic, S.; Chen, F.; Rakov, D.; Mazouzi, D.; Gautier, N.; Kerr, R.; Lestriez, B.; Le Bideau, J.; Howlett, P. C.; Guyomard, D.; Forsyth, M.; Dupre, N. Tuning the Formation and Structure of the Silicon Electrode/Ionic Liquid Electrolyte Interphase in Superconcentrated Ionic Liquids. *ACS Appl. Mater. Interfaces* **2021**, *13* (24), 28281–28294. https://doi.org/10.1021/acsami.1c06465.

(266) Nayak, P. K.; Yang, L.; Brehm, W.; Adelhelm, P. From Lithium-Ion to Sodium-Ion Batteries: Advantages, Challenges, and Surprises. *Angew. Chem. Int. Ed.* **2018**, *57* (1), 102–120. https://doi.org/10.1002/anie.201703772.

(267) Betz, J.; Bieker, G.; Meister, P.; Placke, T.; Winter, M.; Schmuch, R. Theoretical versus Practical Energy: A Plea for More Transparency in the Energy Calculation of Different Rechargeable Battery Systems. *Adv. Energy Mater.* **2019**, *9* (6), 1803170. https://doi.org/10.1002/aenm.201803170.

(268) Liang, S.; Cheng, Y.-J.; Zhu, J.; Xia, Y.; Müller-Buschbaum, P. A Chronicle Review of Nonsilicon (Sn, Sb, Ge)-Based Lithium/Sodium-Ion Battery Alloying

Anodes. *Small Methods* **2020**, *4* (8), 2000218. https://doi.org/10.1002/smtd.202000218.

(269) Azam, M. A.; Safie, N. E.; Ahmad, A. S.; Yuza, N. A.; Zulkifli, N. S. A. Recent Advances of Silicon, Carbon Composites and Tin Oxide as New Anode Materials for Lithium-Ion Battery: A Comprehensive Review. *J. Energy Storage* **2021**, *33*, 102096. https://doi.org/10.1016/j.est.2020.102096.

(270) K. Vesborg, P. C.; F. Jaramillo, T. Addressing the Terawatt Challenge: Scalability in the Supply of Chemical Elements for Renewable Energy. *RSC Adv.* **2012**, *2* (21), 7933–7947. https://doi.org/10.1039/C2RA20839C.

(271) Zhang, R.; Upreti, S.; Whittingham, M. S. Tin-Iron Based Nano-Materials as Anodes for Li-Ion Batteries. *J. Electrochem. Soc.* **2011**, *158* (12), A1498. https://doi.org/10.1149/2.108112jes.

(272) Qin, J.; Liu, D.; Zhang, X.; Zhao, N.; Shi, C.; Liu, E.-Z.; He, F.; Ma, L.; Li, Q.; Li, J.; He, C. One-Step Synthesis of SnCo Nanoconfined in Hierarchical Carbon Nanostructures for Lithium Ion Battery Anode. *Nanoscale* **2017**, *9* (41), 15856–15864. https://doi.org/10.1039/C7NR04786J.

(273) Tian, M.; Wang, W.; Lee, S.-H.; Lee, Y.-C.; Yang, R. Enhancing Ni–Sn Nanowire Lithium-Ion Anode Performance by Tailoring Active/Inactive Material Interfaces. *J. Power Sources* **2011**, *196* (23), 10207–10212. https://doi.org/10.1016/j.jpowsour.2011.08.062.

(274) Todd, A. D. W.; Ferguson, P. P.; Fleischauer, M. D.; Dahn, J. R. Tin-Based Materials as Negative Electrodes for Li-Ion Batteries: Combinatorial Approaches

and Mechanical Methods. *Int. J. Energy Res.* **2010**, *34* (6), 535–555. https://doi.org/10.1002/er.1669.

(275) Lee, K. T.; Jung, Y. S.; Oh, S. M. Synthesis of Tin-Encapsulated Spherical Hollow Carbon for Anode Material in Lithium Secondary Batteries. *J. Am. Chem. Soc.* **2003**, *125* (19), 5652–5653. https://doi.org/10.1021/ja0345524.

(276) Shirzadi, A. A.; Kozieł, T.; Cios, G.; Bała, P. Development of Auto Ejection Melt Spinning (AEMS) and Its Application in Fabrication of Cobalt-Based Ribbons. *J. Mater. Process. Technol.* **2019**, *264*, 377–381. https://doi.org/10.1016/j.jmatprotec.2018.09.028.

(277) Edison, E.; Sreejith, S.; Madhavi, S. Melt-Spun Fe–Sb Intermetallic Alloy Anode for Performance Enhanced Sodium-Ion Batteries. *ACS Appl. Mater. Interfaces* **2017**, *9* (45), 39399–39406. https://doi.org/10.1021/acsami.7b13096.

(278) Wang, C.; Xiufang Bian; Yinghui Yang; Chao Yuan; Junzhang Wang; Mengchun Yu; Rongzhang Guan; Dujiang Lu. Composite of Tin and Silicon with Nanostructure as High Performance Lithium-Ion Battery Anode. *Int J Electrochem Sci* **2020**, *15*, 3054–3067.

(279) Zhang, R.; Wang, Z.; Ma, W.; Yu, W.; Lu, S.; Liu, X. Improved Sodium-Ion Storage Properties by Fabricating Nanoporous CuSn Alloy Architecture. *RSC Adv.* **2017**, *7* (47), 29458–29463. https://doi.org/10.1039/C7RA03718J.

(280) Sun, Z. B.; Wang, X. D.; Li, X. P.; Zhao, M. S.; Li, Y.; Zhu, Y. M.; Song, X. P. Electrochemical Properties of Melt-Spun Al–Si–Mn Alloy Anodes for Lithium-Ion Batteries. *J. Power Sources* **2008**, *182* (1), 353–358. https://doi.org/10.1016/j.jpowsour.2008.03.053.

(281) Harris, P. J. F. New Perspectives on the Structure of Graphitic Carbons. *Crit. Rev. Solid State Mater. Sci.* **2005**, *30* (4), 235–253. https://doi.org/10.1080/10408430500406265.

(282) Wang, G. X.; Ahn, J.-H.; Lindsay, M. J.; Sun, L.; Bradhurst, D. H.; Dou, S. X.; Liu, H. K. Graphite–Tin Composites as Anode Materials for Lithium-Ion Batteries. *J. Power Sources* **2001**, *97–98*, 211–215. https://doi.org/10.1016/S0378-7753(01)00619-X.

(283) Chang, C.-C.; Liu, S.-J.; Wu, J.-J.; Yang, C.-H. Nano-Tin Oxide/Tin Particles on a Graphite Surface as an Anode Material for Lithium-Ion Batteries. *J. Phys. Chem. C* **2007**, *111* (44), 16423–16427. https://doi.org/10.1021/jp073379l.

(284) Nobili, F.; Mancini, M.; Stallworth, P. E.; Croce, F.; Greenbaum, S. G.; Marassi, R. Tin-Coated Graphite Electrodes as Composite Anodes for Li-Ion Batteries. Effects of Tin Coatings Thickness toward Intercalation Behavior. *J. Power Sources* **2012**, *198*, 243–250. https://doi.org/10.1016/j.jpowsour.2011.09.075.

(285) Ding, J.; Zhou, H.; Zhang, H.; Stephenson, T.; Li, Z.; Karpuzov, D.; Mitlin, D. Exceptional Energy and New Insight with a Sodium–Selenium Battery Based on a Carbon Nanosheet Cathode and a Pseudographite Anode. *Energy Environ. Sci.* **2017**, *10* (1), 153–165. https://doi.org/10.1039/C6EE02274J.

(286) Chao, S.-C.; Song, Y.-F.; Wang, C.-C.; Sheu, H.-S.; Wu, H.-C.; Wu, N.-L. Study on Microstructural Deformation of Working Sn and SnSb Anode Particles for Li-Ion Batteries by in Situ Transmission X-Ray Microscopy. *J. Phys. Chem. C* **2011**, *115* (44), 22040–22047. https://doi.org/10.1021/jp206829q.

(287) Asenbauer, J.; Eisenmann, T.; Kuenzel, M.; Kazzazi, A.; Chen, Z.; Bresser, D. The Success Story of Graphite as a Lithium-Ion Anode Material – Fundamentals, Remaining Challenges, and Recent Developments Including Silicon (Oxide) Composites. *Sustain. Energy Fuels* **2020**. https://doi.org/10.1039/D0SE00175A.

(288) Li, Y.; Lu, Y.; Adelhelm, P.; Titirici, M.-M.; Hu, Y.-S. Intercalation Chemistry of Graphite: Alkali Metal Ions and Beyond. *Chem. Soc. Rev.* **2019**, *48* (17), 4655–4687. https://doi.org/10.1039/C9CS00162J.

(289) Li, Y.; Wu, F.; Li, Y.; Liu, M.; Feng, X.; Bai, Y.; Wu, C. Ether-Based Electrolytes for Sodium Ion Batteries. *Chem. Soc. Rev.* **2022**. https://doi.org/10.1039/D1CS00948F.

(290) Song, M.; Wang, C.; Du, D.; Li, F.; Chen, J. A High-Energy-Density Sodium-Ion Full Battery Based on Tin Anode. *Sci. China Chem.* **2019**, *62* (5), 616–621. https://doi.org/10.1007/s11426-018-9422-y.

(291) Xu, Y.; Zhu, Y.; Liu, Y.; Wang, C. Electrochemical Performance of Porous Carbon/Tin Composite Anodes for Sodium-Ion and Lithium-Ion Batteries. *Adv. Energy Mater.* **2013**, *3* (1), 128–133. https://doi.org/10.1002/aenm.201200346.

(292) De Sutter, L.; Berckmans, G.; Marinaro, M.; Wohlfahrt-Mehrens, M.; Berecibar, M.; Van Mierlo, J. Mechanical Behavior of Silicon-Graphite Pouch Cells under External Compressive Load: Implications and Opportunities for Battery Pack Design. *J. Power Sources* **2020**, *451*, 227774. https://doi.org/10.1016/j.jpowsour.2020.227774.

(293) Moyassari, E.; Roth, T.; Kücher, S.; Chang, C.-C.; Hou, S.-C.; Spingler, F. B.; Jossen, A. The Role of Silicon in Silicon-Graphite Composite Electrodes

Regarding Specific Capacity, Cycle Stability, and Expansion. *J. Electrochem. Soc.* **2022**, *169* (1), 010504. https://doi.org/10.1149/1945-7111/ac4545.

(294) Wang, K.; Joshi, Y.; Chen, H.; Schmitz, G. In-Situ Analysis of Solid-Electrolyte Interphase Formation and Cycle Behavior of Sn Battery Anodes. *J. Power Sources* **2022**, *535*, 231439. https://doi.org/10.1016/j.jpowsour.2022.231439.

(295) Wang, P.; Hu, J.; Cao, G.; Zhang, S.; Zhang, P.; Liang, C.; Wang, Z.; Shao, G. Suppression on Allotropic Transformation of Sn Planar Anode with Enhanced Electrochemical Performance. *Appl. Surf. Sci.* **2018**, *435*, 1150–1158. https://doi.org/10.1016/j.apsusc.2017.11.079.

(296) Nobili, F.; Mancini, M.; Dsoke, S.; Tossici, R.; Marassi, R. Low-Temperature Behavior of Graphite–Tin Composite Anodes for Li-Ion Batteries. *J. Power Sources* **2010**, *195* (20), 7090–7097. https://doi.org/10.1016/j.jpowsour.2010.05.001.

(297) Li, M.-Q.; Qu, M.-Z.; He, X.-Y.; Yu, Z.-L. Electrochemical Performance of Si/Graphite/Carbon Composite Electrode in Mixed Electrolytes Containing LiBOB and LiPF6. *J. Electrochem. Soc.* **2009**, *156* (4), A294. https://doi.org/10.1149/1.3076196.

(298) Sopicka-Lizer, M. *High-Energy Ball Milling: Mechanochemical Processing of Nanopowders*; Elsevier, 2010.

(299) Dong, H.; Fu, X.; Wang, J.; Wang, P.; Ding, H.; Song, R.; Wang, S.; Li, R.; Li, S. In-Situ Construction of Porous Si@C Composites with LiCl Template to Provide Silicon Anode Expansion Buffer. *Carbon* **2021**, *173*, 687–695. https://doi.org/10.1016/j.carbon.2020.11.042.

(300) Wu, H.; Zheng, L.; Du, N.; Sun, B.; Ma, J.; Jiang, Y.; Gong, J.; Chen, H.; Wang, L. Constructing Densely Compacted Graphite/Si/SiO2 Ternary Composite Anodes for High-Performance Li-Ion Batteries. *ACS Appl. Mater. Interfaces* **2021**, *13* (19), 22323–22331. https://doi.org/10.1021/acsami.1c01877.

(301) Sharma, S. S.; Manthiram, A. Towards More Environmentally and Socially Responsible Batteries. *Energy Environ. Sci.* **2020**, *13* (11), 4087–4097. https://doi.org/10.1039/D0EE02511A.

(302) Tsai, W.-T. Environmental Hazards and Health Risk of Common Liquid Perfluoro-n-Alkanes, Potent Greenhouse Gases. *Environ. Int.* **2009**, *35* (2), 418–424. https://doi.org/10.1016/j.envint.2008.08.009.

(303) Katz, M. H. Multivariable Analysis: A Primer for Readers of Medical Research. *Ann. Intern. Med.* **2003**, *138* (8), 644–650. https://doi.org/10.7326/0003-4819-138-8-200304150-00012.

(304) Tetrault, J. M.; Sauler, M.; Wells, C. K.; Concato, J. Reporting of Multivariable Methods in the Medical Literature. *J. Investig. Med.* **2008**, *56* (7), 954–957. https://doi.org/10.2310/JIM.0b013e31818914ff.

(305) Ramprasad, R.; Batra, R.; Pilania, G.; Mannodi-Kanakkithodi, A.; Kim, C. Machine Learning in Materials Informatics: Recent Applications and Prospects. *Npj Comput. Mater.* **2017**, *3* (1), 54. https://doi.org/10.1038/s41524-017-0056-5.

(306) Xue, D.; Balachandran, P. V.; Hogden, J.; Theiler, J.; Xue, D.; Lookman, T. Accelerated Search for Materials with Targeted Properties by Adaptive Design. *Nat. Commun.* **2016**, *7*, 11241. https://doi.org/10.1038/ncomms11241.

(307) Maier, W. F.; Stöwe, K.; Sieg, S. Combinatorial and High-Throughput Materials Science. *Angew. Chem. Int. Ed.* **2007**, *46* (32), 6016–6067. https://doi.org/10.1002/anie.200603675.

(308) Oliynyk, A. O.; Mar, A. Discovery of Intermetallic Compounds from Traditional to Machine-Learning Approaches. *Acc. Chem. Res.* **2018**, *51* (1), 59–68. https://doi.org/10.1021/acs.accounts.7b00490.

(309) Boukherroub, R.; Wayner, D. D. M.; Lockwood, D. J.; Canham, L. T. Passivated Luminescent Porous Silicon. *J. Electrochem. Soc.* **2001**, *148* (9), H91. https://doi.org/10.1149/1.1385850.

(310) Cao, B.; Adutwum, L. A.; Oliynyk, A. O.; Luber, E. J.; Olsen, B. C.; Mar, A.; Buriak, J. M. How To Optimize Materials and Devices *via* Design of Experiments and Machine Learning: Demonstration Using Organic Photovoltaics. *ACS Nano* **2018**, *12* (8), 7434–7444. https://doi.org/10.1021/acsnano.8b04726.

(311) Sun, W.; Zheng, Y.; Yang, K.; Zhang, Q.; Shah, A. A.; Wu, Z.; Sun, Y.; Feng, L.; Chen, D.; Xiao, Z.; Lu, S.; Li, Y.; Sun, K. Machine Learning–Assisted Molecular Design and Efficiency Prediction for High-Performance Organic Photovoltaic Materials. *Sci. Adv.* **2019**, *5* (11), eaay4275. https://doi.org/10.1126/sciadv.aay4275.

(312) MacLeod, B. P.; Parlane, F. G. L.; Morrissey, T. D.; Häse, F.; Roch, L. M.; Dettelbach, K. E.; Moreira, R.; Yunker, L. P. E.; Rooney, M. B.; Deeth, J. R.; Lai, V.; Ng, G. J.; Situ, H.; Zhang, R. H.; Elliott, M. S.; Haley, T. H.; Dvorak, D. J.; Aspuru-Guzik, A.; Hein, J. E.; Berlinguette, C. P. Self-Driving Laboratory for

Accelerated Discovery of Thin-Film Materials. *Sci. Adv.* **2020**, *6* (20). https://doi.org/10.1126/sciadv.aaz8867.

(313) Kirkey, A.; Luber, E. J.; Cao, B.; Olsen, B. C.; Buriak, J. M. Optimization of the Bulk Heterojunction of All-Small-Molecule Organic Photovoltaics Using Design of Experiment and Machine Learning Approaches. *ACS Appl. Mater. Interfaces* **2020**, *12* (49), 54596–54607. https://doi.org/10.1021/acsami.0c14922.

(314) Ward, L.; Dunn, A.; Faghaninia, A.; Zimmermann, N. E. R.; Bajaj, S.; Wang, Q.; Montoya, J.; Chen, J.; Bystrom, K.; Dylla, M.; Chard, K.; Asta, M.; Persson, K. A.; Snyder, G. J.; Foster, I.; Jain, A. Matminer: An Open Source Toolkit for Materials Data Mining. *Comput. Mater. Sci.* **2018**, *152*, 60–69. https://doi.org/10.1016/j.commatsci.2018.05.018.

(315) Pedregosa, F.; Varoquaux, G.; Gramfort, A.; Michel, V.; Thirion, B.; Grisel, O.; Blondel, M.; Prettenhofer, P.; Weiss, R.; Dubourg, V.; Vanderplas, J.; Passos, A.; Cournapeau, D.; Brucher, M.; Perrot, M.; Duchesnay, É. Scikit-Learn: Machine Learning in Python. *J Mach Learn Res* **2011**, *12*, 2825–2830.

(316) Leardi, R. Experimental Design in Chemistry: A Tutorial. *Anal. Chim. Acta* **2009**, *652* (1), 161–172. https://doi.org/10.1016/j.aca.2009.06.015.